

Connecting simulations, functionals and machine learning to describe correlations and forces in equilibrium and nonequilibrium fluids

Von der Universität Bayreuth
zur Erlangung des Grades eines
Doktors der Naturwissenschaften (Dr. rer. nat.)
genehmigte Abhandlung

von

Florian Sammüller

aus Tirschenreuth

1. Gutachter: Prof. Matthias Schmidt
2. Gutachter: Prof. Robert Evans
3. Gutachterin: Prof. Marjolein Dijkstra

Tag der Einreichung: 22.02.2024

Tag des Kolloquiums: 22.05.2024

Zusammenfassung

In dieser Arbeit werden verschiedene Techniken zur Beschreibung der Physik von inhomogenen Flüssigkeiten im Gleichgewicht und Nichtgleichgewicht untersucht. Insbesondere werden hierbei Korrelationen und Kräfte betrachtet, die sich durch die nicht-trivialen Wechselwirkungen in klassischen Vielteilchensystemen ergeben. Die Teilchenmodelle in den untersuchten Systemen reichen von simplen Paar-Wechselwirkungen wie beispielsweise in Hart-Kugel- und Lennard-Jones-Fluiden bis hin zu komplexen Interaktionstypen, die unter anderem zur Charakterisierung von Wasser und kolloidalen Gelen verwendet werden. Methodisch werden drei Herangehensweisen näher betrachtet und verknüpft: Computersimulationen von Vielteilchensystemen, funktionale Theorien und maschinelles Lernen.

Im Rahmen der Vielteilchensimulationen wird eine effiziente numerische Methode für überdämpfte Brownsche Dynamik (BD) entwickelt und verwendet. Bei BD wird angenommen, dass sich Teilchen in einem implizit modellierten Lösungsmittel befinden, welches dissipative und stochastische Kräfte ausübt und dabei die Trägheit der Teilchen unterdrückt. Obwohl dieses dynamische Modell häufig theoretische Ansätze erleichtert, erweist sich die Anwendung robuster numerischer Methoden auf die resultierenden Langevin-Bewegungsgleichungen als äußerst schwierig. Adaptive BD wird hier als neue Simulationsmethode und als Alternative zu herkömmlichen Integrationsalgorithmen mit festem Zeitschritt dargestellt. Durch die automatische Anpassung der Zeitschrittlänge kann mit adaptiver BD der numerische Fehler in der Zeitentwicklung der Trajektorien kontrolliert und beschränkt werden. Dadurch erhält man ein auch in anspruchsvollen Situationen numerisch stabiles sowie effizientes und genaues Verfahren, welches die erforderliche Statistik der Zufallskräfte erhält. Neben anderen bekannten Methoden wie Monte Carlo wird adaptive BD in dieser Arbeit als Grundpfeiler für Vielteilchensimulationen verwendet.

Während solche computergestützten Experimente viel Einsicht in konkrete Systeme erlauben, ist auch eine theoretische Beschreibung der beobachteten Phänomene erstrebenswert, welche ohne eine explizite Vielteilchenmodellierung auskommt. Im Gleichgewicht ist durch die klassische Dichtefunktionaltheorie (DFT) ein formal exaktes funktionales Minimierungsprinzip etabliert, in welchem das Dichteprofil als zentraler Ordnungsparameter agiert. Powerfunktionaltheorie (PFT) kann als entsprechendes Analogon im Nichtgleichgewicht herangezogen werden, wobei die funktionalen Abbildungen eine zusätzliche Abhängigkeit vom Stromprofil aufweisen. Insbesondere erlaubt PFT eine klare Trennung von Gleichgewichts- und Nichtgleichgewichtsbeiträgen im internen Kraftprofil, welche jeweils als adiabatische und superadiabatische Kräfte bezeichnet werden. In dieser Arbeit wird PFT genutzt, um superadiabatische Kräfte in relevan-

ten Nichtgleichgewichtsumgebungen zu untersuchen, wobei speziell ein inhomogen geschertes kolloidales Gel sowie der Kompressionsfluss einer Lennard-Jones-Flüssigkeit betrachtet werden.

Die Anwendung des Noether-Theorems auf thermische Vielteilchensysteme verschafft weitere nützliche Erkenntnisse. Summenregeln, welche Mittelwerte verschiedener Observablen miteinander verknüpfen und in der statistischen Mechanik analog zu Erhaltungssätzen sind, können durch das Ausnutzen von fundamentalen Invarianzen des Phasenraums gewonnen werden. Dies ist unter anderem zur Herleitung einer kraftbasierten DFT nützlich, welche hier anhand von numerischen Daten untersucht wird. Das Noether-Konzept erlaubt auch Einsichten in die Struktur von homogenen Flüssigkeiten, wobei mittels Summenregeln zweiter Ordnung neue Arten von radialen Verteilungsfunktionen in den Fokus rücken. Diese bisher unbekanntes Größen werden in Computersimulationen gemessen, um deren erwartete Zusammenhänge für eine Vielzahl verschiedener Modellflüssigkeiten zu verifizieren und zu interpretieren. Außerdem wird gezeigt, dass durch eine Generalisierung der Noether-Invarianz auf beliebige Phasenraumfunktionen eine Hierarchie von Hyperkraft-Summenregeln resultiert, welche relevant für kraftbasierte Samplingtechniken und Konsistenzchecks in Simulationen ist.

Neben den numerischen und funktionalen Methoden kann maschinelles Lernen als weiteres hilfreiches Mittel zur Beschreibung der statistischen Mechanik von inhomogenen Fluiden herangezogen werden. Hierzu werden Verfahren des überwachten maschinellen Lernens entwickelt, mittels derer neuronale Netzwerke zur Repräsentation von lokalen funktionalen Zusammenhängen genutzt werden können. Im dynamischen Fall beschreibt das neuronale Funktional die durch PFT vorgegebene kinematische Abbildung von Dichte- und Stromprofil zur lokalen internen Kraft. Solch ein neuronales Funktional wird hier mit Simulationsdaten aus adaptiver BD trainiert, um stationäre Zustände einer getriebenen Lennard-Jones-Flüssigkeit genau vorherzusagen und zu konzipieren, wodurch systematische Unzulänglichkeiten von dynamischer DFT bewältigt werden. Im Gleichgewicht wird das neuronale Funktional genutzt, um gemäß DFT die Abbildung vom Dichteprofil zur direkten Korrelationsfunktion zu repräsentieren. Das neuronale Korrelationsfunktional erweist sich dabei als vielseitiges Werkzeug zur Untersuchung struktureller und thermodynamischer Eigenschaften von Gleichgewichtsflüssigkeiten. Insbesondere stellt die Implementierung einer neuronalen Funktionalrechenmethode ein zentrales Konzept dar, welches am Beispiel der Hart-Kugel-Flüssigkeit detailliert erläutert wird. Außerdem ermöglicht die Methode eine neuronale DFT zur selbstkonsistenten Berechnung von Dichteprofilen, welche nahezu Simulationsgenauigkeit liefert und effizient auf Multiskalenprobleme anwendbar ist.

Abstract

In this thesis, different techniques for the description of inhomogeneous fluids in and out of equilibrium are investigated. We focus in particular on a thorough account of correlations and forces, which arise nontrivially from interparticle interactions in classical many-body systems. The constituent particles in the considered systems range from models with simple pair interactions such as the hard sphere and Lennard-Jones fluid to more complex interaction types as used in studies of water and of colloidal gels. Our methodology is threefold, as we base the investigations on many-body computer simulations, on functional theories and on machine learning techniques.

Regarding the computational approach, we develop and utilize an efficient numerical method for overdamped Brownian dynamics (BD) simulations. In BD, particles are assumed to be suspended in an implicit solvent, which gives rise to both dissipative and stochastic forces and which suppresses the inertia of the particles. This type of dynamical description commonly poses conceptual advantages for theoretical developments, but the application of robust numerical methods to the resulting Langevin equations of motion turns out to be challenging. We remedy this situation by presenting adaptive BD as a more powerful alternative to common fixed-timestep integration algorithms. By automatic adjustment of the timestep length, adaptive BD facilitates to control and bound the propagation of numerical errors on the trajectory level. This yields a performant and accurate integration scheme that is numerically stable even in demanding scenarios, thereby addressing the problem of preserving the correct statistics of the random forces. Throughout this work, adaptive BD is used among other standard techniques such as Monte Carlo as a staple of many-body simulation methods.

While such *in silico* experiments contribute much to the understanding of specific systems, we also aim for a theoretical description of the observed phenomena which does not necessitate to invoke the many-body picture explicitly. In equilibrium, classical density functional theory (DFT) establishes a formally exact functional minimization principle in which the one-body density profile acts as the central order parameter. Power functional theory (PFT) can be viewed as the analogous framework in nonequilibrium, where the functional relations possess additional dependence on the one-body current. Specifically, PFT allows for a systematic splitting of the resulting internal force profile into an adiabatic and superadiabatic part, where the latter constitutes the genuine nonequilibrium contribution. We use PFT in this work to account for the occurring superadiabatic forces in relevant nonequilibrium environments and investigate in particular both an inhomogeneously sheared colloidal gel former and compressional flows of the Lennard-Jones fluid.

Noether's theorem provides further useful insight when applied to thermal many-

body systems. By exploiting fundamental invariance properties of phase space under continuous transformations, one gains access to corresponding sum rules, which connect averages of different observables and which serve as the statistical mechanical equivalent of conservation laws. This proves to be useful for the development of a force-based DFT, which we investigate by comparison to numerical data. The Noether framework is valuable also in bulk liquids, where second-order invariance generates sum rules for novel kinds of radial correlation functions. Via computer simulations we measure and subsequently interpret the resulting quantities and verify their expected interrelation for a broad range of diverse model fluids. Additionally, the generalization of Noether invariance to arbitrary phase space functions yields hierarchies of hyperforce sum rules, which are shown to be practically relevant for force-sampling techniques and consistency checks in many-body simulations.

With the numerical and functional techniques at hand, machine learning is incorporated as a further efficacious means for describing the statistical mechanics of inhomogeneous fluids. To this end, we develop and utilize supervised training procedures which yield neural networks that act as representations of local functional relationships. For the dynamical case, the resulting neural functional is constructed to capture the kinematic map from the density and current profile to the local internal force as prescribed by PFT. We show that such a neural functional can be trained based on adaptive BD simulations in order to accurately predict and design the steady state of a driven Lennard-Jones fluid, thereby overcoming systematic deficiencies of dynamical DFT. In equilibrium, the neural network is devised to represent the DFT map from the density profile to the one-body direct correlation functional. This neural correlation functional turns out to be a versatile tool for the investigation of structural and thermodynamic properties of fluid equilibria via the successful implementation of a neural functional calculus, which we exemplify in detail for the hard sphere fluid. The framework further realizes a neural DFT for the self-consistent determination of density profiles, which retains near-simulation accuracy and which serves as an efficient method for multiscale predictions.

Contents

1	Introduction	1
1.1	Survey of relevant soft matter physics and outline of this work	1
1.2	Particle models	5
1.3	Statistical mechanics	8
2	Many-body simulation methods	10
2.1	Monte Carlo	10
2.2	Fundamentals of Brownian dynamics and prerequisites for adaptivity . .	11
2.3	Adaptive Brownian dynamics: an overview	14
3	Functional techniques and thermal Noether invariance	18
3.1	Density functional theory	18
3.2	Power functional theory	21
3.3	Sum rules from applications of Noether’s theorem	24
4	Machine learning and neural functionals	28
4.1	Neural networks and supervised machine learning procedures	28
4.2	Application in equilibrium and nonequilibrium	31
4.3	Neural functional theory	33
5	Conclusions and outlook	36
	Bibliography	40
6	Publications	52
6.1	List of publications	52
6.2	Author’s contributions	53
6.3	“Adaptive Brownian dynamics”	56
6.4	“Inhomogeneous steady shear dynamics of a three-body colloidal gel former”	71
6.5	“Comparative study of force-based classical density functional theory” .	85
6.6	“Noether-constrained correlations in equilibrium liquids”	95
6.7	“Hyperforce balance via thermal Noether invariance of any observable” .	105
6.8	“Perspective: How to overcome dynamical density functional theory” . .	117
6.9	“Neural functional theory for inhomogeneous fluids: Fundamentals and applications”	148
6.10	“Why neural functionals suit statistical mechanics”	169

A Efficient evaluation of the Stillinger-Weber potential	192
B Measuring force-force and force-gradient correlations	194
C Neural functional theory for inhomogeneous fluids – Tutorial	196
Eidesstattliche Versicherung	219

1 Introduction

1.1 Survey of relevant soft matter physics and outline of this work

Soft matter systems, as they form the inspiration for the present research [1–12], are ubiquitous both in nature and in technological applications. They display a broad range of highly relevant phenomena, with many of them remaining to be fully understood yet [13]. The oftentimes intricate behavior can be traced back to the coupled motion of the constituent particles, which is caused and influenced primarily by their mutual interactions. Conceptually, it is this coupling of the microscopic degrees of freedom that needs to be tackled in order to describe such systems and to predict their resulting properties quantitatively. Common theoretical techniques are naturally rooted in statistical mechanics, where progress in the last few decades has been driven besides pen and paper derivations also by the rapidly increasing availability of computational resources and by a wealth of novel simulation methods. Not least, recent advances in machine learning have added to this evolution, thereby complementing conventional analytic and numerical approaches.

Simple fluids [14] arguably form the basis of soft matter. They are modeled as collections of particles which interact via rather rudimentary and usually isotropic pair potentials. Despite the apparent simplicity, their collective behavior turns out to be highly nontrivial though. In particular, certain prototypical model systems may account surprisingly well for many properties of real fluids, such as for the occurrence of phase transitions and coexistence as well as for interfacial and surface phenomena [15, 16]. The liquid phase thereby constitutes a noteworthy and rather peculiar state of matter [17, 18], as it is disordered while still possessing a high degree of correlation on a microscopic level. These features separate liquids clearly from solids, where particles are arranged in a lattice, and from a low-density gas, where interparticle interactions are scarce and correlations often become negligible. The properties of liquids have ramifications in bulk and also in spatially inhomogeneous external environments, as occur e.g. in the vicinity of substrates or via confinement in narrow pores. When subjected to such conditions, the fluid becomes spatially inhomogeneous as well, and its resulting state is influenced largely by the mediation of interparticle correlations.

There is a wide array of soft matter systems that go beyond these simple models and which are hence often referred to as complex fluids [19, 20]. Pertinent examples include mixtures, liquid crystals, polymer melts, glasses, gels and various forms of active matter [21]. In this regard, the special role of colloids must be emphasized,

as they are commonly employed to realize both simple and beyond-simple fluids in experiments as well as to carry out fundamental theoretical work. Contrary to atomic and molecular fluids, colloidal suspensions consist of mesoscopic particles on the nano- or microscale which are dispersed in a solvent. From an experimental point of view, the colloidal size often allows to make direct observations of their motion and interaction, e.g. via atomic force [22], scanning electron [23] and in situ confocal microscopy [24–26], thus complementing typical light, x-ray or neutron scattering techniques [27–29]. A further practical advantage is the possibility of manufacturing colloidal particles with precisely tailored interactions between them [30–33]. This facilitates both the synthesis of increasingly complex particle types [34–36] and the accurate comparison of experimental data to theoretical and simulation results for corresponding model Hamiltonians. Besides their use for research purposes, complex fluids and in particular colloidal systems are abundant in everyday life, where they occur both naturally in living matter [37] as well as in common household items [38, 39]. Essentially, the possibility to adjust macroscopic properties of a substance via the careful fabrication of its constituent particles gives colloids their prominent role in industrial and consumer products [40–42]. This link between the microscopic and macroscopic behavior of soft matter is hence deservedly a focal point of theoretical and computational physics. Here, one is interested particularly in finding generic methods to describe and predict this interrelation. Due to the many-body nature of the problems at hand, this is by no means trivial, and different coarse-graining techniques have to be invoked to reduce the behavior of individual particles to more manageable and insightful statistical quantities.

Many-body computer simulations have fared very well for the coarse-graining task, with methods that were conceptualized some 70 years ago still being in prominent use today [43]. Over the last decades, a variety of numerical algorithms have been established [44], and their development has been accompanied and aided by the tremendous progress of computational resources. Large-scale investigations are not out of reach today [45], but in general the resource demand of particle-based simulations is still a prime concern. Therefore, advanced algorithms are desired which aim to make specific parts of a simulation program more efficient, such as the evaluation of interparticle interactions or the evolution of the system state. How particles evolve during a simulation run depends on the applied scheme. Broadly speaking, one can distinguish between two categories:¹ Monte Carlo methods are based on an entirely statistical exploration of the high-dimensional phase space, while molecular dynamics algorithms approximate the physical trajectories of particles by numerically solving their equations of motion. Whereas Monte Carlo usually implies equilibrium conditions, relying on a physical time evolution of particle trajectories is typically also applicable in nonequilibrium scenarios [47]. In the category of trajectory-based methods, a special type of dynamics is founded on the observable Brownian motion [48] of particles on the mesoscale, as we focus on in this work. Brownian dynamics (BD) [14, 44] is particularly relevant for colloids, as it assumes the motion of a particle to be driven besides colloidal interactions also by

¹There are also hybrid schemes which thrive on a combination of techniques [46].

collisions with much smaller solvent particles. However, the motion of the latter is not considered explicitly. Instead, only the statistical effects of random collision events are modeled, which simplifies the microscopic description. Several schemes for BD simulations exist, but they are commonly restricted by certain limitations, which can be traced back to the difficulty of treating the underlying stochastic differential equation numerically. We discuss these conventional methods [49–52] below and present adaptive Brownian dynamics [1] as an improved algorithm, which we apply throughout this work in various simulations of simple and complex fluids in and out of equilibrium.

On the theoretical side, functional methods have proven to be useful to get to grips with the coupled many-body problem. Classical density functional theory (DFT) [53] provides a modern and formally exact framework for describing the thermodynamic equilibrium of a system which may be spatially inhomogeneous. Central to the approach is a minimization principle of a thermodynamic potential that is expressed as a functional of the one-body density profile. The contribution due to internal correlations constitutes the nontrivial part of this functional, for which, depending on the type of considered fluid, a suitable (approximate) representation has to be found. For nonequilibrium systems, power functional theory (PFT) [54, 55] is the analogous framework and it establishes the existence of a functional map from the one-body density and current profiles to the internal force profile. In particular, one can uniquely identify superadiabatic forces, which are genuine out-of-equilibrium contributions that are commonly assumed to be negligible in approximate descriptions such as dynamical density functional theory (DDFT). This so-called adiabatic approximation is uncontrolled though. We explore in this work systems which show highly relevant superadiabatic phenomena such as viscous response under shear [2] and develop power functional theories to account for these effects.

In connection to the functional point of view, symmetries and invariances of general thermal many-body systems can be exploited via Noether’s theorem with the aim of gaining relations that characterize statistical mechanical correlation functions [56–59]. These sum rules, which provide exact constraints for averages of different phase space functions, are a fundamental theoretical tool and prove to be useful also in practical applications. Specifically, we derive novel types of force-gradient and force-force correlation functions, which can be measured in bulk equilibrium fluids for different types of particle interactions [4]. Furthermore, we illustrate a generic framework to obtain hierarchies of Noether sum rules for arbitrary observables and give examples for their use in computer simulations of inhomogeneous fluids [5]. The investigation of Noether identities also allows for a reformulation of DFT which operates on the level of forces and which we here gauge against conventional DFT by comparison to simulation data [3].

As a means to connect the advantages of the presented theoretical approaches with computational methods, we lastly turn to the application of machine learning for an in-depth quantitative description of many-body systems in and out of equilibrium. For this, we develop generic procedures for constructing and using neural functionals, which are neural networks that are trained with suitable simulation data to represent func-

tional maps as given either via DFT in equilibrium or via PFT in nonequilibrium. For the dynamical case, we exemplify the neural functional framework for the steady uniaxial flow of a Lennard-Jones fluid [6], where we find our method to overcome inherent limitations of DDFT. In equilibrium, we revisit the well-studied hard sphere fluid in order to evaluate the capabilities of functional machine learning via benchmarks to analytic and simulation results [7]. A neural correlation functional is acquired in a supervised training routine, which facilitates to investigate the full structure and thermodynamics of homogeneous and heterogeneous fluid states. The use of the neural functional in a self-consistent scheme for the calculation of density profiles outperforms all common analytic approximations and the method directly applies to multiscale problems. Additionally, the neural functional provides highly accurate and computationally cheap access to fundamental quantities that are difficult to obtain by other means, such as the free energy and the hierarchy of direct correlation functions. Our machine learning framework therefore exceeds the mere interpolation of training data and it can be considered to form the basis of a standalone neural functional theory. We further elucidate the different techniques used within this approach by an instructive application to the one-dimensional hard rod system [8], where the exact solution due to Percus [60] provides clear-cut reference.

In the following, we give an overview of the structure of this thesis and of the related publications [1–8]. We use many-body simulations, functional theories and machine learning for the investigation of soft matter and explore in particular means to interrelate the different methodologies as illustrated in Fig. 1. Fundamentals of general many-body simulations are presented in Chapter 2 and we give an outline of adaptive BD as described in detail in Ref. [1]. Adaptive BD is used throughout this work and proves to be useful for equilibrium and nonequilibrium simulations. The method is applied specifically to examine an inhomogeneously sheared colloidal gel former, which exhibits superadiabatic forces that we describe and characterize in Ref. [2]. We turn to functional theories in Chapter 3 and present the core ideas of DFT and PFT as well as the derivation of sum rules which arise as a consequence of thermal Noether invariance. In this regard, a quantitative comparison of a recent reformulation of DFT in terms of forces (“force-DFT” [61]) is performed in Ref. [3]. Gaining access to sum rules of pair correlation functions from the application of second-order Noether invariance is described in Ref. [4], where we verify and interpret the arising two-body identities for various model fluids in bulk. A generalization of the Noether framework to arbitrary phase space functions results in hyperforce balance equations, which form a broad class of both known and novel sum rules as laid out in Ref. [5]. In Chapter 4, we complement and unify the computational and functional treatments via the development of generic machine learning routines for training neural networks with simulation data in order to obtain representations of functional relationships on the one-body level. The application of this concept to inhomogeneous nonequilibrium flow, where PFT prescribes the functional kinematic map, is exemplified for uniaxially driven Lennard-Jones systems in Ref. [6]. For thermal equilibrium, Ref. [7] gives an in-depth account on the capabilities of the neural functional framework, where the focus is put on a quantitative compar-

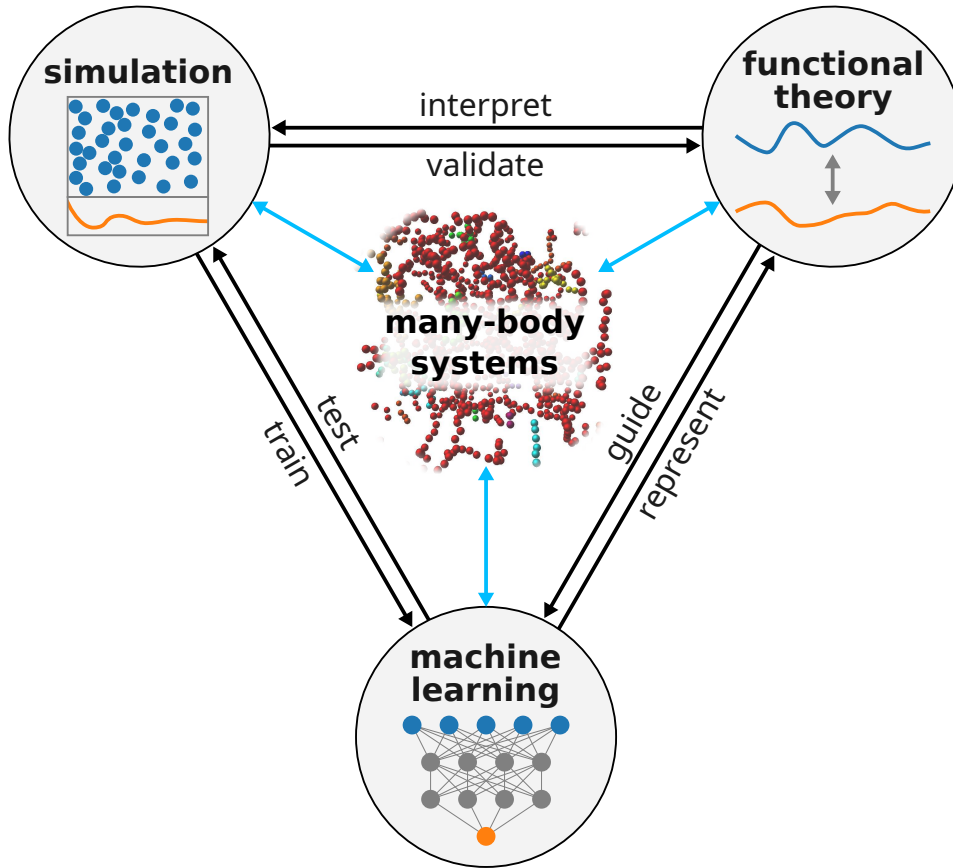


Figure 1: Overview of the different approaches for the description of classical many-body systems in and out of equilibrium which are set forth and interrelated in this work.

ison to state-of-the-art analytic treatments, predominantly regarding the well-studied hard sphere fluid. Ref. [8] serves as a pedagogical and instructive topical review of the underlying aspects of the neural functional theory including the pertinent simulation methods, functional principles and machine learning techniques.

1.2 Particle models

As illustrated in the previous section, the physics of thermal many-body systems is determined primarily by the type of interparticle interaction. In the following, we present different particle models that are used throughout this work and in the related publications [1–8]. For each model, we specify its microscopic behavior in terms of the interaction potential. A brief overview of possible use cases in theory and in simulation

is provided and we illustrate some of the arising physical properties. The considered interaction types range from simple reference systems to representations of complex fluids.

Hard spheres

The hard sphere model is arguably the simplest reference system for the realization of short-range repulsion. It is characterized by the pairwise interparticle potential

$$\phi_{\text{HS}}(r) = \begin{cases} \infty & r < \sigma, \\ 0 & r \geq \sigma, \end{cases} \quad (1.1)$$

where r denotes the distance of two particles with diameter σ . The purely geometric nature of Eq. (1.1) makes the hard sphere system particularly amenable to theoretical techniques, see Sec. 3.1 for its treatment in DFT and note that the hard rod fluid in one spatial dimension is tractable to the degree of exact results [8, 60]. However, due to its nonanalytic character, the hard sphere model is not suitable for the straightforward application of force-based simulation schemes. Besides resorting to energy-based methods such as Monte Carlo (see Sec. 2.1), event-driven algorithms enable the determination of trajectories by the explicit numerical evaluation of particle collisions [3, 62, 63].

Hard-core repulsion is a common idealized feature of many colloids [33, 64] as well as a reasonable approximation of the short-ranged repulsive part of molecular or atomic interactions [14, 65]. The hard sphere fluid shows no liquid-gas phase transition, but despite the lack of attractive interaction, a face centered cubic crystal forms for sufficiently large density. Hard-sphere freezing, albeit having been highly debated [66] until its experimental confirmation [30], has been observed already in very early simulation work [67] and it is sometimes referred to as the Kirkwood-Alder transition [68]. Fluid states of this model, both of spatially homogeneous and heterogeneous nature, are here revisited in the context of novel DFT [3, 61] and machine learning techniques [7, 8], see also Secs. 3.3 and 4.2 for brief descriptions.

Lennard-Jones fluid

The Lennard-Jones (LJ) interaction potential is given by

$$\phi_{\text{LJ}}(r) = 4\epsilon \left[\left(\frac{\sigma}{r} \right)^{12} - \left(\frac{\sigma}{r} \right)^6 \right], \quad (1.2)$$

where ϵ sets the energy scale and σ determines the particle size. The LJ potential is commonly used for the description of simple atomic fluids such as noble gases, as it is constructed to capture both the attractive interaction due to van der Waals forces as well as the repulsion at small separation distance.

In many-body computer simulations, it is common practice to truncate and to possibly shift the LJ potential in order to reduce the number of interactions that need to

be evaluated. For truncation, one sets $\phi_{\text{LJT}}(r) = \phi_{\text{LJ}}(r)$ for $r \leq r_c$ and $\phi_{\text{LJT}}(r) = 0$ for $r > r_c$, where a typical choice of the cutoff radius is $r_c = 2.5\sigma$. Unless noted otherwise, we apply this truncation in the considered LJ systems. Further shifting of the potential according to $\phi_{\text{LJTS}}(r) = \phi_{\text{LJ}}(r) - \phi_{\text{LJ}}(r_c)$ for $r \leq r_c$ while retaining $\phi_{\text{LJTS}}(r) = 0$ for $r > r_c$ prevents a discontinuity at $r = r_c$. One should keep in mind that the thermodynamic properties of the LJ fluid change significantly when the pair potential (1.2) is truncated and possibly shifted, which is particularly relevant for the interpretation of results from different simulation methods [69]. Below a critical point, which depends on the value of r_c and on the applied shifting, the LJ fluid exhibits a liquid-gas phase transition.

The Weeks-Chandler-Andersen (WCA) potential [70] is recovered as a special case of the LJ potential via $\phi_{\text{WCA}}(r) = \phi_{\text{LJTS}}(r)$ if the cutoff radius is chosen to be located at the minimum of the potential well of Eq. (1.2), $r_c = \sqrt[6]{2}\sigma$. The WCA potential hence only consists of a repulsive contribution and it can be used as a qualitatively similar alternative to hard-core repulsion. Force-based simulations [1, 4–6] are feasible for the truncated and shifted LJ potential and hence also for the WCA fluid.

Stillinger-Weber potential

The Stillinger-Weber (SW) potential is representative of more complex fluids. Originally conceived for computer simulations of silicon [71], the potential has since been adapted to also account for the behavior of water [72, 73] and of colloidal gels [74, 75]. Its pairwise contribution

$$\phi_{\text{SW},2}(r) = A\epsilon \left[B \left(\frac{\sigma}{r} \right)^p - \left(\frac{\sigma}{r} \right)^q \right] \exp \left(\frac{\sigma}{r - a\sigma} \right) \quad (1.3)$$

is a generalized variant of the LJ potential with additional parameters A , B , p , q and a . Besides the two-body term (1.3), the SW potential possesses a three-body contribution

$$\phi_{\text{SW},3}(r, r', \theta) = \lambda\epsilon (\cos \theta - \cos \theta_0)^2 \exp \left(\frac{\gamma\sigma}{r - a\sigma} \right) \exp \left(\frac{\gamma\sigma}{r' - a\sigma} \right) \quad (1.4)$$

with parameters γ , λ and θ_0 , where r and r' denote the distances of two particles to a central particle and θ is the intermediate angle of the particle triplet. The parameter λ sets the strength of the three-body contribution and θ_0 tunes the preferred three-body angle, i.e. the angular configuration of minimum energy.

Both Eqs. (1.3) and (1.4) vanish continuously at pairwise distances of $a\sigma$ beyond which they are set to zero. The SW potential can thus profit from common optimizations in many-body simulations which reduce the number of evaluations of short-ranged particle interactions [44]. Note, however, that for the three-body part (1.4), the interactions can be moderated in a range of $2a\sigma$ by an intermediate central particle. Due to the specific multiplicative nature of the SW potential, an alternative representation can be derived, which avoids the direct evaluation of the three-body term (1.4) in a

triple sum when calculating the total internal energy and particle forces. Details of this optimized evaluation scheme are given in Appendix A and in Ref. [75].

Both in the original publication of Stillinger and Weber [71] as well as for the monatomic water model by Molinero and Moore [72], the preferred three-body angle has been set to $\theta_0 = \arccos(-1/3) \approx 109.47^\circ$ in order to account for the tetrahedral nature of the underlying atomic or molecular interactions. In other works [74, 75], different choices of θ_0 have been considered. In particular, for significantly decreased cardinality of the particles, as obtained e.g. by setting $\theta_0 = 180^\circ$, the SW potential was found to be a suitable representation of a colloidal gel former. We investigate the structure [2, 4] of the monatomic water model and of the colloidal gel with simulations [1], cf. Sec. 2.3, and with theoretical tools that are summarized in Secs. 3.2 and 3.3.

Further particle models

Apart from the three models that were laid out above, we also consider further fluid types in supporting roles, where we focus primarily on studying novel types of pair correlation functions, see Ref. [4]. We give a brief overview of the considered models in the following.

Treating long-range interactions in many-body systems is a pertinent problem in theoretical and simulation work [44, 76]. While we do not deal explicitly with Coulombic repulsion, we consider the Yukawa potential [77] as a model which incorporates screened electrostatic interactions between charged particles. Orientational degrees of freedom become relevant when dipolar interactions are taken into account. In this regard, we study the soft-sphere dipolar and the Stockmayer fluid [78, 79], which both consist of a repulsive core and a dipolar interaction term (the Stockmayer fluid includes additional Lennard-Jones-like isotropic attraction). Besides dipolar interactions giving rise to non-trivial orientational configurations, we also consider the uniaxial Gay-Berne interaction potential [80], which models a class of elongated or oblate anisotropic particles. The focus is thereby put on accounting for the pair correlations that arise in isotropic and nematic phases of the Gay-Berne fluid.

1.3 Statistical mechanics

We complete the microscopic picture and introduce notation by laying out the statistical mechanics of classical many-body systems [14] in the following. In general, the standard Hamiltonian

$$H(\mathbf{r}^N, \mathbf{p}^N) = \sum_{i=1}^N \frac{\mathbf{p}_i^2}{2m_i} + U(\mathbf{r}^N) \quad (1.5)$$

is considered, where N is the number of particles with positions $\mathbf{r}^N \equiv (\mathbf{r}_1, \mathbf{r}_2, \dots, \mathbf{r}_N)$ and momenta $\mathbf{p}^N \equiv (\mathbf{p}_1, \mathbf{p}_2, \dots, \mathbf{p}_N)$, and m_i is the mass of particle i . The potential energy $U(\mathbf{r}^N) = u(\mathbf{r}^N) + \sum_{i=1}^N V_{\text{ext}}(\mathbf{r}_i)$ consists of the interparticle energy $u(\mathbf{r}^N)$ and

of a contribution due to an external potential $V_{\text{ext}}(\mathbf{r})$ which depends on position \mathbf{r} . Specifically, for pairwise interactions,

$$u(\mathbf{r}^N) = \sum_{i=1}^N \sum_{j>i}^N \phi(r_{ij}) \quad (1.6)$$

with the pair potential $\phi(r)$ and $\mathbf{r}_{ij} = \mathbf{r}_j - \mathbf{r}_i$ such that $r_{ij} = |\mathbf{r}_{ij}|$ is the distance of particles i and j . For particle types with additional three-body interactions, such as for the SW potential,

$$u(\mathbf{r}^N) = \sum_{i=1}^N \sum_{j>i}^N \phi_2(r_{ij}) + \sum_{i=1}^N \sum_{j \neq i}^N \sum_{k>j}^N \phi_3(r_{ij}, r_{ik}, \theta_{ijk}), \quad (1.7)$$

where $\phi_2(r)$ is the pairwise contribution, e.g. Eq. (1.3), $\phi_3(r, r', \theta)$ is the three-body interaction term, e.g. Eq. (1.4), and θ_{ijk} is the intermediate angle of \mathbf{r}_{ij} and \mathbf{r}_{ik} .

For thermal equilibrium in the grand ensemble, the chemical potential μ , the absolute temperature T and the volume V of the three-dimensional system are fixed. The phase space distribution function then assumes the Boltzmann form

$$\Psi_{\text{eq}} = \frac{1}{\Xi} e^{-\beta(H-\mu N)} \quad (1.8)$$

with inverse temperature $\beta = 1/(k_B T)$ and Boltzmann constant k_B . The grand partition sum $\Xi = \text{Tr} e^{-\beta(H-\mu N)}$ normalizes the phase space distribution function and the grand canonical trace over phase space is defined as

$$\text{Tr} \cdot = \sum_{N=0}^{\infty} \frac{1}{N! h^{3N}} \int d\mathbf{r}^N \int d\mathbf{p}^N \cdot, \quad (1.9)$$

where h denotes the Planck constant. Averages of a phase space function $\hat{A} = \hat{A}(\mathbf{r}^N, \mathbf{p}^N)$ can then be evaluated via $\langle \hat{A} \rangle \equiv \text{Tr} \Psi_{\text{eq}} \hat{A}$. A prime example is the one-body density profile $\rho(\mathbf{r}) = \langle \hat{\rho}(\mathbf{r}) \rangle$, which follows from an average of the density operator $\hat{\rho}(\mathbf{r}) = \sum_{i=1}^N \delta(\mathbf{r} - \mathbf{r}_i)$, where $\delta(\cdot)$ denotes the Dirac distribution.

If the canonical ensemble is considered, the particle number N rather than the chemical potential μ is kept fixed. In this case, the phase space distribution function is given by $\Psi_{\text{eq},N} = e^{-\beta H}/Z_N$ with the canonical trace $\text{Tr}_N \cdot = (N! h^{3N})^{-1} \int d\mathbf{r}^N \int d\mathbf{p}^N \cdot$ and the canonical partition sum $Z_N = \text{Tr}_N e^{-\beta H}$. The evaluation of averages remains identical upon replacing the trace and distribution function with their canonical forms. Note that in both ensembles, the momentum integrals can be performed analytically for Hamiltonians of the form (1.5) if the considered observable $\hat{A} = \hat{A}(\mathbf{r}^N)$ does not depend on momenta. If all particles have identical mass m , this yields the inverse of the thermal wavelength $\Lambda = h/\sqrt{2\pi m k_B T}$ for each inertial degree of freedom.

2 Many-body simulation methods

2.1 Monte Carlo

In equilibrium, Monte Carlo methods are an efficient tool for the simulation of many-body systems in order to obtain averages of relevant observables [3–5, 7, 8]. The fundamental Monte Carlo concept is the stochastic evaluation of the phase space integrals laid out in Sec. 1.3. We point to Ref. [44] for a detailed and pedagogical account of these methods and summarize in the following the most pertinent aspects.

The objective of standard Monte Carlo schemes is the generation of microstates according to their known Boltzmann weights in order to sample the thermal equilibrium of a considered system. For this, the condition of detailed balance is usually imposed as a sufficient prerequisite for the reproduction of the given distribution of states. One thereby demands that the transition from a state A (e.g. a particle configuration \mathbf{r}^N) into a new state B is exactly as probable as the reverse transition $B \rightarrow A$, hence keeping the equilibrium distribution intact. Therefore,

$$P(A)\Pi(A \rightarrow B) = P(B)\Pi(B \rightarrow A), \quad (2.1)$$

where P denotes the probability of a given state and Π is the “transition matrix” [81, 82]. In practice, $\Pi(A \rightarrow B) = \alpha(A \rightarrow B)\text{acc}(A \rightarrow B)$, where α is the probability of a *trial* move and acc is the probability of actually accepting a new state B given the previous state A . For simplification, one usually chooses α to be symmetric¹ such that Eq. (2.1) becomes $P(A)\text{acc}(A \rightarrow B) = P(B)\text{acc}(B \rightarrow A)$. A natural choice due to Metropolis et al. [43] for an acceptance probability that fulfills this relation is

$$\text{acc}(A \rightarrow B) = \min\left(1, \frac{P(B)}{P(A)}\right). \quad (2.2)$$

From here, concrete expressions can be derived for a given ensemble by identifying P with the relevant equilibrium distribution of states. In the canonical ensemble, a state is specified by the particle configuration \mathbf{r}^N , and one arrives at

$$\text{acc}(\mathbf{r}^N \rightarrow \tilde{\mathbf{r}}^N) = \min\left(1, e^{-\beta(U(\tilde{\mathbf{r}}^N) - U(\mathbf{r}^N))}\right) \quad (2.3)$$

for the acceptance probability of moving the particles² from \mathbf{r}^N to new positions $\tilde{\mathbf{r}}^N$.

¹There is much freedom in constructing useful biased Monte Carlo schemes where α is not symmetric, see e.g. Chapter 12 in Ref. [44].

²The displacement of individual particles usually occurs sequentially in so-called *sweeps*.

In the grand canonical ensemble, transitions not only include particle displacements, but also the exchange of particles with a (virtual) reservoir. Therefore, in addition to the acceptance ratio (2.3) of changing particle positions, random particle insertions and removals are performed as specified by the rules

$$\text{acc}(\mathbf{r}^N \rightarrow \mathbf{r}^{N+1}) = \min \left(1, \frac{V}{\Lambda^3(N+1)} e^{\beta(\mu - U(\mathbf{r}^{N+1}) + U(\mathbf{r}^N))} \right), \quad (2.4)$$

$$\text{acc}(\mathbf{r}^N \rightarrow \mathbf{r}^{N-1}) = \min \left(1, \frac{\Lambda^3 N}{V} e^{-\beta(\mu + U(\mathbf{r}^{N-1}) - U(\mathbf{r}^N))} \right), \quad (2.5)$$

where Λ is the thermal wavelength.³ The new states with one inserted and one removed particle are denoted by \mathbf{r}^{N+1} and \mathbf{r}^{N-1} , respectively.

2.2 Fundamentals of Brownian dynamics and prerequisites for adaptivity

The Monte Carlo methods presented in Sec. 2.1 are useful for but also limited to the investigation of statistical equilibrium quantities. If one wishes to explore dynamical processes on the trajectory level, which are interesting already in equilibrium [4, 83, 84] and become particularly relevant for nonequilibrium phenomena [1, 2, 6], further simulation methods are required.

Langevin dynamics [47, 85] provides one such approach which is suitable specifically for the description of colloidal systems. The Langevin equation of motion

$$m_i \ddot{\mathbf{r}}_i(t) = \mathbf{f}_i(\mathbf{r}^N(t), t) - \gamma_i \dot{\mathbf{r}}_i(t) + \sqrt{2k_B T \gamma_i} \mathbf{R}_i(t) \quad (2.6)$$

for particle i incorporates a random force $\sqrt{2k_B T \gamma_i} \mathbf{R}_i(t)$ and the total deterministic force $\mathbf{f}_i(\mathbf{r}^N(t), t)$, which may generally depend on the momentary particle configuration $\mathbf{r}^N(t)$ and on time t ; time derivatives are denoted by overdots. The forces are counteracted by a friction force $\gamma_i \dot{\mathbf{r}}_i(t)$ due to the motion in the solvent,⁴ where γ_i is the friction constant. Note that Eq. (2.6) is a second-order differential equation, which can be reformulated as a system of first-order equations using the momentum $\mathbf{p}_i(t) = m_i \dot{\mathbf{r}}_i(t)$ of particle i .

Crucially, to yield a sound statistical description of collisions with implicit solvent particles, the random force must be unbiased,

$$\langle \mathbf{R}_i(t) \rangle = 0, \quad (2.7)$$

as well as uncorrelated between particles and in time,

$$\langle \mathbf{R}_i(t) \mathbf{R}_j(t') \rangle = \mathbb{1} \delta_{ij} \delta(t - t'), \quad (2.8)$$

³In practice, one usually works in reduced units where $\Lambda = \sigma = 1$.

⁴We do not consider the mediation of hydrodynamic interactions via the solvent [49].

where $\mathbb{1}$ is the 3×3 identity matrix, δ_{ij} denotes the Kronecker delta and $\delta(\cdot)$ is the Dirac distribution; an outer product is implied in the correlation function on the left hand side of Eq. (2.8). The prefactor of the random force in Eq. (2.6) arises as a consequence of a fluctuation-dissipation theorem and yields equilibrium behavior which is consistent with the statistical mechanics as described in Sec. 1.3.

A further simplification of the particle dynamics arises by considering the Langevin equation in the overdamped limit [2, 6]. The inertia of the particles is thereby assumed to vanish instantaneously such that Eq. (2.6) becomes

$$\dot{\mathbf{r}}_i(t) = \frac{1}{\gamma_i} \mathbf{f}_i(\mathbf{r}^N(t), t) + \sqrt{\frac{2k_B T}{\gamma_i}} \mathbf{R}_i(t), \quad (2.9)$$

which is the equation of motion for (overdamped) Brownian dynamics, where the positions \mathbf{r}^N remain as the sole relevant microscopic degrees of freedom. This simplification comes with many crucial benefits for theoretical descriptions (see e.g. Sec. 3.2), but counterintuitively, the treatment of Eq. (2.9) in simulation is more problematic than one might expect at first sight. In the following, we give an outline of conventional numerical algorithms for BD before illustrating an adaptive timestepping method [1] which overcomes many of their drawbacks.

For the implementation of Eq. (2.9) in computer simulations, one is faced with the task of finding an appropriate discretization scheme in order to evolve the particle configuration \mathbf{r}^N numerically in time. The simplest treatment of a first-order stochastic differential equation (SDE) such as Eq. (2.9) can be derived as follows: a fixed discretization interval Δt is chosen, the time derivative is approximated by a finite difference and the accumulated effect of the stochastic term during the interval Δt is considered. After rearrangement, this yields the standard Euler-Maruyama method [52, 86], which reads

$$\mathbf{r}_{i,k+1} = \mathbf{r}_{i,k} + \frac{1}{\gamma_i} \mathbf{f}_i(\mathbf{r}_k^N, t_k) \Delta t + \sqrt{\frac{2k_B T}{\gamma_i}} \mathbf{R}_{i,k} \quad (2.10)$$

when applied to the overdamped Langevin equation (2.9). Eq. (2.10) yields a numerical approximation $\mathbf{r}_k^N \approx \mathbf{r}^N(t_k)$ of the time evolution of the particle configuration at times $t_k = k\Delta t$, $k > 0$, iteratively from a given initial configuration $\mathbf{r}^N(0) = \mathbf{r}_0^N$. The random vectors $\mathbf{R}_{i,k}$ are drawn independently in each step and for each particle according to $\mathbf{R}_{i,k} \sim \mathcal{N}(0, \Delta t) = \sqrt{\Delta t} \mathcal{N}(0, 1)$ from a multivariate normal distribution \mathcal{N} with vanishing mean and variance Δt (the process of drawing a random contribution from a given distribution is denoted by the tilde). This specific construction of the random vectors $\mathbf{R}_{i,k}$ is in agreement with the properties (2.7) and (2.8).

As can already be guessed from its name, the Euler-Maruyama method is the generalization of the Euler method for ordinary differential equations (ODEs) to the case of SDEs, and it differs solely in the (straightforward) addition of the random term. Whereas the Euler method for ODEs is rarely used and has been superseded by more accurate and more efficient schemes which are arguably textbook knowledge [87], the

Euler-Maruyama method is still commonly applied for the numerical solution of SDEs and in particular for conventional BD simulations. Although higher-order [50] or implicit [51] timestepping may be incorporated, the treatment of the stochastic term generally remains crude when attempting to devise more advanced methods, thus somewhat limiting their practical utility. One might wonder why this is the case, especially when keeping many-body simulations in mind, which have significant potential of benefiting from more efficient algorithms.

In the following, we give a brief overview of the numerical treatment of SDEs and the subtleties which arise in the construction of improved methods (more background can be found e.g. in Ref. [52]). For this, we first consider general SDEs of the form

$$dX(t) = f(X(t), t) dt + g(X(t), t) dW(t), \quad (2.11)$$

where X is the dependent random variable, W is a Wiener process (i.e. Brownian motion), and f and g are prescribed general functions. The Euler-Maruyama method for this general SDE then becomes

$$X_{k+1} = X_k + f(X_k, t_k)\Delta t + g(X_k, t_k)R_k, \quad (2.12)$$

where a Wiener increment R_k is drawn in each step k from a normal distribution as shown above.

A first clear distinction to the numerical treatment of ODEs arises when determining the order of convergence of a given integration scheme, e.g. of Eq. (2.12). Since both the true solution $X(t_k)$ as well as the approximation X_k are inherently stochastic, the convergence of numerical methods for SDEs may be considered with respect to averages or with respect to individual realizations of the random process. For disambiguation, this is referred to as *weak* and *strong* convergence, respectively. The order of convergence is then defined as the exponent p of the power law Δt^p which bounds the behavior of the error of X_k to $X(t_k)$ in the weak or strong sense for $\Delta t \rightarrow 0$. While the order of convergence can easily be determined for ODE methods in general, the distinction between weak and strong convergence and the fact that p may depend on the concrete form of the functions f and g complicates this problem for SDEs. As an example, the Euler-Maruyama method possesses a strong order of convergence of $p = 1/2$ for general forms⁵ of g , but $p = 1$ (as for the Euler method for ODEs) if the noise is additive, i.e. $g(X(t), t) = \text{const.}$ in Eq. (2.11). This is exactly the case for the overdamped Langevin equation (2.9), and one can hence focus on the deterministic part⁶ for obtaining higher-order schemes for BD [50, 51].

A second difficulty in the treatment of SDEs arises when the use of adaptive methods is considered, for which the discretization interval no longer remains constant in

⁵For general forms of g , the Milstein method [88] and Runge-Kutta methods for SDEs [52, 89] provide numerical schemes with higher order of strong convergence. This becomes relevant in BD when including hydrodynamic interactions for which the noise term is no longer additive.

⁶The properties of f can also be exploited for the construction of improved schemes. For BD, the Leimkuhler-Matthews method [90, 91] is a feasible and simple alternative to standard Euler-Maruyama integration if the deterministic force is known to be conservative.

each step. Instead, automatic adjustment of Δt shall control the discretization error with the goal of obtaining a stable and accurate time propagation that still remains efficient. Recall that for ODEs, a popular adaptive integration scheme is the Runge-Kutta-Fehlberg method [92], for which two embedded Runge-Kutta steps of different order are used to estimate the discretization error and to hence adapt the value of Δt optimally. A crucial mechanism in adaptive methods is the occurrence of rejections. If a step is performed with a given discretization interval Δt and the resulting local error is deemed too large, the step is undone a posteriori and retried with a smaller value of Δt . This procedure poses fundamental challenges when applied to SDEs. Here, a timestep includes drawing a random contribution which needs to satisfy precise statistical relations, see e.g. Eqs. (2.7) and (2.8). By naively discarding and redrawing these contributions, the random process is altered implicitly and its desired properties are violated, which leads to unphysical results in the case of BD simulations. Hence, if one wishes to incorporate adaptive timestepping due to its undeniable benefits, one must ensure the correct generation of the given random process under the premise of occasional rejections.

2.3 Adaptive Brownian dynamics: an overview

In the following, we show that it is possible to construct an efficient adaptive method for BD and hence summarize the main findings of Ref. [1]. Following the above considerations, a simple scheme with different orders of strong convergence can be obtained by complementing the Euler-Maruyama method with a Heun step (i.e. the trapezoidal rule) as follows:

$$\bar{\mathbf{r}}_{i,k+1} = \mathbf{r}_{i,k} + \frac{1}{\gamma_i} \mathbf{f}_i(\mathbf{r}_k^N, t_k) \Delta t_k + \sqrt{\frac{2k_B T}{\gamma_i}} \mathbf{R}_{i,k}, \quad (2.13)$$

$$\mathbf{r}_{i,k+1} = \mathbf{r}_{i,k} + \frac{1}{2\gamma_i} \left(\mathbf{f}_i(\mathbf{r}_k^N, t_k) + \mathbf{f}_i(\bar{\mathbf{r}}_{k+1}^N, t_{k+1}) \right) \Delta t_k + \sqrt{\frac{2k_B T}{\gamma_i}} \mathbf{R}_{i,k}. \quad (2.14)$$

The Euler-Maruyama step (2.13) produces an intermediate configuration $\bar{\mathbf{r}}_{k+1}^N$ at time $t_{k+1} = t_k + \Delta t_k$, which is taken as input to the Heun step (2.14) to yield an improved estimate of the deterministic force which acts during the time interval $[t_k, t_{k+1}]$. Note that the random contributions \mathbf{R}_k^N in Eqs. (2.13) and (2.14) are identical and that only one additional evaluation of the particle forces \mathbf{f}^N is required in Eq. (2.14), thus constituting an embedded scheme. While this numerical integration procedure could be used as-is with a constant timestep, our main goal is the implementation of adaptivity. Hence, the discrepancy of the Euler ($\bar{\mathbf{r}}_{k+1}^N$) and the Heun (\mathbf{r}_{k+1}^N) step serves to evaluate a scalar error measure, for which a tolerance is imposed. The adaptation of Δt_k then proceeds similar to that of ODE integrators and further technical details of the algorithm are given in Ref. [1]. In particular, if the discrepancy of $\bar{\mathbf{r}}_{k+1}^N$ and \mathbf{r}_{k+1}^N lies above the predefined tolerance, the trial step is rejected and reevaluated after decreasing the timestep Δt_k .

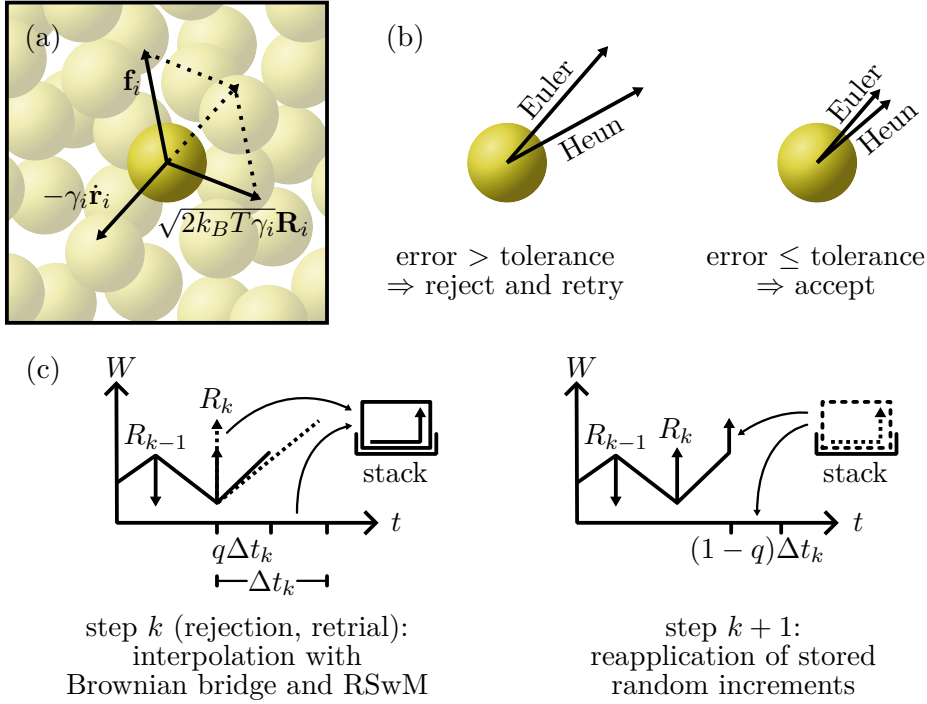


Figure 2: (a) The microscopic force balance in the overdamped Langevin equation (2.9) for particle i consists of a deterministic force \mathbf{f}_i and of a random force $\sqrt{2k_B T \gamma_i} \mathbf{R}_i$, which are counteracted by the friction force $\gamma_i \dot{\mathbf{r}}_i$ exerted by the implicit solvent. (b) Adaptive BD propagates the particles according to the embedded Heun-Euler integration scheme (2.13) and (2.14), which enables to control the accuracy of the time evolution via a tolerance criterion that may result in rejections of trial steps. (c) In case of rejection, the random increment R_k is interpolated with the Brownian bridge theorem (2.15) to retain the desired Wiener process $W(t)$. Rejection sampling with memory (RSwM) facilitates the efficient storage and reapplication of rejected parts of random increments, which is illustrated here for a simplified one-dimensional random process.

The crucial part of adaptive BD is the construction of the random contributions \mathbf{R}_k^N and their handling after such rejections. The problem of generating a given random process iteratively while allowing rejections has also been considered by Rackauckas and Nie [93] in 2017, and they have coined a family of “Rejection Sampling with Memory” (RSwM) algorithms as viable solutions. Central to these methods is the Brownian bridge theorem [52], which concretely specifies how to interpolate a Wiener process, cf. Eq. (2.11). If the state of such a random process is known at two points, e.g. $W(0) = 0$ and $W(\Delta t) = R$, the Brownian bridge theorem yields

$$W(q\Delta t) \sim \mathcal{N}(qR, (1-q)q\Delta t) \quad (2.15)$$

as an interpolation rule for the construction of an intermediate point $W(q\Delta t)$ where $0 < q < 1$. Recall that in Eq. (2.15), the arguments qR and $(1-q)q\Delta t$ prescribe the

expectation value and the variance of the normal distribution \mathcal{N} . Hence, the Brownian bridge (2.15) can be used after the rejection of a Heun-Euler step (2.13) and (2.14) with length Δt to draw new Wiener increments for the retrial of the timestep with a decreased discretization interval $q\Delta t$. The refined random process will then still satisfy the desired properties (2.7) and (2.8) of Brownian motion.

Importantly, the remaining part of the rejected random increment, i.e. the contribution corresponding to the time interval $[q\Delta t, \Delta t]$, must still be retained. For this, RSwM provides an efficient bookkeeping scheme, which ensures that rejected random increments are stored and reused efficiently in subsequent timesteps. The fully general method RSwM3 [93, 94] serves as the basis for adaptive BD, and it enables continuous variation of the time interval and the correct handling of edge cases such as re-rejections.⁷ The use of RSwM3 in adaptive BD and further details of the algorithm are described in Ref. [1] and an implementation is provided in Ref. [9]. An illustration of the embedded Heun-Euler scheme in adaptive BD as well as a sketch of RSwM is shown in Fig. 2.

Applications and results

Adaptive BD is useful especially for nonequilibrium simulations, but it turns out to be favorable already in equilibrium and under bulk conditions. This has been shown in Ref. [1], where different benchmarks were performed for the Lennard-Jones fluid. With adaptive BD, the heuristic choice of a suitable timestep length Δt is spared, and one instead imposes a tolerance criterion for the error of individual steps, which is universal across a broad range of relevant applications. The rapid adaptation of Δt leads on average to a significantly larger timestep and hence to an efficiency gain compared to the standard Euler-Maruyama scheme, but it also ensures the stability and accuracy in situations where the use of fixed-timestep integration methods is bound to fail. As an example, we have investigated the behavior of a colloidal Lennard-Jones system in which evaporation of the implicit solvent is modeled by a time-dependent external potential [1, 95]. The successful automatic choice of Δt reflects the changing environment as the colloidal suspension becomes denser, and the complex stratification dynamics can be resolved up to and within the arrangement of the colloidal particles into a lattice.

We have also employed adaptive BD for the simulation of an inhomogeneously sheared colloidal gel [2] (see also Sec. 3.2 for the PFT point of view). This study demonstrates that the method is particularly useful for nonequilibrium investigations and that more complex interaction types such as the SW potential pose no difficulties for its application. While the timestep would have to be adjusted manually in conventional methods to accommodate for the variable strength of the applied shear force, adaptive BD automates this choice based on the quasi-universal tolerance criterion.

The benefits of automatic timestep adjustment have been particularly relevant for the machine learning investigations (cf. Chapter 4) of Ref. [6], where training and test

⁷We have rectified a subtle error in the original RSwM3 algorithm regarding the treatment of re-rejections, see Appendix B in Ref. [1] for details.

simulations of the LJ fluid have been performed with adaptive BD. As the generation of this reference data set required 1000 simulation runs with vastly different randomized equilibrium and nonequilibrium conditions, it would have been very cumbersome to be obliged to rely on fixed-timestep integrators due to their lack of stability, accuracy and efficiency.

As adaptive BD bounds the local error on the trajectory level by the comparison of forces, the method is also suitable for the accurate measurement of force-related observables. This feature was used advantageously to obtain some of the results of Refs. [4, 5]. Specifically, different types of force correlation functions have been investigated in simulation in order to verify their interrelation via sum rules due to Noether invariance (cf. Sec. 3.3).

Recently, adaptive BD has also been considered in other works as a favorable alternative to usual fixed-timestep Euler-Maruyama integration. In particular, the method has been used for the simulation of topologically protected colloidal transport that may be controlled in corresponding experiments by magnetic patterns or optical tweezers [96, 97]. Adaptive timestepping has also been discussed to play a crucial role in performant simulations of more complex biophysical systems [98, 99], for which adaptive BD provides a practical toolbox that may help to mitigate many of the arising subtleties.

3 Functional techniques and thermal Noether invariance

3.1 Density functional theory

The simulation techniques presented in Chapter 2 facilitate the measurement of one-body quantities [1, 3, 7, 8] such as the density profile $\rho(\mathbf{r})$ as well as of more intricate correlation functions [4, 5] via sampling of many-body configurations. In equilibrium, simulations hence provide practical access to the functional mapping from the prescribed external potential to the measured density profile, i.e. $V_{\text{ext}}(\mathbf{r}) \rightarrow \rho(\mathbf{r})$, which is in accordance with common physical intuition of cause and effect (thereby ignoring subtleties at phase coexistence). Less obviously, and much to the benefit of theoretical and application-oriented methods, one can show that the inverse functional relationship

$$\rho(\mathbf{r}) \rightarrow V_{\text{ext}}(\mathbf{r}) \quad (3.1)$$

is also uniquely determined for fixed but arbitrary interparticle interactions, temperature and chemical potential, provided that $\rho(\mathbf{r})$ is restricted to physically accessible profiles. This landmark result, which was first proven for classical systems by Evans [53] in 1979, serves as the bedrock of classical density functional theory (DFT).

Reformulating the statistical mechanics of many-body systems (cf. Sec. 1.3) in terms of functional relationships with respect to $\rho(\mathbf{r})$ yields a powerful framework for the description of fluid equilibria [14], and we give some details in the following. As $V_{\text{ext}}(\mathbf{r})$ appears explicitly in the Hamiltonian and hence in the Boltzmann distribution function Ψ_{eq} , see Eq. (1.8), it is clear that the DFT map (3.1) implies a formal functional relationship on $\rho(\mathbf{r})$ for every related quantity. In particular, the grand potential $\Omega = -k_B T \ln \Xi$, which follows from the grand partition sum Ξ in the many-body picture, becomes a unique functional $\Omega[\rho]$ with respect to the one-body density profile (functional relationships are indicated by square brackets). The role of $\Omega[\rho]$ as a thermodynamic potential remains valid, such that functional minimization determines the true equilibrium state,

$$\frac{\delta \Omega[\rho]}{\delta \rho(\mathbf{r})} = 0 \quad (\text{min}), \quad (3.2)$$

where $\delta/\delta\rho(\mathbf{r})$ is a functional derivative with respect to the density profile. More explicit results are obtained by writing out ideal, external and internal contributions of the grand potential according to

$$\Omega[\rho] = F_{\text{id}}[\rho] + F_{\text{exc}}[\rho] + \int d\mathbf{r} \rho(\mathbf{r}) (V_{\text{ext}}(\mathbf{r}) - \mu). \quad (3.3)$$

Contrary to the ideal gas free energy

$$F_{\text{id}}[\rho] = k_B T \int d\mathbf{r} \rho(\mathbf{r}) \left(\ln(\rho(\mathbf{r})\Lambda^d) - 1 \right), \quad (3.4)$$

which can be derived exactly, the excess free energy $F_{\text{exc}}[\rho]$ constitutes the nontrivial part of the grand potential $\Omega[\rho]$ and it has to be determined for the specific fluid model under consideration [3, 7, 8]. Note that the thermal wavelength in Eq. (3.4) can be set to $\Lambda = \sigma = 1$ without losing generality and that the parametric dependence of $F_{\text{id}}[\rho]$ and $F_{\text{exc}}[\rho]$ on temperature T is suppressed in the notation.

Using Eq. (3.3) in the minimization principle (3.2), one arrives at

$$\rho(\mathbf{r}) = e^{-\beta(V_{\text{ext}}(\mathbf{r}) - \mu) + c_1(\mathbf{r}; [\rho])}, \quad (3.5)$$

which constitutes the Euler-Lagrange equation of classical DFT. The effects of the internal interactions are captured in Eq. (3.5) by the one-body direct correlation functional

$$c_1(\mathbf{r}; [\rho]) = -\frac{\delta F_{\text{exc}}[\rho]}{\delta \rho(\mathbf{r})}, \quad (3.6)$$

which follows from functional differentiation of the excess free energy and hence retains the functional dependence on $\rho(\mathbf{r})$. By iterating multiple functional derivatives with respect to $\rho(\mathbf{r})$, the hierarchy of direct correlation functions can be accessed [7, 8]. In particular, the two-body direct correlation function is given by

$$c_2(\mathbf{r}, \mathbf{r}'; [\rho]) = \frac{\delta c_1(\mathbf{r}; [\rho])}{\delta \rho(\mathbf{r}')}. \quad (3.7)$$

As an important object in liquid integral equation theory [14], the two-body direct correlation functional determines the pair structure of fluids via the Ornstein-Zernike (OZ) equation [100]

$$h(\mathbf{r}, \mathbf{r}') = c_2(\mathbf{r}, \mathbf{r}') + \int d\mathbf{r}'' c_2(\mathbf{r}, \mathbf{r}'') \rho(\mathbf{r}'') h(\mathbf{r}'', \mathbf{r}'). \quad (3.8)$$

Here, $h(\mathbf{r}, \mathbf{r}')$ is the total correlation function, which is associated in bulk fluids to the radial distribution function $g(r) = g(|\mathbf{r} - \mathbf{r}'|) = h(\mathbf{r}, \mathbf{r}') + 1$, see also Refs. [4, 7] for numerical work.

The two-body direct correlation function plays a further important role in a reformulation of DFT which is based on forces. This force-DFT [61] relies on the calculation of $c_2(\mathbf{r}, \mathbf{r}'; [\rho])$ from a given form of $F_{\text{exc}}[\rho]$ by functional differentiation, see Eqs. (3.6) and (3.7). The two-body density $\rho^{(2)}(\mathbf{r}, \mathbf{r}'; [\rho]) = \rho(\mathbf{r})\rho(\mathbf{r}') (h(\mathbf{r}, \mathbf{r}'; [\rho]) + 1)$ is then accessed explicitly as a functional of $\rho(\mathbf{r})$ via inversion of the OZ equation (3.8) [101], and it serves as an auxiliary quantity during the minimization of the grand potential. For approximate forms of $F_{\text{exc}}[\rho]$, force-DFT results differ from those of conventional (“potential”) DFT. We have investigated the subtle discrepancies of both routes for

the hard sphere fluid in Ref. [3] and have followed therein the suggestion of Ref. [61] to construct and examine an improved hybrid scheme. Further details of the fundamentals of force-DFT are given in Sec. 3.3 and in Refs. [3, 61].

In concrete applications of conventional DFT, Eqs. (3.5) and (3.6) are central for the prediction of inhomogeneous fluid equilibria. The Euler-Lagrange equation (3.5) determines the true density profile implicitly, and it can hence be solved either by straightforward self-consistent iteration [7, 8] or by more sophisticated root-finding methods [102]. A simple and effective scheme is the Picard iteration with mixing parameter α , in which $\rho(\mathbf{r})$ is iterated until convergence according to

$$\rho(\mathbf{r}) \leftarrow (1 - \alpha)\rho(\mathbf{r}) + \alpha e^{-\beta(V_{\text{ext}}(\mathbf{r}) - \mu) + c_1(\mathbf{r}; [\rho])}. \quad (3.9)$$

Although the computational effort of a DFT minimization may be orders of magnitude lower than in a corresponding many-body simulation, the core difficulty of DFT lies in the necessity of finding an accurate functional expression for $c_1(\mathbf{r}; [\rho])$ or equivalently for $F_{\text{exc}}[\rho]$; we recall Eq. (3.6). Since this amounts exactly to solving the many-body problem, copious use of various approximation techniques is expected for all but the most simple types of model fluids.¹

In the following, we proceed analytically and illustrate approximations of $F_{\text{exc}}[\rho]$ for the three-dimensional hard sphere fluid as obtained from fundamental measure theory (FMT) [103]. The terminology can be traced back to the use of fundamental properties of spheres which reflect their purely geometric nature. Specifically, the fundamental geometric measures of spheres are incorporated via the weight functions²

$$\omega_3(\mathbf{r}) = \Theta(R - |\mathbf{r}|), \quad (3.10)$$

$$\omega_2(\mathbf{r}) = \delta(R - |\mathbf{r}|), \quad (3.11)$$

$$\omega_2(\mathbf{r}) = \delta(R - |\mathbf{r}|)\hat{\mathbf{e}}_{\mathbf{r}}, \quad (3.12)$$

with $R = \sigma/2$, $\hat{\mathbf{e}}_{\mathbf{r}} = \mathbf{r}/|\mathbf{r}|$ and additional linearly dependent weights $\omega_0(\mathbf{r}) = \omega_1(\mathbf{r})/R = \omega_2(\mathbf{r})/(4\pi R^2)$ and $\omega_1(\mathbf{r}) = \omega_2(\mathbf{r})/(4\pi R)$. Weighted densities

$$n_\alpha(\mathbf{r}) = (\rho \star \omega_\alpha)(\mathbf{r}) = \int d\mathbf{r}' \rho(\mathbf{r}') \omega_\alpha(\mathbf{r} - \mathbf{r}') \quad (3.13)$$

follow from convolution of the density profile with the weight functions $\omega_\alpha(\mathbf{r})$, $\alpha = 0, 1, 2, 3, \mathbf{1}, \mathbf{2}$. These serve as the basis to express the excess free energy via

$$F_{\text{exc}}[\rho] = k_B T \int d\mathbf{r} \Phi(\{n_\alpha\}). \quad (3.14)$$

¹The one-dimensional hard rod system is one of the very few fluid models for which an exact expression of $F_{\text{exc}}[\rho]$ has been found [60]. See also Ref. [8] for a survey of its analytic treatment and a perspective on neural functional methods (cf. Chapter 4).

²Alternatively to the scalar and vectorial Rosenfeld weights [103] shown here, an equivalent representation in terms of only scalar functions is possible [104, 105].

For use in the iteration (3.9), functional differentiation of the FMT excess free energy (3.14) yields the result

$$c_1(\mathbf{r}; [\rho]) = - \sum_{\alpha} \left(\frac{\partial \Phi}{\partial n_{\alpha}} \star \frac{\delta n_{\alpha}}{\delta \rho} \right) (\mathbf{r}) \quad (3.15)$$

for the one-body direct correlation functional, where an inner product is implied for vectorial terms.

Concrete FMT functionals differ in the algebraic structure of the excess free energy density $\Phi(\{n_{\alpha}\})$. In the original formulation of Rosenfeld [103],

$$\Phi(\{n_{\alpha}\}) = -n_0 \ln(1 - n_3) + \frac{n_1 n_2 - n_1 \cdot n_2}{1 - n_3} + \frac{n_2^3 - 3n_2 n_2^2}{24\pi(1 - n_3)^2}. \quad (3.16)$$

An improvement over the Rosenfeld result (3.16) could be achieved with the derivation of the White Bear and White Bear MkII functionals [106–108], whereby the latter arguably serves as the state-of-the-art treatment of hard-core repulsion in DFT.

Applications of DFT are based on the self-consistent calculation of the density profile (and further related quantities [109–112]) via an iteration scheme such as Eq. (3.9). Conventionally, a suitable analytic expression for $F_{\text{exc}}[\rho]$, e.g. the FMT result (3.14), has to be specified, which gives rise to the one-body direct correlation functional $c_1(\mathbf{r}; [\rho])$ that appears in the Euler-Lagrange equation (3.5) and in the Picard iteration (3.9). Prior to the actual implementation of $c_1(\mathbf{r}; [\rho])$, it is common practice to specialize analytically to a simplified geometry, e.g. to planar [3, 7] or spherical symmetry as is relevant for adsorption on model substrates and for the investigation of surface-induced phenomena [113–117]. The convolutional structure of the FMT expression (3.15) for $c_1(\mathbf{r}; [\rho])$ remains intact in both planar and spherical geometry after integrating out over invariant coordinates [108].

As an alternative approach to analytic treatments, we present in Chapter 4 machine learning methods for the determination of central functional objects from simulation data and for the implementation of a corresponding neural DFT [7, 8]. For hard spheres, the neural functional framework supersedes FMT in accuracy and it can also be readily applied to different types of model fluids. Similarly, neural functionals can be trained and used in nonequilibrium, where the existence of an exact functional map is established by PFT. In the following, we outline relevant approaches for the description of dynamical systems.

3.2 Power functional theory

Before detailing PFT, we give an overview of dynamical density functional theory (DDFT) [3, 6, 53, 118, 119], which serves as an approximate method to investigate time-dependent systems. The dynamical behavior is thereby assumed to be determined by a sequence of equilibrium states, which are in turn described by DFT. The time

evolution then follows from the continuity equation

$$\frac{\partial \rho(\mathbf{r}, t)}{\partial t} = -\nabla \cdot \mathbf{J}(\mathbf{r}, t), \quad (3.17)$$

where the current is given by

$$\mathbf{J}(\mathbf{r}, t) = -\frac{1}{\gamma} \rho(\mathbf{r}, t) \nabla [k_B T \ln \rho(\mathbf{r}, t) + V_{\text{ext}}(\mathbf{r}, t) - k_B T c_1(\mathbf{r}, t; [\rho])]. \quad (3.18)$$

The one-body direct correlation functional $c_1(\mathbf{r}, t; [\rho])$ is defined as before via the functional derivative of $F_{\text{exc}}[\rho]$, see Eq. (3.6), and it inherits the explicit time dependence from $\rho(\mathbf{r}, t)$. The gradient structure of Eq. (3.18) renders DDFT oblivious to certain types of dynamical scenarios and in particular to the effects of nonconservative force fields as occur e.g. in sheared fluids [2, 120, 121]. Additionally, the implication of equilibrium conditions, which is referred to as the adiabatic approximation, results in omissions and defects that are generally hard to judge a priori [6, 122].

Alternatively to the usual functional derivative of the excess free energy, $c_1(\mathbf{r}, t; [\rho])$ in Eq. (3.18) can be expressed in terms of a force integral (see Sec. 3.3), which results in a force-DDFT [3, 61]. For approximate forms of $F_{\text{exc}}[\rho]$, force-DDFT yields results slightly different from those of conventional DDFT, and explicit comparisons for the Rosenfeld FMT functional (3.16) are presented in Ref. [3]. Interestingly, force-DDFT enables a formal extension of DDFT to obtain an additional equation of motion for the two-body density $\rho^{(2)}(\mathbf{r}, \mathbf{r}', t)$, which is coupled to that of the one-body density $\rho(\mathbf{r}, t)$. Applying the adiabatic approximation only at this level is practically feasible and results in a ‘‘superadiabatic DDFT’’ [123, 124], which may mitigate certain limitations of the conventional method.

Instead of climbing up the ladder of higher-order correlation functions, PFT [54, 55] offers a formally exact framework for the investigation of nonequilibrium systems which remains grounded on the one-body level. For overdamped motion,³ cf. Eq. (2.9), the kinematic map of PFT invokes besides the instantaneous density profile $\rho(\mathbf{r}, t)$ a causal functional dependence on the current $\mathbf{J}(\mathbf{r}, t)$, i.e. on its history at all earlier times t . Analogously to DFT, see Eq. (3.2), a minimization principle

$$\frac{\delta R_t[\rho, \mathbf{J}]}{\delta \mathbf{J}(\mathbf{r}, t)} = 0 \quad (3.19)$$

can be formulated, where the functional derivative of the total power functional $R_t[\rho, \mathbf{J}]$ is evaluated for fixed density and at fixed time t . By writing out ideal, internal and external contributions [55] and performing the functional minimization (3.19), one arrives at the force density balance

$$\gamma \mathbf{J}(\mathbf{r}, t) = \mathbf{F}_{\text{int}}(\mathbf{r}, t; [\rho, \mathbf{J}]) + \rho(\mathbf{r}, t) \mathbf{f}_{\text{ext}}(\mathbf{r}, t) - k_B T \nabla \rho(\mathbf{r}, t), \quad (3.20)$$

³The assumption of overdamped BD is crucial for the existence of the functional relations presented here. While PFT can also be formulated for inertial systems, the functional mapping then incorporates $\dot{\mathbf{J}}(\mathbf{r}, t)$, i.e. the time derivative of the current, as an additional variational field [55, 125].

which constitutes together with the continuity equation (3.17) the formally exact equations of motion of PFT. Note that all quantities in Eq. (3.20) are also defined as microscopic averages $\langle \sum_{i=1}^N a_i \delta(\mathbf{r} - \mathbf{r}_i) \rangle$ and are hence accessible in simulation [2, 6]. In particular, setting a_i to the velocity \mathbf{v}_i of particle i yields the current $\mathbf{J}(\mathbf{r}, t)$ (see Ref. [126] for sampling techniques in BD), and $a_i = -\nabla_i u(\mathbf{r}^N)$ determines the internal force density $\mathbf{F}_{\text{int}}(\mathbf{r}, t)$, where ∇_i denotes the gradient with respect to coordinate \mathbf{r}_i .

The nontrivial functional dependence in Eq. (3.19) is passed down to $\mathbf{F}_{\text{int}}(\mathbf{r}, t; [\rho, \mathbf{J}])$ in Eq. (3.20). In the adiabatic approximation, the functional dependence on $\mathbf{J}(\mathbf{r}, t)$ is dropped, and identification with the DDFT current (3.18) reveals that the adiabatic force density

$$\mathbf{F}_{\text{ad}}(\mathbf{r}, t; [\rho]) = \rho(\mathbf{r}, t) k_B T \nabla c_1(\mathbf{r}, t; [\rho]) \quad (3.21)$$

is defined directly via the (equilibrium) one-body direct correlation functional. However, a surplus generally remains in the full nonequilibrium internal force density, which hence constitutes the superadiabatic part

$$\mathbf{F}_{\text{sup}}(\mathbf{r}, t; [\rho, \mathbf{J}]) = -\rho(\mathbf{r}, t) \frac{\delta P_{\text{exc}}[\rho, \mathbf{J}]}{\delta \mathbf{J}(\mathbf{r}, t)}. \quad (3.22)$$

Its generating functional, the superadiabatic free power functional $P_{\text{exc}}[\rho, \mathbf{J}]$, is at the center of attention of PFT studies, as it models the genuine out-of-equilibrium effects in many relevant applications [2, 6, 121, 122, 127]. Thus, in total,

$$\mathbf{F}_{\text{int}}(\mathbf{r}, t; [\rho, \mathbf{J}]) = \mathbf{F}_{\text{ad}}(\mathbf{r}, t; [\rho]) + \mathbf{F}_{\text{sup}}(\mathbf{r}, t; [\rho, \mathbf{J}]) \quad (3.23)$$

determines the dynamical behavior of a given system by entering the force density balance (3.20). For concrete applications [2, 6], functional forms have to be provided for both the adiabatic (see Sec. 3.1) and the superadiabatic contribution. In the following, we specialize to nonequilibrium steady states, such that the explicit time dependence vanishes in the previous equations and the current $\mathbf{J}(\mathbf{r})$ enters only in the form of its stationary profile instead of its whole history.

Approximations for the superadiabatic part can be obtained analytically, e.g. by simple semi-local expansions in terms of gradients of the one-body velocity profile $\mathbf{v}(\mathbf{r}) = \mathbf{J}(\mathbf{r})/\rho(\mathbf{r})$ [6, 122, 128]; note that the functional minimization (3.19) may be formulated equally with respect to $\mathbf{v}(\mathbf{r})$ instead of $\mathbf{J}(\mathbf{r})$. Further analysis enables to split the superadiabatic force density into two additive contributions,

$$\mathbf{F}_{\text{sup}}(\mathbf{r}; [\rho, \mathbf{v}]) = \mathbf{F}_{\text{flow}}(\mathbf{r}; [\rho, \mathbf{v}]) + \mathbf{F}_{\text{struc}}(\mathbf{r}; [\rho, \mathbf{v}]). \quad (3.24)$$

These can be distinguished uniquely with respect to their transformation properties under motion reversal, i.e. by considering a (hypothetical) system where $\rho(\mathbf{r})$ is identical but the flow direction is inverted such that $\mathbf{v}(\mathbf{r}) \rightarrow -\mathbf{v}(\mathbf{r})$. Whereas the flow force density $\mathbf{F}_{\text{flow}}(\mathbf{r})$ also flips its direction in the transformed system, the structural force density $\mathbf{F}_{\text{struc}}(\mathbf{r})$ remains unchanged. Terms of an analytic superadiabatic power functional can hence be directly identified to describe flow or structural forces by considering their order in $\mathbf{v}(\mathbf{r})$. This distinction is valuable as it allows for a clear separation of the physical origin of the observed nonequilibrium forces [2, 6].

Applications and results

In Ref. [2], we have performed investigations of a colloidal gel former [74, 75] as described on the many-body level by the SW potential (1.3) and (1.4), which shows significant superadiabatic effects in nonequilibrium steady states. External driving by a sinusoidal shear force profile $\mathbf{f}_{\text{ext}}(\mathbf{r})$ causes the gel to form two flow channels. Via adaptive BD simulations [1] of the stationary flow, a significant density modulation could be measured, which is maintained by a considerable structural superadiabatic force density profile $\mathbf{F}_{\text{struc}}(\mathbf{r})$. Additionally, the viscoelastic behavior of the colloidal gel leads to the development of a superadiabatic flow force density $\mathbf{F}_{\text{flow}}(\mathbf{r})$ with a phenomenology which is clearly distinct to that of viscous forces in simple fluids. In particular, $\mathbf{F}_{\text{flow}}(\mathbf{r})$ acts at the sides of the flow channels in the same direction as the external force for sufficient driving, which is caused microscopically by the dynamical formation of particle chains that drag along connected strands. The resulting behavior of $\mathbf{F}_{\text{flow}}(\mathbf{r}; [\rho, \mathbf{v}])$ can be described successfully by a simple analytic power functional based on an expansion in gradients of $\mathbf{v}(\mathbf{r})$ and $\rho(\mathbf{r})$, see Eqs. (19)–(21) in Ref. [2].

Further use of PFT has been made in Ref. [6], where we have investigated machine learning techniques which aim to capture the functional kinematic map from simulation data. Specifically, we have considered the steady flow of the supercritical LJ fluid in planar geometry as caused by diverse inhomogeneous external force profiles. The neural network, which has been trained with adaptive BD [1] simulation data (see Sec. 2.3), is capable of accurately predicting superadiabatic forces in systems that were not included in the training, which serves as a data-driven verification of the existence of the PFT kinematic map (3.23). Additionally, the analytic approach based on a simple gradient expansion proves to be useful as it shows qualitative agreement across a wide range of external force profiles.

3.3 Sum rules from applications of Noether’s theorem

As shown in Secs. 3.1 and 3.2, both DFT and PFT operate on a specific set of one-body profiles, with $\rho(\mathbf{r})$ being the sole central quantity in equilibrium. However, in certain applications, further relevant observables are often worthwhile to consider in order to gain additional physical insight. In particular, the consideration of one-body forces is natural in dynamical systems, and it has also led in equilibrium to recent progress, e.g. in the form of advanced numerical sampling schemes [44, 129–131]. One might then wonder whether these additional quantities, which usually arise from averages of different phase space functions, are connected in some way, and if so, how to acquire explicit analytic constraints for their interrelation.

The application of Noether’s theorem [132, 133] to thermal many-body systems [56–59] offers a powerful toolbox for the derivation of such *sum rules*, and we give an overview of well-known and recent results [4, 5] in this section. As a general starting point, a canonical transformation [134] is defined via a shifting field $\epsilon(\mathbf{r})$ which acts on

phase space according to

$$\mathbf{r}_i \rightarrow \mathbf{r}_i + \boldsymbol{\epsilon}(\mathbf{r}_i), \quad (3.25)$$

$$\mathbf{p}_i \rightarrow (\mathbb{1} + \nabla_i \boldsymbol{\epsilon}(\mathbf{r}_i))^{-1} \cdot \mathbf{p}_i, \quad (3.26)$$

and which conserves the phase space volume element $d\mathbf{r}^N d\mathbf{p}^N$ by construction. Formally, quantities in the transformed system then acquire a functional dependence on $\boldsymbol{\epsilon}(\mathbf{r})$. However, the transformation (3.25) and (3.26) can be viewed as a mere reparametrization, such that results of integrals over phase space must be invariant with respect to this coordinate change. Hence, for an arbitrary quantity A which is obtained from phase space integration, one can conclude that $A[\boldsymbol{\epsilon}] = A$ or equivalently

$$\frac{\delta A[\boldsymbol{\epsilon}]}{\delta \boldsymbol{\epsilon}(\mathbf{r})} = 0. \quad (3.27)$$

This functional derivative can be performed explicitly in equilibrium⁴ if $A = \langle \hat{A} \rangle$ is given as an average of an arbitrary phase space function $\hat{A}(\mathbf{r}^N, \mathbf{p}^N)$, see Ref. [5] for the derivation and the general result. In the following, we restrict ourselves to observables $\hat{A} = \hat{A}(\mathbf{r}^N)$ that depend only on positional degrees of freedom. Evaluating Eq. (3.27) at vanishing shifting field $\boldsymbol{\epsilon}(\mathbf{r}) = 0$ then yields the local sum rule [5]

$$\beta \langle \hat{\mathbf{F}}_{\text{int}}(\mathbf{r}) \hat{A} \rangle - \beta \langle \hat{\rho}(\mathbf{r}) \hat{A} \rangle \nabla V_{\text{ext}}(\mathbf{r}) = \nabla \langle \hat{\rho}(\mathbf{r}) \hat{A} \rangle - \left\langle \sum_{i=1}^N (\nabla_i \hat{A}) \delta(\mathbf{r} - \mathbf{r}_i) \right\rangle. \quad (3.28)$$

Useful concrete relations can be acquired by suitable choices of \hat{A} and we emphasize first the seemingly trivial case $\hat{A} = 1$, which recovers the Yvon-Born-Green (YBG) relation [14]

$$\mathbf{F}_{\text{int}}(\mathbf{r}) - \rho(\mathbf{r}) \nabla V_{\text{ext}}(\mathbf{r}) - k_B T \nabla \rho(\mathbf{r}) = 0. \quad (3.29)$$

The YBG equation (3.29) is the force density balance in equilibrium, cf. Eq. (3.20) with $\mathbf{J}(\mathbf{r}, t) = 0$, and it emerges here fundamentally from the invariance properties of phase space.⁵ Eq. (3.28) can hence be considered to form a *hyperforce*⁶ sum rule as it is the generalization of the YBG force balance (3.29) to correlation functions including the arbitrary configuration-dependent operator \hat{A} .

In Eq. (3.29), the internal force density is given explicitly for the case of pairwise internal interactions as the force integral

$$\mathbf{F}_{\text{int}}(\mathbf{r}) = - \int d\mathbf{r}' \rho^{(2)}(\mathbf{r}, \mathbf{r}') \nabla \phi(|\mathbf{r} - \mathbf{r}'|). \quad (3.30)$$

⁴Many equilibrium identities can also be obtained from partial integration of carefully chosen phase space averages.

⁵Alternatively, the YBG equation (3.29) can be obtained by choosing $A = \Omega$ and exploiting its invariance in Eq. (3.27) [61]. A further standard route towards deriving the YBG relation proceeds by integrating over $N - 1$ positional coordinates of the Smoluchowski equation [14].

⁶The terminology can be traced back to Hirschfelder's hypervirial theorems [135], which form a set of related but more abstract sum rules.

By comparison to Eq. (3.21) and recalling that $\mathbf{F}_{\text{int}}(\mathbf{r}) = \mathbf{F}_{\text{ad}}(\mathbf{r})$ in equilibrium, it is clear that this integral offers an alternative way to obtain the one-body direct correlation function $c_1(\mathbf{r})$ to be used in DFT calculations, see e.g. Eq. (3.9). This is the central mechanism of force-DFT, which exploits Eq. (3.30) and the fact that $\rho^{(2)}(\mathbf{r}, \mathbf{r}'; [\rho])$ is indeed practically accessible in planar and spherical geometry as a functional of $\rho(\mathbf{r})$ by inversion of the OZ equation (3.8). Ref. [61] gives a detailed technical account of the method and Ref. [3] conducts a quantitative comparison of conventional and force-(D)DFT on the basis of the Rosenfeld FMT for the hard sphere fluid.

We return to the search for more general sum rules and point to Ref. [5], where explicit results of Eq. (3.28) for various choices of \hat{A} are given. In particular, we reiterate here the possibility of obtaining global sum rules either by spatial integration of the local identity (3.28) across the system volume or by considering a constant shifting field $\epsilon(\mathbf{r}) = \epsilon_0$ in the variation (3.27). As an example, this yields the vanishing of the total internal force $\mathbf{F}_{\text{int}}^{\text{tot}} = \int d\mathbf{r} \mathbf{F}_{\text{int}}(\mathbf{r}) = 0$, which is expected due to Newton's third law. In equilibrium, expressing the internal force density in terms of the one-body direct correlation function via Eq. (3.21) and performing a functional derivative produces the identity [7, 8, 56]

$$\nabla c_1(\mathbf{r}) = \int d\mathbf{r}' c_2(\mathbf{r}, \mathbf{r}') \nabla' \rho(\mathbf{r}'), \quad (3.31)$$

which is an example of a sum rule that connects different members of the hierarchy of direct correlation functions with each other. Additionally, one obtains

$$\int d\mathbf{r} \rho(\mathbf{r}) \int d\mathbf{r}' \rho(\mathbf{r}') \nabla c_2(\mathbf{r}, \mathbf{r}') = 0 \quad (3.32)$$

as a consequence of Eq. (3.31) and $\mathbf{F}_{\text{int}}^{\text{tot}} = 0$ [7, 8, 56].

Noether invariance can also be utilized to reveal further physical insight into the nature of pair correlations in many-body systems. In this regard, novel types of two-body correlation functions emerge from second-order invariance,

$$\frac{\delta^2 A[\epsilon]}{\delta \epsilon(\mathbf{r}) \delta \epsilon(\mathbf{r}')} = 0. \quad (3.33)$$

This has been considered in Ref. [4], where choosing A as the grand potential Ω , see Sec. 1.3, leads to the bulk identity

$$\nabla \nabla g(r) + \mathbf{g}_{\nabla f}(r) + \mathbf{g}_{ff}(r) = 0. \quad (3.34)$$

Besides the standard radial distribution function $g(r)$, the force-gradient and force-force correlation functions

$$\mathbf{g}_{\nabla f}(r) = \frac{\beta}{\rho_b^2} \left\langle \sum_{i=1}^N \sum_{j \neq i}^N \delta(\mathbf{r} - \mathbf{r}_i) \delta(\mathbf{r} - \mathbf{r}_j) \nabla_i \mathbf{f}_j \right\rangle, \quad (3.35)$$

$$\mathbf{g}_{ff}(r) = \frac{\beta^2}{\rho_b^2} \left\langle \sum_{i=1}^N \sum_{j \neq i}^N \delta(\mathbf{r} - \mathbf{r}_i) \delta(\mathbf{r} - \mathbf{r}_j) \mathbf{f}_i \mathbf{f}_j \right\rangle, \quad (3.36)$$

appear in the sum rule (3.34). These (3×3) -tensorial quantities are specified due to isotropy of the bulk fluid with density ρ_b by a radial (\parallel) and two equivalent tangential (\perp) components, such that Eq. (3.34) reduces to the scalar identities

$$g''(r) + g_{\nabla f \parallel}(r) + g_{ff \parallel}(r) = 0, \quad (3.37)$$

$$\frac{g'(r)}{r} + g_{\nabla f \perp}(r) + g_{ff \perp}(r) = 0. \quad (3.38)$$

In particular, for pair potentials, the force-gradient correlation function can be evaluated explicitly, which yields $g_{\nabla f \parallel}(r) = \beta g(r) \phi''(r)$ and $g_{\nabla f \perp}(r) = \beta g(r) \phi'(r)/r$. All quantities in Eqs. (3.37) and (3.38) are accessible in simulation for both simple and complex fluids and we give further details for their sampling in Appendix B. An in-depth mathematical account of the derivations, in particular concerning the subtle treatment of kinetic contributions, is presented in Ref. [136].

Applications and results

In Ref. [5], we demonstrate that many concrete sum rules that emerge from the hyperforce identity (3.28) via suitable choices of \hat{A} turn out to be useful gauges of sufficient equilibration in simulations. Further, one may utilize certain relations for advanced force-sampling techniques [44, 129–131, 137, 138], which aim to acquire reduced-variance measurements of relevant averages as compared to standard histogram-based methods. Hence, despite their arguably formal character, Noether sum rules are relevant in practice for the interpretation of numerical data, as a means to control both simulation quality and consistency, and for the development of enhanced sampling methods.

These implications are also supported by the findings of Ref. [4], which focuses primarily on the investigation of the novel correlation functions (3.35) and (3.36) and their connection via the Noether sum rule (3.34). We have performed GCMC and adaptive BD [1] simulations for various fluid models with affirmative results for the validity of this identity. From a physical point of view, the quantities $\mathbf{g}_{\nabla f}(r)$ and $\mathbf{g}_{ff}(r)$ carry much information about interactions and forces between particles within the bulk fluid, which are not easily deducible from $g(r)$ alone. Interesting results have been obtained especially for the colloidal gel as modeled by the SW potential, which shows markedly different behavior to simple fluids in the force-gradient and force-force correlations. The sum rule holds generically in equilibrium systems irrespective of the interaction type, which has been exemplified explicitly for Yukawa, soft-sphere dipolar, Stockmayer and Gay-Berne particles, see the supplementary material of Ref. [4] for further details.

In Refs. [6–8], Noether sum rules have proven to be useful in particular by providing constraints for the central functionals of DFT and PFT. The global vanishing of the internal force $\mathbf{F}_{\text{int}}^{\text{tot}} = 0$ could be utilized for the construction of analytic power functionals in Ref. [6], and it served to judge the quality of the trained neural network, see also Sec. 4.2. In Refs. [7, 8], the sum rules (3.31) and (3.32) facilitated to gauge the accuracy of the neural correlation functional in applications as well as the validity of the neural functional calculus (cf. Sec. 4.3).

4 Machine learning and neural functionals

4.1 Neural networks and supervised machine learning procedures

The functional theories presented in Chapter 3 formally allow for the effective description of many-body systems on the level of one-body profiles. However, the crux of both DFT and PFT lies in the determination of the central functional maps, with the focus being usually put on the generating functionals $F_{\text{exc}}[\rho]$ and $P_{\text{exc}}[\rho, \mathbf{J}]$. Most commonly, there is no clear path to the analytic derivation of such functionals for a given type of fluid model. Instead, one usually needs to trace the considered problem back to a known reference system, e.g. the hard sphere fluid (cf. Sec. 3.1), or use crude approximations such as a mean-field ansatz [14] or a gradient expansion (cf. Sec. 3.2). In this chapter, we show how neural networks and supervised machine learning routines facilitate to extract functional relationships effectively from numerical data (we recall the overview of simulation methods in Chapter 2). The proposed hybrid approach can be applied to predict and design inhomogeneous fluids both in and out of equilibrium [6], and the trained neural networks also form the foundation of a fundamental theoretical framework [7, 8]. We give in the following some background to relevant machine learning techniques [139] and to the general training strategy before turning to concrete applications.

Neural networks constitute the central objects of our machine learning method. Formally, they correspond to mathematical functions which map a given input to an output. A standard feedforward neural network may thereby consist of multiple layers $l = 0, \dots, n - 1$, which each take a vector \mathbf{x}_l as input from which an output vector

$$\mathbf{x}_{l+1} = f_l(\Theta_l \cdot \mathbf{x}_l + \mathbf{b}_l) \quad (4.1)$$

of possibly different size is produced and subsequently passed to the next layer. The neural network is parameterized by the matrices $\{\Theta_l\}$ and the vectors $\{\mathbf{b}_l\}$ of each layer, which are referred to as *weights* and *biases*, respectively. Activation functions $\{f_l\}$ realize a nonlinear map from the input $\mathbf{x} = \mathbf{x}_0$ to the output $\mathbf{y}^* = \mathbf{x}_n$ of the neural network and they are applied separately to each node (i.e. component) within a layer.

As can be proven rigorously [140], neural networks serve as universal approximators for a broad class of functions, such that adjustments of the weights and biases suffice to represent virtually arbitrary input-output mappings. Within supervised machine learning, this adaptation happens on the basis of training data and it can be formulated as an optimization problem. Given a dataset of inputs \mathbf{x} and corresponding outputs \mathbf{y} , the

trainable parameters $\{\Theta_l\}$ and $\{\mathbf{b}_l\}$ are iteratively changed with the goal of minimizing a suitable loss function (e.g. the mean squared error), which measures the discrepancy of the neural network predictions $\mathbf{y}^*(\mathbf{x})$ to the known target outputs \mathbf{y} . Successful training then results in a neural network which accurately represents the underlying relationship of the training data and which is also able to generalize faithfully to unseen inputs. Powerful optimization algorithms [141] enable the efficient¹ adaptation of the neural network parameters during training by relying on the use of automatic differentiation for the backpropagation of errors. As automatic differentiation is also relevant in Refs. [7, 8] and in Sec. 4.3 for the development of a neural functional calculus, we give a brief overview of the concept in the following (see Ref. [142] for an in-depth account of differentiable programming).

By applying the chain rule to a composite function, e.g. the neural network composed of the layers (4.1), one generally obtains an iterative relation

$$\frac{\partial y}{\partial x} = \frac{\partial x_n}{\partial x_{n-1}} \frac{\partial x_{n-1}}{\partial x_{n-2}} \cdots \frac{\partial x_1}{\partial x_0} \quad (4.2)$$

as its derivative, where we have simplified for now to the scalar case. To evaluate the right hand side of Eq. (4.2), the fundamental derivatives $\partial x_i / \partial x_{i-1}$, $i = 1, \dots, n$, can be collected either from the inside starting with $\partial x_1 / \partial x_0$ or from the outside starting with $\partial x_n / \partial x_{n-1}$, which constitutes forward and reverse mode differentiation, respectively. We focus here on the latter, which enables to calculate derivatives with respect to multiple variables simultaneously when considering vectorial inputs. Contrary to the case of forward accumulation, reverse mode autodifferentiation requires two computational passes, as the function has to be evaluated first in order to perform a bottom-up agglomeration of derivatives. For this task, implementations commonly use computational graphs to record the encountered subexpressions of a function during the first evaluation. The chain rule (4.2) is then applied programmatically on this graph, based on which the backwards pass (sometimes referred to as backpropagation or pullback) is carried out. Automatic differentiation hence facilitates to obtain the derivative of a function, which may be more general than a closed-form mathematical expression, efficiently in the form of executable code. Importantly, albeit relying on the chain rule (4.2) and on the evaluation of the considered function, autodifferentiation is clearly distinct from numerical differentiation, and it also circumvents the disadvantages that come with the manipulation of symbolic derivatives.²

The application of supervised machine learning is particularly useful for problems where the existence of a certain mapping is guaranteed, but where conventional methods fail to obtain useful representations. This is exactly the case in the functional treatment

¹Besides the prowess of these nonlinear optimizers, modern specialized hardware and comprehensive machine learning frameworks have supported the rapid development of artificial intelligence methods in recent years.

²As Alan Edelman, mathematician and cofounder of the Julia [143] programming language, puts it in one of his MIT lecture notes: “The first time I heard about automatic differentiation, it was easy for me to imagine what it was. I was wrong.” [144]

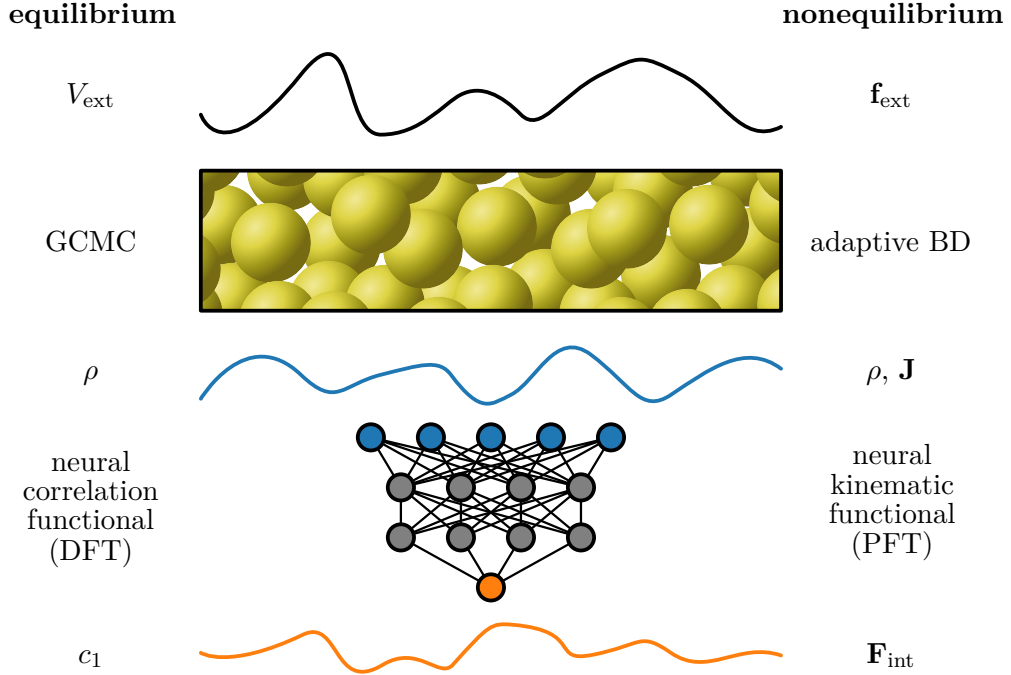


Figure 3: The general workflow for obtaining a neural functional is analogous for equilibrium and nonequilibrium and it consists of a data generation and of a training step. For the generation of reference data, many-body simulations with randomized external environments are performed. This yields a set of one-body profiles, which serve during training of the neural network as input and target output according to the underlying functional theory. After successful training, the neural network acts as a local representation of the respective functional mapping, and it can be applied in various predictive tasks.

of the statistical mechanics of general many-body systems. Here one can leverage on the existence of the functional maps laid out in Secs. 3.1 and 3.2, which are usually very hard to determine though. To make this problem amenable to the utilization of machine learning and neural networks, some care is required in the construction of the specific input-output mappings, and we deviate here from procedures reported in other recent work [145–147]. Our strategy, which results in a flexible and efficient method for the training and application of *neural functionals* [7], is described in the following and Fig. 3 serves as an illustration of the general workflow. A practical survey of the presented techniques is given in Ref. [8] together with more theoretical and physical background (see also Ref. [12] for a hands-on programming tutorial which focuses on the one-dimensional hard rod fluid in equilibrium).

Contrary to most analytic treatments, the generating functionals $F_{\text{exc}}[\rho]$ and $P_{\text{exc}}[\rho, \mathbf{J}]$ are not the primary targets in our machine learning routine. Instead, we rest the investigation on the generated one-body profiles $c_1(\mathbf{r}; [\rho])$ and $\mathbf{F}_{\text{int}}(\mathbf{r}; [\rho, \mathbf{J}])$, as these quantities

are directly accessible in simulation.³ Specifically, $\mathbf{F}_{\text{int}}(\mathbf{r})$ follows from straightforward sampling of the internal force operator [6], and $c_1(\mathbf{r})$ can be recovered pointwise by rearranging Eq. (3.5) and inputting the sampled density profile $\rho(\mathbf{r})$ together with the given chemical and external potential [7]. Crucially, the specific form of the input-output mapping that reflects the functional dependence of these one-body fields is constructed in a *local* manner. Rather than taking the neural network to yield whole profiles at once, we consider the functional relationship separately at individual spatial locations, i.e. in the sense of $c_1(\mathbf{r})[\rho]$ and $\mathbf{F}_{\text{int}}(\mathbf{r})[\rho, \mathbf{J}]$ for each position \mathbf{r} . This local learning approach has numerous essential benefits [6–8]. The most important aspect during training is the much increased data efficiency, as one can extract many input-output pairs (one pair for each discrete location of the sampled profiles) from the data of a single simulation run. A further practical consequence of the local nature of the resulting neural functional is its straightforward applicability to virtually arbitrary system sizes, which is put to use for multiscale predictions, cf. Sec. 4.2. Lastly, invoking knowledge about the physical properties of $c_1(\mathbf{r}; [\rho])$ and $\mathbf{F}_{\text{int}}(\mathbf{r}; [\rho, \mathbf{J}])$ helps to reduce the complexity of the functional mapping and hence to support an efficient training process. For the considered short-ranged interparticle potentials, the functional dependence on the input profiles quickly decays with increasing distance, such that the input range can be restricted to a rather narrow window around the location of interest.

4.2 Application in equilibrium and nonequilibrium

In the following, we apply the techniques laid out in Sec. 4.1 to systems in and out of equilibrium and summarize the main results of Refs. [6, 7]. We specialize in both cases to planar geometry, where the inhomogeneities occur along the z -axis while the x - and y -directions remain translationally invariant. Inhomogeneous environments are realized by imposing an external force profile which only consists of a nonvanishing z -component $f_{\text{ext},z}(z)$. Recall that in equilibrium, this external force is necessarily conservative and it is therefore generated by an external potential $V_{\text{ext}}(z)$ via $f_{\text{ext},z}(z) = -\partial V_{\text{ext}}(z)/\partial z$.

We consider this setup first in nonequilibrium, where $f_{\text{ext},z}(z)$ remains general and may cause a nonvanishing current $J_z(z)$. Note that due to the specific geometry, the current is restricted via the continuity equation (3.17) to spatially constant profiles $J_z(z) = J_{z,0}$. To exemplify our machine learning framework, we consider in Ref. [6] the supercritical LJ fluid at a constant temperature of $k_B T = 1.5\epsilon$. Reference data for training and testing of the neural network is acquired in adaptive BD simulations [1]. Specifically, we generate 1000 inhomogeneous external force profiles via randomized combinations of Fourier components and measure in the respective simulations the profiles $\rho(z)$, $J_z(z)$ and $F_{\text{int},z}(z)$. A neural network is then trained on the grounds

³In equilibrium, one could also try to base the investigation on the internal force density profile, which is connected to the gradient of $c_1(\mathbf{r})$, cf. Eq. (3.21). We opt for the one-body direct correlation function due to practical reasons, e.g. to be able to apply its neural representation directly in the self-consistent iteration (3.9) and in the neural functional calculus (cf. Sec. 4.3).

of this simulation data to capture the functional kinematic map $\rho(z), J_z(z) \rightarrow F_{\text{int},z}(z)$ locally as given by PFT and as described in Sec. 4.1. The network realizes the nonlinear mapping via multiple hidden layers with convolutional and fully-connected architectures [139].

Multiple tests are performed to assess the capabilities of the resulting neural functional for $F_{\text{int},z}(z; [\rho, J_z])$. In an exemplary system with a sinusoidal density profile and different values of the (spatially constant) current, predictions from the neural functional are compared in detail to adaptive BD simulation data. The comparison reveals the validity of the inferred results and the successful determination of adiabatic and superadiabatic contributions, which are quantitatively in line with the reference data and which also shed light on the qualitative agreement of analytic approximations, see Fig. 2 in Ref. [6]. The neural functional can further be applied to determine the external force profile which yields a specific target density and current, cf. Fig. 4 of Ref. [6]. Such inverse design of nonequilibrium flow is feasible by rearrangement of the force balance equation (3.20), in which the internal force density is evaluated via the neural network. This use case hence serves as a performant alternative to the simulation-based and computationally expensive custom flow method [126]. As a special case, one recovers the adiabatic construction, i.e. the determination of an equilibrium reference system with a density profile identical to that of a given nonequilibrium scenario. Additionally, the deficiencies of DDFT due to the adiabatic approximation can be quantified with the availability of the neural functional by comparing results for nonvanishing flow against those obtained from artificially setting $J_z(z) = 0$. The inherent shortcomings of DDFT turn out to be significant in many relevant scenarios. In total, the proposed machine learning method offers a viable means of capturing the kinematic map of PFT, which has versatile use in applications that require the accurate prediction of nonequilibrium internal forces.

We next restrict to the case of systems in thermal equilibrium, where we investigate the representation of $c_1(z; [\rho])$ via a neural network. The availability of fairly accurate analytic approximations (cf. Sec. 3.1) makes the hard sphere fluid a prime candidate for benchmarking the machine learning framework, and we hence put our focus on this fluid model in the following and in Ref. [7]. Reference data is obtained via GCMC simulations (see Sec. 2.1) with randomized values of the chemical potential and inhomogeneous external potentials that are generated from a combination of sinusoidal contributions, linear segments and hard walls. In total, we use 450 simulations for the training of the neural correlation functional and retain the results of 150 additional simulation runs for tests. The specific nature of the neural correlation functional allows for a wide array of applications, and we focus first on the self-consistent calculation of density profiles via neural DFT. The method is based as before on a minimization scheme, e.g. the Picard iteration (3.9), in which $c_1(z; [\rho])$ is now evaluated with the trained neural network instead of being given by an analytic expression. A comparison reveals that neural DFT clearly outperforms implementations of the analytic hard sphere FMT treatment in terms of accuracy of the resulting self-consistent density profiles, which serves as a severe test of the underlying neural network predictions for $c_1(z; [\rho])$. Importantly,

computations involving the neural network remain performant on modern hardware as they are amenable to highly parallel evaluation, e.g. on graphics processing units (GPUs). Together with the local nature of the neural functional mapping, this allows for a significant increase of the system size, which becomes relevant when considering multiscale problems. We exemplify the application “beyond the box” [7] for the case of gravitational sedimentation-diffusion equilibrium, where neural DFT reproduces both the slowly decreasing density within the sedimentation column as well as the layered structure at its boundaries. In contrast, performing many-body simulations of such large-scale systems would hardly be feasible. Neural DFT hence facilitates to fuse the numerical efficacy of DFT calculations with a simulation-based description of internal correlations via the neural correlation functional.

Besides the application for the prediction of density profiles, much more information about the structure and thermodynamics of the underlying fluid can be obtained both in homogeneous and heterogeneous conditions. For this, we describe in the following the implementation of functional calculus on the basis of the neural network, which leads to the development and investigation of a neural functional theory.

4.3 Neural functional theory

Formally, the availability of a thermodynamic potential suffices to describe the thermal equilibrium of a many-body system in its entirety. From the view point of conventional DFT, the grand potential $\Omega[\rho]$, expressed as a functional of the density profile, forms the outset for symbolic calculations in order to derive further results. The excess free energy $F_{\text{exc}}[\rho]$ thereby constitutes the nontrivial term for the description of internal interactions. An example is given by the hierarchy of direct correlation functions, which is obtained via (usually analytic) functional differentiation of $F_{\text{exc}}[\rho]$. As laid out in Sec. 4.1, our machine learning method operates instead on the level of the one-body direct correlation functional $c_1(\mathbf{r}; [\rho])$, and it relies on its representation via a neural network. While this is arguably no less fundamental than an analytic expression of $F_{\text{exc}}[\rho]$, a neural-network-based functional for $c_1(\mathbf{r}; [\rho])$ constitutes a different starting point for derivations, and symbolic calculations are no longer suitable to access related quantities.

In the following, we show alternatives to standard analytic treatments in order to implement functional differentiation and integration methods that remain applicable to the neural correlation functional. For an efficient and accurate evaluation of functional derivatives, we refer to the use of automatic differentiation as laid out in Sec. 4.1. Instead of applying autodifferentiation with respect to the network parameters as was the case during training, we here perform the derivative with respect to the input density profile.⁴ This gives direct access to the two-body direct correlation functional $c_2(\mathbf{r}, \mathbf{r}'; [\rho])$ within the considered geometry up to normalization with the discretization

⁴Machine learning libraries provide ready-to-use implementations of reverse mode automatic differentiation, which make this task feasible in a few lines of code, see Refs. [11, 12] for examples.

interval of the input layer [7, 8, 11, 12].

To complete the calculus, we invoke functional line integration [7, 8, 148, 149], which is the inverse operation of functional differentiation and which amounts formally to performing a line integral in function space. By choosing a linear parametrization⁵ $\rho_a(\mathbf{r}) = a\rho(\mathbf{r})$, one obtains

$$\beta F_{\text{exc}}[\rho] = - \int d\mathbf{r} \rho(\mathbf{r}) \int_0^1 da c_1(\mathbf{r}; [\rho_a]) \quad (4.3)$$

as an explicit and practically accessible expression to recover the excess free energy from a given one-body direct correlation functional, which constitutes the inverse of Eq. (3.6). The functional line integral (4.3) can be evaluated straightforwardly with the neural network by discretization of the integrals [11, 12]. We put the neural functional calculus to use and summarize in the following how the presented techniques enable the formulation of a self-contained neural functional theory.

Gaining access to $c_2(\mathbf{r}, \mathbf{r}', [\rho])$ allows to investigate in detail the pair structure of a fluid. This is already highly relevant in bulk conditions with constant density $\rho(z) = \rho_b$; we specialize here again to the considered planar geometry. The bulk direct correlation function $\bar{c}_2^b(z)$ retains only one spatial degree of freedom due to translational invariance, and it follows directly from the autodifferentiated neural network (note that we obtain the planar projection due to our geometrical setup, which is indicated by the overbar). By transforming to Fourier space, the total correlation function $\tilde{h}(k)$ can be calculated via the OZ equation (3.8), from which the static structure factor is obtained as $S(k) = 1 + \rho_b \tilde{h}(k)$. The latter is central for characterizing two-body correlations in a bulk fluid, and its inverse Fourier transform is directly related to the radial distribution function $g(r)$. We have hence demonstrated these fundamental objects to be accessible to high accuracy by applying the neural functional in the presented calculus [7]. In principle, the hierarchy of direct correlation functions follows from successive autodifferentiation, and we have exemplified this in the supplementary material of Ref. [7] by considering the three-body member $\bar{c}_3^b(z, z')$ in bulk. Recall that imposing bulk conditions serves as a nontrivial test of the neural functional since its training only included inhomogeneous reference data.

A further quantity of interest in a homogeneous fluid is its equation of state, which can be obtained via multiple routes [7] from the neural network, e.g. by evaluating $F_{\text{exc}}[\rho_b]$ with the functional line integral (4.3). Comparison to the pertinent literature reveals that the neural equation of state for the well-studied hard sphere fluid outperforms highly accurate analytic results such as the Carnahan-Starling equation of state [150], cf. Fig. 4 in Ref. [7]. Additionally, we find our results to be on par with simulation-based equations of state [151]. This serves as a further verification of the validity of the neural functional calculus, which hence spans up the complete bulk theory of the considered fluid.

⁵Different choices for the parametrization of the functional line integral are conceivable and lead in general to different explicit results akin to Eq. (4.3).

In inhomogeneous environments, Eq. (4.3) remains applicable and allows to recover precise free energy values, which demonstrates the formal equivalence of our method to the usual treatment of $F_{\text{exc}}[\rho]$ as the central functional object. The two-body direct correlation function $\bar{c}_2(z, z'; [\rho])$ retains the second spatial coordinate in heterogeneous planar environments, and it may be utilized both as a standalone object, but also for further severe tests of the neural functional. For instance, verifying the adherence to the symmetry requirement $\bar{c}_2(z, z'; [\rho]) = \bar{c}_2(z', z; [\rho])$ and to the Noether sum rules (3.31) and (3.32) facilitates to check the validity of the neural functional results [7, 8]. Judging the inference quality of a neural network for unseen data is in general a difficult issue,⁶ and we adopt here a line of action which is arguably inverse to that of physics-informed machine learning [155]. Instead of prescribing certain physical relations during training, e.g. in the form of an additional loss term, we base the training solely on the encountered simulation data and determine only a posteriori the conformance of the neural functional to identities that arise from the underlying physics. This yields the possibility of consistency checks at the time of inference, which gives quantitative guidance for the accuracy and uncertainty of predictions. The merit of the neural functional theory is therefore not only its standalone application to gain insight into the physics of the underlying fluid, but also its pertinence for the verification of neural network results.

⁶Some other machine learning techniques such as Bayesian inference methods [152] provide intrinsic uncertainty measures and have been applied recently in a classical DFT context [153, 154].

5 Conclusions and outlook

In this thesis and in the corresponding publications [1–8], we have studied different means for the investigation of soft matter systems in and out of equilibrium. Specifically, we have taken many-body simulations, functional theories and machine learning as our methodological cornerstones and have considered applications to concrete problems as well as the development of generic techniques to interrelate the different approaches. In the examined soft matter systems, which range from simple reference models to complex fluid types, we have focused on describing and predicting the arising internal forces and correlations, in particular for cases where spatial inhomogeneity is introduced. Accurately determining equilibrated or driven states of inhomogeneous fluids is a topical problem that necessitates the use of various coarse-graining techniques to address the interplay of the constituting particles that comprise the coupled many-body system.

Particle-based simulations serve as a powerful bottom-up approach for this task, and we have given in Chapter 2 a survey of different pertinent methods. Whereas Monte Carlo techniques are well-established for predicting equilibrium properties, going to nonequilibrium requires to specify the dynamical behavior of the many-body system, which can then be tackled numerically. BD provides a suitable description particularly for the motion of colloidal particles by incorporating dissipative and fluctuating forces of an implicit solvent in the overdamped Langevin equations of motion. However, the stochastic nature renders numerical treatments challenging, and one is typically left with simplistic but inefficient and oftentimes even unreliable integration schemes. We have presented in this work adaptive BD [1] as a feasible alternative to conventional BD simulations. The method is centered around a flexible adaptive timestepping algorithm that incorporates the correct handling of random processes [93], which is crucial for retaining the essential properties of Brownian motion.

The advantages of adaptive BD over conventional methods in terms of efficiency, accuracy and stability have been exemplified both in simple [1, 5, 6] and complex fluids [2, 4], where the latter pose no practical difficulties for its application. Useful extensions of the method could incorporate orientational diffusion and self-propelled motion, as is relevant e.g. for the simulation of various types of active matter [156–159]. Conceptually, the inclusion of additional forces and random processes in the equations of motion is not detrimental to the application of the fundamental ideas of adaptive BD (technical details such as the specific adaptation criterion might have to be adjusted). Similarly, a possible future task is the implementation of hydrodynamic interactions [49, 160] that are mediated by the implicit solvent. While rejection sampling with memory remains applicable for the construction of the random process, the embedded integration schemes (2.13) and (2.14) must be reconsidered due to more intricate stochastic forces

that influence numerical methods in their order of strong convergence.

The presented simulation methods are useful besides their standalone application also for the verification and discovery of theoretical results. We have used simulation-based investigations specifically in tandem with functional theories, which provide formally exact coarse-grained descriptions both for equilibrium and nonequilibrium systems in terms of functional relationships on the level of one-body fields. The density profile $\rho(\mathbf{r})$ is unambiguously the central quantity for determining fluid equilibria within DFT, where the nontrivial effects of specific interparticle interactions are captured by a universal one-body direct correlation functional $c_1(\mathbf{r}; [\rho])$. A recent reformulation that detours to forces (“force-DFT” [61]) provides an alternative to the conventional formalism regarding the concrete evaluation of this functional. With simulation data serving as reference, we have compared both DFT routes [3] for the case of the hard sphere fluid. A linear combination of standard and force-based DFT [3, 61] leads to improved results for the density profile as compared to the predictions of the individual methods, which shows the practical utility of force-DFT besides its formal relevance. It would be interesting in the future to evaluate force-DFT for other fluid models and to perform further quantitative assessments of superadiabatic DDFT [123, 124], which constitutes its nonequilibrium extension.

PFT offers a genuine functional nonequilibrium theory and it establishes a kinematic map from the history of the density and current profiles to the instantaneous internal force density profile $\mathbf{F}_{\text{int}}(\mathbf{r}, t; [\rho, \mathbf{J}])$. For simplification, we have specialized here to planar steady states, for which PFT facilitates to investigate the arising superadiabatic (out-of-equilibrium) force contributions, which generally consist of structural and flow components. As compared to the case of simple fluids [120, 122], an unusual phenomenology of these contributions could be observed in an inhomogeneously sheared colloidal gel former [2] modeled by a modified Stillinger-Weber potential [74, 75]. Despite the intricate behavior of this complex fluid, a simple analytic power functional obtained from a gradient expansion accounts for the occurring superadiabatic forces, which demonstrates the generality of the PFT formalism.

Besides the development of concrete analytic functional approximations, we have also taken advantage of fundamental invariance properties of phase space in order to derive exact sum rules which interrelate averages of different phase space functions. The application of Noether’s theorem lies at the core of these derivations, which result in a set of hyperforce balance equations [5] and in relations that feature novel types of pair correlation functions [4]. The hyperforce framework can be put to use in simulations, where it is directly connected to recent developments regarding reduced-variance sampling methods [5, 129–131]. We emphasize in this context that Noether invariance naturally gives rise to observables that would arguably not be considered ad hoc, but which can be endowed with well-founded physical meaning. Regarding the characterization of pair correlations in bulk, we have showcased sum rules that contain besides the standard radial distribution function also force-force and force-gradient correlation functions [4]. The validity of these sum rules has been verified in simulation for fluids consisting of various isotropic and anisotropic particle models. Commonly, the novel types of pair

correlation functions give additional insight into the structure of the underlying bulk fluid that goes far beyond the information provided by the radial distribution function alone.

Although conceptually powerful, the use of DFT and PFT is limited in concrete applications by the availability of suitable approximations for the central functionals. We have hence developed generic machine learning techniques to remedy this restriction. Specifically, neural networks act in our framework as representations of functional maps on the one-body level after being trained with simulation data of inhomogeneous systems. The resulting neural functionals can be applied straightforwardly as surrogates in the respective theories, which leads to substantially improved results compared to conventional analytic treatments. In nonequilibrium, we have exemplified the machine learning routine for a uniaxially driven Lennard-Jones fluid [6], where adaptive BD [1] simulation data served as reference during training. Various applications of the neural network demonstrate the utility of this approach, e.g. for the accurate prediction of superadiabatic forces and for the inverse design of nonequilibrium flow. We recall that a crucial prerequisite for the success of this method is the *local* representation of the kinematic mapping via the neural network, which hence also remains applicable to systems of different sizes.

In equilibrium, attaining analytic density functionals from first principles for certain reference models is not as bleak as in nonequilibrium. For instance, FMT provides a set of accurate approximations for the description of hard sphere fluids. Nevertheless, using the machine learning framework in conjunction with randomized GCMC simulation data still supersedes state-of-the-art FMT in accuracy [7] when applied in the self-consistent calculation of density profiles. Due to the local nature of the neural network, this neural DFT generalizes straightforwardly to multiscale predictions, as is relevant e.g. for predicting gravitational sedimentation-diffusion equilibrium. Importantly, the neural correlation functional that represents $c_1(\mathbf{r}; [\rho])$ acts not only as an interpolation device, but it rather forms a genuine mathematical object that spans up a self-contained neural functional theory. Via automatic differentiation and functional line integration, related quantities such as higher-order correlation functions and the free energy can be accessed, which reveal the complete structure and thermodynamics of the fluid both in homogeneous and heterogeneous environments [7]. We have provided a survey of the neural functional theory also for the one-dimensional hard rod fluid [8], where we exemplify the underlying concepts of simulation, DFT and machine learning.

The neural functional framework is particularly useful when applied to different fluid models which lack satisfactory analytic treatments. This has been illustrated for the supercritical Lennard-Jones fluid [7], where results clearly outperform conventional theoretical approaches that combine a hard sphere reference for the repulsive part of the interactions with a mean-field description of attraction. In the ongoing research, we aim at including the parametric temperature dependence in the neural functional theory to account for the liquid-vapor phase transition, wetting and drying on substrates [16, 114] and critical behavior. Although seemingly daunting at first sight, focusing on a well-defined functional mapping of (commonly short-ranged) direct correlations is

arguably a promising approach to tackle such emergent phenomena. Recall that even simple mean-field treatments recover these effects qualitatively and sometimes even semi-quantitatively, and that our neural functional framework offers a way to overcome remaining quantitative discrepancies via the controlled incorporation of simulation data. In this regard, the data-driven discovery of functional mappings bears good prospects to address such phenomena also in beyond-simple fluids, as relevant e.g. for dealing with the topical problem of predicting solvation in water accurately across length scales [161, 162].

Lastly, it might be feasible to extend the neural functional framework to problems that involve additional degrees of freedom. This is pertinent for instance to include the orientation dependence of anisotropic particles and molecules [163, 164] as well as in generalized spatial geometries. As an intermediate step of the latter, we retain planar geometry in our ongoing research but incorporate nonequilibrium flow with nonvanishing lateral components. Recall that in this work and in Ref. [6], we have considered uniaxial flow, where the z -component is the only nontrivial contribution in the functional mapping of the internal force density profile $F_{\text{int},z}(z; [\rho, J_z])$. For representing additional x - and y -components in the more general mapping $\mathbf{F}_{\text{int}}(z; [\rho, \mathbf{J}])$, the neural network must be modified to take the four profiles $\rho(z)$, $J_x(z)$, $J_y(z)$ and $J_z(z)$ as functional input in order to infer the three components of the local internal force, as given by three scalar values of the output layer. Apart from this modification, the machine learning routines proceed analogously and yield promising results in predictive applications, in the inverse design via custom flow and in an extension to include time dependence [165]. Exploiting symmetry properties has proven to be crucial in this constrained case already, and it is expected to be particularly relevant when considering full three-dimensional inhomogeneity both in and out of equilibrium. Besides the use of data augmentation [139], equivariant neural networks [166, 167] and their recent applications in the natural sciences [168, 169] seem favorable for taming the curse of dimensionality that comes with a fully generalized geometrical setup.

Bibliography

- [1] F. Sammüller and M. Schmidt, “Adaptive Brownian dynamics”, *J. Chem. Phys.* **155**, 134107 (2021), see Sec. 6.3.
- [2] F. Sammüller, D. de las Heras, and M. Schmidt, “Inhomogeneous steady shear dynamics of a three-body colloidal gel former”, *J. Chem. Phys.* **158**, 054908 (2023), see Sec. 6.4.
- [3] F. Sammüller, S. Hermann, and M. Schmidt, “Comparative study of force-based classical density functional theory”, *Phys. Rev. E* **107**, 034109 (2023), see Sec. 6.5.
- [4] F. Sammüller, S. Hermann, D. de las Heras, and M. Schmidt, “Noether-constrained correlations in equilibrium liquids”, *Phys. Rev. Lett.* **130**, 268203 (2023), see Sec. 6.6.
- [5] S. Robitschko, F. Sammüller, M. Schmidt, and S. Hermann, “Hyperforce balance via thermal Noether invariance of any observable”, *Commun. Phys.* **7**, 103 (2024), see Sec. 6.7.
- [6] D. de las Heras, T. Zimmermann, F. Sammüller, S. Hermann, and M. Schmidt, “Perspective: How to overcome dynamical density functional theory”, *J. Phys. Condens. Matter* **35**, 271501 (2023), see Sec. 6.8.
- [7] F. Sammüller, S. Hermann, D. de las Heras, and M. Schmidt, “Neural functional theory for inhomogeneous fluids: Fundamentals and applications”, *Proc. Natl. Acad. Sci.* **120**, e2312484120 (2023), see Sec. 6.9.
- [8] F. Sammüller, S. Hermann, and M. Schmidt, “Why neural functionals suit statistical mechanics”, *J. Phys. Condens. Matter* **36**, 243002 (2024), see Sec. 6.10.
- [9] F. Sammüller, *MBD, A simulation tool for classical many-body dynamics*, <https://gitlab.uni-bayreuth.de/bt306964/mbd>.
- [10] F. Sammüller, *ClassicalDFT.jl, A Julia package for classical density functional theory*, <https://gitlab.uni-bayreuth.de/bt306964/ClassicalDFT.jl>.
- [11] F. Sammüller, S. Hermann, D. de las Heras, and M. Schmidt, *Neural functional theory for inhomogeneous fluids: Fundamentals and applications*, deposited in Zenodo, doi:10.5281/zenodo.8380003, 2023.
- [12] F. Sammüller, *Neural functional theory for inhomogeneous fluids – Tutorial*, <https://github.com/sfalmo/NeuralDFT-Tutorial>, see Appendix C.
- [13] J. van der Gucht, “Grand challenges in soft matter physics”, *Front. Phys.* **6**, 87 (2018).

-
- [14] J.-P. Hansen and I. R. McDonald, *Theory of simple liquids*, 4th ed. (Academic Press, Oxford, 2013).
- [15] P. G. de Gennes, “Wetting: statics and dynamics”, *Rev. Mod. Phys.* **57**, 827–863 (1985).
- [16] R. Evans, M. C. Stewart, and N. B. Wilding, “Drying and wetting transitions of a Lennard-Jones fluid: Simulations and density functional theory”, *J. Chem. Phys.* **147**, 044701 (2017).
- [17] J. A. Barker and D. Henderson, “What is ‘liquid’? Understanding the states of matter”, *Rev. Mod. Phys.* **48**, 587–671 (1976).
- [18] V. F. Weisskopf, “About liquids”, *Trans. N. Y. Acad. Sci.* **38**, 202–218 (1977).
- [19] P. G. de Gennes, “Soft matter”, *Rev. Mod. Phys.* **64**, 645–648 (1992).
- [20] R. Evans, D. Frenkel, and M. Dijkstra, “From simple liquids to colloids and soft matter”, *Phys. Today* **72**, 38–39 (2019).
- [21] S. R. Nagel, “Experimental soft-matter science”, *Rev. Mod. Phys.* **89**, 025002 (2017).
- [22] W. A. Ducker, T. J. Senden, and R. M. Pashley, “Direct measurement of colloidal forces using an atomic force microscope”, *Nature* **353**, 239–241 (1991).
- [23] M. Schulz and J. L. Keddie, “A critical and quantitative review of the stratification of particles during the drying of colloidal films”, *Soft Matter* **14**, 6181–6197 (2018).
- [24] C. P. Royall, A. A. Louis, and H. Tanaka, “Measuring colloidal interactions with confocal microscopy”, *J. Chem. Phys.* **127**, 044507 (2007).
- [25] C. P. Royall, J. Dzubiella, M. Schmidt, and A. van Blaaderen, “Nonequilibrium sedimentation of colloids on the particle scale”, *Phys. Rev. Lett.* **98**, 188304 (2007).
- [26] J. Dong, F. Turci, R. L. Jack, M. A. Faers, and C. P. Royall, “Direct imaging of contacts and forces in colloidal gels”, *J. Chem. Phys.* **156**, 214907 (2022).
- [27] B. Chu, “Laser light scattering”, *Annu. Rev. Phys. Chem.* **21**, 145–174 (1970).
- [28] A. J. Greenfield, J. Wellendorf, and N. Wisner, “X-ray determination of the static structure factor of liquid Na and K”, *Phys. Rev. A* **4**, 1607–1616 (1971).
- [29] J. L. Yarnell, M. J. Katz, R. G. Wenzel, and S. H. Koenig, “Structure factor and radial distribution function for liquid argon at 85 °K”, *Phys. Rev. A* **7**, 2130–2144 (1973).
- [30] P. N. Pusey and W. van Megen, “Phase behaviour of concentrated suspensions of nearly hard colloidal spheres”, *Nature* **320**, 340–342 (1986).
- [31] G. Bryant, S. R. Williams, L. Qian, I. K. Snook, E. Perez, and F. Pincet, “How hard is a colloidal ‘hard-sphere’ interaction?”, *Phys. Rev. E* **66**, 060501 (2002).

- [32] M. E. Leunissen, C. G. Christova, A.-P. Hynninen, C. P. Royall, A. I. Campbell, A. Imhof, M. Dijkstra, R. van Roij, and A. van Blaaderen, “Ionic colloidal crystals of oppositely charged particles”, *Nature* **437**, 235–240 (2005).
- [33] C. P. Royall, W. C. K. Poon, and E. R. Weeks, “In search of colloidal hard spheres”, *Soft Matter* **9**, 17–27 (2013).
- [34] D. Dendukuri, D. C. Pregibon, J. Collins, T. A. Hatton, and P. S. Doyle, “Continuous-flow lithography for high-throughput microparticle synthesis”, *Nat. Mater.* **5**, 365–369 (2006).
- [35] A. van Blaaderen, “Colloids get complex”, *Nature* **439**, 545–546 (2006).
- [36] D. Mukhija and M. J. Solomon, “Nematic order in suspensions of colloidal rods by application of a centrifugal field”, *Soft Matter* **7**, 540–545 (2011).
- [37] M. F. Brown, “Soft matter in lipid–protein interactions”, *Annu. Rev. Biophys.* **46**, 379–410 (2017).
- [38] T. A. Vilgis, “Soft matter food physics—the physics of food and cooking”, *Rep. Prog. Phys.* **78**, 124602 (2015).
- [39] H. M. van der Kooij and J. Sprakel, “Watching paint dry, more exciting than it seems”, *Soft Matter* **11**, 6353–6359 (2015).
- [40] S. A. Wissing and R. H. Müller, “A novel sunscreen system based on tocopherol acetate incorporated into solid lipid nanoparticles”, *Int. J. Cosmet. Sci.* **23**, 233–243 (2001).
- [41] F. Deplace, C. Carelli, S. Mariot, H. Retsos, A. Chateauminois, K. Ouzineb, and C. Creton, “Fine tuning the adhesive properties of a soft nanostructured adhesive with rheological measurements”, *J. Adhes.* **85**, 18–54 (2009).
- [42] E. Tekin, P. J. Smith, and U. S. Schubert, “Inkjet printing as a deposition and patterning tool for polymers and inorganic particles”, *Soft Matter* **4**, 703–713 (2008).
- [43] N. Metropolis, A. W. Rosenbluth, M. N. Rosenbluth, A. H. Teller, and E. Teller, “Equation of state calculations by fast computing machines”, *J. Chem. Phys.* **21**, 1087–1092 (1953).
- [44] D. Frenkel and B. Smit, *Understanding molecular simulation: From algorithms to applications*, 3rd ed. (Academic Press, Oxford, 2023).
- [45] N. Tchipev, S. Seckler, M. Heinen, J. Vrabec, F. Gratl, M. Horsch, M. Bernreuther, C. W. Glass, C. Niethammer, N. Hammer, B. Krischok, M. Resch, D. Kranzlmüller, H. Hasse, H.-J. Bungartz, and P. Neumann, “TweTriS: twenty trillion-atom simulation”, *Int. J. High Perform. Comput. Appl.* **33**, 838–854 (2019).
- [46] P. J. Rossky, J. D. Doll, and H. L. Friedman, “Brownian dynamics as smart Monte Carlo simulation”, *J. Chem. Phys.* **69**, 4628–4633 (1978).

-
- [47] R. Zwanzig, *Nonequilibrium statistical mechanics* (Oxford University Press, New York, 2001).
- [48] E. Frey and K. Kroy, “Brownian motion: a paradigm of soft matter and biological physics”, *Ann. Phys.* **517**, 20–50 (2005).
- [49] D. L. Ermak and J. A. McCammon, “Brownian dynamics with hydrodynamic interactions”, *J. Chem. Phys.* **69**, 1352–1360 (1978).
- [50] A. Iniesta and J. de la Torre, “A second-order algorithm for the simulation of the Brownian dynamics of macromolecular models”, *J. Chem. Phys.* **92**, 2015–2018 (1990).
- [51] M. Fixman, “Implicit algorithm for Brownian dynamics of polymers”, *Macromolecules* **19**, 1195–1204 (1986).
- [52] P. E. Kloeden and E. Platen, *Numerical solution of stochastic differential equations* (Springer, Berlin, Heidelberg, 1992).
- [53] R. Evans, “The nature of the liquid-vapour interface and other topics in the statistical mechanics of non-uniform, classical fluids”, *Adv. Phys.* **28**, 143–200 (1979).
- [54] M. Schmidt and J. M. Brader, “Power functional theory for Brownian dynamics”, *J. Chem. Phys.* **138**, 214101 (2013).
- [55] M. Schmidt, “Power functional theory for many-body dynamics”, *Rev. Mod. Phys.* **94**, 015007 (2022).
- [56] S. Hermann and M. Schmidt, “Noether’s theorem in statistical mechanics”, *Commun. Phys.* **4**, 176 (2021).
- [57] S. Hermann, “Forces and symmetries in the statistical mechanics of active and thermal many-body systems”, PhD thesis (Universität Bayreuth, 2022).
- [58] S. Hermann and M. Schmidt, “Why Noether’s theorem applies to statistical mechanics”, *J. Phys.: Condens. Matter* **34**, 213001 (2022).
- [59] S. Hermann and M. Schmidt, “Variance of fluctuations from Noether invariance”, *Commun. Phys.* **5**, 276 (2022).
- [60] J. K. Percus, “Equilibrium state of a classical fluid of hard rods in an external field”, *J. Statist. Phys.* **15**, 505–511 (1976).
- [61] S. M. Tschopp, F. Sammüller, S. Hermann, M. Schmidt, and J. M. Brader, “Force density functional theory in- and out-of-equilibrium”, *Phys. Rev. E* **106**, 014115 (2022).
- [62] B. J. Alder, “Studies in molecular dynamics. III. A mixture of hard spheres”, *J. Chem. Phys.* **40**, 2724–2730 (1964).
- [63] A. Scala, T. Voigtmann, and C. D. Michele, “Event-driven Brownian dynamics for hard spheres”, *J. Chem. Phys.* **126**, 134109 (2007).

- [64] C. P. Royall, P. Charbonneau, M. Dijkstra, J. Russo, F. Smallenburg, T. Speck, and C. Valeriani, “Colloidal hard spheres: triumphs, challenges and mysteries”, 2023, arXiv:2305.02452.
- [65] J. A. Barker and D. Henderson, “Perturbation theory and equation of state for fluids. II. A successful theory of liquids”, *J. Chem. Phys.* **47**, 4714–4721 (1967).
- [66] D. Frenkel, “Order through disorder: entropy strikes back”, *Phys. World* **6**, 24–25 (1993).
- [67] B. J. Alder and T. E. Wainwright, “Phase transition for a hard sphere system”, *J. Chem. Phys.* **27**, 1208–1209 (1957).
- [68] A. P. Gast and W. B. Russel, “Simple ordering in complex fluids”, *Phys. Today* **51**, 24–30 (1998).
- [69] A. Trokhymchuk and J. Alejandre, “Computer simulations of liquid/vapor interface in Lennard-Jones fluids: some questions and answers”, *J. Chem. Phys.* **111**, 8510–8523 (1999).
- [70] J. D. Weeks, D. Chandler, and H. C. Andersen, “Role of repulsive forces in determining the equilibrium structure of simple liquids”, *J. Chem. Phys.* **54**, 5237–5247 (1971).
- [71] F. H. Stillinger and T. A. Weber, “Computer simulation of local order in condensed phases of silicon”, *Phys. Rev. B* **31**, 5262–5271 (1985).
- [72] V. Molinero and E. B. Moore, “Water modeled as an intermediate element between carbon and silicon”, *J. Phys. Chem. B* **113**, 4008–4016 (2008).
- [73] M. K. Coe, R. Evans, and N. B. Wilding, “The coexistence curve and surface tension of a monatomic water model”, *J. Chem. Phys.* **156**, 154505 (2022).
- [74] S. Saw, N. L. Ellegaard, W. Kob, and S. Sastry, “Structural relaxation of a gel modeled by three body interactions”, *Phys. Rev. Lett.* **103**, 248305 (2009).
- [75] S. Saw, N. L. Ellegaard, W. Kob, and S. Sastry, “Computer simulation study of the phase behavior and structural relaxation in a gel-former modeled by three-body interactions”, *J. Chem. Phys.* **134**, 164506 (2011).
- [76] M. Deserno and C. Holm, “How to mesh up Ewald sums. I. A theoretical and numerical comparison of various particle mesh routines”, *J. Chem. Phys.* **109**, 7678–7693 (1998).
- [77] M. O. Robbins, K. Kremer, and G. S. Grest, “Phase diagram and dynamics of Yukawa systems”, *J. Chem. Phys.* **88**, 3286–3312 (1988).
- [78] M. J. Stevens and G. S. Grest, “Structure of soft-sphere dipolar fluids”, *Phys. Rev. E* **51**, 5962–5975 (1995).
- [79] S. H. L. Klapp, “Dipolar fluids under external perturbations”, *J. Phys. Condens. Matter* **17**, R525–R550 (2005).

-
- [80] J. G. Gay and B. J. Berne, “Modification of the overlap potential to mimic a linear site–site potential”, *J. Chem. Phys.* **74**, 3316–3319 (1981).
- [81] W. K. Hastings, “Monte Carlo sampling methods using Markov chains and their applications”, *Biometrika* **57**, 97–109 (1970).
- [82] J.-S. Wang and R. H. Swendsen, “Transition matrix Monte Carlo method”, *J. Stat. Phys.* **106**, 245–285 (2002).
- [83] L. L. Treffenstädt and M. Schmidt, “Universality in driven and equilibrium hard sphere liquid dynamics”, *Phys. Rev. Lett.* **126**, 058002 (2021).
- [84] L. L. Treffenstädt, T. Schindler, and M. Schmidt, “Dynamic decay and superadiabatic forces in the van Hove dynamics of bulk hard sphere fluids”, *SciPost Phys.* **12**, 133 (2022).
- [85] P. Langevin, “Sur la théorie du mouvement brownien”, *C. R. Acad. Sci. Paris* **146**, 530–533 (1908).
- [86] G. Maruyama, “Continuous Markov processes and stochastic equations”, *Rend. Circ. Mat. Palermo* **4**, 48–90 (1955).
- [87] J. C. Butcher, *Numerical methods for ordinary differential equations*, 3rd ed. (Wiley, Chichester, 2016).
- [88] G. N. Mil’shtejn, “Approximate integration of stochastic differential equations”, *Theory Probab. Its Appl.* **19**, 557–562 (1975).
- [89] K. Burrage and P. Burrage, “High strong order explicit Runge-Kutta methods for stochastic ordinary differential equations”, *Appl. Numer. Math.* **22**, 81–101 (1996).
- [90] B. Leimkuhler and C. Matthews, “Rational construction of stochastic numerical methods for molecular sampling”, *Appl. Math. Res. Express* **2013**, 34–56 (2012).
- [91] B. Leimkuhler, C. Matthews, and M. V. Tretyakov, “On the long-time integration of stochastic gradient systems”, *Proc. R. Soc. A* **470**, 20140120 (2014).
- [92] E. Fehlberg, “Klassische Runge-Kutta-Formeln vierter und niedrigerer Ordnung mit Schrittweiten-Kontrolle und ihre Anwendung auf Wärmeleitungsprobleme”, *Computing* **6**, 61–71 (1970).
- [93] C. Rackauckas and Q. Nie, “Adaptive methods for stochastic differential equations via natural embeddings and rejection sampling with memory”, *Discrete Contin. Dyn. Syst. - B* **22**, 2731–2761 (2017).
- [94] C. Rackauckas and Q. Nie, “DifferentialEquations.jl – a performant and feature-rich ecosystem for solving differential equations in Julia”, *J. Open Res. Softw.* **5**, 15 (2017).
- [95] B. He, I. Martin-Fabiani, R. Roth, G. I. Tóth, and A. J. Archer, “Dynamical density functional theory for the drying and stratification of binary colloidal dispersions”, *Langmuir* **37**, 1399–1409 (2021).

- [96] N. C. X. Stuhlmüller, T. M. Fischer, and D. de las Heras, “Colloidal transport in twisted lattices of optical tweezers”, *Phys. Rev. E* **106**, 034601 (2022).
- [97] N. C. X. Stuhlmüller, F. Farrokhzad, P. Kuświk, F. Stobiecki, M. Urbaniak, S. Akhundzada, A. Ehresmann, T. M. Fischer, and D. de las Heras, “Simultaneous and independent topological control of identical microparticles in non-periodic energy landscapes”, *Nat. Commun.* **14**, 7517 (2023).
- [98] A. J. Bryer, J. S. Rey, and J. R. Perilla, “Performance efficient macromolecular mechanics via sub-nanometer shape based coarse graining”, *Nat. Commun.* **14**, 2014 (2023).
- [99] A. Muñoz-Chicharro, L. W. Votapka, R. E. Amaro, and R. C. Wade, “Brownian dynamics simulations of biomolecular diffusional association processes”, *WIREs Comput. Mol. Sci.* **13**, e1649 (2022).
- [100] L. S. Ornstein and F. Zernike, “Accidental deviations of density and opalescence at the critical point of a single substance”, *Proc. Sect. Sci. K. Ned. Akad. Wet. Amst.* **17**, 793–806 (1914).
- [101] S. M. Tschopp and J. M. Brader, “Fundamental measure theory of inhomogeneous two-body correlation functions”, *Phys. Rev. E* **103**, 042103 (2021).
- [102] M. Edelmann and R. Roth, “A numerical efficient way to minimize classical density functional theory”, *J. Chem. Phys.* **144**, 074105 (2016).
- [103] Y. Rosenfeld, “Free-energy model for the inhomogeneous hard-sphere fluid mixture and density-functional theory of freezing”, *Phys. Rev. Lett.* **63**, 980–983 (1989).
- [104] E. Kierlik and M. L. Rosinberg, “Free-energy density functional for the inhomogeneous hard-sphere fluid: application to interfacial adsorption”, *Phys. Rev. A* **42**, 3382–3387 (1990).
- [105] S. Phan, E. Kierlik, M. L. Rosinberg, B. Bildstein, and G. Kahl, “Equivalence of two free-energy models for the inhomogeneous hard-sphere fluid”, *Phys. Rev. E* **48**, 618–620 (1993).
- [106] R. Roth, R. Evans, A. Lang, and G. Kahl, “Fundamental measure theory for hard-sphere mixtures revisited: the White Bear version”, *J. Phys. Condens. Matter* **14**, 12063–12078 (2002).
- [107] H. Hansen-Goos and R. Roth, “Density functional theory for hard-sphere mixtures: the White Bear version mark II”, *J. Phys. Condens. Matter* **18**, 8413–8425 (2006).
- [108] R. Roth, “Fundamental measure theory for hard-sphere mixtures: a review”, *J. Phys. Condens. Matter* **22**, 063102 (2010).
- [109] R. Evans and M. C. Stewart, “The local compressibility of liquids near non-adsorbing substrates: a useful measure of solvophobicity and hydrophobicity?”, *J. Phys. Condens. Matter* **27**, 194111 (2015).

-
- [110] T. Eckert, N. C. X. Stuhlmüller, F. Sammüller, and M. Schmidt, “Fluctuation profiles in inhomogeneous fluids”, *Phys. Rev. Lett.* **125**, 268004 (2020).
- [111] M. K. Coe, “Hydrophobicity across length scales: the role of surface criticality”, PhD thesis (University of Bristol, 2021).
- [112] T. Eckert, N. C. X. Stuhlmüller, F. Sammüller, and M. Schmidt, “Local measures of fluctuations in inhomogeneous liquids: statistical mechanics and illustrative applications”, *J. Phys. Condens. Matter* **35**, 425102 (2023).
- [113] R. Evans and N. B. Wilding, “Quantifying density fluctuations in water at a hydrophobic surface: evidence for critical drying”, *Phys. Rev. Lett.* **115**, 016103 (2015).
- [114] R. Evans, M. C. Stewart, and N. B. Wilding, “A unified description of hydrophilic and superhydrophobic surfaces in terms of the wetting and drying transitions of liquids”, *Proc. Natl. Acad. Sci.* **116**, 23901–23908 (2019).
- [115] M. K. Coe, R. Evans, and N. B. Wilding, “Measures of fluctuations for a liquid near critical drying”, *Phys. Rev. E* **105**, 044801 (2022).
- [116] M. K. Coe, R. Evans, and N. B. Wilding, “Density depletion and enhanced fluctuations in water near hydrophobic solutes: identifying the underlying physics”, *Phys. Rev. Lett.* **128**, 045501 (2022).
- [117] M. K. Coe, R. Evans, and N. B. Wilding, “Understanding the physics of hydrophobic solvation”, *J. Chem. Phys.* **158**, 034508 (2023).
- [118] U. M. B. Marconi and P. Tarazona, “Dynamic density functional theory of fluids”, *J. Chem. Phys.* **110**, 8032–8044 (1999).
- [119] M. te Vrugt, H. Löwen, and R. Wittkowski, “Classical dynamical density functional theory: from fundamentals to applications”, *Adv. Phys.* **69**, 121–247 (2020).
- [120] N. C. Stuhlmüller, T. Eckert, D. de las Heras, and M. Schmidt, “Structural nonequilibrium forces in driven colloidal systems”, *Phys. Rev. Lett.* **121**, 098002 (2018).
- [121] L. L. Treffenstädt and M. Schmidt, “Memory-induced motion reversal in Brownian liquids”, *Soft Matter* **16**, 1518–1526 (2020).
- [122] D. de las Heras and M. Schmidt, “Flow and structure in nonequilibrium Brownian many-body systems”, *Phys. Rev. Lett.* **125**, 018001 (2020).
- [123] S. M. Tschopp and J. M. Brader, “First-principles superadiabatic theory for the dynamics of inhomogeneous fluids”, *J. Chem. Phys.* **157**, 234108 (2022).
- [124] S. M. Tschopp, H. D. Vuijk, and J. M. Brader, “Superadiabatic dynamical density functional study of Brownian hard-spheres in time-dependent external potentials”, *J. Chem. Phys.* **158**, 234904 (2023).
- [125] M. Schmidt, “Power functional theory for Newtonian many-body dynamics”, *J. Chem. Phys.* **148**, 044502 (2018).

- [126] D. de las Heras, J. Renner, and M. Schmidt, “Custom flow in overdamped Brownian dynamics”, *Phys. Rev. E* **99**, 023306 (2019).
- [127] L. Treffenstädt, “Superadiabatic forces in the dynamics of the hard sphere fluid”, PhD thesis (Universität Bayreuth, 2022).
- [128] D. de las Heras and M. Schmidt, “Velocity gradient power functional for Brownian dynamics”, *Phys. Rev. Lett.* **120**, 028001 (2018).
- [129] D. Borgis, R. Assaraf, B. Rotenberg, and R. Vuilleumier, “Computation of pair distribution functions and three-dimensional densities with a reduced variance principle”, *Mol. Phys.* **111**, 3486–3492 (2013).
- [130] D. de las Heras and M. Schmidt, “Better than counting: density profiles from force sampling”, *Phys. Rev. Lett.* **120**, 218001 (2018).
- [131] B. Rotenberg, “Use the force! Reduced variance estimators for densities, radial distribution functions, and local mobilities in molecular simulations”, *J. Chem. Phys.* **153**, 150902 (2020).
- [132] E. Noether, “Invariante Variationsprobleme”, *Nachr. d. König. Gesellsch. d. Wiss. zu Göttingen, Math.-Phys. Klasse* **1918**, 235–257 (1918).
- [133] E. Noether, “Invariant variation problems”, trans. by M. A. Tavel, *Transport Theor. Stat.* **1**, 186–207 (1971).
- [134] H. Goldstein, C. P. Poole, and J. L. Safko, *Classical mechanics*, 3rd ed. (Addison Wesley, San Francisco, 2008).
- [135] J. O. Hirschfelder, “Classical and quantum mechanical hypervirial theorems”, *J. Chem. Phys.* **33**, 1462–1466 (1960).
- [136] S. Hermann, F. Sammüller, and M. Schmidt, “Noether invariance theory for the equilibrium force structure of soft matter”, *J. Phys. A: Math. Theor.* **57**, 175001 (2024).
- [137] S. W. Coles, D. Borgis, R. Vuilleumier, and B. Rotenberg, “Computing three-dimensional densities from force densities improves statistical efficiency”, *J. Chem. Phys.* **151**, 064124 (2019).
- [138] S. W. Coles, E. Mangaud, D. Frenkel, and B. Rotenberg, “Reduced variance analysis of molecular dynamics simulations by linear combination of estimators”, *J. Chem. Phys.* **154**, 191101 (2021).
- [139] F. Chollet, *Deep Learning with Python*, 2nd ed. (Manning, Shelter Island, 2021).
- [140] K. Hornik, M. Stinchcombe, and H. White, “Multilayer feedforward networks are universal approximators”, *Neural Netw.* **2**, 359–366 (1989).
- [141] D. P. Kingma and J. Ba, “Adam: a method for stochastic optimization”, 2014, arXiv:1412.6980.

-
- [142] A. G. Baydin, B. A. Pearlmutter, A. A. Radul, and J. M. Siskind, “Automatic differentiation in machine learning: a survey”, *J. Mach. Learn. Res.* **18**, 1–43 (2018).
- [143] J. Bezanson, A. Edelman, S. Karpinski, and V. B. Shah, “Julia: a fresh approach to numerical computing”, *SIAM Rev.* **59**, 65–98 (2017).
- [144] A. Edelman, “Autodiff: Calculus from another angle”, <https://mitmath.github.io/18.0002/Autodiff.html>, 2018, video lecture 36 in *18.065 Matrix methods in data analysis, signal processing, and machine learning*, MIT OpenCourseWare.
- [145] S.-C. Lin and M. Oettel, “A classical density functional from machine learning and a convolutional neural network”, *SciPost Phys.* **6**, 025 (2019).
- [146] S.-C. Lin, G. Martius, and M. Oettel, “Analytical classical density functionals from an equation learning network”, *J. Chem. Phys.* **152**, 021102 (2020).
- [147] P. Cats, S. Kuipers, S. de Wind, R. van Damme, G. M. Coli, M. Dijkstra, and R. van Roij, “Machine-learning free-energy functionals using density profiles from simulations”, *APL Mater.* **9**, 031109 (2021).
- [148] R. Evans, “Density functionals in the theory of nonuniform fluids”, in *Fundamentals of inhomogeneous fluids*, edited by D. Henderson (Marcel Dekker, New York, 1992) Chap. 3, pp. 85–176.
- [149] J. M. Brader and M. Schmidt, “Free power dissipation from functional line integration”, *Mol. Phys.* **113**, 2873–2880 (2015).
- [150] N. F. Carnahan and K. E. Starling, “Equation of state for nonattracting rigid spheres”, *J. Chem. Phys.* **51**, 635–636 (1969).
- [151] J. Kolafa, S. Labík, and A. Malijevský, “Accurate equation of state of the hard sphere fluid in stable and metastable regions”, *Phys. Chem. Chem. Phys.* **6**, 2335–2340 (2004).
- [152] S. Theodoridis, *Machine learning: a Bayesian and optimization perspective* (Elsevier, London, 2015).
- [153] P. Yatsyshin, S. Kalliadasis, and A. B. Duncan, “Physics-constrained Bayesian inference of state functions in classical density-functional theory”, *J. Chem. Phys.* **156**, 074105 (2022).
- [154] A. Malpica-Morales, P. Yatsyshin, M. A. Durán-Olivencia, and S. Kalliadasis, “Physics-informed Bayesian inference of external potentials in classical density-functional theory”, *J. Chem. Phys.* **159**, 104109 (2023).
- [155] G. E. Karniadakis, I. G. Kevrekidis, L. Lu, P. Perdikaris, S. Wang, and L. Yang, “Physics-informed machine learning”, *Nat. Rev. Phys.* **3**, 422–440 (2021).
- [156] J. R. Howse, R. A. L. Jones, A. J. Ryan, T. Gough, R. Vafabakhsh, and R. Golestanian, “Self-motile colloidal particles: from directed propulsion to random walk”, *Phys. Rev. Lett.* **99**, 048102 (2007).

- [157] P. Romanczuk, M. Bär, W. Ebeling, B. Lindner, and L. Schimansky-Geier, “Active Brownian particles: From individual to collective stochastic dynamics”, *Eur. Phys. J. Special Topics* **202**, 1–162 (2012).
- [158] M. E. Cates and J. Tailleur, “When are active Brownian particles and run-and-tumble particles equivalent? Consequences for motility-induced phase separation”, *Europhys. Lett.* **101**, 20010 (2013).
- [159] D. Martin, J. O’Byrne, M. E. Cates, É. Fodor, C. Nardini, J. Tailleur, and F. van Wijland, “Statistical mechanics of active Ornstein-Uhlenbeck particles”, *Phys. Rev. E* **103**, 032607 (2021).
- [160] M. C. Marchetti, J. F. Joanny, S. Ramaswamy, T. B. Liverpool, J. Prost, M. Rao, and R. A. Simha, “Hydrodynamics of soft active matter”, *Rev. Mod. Phys.* **85**, 1143–1189 (2013).
- [161] S. Zhao, R. Ramirez, R. Vuilleumier, and D. Borgis, “Molecular density functional theory of solvation: From polar solvents to water”, *J. Chem. Phys.* **134**, 194102 (2011).
- [162] A. T. Bui and S. J. Cox, “A classical density functional theory for solvation across length scales”, 2024, arXiv:2402.02873.
- [163] G. Jeanmairet, M. Levesque, R. Vuilleumier, and D. Borgis, “Molecular density functional theory of water”, *J. Phys. Chem. Lett.* **4**, 619–624 (2013).
- [164] L. Ding, M. Levesque, D. Borgis, and L. Belloni, “Efficient molecular density functional theory using generalized spherical harmonics expansions”, *J. Chem. Phys.* **147**, 094107 (2017).
- [165] T. Zimmermann, F. Sammüller, S. Hermann, M. Schmidt, and D. de las Heras, “Neural power functional theory for non-equilibrium many-body colloidal systems”, in preparation, 2024.
- [166] T. Cohen and M. Welling, “Group equivariant convolutional networks”, in Proceedings of the 33rd international conference on machine learning, edited by M. F. Balcan and K. Q. Weinberger, *Proceedings of Machine Learning Research* **48** (2016), pp. 2990–2999.
- [167] V. G. Satorras, E. Hoogeboom, and M. Welling, “E(n) equivariant graph neural networks”, in Proceedings of the 38th international conference on machine learning, Vol. 139, edited by M. Meila and T. Zhang, *Proceedings of Machine Learning Research* (2021), pp. 9323–9332.
- [168] S. Batzner, A. Musaelian, L. Sun, M. Geiger, J. P. Mailoa, M. Kornbluth, N. Molinari, T. E. Smidt, and B. Kozinsky, “E(3)-equivariant graph neural networks for data-efficient and accurate interatomic potentials”, *Nat. Commun.* **13**, 2453 (2022).

- [169] A. Musaelian, S. Batzner, A. Johansson, L. Sun, C. J. Owen, M. Kornbluth, and B. Kozinsky, “Learning local equivariant representations for large-scale atomistic dynamics”, *Nat. Commun.* **14**, 579 (2023).
- [170] N. Tchipev, A. Wafai, C. W. Glass, W. Eckhardt, A. Heinecke, H.-J. Bungartz, and P. Neumann, “Optimized force calculation in molecular dynamics simulations for the Intel Xeon Phi”, in *Euro-Par 2015: parallel processing workshops* (Springer, Cham, 2015), pp. 774–785.
- [171] T. A. Weber and F. H. Stillinger, “Melting of square crystals in two dimensions”, *Phys. Rev. E* **48**, 4351–4358 (1993).
- [172] D. V. Makhov and L. J. Lewis, “Isotherms for the liquid-gas phase transition in silicon from NPT Monte Carlo simulations”, *Phys. Rev. B* **67**, 153202 (2003).
- [173] M. P. Allen and G. Germano, “Expressions for forces and torques in molecular simulations using rigid bodies”, *Mol. Phys.* **104**, 3225–3235 (2006).

6 Publications

6.1 List of publications

The following table lists all publications that contribute to this thesis. Additionally, we give a detailed graphical categorization into the topics considered in this work (recall the overview Fig. 1). The subject indexing is performed with respect to the types of physical systems and phenomena as well as regarding the methodologies used for their investigation.

Ref.	Publication	Pages
[1]	F. Sammüller and M. Schmidt, “Adaptive Brownian dynamics”, <i>J. Chem. Phys.</i> 155 , 134107 (2021)	56–70
[2]	F. Sammüller, D. de las Heras, and M. Schmidt, “Inhomogeneous steady shear dynamics of a three-body colloidal gel former”, <i>J. Chem. Phys.</i> 158 , 054908 (2023)	71–84
[3]	F. Sammüller, S. Hermann, and M. Schmidt, “Comparative study of force-based classical density functional theory”, <i>Phys. Rev. E</i> 107 , 034109 (2023)	85–94
[4]	F. Sammüller, S. Hermann, D. de las Heras, and M. Schmidt, “Noether-constrained correlations in equilibrium liquids”, <i>Phys. Rev. Lett.</i> 130 , 268203 (2023)	95–104
[5]	S. Robitschko, F. Sammüller, M. Schmidt, and S. Hermann, “Hyperforce balance via thermal Noether invariance of any observable”, <i>Commun. Phys.</i> 7 , 103 (2024)	105–116
[6]	D. de las Heras, T. Zimmermann, F. Sammüller, S. Hermann, and M. Schmidt, “Perspective: How to overcome dynamical density functional theory”, <i>J. Phys. Condens. Matter</i> 35 , 271501 (2023)	117–147
[7]	F. Sammüller, S. Hermann, D. de las Heras, and M. Schmidt, “Neural functional theory for inhomogeneous fluids: Fundamentals and applications”, <i>Proc. Natl. Acad. Sci.</i> 120 , e2312484120 (2023)	148–168
[8]	F. Sammüller, S. Hermann, and M. Schmidt, “Why neural functionals suit statistical mechanics”, <i>J. Phys. Condens. Matter</i> 36 , 243002 (2024)	169–191

	Ref.							
	[1]	[2]	[3]	[4]	[5]	[6]	[7]	[8]
Systems								
Simple fluids	Core topic	Some overlap	Core topic					
Complex fluids	Not considered	Core topic	Not considered	Core topic	Not considered	Not considered	Not considered	Not considered
Equilibrium	Some overlap	Not considered	Core topic	Core topic	Core topic	Not considered	Core topic	Core topic
Nonequilibrium	Core topic	Core topic	Some overlap	Not considered	Not considered	Core topic	Not considered	Some overlap
Methods								
Monte Carlo	Not considered	Not considered	Core topic	Some overlap	Core topic	Not considered	Core topic	Core topic
Adaptive BD	Core topic	Core topic	Not considered	Core topic	Some overlap	Core topic	Not considered	Not considered
DFT	Not considered	Not considered	Core topic	Not considered	Not considered	Not considered	Core topic	Core topic
PFT	Not considered	Core topic	Not considered	Not considered	Not considered	Core topic	Not considered	Some overlap
Noether invariance	Not considered	Not considered	Some overlap	Core topic	Core topic	Some overlap	Some overlap	Some overlap
Machine learning	Not considered	Core topic	Core topic	Core topic				

6.2 Author's contributions

In an initial research phase, the author recognized the lack of an adaptive timestepping algorithm for overdamped Brownian dynamics simulations of many-body systems. Based on his investigation of numerical treatments of stochastic differential equations, he identified a recent generation scheme of random numbers [93] to be applicable to this problem. For Ref. [1], he conceptualized and implemented the adaptive BD algorithm and performed benchmarks for various physical model systems.

For Ref. [2], the Stillinger-Weber [71] interaction potential has been implemented and optimized by the author in order to replicate a colloidal gel [74]. He found this gel former to display extensive and unusual superadiabatic effects when driven by an inhomogeneous shear profile, as investigated with adaptive BD simulations. A power functional theory that accounts for the observed superadiabatic phenomena of the sheared colloidal gel was developed by the author together with his supervisor.

In Ref. [3], a recent DFT formalism based on forces [61] has been gauged via comparison to many-body simulation data. The author generated these simulation results by implementing and performing canonical and grand canonical Monte Carlo simulations of hard sphere systems and by gathering data for the dynamical case with a preexisting event-driven BD program [63, 127]. A hybrid DFT scheme has further been investigated, for which the author conducted the numerical evaluations.

Together with the coauthors, the author derived the second-order Noether sum rules in Ref. [4] and he identified simplifications for the case of pair interactions. He developed numerical procedures to measure the relevant correlation functions and to verify their interrelation via adaptive BD and GCMC simulations for different types of model fluids, many of which have been implemented specifically for this study.

For Ref. [5], the author derived in collaboration with the coauthors applications of global and locally resolved hyperforce sum rules and he identified connections to existing

literature. He further assisted in the preparation of computer simulations and in the analysis of numerical results.

For Ref. [6], the author contributed in close collaboration with the coauthors to the development of the presented machine learning framework and he conceptualized the specific input-output data pairing to capture functional maps from local information by a neural network. Reference data for training and testing of the neural network has been acquired by the author via adaptive BD simulations, for which he developed an automated generation protocol of randomized nonequilibrium environments.

For Ref. [7], the author transferred and generalized the concepts of Ref. [6] to fluid equilibria. He developed and evaluated a supervised machine learning procedure for training a neural network with randomized GCMC reference data, which he exemplified in detail for the hard sphere fluid. The author investigated applications of the resulting neural correlation functional by designing suitable functional calculus routines as well as a neural DFT for the self-consistent determination of density profiles [11]. For the task of comparison to analytic DFT methods, the author implemented a custom DFT library [10] with different types of FMT functionals.

Ref. [8] gives more theoretical background and a practitioner's account on different aspects of the neural functional method, for which the author independently prepared a programming tutorial as supplementary material [12]. The tutorial is provided in the form of a Jupyter notebook with explanatory text and code examples (see Appendix C for a typeset version). It exemplifies GCMC simulations, DFT calculations, machine learning routines and differential programming as the building blocks of the neural functional framework concretely for the one-dimensional hard rod fluid.

The first versions of Refs. [1, 2, 7] as well as Secs. III to V of Ref. [3] were written independently by the author. For all publications, the author was involved significantly in the revision of the manuscript and in the response to referee comments. The author has also contributed to Refs. [61, 110, 112, 136], which are not part of this cumulative thesis in order to provide thematic focus.

Software

Unless otherwise noted, many-body simulations have been performed and analyzed with MBD [9], which is a modular program written by the author in C++ for the simulation of many-body systems in and out of equilibrium [9]. It provides multiple types of particle interactions which are evaluated efficiently in parallel via colored cell lists [44, 170]. Different methods for Monte Carlo as well as molecular and Brownian dynamics simulations (in particular adaptive BD [1]) are implemented. MBD comes with tools that simplify common use cases such as parallel runs on high performance computing clusters and with a Python module for the analysis of output data. For Ref. [7], the Julia [143] package `ClassicalDFT.jl` [10] has been developed by the author. `ClassicalDFT.jl` facilitates to carry out classical DFT calculations and it contains implementations of FMT [103, 106–108] and mean-field functionals, which can be applied to problems in planar and in spherical geometry. Additionally, for Ref. [7], utilities for the automated

generation of reference simulation data and for the training and evaluation of neural functionals have been written in Python using the machine learning frameworks Keras and TensorFlow [139]. This code is published along with simulation data and trained models in Ref. [11]. Complementary to Ref. [8], an instructive tutorial is provided online [12], in which simulation, DFT and machine learning techniques are illustrated with interactive Julia code examples and exercises. A typeset version of the tutorial is given in Appendix C, and it includes illustrations taken from Ref. [8] as well as typical output from straightforward evaluation of the code cells.

Adaptive Brownian Dynamics Cite as: J. Chem. Phys. **155**, 134107 (2021); doi: 10.1063/5.0062396

Submitted: 5 July 2021 • Accepted: 19 August 2021 •

Published Online: 1 October 2021



View Online



Export Citation



CrossMark

Florian Sammüller^{a)}  and Matthias Schmidt^{b)} 

AFFILIATIONS

Theoretische Physik II, Physikalisches Institut, Universität Bayreuth, D-95447 Bayreuth, Germany

^{a)} Author to whom correspondence should be addressed: florian.sammueler@uni-bayreuth.de^{b)} Electronic mail: Matthias.Schmidt@uni-bayreuth.de

ABSTRACT

A framework for performant Brownian Dynamics (BD) many-body simulations with adaptive timestepping is presented. Contrary to the Euler–Maruyama scheme in common non-adaptive BD, we employ an embedded Heun–Euler integrator for the propagation of the overdamped coupled Langevin equations of motion. This enables the derivation of a local error estimate and the formulation of criteria for the acceptance or rejection of trial steps and for the control of optimal stepsize. Introducing erroneous bias in the random forces is avoided by rejection sampling with memory due to Rackauckas and Nie, which makes use of the Brownian bridge theorem and guarantees the correct generation of a specified random process even when rejecting trial steps. For test cases of Lennard-Jones fluids in bulk and in confinement, it is shown that adaptive BD solves performance and stability issues of conventional BD, already outperforming the latter even in standard situations. We expect this novel computational approach to BD to be especially helpful in long-time simulations of complex systems, e.g., in non-equilibrium, where concurrent slow and fast processes occur.

Published under an exclusive license by AIP Publishing. <https://doi.org/10.1063/5.0062396>

I. INTRODUCTION

Computer simulations have long become an established tool in the investigation of physical phenomena.^{1–3} Complementing experimental results, they build the foundation for the exploration of increasingly complex dynamical systems. From the standpoint of classical statistical mechanics, the simulation of a many-body system consisting of discrete interacting particles can reveal information about its structural correlation as well as its thermodynamic properties. Naturally, this opens up the possibility of tackling many problems in the fields of materials science, soft matter, and biophysics, such as investigating the dynamics of macromolecules,⁴ predicting rheological properties of fluids,^{5–7} or exploring non-equilibrium processes that occur, e.g., in colloidal suspensions under the influence of external forcing.⁸

With the ever-increasing capabilities of computer hardware, a variety of different computational methods have emerged since the middle of the last century. Conceptually, at least three distinct classes of particle-based simulation frameworks can be identified: (i) Monte-Carlo (MC), which relies on the stochastic exploration of phase space; (ii) Molecular Dynamics (MD), in which the set of ordinary differential equations (ODEs) of Hamiltonian dynamics is integrated to obtain particle trajectories; and (iii) Langevin Dynamics, where random processes are incorporated into the Newtonian

equations of motion so that the evolution of a system is obtained by numerical integration of then stochastic differential equations (SDEs). Brownian Dynamics (BD) can be seen as a special case of (iii), since the underlying stochastic Langevin equation is thereby considered in the overdamped limit where particle inertia vanishes and only particle coordinates remain as the sole microscopic degrees of freedom.

Notably, a broad range of refined methods have been developed in all three categories, sometimes even intersecting those. Important examples of such extensions are kinetic Monte-Carlo for the approximation of time evolution from reaction rates,⁹ the addition of thermostats in MD to model thermodynamic coupling,^{10,11} event-driven algorithms that enable both MD and BD in hard-particle systems,^{12,13} and the adaptation of molecular algorithms to modern hardware.¹⁴ Improvements in the calculation of observables from the resulting particle configurations have been made as well, e.g., by modifying their generation in MC (umbrella sampling, transition matrix MC,¹⁵ Wang-Landau sampling¹⁶) or by utilizing advanced evaluation schemes in MD and BD, such as force sampling^{17–19} or adaptive resolution MD.²⁰

The efficiency and accuracy of a certain algorithm are always primary concerns, as these properties are essential for applicability and practicability in real-world problems. One therefore aims to design procedures that are both as fast and as precise as possible—yet

it is no surprise that those two goals might often be conflicting. In particular, in BD, where stochastic processes complicate the numerical treatment, the development of more sophisticated algorithms apparently lacks behind that of MD, for example, and one often resorts to alternative or combined simulation techniques.^{21,22} If the full dynamical description of BD is indeed considered, the equations of motion are usually integrated with the simple Euler–Maruyama method,²³ where stochasticity is accounted for in each equidistant step via normally distributed random numbers. This can lead to inaccuracies and stability problems, making BD seem inferior to other computational methods.

In this work, we propose a novel approach to BD simulations, which rectifies the above shortcomings of conventional BD. To achieve this, we employ an adaptive timestepping algorithm that enables the control of the numerical error as follows. The common Euler–Maruyama method is complemented with a higher-order Heun step to obtain an embedded integrator pair for an estimation of the local discretization error per trial step. By comparison of this error estimate with a prescribed tolerance, the trial step is either accepted or it is rejected and then retried with a smaller stepsize. Particular care is required after rejections so as to not introduce a bias in the random forces, which would violate their desired properties. We therefore use Rejection Sampling with Memory (RSwM)²⁴ to retain a Gaussian random process even in a scenario where already determined random increments may conditionally be discarded. RSwM is a recently developed algorithm for the adaptive generation of random processes in the numerical solution of SDEs, which we improve and specialize to our context of overdamped Brownian motion and thereby formulate a method for adaptive BD simulations.

We demonstrate the practical advantages of adaptive BD over common BD in simulation results for prototypical bulk equilibrium systems and for more involved cases in non-equilibrium. A notable example that we investigate is the drying of colloidal films at planar surfaces. In particular, when dealing with non-trivial mixtures, as, e.g., present in common paints and coatings, the dynamics of this process can be inherently complex and its quantitative description turns out to be a major challenge.^{25,26} This stands in contrast to the necessity of understanding and predicting stratification processes in those systems. Stratification leads to a dried film that has multiple layers differing in the concentration of constituent particle species, thereby influencing macroscopic properties of the resulting colloidal film. Therefore, controlling this process is an important measure to tailor colloidal suspensions to their field of application. Advances in this area have been made experimentally,^{27,28} by utilizing functional many-body frameworks like dynamical density functional theory (DDFT),²⁹ and with molecular simulations such as conventional BD.³⁰ By employing the adaptive BD method, we are able to capture the complex dynamical processes occurring in those systems even in the final dense state. Close particle collisions and jammed states are resolved with the required adjustment of the timestep, necessary for the stability and accuracy of the simulation run in those circumstances. This cannot be achieved easily with common BD.

This paper is structured as follows. In Sec. II, a brief and non-rigorous mathematical introduction to the numerical solution of SDEs is given. Particularly, we illustrate the prerequisites for adaptive and higher-order algorithms in the case of general SDEs and emphasize certain pitfalls. In Sec. III, these considerations are

applied to the case of Brownian motion. We construct the embedded Heun–Euler integration scheme in Sec. III A and incorporate RSwM in Sec. III B, which yields the adaptive BD method. Observables can then be sampled from the resulting particle trajectories with the means illustrated in Sec. III C. In Sec. IV, simulation results of the above-mentioned Lennard-Jones systems are shown and the practical use of adaptive BD is confirmed. In Sec. V, we conclude with a summary of the shown concepts, propose possible improvements for the adaptation of timesteps, and present further ideas for use cases.

II. NUMERICS OF STOCHASTIC DIFFERENTIAL EQUATIONS

Brownian dynamics of a classical many-body system of N particles in d spatial dimensions with positions $\mathbf{r}^N(t) = (\mathbf{r}^{(1)}(t), \dots, \mathbf{r}^{(N)}(t))$ at time t and temperature T is described by the overdamped Langevin equation. The trajectory of particle i satisfies

$$\dot{\mathbf{r}}^{(i)}(t) = \frac{1}{\gamma^{(i)}} \mathbf{F}^{(i)}(\mathbf{r}^N(t)) + \sqrt{\frac{2k_B T}{\gamma^{(i)}}} \mathbf{R}^{(i)}(t), \quad (1)$$

where $\mathbf{F}^{(i)}(\mathbf{r}^N(t))$ is the total force (composed of external and interparticle contributions) acting on particle i , $\gamma^{(i)}$ is the friction coefficient of particle i , and k_B is Boltzmann’s constant; the dot denotes a time derivative. In Eq. (1), the right-hand side consists of a deterministic (first summand) and a random contribution (second summand). The random forces are modeled via multivariate Gaussian white noise processes $\mathbf{R}^{(i)}(t)$ that satisfy

$$\langle \mathbf{R}^{(i)}(t) \rangle = 0, \quad (2)$$

$$\langle \mathbf{R}^{(i)}(t) \mathbf{R}^{(j)}(t') \rangle = \mathbf{I} \delta_{ij} \delta(t - t'), \quad (3)$$

where $\langle \cdot \rangle$ denotes an average over realizations of the random process, \mathbf{I} is the $d \times d$ unit matrix, δ_{ij} denotes the Kronecker delta, and $\delta(\cdot)$ is the Dirac delta function.

One can recognize that Eq. (1) has the typical form of an SDE,

$$dX(t) = f(X(t), t)dt + g(X(t), t)dW(t), \quad (4)$$

if the dependent random variable X is identified with the particle positions \mathbf{r}^N and W is a Wiener process corresponding to the integral of the Gaussian processes $\mathbf{R}^N = (\mathbf{R}^{(1)}, \dots, \mathbf{R}^{(N)})$. As we do not consider hydrodynamic interactions, the random forces in Eq. (1) are obtained by a mere scaling of $\mathbf{R}^{(i)}(t)$ with the constant prefactors $\sqrt{2k_B T/\gamma^{(i)}}$. Therefore, the noise in BD is additive, since $g(X(t), t) = \text{const.}$ in the sense of Eq. (4). This is a crucial property for the construction of a simple higher-order integrator below in Sec. III.

In computer simulations, particle trajectories are obtained from Eq. (1) by numerical integration. Contrary to the numerics of ODEs, where higher-order schemes and adaptivity are textbook material, the derivation of corresponding methods for SDEs poses several difficulties that we address below. Due to the complications, SDEs of type (4) are often integrated via the Euler–Maruyama method instead, which follows the notion of the explicit Euler scheme for ODEs. Thereby, the true solution of Eq. (4) with initial value

$X(0) = X_0$ is approximated in $t \in [0, T]$ by partitioning the time interval into n equidistant subintervals of length $\Delta t = T/n$. Then, for $0 \leq k < n$, a timestep is defined by

$$X_{k+1} = X_k + f(X_k, t_k)\Delta t + g(X_k, t_k)\Delta W_k \quad (5)$$

with Wiener increments ΔW_k . An Euler–Maruyama step is also incorporated in the adaptive BD method that we construct below, applying Eq. (5) to the overdamped Langevin equation (1).

Crucially, the random increments ΔW_k in each Euler–Maruyama step (5) have to be constructed from independent and identically distributed normal random variables with expectation value $E(\Delta W_k) = 0$ and variance $\text{Var}(\Delta W_k) = \Delta t$. In practice, this is realized by drawing a new random number R (or vector thereof) from a pseudo-random number generator obeying the normal distribution $\mathcal{N}(0, \Delta t) = \sqrt{\Delta t}\mathcal{N}(0, 1)$ in each step k and setting $\Delta W_k = R$ in Eq. (5). The process of obtaining such a scalar (or vectorial) random increment R will be denoted in the following by

$$R \sim \mathcal{N}(\mu, \eta), \quad (6)$$

where $\mathcal{N}(\mu, \eta)$ is a scalar (or multivariate) normal distribution with expectation value μ and variance η .

As in the case of ODEs, an important measure for the quality of an integration method is its order of convergence. However, what convergence exactly means in the case of SDEs must be carefully reconsidered due to their stochasticity. We refer the reader to the pertinent literature (see, e.g., Ref. 23) and only summarize the key concepts and main results in the following.

Since both the approximation X_k and the true solution $X(t_k)$ are random variables, one can define two distinct convergence criteria. For a certain method with discretization $\Delta t \rightarrow 0$, *weak convergence* captures the error of average values, whereas *strong convergence* assesses the error of following a specific realization of a random process. One can show that the Euler–Maruyama method has a strong convergence order of 0.5, i.e., when increasing or decreasing the stepsize Δt , the error of the numerical solution only scales with $\Delta t^{0.5}$. For general $g(X(t), t)$ in Eq. (4), the construction of schemes with higher strong order is complicated due to the occurrence of higher-order stochastic integrals. Practically, this means that the careful evaluation of additional random variables is necessary in each iteration step. These random variables then enable the approximation of the stochastic integrals. There exist schemes of Runge–Kutta type with strong orders up to 2 although only strong order 1 and 1.5 Runge–Kutta methods are mostly used due to practical concerns.^{31,32}

In order to incorporate adaptivity, one needs a means of comparison of two integration schemes of different strong order to formulate a local error estimate for the proposed step. If the error that occurs in a specific timestep is too large (we define below precisely what we mean by that), the step is rejected and a retrieval with a smaller value of Δt is performed. Otherwise, the step is accepted and, based on the previously calculated error, a new optimized stepsize is chosen for the next step, which hence can be larger than the previous one. This protocol makes an optimal and automatic control of the stepsize possible, meaning that Δt can be both reduced when the propagation of the SDE is difficult and increased when the error estimate allows us to do so. Similar to the case of ODEs,

it is computationally advantageous to construct so-called embedded integration schemes, analogous to, e.g., Runge–Kutta–Fehlberg integrators,³³ which minimize the number of costly evaluations of the right-hand side of Eq. (4). Developments have been made in this direction, e.g., with embedded stochastic Runge–Kutta methods.³⁴

There is still one caveat to consider when rejecting a step, in that one has to be careful to preserve the properties of the Wiener process. In the naive approach of simply redrawing new uncorrelated random increments, rejections would alter the random process implicitly. The reason lies in the introduction of an undesired bias. Since large random increments (generally causing larger errors) get rejected more often, the variance of the Wiener process would be systematically decreased, ultimately violating its desired properties. To avoid this effect, it must be guaranteed that once a random increment is chosen, it will not be discarded until the time interval it originally applied to has passed. Consequently, when rejecting a trial step and retrying the numerical propagation of the SDE with smaller time intervals, new random increments cannot be drawn independently for those substeps anymore. The new random increments must instead be created based on the rejected original timestep such that an unbiased Brownian path is still followed.

The formal framework to the above procedure is given by the so-called Brownian bridge theorem,³⁵ which interpolates a Wiener process between known values at two timepoints. If $W(0) = 0$ and $W(\Delta t) = R$ are given (e.g., due to the previous rejection of a timestep of length Δt where the random increment R has been drawn), then a new intermediate random value must be constructed by

$$W(q\Delta t) \sim \mathcal{N}(qR, (1-q)q\Delta t), \quad 0 < q < 1 \quad (7)$$

such that the statistical properties of the to-be-simulated Wiener process are left intact and a substep $q\Delta t$ can be tried. The value of q thereby sets the fraction of the original time interval to which the Wiener process shall be interpolated. Equation (7) extends naturally (i.e., component-wise) to the multivariate case and it hence enables the construction of interpolating random vectors in a straightforward manner.

With this idea in mind, several adaptive timestepping algorithms for SDEs have been designed.^{36–42} Still, most of these approaches are quite restrictive in the choice of timesteps (e.g., only allowing discrete variations such as halving or doubling),^{36,42} involve the deterministic or random part only separately into an *a priori* error estimation,^{39,41,43} or store rejected timesteps in a costly manner, e.g., in the form of Brownian trees.³⁶ In particular, the above methods rely on precomputed Brownian paths and do not illustrate an ad hoc generation, which is desirable from a performance and memory consumption standpoint in a high-dimensional setting like BD.

In contrast, a very flexible and performant class of adaptive timestepping algorithms called Rejection Sampling with Memory (RSwM) has recently been developed by Rackauckas and Nie.²⁴ Their work provides the arguably optimal means for the adaptive numerical solution of SDEs while still being computationally efficient in the generation of random increments as well as in the handling of rejections. We therefore use RSwM in the construction of an adaptive algorithm and specialize the method to Brownian motion in the following.

III. APPLICATION TO BROWNIAN DYNAMICS

Based on the remarks of Sec. II, we next proceed to apply the general framework to the case of BD with the overdamped Langevin equation (1) forming the underlying SDE. An embedded integration scheme is constructed, which allows the derivation of an error estimate and an acceptance criterion in each step. Furthermore, the application of RSwM for handling rejected timesteps in BD is shown and discussed. We also illustrate how the calculation of observables from sampling of phase space functions has to be altered in a variable timestep scenario.

A. Embedded Heun–Euler method

Regarding the overdamped Langevin equation (1), a major simplification exists compared to the general remarks made in Sec. II. Due to the noise term being trivial, some higher-order schemes can be constructed by only evaluating the deterministic forces for different particle configurations. Crucially, no iterated stochastic integrals are needed, which would have to be approximated in general higher strong-order integrators by using additional random variables.³² In the following, we apply a scheme similar to the one suggested by Lamba *et al.*⁴¹ for general SDEs to Eq. (1) and term it *embedded Heun–Euler method* due to its resemblance to the corresponding ODE integrators. Two different approximations $\tilde{\mathbf{r}}_{k+1}^N$ and \mathbf{r}_{k+1}^N are calculated in each trial step by

$$\tilde{\mathbf{r}}_{k+1}^{(i)} = \mathbf{r}_k^{(i)} + \frac{1}{\gamma^{(i)}} \mathbf{F}^{(i)}(\mathbf{r}_k^N) \Delta t_k + \sqrt{\frac{2k_B T}{\gamma^{(i)}}} \mathbf{R}_k^{(i)}, \quad (8)$$

$$\mathbf{r}_{k+1}^{(i)} = \mathbf{r}_k^{(i)} + \frac{1}{2\gamma^{(i)}} \left(\mathbf{F}^{(i)}(\mathbf{r}_k^N) + \mathbf{F}^{(i)}(\tilde{\mathbf{r}}_{k+1}^N) \right) \Delta t_k + \sqrt{\frac{2k_B T}{\gamma^{(i)}}} \mathbf{R}_k^{(i)}. \quad (9)$$

Equation (8) is the conventional Euler–Maruyama step and hence constitutes the application of Eq. (5) to the overdamped Langevin equation (1). Equation (9) resembles the second order Heun algorithm or midpoint scheme for ODEs⁴⁵ and has been formally derived for SDEs in the context of stochastic Runge–Kutta methods.⁴⁵ Since the deterministic forces \mathbf{F}^N are evaluated at the initial particle configuration \mathbf{r}_k^N in both Eqs. (8) and (9), we have constructed an embedded integration method. This is favorable regarding computational cost, since the numerical result of $\mathbf{F}^N(\mathbf{r}_k^N)$ is evaluated once in Eq. (8) and reused in Eq. (9). Only one additional computation of the deterministic forces at the intermediate particle configuration $\tilde{\mathbf{r}}_{k+1}^N$ is then needed in the Heun step (9).

In each trial step, the same realization of random vectors \mathbf{R}_k^N must be used in both Eqs. (8) and (9). Recall that the random displacements have to obey the properties of multivariate Wiener increments to model the non-deterministic forces. In conventional BD with fixed stepsize $\Delta t_k = \Delta t = \text{const.}$, these random vectors can therefore be drawn independently via $\mathbf{R}_k^{(i)} \sim \mathcal{N}(0, \Delta t)$ for each particle i . If rejections of trial steps are possible, $\mathbf{R}_k^{(i)}$ must instead be constructed as described in Sec. III B.

When the embedded Heun–Euler step (8) and (9) is applied to BD, the improvement over the conventional method is twofold. First, the Heun step (9) can be used as a better propagation method as already analyzed by Fixman⁴⁶ and Iniesta and García de la Torre.⁴⁷

Several further higher-order schemes, mostly of Runge–Kutta type, have been used in BD simulations.^{45,48} These methods often lead to increased accuracy and even efficiency due to bigger timesteps becoming achievable, which outweighs the increased computational cost per step. Since the prefactor of the random force is trivial (i.e., constant) in the overdamped Langevin equation (1), higher strong-order schemes are easily constructable. This situation stands in contrast to the more complicated SDEs of type (4) with general noise term $g(X(t), t)$.

Second, with two approximations of different order at hand, assessing their discrepancy allows us to obtain an estimate of the discretization error in each step, which is a fundamental prerequisite in the construction of adaptive timestepping algorithms. For this, we exploit the additive structure of the noise term in Eq. (1) again and recognize that such an error estimate can be obtained by only comparing the deterministic parts of Eqs. (8) and (9). Nevertheless, note that the random displacements are already contained in $\tilde{\mathbf{r}}_{k+1}^N$. This makes the deterministic part of Eq. (9) implicitly dependent on the realization of \mathbf{R}_k^N , which is opposed to Ref. 41 where an error estimate is defined without involving the random increments at all.

At a given step $k \rightarrow k+1$, one can construct the automatic choice of an appropriate Δt_k . For this, the error of a trial step with length Δt is evaluated.

We define a particle-wise error

$$E^{(i)} = \|\Delta \tilde{\mathbf{r}}^{(i)} - \Delta \mathbf{r}^{(i)}\| = \frac{\Delta t}{2\gamma^{(i)}} \|\mathbf{F}^{(i)}(\tilde{\mathbf{r}}_{k+1}^N) - \mathbf{F}^{(i)}(\mathbf{r}_k^N)\|, \quad (10)$$

with $\Delta \tilde{\mathbf{r}}^{(i)} = \tilde{\mathbf{r}}_{k+1}^{(i)} - \mathbf{r}_k^{(i)}$ and $\Delta \mathbf{r}^{(i)} = \mathbf{r}_{k+1}^{(i)} - \mathbf{r}_k^{(i)}$. For each particle i , this error is compared to a tolerance

$$\tau^{(i)} = \epsilon_{\text{abs}} + \epsilon_{\text{rel}} \|\Delta \mathbf{r}^{(i)}\| \quad (11)$$

consisting of an absolute and a relative part with user-defined coefficients ϵ_{abs} and ϵ_{rel} . Note that $\Delta \mathbf{r}^{(i)}$ is used in Eq. (11), since it captures the true particle displacement more accurately than $\Delta \tilde{\mathbf{r}}^{(i)}$ due to its higher order. Additionally, we stress that $\Delta \mathbf{r}^{(i)}$ decreases on average for shorter timesteps such that $\tau^{(i)}$ indirectly depends on the trial Δt , which limits the accumulation of errors after multiple small steps.

Then, a total error estimate

$$\mathcal{E} = \left\| \left(\frac{E^{(i)}}{\tau^{(i)}} \right)_{1 \leq i \leq N} \right\| \quad (12)$$

can be calculated for the trial step. While the Euclidean norm is the canonical choice in Eq. (10), there is a certain freedom of choosing an appropriate norm $\|\cdot\|$ in Eq. (12). The two- or ∞ -norm defined as

$$\left\| (x^{(i)})_{1 \leq i \leq N} \right\|_2 = \sqrt{\frac{1}{N} \sum_{i=1}^N |x^{(i)}|^2}, \quad (13)$$

$$\left\| (x^{(i)})_{1 \leq i \leq N} \right\|_\infty = \max_{1 \leq i \leq N} |x^{(i)}|, \quad (14)$$

respectively, may both come up as natural and valid options (note that we normalize the standard two-norm by \sqrt{N} to obtain an intensive quantity). However, in Eq. (12), where a reduction from

particle-wise errors to a global scalar error takes place, this has crucial implications to the kind of error that is being controlled. If the two-norm is used, then ϵ_{abs} and ϵ_{rel} set the *mean* absolute and relative tolerance for all particles. In practice for large particle number N , this can lead to substantial single-particle errors becoming lost in the global average. Therefore, it is advisable to use the ∞ -norm for the reduction in Eq. (12) to be able to set a *maximum single-particle* absolute and relative tolerance, i.e., if $\mathcal{E} < 1$, $E^{(i)} < \tau^{(i)}$ for all $i = 1, \dots, N$.

Following the design of adaptive ODE solvers and ignoring stochasticity, an expansion of an embedded pair of methods with orders p and $p - 1$ shows that an error estimate of type (12) is of order p . Thus, a timestep of length $q\Delta t$ with

$$q = \mathcal{E}^{-\frac{1}{p}} \quad (15)$$

could have been chosen to marginally satisfy the tolerance requirement $\mathcal{E} < 1$.

Considering the recommendation of Ref. 24, which discusses the application of such a timestep scaling factor to embedded methods for SDEs, we set

$$q = \left(\frac{1}{\alpha \mathcal{E}} \right)^2. \quad (16)$$

Here, both a more conservative exponent is chosen than in Eq. (15) and also a safety factor $\alpha = 2$ is introduced, as we want to account for stochasticity and for the low order of our integrators, which results in a low order of the error estimate (12).

With the choice (16), one can distinguish two possible scenarios in each trial step:

- $q \geq 1$: Accept the trial step, i.e., set $\Delta t_k = \Delta t$ and advance the particle positions with Eq. (9), and then continue with $k + 1 \rightarrow k + 2$.
- $q < 1$: Reject the trial step and retry $k \rightarrow k + 1$ with a smaller timestep.

In both cases, the timestep is adapted afterward via $\Delta t \leftarrow q\Delta t$. Here and in the following, the notation $a \leftarrow b$ denotes an assignment of the value b to the variable a .

It is advisable to restrict the permissible range of values for q by defining lower and upper bounds $q_{\min} \leq q \leq q_{\max}$ such that the adaptation of Δt is done with

$$q \leftarrow \min(q_{\max}, \max(q_{\min}, q)). \quad (17)$$

While commonly chosen as $q_{\max} \approx 10$ and $q_{\min} \approx 0.2$ for ODE solvers, due to stochasticity and the possibility of drawing “difficult” random increments, q_{\min} should certainly be decreased in the case of SDEs to avoid multiple re-rejections. Vice versa, a conservative choice of q_{\max} prevents an overcorrection of the timestep in the case of “fortunate” random events. We set $q_{\max} = 1.2$ and $q_{\min} = 0.001$ in practical applications to achieve a rapid adaptation in the case of rejected trial steps and a careful approach to larger timesteps after accepted moves.

One can also impose limits for the range of values of Δt , such as a maximum bound $\Delta t_{\max} \geq \Delta t$. Restriction by a minimum

value $\Delta t_{\min} \leq \Delta t$, however, could lead to a forced continuation of the simulation with an actual local error that lies above the user-defined tolerance. Thus, this is not recommended. In our test cases described below, we see no need to restrict the timestep as the adaptive algorithm does not show unstable behavior without such a restriction.

Most concepts of this section can be generalized in a straightforward manner to non-overdamped Langevin dynamics, where particle inertia is explicitly considered in the stochastic equations of motion. However, the embedded Heun–Euler method (8) and (9) might not be a suitable integration scheme in this case. We therefore outline the modifications that are necessary in the construction of an adaptive algorithm for general Langevin dynamics in Appendix A.

B. Rejection sampling with memory in BD

We still have to prescribe the generation of the random vectors \mathbf{R}_k^N that appear in both Eqs. (8) and (9). For clarity, we consider a single trial step and denote the set of corresponding random increments with \mathbf{R} (the sub- and superscript is dropped). Obviously, \mathbf{R} can no longer be chosen independently in general but has to incorporate previously rejected timesteps as long as they are relevant, i.e., as long as their original time interval has not passed yet. For this, we apply the Rejection Sampling with Memory (RSwM) algorithm to BD. Rackauckas and Nie²⁴ described three variants of RSwM, which they refer to as RSwM1, RSwM2, and RSwM3 and which differ in generality of the possible timesteps and algorithmic complexity. We aim to reproduce RSwM3 because it enables optimal timesteping and still ensures correctness in special but rare cases such as re-rejections.

Common to all of the RSwM algorithms is storing parts of rejected random increments onto a stack S_f . We refer to elements of this stack as *future information*, since they have to be considered in the construction of future steps. This becomes relevant as soon as a step is rejected due to a too large error. Then, a retry is performed by decreasing Δt and drawing bridging random vectors via Eq. (7). The difference between rejected and bridging random vectors must not be forgotten but rather be stored on the future information stack, cf. Fig. 1.

On the other hand, if a step is accepted, new random vectors have to be prepared for the next time interval Δt . If no future information is on the stack, this can be done conventionally via drawing Gaussian distributed random vectors according to $\mathbf{R} \sim \mathcal{N}(0, \Delta t)$. If the stack S_f is not empty and thus future information is available, then elements of the stack are popped one after another, i.e., they are taken successively from the top. The random vectors as well as the time interval of each popped element are accumulated in temporary variables, which then hold the sum of those respective time intervals and random vectors. The stack could be empty before the accumulated time reaches Δt , i.e., there could still be a difference Δt_{gap} . In this case, one draws new random vectors $\mathbf{R}_{\text{gap}} \sim \mathcal{N}(0, \Delta t_{\text{gap}})$ to compensate for the difference and adds them to the accumulated ones, cf. Fig. 2, before attempting the trial step. Otherwise, if the future information reaches further than Δt , then there is one element that passes Δt . One takes this element, splits it in “before Δt ” and “after Δt ,” and draws bridging random vectors for “before Δt ” according to Eq. (7), which are again added to the accumulated ones. The rest of this element (“after Δt ”) can be pushed back to the future information stack

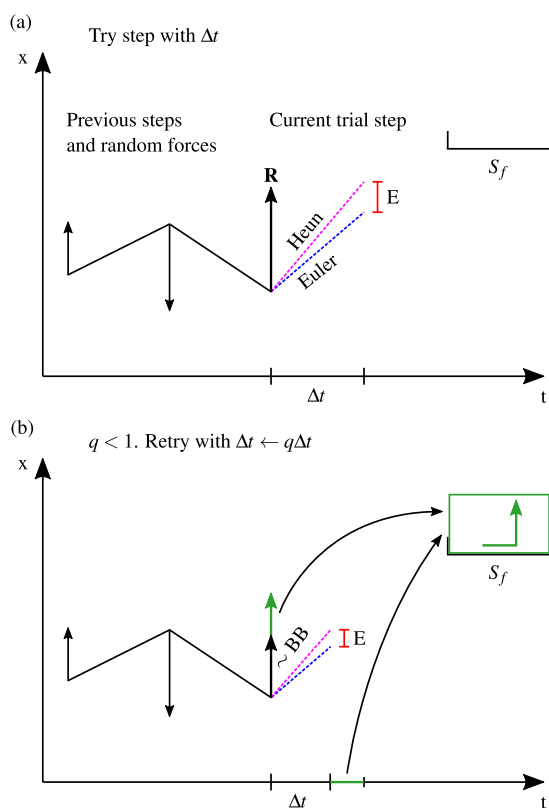


FIG. 1. The trial step is rejected (a) and a retrial with a smaller value of Δt is performed (b) if the discrepancy between Eqs. (8) and (9) is large. To preserve the properties of the Brownian motion, the Brownian bridge (BB) theorem (7) is used to interpolate the random process at the intermediate timepoint $q\Delta t$. The difference between the bridged random sample and the rejected original random sample is stored along with the remaining time difference onto the stack S_f . This is indicated in (b), where S_f now contains one element that holds the residual time interval (horizontal segment) and random increment (vertical arrow). Thus, in future steps, the Brownian path can be reconstructed from elements on S_f and the properties of the Wiener process remain intact. Note that for correctness in the case of re-rejections, one requires a second stack S_u as explained below and in Fig. 4.

and the step Δt can be tried with the accumulated vectors set as \mathbf{R} in Eqs. (8) and (9), cf. Fig. 3.

At this stage, we have constructed RSwM2 for BD, which is not capable of handling all edge cases yet as pointed out in Ref. 24. If future information is popped from the stack to prepare \mathbf{R} for the next step, and this next step is then rejected, we have lost all popped information unrecoverably. To circumvent this, one adds a second stack S_u that stores information that is currently used for the construction of \mathbf{R} . We refer to elements of this stack as *information in use*. If a step is rejected, the information in use can be moved back to the future information stack so that no elements are lost in multiple retries, cf. Fig. 4. With this additional bookkeeping, correctness

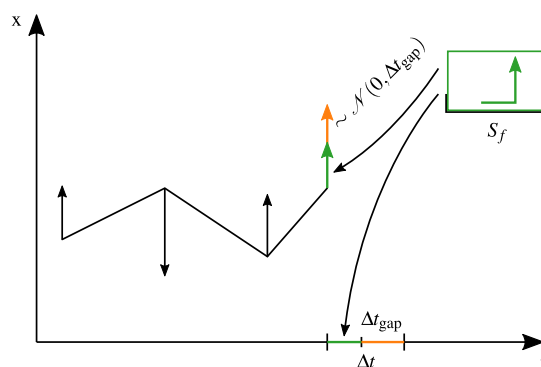


FIG. 2. After an accepted step has been performed, a new random increment is prepared for the next trial step of length Δt . If available, future information—stemming from previously rejected trial steps—has to be incorporated in the generation of new random vectors in order to retain the properties of Brownian motion. In the shown case, the future information stack contains one element, which is popped and accumulated to the new random increment and time interval. The stack is now empty and a difference Δt_{gap} to the goal timestep Δt remains. For this gap, a new uncorrelated random increment has to be generated from $\mathcal{N}(0, \Delta t_{\text{gap}})$ to complete the preparation of the next trial step.

and generality are ensured in all cases and the RSwM3 algorithm is complete.

Notably, with the structuring of information into stacks where only the top element is directly accessible (“last in first out”), the chronological time order is automatically kept intact so that one only has to store time intervals and no absolute timepoints. Furthermore, searching or sorting of elements is prevented entirely, which makes all operations $\mathcal{O}(1)$ and leads to efficient implementations.

We point out that the original RSwM3 rejection branch as given in Ref. 24 was not entirely correct and draw a comparison to our rectifications in Appendix B, which have been brought to attention⁴⁹ and have since been fixed in the reference implementation `DifferentialEquations.jl`.⁵⁰ Crucially, the correction not only applies to the case of BD but is rather relevant for the solution of general SDEs as well. A full pseudocode listing of one adaptive BD trial step utilizing RSwM3 is given in Algorithm 2 in Appendix C along with further explanation of technical details.⁵¹

C. Sampling of observables

Within BD, observables can be obtained from the sampling of configuration space functions. As an example, consider the one-body density profile $\rho(\mathbf{r})$, which is defined as the average of the density operator $\hat{\rho}(\mathbf{r}, \mathbf{r}^N) = \sum_{i=1}^N \delta(\mathbf{r} - \mathbf{r}_i)$.

In simulations of equilibrium or steady states, one can use a time average over a suitably long interval $[0, T]$ to measure such quantities, i.e., for a general operator $\hat{A}(X, \mathbf{r}^N)$,

$$A(X) \approx \frac{1}{T} \int_0^T dt \hat{A}(X, \mathbf{r}^N(t)). \quad (18)$$

Note that the remaining dependence on X can consist of arbitrary scalar or vectorial quantities or also be empty. For example,

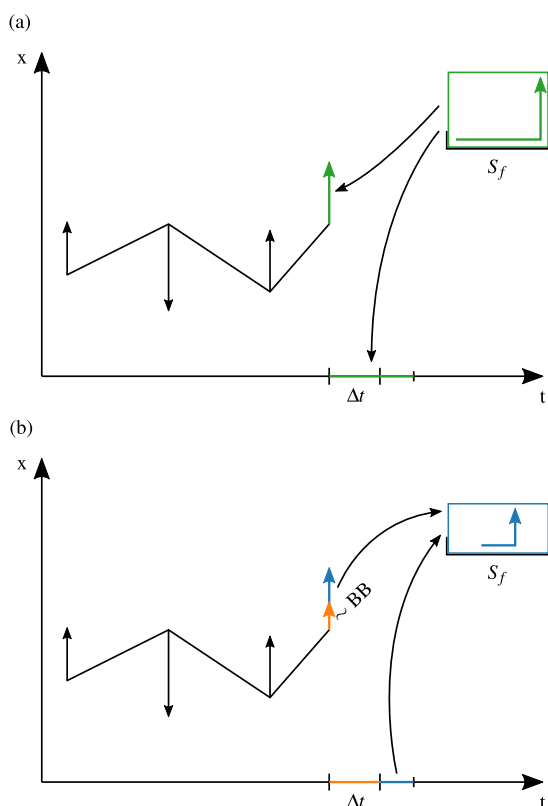


FIG. 3. The situation is similar to Fig. 2, where a step is rejected (a) and then retried (b). Here, the future information reaches further than the goal timestep Δt . In this case, the Brownian bridge (BB) has to be applied for the interpolation of an element from the future information stack. Generally, one pops the elements of the future stack S_f one after another and accumulates the random increments and time intervals until the element that crosses Δt is reached, to which the bridging theorem is then applied. In the shown example, the interpolation is done with the first element of S_f , since it already surpasses Δt . Similar to Fig. 1, the remainder of the bridged increment and time interval is pushed back onto S_f .

$X = (\mathbf{r}, \mathbf{r}')$ or $X = \mathbf{r}$ for general two- or one-body fields, $X = r$ for the isotropic radial distribution function, or $X = \emptyset$ for bulk quantities such as pressure or heat capacity.

Practically, $\hat{A}(X, \mathbf{r}^N)$ is evaluated in each step and an X -resolved histogram is accumulated, which yields $A(X)$ after normalization. Considering the numerical discretization of $[0, T]$ into n timesteps of constant length Δt within a conventional BD simulation, Eq. (18) is usually implemented as

$$A(X) \approx \frac{1}{n} \sum_{k=1}^n \hat{A}(X, \mathbf{r}_k^N). \quad (19)$$

In adaptive BD with varying timestep lengths, one cannot use Eq. (19) directly, since this would cause disproportionately many contributions to $A(X)$ from small timesteps and would thus lead

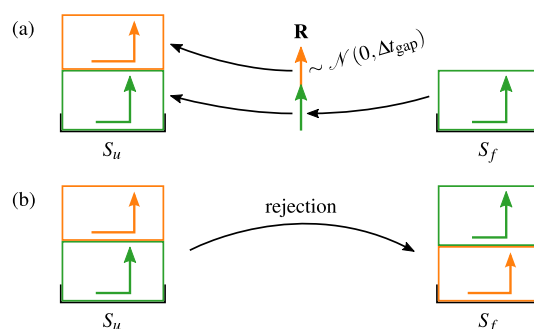


FIG. 4. To keep track of the random increments that are used in the construction of \mathbf{R} , a second stack S_u is introduced. In (a), the situation of Fig. 2 is shown as an example, where \mathbf{R} consists of an element of S_f (stemming from a previous rejection) and a Gaussian contribution $\mathbf{R}_{\text{gap}} \sim \mathcal{N}(0, \Delta t_{\text{gap}})$. In the case of rejection, the elements that were popped from S_f as well as newly drawn increments such as \mathbf{R}_{gap} would be lost unrecoverably. By using S_u as an intermediate storage, all contributions to \mathbf{R} can be transferred back to S_f such that no information about drawn random increments is lost and the same Brownian path is still followed. These considerations apply as well when random vectors are drawn via the Brownian bridge theorem, as, e.g., in Figs. 1 and 3.

to a biased evaluation of any observable. Formally, the quadrature in Eq. (18) now has to be evaluated numerically at non-equidistant integration points.

Therefore, if the time interval $[0, T]$ is discretized into n non-equidistant timepoints $0 = t_1 < t_2 < \dots < t_n < t_{n+1} = T$ and $\Delta t_k = t_{k+1} - t_k$,

$$A(X) \approx \frac{1}{T} \sum_{k=1}^n \Delta t_k \hat{A}(X, \mathbf{r}_k^N) \quad (20)$$

constitutes a generalization of Eq. (19) for this case that enables a straightforward sampling of observables within adaptive BD.

An alternative technique can be employed in scenarios where the state of the system shall be sampled on a sparser time grid than the one given by the integration timesteps. Then, regular sampling points can be defined that must be hit by the timestepping procedure (e.g., by artificially shortening the preceding step). On this regular time grid, Eq. (19) can be used again. In particular, in non-equilibrium situations and for the measurement of time-dependent correlation functions such as the van Hove two-body correlation function,⁵²⁻⁵⁷ this method might be beneficial since quantities can still be evaluated at certain timepoints rather than having to construct a time-resolved histogram consisting of finite time intervals. Note, however, that timestepping to predefined halting points is not yet considered in Algorithm 2.

IV. SIMULATION RESULTS

To test and illustrate the adaptive BD algorithm, we investigate the truncated and shifted Lennard-Jones fluid with interaction potential

$$\Phi_{\text{LJTS}}(r) = \begin{cases} \Phi_{\text{LJ}}(r) - \Phi_{\text{LJ}}(r_c), & r < r_c \\ 0, & r \geq r_c, \end{cases} \quad (21)$$

where

$$\Phi_{\text{LJ}}(r) = 4\epsilon \left[\left(\frac{\sigma}{r} \right)^{12} - \left(\frac{\sigma}{r} \right)^6 \right] \quad (22)$$

and r is the interparticle distance. We set a cutoff radius of $r_c = 2.5\sigma$ throughout Secs. IV A and IV B and use reduced Lennard-Jones units that yield the reduced timescale $\tau = \sigma^2\gamma/\epsilon$.

A common problem in conventional BD simulations is the choice of an appropriate timestep. Obviously, a too small value of Δt —while leading to accurate trajectories—has a strong performance impact, hindering runs that would reveal long-time behavior and prohibiting extensive sampling periods, which are desirable from the viewpoint of the time average (20). Still, Δt must be kept below a certain threshold above which results might be wrong or the simulation becomes unstable. Unfortunately, due to the absence of any intrinsic error estimates, judgment of a chosen Δt is generally not straightforward. For instance, one can merely observe the stability of a single simulation run and accept Δt if sensible output is produced and certain properties of the system (such as its energy) are well-behaved. Another possibility is the costly conduction of several simulation runs with differing timesteps, thereby cross-validating gathered results. Consequently, a true *a priori* choice of the timestep is not possible in general and test runs cannot always be avoided.

With adaptive timestepping, this problem is entirely prevented as one does not need to make a conscious choice for Δt at all. Instead, the maximum local error of a step is restricted by the user-defined tolerance (11), ensuring correctness of results up to a controllable discretization error. This does come at the moderate cost of overhead due to the additional operations per step necessary in the embedded Heun–Euler method and the RSWM algorithm. However, as we demonstrate in the following, the benefits of this method far outweigh the cost even in simple situations.

A. Lennard-Jones bulk fluid in equilibrium

In the following, we compare results from conventional BD to those obtained with adaptive BD. We first consider a bulk system of size $7 \times 7 \times 6\sigma^3$ with periodic boundary conditions at temperature $k_B T = 0.8\epsilon$ consisting of $N = 100$ Lennard-Jones particles initialized on a simple cubic lattice. In the process of equilibration, a gaseous and a liquid phase emerge, and the system therefore becomes inhomogeneous.

With non-adaptive Euler–Maruyama BD, a timestep $\Delta t_{\text{fix}} = 10^{-4}\tau$ is chosen to consistently converge to this state. This value is small enough to avoid severe problems that occur reproducibly for $\Delta t_{\text{fix}} \gtrsim 5 \cdot 10^{-4}\tau$, where the simulation occasionally crashes or produces sudden jumps in energy due to faulty particle displacements.

In contrast, the timestepping of an adaptive BD simulation run is shown both as a timeseries and as a histogram in Fig. 5. The tolerance coefficients in Eq. (11) are thereby set to $\epsilon_{\text{abs}} = 0.05\sigma$ and $\epsilon_{\text{rel}} = 0.05$ and the ∞ -norm is used in the reduction from particle-wise to global error (12). One can see that large stepsizes up to $\Delta t \approx 6 \cdot 10^{-4}\tau$ occur without the error exceeding the tolerance threshold. The majority of steps can be executed with a timestep larger than the value $\Delta t_{\text{fix}} = 10^{-4}\tau$. On the other hand, the algorithm is able to detect moves that would cause large errors where it decreases Δt appropriately. It is striking that in the shown sample, minimum timesteps as small as $\Delta t = 3 \cdot 10^{-6}\tau$ occur. This is far

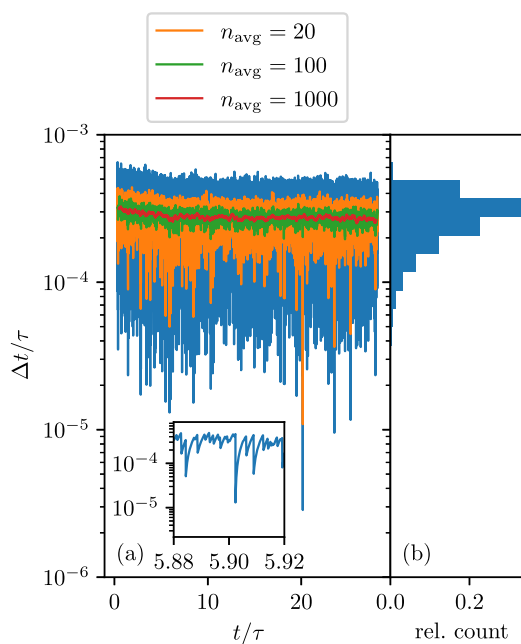


FIG. 5. The evolution of chosen timesteps for accepted moves is shown in (a). To accentuate the distribution of values of Δt further, moving averages taken over the surrounding n_{avg} points of a respective timestep record are depicted. One can see that the timestep Δt varies rapidly in a broad range between $\Delta t \approx 3 \cdot 10^{-6}\tau$ and $\Delta t \approx 6 \cdot 10^{-4}\tau$ around a mean value of $\Delta t \approx 2.8 \cdot 10^{-4}\tau$. In the inset of (a), a close-up of the timestep behavior is given, which reveals the rapid reduction of Δt at jammed states and the quick recovery afterward. In (b), the relative distribution of the data in (a) is illustrated. It is evident that the majority of steps can be executed with a large timestep, leading to increased performance of the BD simulation. On the other hand, in the rare event of a step that would produce large errors, the timestep is decreased appropriately to values far below those that would be chosen in a fixed-timestep BD run.

below the stepsize of $\Delta t_{\text{fix}} = 10^{-4}\tau$ chosen in the fixed-timestep BD run above, which indicates that although the simulation is stable for this value, there are still steps that produce substantial local errors in the particle trajectories. For even larger values of Δt_{fix} , it is those unresolved collision events that cause unphysical particle displacements, which then cascade and crash the simulation run. In comparison, the adaptive BD run yields a mean timestep of $\bar{\Delta t} = 3 \cdot 10^{-4}\tau$, which is larger than the heuristically chosen fixed timestep.

1. Performance and overhead

Per step, due to an additional evaluation via the Heun method (9), twice the computational effort is needed to calculate the deterministic forces compared to a single evaluation of the Euler–Maruyama step (8). This procedure alone has the benefit of increased accuracy though, and it hence makes larger timesteps feasible.

The computational overhead due to adaptivity with RSWM3 comes mainly from storing random increments on both stacks and

applying this information in the construction of new random forces. Therefore, potential for further optimization lies in a cache-friendly organization of the stacks in memory as well as in circumventing superfluous access and copy instructions altogether. The latter considerations suggest that avoiding rejections, and more importantly, avoiding re-rejections, is crucial for good performance and reasonable memory consumption of the algorithm. As already noted, in practice, this can be accomplished with a small value of q_{\min} that allows for a rapid reduction of Δt in the case of unfortunate random events and a conservative value of q_{\max} to avoid too large timestepping after moves with fortunate random increments. In our implementation, the cost of RSwM routines is estimated to lie below 10% of the total runtime in common situations.

B. Non-equilibrium—Formation of colloidal films

While the benefits of adaptive BD are already significant in equilibrium, its real advantages over conventional BD become particularly clear in non-equilibrium situations. Due to the rich phenomenology—which still lacks a thorough understanding—and the important practical applications, the dynamics of colloidal suspensions near substrates and interfaces has been the center of attention in many recent works.^{25–30,58} Nevertheless, the simulation of time-dependent interfacial processes is far from straightforward, and especially for common BD, stability issues are expected with increasing packing fraction.

In the following, we apply adaptive BD to systems of Lennard-Jones particles and simulate evaporation of the implicit solvent. This is done by introducing an external potential that models the fixed substrate surface as well as a moving air–solvent interface. As in Ref. 29, we set

$$V_{\text{ext}}^{(i)}(z, t) = B \left(e^{-\kappa(z-\sigma^{(i)}/2)} + e^{\kappa(z+\sigma^{(i)}/2-L(t))} \right) \quad (23)$$

to only vary in the z -direction and assume periodic boundary conditions in the remaining two directions. The value of κ controls the softness of the substrate and the air–solvent interface, while B sets their strength. We distinguish between the different particle sizes $\sigma^{(i)}$ to account for the offset of the particle centers where the external potential is evaluated. The position $L(t)$ of the air–solvent interface is time-dependent and follows a linear motion $L(t) = L_0 - vt$ with initial position L_0 and constant velocity v .

In the following, systems in a box that is elongated in the z -direction are considered. To ensure dominating non-equilibrium effects, values for the air–solvent interface velocities are chosen, which yield large Péclet numbers $\text{Pe}^{(i)} = L_0 v / D^{(i)} \gg 1$, where $D^{(i)} = k_B T / \gamma^{(i)}$ is the Einstein–Smoluchowski diffusion coefficient and $\gamma^{(i)} \propto \sigma^{(i)}$ due to Stokes.

When attempting molecular simulations of such systems in a conventional approach, one is faced with a non-trivial choice of the timestep length Δt_{fix} since it has to be large enough to be efficient in the dilute phase but also small enough to capture the motion of the dense final state of system. A cumbersome solution would be a subdivision of the simulation into subsequent time intervals, thereby choosing timesteps that suit the density of the current state. This method is beset by problems as the density profile becomes inhomogeneous and is not known *a priori*.

We show that by employing the adaptive BD method of Sec. III, these issues become non-existent. Concerning the physical results of the simulation runs, the automatically chosen timestep is indeed closely connected to the increasing packing fraction as well as to the structural properties of the respective colloidal system, as will be discussed below. Similar test runs as the ones shown in the following but carried out with constant timestepping and a naive choice of Δt_{fix} frequently lead to instabilities in the high-density regimes, ultimately resulting in unphysical trajectories or crashes of the program. Due to the possibility of stable and accurate simulations of closely packed phases with adaptive BD, we focus on the investigation of the final conformation of the colloidal suspension.

1. Single species, moderate driving

First, a single species Lennard-Jones system is studied and the box size is chosen as $8 \times 8 \times 50\sigma^3$. The Lennard-Jones particles are initialized on a simple cubic lattice with lattice constant 2σ and the velocity of the air–solvent interface is set to $v = 1\sigma/\tau$. We set $\epsilon_{\text{abs}} = 0.01\sigma$ to accommodate for smaller particle displacements in the dense phase and relax the relative tolerance to $\epsilon_{\text{rel}} = 0.1$.

As one can see in Fig. 6, the timestep is automatically adjusted as a reaction to the increasing density. In the course of the simulation run, the average number density increases from $\sim 0.07\sigma^{-3}$ to $1.4\sigma^{-3}$ although the particles first accumulate near the air–solvent interface. Astonishingly, even the freezing transition at the end of the simulation run can be captured effortlessly. This illustrates the influence of collective order on the chosen timestep. With rising density of the Lennard-Jones fluid, the timestep decreases on average due to the shorter mean free path of the particles and more frequent collisions. At this stage, Δt varies significantly and very small timesteps maneuver the system safely through jammed states of the disordered fluid. In the process of crystallization, the timestep decreases rapidly to accommodate for the reduced free path of the particles before it shortly relaxes to a plateau when crystal order is achieved. Additionally, the variance of Δt decreases and, contrary to the behavior in the liquid phase, fewer jammed states can be observed. This is due to the crystal order of the solid phase, which prevents frequent close encounters of particles and hence alleviates the need for a rapid reduction of Δt .

2. Single species, strong driving

If the evaporation rate is increased via a faster moving air–solvent interface, the final structure of the colloidal suspension is altered. Particularly, with rising air–solvent velocity v , a perfect crystallization process is hindered and defects in the crystal structure occur. This is reflected in the timestepping evolution, as jammed states still happen frequently in the dense regime due to misaligned particles. Therefore, unlike in the previous case of no defects, sudden jumps to very small timesteps can still be observed as depicted in Fig. 7.

If the velocity of the air–solvent interface is increased even further, amorphous states can be reached, where no crystal order prevails. Nevertheless, our method is still able to resolve the particle trajectories of those quenched particle configurations so that the simulation remains both stable and accurate even in such demanding circumstances.

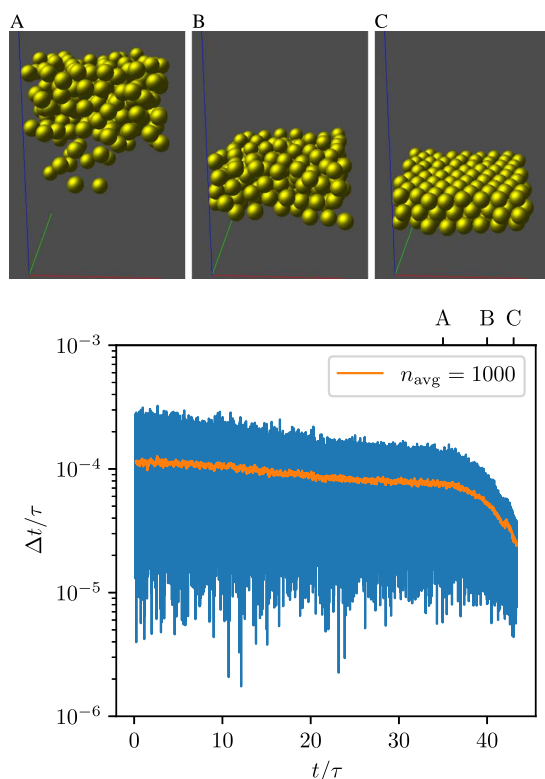


FIG. 6. The timestepping evolution in a system with moving interface modeled via Eq. (23) with parameters $B = 7000\epsilon$, $\kappa = 1/\sigma$ (adapted from Ref. 29), and $v = 1\sigma/\tau$ is shown. We depict both the actual timeseries whose envelope visualizes the maximum and minimum values of Δt and a moving average over the surrounding n_{avg} points to uncover the mean chosen timestep. As the density increases and the propagation of the overdamped Langevin equation becomes more difficult, the timestep is systematically decreased. This is an automatic process that needs no user input and that can even handle the freezing transition which occurs at the end of the simulation. To illustrate this process, typical snapshots of the system are given at different timepoints, which are marked in the timestepping plot as A, B, and C and correspond to a dilute, a prefrozen, and a crystallized state. In particular, in the transition from B to C, frequent particle collisions occur, which are resolved carefully by the adaptive BD method.

3. Binary mixture

Returning to stratification phenomena, we consider mixtures of particles differing in size. Depending on the Péclet numbers of the big (subscript b) and small (subscript s) particle species and their absolute value (i.e., if $Pe \ll 1$ or $Pe \gg 1$), different structures of the final phase can emerge, ranging from “small-on-top” or “big-on-top” layering to more complicated conformations.²⁹ For large Péclet numbers $1 \ll Pe_s < Pe_b$, studies of Fortini *et al.*⁵⁸ have shown the formation of a “small-on-top” structure, i.e., the accumulation of the small particle species near the moving interface. Additionally, in the immediate vicinity of the air–solvent boundary,

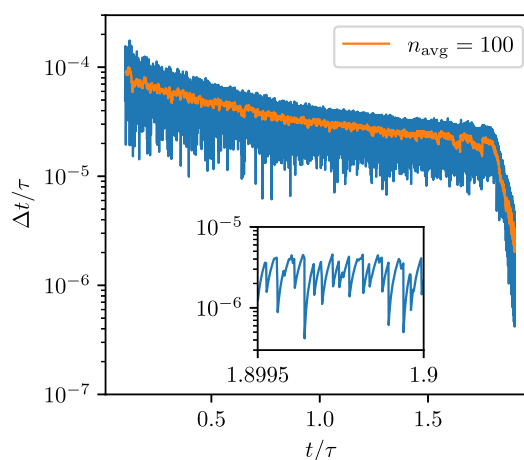


FIG. 7. Time evolution and moving average of the timestep Δt for the air–solvent interface velocity being increased to $v = 50\sigma/\tau$ in a larger system of box size $10 \times 10 \times 100\sigma^3$. In this case, defects are induced during the crystallization process, which prevent a perfect crystal order of the final particle configuration. Jammed states still occur frequently, and the timestep has to accommodate rapidly to resolve particle displacements correctly. This is depicted in the inset, which shows that sudden jumps to small values of Δt still occur in the high-density regime, indicating error-prone force evaluations due to prevailing defects in the crystal structure.

a thin layer of big particles remains trapped due to their low mobility.

In the following, a binary mixture of Lennard-Jones particles with diameters $\sigma_b = \sigma$ and $\sigma_s = 0.5\sigma$ is simulated in a system of size $10 \times 10 \times 100\sigma^3$ and the velocity of the air–solvent interface is set to $v = 1\sigma/\tau$ as before. We initialize $N_b = 768$ big and $N_s = 4145$ small particles uniformly in the simulation domain and particularly focus in our analysis on the structure of the final dense phase.

As the simulation advances in time, the observations of Fortini *et al.*⁵⁸ can be verified. A thin layer of big particles at the air–solvent interface followed by a broad accumulation of small particles emerges. The timestepping evolution shows similar behavior to the single species case shown in Fig. 6. On average, the value of Δt decreases and throughout the simulation, jumps to low values occur repeatedly when interparticle collisions have to be resolved accurately.

As the system approaches the dense regime, the finalizing particle distribution of the dried colloidal suspension can be investigated. One can see that a thin layer of big particles develops in close proximity to the substrate, similar to the one forming throughout the simulation at the air–solvent interface. This process can again be explained by the lower mobility of the big particles compared to the small ones, which prevents a uniform diffusion away from the substrate.

Moreover, as the packing fraction increases further, the structure of the interfacial layers of the trapped big species changes. While only a single peak is visible at first, a second peak develops in the last stages of the evaporation process. This phenomenon occurs both at

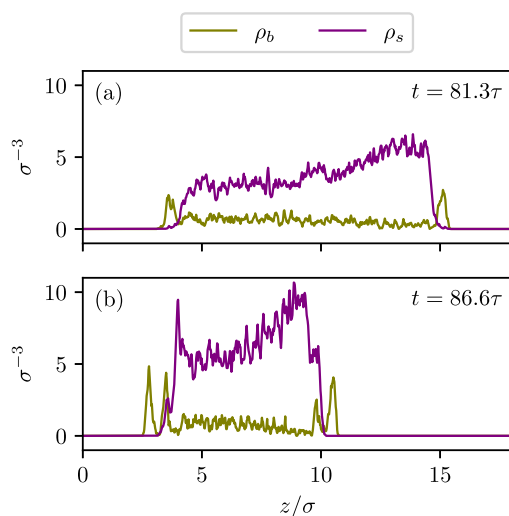


FIG. 8. The density profiles $\rho_b(z)$ and $\rho_s(z)$ of the big and small particle species in a stratifying colloidal suspension of a binary Lennard-Jones mixture with particle diameters $\sigma_b = \sigma$ and $\sigma_s = 0.5\sigma$ are shown at two timepoints of the simulation. In (a), single layers of the big species have already emerged near the substrate and the air–solvent interface, which enclose the dominating small particles in the middle of the box. At a later time (b) when the air–solvent interface has moved further toward the substrate and the packing fraction has hence increased, a second layer of the big particles forms at both interfaces and the final concentration gradient of the small species manifests within the dried film. Crucially, the intricate details of the final conformation demand an accurate numerical treatment of the dynamics of the closely packed colloidal suspension, to which adaptive BD offers a feasible solution.

the substrate and at the air–solvent interface although its appearance happens earlier and more pronounced at the former.

Even for this simple model mixture of colloidal particles that differ only in diameter, the final conformation after evaporation of the implicit solvent possesses an intricate structure. Both at the substrate and at the top of the film, primary and secondary layers of the big particle species build up. Those layers enclose a broad accumulation of the small particle species, which is by no means uniform but rather develops a concentration gradient in the positive z -direction, outlined by peaks of the respective density profile close to the big particle layers. The formation of the described final state is illustrated in Fig. 8, where the density profiles of both particle species are shown for two timepoints at the end of the simulation run.

V. CONCLUSION

In this work, we have constructed a novel method for BD simulations by employing recently developed algorithms for the adaptive numerical solution of SDEs to the case of Brownian motion as described on the level of the overdamped Langevin equation (1). For the evaluation of a local error estimate in each trial step, we have complemented the simple Euler–Maruyama scheme (8) found in common BD with a higher-order Heun step (9). By comparison of their discrepancy with a user-defined tolerance (11)

composed of an absolute and a relative contribution, we were able to impose a criterion (16) for the acceptance or rejection of the trial step and for the adaptation of Δt . Special care was thereby required in the reduction from particle-wise errors (10) to a global scalar error estimate (12).

Due to the stochastic nature of Brownian motion, the rejection and subsequent retrial of a timestep could not be done naively by redrawing uncorrelated random vectors in this case. Instead, a sophisticated method had to be employed to ensure the validity of the statistical properties of the random process in Eq. (1) and hence to avoid biased random forces from a physical point of view. We have illustrated that the Brownian bridge theorem (7) resolves this problem formally and that RSwM²⁴ provides a feasible implementation method based on this theorem. Hence, we specialized RSwM to the case of Brownian motion in Sec. III B and constructed the fully adaptive BD scheme outlined in Algorithm 2. A correction to the original algorithm of Ref. 24 is given in Appendix B, and a generalization of adaptive BD to non-overdamped Langevin dynamics is outlined in Appendix A.

To test our framework, we applied the adaptive BD method to both equilibrium and non-equilibrium Lennard-Jones systems focusing on the analysis of individual trajectories. Even in the standard case of a phase-separating bulk fluid, we could verify that the use of RSwM induced no significant computational overhead and that a performance gain could be achieved compared to the fixed-timestep Euler–Maruyama method. This is complemented by practical convenience, since Δt needs not be chosen *a priori*.

The real advantages of adaptive BD become clear in more demanding situations where a fixed timestep would ultimately lead to inaccuracy and instability of the simulation without manual intervention. We have shown this with non-equilibrium systems of drying colloidal suspensions and have modeled the rapid evaporation of the implicit solvent by a moving interface as in Ref. 29. With our method, we achieved efficient timestepping and unconditional stability of the simulation even in the final stages where the packing fraction increases rapidly and the final structural configuration of the dried film develops. Particularly, in a single-species Lennard-Jones system, the freezing transition could be captured effortlessly even if crystal defects remained as a result of strong external driving. In the more elaborate case of a binary mixture of different-size particles, the intricate structure of the colloidal film could be resolved accurately. Here, we reported the development of a dual layer of the big particle species both at the substrate and at the top interface, while a concentration gradient of the small particle species could be observed in between. This shows that the method can be used to predict the arrangement of stratified films efficiently and with great detail, which could be helpful in the determination of their macroscopic properties.

We expect similar benefits in all sorts of situations where fundamental changes within the system call for more accurate or more relaxed numerical timestepping. For instance, this could be the case in sheared systems,^{59,60} for sedimenting^{61,62} or cluster-forming⁶³ colloidal suspensions, in microrheological simulations,⁶⁴ for phase transitions and especially the glass transition,⁶⁵ in the formation of crystals and quasicrystals,^{66,67} in active matter,^{68–71} possibly including active crystallization,^{72,73} as well as for responsive colloids.⁷⁴ In any respect, adaptive BD can help in a more accurate measurement of observables, since the evaluation of the average (20) is not

hampered by erroneous particle configurations, which might occur in conventional BD. In particular, for quantities with a one-sided bias such as absolute or square values of particle forces and velocities, the abundance of outliers in the set of samples used in Eq. (20) is essential to yield valid results.

We finally illustrate possible improvements of the adaptive BD method itself, where several aspects come to mind. First, the choices of the parameters α in Eq. (16) as well as q_{\min} and q_{\max} in Eq. (17) were made mostly heuristically. We note that in Ref. 24, the influence of those parameters on the performance of the algorithm has been investigated but emphasize that results could vary for our high-dimensional setting of Brownian motion.

Second, recently developed adaptation methods for the step-size that employ control theory could be helpful. Thereby, Δt is not merely scaled after each trial step by a locally determined factor q as evaluated in Eq. (16). Instead, one constructs a proportional-integral-derivative (PID) controller for the selection of new timesteps. This means that the adaptation is now not only influenced proportionally by the error estimate of the current step, but rather it is also determined by integral and differential contributions, i.e., the memory of previous stepsizes and the local change of the stepsize. Adaptive timestepping with control theory has already been applied to ODEs^{75–77} and SDEs.⁴⁰ This method could help in our case to reduce the number of unnecessarily small steps even further. In our present implementation, a conservatively chosen q_{\max} in Eq. (17) keeps the number of rejections low because it restricts the growth of Δt after moves with coincidentally low error. However, it also has the effect of preventing a fast relaxation of Δt after a sudden drop, e.g., due to an unfortunate random event. Then, many steps are needed for Δt to grow back to its nominal value because the maximum gain in each step is limited by q_{\max} . With a control theory approach, a mechanism could be established, which permits sudden drops to low values of Δt but still ensures a rapid relaxation afterward.

Finally, the adaptive BD method could be augmented to include hydrodynamic interactions. This requires a careful treatment of the random forces, as they now incorporate the particle configuration \mathbf{r}^N . Therefore, the noise is no longer additive, which complicates the numerical scheme necessary for a correct discretization of the overdamped Langevin equation. Still, instead of Eqs. (8) and (9), existing methods for SDEs with non-additive noise could be employed within the presented framework to yield an adaptive timestepping procedure for BD with hydrodynamic interactions.

In summary, to capture the dynamics of systems that undergo structural changes such as the ones shown above, and to gain further understanding of the implications regarding, e.g., the resulting macroscopic properties, sophisticated simulation methods are needed. Adaptive BD provides the means to treat these problems with great accuracy while still being computationally feasible and robust, which is a crucial trait from a practical standpoint.

ACKNOWLEDGMENTS

We thank Christopher Rackauckas, Tobias Eckert, and Daniel de las Heras for useful comments. This work was supported by the German Research Foundation (DFG) via Project No. 436 306 241.

APPENDIX A: GENERALIZATION TO LANGEVIN DYNAMICS

In the following, we transfer the concepts of Sec. III to general (non-overdamped) Langevin dynamics. Thereby, the momenta of particles with masses $m^{(i)}$, $i = 1, \dots, N$, are explicitly considered in the Langevin equation

$$m^{(i)}\dot{\mathbf{r}}^{(i)}(t) = \mathbf{F}^{(i)}(\mathbf{r}^N(t)) - \gamma^{(i)}\dot{\mathbf{r}}^{(i)}(t) + \sqrt{2\gamma^{(i)}k_B T}\mathbf{R}^{(i)}(t), \quad (\text{A1})$$

where the notation is that of Eq. (1). Depending on the choice of $\gamma^{(i)}$, two special cases can be identified. BD is recovered in the diffusive regime for large $\gamma^{(i)}$. On the other hand, for vanishing friction and random forces, i.e., $\gamma^{(i)} = 0$, deterministic Hamiltonian equations of motion are obtained.

The SDE (A1) can be reformulated as a pair of first-order equations for the particle positions \mathbf{r}^N and velocities $\mathbf{v}^N = \dot{\mathbf{r}}^N$,

$$m^{(i)}\dot{\mathbf{v}}^{(i)}(t) = \mathbf{F}^{(i)}(\mathbf{r}^N(t)) - \gamma^{(i)}\mathbf{v}^{(i)}(t) + \sqrt{2\gamma^{(i)}k_B T}\mathbf{R}^{(i)}(t), \quad (\text{A2a})$$

$$\dot{\mathbf{r}}^{(i)}(t) = \mathbf{v}^{(i)}(t). \quad (\text{A2b})$$

From a numerical perspective, the treatment of Eq. (A2) differs significantly from that of the overdamped Langevin equation (1), since the second-order nature makes more involved timestepping procedures for \mathbf{r}^N and \mathbf{v}^N possible.

This can be illustrated easily when Eqs. (A2a) and (A2b) are considered in the Hamiltonian case. Then, via the separation of \mathbf{r}^N and \mathbf{v}^N , simple semi-implicit methods are readily available, such as the Euler-Cromer or the well-known velocity Verlet method that is commonly used in MD.^{78,79} From a fundamental point of view, the use of symplectic algorithms is necessary for Hamiltonian systems to ensure the correct description of physical conservation laws and hence to achieve numerical stability for long-time behavior. While the above-mentioned integrators possess this property, most explicit algorithms like the forward Euler and classic Runge–Kutta method fail in this regard.

When going from Hamiltonian to Langevin dynamics, one is faced with an appropriate generalization of the familiar deterministic integration schemes to include dissipative and random forces. This is addressed by so-called quasi-symplectic methods, which are integrators for SDEs of type (A2) that degenerate to symplectic ones when both the noise and the friction term vanish.⁸⁰ Still, it is not straightforward to construct schemes that are suitable for arbitrary $\gamma^{(i)}$, and different strategies have been used in Langevin-based molecular simulations.^{81–86}

To incorporate adaptive timestepping, one must again choose an integrator pair of different order to calculate an error estimation per step. The above considerations suggest, however, that at least for the higher-order method, a quasi-symplectic scheme is advisable for optimal efficiency and accuracy as it is expected to perform better than a naive application of the embedded Heun–Euler method (8) and (9) to general Langevin dynamics. Nevertheless, the latter could still be an adequate option when friction dominates.

Then, with the formalism described in Sec. III, the acceptance or rejection of trial steps and the use of RSwM is straightforward so that adaptive algorithms involving the Langevin equation (A1)

could be a feasible means for the simulation of dissipative particle dynamics in the future.

APPENDIX B: CORRECTNESS OF RSWM3 REJECTION BRANCH

Although the effect is likely subtle or even unmeasurable in most situations, in the original RSWM3 algorithm as described in Ref. 24 and formerly implemented in DifferentialEquations.jl,⁵⁰ the $q < 1$ branch was handled incorrectly. We list a pseudocode version thereof in Algorithm 1, where a specialization to our case of BD is already performed for ease of comparison with Algorithm 2.

To see why Algorithm 1 fails in some cases, consider multiple elements present on the stack S_u , e.g., as depicted in Fig. 9 where S_u contains three elements. Then, in lines 2–11 of Algorithm 1, elements are transferred successively from S_u back to S_f and their time intervals are accumulated in Δt_s as long as the remainder $\Delta t - \Delta t_s$ is still larger than the next goal timestep $q\Delta t$ (this is only the case for the green element in Fig. 9). After that, the Brownian bridge theorem is applied to $(\Delta t_K, \mathbf{R}_K) = (\Delta t - \Delta t_s, \mathbf{R} - \mathbf{R}_s)$. Therefore, the interpolation includes all the remaining elements of the stack S_u , i.e., the blue and violet one in Fig. 9, which implies that intermediate values of the Brownian path are not considered if S_u holds two or more elements at this point.

To yield a valid interpolation in this situation, the Brownian bridge must instead only be applied to the immediately following single element at the top of S_u (the blue one in Fig. 9). In Algorithm 2, lines 4–19 therefore replace the logic of Algorithm 1, which fixes the above issue by always considering only the single element that crosses $q\Delta t$ in the application of Eq. (7). This element is then interpolated at $q\Delta t$, for which the variable Δt_M is introduced to yield the corresponding fraction q_M of the element. Note that S_u always contains at least one element when entering the rejection branch (assuming a proper initialization of the simulation, cf. Appendix C).

ALGORITHM 1. Former $q < 1$ branch of RSWM3 where the bridge theorem might be applied to a wrong interval.

```

1:  $\Delta t_s \leftarrow 0, \mathbf{R}_s \leftarrow 0$ 
2: while  $S_u$  not empty do
3:   Pop top of  $S_u$  as  $(\Delta t_u, \mathbf{R}_u)$ 
4:   if  $\Delta t_s + \Delta t_u < (1 - q)\Delta t$  then
5:      $\Delta t_s \leftarrow \Delta t_s + \Delta t_u, \mathbf{R}_s \leftarrow \mathbf{R}_s + \mathbf{R}_u$ 
6:     Push  $(\Delta t_u, \mathbf{R}_u)$  onto  $S_f$ 
7:   else
8:     Push  $(\Delta t_u, \mathbf{R}_u)$  back onto  $S_u$ 
9:   break
10:  end if
11: end while
12:  $\Delta t_K \leftarrow \Delta t - \Delta t_s, \mathbf{R}_K \leftarrow \mathbf{R} - \mathbf{R}_s$ 
13:  $q_K \leftarrow q\Delta t / \Delta t_K$ 
14:  $\mathbf{R}_{\text{bridge}} \sim \mathcal{N}(q_K \mathbf{R}_K, (1 - q_K)q_K \Delta t_K)$ 
15: Push  $((1 - q_K)\Delta t_K, \mathbf{R}_K - \mathbf{R}_{\text{bridge}})$  onto  $S_f$ 
16:  $\Delta t \leftarrow q\Delta t, \mathbf{R} \leftarrow \mathbf{R}_{\text{bridge}}$ 

```

ALGORITHM 2. Embedded Heun–Euler trial step with RSWM3.

```

1: Calculate  $\bar{\mathbf{r}}_{k+1}$  and  $\mathbf{r}_{k+1}$  via Eqs. (8) and (9)
2: Calculate  $q$  via Eqs. (10)–(12), (16), and (17)
3: if  $q < 1$  then ▷ cf. Fig. 1, Appendix B
4:    $\Delta t_s \leftarrow 0, \mathbf{R}_s \leftarrow 0$ 
5:   while  $S_u$  not empty do
6:     Pop top of  $S_u$  as  $(\Delta t_u, \mathbf{R}_u)$ 
7:      $\Delta t_s \leftarrow \Delta t_s + \Delta t_u, \mathbf{R}_s \leftarrow \mathbf{R}_s + \mathbf{R}_u$ 
8:     if  $\Delta t_s < (1 - q)\Delta t$  then
9:       Push  $(\Delta t_u, \mathbf{R}_u)$  onto  $S_f$ 
10:    else
11:       $\Delta t_M \leftarrow \Delta t_s - (1 - q)\Delta t$ 
12:       $q_M \leftarrow \Delta t_M / \Delta t_u$ 
13:       $\mathbf{R}_{\text{bridge}} \sim \mathcal{N}(q_M \mathbf{R}_u, (1 - q_M)q_M \Delta t_u)$ 
14:      Push  $((1 - q_M)\Delta t_u, \mathbf{R}_u - \mathbf{R}_{\text{bridge}})$  onto  $S_f$ 
15:      Push  $(q_M \Delta t_u, \mathbf{R}_{\text{bridge}})$  onto  $S_u$ 
16:      break
17:    end if
18:  end while
19:  $\Delta t \leftarrow q\Delta t, \mathbf{R} \leftarrow \mathbf{R} - \mathbf{R}_s + \mathbf{R}_{\text{bridge}}$ 
20: else
21: Do step:  $t \leftarrow t + \Delta t, \mathbf{r}_k \leftarrow \mathbf{r}_{k+1}, \Delta t \leftarrow q\Delta t$ 
22: Empty  $S_u, \Delta t_s \leftarrow 0, \mathbf{R} \leftarrow 0$ 
23: while  $S_f$  not empty do
24:   Pop top of  $S_f$  as  $(\Delta t_f, \mathbf{R}_f)$ 
25:   if  $\Delta t_s + \Delta t_f < \Delta t$  then
26:      $\Delta t_s \leftarrow \Delta t_s + \Delta t_f, \mathbf{R} \leftarrow \mathbf{R} + \mathbf{R}_f$ 
27:     Push  $(\Delta t_f, \mathbf{R}_f)$  onto  $S_u$ 
28:   else ▷ cf. Fig. 3
29:      $q_M \leftarrow (\Delta t - \Delta t_s) / \Delta t_f$ 
30:      $\mathbf{R}_{\text{bridge}} \sim \mathcal{N}(q_M \mathbf{R}_f, (1 - q_M)q_M \Delta t_f)$ 
31:     Push  $((1 - q_M)\Delta t_f, \mathbf{R}_f - \mathbf{R}_{\text{bridge}})$  onto  $S_f$ 
32:     Push  $(q_M \Delta t_f, \mathbf{R}_{\text{bridge}})$  onto  $S_u$ 
33:      $\Delta t_s \leftarrow \Delta t_s + q_M \Delta t_f, \mathbf{R} \leftarrow \mathbf{R} + \mathbf{R}_{\text{bridge}}$ 
34:     break
35:   end if
36: end while
37:  $\Delta t_{\text{gap}} \leftarrow \Delta t - \Delta t_s$ 
38: if  $\Delta t_{\text{gap}} > 0$  then ▷ cf. Fig. 2
39:    $\mathbf{R}_{\text{gap}} \sim \mathcal{N}(0, \Delta t_{\text{gap}})$ 
40:    $\mathbf{R} \leftarrow \mathbf{R} + \mathbf{R}_{\text{gap}}$ 
41:   Push  $(\Delta t_{\text{gap}}, \mathbf{R}_{\text{gap}})$  onto  $S_u$ 
42: end if
43: end if

```

APPENDIX C: IMPLEMENTATION OF EMBEDDED HEUN–EULER TRIAL STEP WITH RSWM3

The embedded Heun–Euler trial step with RSWM3 is the integral part of the adaptive BD method, for which we provide a pseudocode implementation in the following and explain its technical details as well as its setting in a full simulation framework. At the beginning of the simulation, S_f must be empty and a finite positive value of the first timestep Δt is chosen heuristically (this choice is irrelevant, however, since the algorithm immediately adapts Δt to acceptable values). Gaussian random increments are drawn for the

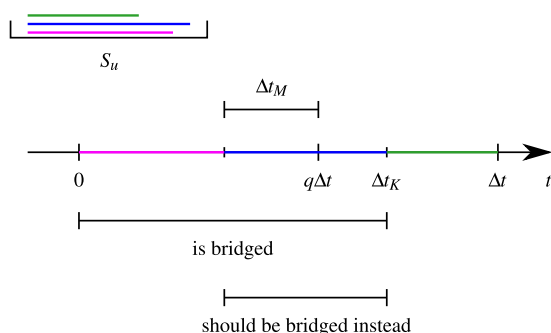


FIG. 9. A scenario is shown for which the original implementation of the RSWM3 rejection branch fails. For clarity, we only display the time intervals that reside on the stack S_u without their corresponding random vectors. In the presented case, the wrong interval (“is bridged”) is selected in the original RSWM3 implementation to which the Brownian bridge theorem (7) is applied. This is fixed in Algorithm 2, where the correct element (“should be bridged”) is considered via the calculation of Δt_M .

initial trial step via $\mathbf{R} \sim \mathcal{N}(0, \Delta t)$, which are pushed onto the stack S_u . This completes the initialization of the simulation run and a loop over trial steps can be started (until a certain simulation time or number of steps is reached).

Then, in each trial step, which is listed in Algorithm 2, the Euler and Heun approximations $\tilde{\mathbf{r}}_{k+1}$ and \mathbf{r}_{k+1} are evaluated via Eqs. (8) and (9) and the adaptation factor q is calculated via Eqs. (16) and (17). This requires an error estimate (12), which is obtained from the two approximations via Eqs. (10) and (11).

If $q < 1$, the proposed step is rejected and a retrial must be performed. For a detailed description of the rejection branch (lines 4–19), we refer to Appendix B, where our changes to the original RSWM3 $q < 1$ case are illustrated as well. If a step is accepted, i.e., $q > 1$, the particle positions and physical time of the system are updated accordingly (line 21) before resetting random increments \mathbf{R} and stack S_u (line 22). Then, in lines 23–42, new random increments are constructed for the next trial step.

For this, elements on S_f stemming from previously rejected steps have to be accounted for as long as parts of them lie within the goal timestep Δt . Therefore, the elements are transferred successively from S_f to S_u and their time intervals and random increments are accumulated in Δt_s and \mathbf{R} . If at some point Δt_s exceeds Δt , the corresponding element is interpolated at Δt via the Brownian bridge theorem (7) in lines 29–34 and one proceeds with the next trial step. Conversely, if all elements of S_f were popped and a gap Δt_{gap} remains between Δt_s and the goal timestep Δt , new Gaussian random increments $\mathbf{R}_{\text{gap}} \sim \mathcal{N}(0, \Delta t_{\text{gap}})$ are drawn, added to \mathbf{R} , and pushed onto S_u in lines 39–41 before attempting the next trial step. Note that the values of \mathbf{R} persist across trial steps and are only reset after accepted moves.

Throughout the algorithm, bookkeeping of random increments and corresponding time intervals is established by pushing those elements that are involved in the current random increment \mathbf{R} onto S_u and by storing elements that become relevant beyond the current step on S_f . This procedure is especially important after bridging an element at the goal timestep, where the two resulting parts

are pushed onto S_u and S_f , respectively (lines 14, 15 and 31, 32). Consequently, no drawn random increments are ever lost.

DATA AVAILABILITY

The data that support the findings of this study are available from the corresponding author upon reasonable request.

REFERENCES

- D. Frenkel and B. Smit, *Understanding Molecular Simulation: From Algorithms to Applications*, Computational Science Series No. 1, 2nd ed. (Academic Press, San Diego, 2002).
- J.-P. Hansen and I. R. McDonald, *Theory of Simple Liquids: With Applications of Soft Matter*, 4th ed. (Elsevier/Academic Press, Amsterdam, 2013).
- M. P. Allen and D. J. Tildesley, *Computer Simulation of Liquids*, reprinted edition (Oxford Science Publications, Clarendon Press, Oxford, 2009).
- M. Karplus and J. A. McCammon, *Nat. Struct. Biol.* **9**, 646 (2002).
- T. M. Squires and J. F. Brady, *Phys. Fluids* **17**, 073101 (2005).
- J. Reinhardt, A. Scacchi, and J. M. Brader, *J. Chem. Phys.* **140**, 144901 (2014).
- A. M. Puertas and T. Voigtmann, *J. Phys.: Condens. Matter* **26**, 243101 (2014).
- T. Geigenfeind, D. de las Heras, and M. Schmidt, *Commun. Phys.* **3**, 23 (2020).
- D. T. Gillespie, *J. Comput. Phys.* **22**, 403 (1976).
- H. C. Andersen, *J. Chem. Phys.* **72**, 2384 (1980).
- S. Nosé, *Mol. Phys.* **52**, 255 (1984).
- B. J. Alder and T. E. Wainwright, *J. Chem. Phys.* **31**, 459 (1959).
- A. Scala, T. Voigtmann, and C. De Michele, *J. Chem. Phys.* **126**, 134109 (2007).
- P. H. Colberg and F. Höfling, *Comput. Phys. Commun.* **182**, 1120 (2011).
- J.-S. Wang, T. K. Tay, and R. H. Swendsen, *Phys. Rev. Lett.* **82**, 476 (1999).
- D. P. Landau, S.-H. Tsai, and M. Exler, *Am. J. Phys.* **72**, 1294 (2004).
- D. de las Heras and M. Schmidt, *Phys. Rev. Lett.* **120**, 218001 (2018).
- B. Rotenberg, *J. Chem. Phys.* **153**, 150902 (2020).
- S. W. Coles, E. Mangaud, D. Frenkel, and B. Rotenberg, *J. Chem. Phys.* **154**, 191101 (2021).
- S. Fritsch, S. Pobleto, C. Junghans, G. Ciccotti, L. Delle Site, and K. Kremer, *Phys. Rev. Lett.* **108**, 170602 (2012).
- P. J. Rossky, J. D. Doll, and H. L. Friedman, *J. Chem. Phys.* **69**, 4628 (1978).
- M. Jardat, O. Bernard, P. Turq, and G. R. Kneller, *J. Chem. Phys.* **110**, 7993 (1999).
- P. E. Kloeden and E. Platen, *Numerical Solution of Stochastic Differential Equations*, 1st ed. (Springer-Verlag Berlin Heidelberg, 1992).
- C. Rackauckas and Q. Nie, *Discrete Contin. Dyn. Syst. - B* **22**, 2731 (2017).
- H. M. van der Kooij and J. Sprakel, *Soft Matter* **11**, 6353 (2015).
- M. Schulz and J. L. Keddie, *Soft Matter* **14**, 6181 (2018).
- D. K. Makepeace, A. Fortini, A. Markov, P. Locatelli, C. Lindsay, S. Moorhouse, R. Lind, R. P. Sear, and J. L. Keddie, *Soft Matter* **13**, 6969 (2017).
- R. E. Trueman, E. Lago Domingues, S. N. Emmett, M. W. Murray, J. L. Keddie, and A. F. Routh, *Langmuir* **28**, 3420 (2012).
- B. He, I. Martin-Fabiani, R. Roth, G. I. Tóth, and A. J. Archer, *Langmuir* **37**, 1399 (2021).
- A. Fortini and R. P. Sear, *Langmuir* **33**, 4796 (2017).
- K. Burrage and P. M. Burrage, *Appl. Numer. Math.* **22**, 81 (1996).
- A. Rößler, *SIAM J. Numer. Anal.* **48**, 922 (2010).
- E. Fehlberg, *Computing* **6**, 61 (1970).
- A. Rößler, *Proc. Appl. Math. Mech.* **2**, 461 (2003).
- O. C. Ibe, *Markov Processes for Stochastic Modeling* (Elsevier, 2013).
- J. G. Gaines and T. J. Lyons, *SIAM J. Appl. Math.* **57**, 1455 (1997).
- S. Mauthner, *J. Comput. Appl. Math.* **100**, 93 (1998).
- P. M. Burrage and K. Burrage, *SIAM J. Sci. Comput.* **24**, 848 (2002).
- H. Lamba, *J. Comput. Appl. Math.* **161**, 417 (2003).
- P. M. Burrage, R. Herdiana, and K. Burrage, *J. Comput. Appl. Math.* **170**, 317 (2004).

- ⁴¹H. Lamba, J. C. Mattingly, and A. M. Stuart, *IMA J. Numer. Anal.* **27**, 479 (2006).
- ⁴²V. Sotiropoulos and Y. N. Kaznessis, *J. Chem. Phys.* **128**, 014103 (2008).
- ⁴³S. Ilie, *J. Chem. Phys.* **137**, 234110 (2012).
- ⁴⁴A. M. Stuart and A. R. Humphries, *Dynamical Systems and Numerical Analysis*, Cambridge Monographs on Applied and Computational Mathematics No. 2 (Cambridge University Press, Cambridge, NY, 1996).
- ⁴⁵R. L. Honeycutt, *Phys. Rev. A* **45**, 600 (1992).
- ⁴⁶M. Fixman, *Macromolecules* **19**, 1195 (1986).
- ⁴⁷A. Iniesta and J. García de la Torre, *J. Chem. Phys.* **92**, 2015 (1990).
- ⁴⁸D. M. Heyes and A. C. Brańka, *Mol. Phys.* **98**, 1949 (2000).
- ⁴⁹This issue has been discussed in <https://github.com/SciML/DiffEqNoiseProcess.jl/pull/80>.
- ⁵⁰C. Rackauckas and Q. Nie, *J. Open Res. Software* **5**, 15 (2017).
- ⁵¹The corresponding implementation in C++ can be found in <https://gitlab.uni-bayreuth.de/bt306964/mbd>.
- ⁵²L. Yeomans-Reyna, H. Acuña-Campa, F. d. J. Guevara-Rodríguez, and M. Medina-Noyola, *Phys. Rev. E* **67**, 021108 (2003).
- ⁵³A. J. Archer, P. Hopkins, and M. Schmidt, *Phys. Rev. E* **75**, 040501 (2007).
- ⁵⁴P. Hopkins, A. Fortini, A. J. Archer, and M. Schmidt, *J. Chem. Phys.* **133**, 224505 (2010).
- ⁵⁵D. Stopper, R. Roth, and H. Hansen-Goos, *J. Phys.: Condens. Matter* **28**, 455101 (2016).
- ⁵⁶D. Stopper, A. L. Thorneywork, R. P. A. Dullens, and R. Roth, *J. Chem. Phys.* **148**, 104501 (2018).
- ⁵⁷L. L. Treffenstädt and M. Schmidt, *Phys. Rev. Lett.* **126**, 058002 (2021).
- ⁵⁸A. Fortini, I. Martín-Fabiani, J. L. De La Haye, P.-Y. Dugas, M. Lansalot, F. D'Agosto, E. Bourgeat-Lami, J. L. Keddie, and R. P. Sear, *Phys. Rev. Lett.* **116**, 118301 (2016).
- ⁵⁹M. Laurati, K. J. Mutch, N. Koumakis, J. Zausch, C. P. Amann, A. B. Schofield, G. Petekidis, J. F. Brady, J. Horbach, M. Fuchs, and S. U. Egelhaaf, *J. Phys.: Condens. Matter* **24**, 464104 (2012).
- ⁶⁰N. Jahreis and M. Schmidt, *Colloid Polym. Sci.* **298**, 895 (2020).
- ⁶¹A. J. Archer and A. Malijevský, *Mol. Phys.* **109**, 1087 (2011).
- ⁶²C. P. Royall, J. Dzubiella, M. Schmidt, and A. van Blaaderen, *Phys. Rev. Lett.* **98**, 188304 (2007).
- ⁶³J. Bleibel, S. Dietrich, A. Domínguez, and M. Oettel, *Phys. Rev. Lett.* **107**, 128302 (2011).
- ⁶⁴I. C. Carpen and J. F. Brady, *J. Rheol.* **49**, 1483 (2005).
- ⁶⁵H. Löwen, J.-P. Hansen, and J.-N. Roux, *Phys. Rev. A* **44**, 1169 (1991).
- ⁶⁶A. J. Archer, A. M. Rucklidge, and E. Knobloch, *Phys. Rev. E* **92**, 012324 (2015).
- ⁶⁷A. J. Archer, A. M. Rucklidge, and E. Knobloch, *Phys. Rev. Lett.* **111**, 165501 (2013).
- ⁶⁸G. Volpe, S. Gigan, and G. Volpe, *Am. J. Phys.* **82**, 659 (2014).
- ⁶⁹T. F. F. Farage, P. Krinninger, and J. M. Brader, *Phys. Rev. E* **91**, 042310 (2015).
- ⁷⁰S. Paliwal, V. Pymidis, L. Filion, and M. Dijkstra, *J. Chem. Phys.* **147**, 084902 (2017).
- ⁷¹S. Paliwal, J. Rodenburg, R. van Roij, and M. Dijkstra, *New J. Phys.* **20**, 015003 (2018).
- ⁷²A. K. Omar, K. Klymko, T. GrandPre, and P. L. Geissler, *Phys. Rev. Lett.* **126**, 188002 (2021).
- ⁷³F. Turci and N. B. Wilding, *Phys. Rev. Lett.* **126**, 038002 (2021).
- ⁷⁴U. Baul and J. Dzubiella, *J. Phys.: Condens. Matter* **33**, 174002 (2021).
- ⁷⁵K. Gustafsson, *ACM Trans. Math. Software* **20**, 496 (1994).
- ⁷⁶G. Söderlind, *Numer. Algorithms* **31**, 281 (2002).
- ⁷⁷G. Söderlind, *ACM Trans. Math. Software* **29**, 1 (2003).
- ⁷⁸L. Verlet, *Phys. Rev.* **159**, 98 (1967).
- ⁷⁹W. C. Swope, H. C. Andersen, P. H. Berens, and K. R. Wilson, *J. Chem. Phys.* **76**, 637 (1982).
- ⁸⁰G. N. Milstein, *IMA J. Numer. Anal.* **23**, 593 (2003).
- ⁸¹K. Burrage, I. Lenane, and G. Lythe, *SIAM J. Sci. Comput.* **29**, 245 (2007).
- ⁸²W. F. van Gunsteren and H. J. C. Berendsen, *Mol. Phys.* **45**, 637 (1982).
- ⁸³A. Brünger, C. L. Brooks, and M. Karplus, *Chem. Phys. Lett.* **105**, 495 (1984).
- ⁸⁴R. D. Skeel and J. A. Izaguirre, *Mol. Phys.* **100**, 3885 (2002).
- ⁸⁵N. Goga, A. J. Rzepiela, A. H. de Vries, S. J. Marrink, and H. J. C. Berendsen, *J. Chem. Theory Comput.* **8**, 3637 (2012).
- ⁸⁶B. Leimkuhler and C. Matthews, *Molecular Dynamics, Interdisciplinary Applied Mathematics* (Springer International Publishing, Cham, 2015), Vol. 39.

Inhomogeneous steady shear dynamics of a three-body colloidal gel former

Cite as: *J. Chem. Phys.* **158**, 054908 (2023); doi: 10.1063/5.0130655

Submitted: 13 October 2022 • Accepted: 15 January 2023 •

Published Online: 3 February 2023



View Online



Export Citation



CrossMark

Florian Sammüller,  Daniel de las Heras,  and Matthias Schmidt^{a)} 

AFFILIATIONS

Theoretische Physik II, Physikalisches Institut, Universität Bayreuth, D-95447 Bayreuth, Germany

Note: This paper is part of the JCP Special Topic on Colloidal Gels.

^{a)} Author to whom correspondence should be addressed: Matthias.Schmidt@uni-bayreuth.de

ABSTRACT

We investigate the stationary flow of a colloidal gel under an inhomogeneous external shear force using adaptive Brownian dynamics simulations. The interparticle forces are derived from the Stillinger–Weber potential, where the three-body term is tuned to enable network formation and gelation in equilibrium. When subjected to the shear force field, the system develops remarkable modulations in the one-body density profile. Depending on the shear magnitude, particles accumulate either in quiescent regions or in the vicinity of maximum net flow, and we deduce this strong non-equilibrium response to be characteristic of the gel state. Studying the components of the internal force parallel and perpendicular to the flow direction reveals that the emerging flow and structure of the stationary state are driven by significant viscous and structural superadiabatic forces. Thereby, the magnitude and nature of the observed non-equilibrium phenomena differ from the corresponding behavior of simple fluids. We demonstrate that a simple power functional theory reproduces accurately the viscous force profile, giving a rationale of the complex dynamical behavior of the system.

© 2023 Author(s). All article content, except where otherwise noted, is licensed under a Creative Commons Attribution (CC BY) license (<http://creativecommons.org/licenses/by/4.0/>). <https://doi.org/10.1063/5.0130655>

I. INTRODUCTION

Gelation in soft matter is a complex and important phenomenon that has many practical applications ranging from the use in household materials to advanced technological processes.^{1–6} A common property of gels is their ability to sustain weak external stresses due to the formation of persistent long-range network structures. From a microscopic point of view, it is the nontrivial correlation of particles arising from their internal interactions that gives gels their characteristic mechanical response.^{7–9}

However, the route to the generation of the network topology can be diverse.¹⁰ One common path to the gelation of colloids involves the crossing of a liquid–gas spinodal, e.g., by a sudden quench in temperature and the subsequent dynamical arrest of heterogeneous dense regions. This arrested spinodal decomposition is non-equilibrium in nature, and it bears similarity to the glass transition although it is driven by interparticle attraction rather than by repulsion.^{11–13} On the other hand, an equilibrium route to gel formation lies open by careful choice of the interparticle interactions in order to prevent macroscopic liquid–gas phase separation and to favor instead the local arrangement of particles into

interconnected clusters or chains. In this spirit, a multitude of interaction potentials have been investigated, which incorporate, for example, limitation of particle connectivity,^{14–17} competing short-range attraction and long-range repulsion,^{18,19} and anisotropy^{20–22} via, e.g., “patchy” interaction sites.^{23–25} The liquid–gas spinodal can sometimes be pushed to very low temperatures and densities, which enables large parts of the phase diagram to be governed by the percolation into dilute networks, as in so called “empty liquids.”^{26–28}

A further class of particle models for colloidal gels that the present work focuses on is based on the inclusion of three-body interactions to the interparticle interaction potential, which consists otherwise only of isotropic pair-interactions.^{29–36} It has been shown that an appropriate choice of the three-body term reproduces the distinctive network topology³⁷ as well as the characteristic nonlinear response to homogeneous shear, including strain hardening and yielding.³³ Especially under external load, the dynamics of such a gel can be intricate, e.g., exhibiting cooperative restructuring of particle bonds³¹ and shear banding.³³

While many studies have considered the response of gels to a linear shear profile up to their breaking point, not much is

known about their viscous flow behavior in *inhomogeneous* external force fields. However, it can be expected that the intrinsic features of a gel former, such as the tendency of particles to percolate, have substantial ramifications in such out-of-equilibrium scenarios. Specifically, one is tempted to assume that some of the genuine non-equilibrium effects^{38,39} already reported for simple fluids (such as shear migration) might even be amplified by additional three-body interactions.

In this work, we show that gels modeled via a modified Stillinger–Weber⁴⁰ potential with a preferred three-body angle of 180° as proposed by Saw, Ellegaard, Kob, and Sastry (SEKS)^{29,30} are indeed highly susceptible to these non-equilibrium effects when sheared by a sinusoidal external force profile. For this, we numerically investigate the behavior of the SEKS model with adaptive Brownian dynamics⁴¹ (adaptive BD), which is a stable and efficient method for the simulation of many-body systems governed by the overdamped Langevin equations of motion. We find that the properties of the emerging stationary state vary strongly with temperature and with the amplitude of the external force profile. Different behaviors occur in the shape of both the density and the internal force profiles as compared to simple fluids. In particular, we show that the superadiabatic (i.e., genuine out-of-equilibrium) contribution to the internal force is substantial in magnitude and that it is responsible for the structural and viscous behavior of the stationary shear flow. This is discussed from a microscopic point of view as well as in a coarse-grained fashion, where we use power functional theory^{42,43} (PFT) to develop a quantitative model for the superadiabatic viscous force. Besides representing a generic situation, the sinusoidal shear flow profile could be seen as a toy model for a mesoscopic convection roll. Convection typically occurs in sedimentation as upward streams alternate with downward streams.⁴⁴

This work is structured as follows: In Sec. II A, the modified Stillinger–Weber potential as well as details for its efficient computation is given. The adaptive BD method and its advantages for our non-equilibrium simulations are laid out in Sec. II B. In Sec. II C, the protocol for the simulation of the stationary flow state is described. In Secs. III A and III B, we show one-body profiles of the density as well as the parallel and perpendicular components of the internal force for a range of simulation parameters and discuss their behavior and interplay. An analogous interpretation on the level of internal stresses is given in Appendix A. In Appendix B, we showcase results for different values of the three-body angle of the Stillinger–Weber potential, and in Appendix C, the unusual non-equilibrium response of the gel is contrasted with numerical results for the simple Lennard-Jones fluid. In Sec. III C, the description of superadiabatic forces with PFT is illustrated and the results are compared with those from simulation. We conclude in Sec. IV and give an outlook to the investigation of further dynamical phenomena observed in our simulations and to a more extensive analysis with PFT.

II. SIMULATION METHOD

A. Particle model

The Stillinger–Weber potential⁴⁰ has originally been used for the simulation of solid and liquid silicon, and it has since been optimized and adapted to other particle types.^{45,46} The interparticle

interactions consist of a two-body potential $u_2(r)$ that models both isotropic attraction and repulsion depending on the distance r between two particles as well as a three-body contribution $u_3(r, r', \Theta)$. This three-body term imposes an energetically favorable angle Θ for three particles where a central particle is separated by the pairwise distances r and r' to two other particles. The directionality of internal interactions is therefore only realized via u_3 . Crucially, there is no need to explicitly incorporate orientational degrees of freedom, which is an advantage both in simulations as well as in a theoretical treatment.

In total, the internal energy potential possesses the form

$$U(\mathbf{r}^N) = \sum_i \sum_{j>i}^N u_2(r_{ij}) + \sum_i \sum_{j \neq i} \sum_{k>j}^N u_3(r_{ij}, r_{ik}, \Theta_{ijk}), \quad (1)$$

with

$$u_2(r) = A\epsilon \left[B \left(\frac{\sigma}{r} \right)^p - \left(\frac{\sigma}{r} \right)^q \right] \exp\left(\frac{\sigma}{r - a\sigma} \right), \quad (2)$$

$$u_3(r, r', \Theta) = \lambda\epsilon [\cos \Theta - \cos \Theta_0]^2 \times \exp\left(\frac{\gamma\sigma}{r - a\sigma} \right) \exp\left(\frac{\gamma\sigma}{r' - a\sigma} \right) \quad (3)$$

for a certain particle configuration $\mathbf{r}^N = \{\mathbf{r}^{(i)}, \dots, \mathbf{r}^{(N)}\}$ of the many-body system with N particles.

The parameters p , q , A , B , a , γ , λ , and Θ_0 can be tuned to alter the shape of the potential. A choice for these quantities, which is used in the present work and varies in some aspects from the one used originally by Stillinger and Weber,⁴⁰ is given in Table I. In particular, following previous studies of Saw *et al.*,^{29,30} we tune Θ_0 to obtain a gel former, which is described in more detail in the following. The formulation in Eqs. (2) and (3) refrains from using absolute units and only involves intrinsic energy (ϵ) and length (σ) scales. In an overdamped system with friction coefficient ζ , all physical quantities can therefore be expressed in a reduced form.

We note that the parameter a sets the cutoff distance since both $u_2(r)$ and $u_3(r, r', \Theta)$ as well as their gradients vanish smoothly for $r \rightarrow a\sigma$ and $r' \rightarrow a\sigma$. The potential is therefore inherently short-ranged (cf. the small value of a in Table I). This is a favorable property for the treatment in computer simulations since it enables the use of neighbor-tracking algorithms to avoid superfluous evaluations for particles beyond the cutoff distance, which substantially reduces the computational cost in large systems.

The parameter Θ_0 in the three-body term $u_3(r, r', \Theta)$ sets the preferred angle of a certain particle triplet (note that u_3 vanishes for $\Theta = \Theta_0$ and that it is otherwise strictly positive for particles within

TABLE I. In Eqs. (2) and (3), we adopt the parameters p , q , A , B , a , and γ of the original Stillinger–Weber⁴⁰ potential and choose the three-body strength λ as determined in Ref. 47. In accordance with Saw *et al.*,^{29,30} a preferred three-body angle of $\Theta_0 = 180^\circ$ then leads to the percolation of interconnected chains, enabling colloidal gelation in equilibrium.

p	q	A	B	a	γ	λ	Θ_0
4	0	7.049 556 27	0.602 224 558 4	1.8	1.2	23.15	180°

the cutoff distance). Most commonly, as discussed in the following, tetrahedral configurations are desired for which one chooses $\cos \Theta_0 = -1/3$. The strength of the three-body interaction term is adjusted via λ , which is often referred to as the tetrahedrality⁴⁷ for the above choice of Θ_0 .

A further computational optimization is employed, which makes use of the concrete structure of $u_3(r, r', \Theta)$ as given in Eq. (3). Via a rewriting of the three-body sum and the introduction of accumulation variables, an evaluation of the total energy and of all particle forces is possible by only iterating twice over all interacting particle pairs. In contrast, a naive implementation would require an iteration over particle triplets. For details of this exact reformulation, which leads to a substantial speedup in our simulations,⁴⁸ consult Ref. 30.

In summary, the versatility and computational efficacy of the Stillinger–Weber potential make it applicable to a wide range of problems. An important example, which conveys its use as an effective interaction potential for more complex particle types, is the monatomic water model of Molinero and Moore.⁴⁷ It has been shown by these authors that thermodynamic and structural properties of water (e.g., for the study of interfacial phenomena⁴⁹) can be captured accurately by this model via an appropriate choice of the absolute values of ϵ and σ as well as the tetrahedrality λ . By comparison with the melting temperature of water, they determined an optimal value of $\lambda = 23.15$, which lies between the respective tetrahedralities of silicon and carbon and which is adopted in our simulations.

While Eq. (3) has initially been conceptualized as a model for tetrahedrally coordinated particles, it is entirely conceivable to alter the preferred three-body angle Θ_0 . A variation of Θ_0 has significant consequences for the spatial correlations of the fluid since the formation of droplets might become energetically unfavorable and the self-assembly into interconnected chains that form open networks is enforced. Therefore, the careful choice of the values of Θ_0 and λ is a means to reduce the effective valency and to suppress the liquid–gas phase transition, making the Stillinger–Weber potential (1) a suitable model for colloidal gels. In the following, we set $\Theta_0 = 180^\circ$ although other values of Θ_0 have been shown to support gelation as well, e.g., as reported in Refs. 29 and 30, where a detailed investigation of the phase diagram and percolation behavior was carried out for various choices of λ and Θ_0 . (In Appendix B, illustrative results are presented for lower values of Θ_0 , which shows that its precise value has little impact on the sheared steady state as long as network formation can occur.) It is worth noting that gelation has also been investigated for other choices of two- and three-body interaction terms u_2 and u_3 apart from those given in Eqs. (2) and (3); see, e.g., Refs. 31–36. For instance, to yield stronger angular rigidity, the cosine difference in Eq. (3) can be exponentiated.^{31–35}

B. Adaptive Brownian dynamics

An important property of gels is their mechanical response to externally imposed strain. As particle bonds within the network are capable of sustaining substantial forces and torques without breaking, a gel exhibits elastic behavior before stiffening⁵⁰ as well as yielding at intermediate and large shear strain due to bending and breaking of bonds, respectively.³³ Numerically, these results can be

obtained, e.g., by performing a linear deformation of the simulation box and measuring the stress tensor. When using non-equilibrium molecular dynamics, adequate thermostating is required,^{51,52} which is not straightforward if spatially inhomogeneous deformations are considered. This is even more problematic if cause and effect are reversed, and an external force profile is applied, which generates a macroscopic net flow that is, hence, not known *a priori*. We circumvent these issues by considering overdamped dynamics, where thermostating is intrinsic.

Furthermore, an advanced numerical integration scheme known as adaptive BD⁴¹ is applied, which improves upon conventional BD simulations as described in the following. We consider the overdamped Langevin equations

$$\dot{\mathbf{r}}^{(i)}(t) = \frac{1}{\zeta} \mathbf{f}^{(i)}(\mathbf{r}^N(t)) + \sqrt{\frac{2k_B T}{\zeta}} \mathbf{R}^{(i)}(t), \quad (4)$$

$i = 1, \dots, N$, as the relevant equations of motion to obtain particle trajectories $\mathbf{r}^N(t)$ in our system consisting of N identical particles. Here, $\mathbf{f}^{(i)}(\mathbf{r}^N(t))$ is the total force acting on particle i , which can be split into external and internal contributions, $\mathbf{f}_{\text{ext}}^{(i)}(\mathbf{r}^{(i)}(t))$ and $\mathbf{f}_{\text{int}}^{(i)}(\mathbf{r}^N(t)) = -\nabla_i U(\mathbf{r}^N(t))$, respectively. The friction coefficient ζ is the same for each (identical) particle, and the over dot denotes a time derivative. The vectors $\mathbf{R}^{(i)}(t)$, $i = 1, \dots, N$, are Gaussian distributed and must therefore satisfy $\langle \mathbf{R}^{(i)}(t) \rangle = 0$ and $\langle \mathbf{R}^{(i)}(t) \mathbf{R}^{(j)}(t') \rangle = \mathbf{I} \delta_{ij} \delta(t - t')$. Here, the angular brackets denote an average over realizations of the random process, \mathbf{I} is the 3×3 -unit-matrix, δ_{ij} is the Kronecker delta, and $\delta(\cdot)$ is the Dirac delta function. Thermostating irrespective of applied external forces and any (possibly inhomogeneous) net flow is inherent in overdamped Brownian dynamics as the temperature-dependent prefactor of the Gaussian random vectors in Eq. (4) determines the average magnitude of the random displacements.

Because Eq. (4) is a set of coupled stochastic differential equations, its numerical treatment requires particular care. Specifically, the use of the Euler–Maruyama method,⁵³ which is usually employed in conventional BD simulations, has serious drawbacks regarding both its stability and accuracy. This is primarily due to using a constant timestep interval Δt , which may lead to faulty particle displacements and erroneous force evaluations when particle collisions are not resolved with the required precision (i.e., with a small enough Δt).

Within adaptive BD,⁴¹ the automatic choice of an appropriate timestep length Δt_k is ensured in each iteration $k \rightarrow k + 1$ by the evaluation of an embedded Heun–Euler integrator,

$$\tilde{\mathbf{r}}_{k+1}^{(i)} = \mathbf{r}_k^{(i)} + \frac{1}{\zeta} \mathbf{f}^{(i)}(\mathbf{r}_k^N) \Delta t_k + \sqrt{\frac{2k_B T}{\zeta}} \mathbf{R}_k^{(i)}, \quad (5)$$

$$\mathbf{r}_{k+1}^{(i)} = \mathbf{r}_k^{(i)} + \frac{1}{2\zeta} \left(\mathbf{f}^{(i)}(\mathbf{r}_k^N) + \mathbf{f}^{(i)}(\tilde{\mathbf{r}}_{k+1}^N) \right) \Delta t_k + \sqrt{\frac{2k_B T}{\zeta}} \mathbf{R}_k^{(i)}, \quad (6)$$

which yields two estimates $\tilde{\mathbf{r}}_{k+1}^N$ and \mathbf{r}_{k+1}^N for the new particle positions at time $t_k + \Delta t_k$. If large discrepancies of $\tilde{\mathbf{r}}_{k+1}^N$ and \mathbf{r}_{k+1}^N are detected, the timestep Δt_k is reduced and the step $k \rightarrow k + 1$ is retried. In such a case of a rejected trial step, one must carefully choose appropriate discrete random increments $\mathbf{R}_k^{(i)}$ to retain the

Gaussian nature of the target random process $\mathbf{R}^{(i)}(t)$. For this, adaptive BD utilizes Rejection Sampling with Memory (RSwM),⁵⁴ which is an efficient algorithm to counteract the rejection of previously drawn random increments. RSwM, hence, guarantees the correct generation of a specified random process. With the numerical treatment of Eq. (4) via adaptive BD, stable and accurate long-time simulations of overdamped many-body systems are possible in equilibrium but also under extreme non-equilibrium conditions, such as when driving the system with a large external force $\mathbf{f}_{\text{ext}}(\mathbf{r})$. A detailed description of adaptive BD is given in Ref. 41.

Hydrodynamic interactions that are mediated by the implicit solvent are neglected in the equations of motion (4). From a computational standpoint, the performance of the simulations turns out to be crucial to obtain accurate results for the quantities of interest, as described in Sec. II C. The numerical treatment of hydrodynamic interactions, which requires both the evaluation of long-ranged forces as well as the generation of appropriately correlated random displacements (e.g., via a Cholesky decomposition of the diffusion matrix⁵⁵), would have a significant impact on the required computational effort. Additionally, within adaptive BD, the Heun–Euler pair (5) and (6) is conceived to handle only additive noise in the underlying stochastic differential equation. Instead of the Heun method (6), one would have to resort to an integration scheme with a sufficient strong order of convergence for general noise terms.⁵³ Moreover, from a physical point of view, we argue that the omission of hydrodynamic interactions simplifies the analysis of the results in Sec. III as all observations are ensured to stem solely from the properties of the Stillinger–Weber particle model. In particular, we show that its ability to form networks is the crucial mechanism that causes the reported out-of-equilibrium response. As hydrodynamic interactions tend to support anisotropic coagulation and transient network states,^{56–58} we expect no significant qualitative change in the reported observations.

C. Simulation protocol

In this work, we model an inhomogeneously sheared system by imposing an external force profile $\mathbf{f}_{\text{ext}}(z)$ that is parallel to the x axis and modulated in the z -direction. The x -component of the force field is sinusoidal with amplitude K such that it complies with the periodic boundary conditions of the cubic simulation box with side length L , i.e.,

$$f_{\text{ext},x}(z) = K \sin\left(2\pi\frac{z}{L}\right). \quad (7)$$

With this choice, Lees–Edwards boundary conditions⁵⁹ as used in simulations with linear shear profiles⁶⁰ are not required because $\mathbf{f}_{\text{ext}}(\mathbf{r})$ and its derivatives are continuous at the periodic boundaries. The application of the time-independent but spatially inhomogeneous shear force (7) is not to be confused with time-dependent oscillatory shear.⁶¹ The considered external force constitutes the lowest-order Fourier mode within the simulation box, and it can, hence, be taken as a generic model for experimentally relevant scenarios, as occur, e.g., in convection⁴⁴ or when inducing inhomogeneous forces with a laser tweezer.

The simulation procedure is as follows: We set $L = 30\sigma$ and initialize $N = 1000$ particles on a regular lattice, which yields a mean number density of $\rho_b \approx 0.037\sigma^{-3}$. This configuration is randomized for a short time (10^4 steps) at a high temperature of $k_B T = 10\epsilon$ using

the adaptive BD method before instantaneously reducing the temperature to the desired value and imposing the sinusoidal external force profile (7). At this point, no particle bonds have formed yet and a flow in the x -direction sets in immediately. From here, the actual production run begins and the respective observables are sampled, which is described in more detail in the following. Due to the nature of the external force profile (7), the system retains translational invariance in the x - y -plane and forms a flow channel in the upper and lower half of the simulation box. Since a transient from the randomized particle distribution into this stationary flow occurs initially, we partition the sampling of the production run into consecutive sections of 10^6 steps. Thus, the sections where a stationary flow has not been reached yet can be discarded, and the remaining ones are averaged over. During individual runs, asymmetric channel populations that persist for a long time are observed. Rather than performing longer simulation runs to yield better time-averages, we average over ~ 50 distinct realizations of a simulation until symmetric profiles are obtained. The typical simulation time of the stationary flow in each individual run is then of the order of $10^5 \tau$ with the Brownian timescale $\tau = \sigma^2 \zeta / \epsilon$.

Using this protocol, a range of external modulation amplitudes K and temperatures T is investigated. For each set of parameters, we obtain the density profile $\rho(\mathbf{r})$ as well as the force density profile $\mathbf{F}(\mathbf{r})$ from sampling of the density operator

$$\hat{\rho}(\mathbf{r}) = \sum_i \delta(\mathbf{r} - \mathbf{r}^{(i)}) \quad (8)$$

and force density operator

$$\hat{\mathbf{F}}(\mathbf{r}) = \sum_i \mathbf{f}^{(i)} \delta(\mathbf{r} - \mathbf{r}^{(i)}), \quad (9)$$

respectively. Thus, $\rho(\mathbf{r}) = \langle \hat{\rho}(\mathbf{r}) \rangle$ and $\mathbf{F}(\mathbf{r}) = \langle \hat{\mathbf{F}}(\mathbf{r}) \rangle$, where angular brackets denote an average over configurations of the stationary flow state obtained according to the above simulation procedure. Specifically, for the force density profile, we focus on its internal contribution

$$\mathbf{F}_{\text{int}}(\mathbf{r}) = \left\langle \sum_i \mathbf{f}_{\text{int}}^{(i)} \delta(\mathbf{r} - \mathbf{r}^{(i)}) \right\rangle \quad (10)$$

to better reveal how the stationary state is stabilized by the internal interaction (1). The internal force density profiles are then normalized by the density to acquire the internal force profile

$$\mathbf{f}_{\text{int}}(\mathbf{r}) = \frac{\mathbf{F}_{\text{int}}(\mathbf{r})}{\rho(\mathbf{r})}. \quad (11)$$

A sufficiently large number of samples is necessary to yield accurate results for the internal force profile as its convergence is slower than that of the density profile.⁶² To investigate possible finite-size effects, which might occur in gels specifically due to their long-range effective correlations, we have conducted additional simulations where the side length L of the box has been doubled while extending the external potential (7) in the z -direction by an additional shear period. No significant impact was found on the behavior of the sheared system compared to the results shown in Sec. III for the original choice of L .

A sketch of the system and of the flow velocity profile resulting from the applied shear force (7) is depicted in Fig. 1, where

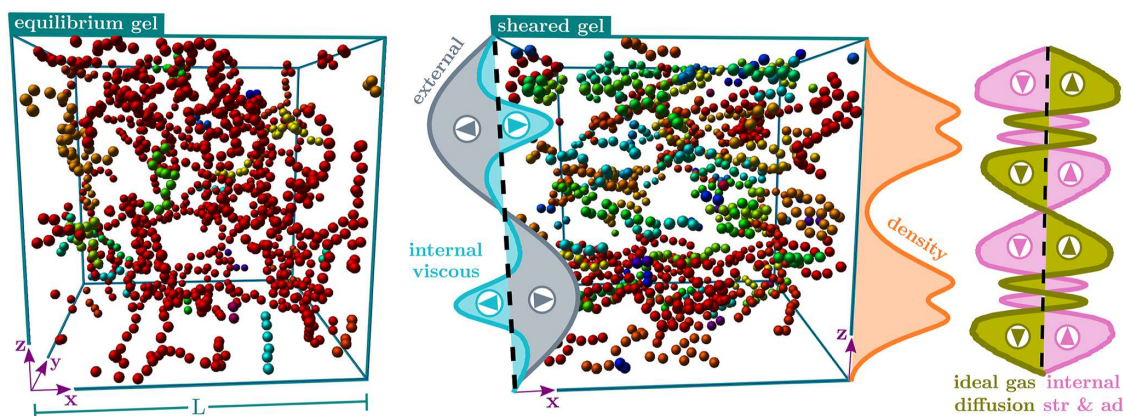


FIG. 1. Characteristic snapshots of an equilibrium gel (left) and a sheared gel in the steady state (right). An animation of the sheared gel is provided in the [supplementary material](#). The particles are colored according to the cluster to which they belong. The simulation box is a cube of side length L , and the temperature is set to $k_B T = 0.1\epsilon$. For the sheared state, an external force amplitude of $K = 5\epsilon/\sigma$ is chosen. The forces acting on the sheared gel are schematically represented: A sinusoidal external force pointing along the x -direction drives the flow of particles, forming two flow channels with the velocity profile (gray) closely following the external force profile (7). In the steady state, a superadiabatic viscous internal force (cyan) emerges that locally either opposes or supports the flow. A strong density modulation (orange) develops along the z -direction. The ideal-gas diffusible force (olive) that tends to homogenize the density profile is balanced by an internal force (pink) along the z -direction, which incorporates both adiabatic and superadiabatic structural components.

we also show characteristic snapshots of the quiescent and of the sheared gel. Additionally, the spatial variations of the one-body profiles are illustrated, and we indicate locally by arrows the directions of the one-body force contributions. Actual simulation results are presented and analyzed in the following, and we highlight the labels of the one-body profiles in subsequent figures according to the colors used in Fig. 1.

III. RESULTS

A. Variation of temperature

For certain state points and values of the amplitude of the external force, large variations in the one-body profiles of density $\rho(\mathbf{r}) = \rho(z)$ and internal force $\mathbf{f}_{\text{int}}(\mathbf{r}) = \mathbf{f}_{\text{int}}(z)$ are observed while the system retains translational symmetry in the x - and y -directions. To investigate the onset and origin of these inhomogeneities, we first vary the temperature T and maintain a large constant amplitude $K = 5\epsilon/\sigma$ of the external force profile. The results are shown in Fig. 2.

The one-body profiles remain almost featureless for $k_B T = 0.3\epsilon$. At $k_B T = 0.2\epsilon$, an inhomogeneous structure begins to appear in the internal force profiles $f_{\text{int},x}(z)$ and $f_{\text{int},z}(z)$. This becomes more clearly visible as variations of the density profile $\rho(z)$ from its bulk value for $k_B T = 0.15\epsilon$. For $k_B T = 0.1\epsilon$, remarkable modulations occur in all three quantities with spatial density variations of the order of the mean bulk density ρ_b itself.

The emergence of structural features in the one-body profiles when decreasing temperature is rapid and continuous. The spatial modulations are significantly stronger than those observed in (non-percolated) simple fluids,³⁸ and we illustrate this in Appendix C via a comparison to results for the dilute Lennard-Jones fluid. Therefore, this effect can be linked to the percolation transition in equilibrium, which sets in at similar thermodynamic state points for the

considered particle model.⁶³ We support this reasoning by an investigation of the cluster size distribution $C(n)$, which gives the probability of finding a random particle in a cluster of size n . As is standard, we define the agglomeration of particles into clusters to be transitive with two particles belonging to the same cluster if their distance is below the cutoff distance $a\sigma$ of the interparticle potential. In Fig. 3, $C(n)$ is shown for varying temperatures in a system sheared according to Eq. (7) with $K = 5\epsilon/\sigma$. One recognizes that the mean cluster size grows with decreasing temperature and that clusters span up to half of the system for $k_B T = 0.1\epsilon$.

Additionally, to better reveal the internal structure of the clusters, we monitor the probabilities of the coordination numbers P_n , i.e., the proportion of particles having n neighboring particles within the cutoff distance $a\sigma$. The behavior of the coordination numbers $n = 0, 1, 2, 3$ is shown in Fig. 4 as a function of inverse temperature. It is apparent that for low temperatures, the structure of the network is dominated by particle chains. Branching still occurs, which interconnects the chains within the flow channels. This shows that even in strongly sheared systems, microscopic correlations are dominated by the three-body contribution to the internal interaction potential (1).

B. Variation of external force amplitude

While the formation of finite-size clusters can be understood as a relic of the equilibrium percolation transition, its effect on the concrete structure of $\rho(z)$ and $\mathbf{f}_{\text{int}}(z)$ turns out to be substantial and can only be explained if genuine non-equilibrium dynamics are considered. In the following, the response of the three-body gel over a range of external force amplitudes K at constant (low) temperature $k_B T = 0.1\epsilon$ is investigated, whereby the system is driven further away from equilibrium with increasing K . The corresponding one-body profiles are shown in Fig. 5.

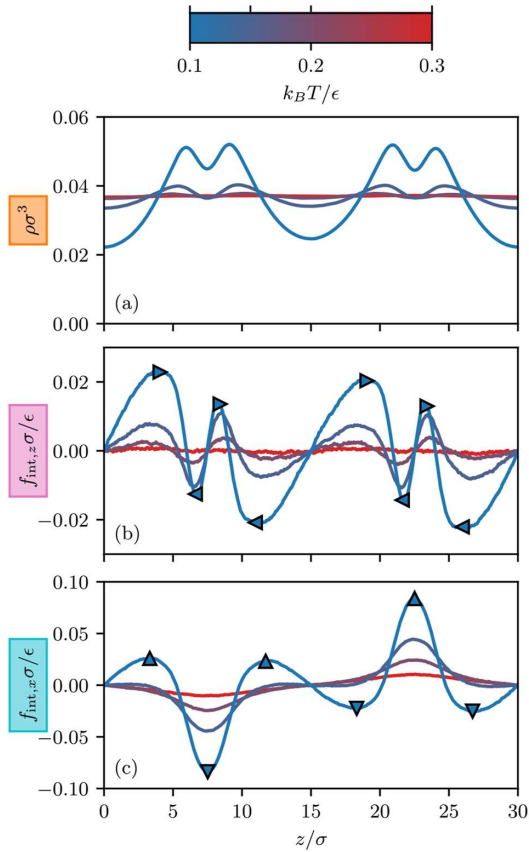


FIG. 2. The density profile $\rho(z)$ (a) as well as the component $f_{\text{int},z}(z)$ (b) and $f_{\text{int},x}(z)$ (c) of the internal force (7) is shown. A constant shear amplitude of $K = 5\epsilon/\sigma$ is maintained, and the temperature is varied with values of $k_B T/\epsilon = 0.1, 0.15, 0.2, 0.3$ (indicated by ticks on the color scale). While $f_{\text{int},z}(z)$ acts parallel to the flow direction, $f_{\text{int},x}(z)$ constitutes a force perpendicular to the flow that leads to the observed density inhomogeneity. This is illustrated by arrows, which accentuate, in particular, the alternating direction in both the parallel and the perpendicular internal force component for low temperature. The onset of structural inhomogeneities in the one-body profiles is continuous and occurs rapidly for decreasing T when the equilibrium percolation transition is encountered.

To rationalize the results, it is instructive to work on the level of forces and to consider the one-body force balance¹³

$$\zeta \mathbf{v}(\mathbf{r}) = \mathbf{f}_{\text{int}}(\mathbf{r}) + \mathbf{f}_{\text{ext}}(\mathbf{r}) - k_B T \nabla \ln \rho(\mathbf{r}). \quad (12)$$

The above relation is exact for arbitrary many-body Hamiltonians, which can be shown, e.g., via an integrating-out of the Smoluchowski equation or in equilibrium, where $\mathbf{v}(\mathbf{r}) = 0$, by an application of Noether's theorem.⁶⁴ The external force $\mathbf{f}_{\text{ext}}(\mathbf{r})$ is imposed in our system via Eq. (7), and $\rho(\mathbf{r})$ as well as $\mathbf{f}_{\text{int}}(\mathbf{r})$ is accessible from their microscopic definitions given in Eqs. (8)–(11). The

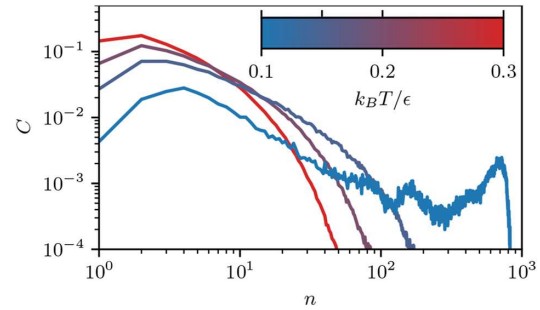


FIG. 3. The cluster size distribution $C(n)$ is shown for different values of the temperature (indicated by ticks on the color scale) at a constant shear amplitude $K = 5\epsilon/\sigma$. Particles tend to form chains when driven by the shear force, cf. Fig. 1, and the mean size of the chains grows when temperature is decreased. Additionally, for $k_B T = 0.1\epsilon$, the occurrence of large clusters that span across a flow channel and include up to half of the particles in the system is observed.

term $-k_B T \nabla \ln \rho(\mathbf{r}) = \mathbf{f}_{\text{id}}(\mathbf{r})$ on the right-hand side of Eq. (12) is the force arising from ideal-gas diffusion. Furthermore, the time dependence has been dropped as we consider a stationary state where $\mathbf{v}(\mathbf{r}) = \mathbf{J}(\mathbf{r})/\rho(\mathbf{r})$ is the time-independent one-body velocity, which can be obtained from the one-body current $\mathbf{J}(\mathbf{r})$. The current obeys the continuity equation $\partial \rho(\mathbf{r}, t)/\partial t = -\nabla \cdot \mathbf{J}(\mathbf{r}, t)$, and it is therefore divergence-free in the present case since the density profile is stationary. We recall that $\mathbf{J}(\mathbf{r})$ is an average of the microscopic operator $\hat{\mathbf{J}}(\mathbf{r}) = \sum_i \mathbf{v}^{(i)} \delta(\mathbf{r} - \mathbf{r}^{(i)})$, and it is thus directly accessible from simulation.⁶⁵

We proceed similar to Ref. 39 and distinguish between adiabatic and superadiabatic contributions to the internal force profile $\mathbf{f}_{\text{int}}(\mathbf{r}) = \mathbf{f}_{\text{ad}}(\mathbf{r}) + \mathbf{f}_{\text{sup}}(\mathbf{r})$. The adiabatic force $\mathbf{f}_{\text{ad}}(\mathbf{r})$ is defined to be

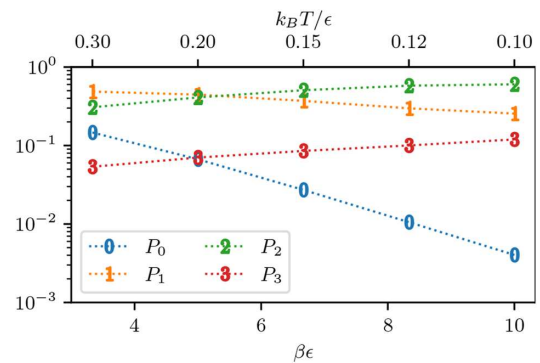


FIG. 4. The probabilities P_n of particles with a coordination number of $n = 0, 1, 2, 3$ are shown as a function of inverse temperature β and for constant shear amplitude $K = 5\epsilon/\sigma$. For low temperatures, individual particles ($n = 0$) as well as particle pairs ($n = 1$) are desorbed into the network as both P_0 and P_1 decrease. The network structure is dominated by chains (P_2 is large) and branching is still viable, as can be deduced from the moderate value of P_3 .

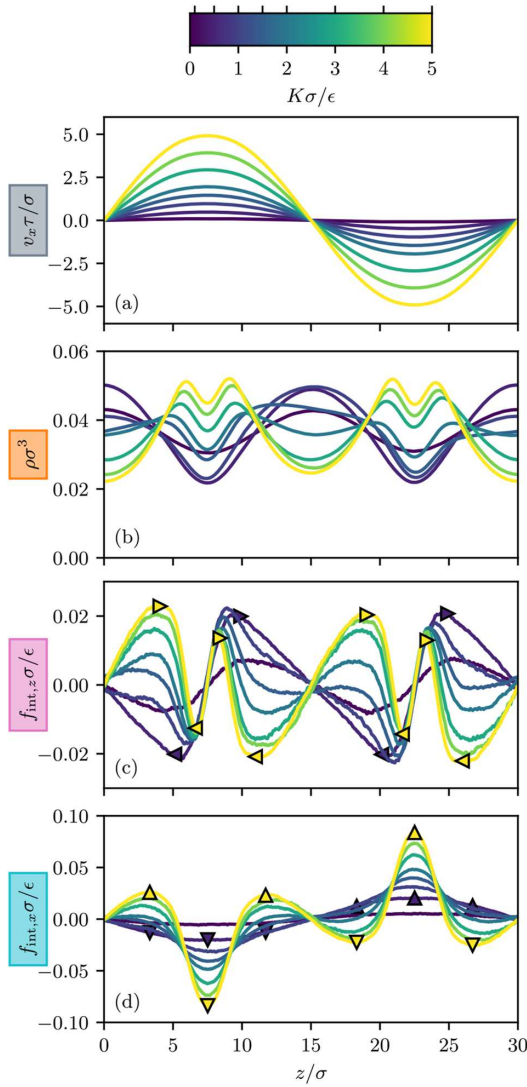


FIG. 5. Similar to Fig. 2, the one-body profiles of velocity $v_x(z)$ (a), density $\rho(z)$ (b), perpendicular internal force $f_{\text{int},z}(z)$ (c), and parallel internal force $f_{\text{int},x}(z)$ (d) are depicted. The temperature is now fixed to $k_B T = 0.1\epsilon$, and the amplitude of the external force is varied with values of $K\sigma/\epsilon = 0.1, 0.5, 1, 1.5, 2, 3, 4, 5$, which are indicated by ticks on the color scale ($K = 0$ corresponds to the bulk state and is not shown). Arrows indicate the local direction of the internal force components for the low (blue) and high (yellow) shear amplitude.

that of a reference equilibrium system, which is constructed to have the same density profile as the original non-equilibrium state. Only the superadiabatic part $\mathbf{f}_{\text{sup}}(\mathbf{r})$ consists of purely out-of-equilibrium forces, which, hence, determine both (inhomogeneous) structure

and flow of a driven colloidal suspension. By specializing to our planar geometry, we now analyze the force profiles in Fig. 5 to determine adiabatic and superadiabatic contributions.

Parallel to the flow, the density remains homogeneous due to translational symmetry such that the x -component of its gradient vanishes. This also implies a vanishing adiabatic force $f_{\text{ad},x}(z) = 0$. The respective component of the internal force therefore only consists of the superadiabatic contribution, i.e., $f_{\text{int},x}(z) = f_{\text{sup},x}(z)$. Hence, the x -component of the force balance Eq. (12) simplifies to

$$\zeta v_x(z) = f_{\text{sup},x}(z) + f_{\text{ext},x}(z), \quad (13)$$

which clarifies that $f_{\text{sup},x}(z)$ plays the role of a viscous force and that it is readily available via the simulation results for $f_{\text{int},x}(z)$ shown in Fig. 5.

In the z -direction, the density varies inhomogeneously, and the internal force therefore consists of both adiabatic and superadiabatic contributions. To distill $f_{\text{sup},z}(z)$ from the data of $f_{\text{int},z}(z)$ in Fig. 5 would require the construction and simulation of an appropriately chosen equilibrium system,^{65,66} which will be considered in the future work. Nevertheless, due to the absence of driving and flow in the z -direction, i.e., $f_{\text{ext},z}(z) = 0$ and $v_z(z) = 0$, the force balance along the z axis reduces to

$$0 = f_{\text{sup},z}(z) + f_{\text{ad},z}(z) - k_B T \frac{\partial \ln \rho(z)}{\partial z}. \quad (14)$$

Therefore, the non-equilibrium force component $f_{\text{sup},z}(z)$ is necessary to stabilize the density gradient, and it can thus be referred to as a structural superadiabatic force. Equation (14) also reveals that the internal force density is straightforwardly related to the derivative of the density profile due to $F_{\text{int},z}(z) = f_{\text{int},z}(z)\rho(z) = k_B T \partial \rho(z) / \partial z$, which can be utilized as a means to “force sample”^{67–69} the density profile with a reduced variance. Additionally, an analogous description of viscous and structural effects on the level of internal stresses is given in Appendix A.

In simple fluids, where the constituent particles only interact via an isotropic pair-potential, non-equilibrium viscous and structural forces have been reported to occur both in an analogous sinusoidal shear profile³⁸ and in more complex two-dimensional flows.³⁹ However, the emerging features of density and force profiles—while being measurable and conceptually important—are rather frugal especially in the quasi-one-dimensional case (cf. Appendix C for results of the sheared Lennard-Jones fluid). The relative variation in density is comparatively small even for moderate external force, and particles consistently accumulate in regions of low shear rates, i.e., at the center of the flow channels. The superadiabatic forces possess a sinusoidal shape such that the structural force drives particles to the center of the channels. The viscous force is Stokes-like in a broad range of shear amplitudes, and it is always opposed to the flow direction. In the following, these observations are compared to the markedly different one-body profiles of the sheared three-body gel illustrated in Fig. 1. The results of the variation of K are shown in Fig. 5.

For small values of the external force amplitude K , the density is sinusoidal in shape but the amplitude is inverted as compared to the simple fluid scenario such that particles accumulate in regions of large velocity gradient. When K is increased, the density maxima

shrink while the depletion at the center of the channels remains pronounced. For large values of K , we observe that particles now tend to flee the regions of high velocity gradient. However, the migration is not simply directed toward the center of the flow channels where the local shear rate vanishes, as would be the case in simple fluids. Instead, the density profile develops a double-peak and retains a depletion zone right at the location of maximum flow velocity. This behavior is reflected in the form of the internal force $f_{\text{int},x}(z)$, which progresses from a sinusoidal profile for small K to a rapidly varying quantity for large K , thereby promoting and maintaining the observed double-peak structure of $\rho(z)$ within the flow channels. The purely superadiabatic viscous force $f_{\text{int},x}(z)$ counteracts partially the flow for low to intermediate K similar to the behavior found in simple fluids. For large external force amplitudes, however, $f_{\text{int},x}(z)$ locally acts in the *same* direction as the flow velocity at the sides of the channels, which is anomalous phenomenology for a viscous force.

The striking signal in both structural and viscous forces can be explained as a consequence of the three-body interaction (1). As the system is weakly sheared, particles can still percolate into a large network for the chosen temperature. With increasing K , bonds are first broken in regions of maximum external force such that particles become mobile and evade these regions—thus, a density depletion zone develops. At even larger K , the formation of an extensive network cannot be maintained and bonds break and dynamically rejoin across the whole system. However, driven by the three-body term in Eq. (1), particles still tend to develop finite-size chains, which then align parallel to the flow direction. The mobility of the individual chains enables the migration to regions of low velocity gradient, and the density profile, hence, inverts. Within the flow channels, the chains organize into two lanes that are slightly offset from the center and thus lead to a double-peak structure in $\rho(z)$. This is because their alignment parallel to the flow is driven by inhomogeneous shear rate, and it can therefore only occur if $\partial v_x(z)/\partial z \neq 0$. Yet, at the extrema of the external force profile, the gradient of the resulting flow vanishes and particle bonds are not aligned. This explains the spatial offset of the chain formation to regions of finite velocity gradient; cf. Fig. 5. The arrangement of particles into aligned chains also clarifies the anomalous behavior of the viscous force $f_{\text{int},x}(z)$ that is encountered in this case and that can, hence, be understood as a dynamical “drag-along.” In summary, the inclusion of three-body terms in the interaction potential greatly affects the response of colloidal suspensions to inhomogeneous shear and results in collective effects, which influence and amplify structural and viscous forces.

C. Power functional theory

We next turn to a theoretical description of the simulation results with PFT^{42,43} and give a brief summary of its core concepts in the following. PFT is based on an exact variational principle that reproduces the time-dependent force balance equation

$$\zeta \mathbf{v}(\mathbf{r}, t) = \mathbf{f}_{\text{ad}}(\mathbf{r}, t) + \mathbf{f}_{\text{sup}}(\mathbf{r}, t) + \mathbf{f}_{\text{ext}}(\mathbf{r}, t) - k_B T \nabla \ln \rho(\mathbf{r}, t). \quad (15)$$

Thereby, the nontrivial contributions $\mathbf{f}_{\text{ad}}(\mathbf{r}, t)$ and $\mathbf{f}_{\text{sup}}(\mathbf{r}, t)$, which together constitute the internal force profile $\mathbf{f}_{\text{int}}(\mathbf{r}, t)$, are made accessible via universal generating functionals of the density profile

$\rho(\mathbf{r}, t)$ and current profile $\mathbf{J}(\mathbf{r}, t)$. Together with the external and diffusive forces (right-hand side), they are balanced by the friction of the overdamped system (left-hand side).

More precisely, the adiabatic force $\mathbf{f}_{\text{ad}}(\mathbf{r}, t)$ incorporates the functional derivative of the intrinsic excess Helmholtz free energy $F_{\text{exc}}[\rho]$,

$$\mathbf{f}_{\text{ad}}(\mathbf{r}, t) = -\nabla \frac{\delta F_{\text{exc}}[\rho]}{\delta \rho(\mathbf{r}, t)}, \quad (16)$$

where brackets denote functional dependencies. If one uses Eq. (16) in Eq. (15) and neglects $\mathbf{f}_{\text{sup}}(\mathbf{r}, t)$, classical dynamical density functional theory (DDFT)⁷⁰ is recovered as an uncontrolled approximation. In the sheared three-body gel, as was shown in Secs. III A and B, the dynamics are governed by genuine out-of-equilibrium effects. Being a purely adiabatic theory by construction, DDFT is strictly unable to reproduce or describe the observed behavior in our system.⁷¹

Instead, in order to go beyond an adiabatic description, superadiabatic forces $\mathbf{f}_{\text{sup}}(\mathbf{r}, t)$ have to be taken into account. Within PFT, this is made possible by functional differentiation of the superadiabatic excess power functional $P_{\text{exc}}[\rho, \mathbf{J}]$,

$$\mathbf{f}_{\text{sup}}(\mathbf{r}, t) = -\frac{\delta P_{\text{exc}}[\rho, \mathbf{J}]}{\delta \mathbf{J}(\mathbf{r}, t)}. \quad (17)$$

The force balance Eq. (15) can then be written as

$$\begin{aligned} \zeta \mathbf{v}(\mathbf{r}, t) = & -\frac{\delta P_{\text{exc}}[\rho, \mathbf{J}]}{\delta \mathbf{J}(\mathbf{r}, t)} - \nabla \frac{\delta F_{\text{exc}}[\rho]}{\delta \rho(\mathbf{r}, t)} \\ & + \mathbf{f}_{\text{ext}}(\mathbf{r}, t) - k_B T \nabla \ln \rho(\mathbf{r}, t), \end{aligned} \quad (18)$$

and it involves both adiabatic and superadiabatic interparticle forces as systematically generated via the respective functionals.

Therefore, if $P_{\text{exc}}[\rho, \mathbf{J}]$ and $F_{\text{exc}}[\rho]$ are known, PFT enables the dynamical description of a system subjected to an arbitrary external force profile $\mathbf{f}_{\text{ext}}(\mathbf{r})$ via Eq. (18) and the continuity equation. This reformulation, which reduces the many-body problem to a variational principle on one-body quantities, is exact, in principle. Crucially, both $P_{\text{exc}}[\rho, \mathbf{J}]$ as well as $F_{\text{exc}}[\rho]$ are intrinsic functionals that depend only on internal interactions and further intrinsic properties of the system (e.g., temperature and density), but not on the externally applied force profile $\mathbf{f}_{\text{ext}}(\mathbf{r}, t)$. In practice, for a certain interparticle interaction potential, approximations for $P_{\text{exc}}[\rho, \mathbf{J}]$ and $F_{\text{exc}}[\rho]$ must be found, which poses a nontrivial problem. For $P_{\text{exc}}[\rho, \mathbf{J}]$, the functional dependence will, in general, be non-local both in space and in time (i.e., non-Markovian) as the history of $\rho(\mathbf{r}, t)$ and $\mathbf{J}(\mathbf{r}, t)$ has to be considered to obtain an accurate dynamical theory for time-dependent problems.

In the following, we use the framework of PFT to develop a model that is capable of reproducing the found anomalous behavior of the viscous force profile in the sheared three-body gel. We focus on the viscous part because it is directly accessible in simulation (we recall that $f_{\text{int},x}(z)$ is purely superadiabatic), which, hence, simplifies the following considerations. Recall also that a stationary state is considered, which implies $\nabla \cdot \mathbf{v}(\mathbf{r}) = 0$ due to the continuity equation and the chosen geometry. Since $\rho(\mathbf{r})$ is time-independent, we perform a change of variables to formulate $P_{\text{exc}}[\rho, \mathbf{v}]$ as a functional of the velocity profile and use $\delta/\delta \mathbf{J}(\mathbf{r}) = \rho(\mathbf{r})^{-1} \delta/\delta \mathbf{v}(\mathbf{r})$. To

yield an approximate explicit expression for $P_{\text{exc}}[\rho, \mathbf{v}]$, a semi-local velocity gradient expansion²² is assumed. Due to being in a stationary state, we can further specialize to a Markovian model such that

$$P_{\text{exc}}[\rho, \mathbf{v}] = \int d\mathbf{r} \phi(\rho(\mathbf{r}), \nabla \mathbf{v}(\mathbf{r})), \quad (19)$$

with a suitable integrand $\phi(\rho(\mathbf{r}), \nabla \mathbf{v}(\mathbf{r}))$.

As in Refs. 38 and 39, we perform the general expansion up to second order in $\nabla \mathbf{v}(\mathbf{r})$ to obtain an expression for the integrand $\phi(\rho(\mathbf{r}), \nabla \mathbf{v}(\mathbf{r}))$. Assuming a local dependence in space and imposing rotational invariance, this expression can be reduced to

$$\phi(\rho(\mathbf{r}), \nabla \mathbf{v}(\mathbf{r})) = \frac{1}{2} \eta \rho(\mathbf{r})^2 (\nabla \times \mathbf{v}(\mathbf{r}))^2, \quad (20)$$

where η is the coefficient of the superadiabatic viscous response. This coefficient depends on intrinsic properties, such as interparticle potential, density, and temperature, but it crucially is independent of the imposed external force profile. Furthermore, the value of η only alters the magnitude of the superadiabatic force profile resulting from Eq. (20) with its shape being fully determined by the forms of $\rho(\mathbf{r})$ and $\mathbf{v}(\mathbf{r})$.

The functional minimization (17) of Eq. (19) with the model integrand (20) results in the superadiabatic force profile

$$\mathbf{f}_{\text{sup}}(\mathbf{r}) = \eta [\rho(\mathbf{r}) \nabla^2 \mathbf{v}(\mathbf{r}) - \rho(\mathbf{r}) \nabla (\nabla \cdot \mathbf{v}(\mathbf{r})) - 2(\nabla \rho(\mathbf{r})) \times (\nabla \times \mathbf{v}(\mathbf{r}))], \quad (21)$$

where the right-hand side can be evaluated for the sheared gel. For this, we approximate $\mathbf{v}(\mathbf{r}) \approx \mathbf{f}_{\text{ext}}(\mathbf{r})/\zeta$ since the magnitude of the viscous force is small compared to $\zeta \mathbf{v}(\mathbf{r})$ and take the density profile from the simulations as the input. The x -component of Eq. (21) then yields the viscous force, which can be compared to the actual simulation data $f_{\text{int},x}(z)$ as shown in Fig. 5. To obtain a quantitative comparison, the value of the transport coefficient η is fitted to match the magnitude of the simulation results universally for the considered shear amplitudes. The superadiabatic force profiles for the viscous force within this PFT description are shown in Fig. 6, where a value of $\eta = 5$ has been used for the viscous coefficient for all considered values of K .

It is apparent that $f_{\text{sup},x}(z)$ displays a double-peak within the flow channels and therefore differs from the simulation results, where only a single peak is observed. However, this inaccuracy is not surprising since the model functional (19) and (20) is obtained merely by an expansion in gradients of the velocity profile. The density enters the functional only locally, and the model is thus expected to fail in regions where higher derivatives (e.g., the curvature) of $\rho(\mathbf{r})$ are significant, such as in the center of the flow channels. To achieve better results in these regions, the integrand (20) of $P_{\text{exc}}[\rho, \mathbf{v}]$ could be augmented by an expansion in $\rho(\mathbf{r})$, which will be considered in future work.

In between the flow channels, the viscous force profiles obtained from Eqs. (19) and (20) match the simulation results across the range of investigated shear amplitudes K . Particularly, the anomalous change in the sign of the viscous force, which we attribute to a dynamical drag-along of particles, is captured by the PFT model as well, and it shows the same K -dependent behavior as in the simulation. The successful reproduction of this phenomenon exemplifies

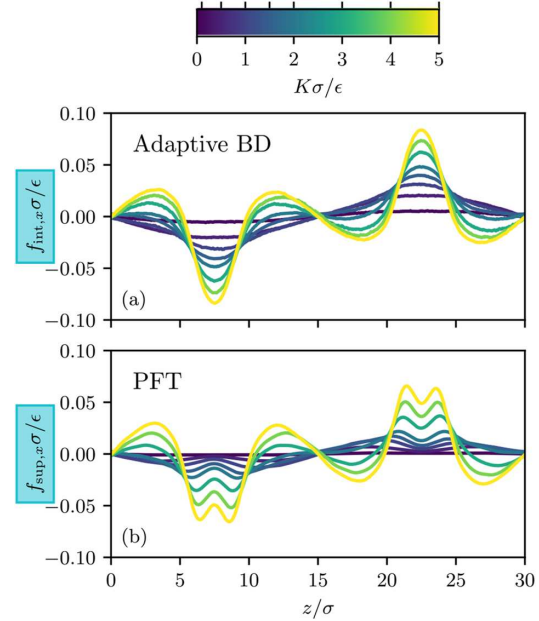


FIG. 6. The superadiabatic viscous force $f_{\text{sup},x}(z)$ is shown as obtained from the model (19) and (20) for $P_{\text{exc}}[\rho, \mathbf{v}]$ with $\eta = 5$. For this, the expression (21) is evaluated with the density profiles from the simulations in Sec. III B. The velocity profiles are approximated analytically by $\mathbf{v}(\mathbf{r}) \approx \mathbf{f}_{\text{ext}}(\mathbf{r})/\zeta$. When comparing the shown PFT results (b) with the adaptive BD simulation data (a) for $f_{\text{int},x}(z)$, good agreement is found. Solely in the center of the flow channels, the simple model for $P_{\text{exc}}[\rho, \mathbf{v}]$ leads to deficiencies due to the complex behavior of $\rho(z)$ in these regions.

that even simple model functionals for the excess power are capable of resolving nontrivial superadiabatic effects and that PFT is a concise framework for their systematic investigation.

IV. CONCLUSION AND OUTLOOK

In this work, we have studied the behavior of a colloidal gel modeled by the Stillinger–Weber potential (1), where the three-body interaction (3) has been modified similar to Refs. 29 and 30. The gel is subjected to a sinusoidal external shear profile. For the numerical investigation, we have utilized adaptive BD,⁴¹ which facilitates to carry out efficient and stable long-time simulation runs to accurately obtain the density and internal force profile in the stationary flow state. Markedly different behaviors have been encountered depending on the chosen temperature T and the amplitude K of the external force profile.

The simulations over a range of temperatures revealed that the effect of the equilibrium percolation transition—which leads to the formation of an extended and dilute network under quiescent bulk conditions—transfers to situations far from equilibrium. Thus, while a system-spanning network is not formed for suf-

ficiently strong inhomogeneous shear, the local arrangement of particles into finite-size chains is still viable, which we have shown via the cluster size distribution $C(n)$. An investigation of the probabilities of the coordination numbers P_n revealed that the clusters are dominated by chains, which interconnect via branching. This clustering effect is crucial to describe the emergence of structure in the density profile $\rho(z)$ and in the parallel and perpendicular component of the internal force $\mathbf{f}_{\text{int}}(z)$ with respect to the flow direction. Note that the global temperature acts as a control parameter for the network formation in our system. In depletion-induced gels, a similar effect could be achieved by a variation of the concentration of the depletion agent to tailor the effective attraction between colloids.^{11–13}

For an in-depth analysis, we have further split the internal force into adiabatic and superadiabatic contributions with the latter being the driving mechanism for genuine out-of-equilibrium effects. Due to the chosen planar geometry, the parallel component of the internal force could be associated directly with a superadiabatic viscous force. The perpendicular component consists of both adiabatic and superadiabatic contributions instead, where the latter is needed to stabilize the emerging density inhomogeneity.

When comparing the found results of the three-body gel with known observations of colloids consisting of simpler particle types,^{38,39} we found anomalous behavior for both viscous and structural effects. This could be attributed to be a direct consequence of the internal three-body contributions. The emerging density modulation is much larger in magnitude and shows a richer phenomenology than in simple fluids, as we have illustrated via a comparison to the Lennard-Jones fluid in Appendix C. In particular, the accumulation of particles can occur both in regions of high and low velocity gradient depending on the applied external force. For large amplitudes of the latter, the formation of particle chains occurs within a double-lane near the center of the flow channels. The superadiabatic viscous force, which generally opposes the flow direction in simple fluids, has been shown here to flip its usual counteracting direction for large K in some regions of the channels. We deduced this “drag-along” to be another consequence of the formation of particle chains. Therefore, in both components of the internal force profile, collective effects are involved, which substantially amplify the non-equilibrium response of the system. As we have shown, colloidal gels are very susceptible to out-of-equilibrium phenomena, and they can, hence, be taken as a prototypical model for future study.

By utilizing PFT, a possible route to a coarse-grained description of the found results was given. This was exemplified for the viscous force profile, where we have shown that a simple excess power functional suffices to reproduce the simulation results and capture the anomalous drag-along in the three-body gel. In the future work, more sophisticated model functionals will be investigated in order to alleviate some deficiencies of this simple description. Building upon the found results, a similar analysis of the structural force profile will be considered. This requires, however, the construction of an equilibrium reference state to perform the splitting of the respective internal force component into adiabatic and superadiabatic contributions.

In the conducted simulations, it was observed that asymmetric channel populations that persist over long time scales occur especially for intermediate values of the shear amplitude. Hence,

another objective for future work is a study of their statistics and stability, possibly being indicative of a dynamical phase transition as reported already in dense colloidal suspensions of simpler particles that exhibit flow-induced ordering or layering phenomena.^{73,74} Further interesting research could incorporate a variation of other parameters of the Stillinger–Weber potential besides Θ_0 to study their impact on the response of the driven system. This is especially important from a practical perspective as the tuning of microscopic interactions to yield desired material properties is a central concept of material science, which has also been applied to colloidal gels under shear.⁷⁵ For a quantitative prediction, hydrodynamic interactions might become relevant, and it would be useful to augment adaptive BD in this regard, possibly accompanied by efficient evaluation schemes of then correlated random increments.^{76,77} Additionally, going beyond the steady state and investigating time-dependent situations, such as transients in a switching protocol of the external force,⁷⁸ could reveal the nature of non-equilibrium memory effects. This is especially interesting from the view point of PFT as memory kernels can be directly incorporated in the theory, such that time-dependent phenomena may provide further assistance in the development of accurate functionals.

SUPPLEMENTARY MATERIAL

See the [supplementary material](#) for an animation of the steady shear flow of the three-body gel at temperature $k_B T = 0.1\epsilon$ and shear amplitude $K = 5\epsilon/\sigma$.

ACKNOWLEDGMENTS

We thank Tobias Eckert and Matthias Fuchs for useful comments. This work was supported by the German Research Foundation (DFG) via Project No. 436306241.

AUTHOR DECLARATIONS

Conflict of Interest

The authors have no conflicts to disclose.

Author Contributions

Florian Sammüller: Formal analysis (lead); Methodology (equal); Software (lead); Writing – original draft (lead). **Daniel de las Heras:** Conceptualization (equal); Methodology (equal); Writing – review & editing (equal). **Matthias Schmidt:** Conceptualization (equal); Methodology (equal); Project administration (equal); Writing – review & editing (equal).

DATA AVAILABILITY

The data that support the findings of this study are available from the corresponding author upon reasonable request.

APPENDIX A: INTERNAL STRESS TENSOR

Instead of working on the level of the force balance Eq. (12) directly, one can consider a similar decomposition of the stress

tensor as a generator of the respective force profiles. For this, we use the definition

$$\nabla \cdot \boldsymbol{\sigma}(\mathbf{r}, t) = \zeta \mathbf{J}(\mathbf{r}, t) \quad (\text{A1})$$

of the total stress tensor $\boldsymbol{\sigma}(\mathbf{r}, t)$. To identify its internal contribution, we multiply Eq. (12) by the density profile $\rho(\mathbf{r}, t)$, which yields the force density balance

$$\zeta \mathbf{J}(\mathbf{r}, t) = \mathbf{F}_{\text{int}}(\mathbf{r}, t) + \mathbf{F}_{\text{ext}}(\mathbf{r}, t) - k_B T \nabla \rho(\mathbf{r}, t). \quad (\text{A2})$$

Insertion of Eq. (A2) into Eq. (A1) and an analogous splitting then gives rise to the definition

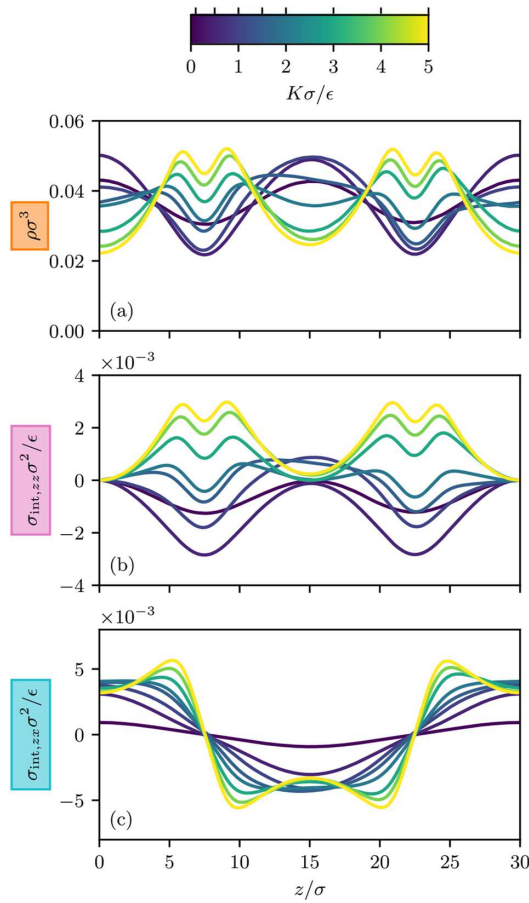


FIG. 7. The density profile (a) as well as structural (b) and viscous (c) components of the internal stress tensor $\sigma_{\text{int}}(z)$ as obtained via Eqs. (A4) and (A5) is shown. The components of the internal stress tensor are scaled by the squared particle diameter divided by the energy scale (σ^2/ϵ). A constant temperature $k_B T = 0.1\epsilon$ is maintained, and values of $K\sigma/\epsilon = 0.1, 0.5, 1, 1.5, 2, 3, 4, 5$ (indicated by ticks on the color scale) are chosen for the shear amplitude as in Fig. 5.

$$\nabla \cdot \sigma_{\text{int}}(\mathbf{r}, t) = \mathbf{F}_{\text{int}}(\mathbf{r}, t) \quad (\text{A3})$$

for the internal stress tensor $\sigma_{\text{int}}(\mathbf{r}, t)$.

In the considered stationary state, the time dependence can be dropped. Obtaining $\sigma_{\text{int}}(\mathbf{r})$ from the sampled force density profile $\mathbf{F}_{\text{int}}(\mathbf{r})$ requires an integration of its spatial components according to Eq. (A3). Pressure-like contributions (corresponding to integration constants) are not accessible from the force density profiles alone and require further suitable measurements in simulation.^{79,80} (The standard Irving–Kirkwood⁸¹ treatment is only valid for pair-potentials.) We omit such constants in the following and only consider relative inhomogeneities of the internal stress. Additionally, a non-unique⁸² divergence-free part of $\sigma_{\text{int}}(\mathbf{r})$ remains undetermined from the integration of Eq. (A3) and is set to zero.

We specialize to the planar geometry of our system, which enables a straightforward integration to obtain two relevant components of $\sigma_{\text{int}}(z)$ via

$$\sigma_{\text{int},zz}(z) = \int dz F_{\text{int},z}(z), \quad (\text{A4})$$

$$\sigma_{\text{int},zx}(z) = \int dz F_{\text{int},x}(z). \quad (\text{A5})$$

Analogous to Fig. 5, where the x - and z -component of the internal force is depicted, we show results for the components $\sigma_{\text{int},zz}(z)$ and $\sigma_{\text{int},zx}(z)$ of the internal stress tensor as obtained by Eqs. (A4) and (A5) in Fig. 7. Here, the integration constants were chosen such that $\sigma_{\text{int},zz}(z)$ vanishes at the boundaries of the box and $\sigma_{\text{int},zx}(z)$ is anti-symmetric under motion reversal ($\mathbf{v}(\mathbf{r}) \rightarrow -\mathbf{v}(\mathbf{r})$).

It is observed that $\sigma_{\text{int},zz}(z)$ reproduces the shape of the density profile, which is consistent with the considerations in the main text; cf. Eq. (14). For $\sigma_{\text{int},zx}(z)$, a sinusoidal shape is obtained at low shear amplitudes. When increasing K , the zx -component of the internal stress tensor develops a secondary structure. This is indicative of the non-linear response of a colloidal gel to applied shear, which manifests itself for inhomogeneous shear in an anomalous behavior of the viscous contribution.

APPENDIX B: VARIATION OF THE THREE-BODY ANGLE

In Fig. 8, we show illustrative results of the sheared three-body gel for different values of the preferred three-body angle Θ_0 . For lower values of Θ_0 , it is increasingly difficult to obtain symmetric profiles. We choose $\Theta_0 = 150^\circ$ as the lowest value to keep away from the liquid–gas binodal and to prevent the formation of droplets within the flow channels, which hinder an accurate sampling. It is apparent from the results that the choice of $\Theta_0 = 180^\circ$ in the main text is not artificial and that similar behavior can be achieved also for lower values of Θ_0 as long as gelation is enforced. When decreasing Θ_0 , one even observes larger local forces at the sides of the flow channels [cf. $f_{\text{int},z}(z)$ and $f_{\text{int},x}(z)$ in Fig. 8] as the desorption of particle strands is enhanced due to the increased ability of branching. We refer to Refs. 29 and 30 for an investigation of the equilibrium behavior of the three-body gel for different values of the three-body angle Θ_0 and the three-body interaction strength λ .

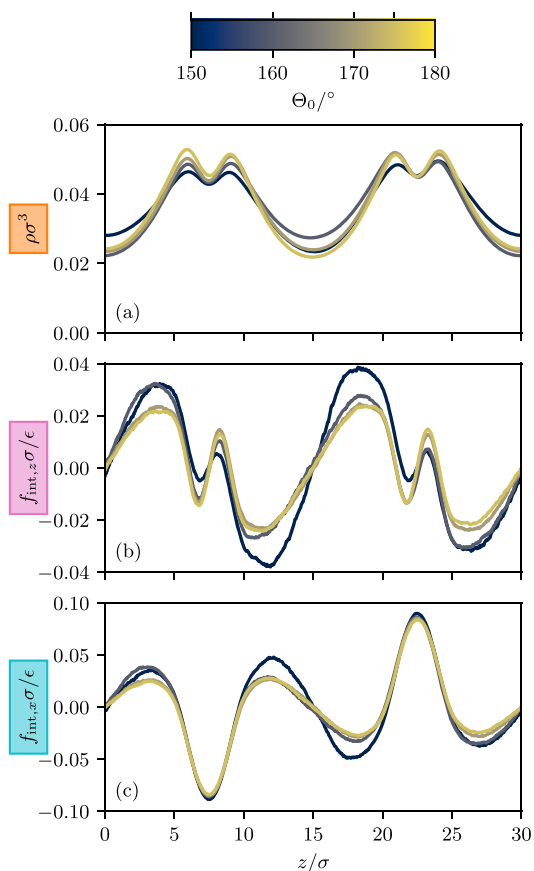


FIG. 8. The density profile $\rho(z)$ (a) as well as the perpendicular (b) and parallel (c) component of the internal force profile $\mathbf{f}_{\text{int}}(z)$ is shown for the sheared three-body gel with modified preferred three-body angles of $\Theta_0 = 175^\circ, 170^\circ, 160^\circ, 150^\circ$ (indicated by ticks on the color scale). We set a temperature of $k_B T = 0.1\epsilon$ and a shear amplitude of $K = 5\epsilon/\sigma$. As network formation also occurs for the above values of Θ_0 and as it is the driving mechanism for the strong superadiabatic response, one can observe similar behavior as for the choice of $\Theta_0 = 180^\circ$ in the main text. Below a value of $\Theta_0 = 150^\circ$, an accurate sampling of the steady state was hindered by the formation of droplets in the flow channels.

APPENDIX C: COMPARISON TO THE LENNARD-JONES FLUID

For comparison, we show the behavior of the truncated Lennard-Jones fluid under an analogous shear protocol as for the three-body gel. The Lennard-Jones interaction potential only consists of the radially isotropic pairwise contribution

$$u_2(r) = \begin{cases} 4\epsilon \left[\left(\frac{\sigma}{r}\right)^{12} - \left(\frac{\sigma}{r}\right)^6 \right], & r \leq r_c, \\ 0, & r > r_c, \end{cases} \quad (\text{C1})$$

with the cutoff distance $r_c = 2.5\sigma$, and it can, hence, be taken as an example of a *simple* fluid or colloidal suspension.

In Fig. 9, the density profile as well as the parallel and perpendicular contribution of the internal force profile is shown for a temperature of $k_B T = 1.5\epsilon$ and for various (large) shear amplitudes K . All other system parameters are adopted from the simulations of the sheared gel, which yields the same low mean density of $\rho_b \approx 0.037\sigma^{-3}$. One recognizes that the superadiabatic response of the Lennard-Jones fluid differs starkly from that of the three-body gel; cf. 5. The density inhomogeneity of the simple liquid is orders of magnitude smaller and possesses a sinusoidal shape that does not change qualitatively for different shear amplitudes. Note that despite driving the Lennard-Jones system with much stronger

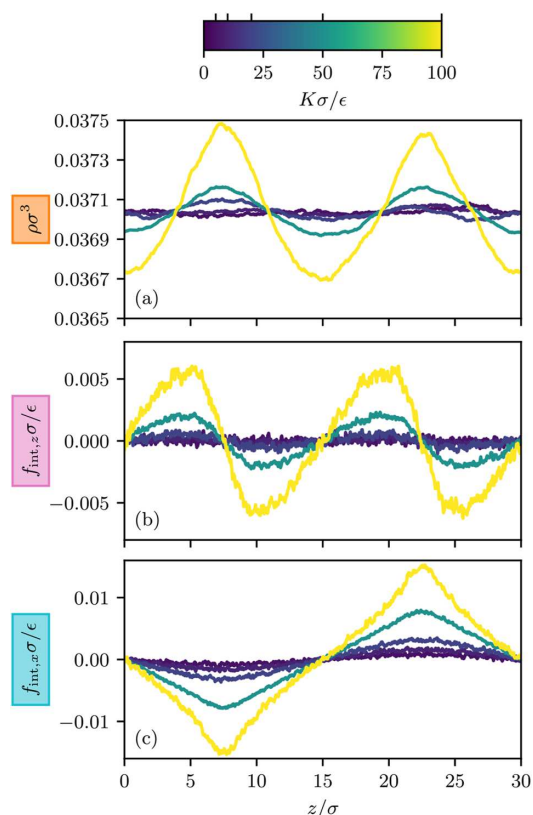


FIG. 9. The steady state behavior of a sheared low-density Lennard-Jones fluid is shown for a temperature of $k_B T = 1.5\epsilon$ and for various shear amplitudes $K\sigma/\epsilon = 5, 10, 20, 50, 100$ (indicated by ticks on the color scale). The superadiabatic response of this representative simple fluid is much weaker than in the sheared three-body gel. The migration of particles always occurs toward the center of the flow channels, where the velocity gradient vanishes, as can be deduced from the density profile $\rho(z)$ (a) and the perpendicular internal force profile $f_{\text{int},z}(z)$ (b). The viscous superadiabatic force $f_{\text{int},x}(z)$ (c) counteracts the flow direction, and unlike in the three-body gel, no drag-along is observed.

external forces, the onset of notable superadiabatic effects occurs only for sufficiently large inhomogeneous shear as opposed to the three-body gel, where a substantial density inhomogeneity develops also for low values of K . In particular, no inversion of the extrema in the density profile $\rho(z)$ is observed, as was the case for the three-body gel when transitioning from low to high shear. The internal force components reflect this situation with both $f_{\text{int},z}(z)$ and $f_{\text{int},x}(z)$ being much smaller and showing less features than in the three-body gel. Especially for $f_{\text{int},x}(z)$, no anomalous drag-along is observed as the superadiabatic viscous force in the Lennard-Jones fluid always counteracts the flow.

REFERENCES

- ¹Q. Chen, S. C. Bae, and S. Granick, “Directed self-assembly of a colloidal kagome lattice,” *Nature* **469**, 381–384 (2011).
- ²Y. Wang, Y. Wang, D. R. Breed, V. N. Manoharan, L. Feng, A. D. Hollingsworth, M. Weck, and D. J. Pine, “Colloids with valence and specific directional bonding,” *Nature* **491**, 51–55 (2012).
- ³S. Sacanna, M. Korpics, K. Rodriguez, L. Colón-Meléndez, S.-H. Kim, D. J. Pine, and G.-R. Yi, “Shaping colloids for self-assembly,” *Nat. Commun.* **4**, 1688 (2013).
- ⁴A. Demortière, A. Snezhko, M. V. Sapozhnikov, N. Becker, T. Proslir, and I. S. Aranson, “Self-assembled tunable networks of sticky colloidal particles,” *Nat. Commun.* **5**, 3117 (2014).
- ⁵Z. M. Sherman, A. M. Green, M. P. Howard, E. V. Anslin, T. M. Truskett, and D. J. Milliron, “Colloidal nanocrystal gels from thermodynamic principles,” *Acc. Chem. Res.* **54**, 798–807 (2021).
- ⁶E. Lattuada, T. Pietrangeli, and F. Sciortino, “Interpenetrating gels in binary suspensions of DNA nanostars,” *J. Chem. Phys.* **157**, 135101 (2022).
- ⁷A. D. Dinsmore and D. A. Weitz, “Direct imaging of three-dimensional structure and topology of colloidal gels,” *J. Phys.: Condens. Matter* **14**, 7581–7597 (2002).
- ⁸J. R. Stokes and W. J. Frith, “Rheology of gelling and yielding soft matter systems,” *Soft Matter* **4**, 1133 (2008).
- ⁹M. Laurati, G. Petekidis, N. Koumakis, F. Cardinaux, A. B. Schofield, J. M. Brader, M. Fuchs, and S. U. Egelhaaf, “Structure, dynamics, and rheology of colloid-polymer mixtures: From liquids to gels,” *J. Chem. Phys.* **130**, 134907 (2009).
- ¹⁰E. Zaccarelli, “Colloidal gels: Equilibrium and non-equilibrium routes,” *J. Phys.: Condens. Matter* **19**, 323101 (2007).
- ¹¹M. E. Cates, M. Fuchs, K. Kroy, W. C. K. Poon, and A. M. Puestas, “Theory and simulation of gelation, arrest and yielding in attracting colloids,” *J. Phys.: Condens. Matter* **16**, S4861–S4875 (2004).
- ¹²C. P. Royall, S. R. Williams, T. Ohtsuka, and H. Tanaka, “Direct observation of a local structural mechanism for dynamic arrest,” *Nat. Mater.* **7**, 556–561 (2008).
- ¹³C. P. Royall, S. R. Williams, and H. Tanaka, “Vitrification and gelation in sticky spheres,” *J. Chem. Phys.* **148**, 044501 (2018).
- ¹⁴E. Zaccarelli, S. V. Buldyrev, E. La Nave, A. J. Moreno, I. Saika-Voivod, F. Sciortino, and P. Tartaglia, “Model for reversible colloidal gelation,” *Phys. Rev. Lett.* **94**, 218301 (2005).
- ¹⁵E. Zaccarelli, I. Saika-Voivod, S. V. Buldyrev, A. J. Moreno, P. Tartaglia, and F. Sciortino, “Gel to glass transition in simulation of a valence-limited colloidal system,” *J. Chem. Phys.* **124**, 124908 (2006).
- ¹⁶B. A. Lindquist, R. B. Jadrich, D. J. Milliron, and T. M. Truskett, “On the formation of equilibrium gels via a macroscopic bond limitation,” *J. Chem. Phys.* **145**, 074906 (2016).
- ¹⁷M. P. Howard, Z. M. Sherman, A. N. Sreenivasan, S. A. Valenzuela, E. V. Anslin, D. J. Milliron, and T. M. Truskett, “Effects of linker flexibility on phase behavior and structure of linked colloidal gels,” *J. Chem. Phys.* **154**, 074901 (2021).
- ¹⁸J. Groenewold and W. K. Kelgel, “Colloidal cluster phases, gelation and nuclear matter,” *J. Phys.: Condens. Matter* **16**, S4877–S4886 (2004).
- ¹⁹M.-A. Suarez, N. Kern, E. Pitard, and W. Kob, “Out-of-equilibrium dynamics of a fractal model gel,” *J. Chem. Phys.* **130**, 194904 (2009).
- ²⁰R. Blaak, M. A. Miller, and J.-P. Hansen, “Reversible gelation and dynamical arrest of dipolar colloids,” *Europhys. Lett.* **78**, 26002 (2007).
- ²¹M. A. Miller, R. Blaak, C. N. Lumb, and J.-P. Hansen, “Dynamical arrest in low density dipolar colloidal gels,” *J. Chem. Phys.* **130**, 114507 (2009).
- ²²L. Rovigatti, J. Russo, and F. Sciortino, “No evidence of gas-liquid coexistence in dipolar hard spheres,” *Phys. Rev. Lett.* **107**, 237801 (2011).
- ²³E. Bianchi, R. Blaak, and C. N. Likos, “Patchy colloids: State of the art and perspectives,” *Phys. Chem. Chem. Phys.* **13**, 6397 (2011).
- ²⁴E. Del Gado and W. Kob, “A microscopic model for colloidal gels with directional effective interactions: Network induced glassy dynamics,” *Soft Matter* **6**, 1547 (2010).
- ²⁵F. Sciortino and E. Zaccarelli, “Reversible gels of patchy particles,” *Curr. Opin. Solid State Mater. Sci.* **15**, 246–253 (2011).
- ²⁶E. Bianchi, J. Largo, P. Tartaglia, E. Zaccarelli, and F. Sciortino, “Phase diagram of patchy liquids: Towards empty liquids,” *Phys. Rev. Lett.* **97**, 168301 (2006).
- ²⁷B. Ruzicka, E. Zaccarelli, L. Zulian, R. Angelini, M. Sztucki, A. Moussaïd, T. Narayanan, and F. Sciortino, “Observation of empty liquids and equilibrium gels in a colloidal clay,” *Nat. Mater.* **10**, 56–60 (2011).
- ²⁸D. de las Heras, J. M. Tavares, and M. M. Telo da Gama, “Phase diagrams of binary mixtures of patchy colloids with distinct numbers of patches: The network fluid regime,” *Soft Matter* **7**, 5615 (2011).
- ²⁹S. Saw, N. L. Ellegaard, W. Kob, and S. Sastry, “Structural relaxation of a gel modeled by three body interactions,” *Phys. Rev. Lett.* **103**, 248305 (2009).
- ³⁰S. Saw, N. L. Ellegaard, W. Kob, and S. Sastry, “Computer simulation study of the phase behavior and structural relaxation in a gel-former modeled by three-body interactions,” *J. Chem. Phys.* **134**, 164506 (2011).
- ³¹J. Colombo, A. Widmer-Cooper, and E. Del Gado, “Microscopic picture of cooperative processes in restructuring gel networks,” *Phys. Rev. Lett.* **110**, 198301 (2013).
- ³²J. Colombo and E. Del Gado, “Self-assembly and cooperative dynamics of a model colloidal gel network,” *Soft Matter* **10**, 4003 (2014).
- ³³J. Colombo and E. Del Gado, “Stress localization, stiffening, and yielding in a model colloidal gel,” *J. Rheol.* **58**, 1089–1116 (2014).
- ³⁴H. Hatami-Marbini and J. B. Coulbaly, “Colloidal particle gel models using many-body potential interactions,” *Phys. Rev. E* **101**, 020601 (2020).
- ³⁵H. Hatami-Marbini, “A computational study of the behavior of colloidal gel networks at low volume fraction,” *J. Phys.: Condens. Matter* **32**, 275101 (2020).
- ³⁶M. Bantawa, W. A. Fontaine-Seiler, P. D. Olmsted, and E. Del Gado, “Microscopic interactions and emerging elasticity in model soft particulate gels,” *J. Phys.: Condens. Matter* **33**, 414001 (2021).
- ³⁷M. Bouzid and E. Del Gado, “Network topology in soft gels: Hardening and softening materials,” *Langmuir* **34**, 773–781 (2018).
- ³⁸N. C. X. Stuhlmüller, T. Eckert, D. de las Heras, and M. Schmidt, “Structural nonequilibrium forces in driven colloidal systems,” *Phys. Rev. Lett.* **121**, 098002 (2018).
- ³⁹D. de las Heras and M. Schmidt, “Flow and structure in nonequilibrium Brownian many-body systems,” *Phys. Rev. Lett.* **125**, 018001 (2020).
- ⁴⁰F. H. Stillinger and T. A. Weber, “Computer simulation of local order in condensed phases of silicon,” *Phys. Rev. B* **31**, 5262–5271 (1985).
- ⁴¹F. Sannüller and M. Schmidt, “Adaptive Brownian dynamics,” *J. Chem. Phys.* **155**, 134107 (2021).
- ⁴²M. Schmidt and J. M. Brader, “Power functional theory for Brownian dynamics,” *J. Chem. Phys.* **138**, 214101 (2013).
- ⁴³M. Schmidt, “Power functional theory for many-body dynamics,” *Rev. Mod. Phys.* **94**, 015007 (2022).
- ⁴⁴C. P. Royall, J. Dzubiella, M. Schmidt, and A. van Blaaderen, “Nonequilibrium sedimentation of colloids on the particle scale,” *Phys. Rev. Lett.* **98**, 188304 (2007).
- ⁴⁵A. S. Barnard and S. P. Russo, “Development of an improved Stillinger–Weber potential for tetrahedral carbon using *ab initio* (Hartree–Fock and MP2) methods,” *Mol. Phys.* **100**, 1517–1525 (2002).
- ⁴⁶M. H. Bhat, V. Molinero, E. Soignard, V. C. Solomon, S. Sastry, J. L. Yarger, and C. A. Angell, “Vitrification of a monatomic metallic liquid,” *Nature* **448**, 787–790 (2007).
- ⁴⁷V. Molinero and E. B. Moore, “Water modeled as an intermediate element between carbon and silicon,” *J. Phys. Chem. B* **113**, 4008–4016 (2009).

- ⁴⁸The simulation code can be found at <https://gidab.uni-bayreuth.de/bt306964/mbd>.
- ⁴⁹M. K. Coe, R. Evans, and N. B. Wilding, "The coexistence curve and surface tension of a monatomic water model," *J. Chem. Phys.* **156**, 154505 (2022).
- ⁵⁰M. Pouzot, T. Nicolai, L. Benyahia, and D. Durand, "Strain hardening and fracture of heat-set fractal globular protein gels," *J. Colloid Interface Sci.* **293**, 376–383 (2006).
- ⁵¹D. J. Evans and G. P. Morriss, "Nonlinear-response theory for steady planar Couette flow," *Phys. Rev. A* **30**, 1528–1530 (1984).
- ⁵²B. D. Todd and P. J. Davis, *Nonequilibrium Molecular Dynamics: Theory, Algorithms and Applications*, 1st ed. (Cambridge University Press, 2017).
- ⁵³P. E. Kloeden and E. Platen, *Numerical Solution of Stochastic Differential Equations*, Applications of Mathematics, Corr. 3rd Print ed. (Springer, Berlin; NY, 1999), Vol. 23.
- ⁵⁴C. Rackauckas and Q. Nie, "Adaptive methods for stochastic differential equations via natural embeddings and rejection sampling with memory," *Discrete Contin. Dyn. Syst. B* **22**, 2731–2761 (2017).
- ⁵⁵D. L. Ermak and J. A. McCammon, "Brownian dynamics with hydrodynamic interactions," *J. Chem. Phys.* **69**, 1352–1360 (1978).
- ⁵⁶H. Tanaka and T. Araki, "Simulation method of colloidal suspensions with hydrodynamic interactions: Fluid particle dynamics," *Phys. Rev. Lett.* **85**, 1338–1341 (2000).
- ⁵⁷N. M. Kovalchuk and V. M. Starov, "Aggregation in colloidal suspensions: Effect of colloidal forces and hydrodynamic interactions," *Adv. Colloid Interface Sci.* **179–182**, 99–106 (2012).
- ⁵⁸C. P. Royall, J. Eggers, A. Furukawa, and H. Tanaka, "Probing colloidal gels at multiple length scales: The role of hydrodynamics," *Phys. Rev. Lett.* **114**, 258302 (2015).
- ⁵⁹A. W. Lees and S. F. Edwards, "The computer study of transport processes under extreme conditions," *J. Phys. C: Solid State Phys.* **5**, 1921–1928 (1972).
- ⁶⁰N. Jahreis and M. Schmidt, "Shear-induced deconfinement of hard disks," *Colloid Polym. Sci.* **298**, 895–906 (2020).
- ⁶¹E. Moghimi, A. R. Jacob, N. Koumakis, and G. Petekidis, "Colloidal gels tuned by oscillatory shear," *Soft Matter* **13**, 2371–2383 (2017).
- ⁶²For one steady state, the profiles were obtained within 1000 CPU hours.
- ⁶³The onset of percolation has been verified in corresponding bulk simulations. In this case, the density profile remains constant and the internal force profile vanishes within numerical accuracy.
- ⁶⁴S. Hermann and M. Schmidt, "Noether's theorem in statistical mechanics," *Commun. Phys.* **4**, 176 (2021).
- ⁶⁵D. de las Heras, J. Renner, and M. Schmidt, "Custom flow in overdamped Brownian dynamics," *Phys. Rev. E* **99**, 023306 (2019).
- ⁶⁶A. Fortini, D. de las Heras, J. M. Brader, and M. Schmidt, "Superadiabatic forces in Brownian many-body dynamics," *Phys. Rev. Lett.* **113**, 167801 (2014).
- ⁶⁷D. Borgis, R. Assaraf, B. Rotenberg, and R. Vuilleumier, "Computation of pair distribution functions and three-dimensional densities with a reduced variance principle," *Mol. Phys.* **111**, 3486–3492 (2013).
- ⁶⁸D. de las Heras and M. Schmidt, "Better than counting: Density profiles from force sampling," *Phys. Rev. Lett.* **120**, 218001 (2018).
- ⁶⁹B. Rotenberg, "Use the force! Reduced variance estimators for densities, radial distribution functions, and local mobilities in molecular simulations," *J. Chem. Phys.* **153**, 150902 (2020).
- ⁷⁰R. Evans, "The nature of the liquid-vapour interface and other topics in the statistical mechanics of non-uniform, classical fluids," *Adv. Phys.* **28**, 143–200 (1979).
- ⁷¹D. de las Heras, T. Zimmermann, F. Sammler, S. Hermann, and M. Schmidt, "Perspective: How to overcome dynamical density functional theory," to be published.
- ⁷²D. de las Heras and M. Schmidt, "Velocity gradient power functional for Brownian dynamics," *Phys. Rev. Lett.* **120**, 028001 (2018).
- ⁷³J. M. Brader and M. Krüger, "Density profiles of a colloidal liquid at a wall under shear flow," *Mol. Phys.* **109**, 1029–1041 (2011).
- ⁷⁴A. Scacchi, M. Krüger, and J. M. Brader, "Driven colloidal fluids: Construction of dynamical density functional theories from exactly solvable limits," *J. Phys. Condens. Matter* **28**, 244023 (2016).
- ⁷⁵N. Koumakis, E. Moghimi, R. Besseling, W. C. K. Poon, J. F. Brady, and G. Petekidis, "Tuning colloidal gels by shear," *Soft Matter* **11**, 4640–4648 (2015).
- ⁷⁶T. Geyer and U. Winter, "An $O(N^2)$ approximation for hydrodynamic interactions in Brownian dynamics simulations," *J. Chem. Phys.* **130**, 114905 (2009).
- ⁷⁷R. R. Schmidt, J. G. H. Cifre, and J. G. de la Torre, "Comparison of Brownian dynamics algorithms with hydrodynamic interaction," *J. Chem. Phys.* **135**, 084116 (2011).
- ⁷⁸L. L. Treffenstädt and M. Schmidt, "Memory-induced motion reversal in Brownian liquids," *Soft Matter* **16**, 1518–1526 (2020).
- ⁷⁹A. P. Thompson, S. J. Plimpton, and W. Mattson, "General formulation of pressure and stress tensor for arbitrary many-body interaction potentials under periodic boundary conditions," *J. Chem. Phys.* **131**, 154107 (2009).
- ⁸⁰K. Shi, E. Smith, E. E. Santiso, and K. E. Gubbins, "A perspective on microscopic pressure (stress) tensor: History, current understanding, and future challenges," *J. Chem. Phys.* (published online 2022).
- ⁸¹J. H. Irving and J. G. Kirkwood, "The statistical mechanical theory of transport processes. IV. The equations of hydrodynamics," *J. Chem. Phys.* **18**, 817–829 (1950).
- ⁸²P. Schofield and J. R. Henderson, "Statistical mechanics of inhomogeneous fluids," *Proc. R. Soc. London, Ser. A* **379**, 231–246 (1982).

Comparative study of force-based classical density functional theoryFlorian Sammüller , Sophie Hermann , and Matthias Schmidt **Theoretische Physik II, Physikalisches Institut, Universität Bayreuth, D-95447 Bayreuth, Germany*

(Received 2 December 2022; accepted 17 February 2023; published 6 March 2023)

We reexamine results obtained with the recently proposed density functional theory framework based on forces (force-DFT) [S. M. Tschopp *et al.*, *Phys. Rev. E* **106**, 014115 (2022)]. We compare inhomogeneous density profiles for hard sphere fluids to results from both standard density functional theory and from computer simulations. Test situations include the equilibrium hard sphere fluid adsorbed against a planar hard wall and the dynamical relaxation of hard spheres in a switched harmonic potential. The comparison to grand canonical Monte Carlo simulation profiles shows that equilibrium force-DFT alone does not improve upon results obtained with the standard Rosenfeld functional. Similar behavior holds for the relaxation dynamics, where we use our event-driven Brownian dynamics data as benchmark. Based on an appropriate linear combination of standard and force-DFT results, we investigate a simple hybrid scheme which rectifies these deficiencies in both the equilibrium and the dynamical case. We explicitly demonstrate that although the hybrid method is based on the original Rosenfeld fundamental measure functional, its performance is comparable to that of the more advanced White Bear theory.

DOI: [10.1103/PhysRevE.107.034109](https://doi.org/10.1103/PhysRevE.107.034109)**I. INTRODUCTION**

Whether any theoretical approach is useful in practice often stems from the accuracy and reliability of its predictions versus the analytical and computational effort it requires. Classical density functional theory (DFT) [1,2] fares very well, ranging from simple local density and square gradient approximations [1,2], which are sufficiently accurate in appropriate circumstances (see, e.g., Refs. [3–5] for studies of colloidal sedimentation) to the nonlocal and nonlinear prowess of Rosenfeld’s fundamental measure theory (FMT) [6,7] to capture hard sphere correlations.

Applying DFT in practice involves solving a variational (minimization) problem, which typically requires the numerical treatment of an implicit integral equation. One obtains static quantities or performs adiabatic time evolution within dynamical DFT (DDFT). The latter task is often done with a simple time-forward integrator, but more advanced methods [8,9] allow to address dynamical optimization problems. Similarly, computational grids in real space range from simple and often very relevant effective one-dimensional geometries [10] to full three-dimensional resolution [11] and pseudospectral methods [8]. Increasing the complexity of the underlying microscopic model trades off well with the achieved broader physical scope, as is the case in including orientational degrees of freedom in liquid crystal formation [12,13] and molecular DFT [14–16] for realistic modeling of molecular liquids.

DFT offers a complete theoretical framework for addressing static problems in many-body statistical physics. The theory is founded on the concept of potentials, including the chemical potential μ as a control parameter, an external potential that adds local variation to μ , and an intrinsic part, which

arises from the interparticle interactions and which induces the coupling of the microscopic degrees of freedom.

In contrast to this basis in potentials, the concept of forces seems almost alien to the framework, or at least redundant. Nevertheless, in a variety of very different fields there appears to be new interest in this old workhorse. We mention the recent and unexpected advances in simulation methodology based on force sampling [17–20] and in the related but different realm of quantum DFT [21–25], as well as in the power functional approach to nonequilibrium many-body dynamics [26]. Both the classical and the quantum force balance were proven to be direct consequences of a thermal Noether symmetry of the system [27,28]. Forces are also central in the recent treatment of motility-induced phase separation by Brady and coworkers [29].

Recently, Tschopp *et al.* [27] developed a force-based alternative to implement density functional theory. Their “force-DFT” comes at an increased computational cost, as two-body functions appear explicitly and need to be manipulated. Nevertheless, the framework still retains formal one-body purity with the two-body density playing the role of an auxiliary variable. The difference between the standard approach to DFT and the force-DFT appears similar to the difference between the virial and compressibility route to determine the equation of state in bulk fluids [2], e.g., on basis of the celebrated Percus-Yevick approximation for the hard sphere fluid. Actually, as could be shown by Tschopp *et al.* [27] via an investigation of the hard wall contact theorem, standard DFT corresponds in this case to the compressibility equation of state while force-DFT satisfies the virial equation of state.

Here we address the question of where the balance of complexity and accuracy tips for the force-DFT. We compare the theoretical results of Ref. [27] against new computer simulation data, involving canonical, grand canonical, and event-driven methods, as is appropriate for carrying out a systematic comparison, as we detail below. We find that the

*Matthias.Schmidt@uni-bayreuth.de

force-DFT per se does not improve on standard DFT in the considered cases, but that an appropriate linear combination of results from the two approaches, which constitutes a simple hybrid scheme, gives much improved results as compared to the standard framework. We hence follow the suggestion raised in the outlook of Ref. [27] that “the virial and compressibility routes could be mixed in the spirit of liquid-state integral-equation theories, using approximations analogous to the Rogers-Young or Carnahan-Starling theories.”

The paper is organized as follows. In Sec. II, a brief summary of the core concepts of DFT is given. Particularly, we highlight the conceptual differences of the force-DFT approach and describe how both routes can be used to formulate a dynamical DFT. In Sec. III, we conduct a thorough reinvestigation of the force-DFT results for the model applications of Ref. [27], thereby comparing these data to results from standard DFT and from simulation. Throughout this work, the hard sphere fluid is considered and the force-DFT results are those that were obtained with the Rosenfeld [6] FMT functional in Ref. [27]. We first turn to the case of imposing a planar hard wall in Sec. III A where the respective connection of standard and force-DFT to the compressibility and virial route is established via the hard wall contact theorem. To obtain numerically accurate results for this equilibrium situation, we perform grand canonical Monte Carlo (GCMC) [30] simulations which are systematically adjusted to enable a comparison with both DFT routes. In Sec. III B, the dynamical behavior of the hard sphere fluid in a switched harmonic potential is considered. For the numerical reproduction of the exact time evolution, we employ event-driven Brownian dynamics simulations (EDBD) [31] that are initialized with particle configurations from canonical Monte Carlo (MC) simulation. The time-dependent density profile obtained with this procedure is compared to results from standard and from force-DDFT. Based on the observations of Secs. III A and III B, we investigate a hybrid scheme in Sec. IV as a means to substantially improve the resulting density profiles via a linear combination of results from the standard and force route. This is illustrated both for the equilibrium and for the dynamical case, where we find much better agreement with simulation results. In particular, we show that hybrid Rosenfeld DFT can compete with standard DFT on the basis of the high-accuracy White Bear [32,33] functionals for the hard wall test case. We conclude in Sec. V and give an outlook to further possible applications of force-DFT and the hybrid scheme.

II. CONCEPTS OF STANDARD DFT AND FORCE-DFT

One of the main goals and motivations behind the development of force-DFT is the possibility to improve upon the results from standard DFT calculations. Usually improvements of DFT involve refinements of the assumed free energy density functional. Two prominent examples are the advanced White Bear versions of FMT [7,32,33]. In contrast, the implementation of force-DFT acknowledges the fact that the exact density functional is not within reach for relevant physical systems and that introducing approximations leads to a theory that is not entirely self-consistent. Starting from the same functional but using different routes to calculate a physical

variable will yield different results except in the formal case of an exactly known functional.

The starting point of both the standard DFT and the force-DFT approach is determining the density $\rho(\mathbf{r})$ self-consistently from solving the Euler-Lagrange equation

$$\ln \rho(\mathbf{r}) - \beta[\mu - V_{\text{ext}}(\mathbf{r})] - c_1(\mathbf{r}) = 0, \quad (1)$$

where $\beta = (k_B T)^{-1}$ denotes the inverse temperature with k_B being Boltzmann’s constant, and μ is the chemical potential. While the thermodynamic state point as well as the external potential $V_{\text{ext}}(\mathbf{r})$ act as control parameters, the one-body direct correlation function $c_1(\mathbf{r})$ arises from internal interactions and it has to be approximated in practice.

Given a suitable approximation for the excess free energy density functional $F_{\text{exc}}[\rho]$, where the brackets indicate functional dependence, one determines the one-body direct correlation function via functional differentiation according to

$$c_1(\mathbf{r}) = -\beta \frac{\delta F_{\text{exc}}[\rho]}{\delta \rho(\mathbf{r})}. \quad (2)$$

In force-DFT one retains Eq. (1) but calculates the direct correlation function from the force integral

$$c_1(\mathbf{r}) = -\nabla^{-1} \cdot \int d\mathbf{r}' \frac{\rho_2(\mathbf{r}, \mathbf{r}'; [\rho])}{\rho(\mathbf{r})} \nabla \beta \phi(|\mathbf{r} - \mathbf{r}'|), \quad (3)$$

where $\nabla^{-1} = 1/(4\pi) \int d\mathbf{r}' (\mathbf{r} - \mathbf{r}')/|\mathbf{r} - \mathbf{r}'|^3$ indicates an integral operator (see, e.g., Refs. [17,18]) and $\phi(r)$ is the pair interaction potential as a function of the interparticle distance r . At face value the expression (3) is based on the two-body level as it depends on the two-body density $\rho_2(\mathbf{r}, \mathbf{r}'; [\rho])$. However, starting from an approximative excess free energy functional $F_{\text{exc}}[\rho]$, the two-body density $\rho_2(\mathbf{r}, \mathbf{r}'; [\rho])$ is determined by functionally differentiating twice to get the two-body direct correlation function $c_2(\mathbf{r}, \mathbf{r}') = -\beta \delta F_{\text{exc}}[\rho] / \delta \rho(\mathbf{r}) \delta \rho(\mathbf{r}')$ and then solving the inhomogeneous Ornstein-Zernike (OZ) equation self-consistently [27]. The last step can be done numerically in planar and spherical geometry (see Refs. [34–36] for the technical details).

Solving the inhomogeneous OZ equations has relevant applications in the study of the structure factor of thin films [37], of capillary waves, and of the wave-number-dependent surface tension [38,39] in lateral systems. Due to this additional self-consistency step and by working on the two-body level, the force-DFT is technically and computationally more complex than standard implementations of DFT based on Eq. (2).

The alternative force route also transfers directly to DDFT, which is then called force-DDFT. Standard DDFT provides a statistical mechanical approach to describe inhomogeneous fluids in nonequilibrium, including the dynamics of adsorption [40,41], lane formation [42,43], or the motion of active microswimmers [44,45] (see the review [46] for a recent and broad overview). This theory is the dynamic extension of DFT and it is intrinsically based on the adiabatic approximation. Efforts to improve the implied approaches [47] include the in principle exact power functional theory, which goes beyond the adiabatic approximation by taking all superadiabatic (above adiabatic) contributions into account [26,48]. Recently, a concrete implementation of a two-body DDFT [49], which is deeply founded on the force route investigated

in this work, has been shown to incorporate superadiabatic effects on the one-body level, thus providing a way to improve upon standard DDFT. Reference [50] discusses the shortcomings of standard DDFT and describes possible ways forward.

The transition from the equilibrium DFT to the nonequilibrium DDFT is in both cases simply based on the continuity equation

$$\frac{\partial \rho(\mathbf{r}, t)}{\partial t} = -\nabla \cdot \mathbf{J}(\mathbf{r}, t). \quad (4)$$

The current $\mathbf{J}(\mathbf{r}, t)$ is equal (up to the friction constant) to the force density and takes into account its internal, external, and diffusive ideal gas contribution. The internal force $\mathbf{f}_{\text{int}}(\mathbf{r}, t)$ is then assumed, as in equilibrium, to be obtained by the gradient of the one-body direct correlation function $\mathbf{f}_{\text{int}}(\mathbf{r}, t) = k_B T \nabla c_1(\mathbf{r}, t)$, which neglects superadiabatic force contributions [26]. Evaluation of $c_1(\mathbf{r}, t)$ can proceed via Eq. (2) for the DDFT route and via Eq. (3) in case of the force-DDFT approach, and differences are expected to occur for approximate forms of the excess free energy functional.

III. COMPARISON TO SIMULATION RESULTS

A. Equilibrium: Hard sphere fluid at a hard wall

We proceed with a comparison of results from both DFT routes to simulation data for the standard case of an equilibrium hard sphere fluid at a hard wall as previously investigated by Tschoop *et al.* [27]. For the DFT treatment of the hard sphere fluid, these authors resorted to the Rosenfeld [6] fundamental measure theory (FMT) functional for modeling $F_{\text{exc}}[\rho]$ in both standard and force-DFT. As this functional is an approximation, we showcase in the following the deviation to numerically exact grand canonical Monte Carlo [30] (GCMC) data.

Imposing a planar hard wall is a conceptually important test case for two reasons. First, large density inhomogeneities are induced in the vicinity of the wall, which reveal deviations of approximative theories very clearly [10]. Second, for arbitrary fluids at a hard wall, the contact theorem

$$\rho(0^+) = \beta P \quad (5)$$

establishes a connection of the bulk pressure P of the fluid to the contact value $\rho(0^+)$ of the density profile. This holds beyond simple fluids as governed by a pair potential because DFT is formally valid for many-body interparticle interactions. As was shown in Ref. [27], standard and force-DFT can be associated respectively in this regard to the compressibility and virial route of liquid integral equation theory [2]. More precisely, it could be proven [27] that

$$\rho_s(0^+) = \beta P_c, \quad (6)$$

$$\rho_f(0^+) = \beta P_v, \quad (7)$$

where $\rho_s(z)$ indicates the density profile as obtained from standard DFT, whereas $\rho_f(z)$ is the density profile obtained with force-DFT as a function of the distance z from the wall. Equations (6) and (7) can be derived by explicit analytical calculation and they connect the respective contact densities ($z = 0^+$) to the compressibility (P_c) and virial (P_v) forms of the pressure which are well-known bulk results from liquid

TABLE I. The values of the chemical potential μ_{sim} for the GCMC simulations that yield matching bulk densities ρ_b with the DFT results (cf. Fig. 1). The reference chemical potentials μ_c that were used in the standard DFT calculations (corresponding to the compressibility route) are listed as well.

$\rho_b \sigma^3$	0.4890	0.6032	0.6908
$\beta \mu_c$	3	5	7
$\beta \mu_{\text{sim}}$	2.9572	4.8930	6.7983

integral equation theory. The two DFT routes thus make these differences accessible locally and away from the wall on the level of the inhomogeneous density profile. As the force-DFT is inherently tailored to simple fluids that are governed by pairwise interparticle interactions [recall Eq. (3)], the force-DFT contact theorem (7) also only holds for simple fluids, whereas Eq. (6) is general. For details of the respective proofs we refer the reader to Ref. [27].

In the present case, the Rosenfeld FMT functional reproduces by construction the Percus-Yevick bulk fluid results. In particular, we recall [2] the compressibility equation of state

$$P_c = \frac{\rho_b}{\beta} \frac{1 + \eta + \eta^2}{(1 - \eta)^3} \quad (8)$$

and the virial equation of state

$$P_v = \frac{\rho_b}{\beta} \frac{1 + 2\eta + 3\eta^2}{(1 - \eta)^2}, \quad (9)$$

where ρ_b is the bulk density and $\eta = \rho_b \sigma^3 \pi/6$ is the packing fraction. The standard Rosenfeld FMT when evaluated at a constant density gives a free energy which is consistent with P_c [7].

In Ref. [27], the comparison was carried out as follows. First, standard DFT calculations were performed for various values of the reduced chemical potential $\beta \mu = 3, 5, 7$, which respectively correspond to bulk densities of $\rho_b \sigma^3 = 0.4890, 0.6032, 0.6908$ (cf. Table I). Then, corresponding force-DFT calculations were carried out, which were set up to yield identical bulk densities for providing a valid comparison via Eqs. (6)–(9). As the control parameter of force-DFT is the mean number of particles (N), instead of the chemical potential μ as is the case in standard DFT, the results for $\langle N \rangle$ obtained from the standard DFT calculations were taken as input for the force-DFT. With this protocol, it could be verified that the contact densities of standard and force-DFT indeed correspond to the compressibility and virial pressures (8) and (9), respectively.

For the following investigations via GCMC simulations, we also want to ensure that the bulk densities match the ones chosen in the DFT calculations. However, as the Percus-Yevick result (8) deviates slightly from the true equation of state, one cannot merely consider a GCMC simulation with the same value of the chemical potential μ as in the standard DFT case. Instead, the value of μ has to be adjusted to obtain the same bulk density as in both DFT routes. For this, we perform preliminary simulation runs of the system which yield the numerically accurate equation of state for the hard sphere fluid; results are shown in Fig. 1. This numerical equation of

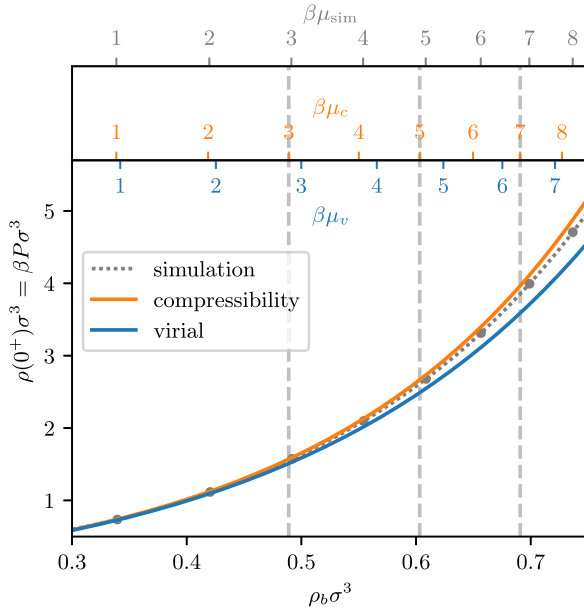


FIG. 1. The equation of state of the hard sphere fluid is shown as obtained from the Percus-Yevick approximation both via the compressibility and the virial route as well as from GCMC simulations (as indicated). Thereby, ρ_b denotes the bulk density and $\rho(0^+) = \beta P$ is the contact density at the hard wall, which can be associated with the bulk pressure P . The upper scales illustrate differences in the chemical potential with respect to the simulation values μ_{sim} that result from the approximative equations of state via the compressibility (μ_c) and virial (μ_v) route (analytical expressions are given in Appendix). Therefore, to yield a valid comparison of the density profiles, μ has to be tuned appropriately in the GCMC simulation to match the considered bulk densities of the standard and force-DFT results, which is illustrated by the gray vertical lines.

state is interpolated at the desired values for the bulk density, which then yields the target values of chemical potential for the actual comparison runs (the numerical values are given in Table I).

The density profiles from the thus prepared GCMC simulations and their comparison to both standard and force-DFT results are shown in Fig. 2. It is observed that the deviation of the contact values at the hard wall indeed reflects the inaccuracies of the Percus-Yevick equation of state. As expected from the bulk results shown in Fig. 1, the GCMC density profile in the vicinity of the wall is enclosed from above and from below by the two DFT profiles. The standard DFT result thereby agrees better with the simulation data. At intermediate separations from the wall, both routes are able to capture the inhomogeneities of the density profile with quite reasonable precision. Although the simulated density profile lies within the two DFT profiles in most parts of the system, there are also regions where the DFT results do not act as a respective upper and lower bound of the true local density. This is most clearly visible for large values of μ [e.g., in Fig. 1(c)] and close to the first density maximum, where both DFT routes underestimate the values of $\rho(z)$ locally. The shape of the

first density maximum of a hard sphere fluid at a hard wall is particularly difficult to reproduce in DFT even when using more elaborate free energy functionals [10,32,33,51] (we return to this point below). While providing a means to yield an additional approximation of $\rho(z)$, force-DFT is not capable to systematically rectify this deficiency in the considered case of the hard sphere fluid adsorbed against a planar hard wall.

B. Dynamics: Hard sphere fluid in a switched harmonic trap

Tschopp *et al.* [27] extended their force-DFT method to out-of-equilibrium situations by replacing the standard form of the one-body direct correlation function $c_1(\mathbf{r})$ by the force integral (3) in the DDFT equation of motion. This yields a dynamical description that is still purely adiabatic, i.e., it approximates the time evolution of the system as a series of equilibrium states. Nevertheless, due to the discrepancies of the two forms of $c_1(\mathbf{r})$ for a given approximate Helmholtz free energy functional, the two routes will in general lead to different dynamical behavior. This has been exemplified in Ref. [27] for the model situation of a hard sphere fluid in a harmonic external potential $V_{ext}(z) = A(z - 5\sigma)^2$, where the strength of the harmonic trap is switched from $A = 0.75k_B T/\sigma^2$ to $A = 0.5k_B T/\sigma^2$ at the initial time $t = 0$.

For a precise numerical investigation of the true time evolution of the system, we employ event-driven Brownian dynamics (EDBD) simulations [31]. Unlike in the equilibrium hard wall comparisons, where the bulk densities of the simulations and the DFT routes were matched to focus solely on structural differences, we now set the total number of particles per lateral system area equal to the corresponding values of the DDFT calculations. Therefore, differences that arise solely from inaccuracies of the associated equations of state are expected and will be most prominent at the center of the trap, where the local density is large. To achieve an accurate and fast initialization of each EDBD run, a preliminary canonical Monte Carlo simulation with identical system parameters is carried out, by which appropriately distributed particle configurations of the initial equilibrium state are obtained. In total, 10^4 EDBD runs are initialized with the above configurations, and the relaxation dynamics after the switching of the harmonic trap is simulated for $0 \leq t/\tau \leq 1$ with the Brownian timescale $\tau = \sigma^2 \gamma / k_B T$ where γ is the friction coefficient. The time evolution of the density profile, attained as an average over all runs, is shown in Fig. 3 for $t/\tau = 0, 0.05, 0.1, 0.2, 0.5, 1$. Additionally, density profiles for the initial and for the final equilibrium states as obtained via canonical Monte Carlo simulations are depicted.

It is apparent that discrepancies which stem from the approximative form of $F_{exc}[\rho]$ emerge for the two DDFT routes. In the considered system, force-DDFT generally yields larger densities at the center of the harmonic trap. For the initial and final equilibrium states, standard DFT provides more accurate results in this region. After toggling the strength of the harmonic potential, both DDFT methods yield similar relaxation dynamics towards their respective equilibrium state. Compared to the simulation results, the density relaxation is marginally too fast in both routes, as is visible especially shortly after switching the potential (cf. Fig. 3,

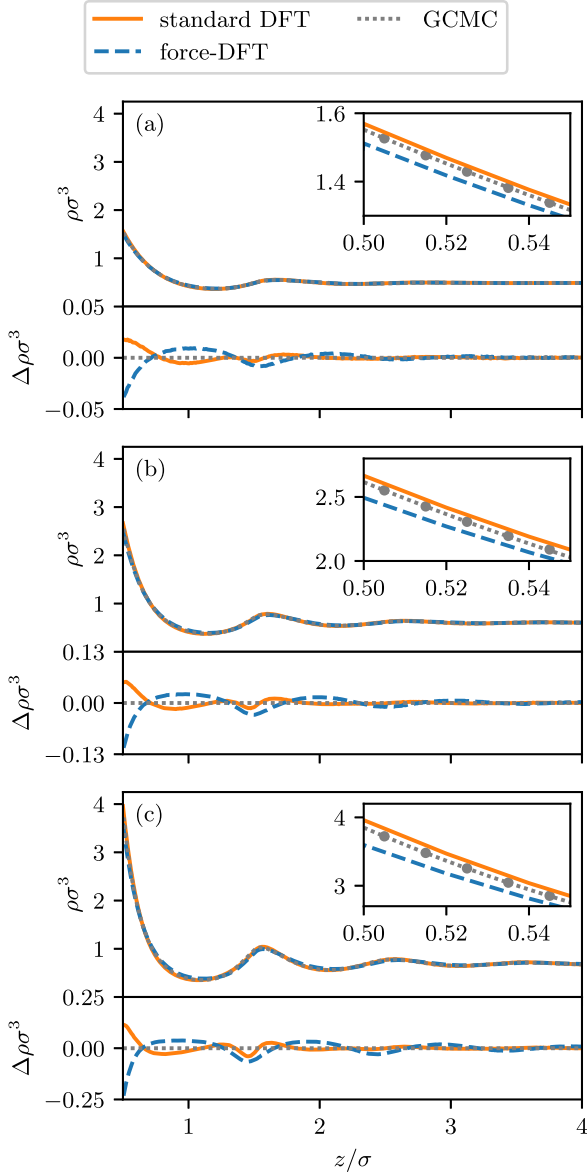


FIG. 2. Density profiles $\rho(z)$ of a hard sphere fluid at a planar hard wall are shown for values $\rho_b = 0.4890\sigma^{-3}$ (a), $\rho_b = 0.6032\sigma^{-3}$ (b), and $\rho_b = 0.6908\sigma^{-3}$ (c) of the bulk density. We compare the results of standard (orange) and force-DFT (blue) to numerically exact density profiles from GCMC simulations (gray). For each value of μ , the absolute error $\Delta\rho(z)$ of the density profiles compared to the simulation result is shown in the respective bottom panel, and the inset plot zooms in on the differences of the two DFT routes close to the hard wall. The simulations were set up to yield the same bulk density as in the DFT results via an appropriate choice of the chemical potential (cf. Fig. 1 and Table I) for a systematic comparison of the resulting contact densities.

$t/\tau = 0.05, 0.1, 0.2$). This is indicative of nonequilibrium forces that go beyond the adiabatic approximation [26,52] and that are neither captured in standard nor in force-DDFT.

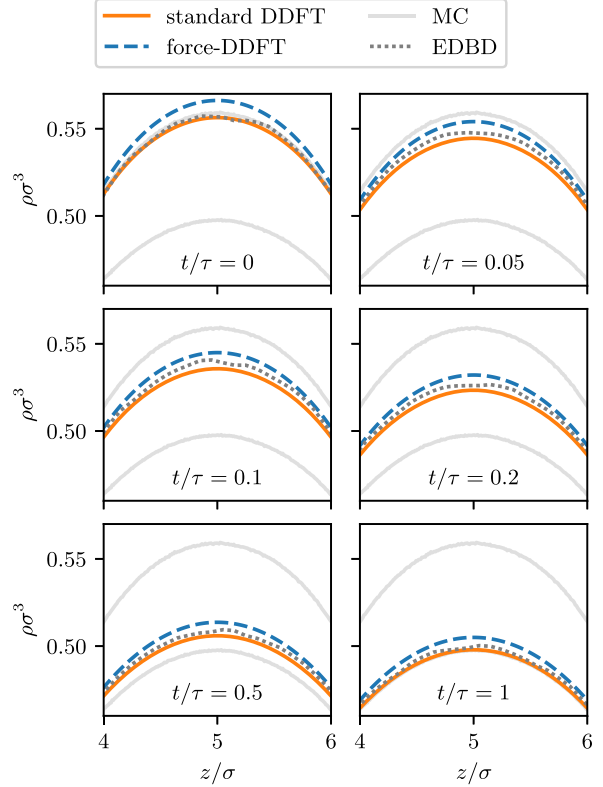


FIG. 3. Time evolution of the density profile $\rho(z)$ of a hard sphere fluid in a harmonic external potential $V_{\text{ext}}(z) = A(z - 5\sigma)^2$ after switching its strength from $A = 0.75k_B T/\sigma^2$ to $A = 0.5k_B T/\sigma^2$ at time $t = 0$. The relaxation dynamics calculated with standard (orange) and force-DDFT (blue) are shown for $t/\tau = 0, 0.05, 0.1, 0.2, 0.5, 1$ and are compared to EDBD simulation results (gray). The initial and final equilibrium profiles (silver) as obtained via MC simulations for both values of A are indicated in each panel for reference.

IV. HYBRID SCHEME

The above comparison of the force-DFT route to standard DFT and simulations reveals that there is no systematic improvement in the resulting density profiles neither in equilibrium (DFT) nor for the dynamical problem (DDFT) considered. Instead, force-DFT and force-DDFT can be viewed as an alternative to the standard formalism for calculating the density profile from a given Helmholtz free energy functional. If this functional is not exact, as is the case for the Rosenfeld FMT functional for the hard sphere fluid, the results of both routes will in general differ, as we have exemplified above. The comparison also uncovers that the numerically exact simulation results are commonly bracketed by standard and force results for the considered hard sphere fluids.

In this spirit, a systematic improvement of the density profile both in equilibrium and in the dynamical scenario is conceivable by an appropriate combination of the two routes, which constitutes a hybrid implementation of DFT. For this,

we construct an approximation of the density profile according to

$$\rho_h \equiv \alpha \rho_s + (1 - \alpha) \rho_f, \quad (10)$$

where the subscripts indicate the results from the hybrid scheme (h), from the standard DFT (s), and from the force-DFT (f). The interpolation parameter α can be tuned to favor standard ($\alpha = 1$) or force-DFT ($\alpha = 0$).

To arrive at an appropriate choice of α for the considered hard sphere fluids, we recall the Carnahan-Starling [53] equation of state

$$p^{CS} = \frac{\rho_b}{\beta} \frac{1 + \eta + \eta^2 - \eta^3}{(1 - \eta)^3} \quad (11)$$

as a superior alternative to the Percus-Yevick results (8) and (9). In particular, similar to the combination in Eq. (10), Eq. (11) can be obtained from the compressibility (P_c^{PY}) and virial (P_v^{PY}) Percus-Yevick equations of state via the linear combination [2]

$$P^{CS} = \frac{2}{3} P_c^{PY} + \frac{1}{3} P_v^{PY}. \quad (12)$$

Due to Eq. (12) and the connection of standard and force-DFT to the compressibility and virial pressure [cf. Eqs. (6) and (7)], we choose $\alpha = \frac{2}{3}$ in the following considerations as a means to obtain improved estimates $\rho_h(\mathbf{r})$ of the density profile via Eq. (10).

The result of this combination of both DFT methods is shown for the hard sphere fluid in equilibrium at the hard wall in Fig. 4. Note that we do not alter the utilized functional, as the hybrid density profile is obtained consistently from a combination of standard and force results (cf. Fig. 2), which were both acquired with the Rosenfeld functional. The local error of the hybrid Rosenfeld density profile decreases in large parts of the system and particularly in the vicinity of the hard wall as compared to the error of the density profiles obtained via the individual routes. Hence, hybrid DFT can be considered as a viable means to improve resulting density profiles while avoiding the often difficult task of refining the Helmholtz excess free energy functional. We further exemplify this in Fig. 4 by depicting additionally the density profiles obtained from standard DFT when using the more advanced White Bear [32] and White Bear MkII [33] functionals, which serve as a benchmark to a common (and the current de facto standard) DFT treatment of the hard sphere fluid. Notably, the hybrid scheme yields similar accuracy as compared to these results, albeit being obtained with the inferior Rosenfeld approximation for $F_{\text{exc}}[\rho]$. In the vicinity of the first density maximum, the hybrid route is still not capable of mitigating the well-known shortcomings of standard FMT completely. Surprisingly, however, the density profile calculated via Eq. (10) match the numerical density profile equally well as both the White Bear and the White Bear MkII functionals employed in standard DFT, in particular for small distances to the hard wall. Close to the first maximum, the agreement to simulation is even better for the former than in the standard White Bear and White Bear MkII treatment. This shows that an appropriate combination of standard and force-DFT via Eq. (10) to yield a hybrid method is a viable means to improve deficiencies of an approximate excess free energy functional, and that its impact on the density profile

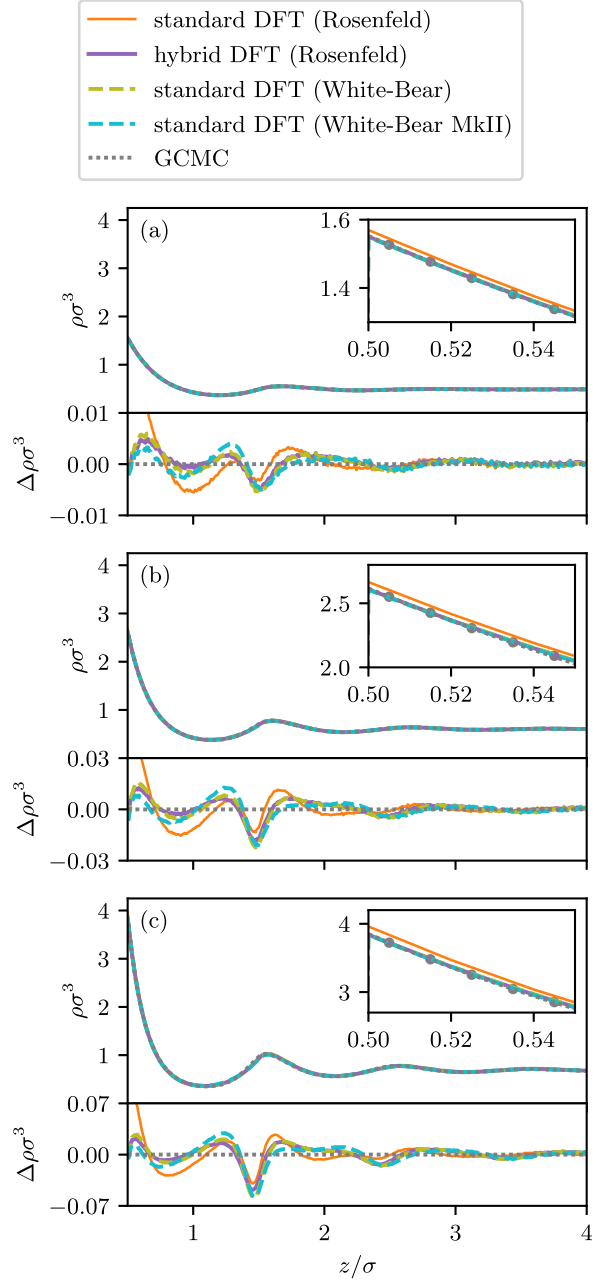


FIG. 4. Hybrid DFT density profiles $\rho(z)$ (purple) for a hard sphere fluid at a hard wall are compared to simulation results as in Fig. 2 (the standard Rosenfeld DFT is replotted in orange). In most parts of the system, this combination of standard and force-DFT via Eq. (10) enables a systematic improvement of the resulting density profile while retaining the Rosenfeld FMT treatment of $F_{\text{exc}}[\rho]$. The largest discrepancy to the numerical GCMC density profiles (gray) still occurs in the vicinity of the first density maximum. For comparison, standard DFT results for the superior White Bear (olive) and White Bear MkII (cyan) functionals are depicted, and an error comparable to hybrid Rosenfeld DFT is found.

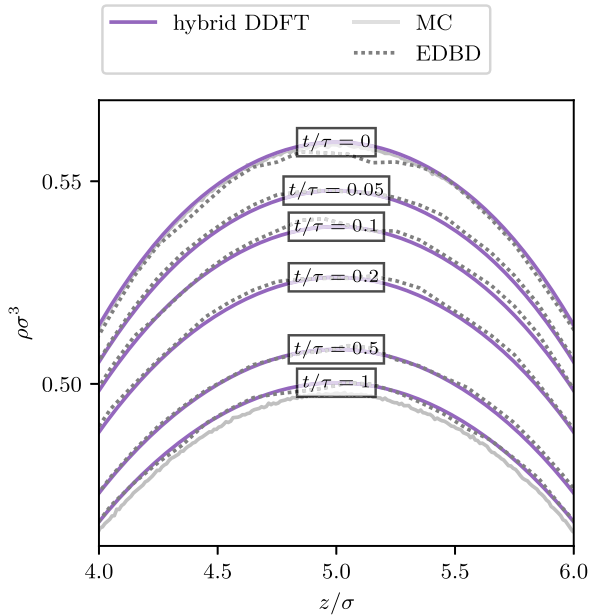


FIG. 5. Hybrid DDFT density profiles $\rho(z)$ (purple) via Eq. (10) for the relaxation of a hard sphere fluid in a harmonic potential as in Fig. 3. The time evolution is again compared to EDBD simulation results (gray) and the initial and final equilibrium profiles are indicated for reference (silver). As in Fig. 4, the combination procedure (10) of standard and force-DDFT yields much better results than the individual routes alone.

may be as significant as when using a superior functional. A tangible choice of the interpolation parameter in Eq. (10) may be obtained via known results for bulk fluids, e.g., by comparison of associated equations of state. While this choice was made analytically with Eq. (12) for the hard sphere fluid above, bulk simulation results might provide guidance to go beyond Carnahan-Starling results or to apply the hybrid scheme to other particle models.

For the dynamical case, the evolution of $\rho_h(z, t)$ in the switched harmonic potential is shown in Fig. 5. We observe that the initial state is captured via the hybrid method much more accurately than by the individual DFT routes. This trend transfers to the relaxation dynamics, where arguably better results can be achieved than with standard and force-DDFT alone. Still, hybrid DDFT remains adiabatic, such that effects beyond the adiabatic assumption are not incorporated by construction. In the considered case, however, this approximation turns out to be reasonable, and the resulting density evolution calculated within DDFT can hence be improved by the combination procedure (10) as we had shown before for equilibrium DFT.

V. CONCLUSIONS AND OUTLOOK

In this work, the recent force-DFT method developed by Tschopp *et al.* [27] was compared in depth to standard DFT and simulation results. For this, we have reexamined the results of Ref. [27] for a hard sphere fluid both in

equilibrium at a hard wall as well as for its relaxation dynamics in a switched harmonic trap. Numerically exact many-body simulations have been carried out to enable the comparison of density profiles from standard and force-DFT calculations with reference data.

We first turned to the prototypical case of subjecting the hard sphere fluid to a hard wall, thereby inducing large density modulations. As shown by Tschopp *et al.* [27] standard and force-DFT are connected via the hard wall contact theorems (6) and (7) to the compressibility and virial expression of the pressure, respectively, which was exemplified in their work with the Rosenfeld FMT functional and the corresponding Percus-Yevick equation of state. Here, we have augmented this investigation with numerically accurate density profiles from GCMC simulations, which have been adjusted to replicate the same bulk density as used in both DFT methods. As expected from the theoretical results of Ref. [27], the numerical contact density is enclosed by the results from standard and from force-DFT and fits more accurately to the former. More importantly, however, with the GCMC data being available, the comparison could be carried out in this work for the complete inhomogeneous structure of the density profile. For intermediate distances from the wall, the numerical density profile shows discrepancies to the results of both DFT routes. In large parts of the system, the GCMC density profile is bracketed by standard and force-DFT results. In the vicinity of the first density maximum, which is difficult to reproduce in standard DFT [10], force-DFT yields no systematic improvement.

We next considered the dynamical relaxation of the hard sphere fluid in a harmonic potential when its strength is instantaneously decreased. In order to complement the force-DDFT results of Ref. [27] with numerical data, we have employed EDBD as an accurate dynamical simulation method for hard sphere fluids under nonequilibrium conditions. Hence, we have initialized 10^4 EDBD runs with particle configurations obtained via canonical MC simulations and have reproduced the relaxation dynamics after the switching of the harmonic trap. The total number of particles as given by the integrated density profile has been matched to the DDFT calculations. We observed that the inaccuracies of the Rosenfeld FMT functional transfer to the dynamical case, such that the numerical density profile lies in-between the results of both DDFT routes. At the center of the trap, force-DDFT overestimates the local value of the density while standard DDFT yields values that are slightly too low. As the dynamical description with force-DDFT is still adiabatic by construction, the relative relaxation dynamics differs only marginally to that in standard DDFT.

With the previous observations for both routes in equilibrium and in the dynamical case, we have investigated a hybrid method via an appropriate linear interpolation of standard and force results as was suggested in Ref. [27]. For the hard sphere fluid modeled with the Rosenfeld FMT functional, an interpolation parameter could be found by considering the associated Percus-Yevick results (8) and (9) and their well-known combination (12) to yield the improved Carnahan-Starling equation of state. We have shown that the application of an analog combination procedure to standard and force results yields substantially improved density

profiles both in equilibrium and in the dynamical scenario. In equilibrium at the hard wall, we have compared the hybrid method with the Rosenfeld functional both to GCMC data and to density profiles calculated with standard DFT when using the highly accurate White Bear and White Bear MkII functionals. It was shown that the hybrid Rosenfeld scheme mitigates many deficiencies of the individual DFT routes. Its deviations from the GCMC data are comparable to those of the standard White Bear and White Bear MkII DFT treatments.

In the time-dependent problem, the hybrid implementation of DDFT captures the relaxation of the hard sphere fluid much better than standard and force-DDFT alone, which we attribute to the more accurate reproduction of the equation of state. Still, the hybrid scheme is purely adiabatic by construction. This is an acceptable approximation in the presented case, but will be inappropriate in other dynamical systems.

In the future, it would be interesting to use more accurate functionals such as White Bear and White Bear MkII in force-DFT and in the hybrid method. As hybrid Rosenfeld DFT already significantly improves upon the individual DFT routes, it is conceivable that a hybrid White Bear (MkII) DFT will lead to a further systematic gain in the accuracy of the resulting density profiles. Moreover, the method could be useful in other systems that may consist of different particle types than the hard sphere fluid, where the derivation of accurate Helmholtz excess free energy functionals poses an even more difficult problem. On the other hand, both standard DFT and force-DFT are equivalent if one can start with the exact free energy functional. Hence, carrying out explicitly an investigation for the one-dimensional hard core (“hard rod”) system using Percus’ exact functional [54] as a practical verification of the formal equivalence of both DFT routes could be a worthwhile future research task. This could be augmented by a force-DFT investigation of the two-dimensional hard disk system, where both highly accurate FMT functionals [55] as well as highly reliable simulation results [56] have been reported.

From a conceptual point of view, force-DFT opens up the possibility to gain further insight into the inner workings of DFT, especially by making the two-body density correlation function directly accessible. This could be used, e.g., in an investigation of the hard sphere pair correlations at the contact shell. Furthermore, one could obtain one-body fluctuation profiles [57] such as the local compressibility [58,59] from integrating over the two-body pair correlation function. This offers an alternative way to access this information besides the common parametric differentiation of the density profile. Of course, standard DFT also allows to compute the pair structure via the inhomogeneous OZ equation (see, e.g., the work carried out by Dietrich and coworkers [34,37,38]). We further point out that higher densities than showcased in this work could be investigated, which becomes a conceptually demanding test case when approaching the freezing transition. Additionally, more advanced hybrid schemes are conceivable, e.g., by using a local mixing parameter $\alpha(\mathbf{r})$, and from a theoretical perspective, self-consistency of standard and force-DFT could be a useful prerequisite in the derivation of accurate excess free energy functionals. This is especially interesting from the viewpoint of FMT, where the construction

and choice of appropriate nonlocal measures is an ongoing research task [60–62]. One could hope that force- and hybrid DFT shed light on the clearly noticeable deficiencies of FMT and provide aid in the derivation of improved hard sphere functionals.

When dynamics are considered, the prospects arising from the force route are even more promising than in equilibrium. A fundamental advantage of the force-DDFT formalism is the possibility to include higher orders in the many-body hierarchy. Recently, Tschopp and Brader [49] exploited this idea by considering the dynamics of the two-body density explicitly via its continuity equation. Applying the adiabatic approximation only at this higher order then yields a systematic extension of standard DDFT that is no longer adiabatic on the one-body level. Further possibilities to break free of the inherent restrictions of standard DDFT are discussed in Ref. [50].

ACKNOWLEDGMENTS

We thank M. Coe for providing a DFT library with implementations of the White Bear and White Bear MkII functionals [63]. J. M. Brader and S. M. Tschopp are thanked for sending us the theoretical data of Ref. [27]. L. L. Trefenstädt is acknowledged for sharing his EDBD code and D. de las Heras and R. Evans for useful discussions. This work is supported by the German Research Foundation (DFG) via Project No. 436306241.

APPENDIX: CHEMICAL POTENTIAL FROM THE PERCUS-YEVICK EQUATION OF STATE

We briefly give some classical results and point out Ref. [64] for an extensive and well-accessible collection of analytical relations for the hard sphere fluid. The Percus-Yevick equation of state

$$P_{c,v} = \frac{\rho_b}{\beta} f_{c,v}(\eta) \quad (\text{A1})$$

can be obtained either via the compressibility (subscript c) or the virial (subscript v) route. The explicit forms of the functions $f_{c,v}(\eta)$ are given in Eqs. (8) and (9) in the main text.

We consider the Helmholtz free energy F and insert Eq. (A1), which yields

$$F = - \int dV P = \frac{N}{\beta} \int d\rho_b \frac{f(\eta(\rho_b))}{\rho_b}. \quad (\text{A2})$$

The chemical potential is then obtained via

$$\mu = \frac{\partial F}{\partial N} = \frac{\partial F/V}{\partial \rho_b} = \frac{1}{\beta} \left(f(\eta) + \int d\rho_b \frac{f(\eta(\rho_b))}{\rho_b} \right). \quad (\text{A3})$$

Thus,

$$\beta\mu_c = \ln(\rho_b) + f_c(\eta) + \frac{3}{2(1-\eta)^2} - \ln(1-\eta) - \frac{5}{2}, \quad (\text{A4})$$

$$\beta\mu_v = \ln(\rho_b) + f_v(\eta) + \frac{6\eta}{1-\eta} + 2\ln(1-\eta) - 1. \quad (\text{A5})$$

- [1] R. Evans, The nature of the liquid-vapour interface and other topics in the statistical mechanics of non-uniform, classical fluids, *Adv. Phys.* **28**, 143 (1979).
- [2] J.-P. Hansen and I. R. McDonald, *Theory of Simple Liquids With Applications to Soft Matter* (Elsevier, Amsterdam, 2013).
- [3] T. Eckert, M. Schmidt, and D. de las Heras, Gravity-induced phase phenomena in plate-rod colloidal mixtures, *Commun. Phys.* **4**, 202 (2021).
- [4] T. Eckert, M. Schmidt, and D. de las Heras, Sedimentation of colloidal plate-sphere mixtures and inference of particle characteristics from stacking sequences, *Phys. Rev. Res.* **4**, 013189 (2022).
- [5] T. Eckert, M. Schmidt, and D. de las Heras, Sedimentation path theory for mass-polydisperse colloidal systems, *J. Chem. Phys.* **157**, 234901 (2022).
- [6] Y. Rosenfeld, Free-Energy Model for the Inhomogeneous Hard-Sphere Fluid Mixture and Density-Functional Theory of Freezing, *Phys. Rev. Lett.* **63**, 980 (1989).
- [7] R. Roth, Fundamental measure theory for hard-sphere mixtures: a review, *J. Phys.: Condens. Matter* **22**, 063102 (2010).
- [8] M. Aduamoah, B. D. Goddard, J. W. Pearson, and J. C. Roden, Pseudospectral methods and iterative solvers for optimization problems from multiscale particle dynamics, *BIT Numer. Math.* **62**, 1703 (2022).
- [9] J. C. Roden, R. D. Mills-Williams, J. W. Pearson, and B. D. Goddard, Multishape: A spectral element method, with applications to dynamic density functional theory and PDE-constrained optimization, [arXiv:2207.05589](https://arxiv.org/abs/2207.05589).
- [10] R. L. Davidchack, B. B. Laird, and R. Roth, Hard spheres at a planar hard wall: Simulations and density functional theory, *Condens. Matter Phys.* **19**, 23001 (2016).
- [11] D. Stopper and R. Roth, Massively parallel GPU-accelerated minimization of classical density functional theory, *J. Chem. Phys.* **147**, 064508 (2017).
- [12] D. de las Heras, E. Velasco, and L. Mederos, Effects of wetting and anchoring on capillary phenomena in a confined liquid crystal, *J. Chem. Phys.* **120**, 4949 (2004).
- [13] D. de las Heras, E. Velasco, and L. Mederos, Capillary Smectization and Layering in a Confined Liquid Crystal, *Phys. Rev. Lett.* **94**, 017801 (2005).
- [14] S. Zhao, R. Ramirez, R. Vuilleumier, and D. Borgis, Molecular density functional theory of solvation: From polar solvents to water, *J. Chem. Phys.* **134**, 194102 (2011).
- [15] G. Jeanmairet, M. Levesque, R. Vuilleumier, and D. Borgis, Molecular Density Functional theory of Water, *J. Phys. Chem. Lett.* **4**, 619 (2013).
- [16] G. Jeanmairet, M. Levesque, and D. Borgis, Tackling solvent effects by coupling electronic and molecular density functional theory, *J. Chem. Theory Comput.* **16**, 7123 (2020).
- [17] B. Rotenberg, Use the force! Reduced variance estimators for densities, radial distribution functions, and local mobilities in molecular simulations, *J. Chem. Phys.* **153**, 150902 (2020).
- [18] D. de las Heras and M. Schmidt, Better Than Counting: Density Profiles from Force Sampling, *Phys. Rev. Lett.* **120**, 218001 (2018).
- [19] A. Purohit, A. J. Schultz, and D. A. Kofke, Force-sampling methods for density distributions as instances of mapped averaging, *Mol. Phys.* **117**, 2822 (2019).
- [20] D. Borgis, R. Assaraf, B. Rotenberg, and R. Vuilleumier, Computation of pair distribution functions and three-dimensional densities with a reduced variance principle, *Mol. Phys.* **111**, 3486 (2013).
- [21] I. V. Tokatly, Quantum many-body dynamics in a lagrangian frame: I. Equations of motion and conservation laws, *Phys. Rev. B* **71**, 165104 (2005).
- [22] I. V. Tokatly, Quantum many-body dynamics in a lagrangian frame: II. Geometric formulation of time-dependent density functional theory, *Phys. Rev. B* **71**, 165105 (2005).
- [23] I. V. Tokatly, Time-dependent deformation functional theory, *Phys. Rev. B* **75**, 125105 (2007).
- [24] M.-L. M. Tchenkoue, M. Penz, I. Theophilou, M. Ruggenthaler, and A. Rubio, Force balance approach for advanced approximations in density functional theories, *J. Chem. Phys.* **151**, 154107 (2019).
- [25] W. Tarantino and C. A. Ullrich, A reformulation of time-dependent Kohn–Sham theory in terms of the second time derivative of the density, *J. Chem. Phys.* **154**, 204112 (2021).
- [26] M. Schmidt, Power functional theory for many-body dynamics, *Rev. Mod. Phys.* **94**, 015007 (2022).
- [27] S. M. Tschopp, F. Sammüller, S. Hermann, M. Schmidt, and J. M. Brader, Force density functional theory in- and out-of-equilibrium, *Phys. Rev. E* **106**, 014115 (2022).
- [28] S. Hermann and M. Schmidt, Force balance in thermal quantum many-body systems from Noether’s theorem, *J. Phys. A: Math. Theor.* **55**, 464003 (2022).
- [29] A. K. Omar, H. Row, S. A. Mallory, and J. F. Brady, Mechanical theory of nonequilibrium coexistence and motility-induced phase separation, [arXiv:2211.12673](https://arxiv.org/abs/2211.12673).
- [30] D. Frenkel and B. Smit, *Understanding Molecular Simulation From Algorithms to Applications* (Elsevier, Amsterdam, 2001).
- [31] A. Scala, T. Voigtmann, and C. D. Michele, Event-driven Brownian dynamics for hard spheres, *J. Chem. Phys.* **126**, 134109 (2007).
- [32] R. Roth, R. Evans, A. Lang, and G. Kahl, Fundamental measure theory for hard-sphere mixtures revisited: The White Bear version, *J. Phys.: Condens. Matter* **14**, 12063 (2002).
- [33] H. Hansen-Goos and R. Roth, Density functional theory for hard-sphere mixtures: The White Bear version mark II, *J. Phys.: Condens. Matter* **18**, 8413 (2006).
- [34] B. Götzemann, A. Haase, and S. Dietrich, Structure factor of hard spheres near a wall, *Phys. Rev. E* **53**, 3456 (1996).
- [35] S. M. Tschopp, H. D. Vuijk, A. Sharma, and J. M. Brader, Mean-field theory of inhomogeneous fluids, *Phys. Rev. E* **102**, 042140 (2020).
- [36] S. M. Tschopp and J. M. Brader, Fundamental measure theory of inhomogeneous two-body correlation functions, *Phys. Rev. E* **103**, 042103 (2021).
- [37] R. Klimpel and S. Dietrich, Structure factor of thin films near continuous phase transitions, *Phys. Rev. B* **60**, 16977 (1999).
- [38] K. R. Mecke and S. Dietrich, Effective Hamiltonian for liquid-vapor interfaces, *Phys. Rev. E* **59**, 6766 (1999).
- [39] F. Höfling and S. Dietrich, Enhanced wavelength-dependent surface tension of liquid-vapour interfaces, *Europhys. Lett.* **109**, 46002 (2015).
- [40] S. Angioletti-Uberti, M. Ballauff, and J. Dzubiella, Dynamic density functional theory of protein adsorption on polymer-coated nanoparticles, *Soft Matter* **10**, 7932 (2014).
- [41] S. Angioletti-Uberti, M. Ballauff, and J. Dzubiella, Competitive adsorption of multiple proteins to nanoparticles: The vroman effect revisited, *Mol. Phys.* **116**, 3154 (2018).

- [42] J. Chakrabarti, J. Dzubiella, and H. Löwen, Dynamical instability in driven colloids, *Europhys. Lett.* **61**, 415 (2003).
- [43] J. Chakrabarti, J. Dzubiella, and H. Löwen, Reentrance effect in the lane formation of driven colloids, *Phys. Rev. E* **70**, 012401 (2004).
- [44] A. M. Menzel, A. Saha, C. Hoell, and H. Löwen, Dynamical density functional theory for microswimmers, *J. Chem. Phys.* **144**, 024115 (2016).
- [45] A. Sharma and J. M. Brader, Brownian systems with spatially inhomogeneous activity, *Phys. Rev. E* **96**, 032604 (2017).
- [46] M. te Vrugt, H. Löwen, and R. Wittkowski, Classical dynamical density functional theory: From fundamentals to applications, *Adv. Phys.* **69**, 121 (2020).
- [47] M. te Vrugt and R. Wittkowski, Perspective: New directions in dynamical density functional theory, *J. Phys.: Condens. Matter* **35**, 041501 (2022).
- [48] M. Schmidt and J. M. Brader, Power functional theory for Brownian dynamics, *J. Chem. Phys.* **138**, 214101 (2013).
- [49] S. M. Tschopp and J. M. Brader, First-principles superadiabatic theory for the dynamics of inhomogeneous fluids *J. Chem. Phys.* **157**, 234108 (2022).
- [50] D. de las Heras, T. Zimmermann, F. Sammüller, S. Hermann, and M. Schmidt, Perspective: How to overcome dynamical density functional theory, [arXiv:2301.12156](https://arxiv.org/abs/2301.12156).
- [51] Y.-X. Yu and J. Wu, Structures of hard-sphere fluids from a modified fundamental-measure theory, *J. Chem. Phys.* **117**, 10156 (2002).
- [52] L. L. Treffenstädt and M. Schmidt, Memory-induced motion reversal in Brownian liquids, *Soft Matter* **16**, 1518 (2020).
- [53] N. F. Carnahan and K. E. Starling, Equation of state for nonattracting rigid spheres, *J. Chem. Phys.* **51**, 635 (1969).
- [54] J. K. Percus, Equilibrium state of a classical fluid of hard rods in an external field, *J. Stat. Phys.* **15**, 505 (1976).
- [55] R. Roth, K. Mecke, and M. Oettel, Communication: Fundamental measure theory for hard disks: Fluid and solid, *J. Chem. Phys.* **136**, 081101 (2012).
- [56] B. Li, Y. Nishikawa, P. Höllmer, L. Carillo, A. C. Maggs, and W. Krauth, Hard-disk pressure computations—a historic perspective, *J. Chem. Phys.* **157**, 234111 (2022).
- [57] T. Eckert, N. C. X. Stuhlmüller, F. Sammüller, and M. Schmidt, Fluctuation Profiles in Inhomogeneous Fluids, *Phys. Rev. Lett.* **125**, 268004 (2020).
- [58] R. Evans and M. C. Stewart, The local compressibility of liquids near non-adsorbing substrates: a useful measure of solvophobicity and hydrophobicity? *J. Phys.: Condens. Matter* **27**, 194111 (2015).
- [59] M. K. Coe, R. Evans, and N. B. Wilding, Density Depletion and Enhanced Fluctuations in Water near Hydrophobic Solutes: Identifying the Underlying Physics, *Phys. Rev. Lett.* **128**, 045501 (2022).
- [60] P. Tarazona, Density Functional for Hard Sphere Crystals: A Fundamental Measure Approach, *Phys. Rev. Lett.* **84**, 694 (2000).
- [61] P. Tarazona, Fundamental measure theory and dimensional interpolation for the hard spheres fluid, *Physica A (Amsterdam)* **306**, 243 (2002).
- [62] P. Tarazona, J. Cuesta, and Y. Martínez-Ratón, Density functional theories of hard particle systems, *Theory and Simulation of Hard-Sphere Fluids and Related Systems*, edited by Á. Mulero (Springer, Berlin, 2008), pp. 247–341.
- [63] The DFT library can be found at https://github.com/marykcoe/cDFT_Package.
- [64] A. Santos, S. B. Yuste, and M. L. de Haro, Structural and thermodynamic properties of hard-sphere fluids, *J. Chem. Phys.* **153**, 120901 (2020).

Noether-Constrained Correlations in Equilibrium Liquids

Florian Sammüller¹, Sophie Hermann¹, Daniel de las Heras¹, and Matthias Schmidt^{1*}
Theoretische Physik II, Physikalisches Institut, Universität Bayreuth, D-95447 Bayreuth, Germany

 (Received 26 January 2023; accepted 12 June 2023; published 30 June 2023)

Liquid structure carries deep imprints of an inherent thermal invariance against a spatial transformation of the underlying classical many-body Hamiltonian. At first order in the transformation field Noether’s theorem yields the local force balance. Three distinct two-body correlation functions emerge at second order, namely the standard two-body density, the localized force-force correlation function, and the localized force gradient. An exact Noether sum rule interrelates these correlators. Simulations of Lennard-Jones, Yukawa, soft-sphere dipolar, Stockmayer, Gay-Berne and Weeks-Chandler-Andersen liquids, of monatomic water and of a colloidal gel former demonstrate the fundamental role in the characterization of spatial structure.

DOI: [10.1103/PhysRevLett.130.268203](https://doi.org/10.1103/PhysRevLett.130.268203)

It is a both surprising and intriguing phenomenon that the liquid phase occurs in the phase diagram at and off coexistence with the gas or the solid phase. Famously it has been argued [1,2] that it needs relying on observations rather than mere theory alone to predict the existence of liquids, as neither the noninteracting ideal gas nor the Einstein crystal form appropriate idealized references. The liquid state [3–6] comprises high spatial symmetry against global translations and rotations, together with the correlated and strongly interacting behavior of the dense constituents, whether they are atoms, molecules, or colloids.

Among the defining features of liquids are the ability to spontaneously form an interface when at liquid-gas coexistence, the viscous response against shearing motion, and the rich pair correlation structure. While the one-body density distribution is homogeneous in bulk (in stark contrast to the microscopic density of a crystal), the joint probability of finding two particles at a given separation distance r is highly nontrivial in a liquid. The pair correlation function $g(r)$ [4], as accessible, e.g., via microscopy [7–10] and scattering [4,11–14] techniques, quantifies this spatial structure on the particle level. At large distances r , the asymptotic decay of $g(r)$ falls into different classes [15–18] with much current interest in electrolytes [19]. The spatial Fourier transform of $g(r)$ yields the static structure factor [4,11–14].

It is a common strategy to exploit the symmetries of a given physical system via Noether’s theorem of invariant variations [20,21]. From symmetries in the dynamical description of the system one systematically obtains conservation laws. Typically the starting point is the action functional, as generalized to a variety of statistical mechanical settings [22–30]. In contrast, we have recently applied Noether’s concept directly to statistical mechanical functionals, such as the free energy [31–34]. This allows us to exploit a specific thermal invariance property of Hamiltonian many-body systems against shifting as performed globally [31–33] or locally resolved in position [34,35].

In this Letter we demonstrate that at the local second-order level the thermal Noether invariance leads to exact identities (“sum rules” [4,36–43]) that form a comprehensive statistical two-body correlation framework. We use simulations to demonstrate the relevance for the investigation of the structure of simple, beyond-simple, and gelled liquids.

We consider systems of N classical particles in three dimensions with positions $\mathbf{r}_1, \dots, \mathbf{r}_N \equiv \mathbf{r}^N$ and momenta $\mathbf{p}_1, \dots, \mathbf{p}_N \equiv \mathbf{p}^N$. The Hamiltonian consists of kinetic, interparticle, and external energy contributions,

$$H = \sum_i \frac{\mathbf{p}_i^2}{2m} + u(\mathbf{r}^N) + \sum_i V_{\text{ext}}(\mathbf{r}_i), \quad (1)$$

where the indices $i = 1, \dots, N$ run over all particles, m indicates the particle mass, $u(\mathbf{r}^N)$ is the interparticle interaction potential, and $V_{\text{ext}}(\mathbf{r})$ is a one-body external potential as a function of position \mathbf{r} .

We consider a canonical transformation [44], where coordinates and momenta change according to the following map [35]:

$$\mathbf{r}_i \rightarrow \mathbf{r}_i + \boldsymbol{\epsilon}(\mathbf{r}_i), \quad (2)$$

$$\mathbf{p}_i \rightarrow [\mathbb{1} + \nabla_i \boldsymbol{\epsilon}(\mathbf{r}_i)]^{-1} \cdot \mathbf{p}_i. \quad (3)$$

Here $\boldsymbol{\epsilon}(\mathbf{r})$ is a spatial “shifting” field that parametrizes the transform, $\mathbb{1}$ indicates the 3×3 -unit matrix, the superscript -1 of a matrix is its inverse, and ∇_i indicates the derivative with respect to \mathbf{r}_i , such that $\nabla_i \boldsymbol{\epsilon}(\mathbf{r}_i)$ is a 3×3 matrix. The transformation (2) and (3) preserves both the phase space volume element and the Hamiltonian [35,44]; its self-adjoint version is applicable to quantum systems [34]. The form of the vector field $\boldsymbol{\epsilon}(\mathbf{r})$ must be such that the

transformation between original and new coordinates is bijective [34].

We consider the shifting field and its gradient to be small and hence Taylor expand. The coordinate transformation (2) is already linear in the displacement field and is hence unaffected. The momentum transformation (3), when expanded as a geometric (Neumann) series to second order, is

$$[\mathbb{1} + \nabla_i \boldsymbol{\epsilon}(\mathbf{r}_i)]^{-1} = \mathbb{1} - \nabla_i \boldsymbol{\epsilon}(\mathbf{r}_i) + [\nabla_i \boldsymbol{\epsilon}(\mathbf{r}_i)]^2 - \dots, \quad (4)$$

where the exponents on the right-hand side imply matrix products such that $[\nabla_i \boldsymbol{\epsilon}(\mathbf{r}_i)]^2 = [\nabla_i \boldsymbol{\epsilon}(\mathbf{r}_i)] \cdot [\nabla_i \boldsymbol{\epsilon}(\mathbf{r}_i)]$, etc. When expressed in the new variables, the Hamiltonian acquires a functional dependence on the shifting field, i.e., $H \rightarrow H[\boldsymbol{\epsilon}]$. It is then straightforward to show [34,35] that the locally resolved one-body force operator $\hat{\mathbf{F}}(\mathbf{r})$ follows from functional differentiation according to

$$-\left. \frac{\delta H[\boldsymbol{\epsilon}]}{\delta \boldsymbol{\epsilon}(\mathbf{r})} \right|_{\boldsymbol{\epsilon}=0} = \hat{\mathbf{F}}(\mathbf{r}), \quad (5)$$

where $\delta/\delta \boldsymbol{\epsilon}(\mathbf{r})$ indicates the functional derivative with respect to the shifting field $\boldsymbol{\epsilon}(\mathbf{r})$. As indicated, $\boldsymbol{\epsilon}(\mathbf{r})$ is set to zero after the derivative has been taken. Similar to the structure of the Hamiltonian (1), the one-body force operator $\hat{\mathbf{F}}(\mathbf{r})$ contains kinetic, interparticle, and external contributions:

$$\hat{\mathbf{F}}(\mathbf{r}) = -\nabla \cdot \sum_i \frac{\mathbf{p}_i \mathbf{p}_i}{m} \delta(\mathbf{r} - \mathbf{r}_i) + \hat{\mathbf{F}}_{\text{int}}(\mathbf{r}) - \hat{\rho}(\mathbf{r}) \nabla V_{\text{ext}}(\mathbf{r}). \quad (6)$$

Here $\delta(\cdot)$ indicates the (three-dimensional) Dirac distribution, $\hat{\mathbf{F}}_{\text{int}}(\mathbf{r}) = -\sum_i \delta(\mathbf{r} - \mathbf{r}_i) \nabla_i u(\mathbf{r}^N)$ is the interparticle one-body force operator [45], and $\hat{\rho}(\mathbf{r}) = \sum_i \delta(\mathbf{r} - \mathbf{r}_i)$ is the standard one-body density operator [4,5]. All considerations so far are general and hold per microstate.

We complement this deterministic description by the statistical mechanics of the grand ensemble at chemical potential μ and temperature T . The grand potential is $\Omega = -k_B T \ln \Xi$, with the grand partition sum $\Xi = \text{Tr} e^{-\beta(H - \mu N)}$. Here k_B indicates the Boltzmann constant, $\beta = 1/(k_B T)$ denotes inverse temperature, and the classical ‘‘trace’’ operation in the grand ensemble is given by $\text{Tr} = \sum_{N=0}^{\infty} (N! h^{3N})^{-1} \int d\mathbf{r}_1 \dots d\mathbf{r}_N \int d\mathbf{p}_1 \dots d\mathbf{p}_N$, where h denotes the Planck constant. The corresponding grand probability distribution is $\Psi = e^{-\beta(H - \mu N)} / \Xi$ and thermal averages are defined via $\langle \cdot \rangle = \text{Tr} \Psi \cdot$, as is standard. A primary example of a thermal average is the density profile being the average of the one-body density operator, i.e., $\rho(\mathbf{r}) = \langle \hat{\rho}(\mathbf{r}) \rangle$.

Via the transformed Hamiltonian $H[\boldsymbol{\epsilon}]$, the grand partition sum acquires functional dependence on the shifting field [34,35], i.e., $\Xi[\boldsymbol{\epsilon}]$, and so does the grand potential, i.e.,

$\Omega[\boldsymbol{\epsilon}]$. Noether invariance [31,32], however, implies that the grand potential does not change under the transformation, and hence

$$\Omega[\boldsymbol{\epsilon}] = \Omega, \quad (7)$$

irrespective of the form of $\boldsymbol{\epsilon}(\mathbf{r})$. The first functional derivative of Eq. (7) with respect to the shifting field $\boldsymbol{\epsilon}(\mathbf{r})$ then yields [34,35] the locally resolved equilibrium force density balance relation $\mathbf{F}(\mathbf{r}) = \langle \hat{\mathbf{F}}(\mathbf{r}) \rangle = 0$ [4,45].

Here we work at the second-order level and hence consider the second derivative of Eq. (7), which yields

$$\left. \frac{\delta^2 \Omega[\boldsymbol{\epsilon}]}{\delta \boldsymbol{\epsilon}(\mathbf{r}) \delta \boldsymbol{\epsilon}(\mathbf{r}')} \right|_{\boldsymbol{\epsilon}=0} = 0. \quad (8)$$

Evaluating the functional derivative on the left-hand side gives

$$\left. \frac{\delta^2 \Omega[\boldsymbol{\epsilon}]}{\delta \boldsymbol{\epsilon}(\mathbf{r}) \delta \boldsymbol{\epsilon}(\mathbf{r}')} \right|_{\boldsymbol{\epsilon}=0} = -\beta \text{cov} \left(\left. \frac{\delta H[\boldsymbol{\epsilon}]}{\delta \boldsymbol{\epsilon}(\mathbf{r})} \right|_{\boldsymbol{\epsilon}=0}, \left. \frac{\delta H[\boldsymbol{\epsilon}]}{\delta \boldsymbol{\epsilon}(\mathbf{r}')} \right|_{\boldsymbol{\epsilon}=0} \right) + \left\langle \frac{\delta^2 H[\boldsymbol{\epsilon}]}{\delta \boldsymbol{\epsilon}(\mathbf{r}) \delta \boldsymbol{\epsilon}(\mathbf{r}')} \right\rangle, \quad (9)$$

where the covariance of two observables (phase space functions) \hat{A} and \hat{B} is defined in the standard way as $\text{cov}(\hat{A}, \hat{B}) = \langle \hat{A} \hat{B} \rangle - \langle \hat{A} \rangle \langle \hat{B} \rangle$. Rewriting the derivative $\delta H[\boldsymbol{\epsilon}]/\delta \boldsymbol{\epsilon}(\mathbf{r})$ as the negative force density operator via Eq. (5), inserting Eq. (9) into Eq. (8), and rearranging gives the following locally resolved two-body Noether sum rule:

$$\beta \langle \hat{\mathbf{F}}(\mathbf{r}) \hat{\mathbf{F}}(\mathbf{r}') \rangle = \left\langle \frac{\delta^2 H[\boldsymbol{\epsilon}]}{\delta \boldsymbol{\epsilon}(\mathbf{r}) \delta \boldsymbol{\epsilon}(\mathbf{r}')} \right\rangle \Big|_{\boldsymbol{\epsilon}=0}. \quad (10)$$

We have replaced $\text{cov}(\hat{\mathbf{F}}(\mathbf{r}), \hat{\mathbf{F}}(\mathbf{r}')) = \langle \hat{\mathbf{F}}(\mathbf{r}) \hat{\mathbf{F}}(\mathbf{r}') \rangle$, because $\langle \hat{\mathbf{F}}(\mathbf{r}) \rangle = 0$ in equilibrium [4,45]. The sum rule (10) relates the force-force correlations at two different positions (left-hand side) with the mean curvature of the Hamiltonian with respect to variation in the shifting field (right-hand side). That such physically meaningful averages are related to each other, at all positions \mathbf{r} and \mathbf{r}' , is highly nontrivial.

We can bring the fundamental Noether two-body sum rule (10) into a more convenient form by multiplying by β , splitting off the trivial kinetic contributions, and introducing the potential energy force operator $\hat{\mathbf{F}}_U(\mathbf{r})$, which combines interparticle and external forces according to $\hat{\mathbf{F}}_U(\mathbf{r}) = \hat{\mathbf{F}}_{\text{int}}(\mathbf{r}) - \hat{\rho}(\mathbf{r}) \nabla V_{\text{ext}}(\mathbf{r})$. Furthermore we focus on the distinct contributions (subscript ‘‘dist’’) such that only pairs of particles with unequal indices are involved and double sums reduce to $\sum_{ij(\neq)} \equiv \sum_{i=1}^N \sum_{j=1, j \neq i}^N$. This allows us to identify from Eq. (10) the following exact distinct two-body Noether identity:

$$\langle \beta \hat{\mathbf{F}}_U(\mathbf{r}) \beta \hat{\mathbf{F}}_U(\mathbf{r}') \rangle_{\text{dist}} = \nabla \nabla' \rho_2(\mathbf{r}, \mathbf{r}') + \left\langle \sum_{ij(\neq)} \delta(\mathbf{r} - \mathbf{r}_i) \delta(\mathbf{r}' - \mathbf{r}_j) \nabla_i \nabla_j \beta u(\mathbf{r}^N) \right\rangle. \quad (11)$$

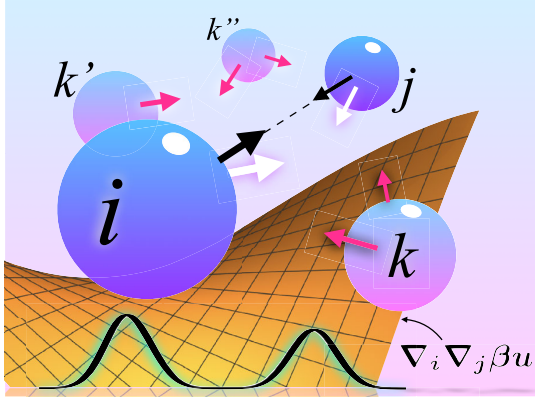


FIG. 1. Illustration of the three different correlation functions that are constrained by thermal Noether invariance. The particles (spheres) exert forces (arrows) onto each other. Particles i and j interact directly with each other (black arrows). The total force (white arrow) on each particle is also determined by the forces that all other particles k, k', k'' exert (pink arrows). The force-force correlations are balanced by the potential energy curvature $\nabla_i \nabla_j \beta u(\mathbf{r}^N)$ (orange surface) and by the two-body density Hessian $\nabla \nabla \rho_2(\mathbf{r}, \mathbf{r}')$ (black curve).

Here the two-body density is defined as is standard: $\rho_2(\mathbf{r}, \mathbf{r}') = \langle \hat{\rho}(\mathbf{r}) \hat{\rho}(\mathbf{r}') \rangle_{\text{dist}} = \langle \sum_{ij(i \neq j)} \delta(\mathbf{r} - \mathbf{r}_i) \delta(\mathbf{r}' - \mathbf{r}_j) \rangle$. The relationship between the different correlators, as graphically illustrated in Fig. 1, holds in general inhomogeneous situations with no need for specific simplifying symmetries.

We demonstrate that this framework has profound implications already for a bulk liquid, where $\rho(\mathbf{r}) = \rho_b = \text{const}$ and $V_{\text{ext}}(\mathbf{r}) = 0$, such that $\hat{\mathbf{F}}_U(\mathbf{r}) = \hat{\mathbf{F}}_{\text{int}}(\mathbf{r})$. In view of the form of the distinct sum rule (11), we use the pair correlation function $g(|\mathbf{r} - \mathbf{r}'|) = \rho_2(\mathbf{r}, \mathbf{r}') / \rho_b^2$, and introduce both the force-force pair correlation function $\mathbf{g}_{ff}(|\mathbf{r} - \mathbf{r}'|) = \beta^2 \langle \hat{\mathbf{F}}_{\text{int}}(\mathbf{r}) \hat{\mathbf{F}}_{\text{int}}(\mathbf{r}') \rangle_{\text{dist}} / \rho_b^2$, and the force gradient correlator $\mathbf{g}_{\nabla f}(|\mathbf{r} - \mathbf{r}'|) = -\langle \sum_{ij(i \neq j)} \delta(\mathbf{r} - \mathbf{r}_i) \delta(\mathbf{r}' - \mathbf{r}_j) \nabla_i \nabla_j \beta u(\mathbf{r}^N) \rangle / \rho_b^2$, which is also the negative mean potential curvature. The identity (11) can then be written succinctly as

$$\nabla \nabla g(r) + \mathbf{g}_{\nabla f}(r) + \mathbf{g}_{ff}(r) = 0, \quad (12)$$

where $r = |\mathbf{r} - \mathbf{r}'|$ denotes the separation distance between the two positions. Both $\mathbf{g}_{ff}(r)$ and $\mathbf{g}_{\nabla f}(r)$ have tensor rank two, i.e., they are 3×3 matrices. Given the central role that $g(r)$ plays in the theory of liquids [4], Eq. (12) is highly remarkable as it allows us to express $g(r)$ via spatial integration of two seemingly entirely different (force-gradient and force-force) correlators. Because of the rotational symmetry of the bulk liquid, the only nontrivial tensor components are

parallel (\parallel) and transversal (\perp) to $\mathbf{r} - \mathbf{r}'$, such that Eq. (12) reduces to

$$g'(r) + g_{\nabla f \parallel}(r) + g_{ff \parallel}(r) = 0, \quad (13)$$

$$g'(r)/r + g_{\nabla f \perp}(r) + g_{ff \perp}(r) = 0, \quad (14)$$

with the prime(s) denoting the derivative(s) with respect to r . In the chosen coordinate system the matrices are diagonal, $\text{diag}(\parallel, \perp, \perp)$, with the first axis being parallel to $\mathbf{r} - \mathbf{r}'$. For molecular liquids of particles with orientational degrees of freedom [4,46–48] our theory, including Eqs. (13) and (14), remains valid upon equilibrium orientational averaging.

For simple fluids, where the particles interact mutually only via a pair potential $\phi(r)$, the force gradient correlator reduces to $\mathbf{g}_{\nabla f}(r) = \beta g(r) \nabla \nabla \phi(r)$ such that

$$g_{\nabla f \parallel}(r) = \beta g(r) \phi''(r), \quad g_{\nabla f \perp}(r) = \beta g(r) \phi'(r)/r. \quad (15)$$

This simplification is due to the reduction of the mixed derivative $\nabla_i \nabla_j u(\mathbf{r}^N) = \nabla_i \nabla_j \sum_{kl(k \neq l)} \phi(|\mathbf{r}_k - \mathbf{r}_l|) / 2 = \nabla_i \nabla_j \phi(|\mathbf{r}_i - \mathbf{r}_j|)$, for $i \neq j$. This allows us to rewrite the curvature correlator in Eqs. (13) and (14), which attain the form $g'(r) + \beta \phi''(r) g(r) + g_{ff \parallel}(r) = 0$ and $g'(r)/r + \beta \phi'(r) g(r)/r + g_{ff \perp}(r) = 0$. In the gas phase the validity can be analytically verified on the second virial level, where $g(r) = \exp[-\beta \phi(r)]$ and the force-force correlations are due to the antiparallel direct forces between a particle pair: $g_{ff \parallel}(r) = -g(r) [\beta \phi'(r)]^2$. Furthermore $g_{ff \perp}(r) = 0$ due to the absence of a third particle at $\rho_b \rightarrow 0$ that could mediate a transversal force.

We substantiate this Noether correlation framework with computer simulations using adaptive Brownian dynamics [49], which is an algorithm that is both fast and allows for tight control of force evaluation errors. We first investigate the Lennard-Jones (LJ) liquid, the purely repulsive Weeks-Chandler-Andersen (WCA) liquid, monatomic water [50,51], and a three-body colloidal gel former [52,53]. The results are summarized in Fig. 2; the top line gives the respective values of T and $\rho_b = N/V$ with box volume $V = (10\sigma)^3$; the LJ potential is truncated at $r/\sigma = 2.5$ with σ denoting the respective particle size. We first discuss the two simple liquids. Both the LJ and the WCA liquid feature pair correlation functions $g(r)$ that display the familiar strongly structured, damped oscillatory form [4,15,16], with a prominent first peak indicating a nearest neighbor correlation shell and subsequent, increasingly washed out oscillations at larger distances. In stark contrast, both the force-gradient (potential curvature) correlator $\mathbf{g}_{\nabla f}(r)$ and the force-force correlator $\mathbf{g}_{ff}(r)$ have very different forms than $g(r)$ itself. The curvature correlator has very strongly localized positive (\parallel) and negative (\perp) peaks near $r = \sigma$. This feature is due to the strong first peak of $g(r)$ combined

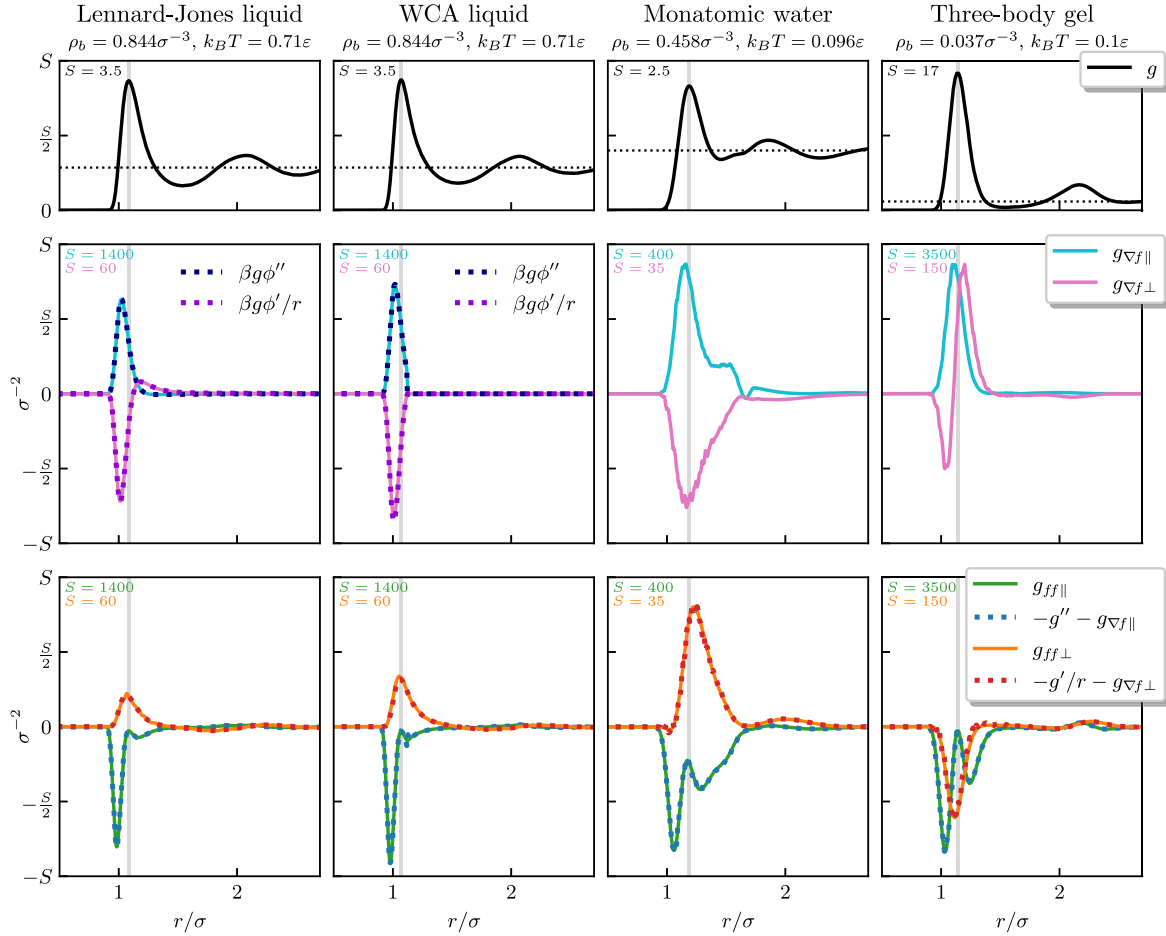


FIG. 2. Simulation results for the two-body correlation functions of the Lennard-Jones liquid (first column), the WCA liquid (second column), monatomic water (third column), and the three-body gel (fourth column). Results are shown as a function of the scaled interparticle distance r/σ . S is a vertical scale factor given in the upper left corner of each panel, and ϵ denotes the energy scale of the respective model fluid. Shown is the pair correlation function $g(r)$ (top row), the potential curvature correlator $\mathbf{g}_{\nabla f}(r)$ (middle row) and the force-force correlator $\mathbf{g}_{ff}(r)$ (bottom row); the latter two correlators have a transversal (\perp) and a parallel (\parallel) tensor component. The results for $\mathbf{g}_{\nabla f}(r)$ for the LJ and WCA liquids are numerically identical to those from the analytical expressions (15) (dashed lines). The directly sampled results for $\mathbf{g}_{ff}(r)$ are numerically identical to those obtained from the Noether sum rules (13) and (14) (dashed lines) for all four systems. Vertical gray lines indicate the position of the first maximum of $g(r)$ as a guide to the eye.

with the properties of $\phi'(r)$ and $\phi''(r)$, as is evident via Eq. (15), which we find to be satisfied to high numerical accuracy. Our results confirm the expectation [16] that $g(r)$ is hardly affected by interparticle attraction. In contrast the force gradient $g_{\nabla f\perp}(r)$ has a clear and significant peak in the attractive region of the LJ potential with no such feature occurring in the purely repulsive WCA liquid.

The force-force correlator $\mathbf{g}_{ff}(r)$ has a similar first peak structure as the curvature correlator, but oscillations extend much further out to larger distances r . Hence $\mathbf{g}_{ff}(r)$ captures also the indirect interactions that are mediated by surrounding particles; we recall Fig. 1. The strong negative double peak of the parallel component indicates

anti-correlated force orientations, which reflect the direct interactions between pairs of particles. Both tensor components of $\mathbf{g}_{ff}(r)$ satisfy the Noether sum rules (13) and (14) to excellent numerical accuracy.

To go beyond simple liquids, we first turn to the monatomic water model by Molinero and Moore [50], which includes three-body interparticle interactions in $u(\mathbf{r}^N)$ that generate the tetrahedral coordination of liquid water. The monatomic water model gives a surprisingly accurate description of the properties of real water, see Ref. [51] for very recent work, while the particles remain spherical and there is no necessity to explicitly invoke molecular orientational degrees of freedom. Hence our

framework (13) and (14) applies. The third column of Fig. 2 demonstrates at ambient conditions that while the shape of $g(r)$ is similar to that in the LJ liquid, both the potential energy curvature and the force-force correlator differ markedly from those of the LJ model. Notably the shape of the double negative peak of $g_{ff\parallel}(r)$ differs and the sign of $g_{ff\perp}(r)$ does not turn negative for distances towards the second shell, as is the case in the LJ liquid. Consistently, the magnitude of the \parallel component is much larger than the \perp component, as direct interparticle interactions are prominent in the former, whereas mediation by third particles is required for the latter.

The three-body gel former by Kob and coworkers [52,53] alters the preferred angle of the three-body interaction term from tetrahedral to stretched (we use 180 degrees [54]). This change induces an affinity for the formation of chains while retaining an ability for their branching and thus the model forms networks in equilibrium. The results shown in the fourth column of Fig. 2 indicate markedly different behavior as compared to the above liquids. While $g(r)$ has the generic long-range decay that one expects of network-forming systems, both the curvature and the force-force correlator are much more specific indicators. In particular we attribute the striking shape of the transversal (\perp) tensor component to the network connectivity. Again the sum rules are satisfied to very good numerical accuracy which we take (i) as a demonstration that the gel state is indeed equilibrated, which distinguishes this model [52,53] from genuine nonequilibrium gel formers, and (ii) as a confirmation of the fitness of the Noether correlators to systematically quantify complex spatial structure formation. This holds beyond the presented model fluids; see the Supplemental Material [55] for results for screened long-ranged interparticle forces of Yukawa type, as well as for dipolar [56–60], Stockmayer [60], and (isotropic and nematic) Gay-Berne fluids [60–62]. For the LJ model, we also contrast the behaviour in the liquid against both the gas and the crystal, where the identities (13) and (14) remain valid [55]. Our equilibrium theory requires proper thermal averaging for the presented identities to hold. A trivial counterexample is a precipitous temperature quench where the distribution of microstates remains instantaneously intact, but β has acquired a new value. Then the sum rule (12) is immediately violated, due to the respective scaling of the correlators $\nabla\nabla g(r)$, $\mathfrak{g}_{\nabla f}(r)$, and $\mathfrak{g}_{ff}(r)$ with powers β^0 , β^1 , and β^2 .

In conclusion, we have formulated and tested a systematic two-body correlation framework based on invariance against an intrinsic symmetry of thermal many-body systems. Formal similarities exist with sum rules for interfacial Hamiltonians [63], as used for studies of wetting [64], and with Takahashi-Ward identities [65,66] of quantum field theory. Future work could relate to the effective temperature [67], to one-dimensional systems [68–70], the

structure of crystals [71–73], gels [52,53,74], glasses [75–77], and the hexatic phase [78], to force-sampling simulation techniques [79–81], and to force-based classical [35,82] and quantum density functional theory [83,84]. Testing sum rules in charged systems is valuable, but can be technically subtle [85]. Connections to three-point [77] and four-point [86,87] correlation functions are interesting, as for a simple fluid $\mathfrak{g}_{ff}(r)$ is given via two position integrals over the four-body density. We have checked that for molecular liquids the general force correlation sum rules (10) and (11) remain valid upon supplementing the dependence on positions \mathbf{r}, \mathbf{r}' with dependence on the molecular orientational degrees of freedom; an analogous structure holds for mixtures of different components. Deriving torque correlation sum rules requires using a local version of the Noether rotational invariance [31].

A particularly exciting prospect is to apply the general identity (11) to the study of interfacial phenomena [38–41,43,51], where the connections with the existing body of sum rules [4,36–43] and the constraints that follow on the allowed correlation function structure at complete drying [88–90] and wetting transitions are worth exploring. Besides measurements of $g(r)$ [7–13], position-resolved forces have recently become accessible by direct imaging in colloidal systems [91], which can facilitate experimental investigations of Noether correlators.

We thank Andrew O. Parry for pointing out Ref. [63] to us, and we are grateful to him, Gerhard Jung, Atreyee Banerjee, Liesbeth Janssen, and Marjolein Dijkstra for useful discussions. This work was supported by the German Research Foundation (DFG) via Project No. 436306241.

*Matthias.Schmidt@uni-bayreuth.de

- [1] V. F. Weisskopf, About liquids, *Trans. N.Y. Acad. Sci.* **38**, 202 (1977).
- [2] R. Evans, D. Frenkel, and M. Dijkstra, From simple liquids to colloids and soft matter, *Phys. Today* No. 2, **72**, 38 (2019).
- [3] J. A. Barker and D. Henderson, What is “liquid”? Understanding the states of matter, *Rev. Mod. Phys.* **48**, 587 (1976).
- [4] J. P. Hansen and I. R. McDonald, *Theory of Simple Liquids*, 4th ed. (Academic Press, London, 2013).
- [5] R. Evans, The nature of the liquid-vapour interface and other topics in the statistical mechanics of non-uniform, classical fluids, *Adv. Phys.* **28**, 143 (1979).
- [6] R. Evans, M. Oettel, R. Roth, and G. Kahl, New developments in classical density functional theory, *J. Phys. Condens. Matter* **28**, 240401 (2016).
- [7] C. P. Royall, A. A. Louis, and H. Tanaka, Measuring colloidal interactions with confocal microscopy, *J. Chem. Phys.* **127**, 044507 (2007).
- [8] A. L. Thorneywork, R. Roth, D. G. A. L. Aarts, and R. P. A. Dullens, Communication: Radial distribution functions in a

- two-dimensional binary colloidal hard sphere system, *J. Chem. Phys.* **140**, 161106 (2014).
- [9] A. Statt, R. Pinchaipat, F. Turci, R. Evans, and C. P. Royall, Direct observation in 3d of structural crossover in binary hard sphere mixtures, *J. Chem. Phys.* **144**, 144506 (2016).
- [10] A. Ramirez-Saito, C. Bechinger, and J. L. Arauz-Lara, Optical microscopy measurement of pair correlation functions, *Phys. Rev. E* **74**, 030401(R) (2006).
- [11] J. L. Yarnell, M. J. Katz, R. G. Wenzel, and S. H. Koenig, Structure factor and radial distribution function for liquid argon at 85K, *Phys. Rev. A* **7**, 2130 (1973).
- [12] P. S. Salmon, Decay of the pair correlations and small-angle scattering for binary liquids and glasses, *J. Phys. Condens. Matter* **18**, 11443 (2006).
- [13] F. S. Carvalho and J. P. Braga, Partial radial distribution functions for a two-component glassy solid, GeSe, from scattering experimental data using an artificial intelligence framework, *J. Mol. Model.* **28**, 99 (2022).
- [14] J. C. Dyre, Simple liquids' quasiuniversality and the hard-sphere paradigm, *J. Phys. Condens. Matter* **28**, 323001 (2016).
- [15] R. Evans, J. R. Henderson, D. C. Hoyle, A. O. Parry, and Z. A. Sabeur, Asymptotic decay of liquid structure: Oscillatory liquid-vapour density profiles and the Fisher-Widom line, *Mol. Phys.* **80**, 755 (1993).
- [16] R. Evans, R. J. F. Leote de Carvalho, J. R. Henderson, and D. C. Hoyle, Asymptotic decay of correlations in liquids and their mixtures, *J. Chem. Phys.* **100**, 591 (1994).
- [17] M. Dijkstra and R. Evans, A simulation study of the decay of the pair correlation function in simple fluids, *J. Chem. Phys.* **112**, 1449 (2000).
- [18] C. Grodon, M. Dijkstra, R. Evans, and R. Roth, Decay of correlation functions in hard-sphere mixtures: Structural crossover, *J. Chem. Phys.* **121**, 7869 (2004).
- [19] P. Cats, R. Evans, A. Härtel, and R. van Roij, Primitive model electrolytes in the near and far field: Decay lengths from DFT and simulations, *J. Chem. Phys.* **154**, 124504 (2021).
- [20] E. Noether, Invariante Variationsprobleme, *Gott. Nachr.* **1918**, 235 (1918), <https://eudml.org/doc/59024>; [M. A. Tavel: Invariant variation problems., *Transp. Theory Stat. Phys.* **1**, 186 (1971)]; For a version in modern typesetting see: Frank Y. Wang, [arXiv:physics/0503066v3](https://arxiv.org/abs/physics/0503066v3).
- [21] N. Byers, E. Noether's discovery of the deep connection between symmetries and conservation laws, [arXiv:physics/9807044](https://arxiv.org/abs/physics/9807044) (1998).
- [22] A. G. Lezcano and A. C. M. de Oca, A stochastic version of the Noether theorem, *Found. Phys.* **48**, 726 (2018).
- [23] J. C. Baez and B. Fong, A Noether theorem for Markov processes, *J. Math. Phys. (N.Y.)* **54**, 013301 (2013).
- [24] I. Marvian and R. W. Spekkens, Extending Noether's theorem by quantifying the asymmetry of quantum states, *Nat. Commun.* **5**, 3821 (2014).
- [25] S. Sasa and Y. Yokokura, Thermodynamic Entropy as a Noether Invariant, *Phys. Rev. Lett.* **116**, 140601 (2016).
- [26] S. Sasa, S. Sugiura, and Y. Yokokura, Thermodynamical path integral and emergent symmetry, *Phys. Rev. E* **99**, 022109 (2019).
- [27] Y. Minami and S. Sasa, Thermodynamic entropy as a Noether invariant in a Langevin equation, *J. Stat. Mech.* (2020) 013213.
- [28] M. Revzen, Functional integrals in statistical physics, *Am. J. Phys.* **38**, 611 (1970).
- [29] Y. A. Budkov and A. L. Kolesnikov, Modified Poisson-Boltzmann equations and macroscopic forces in inhomogeneous ionic fluids, *J. Stat. Mech.* (2022) 053205.
- [30] P. E. Brandyshev and Y. A. Budkov, Noether's second theorem and covariant field theory of mechanical stresses in inhomogeneous ionic fluids, *J. Chem. Phys.* **158**, 174114 (2023).
- [31] S. Hermann and M. Schmidt, Noether's theorem in statistical mechanics, *Commun. Phys.* **4**, 176 (2021).
- [32] S. Hermann and M. Schmidt, Why Noether's theorem applies to statistical mechanics, *J. Phys. Condens. Matter* **34**, 213001 (2022) (Topical Review).
- [33] S. Hermann and M. Schmidt, Variance of fluctuations from Noether invariance, *Commun. Phys.* **5**, 276 (2022).
- [34] S. Hermann and M. Schmidt, Force balance in thermal quantum many-body systems from Noether's theorem, *J. Phys. A* **55**, 464003 (2022).
- [35] S. M. Tschopp, F. Sammüller, S. Hermann, M. Schmidt, and J. M. Brader, Force density functional theory in- and out-of-equilibrium, *Phys. Rev. E* **106**, 014115 (2022).
- [36] J. R. Henderson, Statistical mechanical sum rules, in *Fundamentals of Inhomogeneous Fluids*, edited by D. Henderson (Dekker, New York, 1992).
- [37] R. Evans, Density functionals in the theory of non-uniform fluids, in *Fundamentals of Inhomogeneous Fluids*, edited by D. Henderson (Dekker, New York, 1992).
- [38] P. J. Upton, Fluids Against Hard Walls and Surface Critical Behavior, *Phys. Rev. Lett.* **81**, 2300 (1998).
- [39] R. Evans and A. O. Parry, Liquids at interfaces: What can a theorist contribute?, *J. Phys. Condens. Matter* **2**, SA15 (1990).
- [40] J. R. Henderson and F. van Swol, On the interface between a fluid and a planar wall: Theory and simulations of a hard sphere fluid at a hard wall, *Mol. Phys.* **51**, 991 (1984).
- [41] J. R. Henderson and F. van Swol, On the approach to complete wetting by gas at a liquid-wall interface, *Mol. Phys.* **56**, 1313 (1985).
- [42] J. O. Hirschfelder, Classical and quantum mechanical hypervirial theorems, *J. Chem. Phys.* **33**, 1462 (1960).
- [43] D. G. Triezenberg and R. Zwanzig, Fluctuation Theory of Surface Tension, *Phys. Rev. Lett.* **28**, 1183 (1972).
- [44] H. Goldstein, C. Poole, and J. Safko, *Classical Mechanics* (Addison-Wesley, New York, 2002). Our generator \mathcal{G} is given as F_2 in their notation.
- [45] M. Schmidt, Power functional theory for many-body dynamics, *Rev. Mod. Phys.* **94**, 015007 (2022).
- [46] S. Zhao, R. Ramirez, R. Vuilleumier, and D. Borgis, Molecular density functional theory of solvation: From polar solvents to water, *J. Chem. Phys.* **134**, 194102 (2011).
- [47] G. Jeanmairet, M. Levesque, R. Vuilleumier, and D. Borgis, Molecular density functional theory of water, *J. Phys. Chem. Lett.* **4**, 619 (2013).
- [48] S. Luukkonen, M. Levesque, L. Belloni, and D. Borgis, Hydration free energies and solvation structures with molecular density functional theory in the hypernetted chain approximation, *J. Chem. Phys.* **152**, 064110 (2020).
- [49] F. Sammüller and M. Schmidt, Adaptive Brownian dynamics, *J. Chem. Phys.* **155**, 134107 (2021).

- [50] V. Molinero and E. B. Moore, Water modeled as an intermediate element between carbon and silicon, *J. Phys. Chem. B* **113**, 4008 (2009).
- [51] M. K. Coe, R. Evans, and N. B. Wilding, The coexistence curve and surface tension of a monatomic water model, *J. Chem. Phys.* **156**, 154505 (2022).
- [52] S. Saw, N. L. Ellegaard, W. Kob, and S. Sastry, Structural Relaxation of a Gel Modeled by Three Body Interactions, *Phys. Rev. Lett.* **103**, 248305 (2009).
- [53] S. Saw, N. L. Ellegaard, W. Kob, and S. Sastry, Computer simulation study of the phase behavior and structural relaxation in a gel-former modeled by three-body interactions, *J. Chem. Phys.* **134**, 164506 (2011).
- [54] F. Sammüller, D. der las Heras, and M. Schmidt, Inhomogeneous steady shear dynamics of a three-body colloidal gel former, *J. Chem. Phys.* **158**, 054908 (2023).
- [55] See Supplemental Material at <http://link.aps.org/supplemental/10.1103/PhysRevLett.130.268203> for simulation results of the Noether correlation functions for the Yukawa, soft-sphere dipolar, Stockmayer, and Gay-Berne models (Fig. 3), as well as for the gas, liquid, and crystal phase of the Lennard-Jones model (Fig. 4).
- [56] P. I. C. Teixeira, J. M. Tavares, and M. M. Telo da Gama, Review article: The effect of dipolar forces on the structure and thermodynamics of classical fluids, *J. Phys. Condens. Matter* **12**, R411 (2000).
- [57] S. H. L. Klapp, Topical review: Dipolar fluids under external perturbations, *J. Phys. Condens. Matter* **17**, R525 (2005).
- [58] M. J. Stevens and G. S. Grest, Structure of soft-sphere dipolar fluids, *Phys. Rev. E* **51**, 5962 (1995).
- [59] J. M. Tavares, J. J. Weis, and M. M. Telo da Gama, Strongly dipolar fluids at low densities compared to living polymers, *Phys. Rev. E* **59**, 4388 (1999).
- [60] M. P. Allen, Topical review: Molecular simulation of liquid crystals, *Mol. Phys.* **117**, 2391 (2019).
- [61] J. G. Gay and B. J. Berne, Modification of the overlap potential to mimic a linear site-site potential, *J. Chem. Phys.* **74**, 3316 (1981).
- [62] J. T. Brown, M. P. Allen, E. Martín del Río, and E. de Miguel, Effects of elongation on the phase behavior of the Gay-Berne fluid, *Phys. Rev. E* **57**, 6685 (1998).
- [63] L. V. Mikhcheev and J. D. Weeks, Sum rules for interface Hamiltonians, *Physica (Amsterdam)* **177A**, 495 (1991).
- [64] A. Squarcini, J. M. Romero-Enrique, and A. O. Parry, Casimir Contribution to the Interfacial Hamiltonian for 3D Wetting, *Phys. Rev. Lett.* **128**, 195701 (2022).
- [65] J. C. Ward, An identity in quantum electrodynamics, *Phys. Rev.* **78**, 182 (1950).
- [66] Y. Takahashi, On the generalized Ward identity, *Nuovo Cimento* **6**, 371 (1957).
- [67] S. Saw, L. Costigliola, and J. C. Dyre, Configurational temperature in active-matter models. I. Lines of invariant physics in the phase diagram of the Ornstein-Uhlenbeck model, *Phys. Rev. E* **107**, 024609 (2023).
- [68] C. W. J. Beenakker, Pair correlation function of the one-dimensional Riesz gas, *Phys. Rev. Res.* **5**, 013152 (2023).
- [69] A. Flack, S. N. Majumdar, and G. Schehr, An exact formula for the variance of linear statistics in the one-dimensional jellium model, *J. Phys. A* **56**, 105002 (2023).
- [70] A. M. Montero and A. Santos, Triangle-well and ramp interactions in one-dimensional fluids: A fully analytic exact solution, *J. Stat. Phys.* **175**, 269 (2019).
- [71] C. Walz and M. Fuchs, Displacement field and elastic constants in nonideal crystals, *Phys. Rev. B* **81**, 134110 (2010).
- [72] J. M. Häring, C. Walz, G. Szamel, and M. Fuchs, Coarse-grained density and compressibility of nonideal crystals: General theory and an application to cluster crystals, *Phys. Rev. B* **92**, 184103 (2015).
- [73] S.-C. Lin, M. Oettel, J. M. Häring, R. Haussmann, M. Fuchs, and G. Kahl, Direct Correlation Function of a Crystalline Solid, *Phys. Rev. Lett.* **127**, 085501 (2021).
- [74] B. A. Lindquist, R. B. Jadrich, D. J. Milliron, and T. M. Truskett, On the formation of equilibrium gels via a macroscopic bond limitation, *J. Chem. Phys.* **145**, 074906 (2016).
- [75] M. K. Nandi, A. Banerjee, C. Dasgupta, and S. M. Bhattacharyya, Role of the Pair Correlation Function in the Dynamical Transition Predicted by Mode Coupling Theory, *Phys. Rev. Lett.* **119**, 265502 (2017).
- [76] L. M. C. Janssen, Mode-coupling theory of the glass transition: A primer, *Front. Phys.* **6**, 97 (2018).
- [77] C. Luo, J. F. Robinson, I. Pihlajamaa, V. E. Debets, C. P. Royall, and L. M. C. Janssen, Many-Body Correlations are Non-Negligible in Both Fragile and Strong Glassformers, *Phys. Rev. Lett.* **129**, 145501 (2022).
- [78] E. P. Bernard and W. Krauth, Two-Step Melting in Two Dimensions: First-Order Liquid-Hexatic Transition, *Phys. Rev. Lett.* **107**, 155704 (2011).
- [79] B. Rotenberg, Use the force! Reduced variance estimators for densities, radial distribution functions, and local mobilities in molecular simulations, *J. Chem. Phys.* **153**, 150902 (2020).
- [80] D. de las Heras and M. Schmidt, Better than Counting: Density Profiles from Force Sampling, *Phys. Rev. Lett.* **120**, 218001 (2018).
- [81] D. Borgis, R. Assaraf, B. Rotenberg, and R. Vuilleumier, Computation of pair distribution functions and three-dimensional densities with a reduced variance principle, *Mol. Phys.* **111**, 3486 (2013).
- [82] F. Sammüller, S. Hermann, and M. Schmidt, Comparative study of force-based classical density functional theory, *Phys. Rev. E* **107**, 034109 (2023).
- [83] C. A. Ullrich and I. V. Tokatly, Nonadiabatic electron dynamics in time-dependent density-functional theory, *Phys. Rev. B* **73**, 235102 (2006).
- [84] M. M. Tchenkoue, M. Penz, I. Theophilou, M. Ruggenthaler, and A. Rubio, Force balance approach for advanced approximations in density functional theories, *J. Chem. Phys.* **151**, 154107 (2019).
- [85] J. M. Falcón-González, C. Contreras-Aburto, M. Lara-Peña, M. Heinen, C. Avendaño, A. Gil-Villegas, and R. Castañeda-Priego, Assessment of the Wolf method using the Stillinger-Lovett sum rules: From strong electrolytes to weakly charged colloidal dispersions, *J. Chem. Phys.* **153**, 234901 (2020).
- [86] Z. Zhang and W. Kob, Revealing the three-dimensional structure of liquids using four-point correlation functions, *Proc. Natl. Acad. Sci. U.S.A.* **117**, 14032 (2020).
- [87] N. Singh, Z. Zhang, A. K. Sood, W. Kob, and R. Ganapathy, Intermediate-range order governs dynamics

- in dense colloidal liquids, *Proc. Natl. Acad. Sci. U.S.A.* **120**, e2300923120 (2023).
- [88] R. Evans, M. C. Stewart, and N. B. Wilding, A unified description of hydrophilic and superhydrophobic surfaces in terms of the wetting and drying transitions of liquids, *Proc. Natl. Acad. Sci. U.S.A.* **116**, 23901 (2019).
- [89] M. K. Coe, R. Evans, and N. B. Wilding, Density Depletion and Enhanced Fluctuations in Water Near Hydrophobic Solutes: Identifying the Underlying Physics, *Phys. Rev. Lett.* **128**, 045501 (2022).
- [90] M. K. Coe, R. Evans, and N. B. Wilding, Understanding the physics of hydrophobic solvation, *J. Chem. Phys.* **158**, 034508 (2023).
- [91] J. Dong, F. Turci, R. L. Jack, M. A. Faers, and C. P. Royall, Direct imaging of contacts and forces in colloidal gels, *J. Chem. Phys.* **156**, 214907 (2022).

Supplementary Information

Noether-Constrained Correlations in Equilibrium Liquids

Florian Sammüller, Sophie Hermann, Daniel de las Heras, and Matthias Schmidt

Theoretische Physik II, Physikalisches Institut, Universität Bayreuth, D-95447 Bayreuth, Germany

(Dated: 7 June 2023, www.mschiid.uni-bayreuth.de)

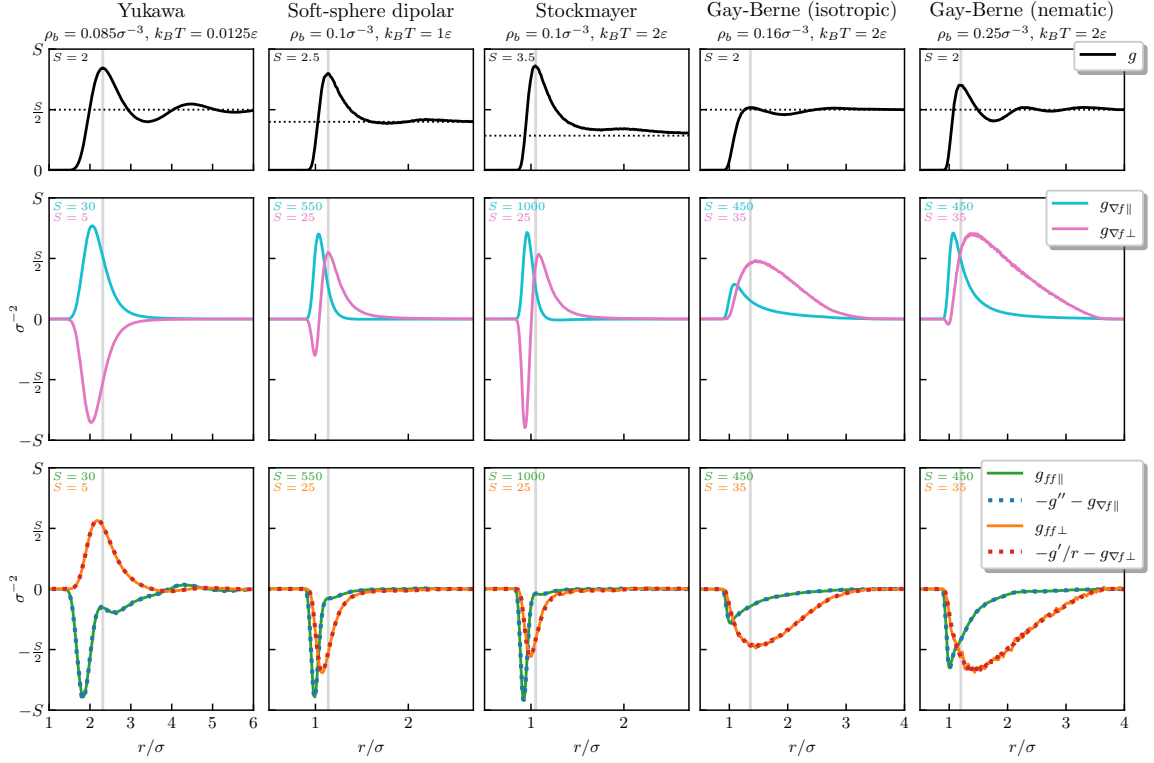


FIG. 3: Correlation functions analogous to Fig. 2 of the main text, but for the Yukawa liquid (first column), the soft-sphere dipolar fluid (second column), the Stockmayer fluid (third column), and the Gay-Berne model in the isotropic (fourth column) and nematic phase (fifth column). The results for the anisotropic models are obtained from canonical Monte Carlo simulations, and they are averaged over the microscopic orientations; the simulation box volume is $V = (20\sigma)^3$ and the long-ranged interactions are cut off at radial distance 10σ . Shown are results for the pair correlation function $g(r)$ (first row) and for the radial (\parallel) and transversal (\perp) components of the two-body force-gradient correlator $g_{\nabla f}(r)$ (second row) and the force-force pair correlator $g_{ff}(r)$ (third row). The respective vertical scale factor S is given in the top left corner of each panel and the scaled values for bulk density ρ_b and temperature T are indicated for each model fluid above the respective column. The results for the Yukawa liquid with inverse screening parameter $\kappa = 2/\sigma$ are qualitatively similar to those of the WCA liquid (second column Fig. 2 of the main text) but here with much longer-ranged decay behaviour. For identical dipolar strength $\mu/\sqrt{\epsilon\sigma^3} = 2$ the results for $g_{\nabla f}^{\perp}(r)$ for both the soft-sphere dipolar fluid [58] and the Stockmayer fluid show strong signatures of chain formation, similar to the behaviour of the three-body gel former (fourth column of Fig. 2 of the main text). The Gay-Berne model (with parameters $\kappa = 3.8, \kappa' = 5$ [62]) features positive-valued $g_{\nabla f}^{\perp}(r)$, which contrasts the behaviour of all other models and which we take to indicate interlocked arrangements of neighboring anisotropic molecules.

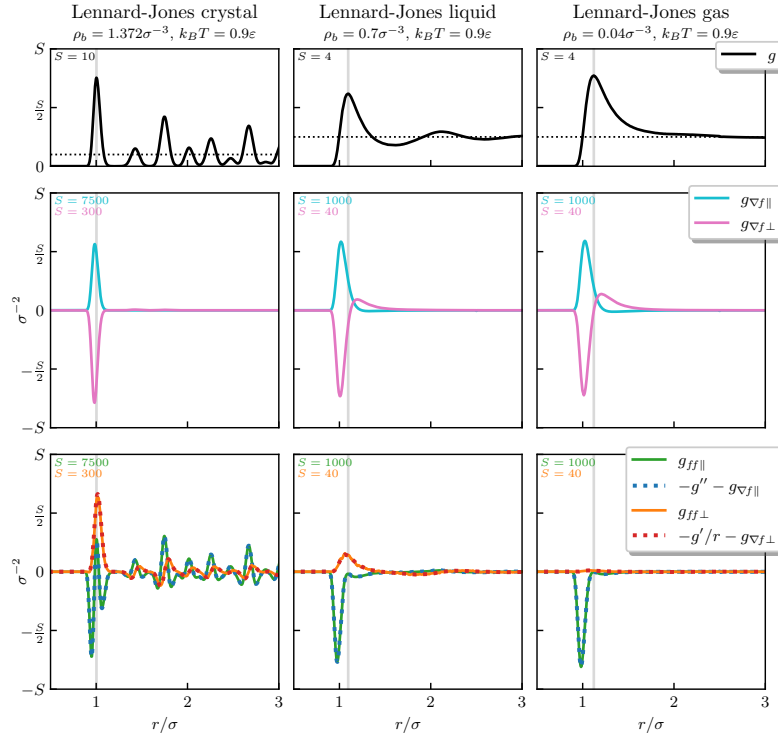
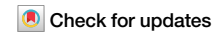


FIG. 4: Comparison of correlation functions for the LJ system in the fcc crystal phase (first column), the liquid (second column), and the gas phase (third column). Shown are the pair correlation function $g(r)$ (top row), the force-gradient correlator $\mathbf{g}_{\nabla f}(r)$ (middle row), and the force-force correlator $\mathbf{g}_{ff}(r)$ (bottom row). The plot style is analogous to Fig. 2 of the main text and to Fig. 3 of this SI. While the results for the gas and for the liquid carry the full structural two-body information, the correlators for the crystal are resolved only as a function of the radial distance r . This representation constitutes an average over global translations and rotations of the general inhomogeneous Noether sum rule, see Eq. (11) of the main text with $|\mathbf{r} - \mathbf{r}'|$ kept fixed. The reduced Noether identities (13) and (14) continue to hold in this averaged sense, as is demonstrated by the data collapse in the lower left panel. This perfect agreement serves as an indirect indication of the validity of the more general Eq. (11), which is applicable in the full inhomogeneous geometry.

<https://doi.org/10.1038/s42005-024-01568-y>

Hyperforce balance via thermal Noether invariance of any observable



Silas Robitschko, Florian Sammüller , Matthias Schmidt & Sophie Hermann

Noether invariance in statistical mechanics provides fundamental connections between the symmetries of a physical system and its conservation laws and sum rules. The latter are exact identities that involve statistically averaged forces and force correlations and they are derived from statistical mechanical functionals. However, the implications for more general observables and order parameters are unclear. Here, we demonstrate that thermally averaged classical phase space functions are associated with exact hyperforce sum rules that follow from translational Noether invariance. Both global and locally resolved identities hold and they relate the mean gradient of a phase-space function to its negative mean product with the total force. Similar to Hirschfelder’s hypervirial theorem, the hyperforce sum rules apply to arbitrary observables in equilibrium. Exact hierarchies of higher-order sum rules follow iteratively. As applications we investigate via computer simulations the emerging one-body force fluctuation profiles in confined liquids. These local correlators quantify spatially inhomogeneous self-organization and their measurement allows for the development of stringent convergence tests and enhanced sampling schemes in complex systems.

The task of predicting thermal averages of phase space functions lies at the center of attention in Statistical Mechanics. Prominent examples include correlation functions and order parameters, but also global quantities such as internal and external energies, entropy, and much more are considered^{1,2}. Significant progress has been reported for problem-specific order parameters that are tailored to capture intricate correlation effects. Recent examples that address the spatial ordering behavior of dense liquids include beyond-two-body correlation functions, as advocated by Kob and coworkers^{3,4} and by Janssen and her coworkers⁵.

In contrast to such freedom of choice, the variables within classical density functional theory^{2,6,7} seem to be a priori uniquely determined by the existence of a generating free energy functional and the associated structure of pairs of conjugate variables, which in particular are the external one-body potential energy $V_{\text{ext}}(\mathbf{r})$ and the density profile $\rho(\mathbf{r})$. However, there are recent extensions to density functional theory to systematically include the local compressibility^{8–10}, which forms a well-accessible order parameter for local particle number fluctuations. Technically, the local compressibility constitutes either a parametric derivative of the equilibrium density profile with respect to the chemical potential or, analogously, the covariance of the local density and the global particle number. A generalization from such chemical particle number fluctuation to thermal fluctuations has been recently performed^{11,12}. Working in the grand ensemble, where the particle

number fluctuates, is thereby crucial to not impose artificial constraints on the system.

Besides the standard thermodynamical thinking in terms of thermal and chemical equilibrium, there is much recent progress from the force point of view. Highly efficient force sampling techniques allow to obtain reliable results within many-body simulations that outperform more straightforward counting methods^{13–19}. Forces are also at the core of power functional theory²⁰ as a systematic approach to formulate coupled many-body dynamics on the one-body level of dynamical correlation functions.

To be specific, in the thermal equilibrium of a spatially inhomogeneous system, the sum of all mean forces necessarily vanishes at each position \mathbf{r} . This is expressed by the following exact sum rule:

$$\mathbf{F}_{\text{int}}(\mathbf{r}) - \rho(\mathbf{r})\nabla V_{\text{ext}}(\mathbf{r}) = k_B T \nabla \rho(\mathbf{r}). \quad (1)$$

Here, $\mathbf{F}_{\text{int}}(\mathbf{r})$ is the localized force density that acts at position \mathbf{r} due to the interparticle interactions with all surrounding particles, ∇ denotes the derivative with respect to \mathbf{r} such that $-\nabla V_{\text{ext}}(\mathbf{r})$ is the external force field, k_B indicates the Boltzmann constant, and T is the absolute temperature.

The sum of the interparticle and external force densities on the left-hand side of Eq. (1) balances the thermal diffusive contribution on its right-hand side. This is a classical result due to Yvon, Born, and Green (YBG)¹,

Theoretische Physik II, Physikalisches Institut, Universität Bayreuth, 95447 Bayreuth, Germany.

 e-mail: Matthias.Schmidt@uni-bayreuth.de; Sophie.Hermann@uni-bayreuth.de

where for particles that mutually interact only via a pair potential, the interparticle force density $\mathbf{F}_{\text{int}}(\mathbf{r})$ is expressed as an integral over the two-body density multiplied by the pair force¹. Higher-order versions of Eq. (1) form a hierarchy. That the first YBG equation (1) has practical consequences for carrying out sampling tasks in simulations is only a quite recent insight. Loosely speaking, *force sampling*^{13–15} amounts to obtaining simulation data for the left-hand side of Eq. (1) and then in a post-processing step dividing by $k_B T$ and building the inverse operation of the spatial derivative on the right-hand side via suitable integration in position. This method yields results for the density profile $\rho(\mathbf{r})$ which feature a significant reduction of statistical noise^{13–19}.

Exploiting Noether's Theorem^{21,22} in statistical mechanics has been performed in a variety of ways^{23–30}. Considering the invariance of statistical mechanical functionals leads very naturally to the notion of statistically averaged forces when spatial displacement is imposed on the system; mean torques emerge when invariance against rotations is addressed^{31,32}. In previous work, we have shown that the statistical Noether concept also applies quantum mechanically³³ and that it gives access to global force fluctuations³⁴. Generalizing to local invariance^{33,35} that is resolved in spatial position facilitated fresh insights into the correlation structure of the liquid state³⁶. Considering the first order in the displacement field yields the thermal equilibrium force balance relationship according to the YBG equation (1)^{33,35}. At second-order hitherto unknown two-body force-gradient and force-force correlators emerge and these, together with the standard pair correlation function, are constrained by exact Noether identities³⁶.

This situation of theory development leaves open the question of whether more general observables that serve as important order parameters and quantifiers of spatial structure will also be affected by the statistical Noether invariance, as one could glean from the generality of the thermal invariance concept. Here we demonstrate that any statistical observable \hat{A} is intrinsically associated with a corresponding hierarchy of exact identities that emerges from its statistical shifting invariance properties. We validate the corresponding exact local and global sum rules for a range of relevant observables via many-body simulations of a confined Lennard-Jones fluid. The results clarify a very intimate link of global and locally resolved correlators and they suggest a very general statistical mechanical structure.

Our framework can be viewed as a generalization of the YBG equation (1) to systematically include the dependence on a further given observable \hat{A} . The equilibrium force balance (1) itself is recovered for the trivial case $\hat{A} = 1$. Such generalization is not uncommon in Statistical Mechanics. The relationship of our theory and the YBG force balance equation is akin Hirschfelder's hypervirial theorem³⁷ as a generalization of the standard virial theorem¹ to also invoke an additional dependence on a given phase space function \hat{A} . Our theory can hence be viewed as a hyperforce balance relationship, and we derive global and local variants below, see Eqs. (4) and (10). We further show that the local version simplifies further to Eq. (11) and more explicitly to Eq. (12) in case of \hat{A} being independent of momenta. As a specific example, our methodology not only allows to sample density gradients, as is possible in force sampling schemes^{13–19}, but also to sample force density gradients. The general method complements existing counting and force-sampling techniques and it gives much inspiration for rigorous statistical mechanical theories based on exact identities. As we lay out, the degree of numerical accuracy to which the Noether sum rules are satisfied can serve as an estimator for sufficient equilibration of slowly converging systems.

Methods

Statistical mechanics

We consider general thermal many-body systems of particles with identical mass m , coordinates $\mathbf{r}_1, \dots, \mathbf{r}_N \equiv \mathbf{r}^N$, and momenta $\mathbf{p}_1, \dots, \mathbf{p}_N \equiv \mathbf{p}^N$, where N denotes the number of particles. The Hamiltonian is of the standard form $H = \sum_i \mathbf{p}_i^2 / (2m) + u(\mathbf{r}^N) + \sum_i V_{\text{ext}}(\mathbf{r}_i)$, where the sums $i = 1, \dots, N$ run over all particles, $u(\mathbf{r}^N)$ is the interparticle interaction potential, and $V_{\text{ext}}(\mathbf{r})$ is an external potential that depends on position \mathbf{r} . Thermal equilibrium is

characterized by a statistical equilibrium ensemble with grand canonical probability distribution $\Psi_{\text{eq}} = \Xi^{-1} e^{-\beta(H-\mu N)}$, where $\beta = 1/(k_B T)$ and μ indicates the chemical potential. The normalization factor of Ψ_{eq} is the partition sum $\Xi = \text{Tr} e^{-\beta(H-\mu N)}$, where the classical trace is defined as $\text{Tr} \cdot = \sum_{N=0}^{\infty} (N! h^{3N})^{-1} \int d\mathbf{r}^N \int d\mathbf{p}^N$, with h indicating Planck's constant. The thermal equilibrium average A of a given phase space function \hat{A} is then obtained as $A = \langle \hat{A} \rangle \equiv \text{Tr} \Psi_{\text{eq}} \hat{A}$, where we have suppressed the dependence of \hat{A} on the phase space variables \mathbf{r}^N and \mathbf{p}^N in the notation, i.e., in full notation we have $\hat{A}(\mathbf{r}^N, \mathbf{p}^N)$ as well as potentially further parametric dependence such as on a generic position variable \mathbf{r} .

Global shifting invariance

To develop the Noether invariance theory, we first consider a global coordinate displacement $\mathbf{r}_i \rightarrow \mathbf{r}_i + \boldsymbol{\epsilon}_0 \equiv \tilde{\mathbf{r}}_i$, where the shifting vector $\boldsymbol{\epsilon}_0 = \text{const}$ is independent of position and acts on all particles in the same way³¹. The tilde indicates the new coordinates. Expressing H as well as the corresponding distribution function Ψ_{eq} in the new coordinates makes averages become formally dependent on the shifting parameter, i.e., $A(\boldsymbol{\epsilon}_0)$. However, the coordinate change can also be viewed as a mere re-parameterization of the phase space integral which induces no change to its value such that $A(\boldsymbol{\epsilon}_0) = A$, with the right-hand side denoting $\langle \hat{A} \rangle$ in the original representation. Partially differentiating both sides of the equation yields:

$$\frac{\partial A(\boldsymbol{\epsilon}_0)}{\partial \boldsymbol{\epsilon}_0} = \frac{\partial}{\partial \boldsymbol{\epsilon}_0} \text{Tr} \Psi_{\text{eq}}(\boldsymbol{\epsilon}_0) \hat{A}(\boldsymbol{\epsilon}_0) = 0, \quad (2)$$

where the second equality arises trivially from $\partial A / \partial \boldsymbol{\epsilon}_0 = 0$, as there is no dependence on $\boldsymbol{\epsilon}_0$.

Carrying out the derivative is straightforward upon using the Boltzmann form of the equilibrium distribution function and noting that the partition sum is independent of $\boldsymbol{\epsilon}_0$. Explicitly we have $\partial \Psi_{\text{eq}}(\boldsymbol{\epsilon}_0) / \partial \boldsymbol{\epsilon}_0 = -\beta \Psi_{\text{eq}}(\boldsymbol{\epsilon}_0) \partial H(\boldsymbol{\epsilon}_0) / \partial \boldsymbol{\epsilon}_0$. Using the product rule of differentiation and evaluating at vanishing displacement $\boldsymbol{\epsilon}_0 = 0$ then leads from Eq. (2) to

$$-\beta \left\langle \left. \frac{\partial H(\boldsymbol{\epsilon}_0)}{\partial \boldsymbol{\epsilon}_0} \right|_{\boldsymbol{\epsilon}_0=0} \hat{A} \right\rangle + \left\langle \left. \frac{\partial \hat{A}(\boldsymbol{\epsilon}_0)}{\partial \boldsymbol{\epsilon}_0} \right|_{\boldsymbol{\epsilon}_0=0} \right\rangle = 0. \quad (3)$$

Observing that here $\partial / \partial \boldsymbol{\epsilon}_0|_{\boldsymbol{\epsilon}_0=0} \equiv \sum_i \nabla_i$ allows to make the derivatives more explicit with ∇_i indicating the partial derivative with respect to \mathbf{r}_i . In the first term in Eq. (3) we have $-\partial H(\boldsymbol{\epsilon}_0) / \partial \boldsymbol{\epsilon}_0|_{\boldsymbol{\epsilon}_0=0} = -\sum_i \nabla_i V_{\text{ext}}(\mathbf{r}_i) \equiv \hat{\mathbf{F}}_{\text{ext}}^0$, which defines the global external force operator $\hat{\mathbf{F}}_{\text{ext}}^0$. Here the global interparticle force due to the mutual interactions between all particles in the system vanishes, $\hat{\mathbf{F}}_{\text{int}}^0 = -\sum_i \nabla_i u(\mathbf{r}^N) \equiv 0$, as is due to Newton's third law or, analogously, to the translational invariance of $u(\mathbf{r}^N)$ against global displacement³¹.

Re-ordering the two terms in Eq. (3) gives the following global hyperforce identity that holds for any given observable $\hat{A}(\mathbf{r}^N, \mathbf{p}^N)$:

$$\beta \langle \hat{\mathbf{F}}_{\text{ext}}^0 \hat{A} \rangle = - \left\langle \sum_i \nabla_i \hat{A} \right\rangle. \quad (4)$$

Here $\hat{A} = \hat{A}(\mathbf{r}^N, \mathbf{p}^N)$ can feature additional parametric dependence, such as on a generic position argument \mathbf{r} . The sum rule (4) relates the correlation of \hat{A} with the external force operator (left-hand side) to the mean negative global coordinate derivative of \hat{A} (right-hand side); here we use the term correlation to imply the average of the product of two observables. As announced in the introduction, Eq. (4) is similar to Hirschfelder's hypervirial theorem³⁷ in the inclusion of the phase space function $\hat{A}(\mathbf{r}^N, \mathbf{p}^N)$ and our hyperforce terminology parallels his use of the term hypervirial.

While Noether invariance enabled us to obtain the global hyperforce identity Eq. (4) constructively, one can verify its validity a posteriori by

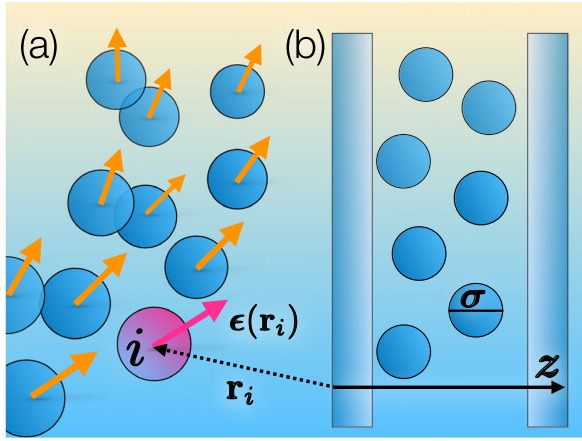


Fig. 1 | Illustrations of the relevant geometries. **a** The shifting field (orange arrows) displaces the coordinates \mathbf{r}_i of all particles i by a vector $\boldsymbol{\epsilon}(\mathbf{r}_i)$; the specific particle i is highlighted in red and all particles are identical. A corresponding change in momenta, see Eq. (6), compensates for the spatial distortion such that the differential phase space volume element (integration measure) remains unchanged. **b** Planar geometry of the confined Lennard-Jones fluid between two smooth parallel soft attractive Lennard-Jones walls; σ is the particle size, z measures the distance across the planar pore, and L is the distance between the two walls.

integration by parts in phase space on the right-hand side. The derivatives ∇_i then act on the probability distribution and exploiting again the Boltzmann form leads to $\hat{A} \sum_i \nabla_i \Psi_{\text{eq}} = -\beta \Psi_{\text{eq}} \hat{A} \sum_i \nabla_i H = \Psi_{\text{eq}} \beta \hat{\mathbf{F}}_{\text{ext}}^0 \hat{A}$, which gives the left-hand side of Eq. (4) upon building the trace. Alternatively one can start with the Yvon theorem¹, $\beta \langle \hat{A} \nabla_i H \rangle = \langle \nabla_i \hat{A} \rangle$, which itself also follows from partial phase space integration¹. Summing the Yvon theorem over all particles i and noting that $\sum_i \nabla_i u(\mathbf{r}^N) \equiv 0$ gives Eq. (4). A similar derivation can also be based on the hypervirial theorem³⁷.

Local shifting invariance

Before presenting explicit applications of Eq. (4) to specific forms of \hat{A} , we first generalize to the fully position-resolved case. In a generalization of the uniform coordinate displacement used for global shifting in the previous subsection, we consider the following local transformation on phase space, as parameterized by a three-dimensional vector field $\boldsymbol{\epsilon}(\mathbf{r})$ ^{33,35}:

$$\mathbf{r}_i \rightarrow \mathbf{r}_i + \boldsymbol{\epsilon}(\mathbf{r}_i), \quad (5)$$

$$\mathbf{p}_i \rightarrow [\mathbb{1} + \nabla_i \boldsymbol{\epsilon}(\mathbf{r}_i)]^{-1} \cdot \mathbf{p}_i. \quad (6)$$

The gradient $\nabla_i \boldsymbol{\epsilon}(\mathbf{r}_i)$ is a 3×3 matrix, $\mathbb{1}$ denotes the 3×3 identity matrix, and the superscript -1 indicates matrix inversion. Figure 1a depicts an illustration of the spatial transformation (5). The momentum transformation (6) has the following Taylor expansion to the lowest order in the displacement field: $\mathbf{p}_i \rightarrow [\mathbb{1} - \nabla_i \boldsymbol{\epsilon}(\mathbf{r}_i)] \cdot \mathbf{p}_i$.

The joint transformation (5) and (6) is canonical^{33,35,38} and it hence preserves the phase space volume element, $d\mathbf{r}_i d\mathbf{p}_i = d\tilde{\mathbf{r}}_i d\tilde{\mathbf{p}}_i$, where the tilde indicates the transformed variables [right-hand sides of Eqs. (5) and (6)]. The Hamiltonian also remains unchanged (up to expressing the original via the new variables). Hence the partition sum Ξ is an invariant under the joint transformation (5) and (6)^{33,35,36}. Together with the invariance of the integration measure, the setup implies that any average $A = \langle \hat{A} \rangle = \text{Tr} \Psi_{\text{eq}} \hat{A}$ is an invariant. This property holds despite the explicit occurrence of the shifting field $\boldsymbol{\epsilon}(\mathbf{r})$ in the integrand, and hence $A[\boldsymbol{\epsilon}] = A$, where the left-hand side carries the apparent dependence on the shifting field and the right-hand side is the average expressed in the original variables where $\boldsymbol{\epsilon}(\mathbf{r})$ is absent. We use the standard notation to express dependence on a function (so-called functional dependence) by bracketed arguments.

From the local Noether invariance, we can conclude from functionally differentiating the equation $A[\boldsymbol{\epsilon}] = A$ with respect to the shifting field that

$$\frac{\delta A[\boldsymbol{\epsilon}]}{\delta \boldsymbol{\epsilon}(\mathbf{r})} = 0. \quad (7)$$

The right-hand side of Eq. (7) vanishes trivially due to the average A being independent of $\boldsymbol{\epsilon}(\mathbf{r})$ in the original representation and hence $\delta A/\delta \boldsymbol{\epsilon}(\mathbf{r}) = 0$. Carrying out the functional derivative on the left-hand side of Eq. (7) requires to functionally differentiate the equilibrium distribution, $\delta \Psi_{\text{eq}}[\boldsymbol{\epsilon}]/\delta \boldsymbol{\epsilon}(\mathbf{r}) = -\beta \Psi_{\text{eq}}[\boldsymbol{\epsilon}] \delta H[\boldsymbol{\epsilon}]/\delta \boldsymbol{\epsilon}(\mathbf{r})$, as follows from the chain rule. This allows to rewrite Eq. (7) upon using the product rule and re-ordering the resulting two terms as

$$-\beta \left\langle \frac{\delta H[\boldsymbol{\epsilon}]}{\delta \boldsymbol{\epsilon}(\mathbf{r})} \Big|_{\boldsymbol{\epsilon}=0} \hat{A} \right\rangle = - \left\langle \frac{\delta \hat{A}[\boldsymbol{\epsilon}]}{\delta \boldsymbol{\epsilon}(\mathbf{r})} \Big|_{\boldsymbol{\epsilon}=0} \right\rangle, \quad (8)$$

where we have evaluated both sides at vanishing shifting field, $\boldsymbol{\epsilon}(\mathbf{r}) = 0$.

Differentiating the transformed Hamiltonian with respect to the shifting field gives $-\delta H[\boldsymbol{\epsilon}]/\delta \boldsymbol{\epsilon}(\mathbf{r})|_{\boldsymbol{\epsilon}=0} = \hat{\mathbf{F}}(\mathbf{r})$ ^{33,35}, where the position-resolved total force operator comprises the following three terms:

$$\hat{\mathbf{F}}(\mathbf{r}) = \nabla \cdot \hat{\boldsymbol{\tau}}(\mathbf{r}) + \hat{\mathbf{F}}_{\text{int}}(\mathbf{r}) - \hat{\rho}(\mathbf{r}) \nabla V_{\text{ext}}(\mathbf{r}). \quad (9)$$

The right-hand side of Eq. (9) features the one-body kinematic stress operator $\hat{\boldsymbol{\tau}}(\mathbf{r}) = -\sum_i \delta(\mathbf{r} - \mathbf{r}_i) \mathbf{p}_i \mathbf{p}_i / m^{20}$, the one-body interparticle force density operator $\hat{\mathbf{F}}_{\text{int}}(\mathbf{r}) = -\sum_i \delta(\mathbf{r} - \mathbf{r}_i) \nabla_i u(\mathbf{r}^N)$ ³⁰, the standard form of the density operator $\hat{\rho}(\mathbf{r}) = \sum_i \delta(\mathbf{r} - \mathbf{r}_i)$ ^{1,2,20}, and the external force field $-\nabla V_{\text{ext}}(\mathbf{r})$. (The force density operator $\hat{\mathbf{F}}(\mathbf{r})$ defined in (9) also arises as the time derivative of the one-body current operator²⁰. In equilibrium the kinematic term in (9) reduces to a diffusive contribution: $\nabla \cdot \langle \hat{\boldsymbol{\tau}}(\mathbf{r}) \rangle = -k_B T \nabla \rho(\mathbf{r})$; we refer the Reader to Schmidt²⁰ for details). Equation (8) can then be written upon carrying out the functional derivatives and using Eq. (9) (on the left-hand side) together with the chain rule (on the right-hand side), as the following hyperforce sum rule that holds for a given form of $\hat{A} = \hat{A}(\mathbf{r}^N, \mathbf{p}^N)$:

$$\beta \langle \hat{\mathbf{F}}(\mathbf{r}) \hat{A} \rangle = - \left\langle \sum_i \delta(\mathbf{r} - \mathbf{r}_i) \nabla_i \hat{A} \right\rangle - \nabla \cdot \left\langle \sum_i \delta(\mathbf{r} - \mathbf{r}_i) \frac{\partial \hat{A}}{\partial \mathbf{p}_i} \mathbf{p}_i \right\rangle, \quad (10)$$

where \hat{A} can again feature additional parametric dependencies, such as on \mathbf{r} .

For cases where the observable under consideration is independent of the momenta, i.e., $\hat{A} \equiv \hat{A}(\mathbf{r}^N)$, the second term on the right-hand side of Eq. (10) vanishes and we obtain the coordinate-based local hyperforce sum rule:

$$\beta \langle \hat{\mathbf{F}}(\mathbf{r}) \hat{A}(\mathbf{r}^N) \rangle = - \left\langle \sum_i \delta(\mathbf{r} - \mathbf{r}_i) \nabla_i \hat{A}(\mathbf{r}^N) \right\rangle. \quad (11)$$

Equation (11) can be viewed as a generalization of the framework developed by Coles et al.¹⁷, where they consider observables of the specific form $\hat{A} = \sum_i a_i \delta(\mathbf{r} - \mathbf{r}_i)$, where a_i is a unique property of particle i only, such as, e.g., its charge or, when taking orientational degrees of freedom into account, its polarization¹⁷.

As a consistency check, from integrating the locally resolved sum rules (10) and (11) over position \mathbf{r} , i.e., applying $\int d\mathbf{r}$ to both sides of these equations, and observing that $\int d\mathbf{r} \delta(\mathbf{r} - \mathbf{r}_i) = 1$, one retrieves the global Noether identity (4). Here the global external force is the only remaining nontrivial global force contribution, $\hat{\mathbf{F}}^0 \equiv \int d\mathbf{r} \hat{\mathbf{F}}(\mathbf{r}) = \hat{\mathbf{F}}_{\text{ext}}^0$, as the global interparticle force vanishes due to Newton’s third law³¹ and there is also no global diffusive effect due to vanishing boundary terms. Hence Eq. (4) continues to hold upon replacing $\hat{\mathbf{F}}_{\text{ext}}^0$ by the global total force operator $\hat{\mathbf{F}}$.

As a further remark, by splitting off the kinetic term in Eq. (11), its left-hand side can be re-written as $\beta\langle\hat{\mathbf{F}}(\mathbf{r})\hat{A}(\mathbf{r}^N)\rangle = \beta\langle\hat{\mathbf{F}}_U(\mathbf{r})\hat{A}(\mathbf{r}^N) - \nabla\langle\hat{\rho}(\mathbf{r})\hat{A}(\mathbf{r}^N)\rangle$, with the potential force density operator being given as the sum of interparticle and external contributions: $\hat{\mathbf{F}}_U(\mathbf{r}) = \hat{\mathbf{F}}_{\text{int}}(\mathbf{r}) - \hat{\rho}(\mathbf{r})\nabla V_{\text{ext}}(\mathbf{r})$.

In summary, the local force decomposition into ideal, interparticle, and external contributions in Eq. (11) allows to obtain the following more explicit form, which holds, as we recall, provided that $\hat{A} = \hat{A}(\mathbf{r}^N)$ is independent of the momenta:

$$\begin{aligned} \beta\langle\hat{\mathbf{F}}_{\text{int}}(\mathbf{r})\hat{A}\rangle - \beta\langle\hat{\rho}(\mathbf{r})\hat{A}\rangle\nabla V_{\text{ext}}(\mathbf{r}) \\ = \nabla\langle\hat{\rho}(\mathbf{r})\hat{A}\rangle - \left\langle\sum_i\delta(\mathbf{r}-\mathbf{r}_i)\nabla_i\hat{A}\right\rangle. \end{aligned} \quad (12)$$

For a given explicit form of \hat{A} , such as in the concrete examples discussed below, the sum rule (12) connects the three irreducible correlators $\langle\hat{\mathbf{F}}_{\text{int}}(\mathbf{r})\hat{A}\rangle$, $\langle\hat{\rho}(\mathbf{r})\hat{A}\rangle$, and $\langle\sum_i\delta(\mathbf{r}-\mathbf{r}_i)\nabla_i\hat{A}\rangle$ in a formally exact and non-trivial way with each other. Setting $\hat{A} = 1$ recovers the YBG equation (which we take to imply thermal averages being taken), as then the last term in Eq. (12) vanishes and the remaining terms constitute Eq. (1). Paralleling the naming convention of the hypervirial theorem, which generalizes the standard virial theorem to include a further observable, Eq. (12) attains the status of a hyper-YBG equation or hyperforce balance relationship. Concrete applications thereof are shown below in the *Results* section.

The correlators on the left-hand sides of the sum rules (4), (10), and (11) also constitute covariances. We recall that the covariance of two observables \hat{A} and \hat{B} , as defined via $\text{cov}(\hat{A}, \hat{B}) = \langle\hat{A}\hat{B}\rangle - \langle\hat{A}\rangle\langle\hat{B}\rangle$ measures the correlation of the fluctuations of the two observables around their respective mean. In the present case the mean force vanishes both globally, $\langle\hat{\mathbf{F}}_{\text{ext}}\rangle = 0$, and locally, $\langle\hat{\mathbf{F}}(\mathbf{r})\rangle = 0$. Hence we can formally subtract the vanishing averages and re-express $\langle\hat{\mathbf{F}}_{\text{ext}}^0\hat{A}\rangle = \text{cov}(\hat{\mathbf{F}}_{\text{ext}}^0, \hat{A})$ as well as $\langle\hat{\mathbf{F}}(\mathbf{r})\hat{A}\rangle = \text{cov}(\hat{\mathbf{F}}(\mathbf{r}), \hat{A})$. Besides the conceptual difference between correlation and covariance, in practical sampling schemes it can be beneficial to work with covariances rather than correlations to reduce statistical noise, as we will demonstrate further below.

That Eq. (11) holds can again be verified a posteriori by phase space coordinate integration by parts on the right-hand side. Due to the product rule two contributions result, one from the Boltzmann factor: $\sum_i\delta(\mathbf{r}-\mathbf{r}_i)\nabla_i\Psi_{\text{eq}} = -\beta\Psi_{\text{eq}}\sum_i\delta(\mathbf{r}-\mathbf{r}_i)\nabla_i H$, and one from the Dirac distribution: $\Psi_{\text{eq}}\sum_i\nabla_i\delta(\mathbf{r}-\mathbf{r}_i) = -\Psi_{\text{eq}}\nabla\hat{\rho}(\mathbf{r})$. Together with the factor \hat{A} their combination yields the left-hand side of Eq. (11) upon identifying $\hat{\mathbf{F}}(\mathbf{r})$ via Eq. (9). The more general Eq. (10) follows analogously upon integrating by parts also with respect to the momenta.

Results

Global shifting applications

We turn to applications and hence consider concrete examples for the general phase space function \hat{A} , which has remained so far unspecified in the above generic hyperforce framework. We start with investigating the global invariance (4), which as we demonstrate constitutes a powerful device both if \hat{A} is a global object or if it is locally resolved via dependence on a position. We first consider the seemingly trivial case $\hat{A} = 1$, for which of course $\langle 1 \rangle = 1$ due to the correct normalization of Ψ_{eq} . The right-hand side of Eq. (4) vanishes and we obtain $\mathbf{F}_{\text{ext}}^0 \equiv \langle\hat{\mathbf{F}}_{\text{ext}}^0\rangle = 0$, i.e., the vanishing of the mean external force in equilibrium³¹. This is intuitively expected, as can be seen by contradiction as follows. If the mean external force did not vanish, then the system would start to move on average³² and hence it would not be in equilibrium.

Addressing the global external force and hence setting $\hat{A} = \hat{\mathbf{F}}_{\text{ext}}^0$ in Eq. (4) leads upon simplifying the right-hand side via $\langle\sum_i\nabla_i\hat{\mathbf{F}}_{\text{ext}}^0\rangle = -\langle\sum_i\nabla_i\nabla_i V_{\text{ext}}(\mathbf{r}_i)\rangle$ to the recently formulated global force-variance relationship $\beta\langle\hat{\mathbf{F}}_{\text{ext}}^0\hat{\mathbf{F}}_{\text{ext}}^0\rangle = \int d\mathbf{r}\rho(\mathbf{r})\nabla\nabla V_{\text{ext}}(\mathbf{r})$ ³⁴. Here the auto-correlation of

the global external force (left-hand side) equals up to a factor β the mean external potential energy curvature (right-hand side).

By iteratively replacing \hat{A} with the composite $\hat{\mathbf{F}}_{\text{ext}}^0\hat{A}$ in Eq. (4), one can systematically generate higher-order sum rules, starting with $\beta\langle\hat{\mathbf{F}}_{\text{ext}}^0\hat{\mathbf{F}}_{\text{ext}}^0\hat{A}\rangle = -\langle\hat{\mathbf{F}}_{\text{ext}}^0\sum_i\nabla_i\hat{A}\rangle - \langle\hat{A}\sum_i\nabla_i\hat{\mathbf{F}}_{\text{ext}}^0\rangle$, where the first term on the right-hand side allows repeated application of Eq. (4) and the second term can be written via the external potential curvature. The result is the following global second-order hyperforce sum rule:

$$\beta^2\langle\hat{\mathbf{F}}_{\text{ext}}^0\hat{\mathbf{F}}_{\text{ext}}^0\hat{A}\rangle = \left\langle\sum_{ij}\nabla_i\nabla_j\hat{A}\right\rangle + \left\langle\hat{A}\sum_i\nabla_i\nabla_i\beta V_{\text{ext}}(\mathbf{r}_i)\right\rangle, \quad (13)$$

where $\hat{A} = \hat{A}(\mathbf{r}^N, \mathbf{p}^N)$. The second term on the right hand of Eq. (13) side can alternatively be written as an integral over a correlation function as follows: $\beta\int d\mathbf{r}\langle\hat{A}\hat{\rho}(\mathbf{r})\rangle\nabla\nabla V_{\text{ext}}(\mathbf{r})$, where $\langle\hat{A}\hat{\rho}(\mathbf{r})\rangle$ is the correlation of \hat{A} and the local density operator. Alternatively to the present route via Eq. (4), the sum rule (13) can equivalently be derived from second-order invariance of $\langle\hat{A}\rangle$ against global shifting and hence calculating $\partial^2 A(\epsilon_0)/\partial\epsilon_0\partial\epsilon_0 = 0$.

Addressing locally resolved correlation functions on the basis of Eq. (4) allows to access a higher degree of spatial resolution. We first consider the case $\hat{A} = \hat{\rho}(\mathbf{r})$, which leads upon re-writing the right-hand side of Eq. (4) via $-\sum_i\nabla_i\hat{\rho}(\mathbf{r}) = -\sum_i\nabla_i\delta(\mathbf{r}-\mathbf{r}_i) = \sum_i\nabla\delta(\mathbf{r}-\mathbf{r}_i) = \nabla\hat{\rho}(\mathbf{r})$ to the following identity:

$$\beta\langle\hat{\mathbf{F}}_{\text{ext}}^0\hat{\rho}(\mathbf{r})\rangle = \nabla\rho(\mathbf{r}), \quad (14)$$

where we recall that on the right-hand side $\rho(\mathbf{r}) = \langle\hat{\rho}(\mathbf{r})\rangle$ is the averaged density profile. Hence building the correlation of the density operator with the global external force acts to spatially differentiate the density profile. We recall that the density gradient $\nabla\rho(\mathbf{r})$, as it occurs on the right-hand side of Eq. (14), follows alternatively from the YBG equation (1), which upon multiplication by β attains the form $\nabla\rho(\mathbf{r}) = \beta\mathbf{F}_{\text{int}}(\mathbf{r}) + \beta\mathbf{F}_{\text{ext}}(\mathbf{r})$, where the external force density is simply given as $\mathbf{F}_{\text{ext}}(\mathbf{r}) = -\rho(\mathbf{r})\nabla V_{\text{ext}}(\mathbf{r})$.

It is interesting to note that Eq. (14), when written in covariance form as $\beta\text{cov}(\hat{\mathbf{F}}_{\text{ext}}^0, \hat{\rho}(\mathbf{r})) = \nabla\rho(\mathbf{r})$, mirrors closely the structure of the thermodynamic identity $\beta\text{cov}(N, \hat{\rho}(\mathbf{r})) = \partial\rho(\mathbf{r})/\partial\mu \equiv \chi_\mu(\mathbf{r})$ with the local compressibility $\chi_\mu(\mathbf{r})$ ⁸⁻¹⁰. Here rather than the spatial gradient, the thermodynamic parametric derivative with respect to chemical potential occurs. Equation (14) can also be viewed as the so-called inverse Lovett-Mou-Buff-Wertheim (LMBW) relation $\beta\int d\mathbf{r}'H_2(\mathbf{r}, \mathbf{r}')\nabla'V_{\text{ext}}(\mathbf{r}') = \nabla\rho(\mathbf{r})$ ^{39,40}, as is obtainable from global translational invariance³¹. Having explicit results for the density covariance $H_2(\mathbf{r}, \mathbf{r}') = \text{cov}(\hat{\rho}(\mathbf{r}), \hat{\rho}(\mathbf{r}'))$ is however not required in the much more straightforward form (14). Furthermore, by summing only over particle pairs with unequal indices we obtain the distinct identity $\langle\hat{\mathbf{F}}_{\text{ext}}^0\hat{\rho}(\mathbf{r})\rangle_{\text{dist}} = \mathbf{F}_{\text{int}}(\mathbf{r})$, which again relates seemingly very different physical objects identically to each other. The derivation is straightforward by starting from Eq. (14), subtracting the self contribution which is the YBG equation (1) in the form $-\beta\rho(\mathbf{r})\nabla V_{\text{ext}}(\mathbf{r}) = -\beta\mathbf{F}_{\text{int}}(\mathbf{r}) + \nabla\rho(\mathbf{r})$, and dividing the result by β .

To validate the Noether invariance theory and to investigate its implications for the use of force sampling methods, we turn to many-body simulations and consider the Lennard-Jones (LJ) fluid as a representative microscopic model. The LJ pair potential $\phi(r)$ between two particles separated by a distance r has the familiar form $\phi(r) = 4\epsilon[(\sigma/r)^{12} - (\sigma/r)^6]$ with the energy scale ϵ and particle size σ both being constants.

As our above statistical mechanical derivations continue to hold canonically, we sample both via adaptive Brownian dynamics (BD)⁴¹ with a fixed number of particles, but also using Monte Carlo simulations in the grand canonical ensemble. Spatial inhomogeneity is induced by confining the system between two planar, parallel LJ walls. Each wall is represented by an external potential contribution $V_{\text{wall}}(z)$ that we choose to be identical to the LJ interparticle potential $\phi(r)$, but instead of the radial distance r

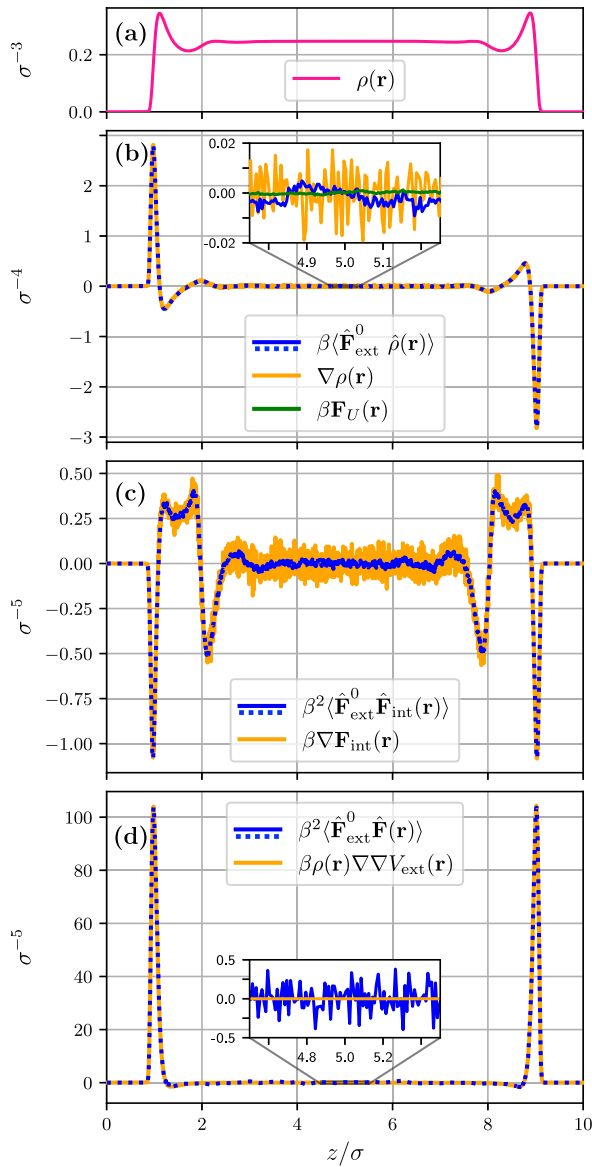


Fig. 2 | Illustration of the sum rules (14), (15), and (16). The simulation results were obtained from adaptive BD sampling of the LJ fluid confined between two parallel planar LJ walls. The profiles are shown as a function of scaled distance z/σ across the planar slit. **a** The density profile $\rho(\mathbf{r})$ of the confined system is shown as a reference. **b** Comparison of the correlator $\beta\langle\hat{\mathbf{F}}_{\text{ext}}^0\hat{\rho}(\mathbf{r})\rangle$ and the density gradient $\nabla\rho(\mathbf{r})$, see Eq. (14); the zoomed inset demonstrates the respective noise levels and it also shows the scaled force density sum $\beta\mathbf{F}_U(\mathbf{r}) = \beta\hat{\mathbf{F}}_{\text{int}}(\mathbf{r}) + \beta\mathbf{F}_{\text{ext}}(\mathbf{r})$ which equals $\nabla\rho(\mathbf{r})$ due to the local force balance. **c** Comparison of $\beta^2\langle\hat{\mathbf{F}}_{\text{ext}}^0\hat{\mathbf{F}}_{\text{int}}(\mathbf{r})\rangle$ and $\beta\nabla\mathbf{F}_{\text{int}}(\mathbf{r})$, see Eq. (15). The former route carries less statistical noise and hence can serve as a starting point for a force sampling scheme. **d** Comparison of $\beta^2\langle\hat{\mathbf{F}}_{\text{ext}}^0\hat{\mathbf{F}}(\mathbf{r})\rangle$ and the local external potential curvature density $\beta\rho(\mathbf{r})\nabla\nabla V_{\text{ext}}(\mathbf{r})$, see Eq. (16).

evaluated as a function of the distance z perpendicular to the wall, $V_{\text{wall}}(z) = 4\epsilon[(\sigma/z)^{12} - (\sigma/z)^6]$. The joint potential of both walls is then $V_{\text{ext}}(z) = V_{\text{wall}}(z) + V_{\text{wall}}(L - z)$, with L indicating the separation distance between the two walls. The specific choice of 12-6-wall potential is made for convenience only and it differs from the physically motivated 9-3-form (see e.g., Evans et al.⁹).

The system is periodic in the two directions perpendicular to the z -direction across the slit; a sketch is shown in Fig. 1b. The wall separation distance is chosen as $L = 10\sigma$, with σ denoting the LJ particle size, and the lateral box length is also set to 10σ . The LJ potential is cut and shifted with a cutoff distance of 2.5σ . The reduced temperature is $k_B T/\epsilon = 2$ with ϵ denoting the LJ energy scale. We use $N = 200$ particles. Sampling is started after 10^8 time steps that are used for equilibration. The subsequent sampling runlength is 3×10^8 time steps which corresponds to $\sim 2000\tau_B$, where $\tau_B = \gamma\sigma^2/\epsilon$ denotes the Brownian timescale with γ being the friction constant. All results that we show for correlators are obtained from evaluation as covariances. Subtracting the residual contribution from the product of the two mean values helps to remove artifacts that occur due to finite sampling.

The density profile of the confined LJ fluid, resolved as a function of the scaled position z/σ across the planar slit, is shown in Fig. 2a. The shape of the spatial density variation features structured packing effects that appear adjacent to each wall and that become damped towards the middle of the pore. Turning to the density gradient, we present simulation results for both sides of Eq. (14) in Fig. 2b. Equation (14) in the specific planar geometry reduces to $\beta\langle\hat{\mathbf{F}}_{\text{ext}}^0\sum_i\delta(z-z_i)/L^2\rangle = \partial\rho(z)/\partial z$, where $\delta(z-z_i)$ is a one-dimensional Dirac distribution, z_i is the component of the vector \mathbf{r}_i across the pore, L^2 is the lateral system area, and the global external force has only a nonvanishing z -component given by $\hat{F}_{\text{ext}}^0 = -\sum_i\partial V_{\text{ext}}(z_i)/\partial z_i$. The density profile is sampled as $\rho(z) = \langle\sum_i\delta(z-z_i)/L^2\rangle$. The comparison of the a priori very different data sets shown in Fig. 2b indicates excellent agreement. That the correlation of the density operator with the global external force operator indeed gives the gradient of the density profile, cf. Eq. (14), is surely not only at first glance very counter-intuitive.

We next consider the one-body interparticle force density operator $\hat{A} = \hat{\mathbf{F}}_{\text{int}}(\mathbf{r})$, for which Eq. (4) yields

$$\beta\langle\hat{\mathbf{F}}_{\text{ext}}^0\hat{\mathbf{F}}_{\text{int}}(\mathbf{r})\rangle = \nabla\mathbf{F}_{\text{int}}(\mathbf{r}). \quad (15)$$

Equation (15) gives access to the gradient of the internal force density (right-hand side) via sampling the correlation of the local internal force density with the global external force (left-hand side). This relationship could be used in a force sampling scheme¹³⁻¹⁹, where one obtains data for the force correlations and via spatial integration obtains the interparticle force density, which we demonstrate below. We first present simulation results to illustrate the validity of Eq. (15) in Fig. 2c. The results for $\beta\langle\hat{\mathbf{F}}_{\text{ext}}^0\hat{\mathbf{F}}_{\text{int}}(\mathbf{r})\rangle$ carry much less statistical noise, as the need for building the numerical derivative $\nabla\mathbf{F}_{\text{int}}(\mathbf{r})$ is avoided. However, this is no panacea, as accurately sampling the correlation of the interparticle force density with the global external force also poses challenges to the overall equilibration of the system.

Addressing the total force density operator $\hat{A} = \hat{\mathbf{F}}(\mathbf{r})$ requires to complement the above-considered interparticle force density $\hat{\mathbf{F}}_{\text{int}}(\mathbf{r})$ with the ideal and external contributions. These two latter terms constitute mere variants of the density operator identity (14). First there is the external force density operator $\hat{A} = \hat{\mathbf{F}}_{\text{ext}}(\mathbf{r}) = -\hat{\rho}(\mathbf{r})\nabla V_{\text{ext}}(\mathbf{r})$ which yields $\beta\langle\hat{\mathbf{F}}_{\text{ext}}^0\hat{\mathbf{F}}_{\text{ext}}(\mathbf{r})\rangle = -[\nabla V_{\text{ext}}(\mathbf{r})]\nabla\rho(\mathbf{r})$, as $\nabla V_{\text{ext}}(\mathbf{r})$ can be taken out of the phase space average on the left-hand side of Eq. (14). Secondly, the diffusive force density, $\hat{A} = -k_B T\nabla\hat{\rho}(\mathbf{r})$, leads trivially to the gradient of Eq. (14).

Collecting all three terms (ideal, interparticle, and external) allows us to obtain for the choice $\hat{A} = \hat{\mathbf{F}}(\mathbf{r})$ a mixed global-local Noether identity:

$$\beta\langle\hat{\mathbf{F}}_{\text{ext}}^0\hat{\mathbf{F}}(\mathbf{r})\rangle = \rho(\mathbf{r})\nabla\nabla V_{\text{ext}}(\mathbf{r}). \quad (16)$$

We present simulation results that validate the sum rule (16) in Fig. 2d. We have checked that via spatial integration these results also validate the global variance identity $\beta\langle\hat{\mathbf{F}}_{\text{ext}}^0\hat{\mathbf{F}}_{\text{ext}}(\mathbf{r})\rangle = \int d\mathbf{r}\rho(\mathbf{r})\nabla\nabla V_{\text{ext}}(\mathbf{r})$ ³⁴, which follows from Eq. (13) with operator $\hat{A} = 1$. For the presently considered system, the global force-force correlation on the left-hand side is only marginally (0.4%) smaller than the global mean potential curvature on the right-hand side.

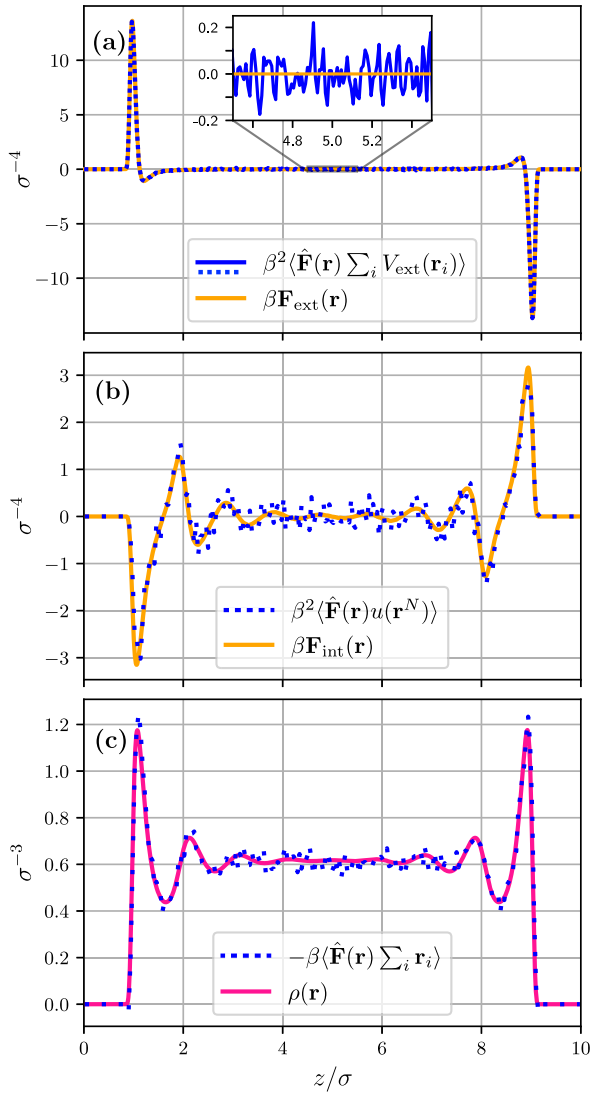


Fig. 3 | Demonstration of Noether sum rules (19), (20), and (21). These identities are respectively based on the global external and interparticle energies and on the center of mass. Shown are results from adaptive BD simulations for the LJ fluid between parallel LJ walls as a function of the scaled distance z/σ . **a** Comparison of $\beta^2 \langle \hat{\mathbf{F}}(\mathbf{r}) \sum_i V_{\text{ext}}(\mathbf{r}_i) \rangle$ and $\beta \mathbf{F}_{\text{ext}}(\mathbf{r}) = -\beta \rho(\mathbf{r}) \nabla V_{\text{ext}}(\mathbf{r})$, see Eq. (19). **b** Comparison of $\beta^2 \langle \hat{\mathbf{F}}(\mathbf{r}) u(\mathbf{r}^N) \rangle$ and $\beta \mathbf{F}_{\text{int}}(\mathbf{r})$, see Eq. (20). **c** Comparison of $-\beta \langle \hat{\mathbf{F}}(\mathbf{r}) \sum_i \mathbf{r}_i \rangle$ and $\rho(\mathbf{r})$, see Eq. (21).

Local shifting applications

We turn to the application of the locally resolved hyperforce sum rules (10) and (11). We recall from the *Methods* section that the seemingly trivial case $\hat{A} = 1$ reduces the local hyperforce identity (11) to the locally resolved force balance relationship $\mathbf{F}(\mathbf{r}) = \langle \hat{\mathbf{F}}(\mathbf{r}) \rangle = 0$. The definition of the total force operator (9) and carrying out the average gives the more explicit form $-k_B T \nabla \rho(\mathbf{r}) + \mathbf{F}_{\text{int}}(\mathbf{r}) - \rho(\mathbf{r}) \nabla V_{\text{ext}}(\mathbf{r}) = 0$, i.e., the first member (1) of the Yvon-Born-Green hierarchy¹. Typically this identity is derived from multiplying the equilibrium probability distribution function Ψ_{eq} by the gradient of the interaction potential and integrating over the degrees of freedom of $N - 1$ particles. We emphasize that arguably the simplest possible application of Eq. (11) yields such a central result of liquid state theory with very little effort. From the Noetherian point of view the result was also obtained from applying the locally resolved transformation (5) and (6) to the

free energy^{33,35}. At the heart of these Noetherian derivations lies the invariance of the Hamiltonian, of the phase space integration measure, and hence of the partition sum.

We next consider setting $\hat{A} = \hat{\mathbf{F}}_{\text{ext}}^0$ in Eq. (10). This constitutes a valuable consistency check with the above global shifting of $\hat{\mathbf{F}}(\mathbf{r})$ that led to Eq. (16) and which we can identically reproduce here. Arguably even more fundamentally the sum rule (16) can be obtained by considering mixed local-global shifting invariance at second order, i.e., building the mixed derivative $\partial(\delta\Omega/\delta\epsilon(\mathbf{r}))/\partial\epsilon_0 = 0$, where the grand potential $\Omega = -k_B T \ln \Xi$ is subject to the combined displacement $\mathbf{r}_i \rightarrow \mathbf{r}_i + \epsilon_0 + \epsilon(\mathbf{r}_i)$. Furthermore increasing the spatial resolution and hence selecting $\hat{A} = \hat{\mathbf{F}}(\mathbf{r})$ in Eq. (10) yields the recent Noether-constrained two-body force-correlation theory, which is discussed in detail by Sammüller et al.³⁶. The theory that is presented therein can hence be viewed as the special case of pure force-dependence within the hyperforce framework.

Reverting back to developing the general theory, here we generalize to higher orders by iteratively replacing $\hat{A}(\mathbf{r}^N, \mathbf{p}^N)$ by $\hat{\mathbf{F}}(\mathbf{r})\hat{A}(\mathbf{r}^N, \mathbf{p}^N)$ in Eq. (8). This leads to the following second-order hyperforce sum rule:

$$\beta^2 \langle \hat{\mathbf{F}}(\mathbf{r}) \hat{\mathbf{F}}(\mathbf{r}') \hat{A} \rangle = \beta \left\langle \hat{A} \frac{\delta^2 H[\epsilon]}{\delta\epsilon(\mathbf{r})\delta\epsilon(\mathbf{r}')} \right\rangle + \left\langle \frac{\delta^2 \hat{A}[\epsilon]}{\delta\epsilon(\mathbf{r})\delta\epsilon(\mathbf{r}')} \right\rangle, \quad (17)$$

where evaluation of the right-hand side at $\epsilon(\mathbf{r}) = 0$ is suppressed in the notation and $\delta^2 H[\epsilon]/\delta\epsilon(\mathbf{r})\delta\epsilon(\mathbf{r}')$ is discussed by Sammüller et al.³⁶. In case of no dependence of \hat{A} on momenta, i.e., $\hat{A} = \hat{A}(\mathbf{r}^N)$, the second term on the right-hand side of Eq. (17) can be made more explicit as

$$\left\langle \frac{\delta^2 \hat{A}[\epsilon, \mathbf{r}^N]}{\delta\epsilon(\mathbf{r})\delta\epsilon(\mathbf{r}')} \right\rangle = \left\langle \sum_{ij} \delta(\mathbf{r} - \mathbf{r}_i) \delta(\mathbf{r}' - \mathbf{r}_j) \nabla_i \nabla_j \hat{A}(\mathbf{r}^N) \right\rangle. \quad (18)$$

We proceed beyond forces by turning to energies with the aim of exploiting their thermal Noether invariance against shifting. We consider both the global external potential energy $\hat{A} = \sum_i V_{\text{ext}}(\mathbf{r}_i)$ as well as the global interparticle energy $\hat{A} = u(\mathbf{r}^N)$. Applying Eq. (11) yields in these two cases respectively the following sum rules:

$$\beta \langle \hat{\mathbf{F}}(\mathbf{r}) \sum_i V_{\text{ext}}(\mathbf{r}_i) \rangle = -\rho(\mathbf{r}) \nabla V_{\text{ext}}(\mathbf{r}), \quad (19)$$

$$\beta \langle \hat{\mathbf{F}}(\mathbf{r}) u(\mathbf{r}^N) \rangle = \mathbf{F}_{\text{int}}(\mathbf{r}). \quad (20)$$

Simulation results that demonstrate the validity of Eqs. (19) and (20) are shown in Fig. 3a, b, respectively. Here we have increased the overall density by reducing the lateral box size to 5σ and we sample $N = 128$ particles over time periods of 2000τ (data shown in Fig. 3a, b) and of 8000τ (data shown in Fig. 3c).

The potential energy identities (19) and (20) can be supplemented by considering the kinetic energy, $\hat{A} = \sum_i \mathbf{p}_i^2 / (2m)$, which leads upon using Eq. (10) to the identity $\beta \langle \hat{\mathbf{F}}(\mathbf{r}) \sum_i \mathbf{p}_i^2 / (2m) \rangle = -k_B T \nabla \rho(\mathbf{r})$. Treating then the entire Hamiltonian, $\hat{A} = H$, follows from adding up all three energy contributions. The result is the compact identity: $\beta \langle \hat{\mathbf{F}}(\mathbf{r}) H \rangle = \mathbf{F}(\mathbf{r}) = 0$. This possibly unexpected behavior also holds for the global entropy. We choose the entropy operator $\hat{A} = \hat{S} \equiv -k_B \ln \Psi_{\text{eq}}$ and obtain from Eq. (10) $k_B^{-1} \langle \hat{\mathbf{F}}(\mathbf{r}) \hat{S} \rangle = \mathbf{F}(\mathbf{r}) = 0$, i.e., the correlation (as well as the covariance) of the entropy operator with the local force density vanishes. This behavior is very different from the nontrivial fluctuation profile that is obtained from the covariance of the density operator with the global entropy^{11,12}.

As a final case, we consider the center of mass $\sum_i \mathbf{r}_i / N$ as a purely mechanical entity. We multiply by N , such that $\hat{A} = \sum_i \mathbf{r}_i$ and obtain from Eq. (11) upon multiplication by -1 the result

$$-\beta \left\langle \hat{\mathbf{F}}(\mathbf{r}) \sum_i \mathbf{r}_i \right\rangle = \rho(\mathbf{r}) \mathbb{1}. \quad (21)$$

Integrating Eq. (21) over position yields a simple relationship between the correlator of the global external force and the center of mass: $\langle \hat{F}_{\text{ext}} \sum_i \mathbf{r}_i \rangle / N = -k_B T \mathbf{1}$, where the mean number of particles is $N = \int d\mathbf{r} \rho(\mathbf{r}) \equiv \langle N \rangle$. Except for an additional sum over all particles, this global relationship is akin to the equipartition theorem. We present simulation results for both sides of the locally resolved Eq. (21) in Fig. 3c. The accurate agreement of the respective profiles confirms that the identity (21) indeed offers a rather unusual route to gain access to the density profile.

Hyperforce sampling and equilibration testing

Besides the unexpected insights into the general correlation structure of equilibrium many-body systems that the thermal Noether invariance delivers, our results are useful for the careful assessment and construction of computer sampling schemes. Force sampling^{13–19} in perhaps its most intuitive form¹⁵ rests on spatial integration of the YBG equation (1) such that the density profile is obtained via $\rho(\mathbf{r}) = \rho_0 + \beta \nabla^{-1} \cdot [\mathbf{F}_{\text{int}}(\mathbf{r}) - \rho(\mathbf{r}) \nabla V_{\text{ext}}(\mathbf{r})]$, where $\rho_0 = \text{const}$ is an integration constant and ∇^{-1} is an inverse ∇ operator. The data input on the right-hand side is obtained via sampling $\mathbf{F}_{\text{int}}(\mathbf{r}) = \langle \hat{\mathbf{F}}_{\text{int}}(\mathbf{r}) \rangle$ and either $\rho(\mathbf{r}) = \langle \hat{\rho}(\mathbf{r}) \rangle$ or $\mathbf{F}_{\text{ext}}(\mathbf{r}) = -\langle \sum_i \delta(\mathbf{r} - \mathbf{r}_i) \nabla_i V_{\text{ext}}(\mathbf{r}_i) \rangle$. The averages denote those that are being carried out in the simulation. In the present planar geometry ∇^{-1} reduces to carrying out a simple position integral, which we make explicit below.

Summarizing, we can compare the results from four different routes: i) counting of particle occurrences in a position-resolved histogram, which constitutes the standard method, ii) force sampling¹⁵ according to Eq. (1), iii) hyperforce sampling according to the global external force correlation in Eq. (14) with spatial integration post-processing, and iv) center-of-mass-based hyperforce sampling according to Eq. (21). These routes are respectively given by the following explicit expressions:

$$\rho(z) = \langle \hat{\rho}(z) \rangle, \tag{22}$$

$$\rho(z) = \rho_0 + \beta \int_0^z dz' \langle \hat{F}_U(z') \rangle, \tag{23}$$

$$\rho(z) = \rho_0 + \beta \int_0^z dz' \langle \hat{F}_{\text{ext}}^0 \hat{\rho}(z') \rangle, \tag{24}$$

$$\rho(z) = -\beta \left\langle \hat{F}(z) \sum_i z_i \right\rangle. \tag{25}$$

Here we choose the integration constant as $\rho_0 = \rho(0) = 0$ due to the divergent wall potential at $z = 0$. The averages on the above right-hand sides denote the actual simulation data, all vectors have been projected onto the z -direction across the pore, and z_i denotes the z -component of the particle position \mathbf{r}_i . In more detail, the operators on the right-hand sides of Eqs. (22) and (23) are explicitly given as $\hat{\rho}(z) = \sum_i \delta(z - z_i) / L^2$ and $\hat{F}_U(z) = \sum_{i,j}^{\text{int}} \delta(z - z_i) / L^2 - \hat{\rho}(z) \partial V_{\text{ext}}(z) / \partial z$, where we recall that L^2 is the lateral system size and the z -component of the interparticle force on particle i is $f_{i,z}^{\text{int}} = -\partial u(\mathbf{r}^N) / \partial z_i$. Furthermore the operators on the right-hand sides of Eqs. (24) and (25) are $\hat{F}_{\text{ext}}^0 = -\sum_i \partial V_{\text{ext}}(z_i) / \partial z_i$, and $\beta \hat{F}(z) = \beta \hat{F}_U(z) - \partial \hat{\rho}(z) / \partial z$.

Results for the density profile from the four routes (22)–(25) are shown in Fig. 4. The simulation parameters are identical as before [Fig. 2]. We display the four different statistical estimators for the density profile, as obtained after increasing runlength of (a) 10^5 , (b) 10^6 , (c) 10^7 , and (d) 3×10^8 simulation steps. We recall that as demonstrated above both in the numerical examples as well as in the formal statistical mechanical derivations, the results from all routes are formally identical. In practice, pronounced differences can be observed and these are due to the simulation averages being mere approximations for the true statistical mechanical equilibrium.

For example the routes (23) and (24) yield less statistical noise due to the spatial integration, but they however can instead accumulate systematic

deviations. The expected differences between the four methods are also consistently demonstrated by the fact that the results from the different routes mutually agree better for increasing runlengths. Nevertheless, in particular, the routes (24) and (25) that involve global quantities are very sensitive to the choice of runlength and they can hence serve as indicators of the overall quality of the sampling routine, even when quantities beyond the density profile are the very aim of the simulation. Having such tools for quality control can be particularly useful when investigating capillary and wetting phenomena^{42–46} where surface phase transitions pose significant challenges for reliable prediction.

The Noetherian hyperforce framework allows us to easily go beyond the density profile and we wish to address the interparticle force density as a target, rather than the mere source that it played in contributing to Eq. (23) above for the force sampling. As a demonstration we use and contrast different estimators for the interparticle force density profile $\mathbf{F}_{\text{int}}(\mathbf{r})$. The traditional counting method of filling a position-resolved histogram forms the baseline and Eq. (15) provides an alternative. These methods are respectively given by

$$F_{\text{int}}(z) = \langle \hat{F}_{\text{int}}(z) \rangle, \tag{26}$$

$$F_{\text{int}}(z) = \beta \int_0^z dz' \langle \hat{F}_{\text{ext}}^0 \hat{F}_{\text{int}}(z') \rangle. \tag{27}$$

Figure 5 presents both canonical averages obtained via adaptive BD⁴¹ as well as grand canonical Monte Carlo data. The chemical potential is chosen as $\mu/c = 1$ and the resulting average number of particles is $\langle N \rangle = 136.5$. In the corresponding adaptive BD simulation runs we have set $N = 136$, which remains sharply fixed in the course of time. The agreement between both sets of results confirms the expectation of independence of the sum rule validity on the choice of ensemble. This is based on the fact that the theoretical derivations continue to hold with fixed N , as we have also explicitly verified. Hence the mechanical effects that the Noether invariance against spatial displacement captures are oblivious to the presence of global particle number fluctuations. We recall that the latter are precisely captured and quantified by the local compressibility^{8–10}.

The comparison of lower and higher quality statistical data, as obtained from sampling every step (see Fig. 5a, b) or only every 1000th step (see Fig. 5c, d) demonstrates that the force correlation method is a sensitive measure of the degree of sampling quality.

Conclusions

In conclusion, we have developed a statistical mechanical hyperforce framework in generalization of the YBG equilibrium force balance relationship (1). Our theory is based on previously developed global^{1,32,34} and local^{13,35} shifting transformations on phase space. These variable transformations leave the thermal physics invariant despite an apparent dependence on the transformation parameter. The parameter is a three-dimensional globally constant vector in case of global symmetry, which applies to the entirety of the system, and a position-dependent three-dimensional vector field for the locally resolved case. Treating the corresponding phase space transformations according to Noether’s invariant variational calculus²¹ allows us to systematically generate exact identities.

Here we have generalized this Noetherian concept to the equilibrium average of an arbitrary given phase space function \hat{A} . The resulting Noether identities couple in a specific manner the forces, which the underlying Hamiltonian generates, to the observable \hat{A} and its gradient with respect to the phase space variables. In the position-resolved case, we obtain localized correlation functions, with the Dirac distribution generating microscopically sharp, but statistically coarse-grained and hence well-accessible correlators. In detail, we have presented the global hyperforce sum rule (4) that applies to any given phase space function \hat{A} . The local versions comprise Eqs. (10) and Eq. (11), where the latter version applies to momentum-independent observables. Decomposing the total force operator into its ideal, interparticle, and external contributions leads to Eq. (12), which

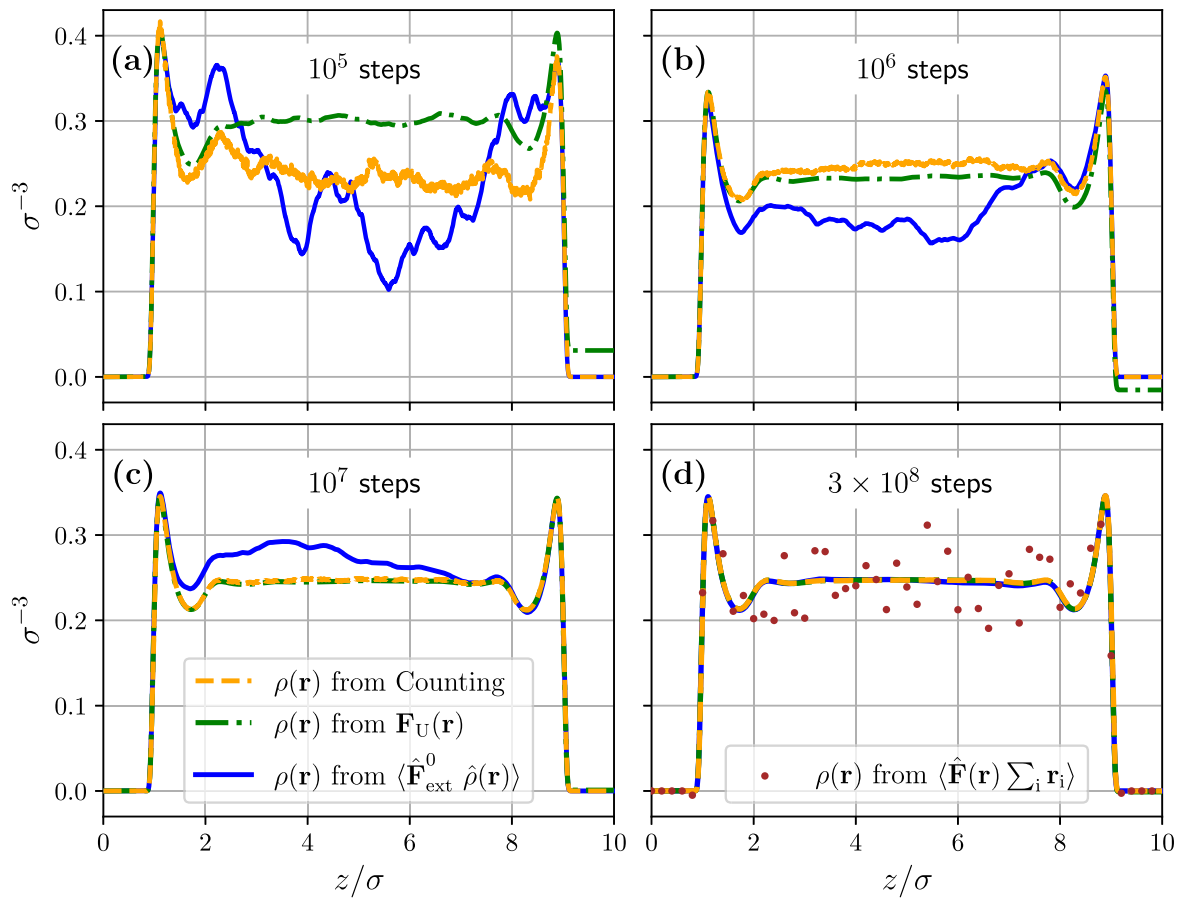


Fig. 4 | Comparison of standard counting against force sampling. We show results from four different routes towards the density profile $\rho(\mathbf{r})$ as obtained after **a** 10^5 , **b** 10^6 , **c** 10^7 , **d** 3×10^8 simulation steps. Shown is data from the standard counting method according to Eq. (22) (orange lines), from force sampling $\mathbf{F}_U(\mathbf{r})$ according to Eq. (23) (green dash-dotted lines), from global external force correlation sampling of

$\langle \hat{\mathbf{F}}_{\text{ext}}^0 \hat{\rho}(\mathbf{r}) \rangle$ according to Eq. (24) (blue solid lines), and from center-of-mass correlation sampling of $\langle \hat{\mathbf{F}}(\mathbf{r}) \sum_i \mathbf{r}_i \rangle$ according to Eq. (25) (red symbols). Results from the latter route are only displayed from the longest run [panel **d**] and they still display considerable scatter, whereas the results from the remaining three methods already agree very satisfactorily.

generalizes the equilibrium force density balance (1). An overview of these general identities is shown in Fig. 6a.

For a variety of relevant concrete choices of the form of \hat{A} , we have demonstrated explicitly their validity via carrying out many-body simulations. This includes forces, energies, and entirely mechanical quantities such as the center of mass; see Fig. 6b for a summary of specific examples. We have shown that the sampling quality and equilibration properties depend significantly on the type of underlying sum rule. We argue that this behavior forms a valuable asset for the systematic assessment of simulation quality.

Our hyperforce identities complement the virial¹, hypervirial³⁷, equipartition¹ and Yvon¹ theorems. Despite certain formal similarities, we emphasize that the underlying phase space invariance is more fundamental than derivations based on ad hoc partial integration. Furthermore, the considered invariance operations naturally lead to correlations with either global or locally resolved forces, which are both simple to interpret and straightforward to acquire in simulations.

We have shown how the global hyperforce identity (4) can alternatively be obtained from the Yvon theorem¹. Hence, as anticipated in the discussion by Rotenberg¹³, the Yvon theorem can indeed be a relevant tool for force sampling. However, the general localized Noether sum rule (10) reaches beyond the Yvon theorem in terms of the momentum effects that are included. We have shown that the derivation of the momentum-independent sum rule (11) based on the Yvon theorem requires to apply

the ad hoc localized choice $\hat{A}\delta(\mathbf{r} - \mathbf{r}_i)$ and summing over i . As a second step, treating the ideal contribution explicitly allows to identify the sequence of emerging terms as the one-body force operator $\hat{\mathbf{F}}(\mathbf{r})$ at any position. Conversely, the Yvon theorem can be derived as a limit case from Noether invariance upon shifting only one given particle i according to $\mathbf{r}_i \rightarrow \mathbf{r}_i + \mathbf{e}_0$, and keeping unchanged all other particles coordinates \mathbf{r}_j with $j \neq i$.

Besides the theoretical connections that the Noether hyperforce sum rules establish, they can serve to carry out tests in theoretical and simulation approaches, with possible fruitful connections to the mapped-averaging force sampling framework¹⁶. The hyperforce sum rules can also provide a starting point, together with the existing body of equilibrium sum rules^{42–46}, for the construction of new inhomogeneous liquid state approximations. We have exemplified the use of sum rules in providing gauges for the equilibration quality of simulation data and we are confident in their future beneficial use in machine-learning approaches such as the recent neural functional theory^{47,48}.

In the context of the use of machine-learning in Statistical Mechanics^{47–54} sum rules were shown to provide tests for the successful construction of neural functionals both in^{47,48} and out of equilibrium⁴⁹. These sum rules amount to specific force properties, such as the vanishing of the global interparticle force⁴⁵ and the interrelation of different orders of direct correlation functions^{47,48}. The present much more general hyperforce framework can form much inspiration for such approaches as well as for the

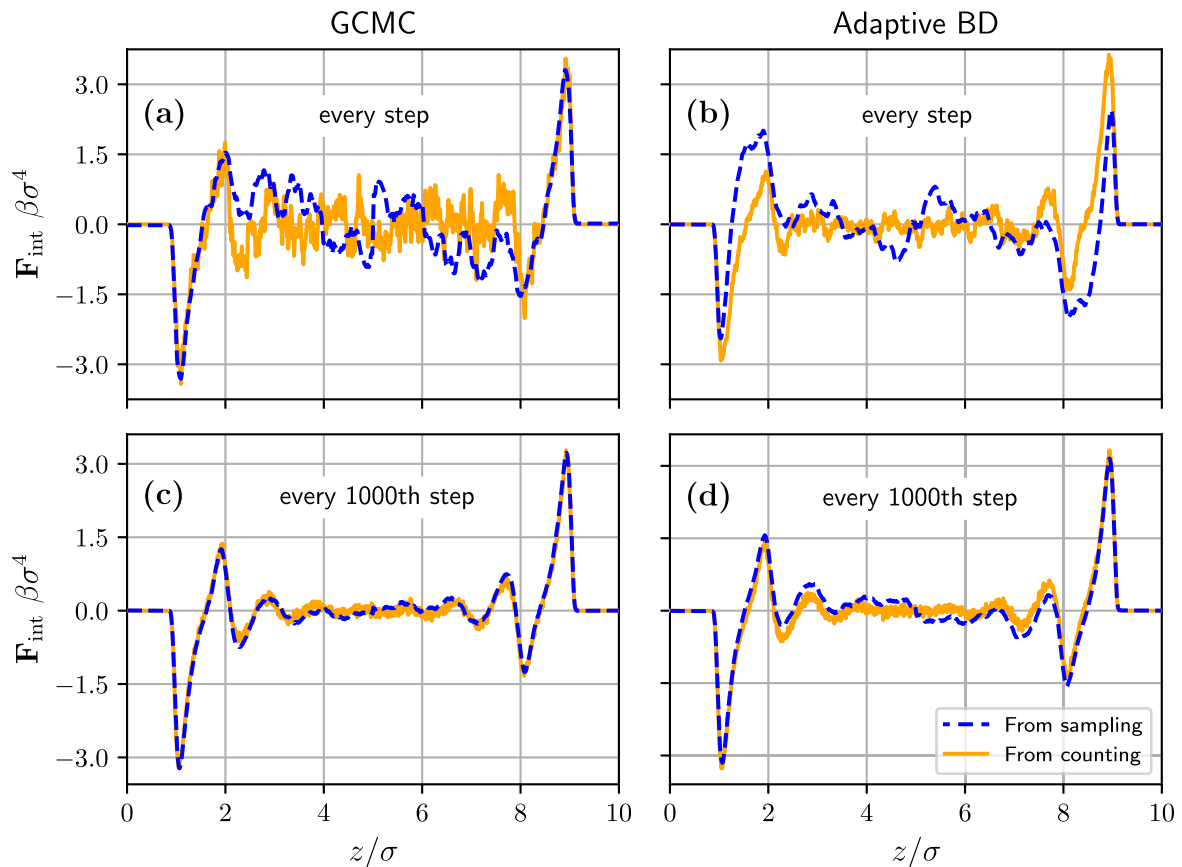


Fig. 5 | Comparison of different statistical estimators for the interparticle one-body force density profile according to Eq. (15). The results are obtained from the standard counting histogram method, $F_{\text{int}}(\mathbf{r}) = \langle \hat{F}_{\text{int}}(\mathbf{r}) \rangle$ (orange lines), and from hyperforce sampling and spatial integration of $\nabla F_{\text{int}}(\mathbf{r}) = \beta \langle \hat{F}_{\text{ext}}^0 \hat{F}_{\text{int}}(\mathbf{r}) \rangle$ (blue lines) with data for the right-hand side forming the basis. These methods are explicitly spelled out in Eqs. (26) and (27). The results stem from sampling 10^5 strongly correlated microstates at every simulation step (a, b) compared to better-

decorrelated configurations obtained from also 10^5 configurations, with the samples being taken only every 1000th simulation step (c, d). Results are shown from grand canonical Monte Carlo simulations (a, c) and from adaptive BD simulations (b, d). The results from sampling are symmetrized with respect to mirroring at the center of the pore, i.e., via building the arithmetic mean $[F_{\text{int}}(z) - F_{\text{int}}(L - z)]/2$, as is common practice in force sampling schemes.

recent force-based density functional theory^{35,55}, which was compared⁵⁵ to standard fundamental measure theory⁵⁶.

Furthermore, investigating hyperforce correlations in ionic systems, recent work^{57–59} addresses both concentration and charge fluctuation behavior, as are also relevant in confined systems⁶⁰, appears to be very promising. This also holds true for further interfacial physics^{42–46} and potentially for the higher-order correlation functions^{3–5}.

In our theoretical derivations we have relied on the grand canonical ensemble, with fixed chemical potential μ and fluctuating number of particles N . Carrying out formal manipulations in this way is often more straightforward than working with fixed N , as is appropriate for a canonical treatment. (Temperature is constant in both ensembles.) A prominent example is to obtain the density profile as a functional derivative $\rho(\mathbf{r}) = \delta\Omega / \delta V_{\text{ext}}(\mathbf{r})$ where crucially μ is kept fixed, rather than N , upon building the functional derivative. This prototypical example demonstrates the elegance of working grand canonically, and one could expect that a similar situation applies to the thermal Noether invariance. This, however, is not the case. Rather the phase space shifting transformation, whether global by a constant ϵ_0 or locally resolved in position via a three-dimensional vector field $\epsilon(\mathbf{r})$, is an entirely mechanical operation that applies equally well canonically. The shifting invariance gives a powerful new route to correlation functions and their sum rules, an alternative to the traditional method of integrating over degrees of freedom, as pioneered by Yvon⁶¹ and Born and Green⁶².

A detailed account of global shifting in the canonical ensemble is provided by Hermann and Schmidt³². The resulting Noether force identities are analogous in form to the results from a grand canonical treatment³¹, with the sole (and trivial) difference of the definition of the respective ensemble averages. Here we find that the analogous situation holds for the hyperforce identities. As they originate from phase space transformations only, they are insensitive to the ensemble differences between the canonical and the grand ensemble. This theoretical fact is corroborated by our computer simulation results, where we have explicitly compared grand canonical Monte Carlo data and canonical results, with the latter obtained via sampling under adaptive BD time evolution⁴¹.

We have used overdamped Brownian time evolution as a means to sample in thermal equilibrium. We find the adaptive Brownian dynamics time stepping algorithm⁴¹ to be a convenient choice for our present purposes. The principle validity of the hyperforce sum rules is nevertheless independent thereof and we expect careful use of either the simpler Euler-Maruyama method^{41,63} or indeed Molecular Dynamics⁶³ to yield identical results. In our BD simulations, we have sampled all correlation functions at equal time as is the appropriate limit in equilibrium time evolution to recover static thermal ensemble averages. We refer to Hermann and Schmidt³¹ for the exploitation of the Noether invariance in nonequilibrium dynamics.

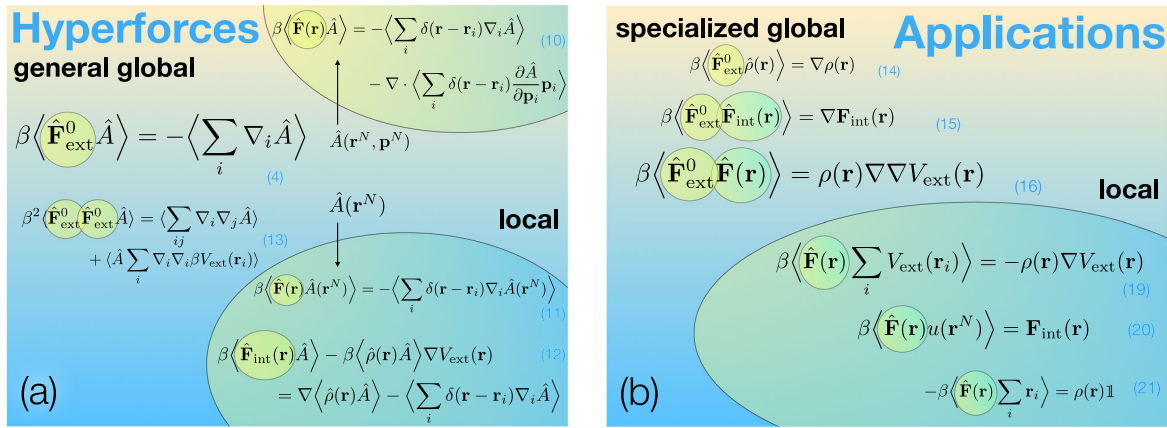


Fig. 6 | Overview of theoretical results. **a** Hyperforce sum rules that relate a given observable with the forces that act in the system. The global sum rules (4) and (13) couple the global external force operator $\hat{\mathbf{F}}_{\text{ext}}^0$ at first and second order with an observable $\hat{A}(\mathbf{r}^N, \mathbf{p}^N)$. The local sum rules (10), (11), and (12) contain the localized force density operator $\hat{\mathbf{F}}(\mathbf{r})$ and its interparticle contribution $\hat{\mathbf{F}}_{\text{int}}(\mathbf{r})$ and they apply for full phase space-dependence $\hat{A}(\mathbf{r}^N, \mathbf{p}^N)$ (upper bubble) or coordinate-only dependence $\hat{A}(\mathbf{r}^N)$ (lower bubble). In the latter case alternative forms involve the

total local force density $\hat{\mathbf{F}}(\mathbf{r})$ or the splitting (1) into its three constituent contributions. **b** Sum rules that result from specific observable choices. Global examples set $\hat{A}(\mathbf{r}^N, \mathbf{p}^N)$ as the density operator $\hat{\rho}(\mathbf{r})$, the interparticle force density operator $\hat{\mathbf{F}}_{\text{int}}(\mathbf{r})$, and the total local force density operator $\hat{\mathbf{F}}(\mathbf{r})$, as corresponds to the sum rules (14), (15), and (16), respectively. The local examples include the total external potential energy $\sum_i V_{\text{ext}}(\mathbf{r}_i)$, the interparticle energy $u(\mathbf{r}^N)$, and the sum of all particle coordinates $\sum_i \mathbf{r}_i$, corresponding to the sum rules (19), (20), and (21), respectively.

As a final note, we return to classical density functional theory and its prowess in the description and incorporation of the fundamental force correlators that emerge from the hyperforce concept. We recall that classical density functional theory is based on a formally exact variational principle which amounts to solving the following Euler-Lagrange equation:

$$k_B T c_1(\mathbf{r}, [\rho]) - V_{\text{ext}}(\mathbf{r}) = k_B T \ln \rho(\mathbf{r}) - \mu. \quad (28)$$

Here $c_1(\mathbf{r}, [\rho])$ is the one-body direct correlation function of inhomogeneous liquid state theory. This is expressed as a density functional via $c_1(\mathbf{r}, [\rho]) = -\beta \delta F_{\text{exc}}[\rho] / \delta \rho(\mathbf{r})$, where $F_{\text{exc}}[\rho]$ is the intrinsic excess Helmholtz free energy functional, which contains the interparticle interactions, and $\delta / \delta \rho(\mathbf{r})$ denotes the functional derivative with respect to the density profile. Solving Eq. (28) for given T, μ , and $V_{\text{ext}}(\mathbf{r})$ yields results for the equilibrium density profile $\rho(\mathbf{r})$, which is hence the central variable of density functional theory.

A multitude of connections with the current invariance theory emerge naturally. From the density profile, using the hyperforce identities one can obtain results for $\langle \hat{\mathbf{F}}(\mathbf{r}) \sum_i \mathbf{r}_i \rangle$ via Eq. (21), for $\langle \hat{\mathbf{F}}_{\text{ext}}^0 \hat{\mathbf{F}}(\mathbf{r}) \rangle$ via Eq. (16), for $\langle \hat{\mathbf{F}}(\mathbf{r}) \sum_i V_{\text{ext}}(\mathbf{r}_i) \rangle$ via Eq. (19), and upon building the gradient of the density profile for $\langle \hat{\mathbf{F}}_{\text{ext}}^0 \hat{\rho}(\mathbf{r}) \rangle$ via Eq. (14).

We can make further progress by noting that within density functional theory the interparticle force density is given by $\mathbf{F}_{\text{int}}(\mathbf{r}) = k_B T \rho(\mathbf{r}) \nabla c_1(\mathbf{r})$, where we have suppressed the functional dependence on the density profile in the notation. That this relationship holds can be seen from building the gradient of Eq. (28) whereby $-\nabla \mu$ vanishes as the chemical potential is constant, multiplying by $\rho(\mathbf{r})$, and comparing term-wise with the force density balance relationship (1).

Having obtained $\mathbf{F}_{\text{int}}(\mathbf{r})$ in this (density functional) way gives access to $\langle \hat{\mathbf{F}}(\mathbf{r}) u(\mathbf{r}^N) \rangle$ via Eq. (20). Building the gradient of the interparticle force density via the product rule yields $\nabla \mathbf{F}_{\text{int}}(\mathbf{r}) = k_B T [\nabla \rho(\mathbf{r})] \nabla c_1(\mathbf{r}) + k_B T \rho(\mathbf{r}) \nabla \nabla c_1(\mathbf{r})$. Again in principle, the right-hand side is straightforward to evaluate in a typical numerical density functional study as data for both $\rho(\mathbf{r})$ and $c_1(\mathbf{r})$ is accessible. As a result, the correlator $\langle \hat{\mathbf{F}}_{\text{ext}}^0 \hat{\mathbf{F}}_{\text{int}}(\mathbf{r}) \rangle$ is available via the hyperforce sum rule (15).

Hence standard results that are obtained within the density functional framework allow to access a wealth of nontrivial force correlation structures.

This additional information is not redundant. We compare with Evans and his coworkers' local compressibility $\chi_\mu(\mathbf{r}) = \partial \rho(\mathbf{r}) / \partial \mu$, where similar to the present force setup, one obtains $\chi_\mu(\mathbf{r})$ from processing the density profile. In practice then analyzing $\chi_\mu(\mathbf{r})$ can shed significantly more light on the physics than what is apparent from the density profile alone, as has been demonstrated in a range of insightful studies on drying at substrates and the important phenomenon of hydrophobicity⁸⁻¹⁰.

Data availability

The data is available from the authors upon reasonable request.

Code availability

The simulation code to generate the data in this study is available online at the following URL: <https://gitlab.uni-bayreuth.de/bt306964/mbd/-/tree/hyperforce>.

Received: 23 October 2023; Accepted: 20 February 2024;

Published online: 21 March 2024

References

- Hansen, J. P. and McDonald, I. R. *Theory of Simple Liquids*, 4th edn. (Academic Press, London, 2013).
- Evans, R. The nature of the liquid-vapour interface and other topics in the statistical mechanics of non-uniform, classical fluids. *Adv. Phys.* **28**, 143 (1979).
- Zhang, Z. & Kob, W. Revealing the three-dimensional structure of liquids using four-point correlation functions. *Proc. Natl Acad. Sci. USA* **117**, 14032 (2020).
- Singh, N., Zhang, Z., Sood, A. K., Kob, W. & Ganapathy, R. Intermediate-range order governs dynamics in dense colloidal liquids. *Proc. Natl Acad. Sci. USA* **120**, e2300923120 (2023).
- Pihlajamaa, I., Laudicina, C. C. L., Luo, C. & Janssen, L. M. C. Emergent structural correlations in dense liquids. *PNAS Nexus* **2**, pgad184 (2023).
- Evans, R. in *Fundamentals of Inhomogeneous Fluids*. Chap. 3. (ed. Henderson, D.) (Dekker, New York, 1992).
- Evans, R., Oettel, M., Roth, R. & Kahl, G. New developments in classical density functional theory. *J. Phys. Condens. Matter* **28**, 240401 (2016).

8. Evans, R. & Stewart, M. C. The local compressibility of liquids near non-adsorbing substrates: a useful measure of solvophobicity and hydrophobicity? *J. Phys. Condens. Matter* **27**, 194111 (2015).
9. Evans, R., Stewart, M. C. & Wilding, N. B. A unified description of hydrophilic and superhydrophobic surfaces in terms of the wetting and drying transitions of liquids. *Proc. Natl Acad. Sci. USA* **116**, 23901 (2019).
10. Coe, M. K., Evans, R. & Wilding, N. B. Density depletion and enhanced fluctuations in water near hydrophobic solutes: identifying the underlying physics. *Phys. Rev. Lett.* **128**, 045501 (2022).
11. Eckert, T., Stuhlmüller, N. C. X., Sammüller, F. & Schmidt, M. Fluctuation profiles in inhomogeneous fluids. *Phys. Rev. Lett.* **125**, 268004 (2020).
12. Eckert, T., Stuhlmüller, N. C. X., Sammüller, F. & Schmidt, M. Local measures of fluctuations in inhomogeneous liquids: Statistical mechanics and illustrative applications. *J. Phys. Condens. Matter* **35**, 425102 (2023).
13. Rotenberg, B. Use the force! Reduced variance estimators for densities, radial distribution functions, and local mobilities in molecular simulations. *J. Chem. Phys.* **153**, 150902 (2020).
14. Borgis, D., Assaraf, R., Rotenberg, B. & Vuilleumier, R. Computation of pair distribution functions and three-dimensional densities with a reduced variance principle. *Mol. Phys.* **111**, 3486 (2013).
15. de las Heras, D. & Schmidt, M. Better than counting: Density profiles from force sampling. *Phys. Rev. Lett.* **120**, 218001 (2018).
16. Purohit, A., Schultz, A. J. & Kofke, D. A. Force-sampling methods for density distributions as instances of mapped averaging. *Mol. Phys.* **117**, 2822 (2019).
17. Coles, S. W., Borgis, D., Vuilleumier, R. & Rotenberg, B. Computing three-dimensional densities from force densities improves statistical efficiency. *J. Chem. Phys.* **151**, 064124 (2019).
18. Coles, S. W., Mangaud, E., Frenkel, D. & Rotenberg, B. Reduced variance analysis of molecular dynamics simulations by linear combination of estimators. *J. Chem. Phys.* **154**, 191101 (2021).
19. Coles, S. W., Morgan, B. J. & Rotenberg, B. RevelsMD: Reduced variance estimators of the local structure in molecular dynamics. <https://arxiv.org/abs/2310.06149> (2023).
20. Schmidt, M. Power functional theory for many-body dynamics. *Rev. Mod. Phys.* **94**, 015007 (2022).
21. Noether, E. Invariante Variationsprobleme. *Nachr. d. Königl. Gesellsch. d. Wiss. zu Göttingen, Math.-Phys. Klasse* **235**, 183 (1918). English translation by M. A. Tavel: Invariant variation problems. *Transp. Theor. Stat. Phys.* **1**, 186 (1971); for a version in modern typesetting see: Frank Y. Wang. <https://arxiv.org/abs/physics/0503066> (2018) .
22. Byers, N. E. Noether’s discovery of the deep connection between symmetries and conservation laws. <https://arxiv.org/abs/physics/9807044> (1998).
23. Baez, J. C. & Fong, B. A Noether theorem for Markov processes. *J. Math. Phys.* **54**, 013301 (2013).
24. Marvian, I. & Spekkens, R. W. Extending Noether’s theorem by quantifying the asymmetry of quantum states. *Nat. Commun.* **5**, 3821 (2014).
25. Sasa, S. & Yokokura, Y. Thermodynamic entropy as a Noether invariant. *Phys. Rev. Lett.* **116**, 140601 (2016).
26. Sasa, S., Sugiura, S. & Yokokura, Y. Thermodynamical path integral and emergent symmetry. *Phys. Rev. E* **99**, 022109 (2019).
27. Revzen, M. Functional integrals in statistical physics. *Am. J. Phys.* **38**, 611 (1970).
28. Budkov, Y. A. & Kolesnikov, A. L. Modified Poisson-Boltzmann equations and macroscopic forces in inhomogeneous ionic fluids. *J. Stat. Mech.* **2022**, 053205 (2022).
29. Brandyshev, P. E. & Budkov, Y. A. Noether’s second theorem and covariant field theory of mechanical stresses in inhomogeneous ionic fluids. *J. Chem. Phys.* **158**, 174114 (2023).
30. Bravetti, A., Garcia-Ariza, M. A. & Tapias, D. Thermodynamic entropy as a Noether invariant from contact geometry. *Entropy* **25**, 1082 (2023).
31. Hermann, S. & Schmidt, M. Noether’s theorem in statistical mechanics. *Commun. Phys.* **4**, 176 (2021).
32. Hermann, S. & Schmidt, M. Why Noether’s theorem applies to statistical mechanics. *J. Phys.: Condens. Matter* **34**, 213001 (2022).
33. Hermann, S. & Schmidt, M. Force balance in thermal quantum many-body systems from Noether’s theorem. *J. Phys. A: Math. Theor.* **55**, 464003 (2022). (Special Issue: *Clartons and the Asymptotics of ideas: the Physics of Michael Berry*).
34. Hermann, S. & Schmidt, M. Variance of fluctuations from Noether invariance. *Commun. Phys.* **5**, 276 (2022).
35. Tschopp, S. M., Sammüller, F., Hermann, S., Schmidt, M. & Brader, J. M. Force density functional theory in- and out-of-equilibrium. *Phys. Rev. E* **106**, 014115 (2022).
36. Sammüller, F., Hermann, S., de las Heras, D. & Schmidt, M. Noether-constrained correlations in equilibrium liquids. *Phys. Rev. Lett.* **130**, 268203 (2023).
37. Hirschfelder, J. O. Classical and quantum mechanical hypervirial theorems. *J. Chem. Phys.* **33**, 1462 (1960).
38. Goldstein, H., Poole, C. & Safko, J. *Classical Mechanics* (Addison-Wesley, New York, 2002).
39. Lovett, R. A., Mou, C. Y. & Buff, F. P. The structure of the liquid-vapor interface. *J. Chem. Phys.* **65**, 570 (1976).
40. Wertheim, M. S. Correlations in the liquid-vapor interface. *J. Chem. Phys.* **65**, 2377 (1976).
41. Sammüller, F. & Schmidt, M. Adaptive Brownian dynamics. *J. Chem. Phys.* **155**, 134107 (2021).
42. Upton, P. J. Fluids against hard walls and surface critical behavior. *Phys. Rev. Lett.* **81**, 2300 (1998).
43. Evans, R. & Parry, A. O. Liquids at interfaces: what can a theorist contribute? *J. Phys. Condens. Matter* **2**, SA15 (1990).
44. Henderson, J. R. & van Swol, F. On the interface between a fluid and a planar wall: theory and simulations of a hard sphere fluid at a hard wall. *Mol. Phys.* **51**, 991 (1984).
45. Henderson, J. R. & van Swol, F. On the approach to complete wetting by gas at a liquid-wall interface. *Mol. Phys.* **56**, 1313 (1985).
46. Triezenberg, D. G. & Zwanzig, R. Fluctuation theory of surface tension. *Phys. Rev. Lett.* **28**, 1183 (1972).
47. Sammüller, F., Hermann, S., de las Heras, D. & Schmidt, M. Neural functional theory for inhomogeneous fluids: Fundamentals and applications. *Proc. Natl Acad. Sci. USA* **120**, e2312484120 (2023).
48. Sammüller, F., Hermann, S. & Schmidt, M. Why neural functionals suit statistical mechanics. <https://arxiv.org/abs/2312.04681> (2023).
49. de las Heras, D., Zimmermann, T., Sammüller, F., Hermann, S. & Schmidt, M. Perspective: how to overcome dynamical density functional theory. *J. Phys. Condens. Matter* **35**, 271501 (2023).
50. Santos-Silva, T., Teixeira, P. I. C., Anquetil-Deck, C. & Cleaver, D. J. Neural-network approach to modeling liquid crystals in complex confinement. *Phys. Rev. E* **89**, 053316 (2014).
51. Lin, S.-C. & Oettel, M. A classical density functional from machine learning and a convolutional neural network. *SciPost Phys.* **6**, 025 (2019).
52. Lin, S.-C., Martius, G. & Oettel, M. Analytical classical density functionals from an equation learning network. *J. Chem. Phys.* **152**, 021102 (2020).
53. Cats, P. et al. Machine-learning free-energy functionals using density profiles from simulations. *APL Mater.* **9**, 031109 (2021).
54. Yatsyshin, P., Kalliadasis, S. & Duncan, A. B. Physics-constrained Bayesian inference of state functions in classical density-functional theory. *J. Chem. Phys.* **156**, 074105 (2022).
55. Sammüller, F., Hermann, S. & Schmidt, M. Comparative study of force-based classical density functional theory. *Phys. Rev. E* **107**, 034109 (2023).

56. Roth, R. Fundamental measure theory for hard-sphere mixtures: a review. *J. Phys. Condens. Matter* **22**, 063102 (2010).
57. Minh, T. H. N., Rotenberg, B. & Marbach, S. Ionic fluctuations in finite volumes: fractional noise and hyperuniformity. *Faraday Discuss.* **246**, 225 (2023).
58. Minh, T. H. N. et al. Electrical noise in electrolytes: a theoretical perspective. *Faraday Discuss.* **246**, 198 (2023).
59. Marbach, S. Intrinsic fractional noise in nanopores: The effect of reservoirs. *J. Chem. Phys.* **154**, 171101 (2021).
60. Minh, T. H. N., Stoltz, G. & Rotenberg, B. Frequency and field-dependent response of confined electrolytes from Brownian dynamics simulations. *J. Chem. Phys.* **158**, 104103 (2023).
61. Yvon, J. La théorie statistique des fluides et l'équation d'état (in French), *Actualités Scientifiques et Industrielles No. 203* (Hermann, Paris, 1935).
62. Born, M. & Green, H. A general kinetic theory of liquids I. The molecular distribution functions. *Proc. R. Soc. Lond., Ser. A* **188**, 10 (1946).
63. Frenkel, D. & Smit, B. *Understanding Molecular Simulation: From Algorithms to Applications*, 3rd edn. (Academic Press, London, 2023).

Acknowledgements

We thank Daniel de las Heras, Jonas Köglmayr, and David Limmer for useful discussions. This work is supported by the German Research Foundation (DFG) via Project No. 436306241. Funded by the Open Access Publishing Fund of the University of Bayreuth.

Author contributions

S.H. and M.S. designed the research. All authors carried out the analytical work. S.R. and F.S. performed the numerical work. All authors wrote the paper.

Funding

Open Access funding enabled and organized by Projekt DEAL.

Competing interests

The authors declare no competing interests.

Additional information

Supplementary information The online version contains supplementary material available at <https://doi.org/10.1038/s42005-024-01568-y>.

Correspondence and requests for materials should be addressed to Matthias Schmidt or Sophie Hermann.

Peer review information *Communications Physics* thanks the anonymous reviewers for their contribution to the peer review of this work. A peer review file is available.

Reprints and permissions information is available at <http://www.nature.com/reprints>

Publisher's note Springer Nature remains neutral with regard to jurisdictional claims in published maps and institutional affiliations.

Open Access This article is licensed under a Creative Commons Attribution 4.0 International License, which permits use, sharing, adaptation, distribution and reproduction in any medium or format, as long as you give appropriate credit to the original author(s) and the source, provide a link to the Creative Commons licence, and indicate if changes were made. The images or other third party material in this article are included in the article's Creative Commons licence, unless indicated otherwise in a credit line to the material. If material is not included in the article's Creative Commons licence and your intended use is not permitted by statutory regulation or exceeds the permitted use, you will need to obtain permission directly from the copyright holder. To view a copy of this licence, visit <http://creativecommons.org/licenses/by/4.0/>.

© The Author(s) 2024

OPEN ACCESS

IOP Publishing

Journal of Physics: Condensed Matter

J. Phys.: Condens. Matter **35** (2023) 271501 (31pp)<https://doi.org/10.1088/1361-648X/acb33>

CrossMark

Perspective

Perspective: How to overcome dynamical density functional theory

Daniel de las Heras ,
Toni Zimmermann ,
Florian Sammüller ,
Sophie Hermann 
and Matthias Schmidt* 

*Theoretische Physik II, Physikalisches
Institut, Universität Bayreuth,
D-95447 Bayreuth, Germany
E-mail:
Matthias.Schmidt@uni-bayreuth.de*

Abstract

We argue in favour of developing a comprehensive dynamical theory for rationalizing, predicting, designing, and machine learning nonequilibrium phenomena that occur in soft matter. To give guidance for navigating the theoretical and practical challenges that lie ahead, we discuss and exemplify the limitations of dynamical density functional theory (DDFT). Instead of the implied adiabatic sequence of equilibrium states that this approach provides as a makeshift for the true time evolution, we posit that the pending theoretical tasks lie in developing a systematic understanding of the dynamical functional relationships that govern the genuine nonequilibrium physics. While static density functional theory gives a comprehensive account of the equilibrium properties of many-body systems, we argue that power functional theory is the only present contender to shed similar insights into nonequilibrium dynamics, including the recognition and implementation of exact sum rules that result from the Noether theorem. As a demonstration of the power functional point of view, we consider an idealized steady sedimentation flow of the three-dimensional Lennard-Jones fluid and machine-learn the kinematic map from the mean motion to the internal force field. The trained model is capable of both predicting and designing the steady state dynamics universally for various target density modulations. This demonstrates the significant potential of using such techniques in nonequilibrium many-body physics and overcomes both the conceptual constraints of DDFT as well as the limited availability of its analytical functional approximations.

Keywords: density functional theory, dynamical density functional theory, power functional theory, Noether theorem, superadiabatic forces, Brownian dynamics, statistical mechanics of liquids

(Some figures may appear in colour only in the online journal)

1. Introduction

The coupled dynamics of the microscopic degrees of freedom in typical soft matter systems generates a wide array of relevant and also often unsolved nonequilibrium phenomena [1, 2]. One central quantity for the characterization of self-assembly and structure formation in complex systems is the microscopically resolved one-body density distribution $\rho(\mathbf{r}, t)$, where \mathbf{r} indicates position and t denotes time. The ‘density profile’ $\rho(\mathbf{r}, t)$ acts as a central order parameter both due to its intuitive physical interpretation and clear cut mathematical definition [3].

* Author to whom any correspondence should be addressed.



Original Content from this work may be used under the terms of the [Creative Commons Attribution 4.0 licence](https://creativecommons.org/licenses/by/4.0/). Any further distribution of this work must maintain attribution to the author(s) and the title of the work, journal citation and DOI.

According to the dynamical density functional theory (DDFT), as originally proposed by Evans in 1979 [4] and put at center stage by Marconi and Tarazona in 1999 [5], the time evolution of the microscopic density profile is assumed to be determined by the following partial differential equation:

$$\frac{\partial \rho(\mathbf{r}, t)}{\partial t} = \gamma^{-1} \nabla \cdot \rho(\mathbf{r}, t) \nabla \left(\frac{\delta F[\rho]}{\delta \rho(\mathbf{r}, t)} + V_{\text{ext}}(\mathbf{r}, t) \right). \quad (1)$$

Here γ is a friction constant, $F[\rho]$ is an intrinsic free energy functional that depends functionally on the density profile, and the external potential $V_{\text{ext}}(\mathbf{r}, t)$ represents interactions of the system with the environment. The system is set into motion by a temporal variation of $V_{\text{ext}}(\mathbf{r}, t)$, such as e.g. step-like switching at an initial time.

The time evolution according to equation (1) conserves the particle number locally and hence it constitutes dynamics of model B type [6]. In standard applications one starts with an equilibrium state of the system and then the dynamics are monitored on the basis of numerical time integration of equation (1), where the time dependence is induced by the temporal variation of $V_{\text{ext}}(\mathbf{r}, t)$. In order to provide reference data and to allow for the generation of benchmark results to assess the quality of the theory, resorting to many-body computer simulations is common, with overdamped Brownian dynamics (BD) being a popular choice. Marconi and Tarazona [5] initially spelled out the connection of these dynamics with DDFT and [7] describes a modern and stable adaptive time-stepping BD simulation algorithm. Comparison of DDFT data with experimental results are more scarce, but notable exceptions include non-equilibrium sedimentation of colloids [8], the self-diffusion of particles in complex fluids [9], the bulk dynamics of Brownian hard disks [10], and the flow profile and drying pattern of dispersion droplets [11].

The DDFT time evolution reaches a stationary state if the gradient on the right hand side of equation (1) vanishes, i.e. provided that the expression inside of the parentheses is constant:

$$\frac{\delta F[\rho]}{\delta \rho(\mathbf{r})} + V_{\text{ext}}(\mathbf{r}) = \mu. \quad (2)$$

Here we have dropped the dependence on time in the notation, as the situation is now static. The constant μ can be identified with the chemical potential, which in a grand canonical statistical mechanical setting is the conjugate control parameter of the mean particle number. Equation (2) is exact in equilibrium, as was shown by Evans [4]. He proved the equilibrium intrinsic free energy functional $F[\rho]$ to exist, to be unique, and to form the starting point for a modern equilibrium theory of spatially inhomogeneous liquids and crystals [12, 13].

In practice one needs to rely on approximations for $F[\rho]$, given a microscopic fluid model under consideration. Once one has solved equation (2) for given values of μ and temperature T (the dependence of $F[\rho]$ on T is suppressed in the notation), then in principle complete knowledge of the thermal system is available. The value of the density functional $F[\rho]$ is the true intrinsic free energy, and higher-order correlation functions are determined via higher-order derivatives of the free energy functional or via test-particle procedures. In particular two-body correlations functions, such as the bulk pair correlation function $g(r)$ as well as its generalization to inhomogeneous systems are accessible. These exhibit defining characteristics of liquids and more general soft matter systems and they are formally fully contained in the static density functional theory framework.

Together with a number of available reliable approximate free energy functionals, density functional theory is a powerful theoretical framework that has been used to elucidate much intricate and complex behaviour in soft matter.

Recent representative highlights include tracing hydrophobicity to critical drying at substrates [14–16], resolving three-dimensional structures of electrolyte aqueous solutions near surfaces [17, 18], and addressing the magnitude of the decay lengths in electrolytes [19]. Rosenfeld’s celebrated hard sphere fundamental measure free energy functional [20–23] is at the core of much of this research activity.

In the following we wish to address whether or not the DDFT has the prowess to play a similar role in nonequilibrium, as is often at least implicitly assumed. We demonstrate on the basis of an explicit and generic example, i.e. that of uniaxial compressional flow of the three-dimensional Lennard-Jones (LJ) fluid, that the DDFT is fundamentally flawed and that in reality, as represented by many-body simulations, recognizing the flow field as a further relevant degree of freedom is required to represent true nonequilibrium. These conclusions are based on analytical power functional approximations, adaptive BD simulation data, and explicit machine learning of the power functional map from motion to the interparticle one-body force field. Neglecting the dependence on the velocity field, via artificially setting its value identically to zero, reduces to the machine-learned functional mapping and hence the adiabatic time evolution of DDFT, albeit here on the basis of the quasi-exact adiabatic forces as they are included in the supervised machine learning.

This Perspective is organized as follows. We first make some key aspects of DDFT explicit in section 2 and describe several prominent shortcomings of this theory. We then give an account of how to go towards the formally exact one-body dynamics in section 3 and provide in section 4 a description of key aspects of the power functional framework, which as we wish to argue overcomes the fundamental defects of DDFT. We describe the exemplary stationary compressional flow situation in section 5 and lay out the application of Noether’s theorem in this statistical mechanical setting in section 6. We present machine learning results for the kinematic functional relationships of the streaming LJ fluid in section 7. This method also yields direct access to the adiabatic force field, as is required for the DDFT time evolution, without the need for involving any prior explicit analytical approximations for the free energy density functional. We give conclusions and an outlook in section 8. Readers who are primarily interested in the machine learning aspects of our work (section 7) are welcome to skip to the [appendix](#) where we lay out our strategy of its use in predicting and designing nonequilibrium many-body dynamics in soft matter.

2. Limits and limitations of adiabatic dynamics

We go into some detail and describe why the DDFT represents adiabatic dynamics in the sense of a temporal sequence of spatially inhomogeneous equilibrium states. The equilibrium intrinsic free energy functional splits into ideal and excess (over ideal gas) contributions according to $F[\rho] = F_{\text{id}}[\rho] + F_{\text{exc}}[\rho]$. Here the excess free energy functional $F_{\text{exc}}[\rho]$ accounts for the effects of the interparticle interactions on the equilibrium properties of the system and it is in general unknown and requires approximations to be made. The ideal gas free energy functional however is exactly given by

$$F_{\text{id}}[\rho] = k_B T \int d\mathbf{r} \rho(\mathbf{r}) [\ln(\rho(\mathbf{r})\Lambda^3) - 1], \quad (3)$$

where k_B denotes the Boltzmann constant, Λ is the thermal de Broglie wavelength, and we consider three-dimensional systems. The functional derivative, as it is relevant for equation (1), is $\delta F_{\text{id}}[\rho]/\delta\rho(\mathbf{r}) = k_B T \ln(\rho(\mathbf{r})\Lambda^3)$.

When disregarding the excess contribution and inserting this result alone into the DDFT equation of motion (1), its right hand side becomes $\gamma^{-1} \nabla \cdot \rho(\mathbf{r}, t) \nabla [k_B T \ln(\rho(\mathbf{r}, t) \Lambda^3) + V_{\text{ext}}(\mathbf{r}, t)]$ with the dependence on Λ being irrelevant due to the spatial gradient operation. The result can be re-written further such that for the case of the ideal gas, where $F_{\text{exc}}[\rho] = 0$ and $F[\rho] = F_{\text{id}}[\rho]$, the equation of motion (1) attains the following form:

$$\frac{\partial \rho(\mathbf{r}, t)}{\partial t} = D_0 \nabla^2 \rho(\mathbf{r}, t) - \nabla \cdot \rho(\mathbf{r}, t) \mathbf{f}_{\text{ext}}(\mathbf{r}, t) / \gamma. \quad (4)$$

Here $D_0 = k_B T / \gamma$ is the diffusion constant, ∇^2 is the Laplace operator and the external force field is given (here) as $\mathbf{f}_{\text{ext}}(\mathbf{r}, t) = -\nabla V_{\text{ext}}(\mathbf{r}, t)$. Equation (4) is the exact drift-diffusion equation for overdamped motion of a mutually noninteracting system, i.e. the ideal gas.

Besides Evans' original proposal [4] based on the continuity equation and undoubtedly his physical intuition, derivations of the DDFT (1) were founded much more recently on Dean's equation of motion for the density operator [5], the Smoluchowski equation [24], a stationary action principle for the density [25], the projection operator formalism [26], a phase-space approach [27], the mean-field approximation [28], a local equilibrium assumption [29], and a non-equilibrium free energy [30]. The question of the well-posedness of the DDFT was addressed [31] and several extensions beyond overdamped BD were formulated, such as e.g. for dynamics including inertia [32–35] and for particles that experience hydrodynamic interactions [35, 36] or undergo chemical reactions [37, 38].

The DDFT was also used beyond the description of fluids, such as e.g. for opinion dynamics [39] and epidemic spreading [40]. Recent reviews of DDFT are given in [41, 42], with [42] giving an updated overview of several very recent directions. The theory is put into a wider perspective, together with much background pedagogical material in [43]. A modern and well-accessible account of the general strategy of dynamical coarse-graining in statistical physics, of which the DDFT can be viewed as being a representative, has recently been given by Schilling [44].

The fact that both the static limit for the fully interacting system (2) as well as the full dynamics of the noninteracting system (4) are exact, taken together with the heft of the DDFT literature, appears to give much credibility to the equation of motion (1). However, despite the range of theoretical techniques employed [5, 24–30] neither of these approaches has provided us with a concrete way of going beyond equation (1). Apart from several case-by-case and rather ad hoc modifications, no systematic or even only practical identification of what is missing has been formulated. (We turn to power functional theory in section 4.) This is a problematic situation as two defects of equation (1) are immediately obvious upon inspection: (i) the description is local in time and there is no natural mechanism for the inclusion of memory while time-locality is not sufficient for general nonequilibrium situations; (ii) only flow that leads to direct changes in the density profile is captured and hence effects of rotational flow, such as shearing, as well as of nonequilibrium effects in compression and expansion are lost (see below).

Here we argue that these defects are indicative of a broader failure of equation (1) to describe nonequilibrium physics. We show that the DDFT is only fit to describe situations in which the dynamics follow an adiabatic path through a sequence of equilibrium states. The description of genuine nonequilibrium dynamics in a functional setting on the one-body level rather requires recognition of the local velocity field as a further relevant physical variable besides the density profile, and this is provided by power functional theory [43]. Before laying out key principles of this approach in section 4, we first describe the microscopically sharp coarse-graining on the one-body level of correlation functions.

3. Towards exact one-body dynamics

Evans based his original derivation [4] of equation (1) on the continuity equation,

$$\frac{\partial \rho(\mathbf{r}, t)}{\partial t} = -\nabla \cdot \mathbf{J}(\mathbf{r}, t), \quad (5)$$

where $\mathbf{J}(\mathbf{r}, t)$ is the microscopically resolved one-body current distribution. Equation (5) is exact in a variety of contexts, including overdamped BD, as described either on the Fokker–Planck level by the Smoluchowski equation or by the corresponding overdamped Langevin equation that governs the trajectories, as they are realized in simulation work [7]. For BD the one-body current distribution is given exactly by [43]:

$$\gamma \mathbf{J}(\mathbf{r}, t) = -k_B T \nabla \rho(\mathbf{r}, t) + \mathbf{F}_{\text{int}}(\mathbf{r}, t) + \rho(\mathbf{r}, t) \mathbf{f}_{\text{ext}}(\mathbf{r}, t). \quad (6)$$

This identity expresses the force density balance of the negative friction force density (left hand side) with the force densities due to ideal thermal diffusion, interparticle interactions, and external influence (three contributions on the right hand side). Here the interparticle force density distribution is given by the statistical average

$$\mathbf{F}_{\text{int}}(\mathbf{r}, t) = -\left\langle \sum_i \delta(\mathbf{r} - \mathbf{r}_i) \nabla_i u(\mathbf{r}^N) \right\rangle_t, \quad (7)$$

where the angular brackets indicate an average at fixed time t over the nonequilibrium many-body distribution, $u(\mathbf{r}^N)$ is the interparticle interaction potential that depends on all particle position coordinates $\mathbf{r}^N \equiv \mathbf{r}_1, \dots, \mathbf{r}_N$ and ∇_i indicates the derivative with respect to the position \mathbf{r}_i of particle i . The formulation of equation (7) is based on the concept of static operators and a dynamically evolving probability distribution. This is analogous to the Schrödinger picture of quantum mechanics. The Heisenberg picture is more closely related to simulation work. Here the probability distribution is that of the initial microstates and the operators move forward in time, i.e. the position $\mathbf{r}_i(t)$ of particle i changes over the course of time. Then the Dirac distribution in equation (7) becomes $\delta(\mathbf{r} - \mathbf{r}_i(t))$, with the generic position variable \mathbf{r} however remaining static. The forces are those that act in the given microstate $\mathbf{r}^N(t)$ at time t , i.e. the interparticle force on particle i at time t is $-\nabla_i u(\mathbf{r}^N(t))$.

In practice, using BD simulations, carrying out the average in equation (7) requires to build the mean over sufficiently many separate realizations of the microscopic evolution of the many-body system that differ in the initial microstate (as e.g. drawn from an equilibrium ensemble) and in the realization of the thermal noise. As equation (7) measures both the probability to find particle i at position \mathbf{r} (via the delta function) and the interparticle force that acts via the negative gradient $-\nabla_i u(\mathbf{r}^N)$, we refer to $\mathbf{F}_{\text{int}}(\mathbf{r}, t)$ as a force density. The corresponding force field $\mathbf{f}_{\text{int}}(\mathbf{r}, t)$ is obtained by simple normalization with the density profile, i.e. $\mathbf{f}_{\text{int}}(\mathbf{r}, t) = \mathbf{F}_{\text{int}}(\mathbf{r}, t) / \rho(\mathbf{r}, t)$. Building this ratio scales out the probability effect and the force field then carries physical units of force, i.e. energy per length.

In equilibrium the definition (7) remains intact. Complementing the statistical average, static density functional theory allows to express the equilibrium force density as being functionally dependent on the density profile via the functional derivative of the excess free energy functional according to:

$$\mathbf{F}_{\text{int}}(\mathbf{r})|_{\text{eq}} = -\rho(\mathbf{r}) \nabla \frac{\delta F_{\text{exc}}[\rho]}{\delta \rho(\mathbf{r})}. \quad (8)$$

Crucially, and in contrast to equation (7), here the internal force density is directly expressed as a density functional. This dependence has superseded the original dependence on the external potential, as is manifest in the probability distribution for building the average (7) in equilibrium.

As a self-consistency check we insert the force density functional (8) into the equilibrium limit of the force density balance (6). The current vanishes in the equilibrium case, $\mathbf{J}(\mathbf{r}, t) \equiv 0$, and we obtain

$$-k_B T \nabla \rho(\mathbf{r}) + \mathbf{F}_{\text{int}}(\mathbf{r})|_{\text{eq}} + \rho(\mathbf{r}) \mathbf{f}_{\text{ext}}(\mathbf{r}) = 0. \quad (9)$$

This result is independent of time and it constitutes the gradient of the static Euler–Lagrange equation (2) when divided by the density profile. (Insert equation (8), identify the ideal gas contribution $-k_B T \nabla \rho(\mathbf{r}) = -\rho(\mathbf{r}) \delta F_{\text{id}}[\rho] / \delta \rho(\mathbf{r})$, and divide by $\rho(\mathbf{r})$.) The classical force density balance result (9) by Yvon, Born and Green [3] has recently been derived from systematically addressing thermal Noether invariance [45, 46] against locally resolved spatial deformations of the statistical ensemble [47–49], as also valid quantum mechanically [49] and at second order in the displacement field [50, 51]; we give a brief account of this theory in section 6 below.

A naive transfer of equation (8) to nonequilibrium lets one simply evaluate the equilibrium excess free energy functional at the instantaneous nonequilibrium density $\rho(\mathbf{r}, t)$. In order to separate this contribution from true static equilibrium, we refer to this force density as being adiabatic (subscript ‘ad’) and to be defined as

$$\mathbf{F}_{\text{ad}}(\mathbf{r}, t) = -\rho(\mathbf{r}, t) \nabla \frac{\delta F_{\text{exc}}[\rho]}{\delta \rho(\mathbf{r}, t)}. \quad (10)$$

We recall that the right hand side offers a concrete computational structure that is of practical usefulness in actual applications, as considerable knowledge about approximative forms of the excess free energy density functional $F_{\text{exc}}[\rho]$ is available. Using the adiabatic force density as a proxy for the true nonequilibrium intrinsic force density distribution (7), i.e. setting $\mathbf{F}_{\text{int}}(\mathbf{r}, t) = \mathbf{F}_{\text{ad}}(\mathbf{r}, t)$ in the force density balance (6) together with the continuity equation (5) leads to the DDFT equation of motion (1). The adiabatic force density approximation is uncontrolled though and the theory inherently yields the dynamics as an adiabatic sequence of equilibrium states. Surely, more than 40 years after the conception of the DDFT [4], we have to be able to do better!

4. Power functional techniques

Power functional theory [43] offers a concrete mathematical structure to go forward. We describe the essential steps that enable one to go beyond the DDFT and to hence address a significantly expanded realm of nonequilibrium physics which equation (1) is oblivious of.

The interparticle force density profile (7) is identified to consist of two contributions according to:

$$\mathbf{F}_{\text{int}}(\mathbf{r}, t) = \mathbf{F}_{\text{ad}}(\mathbf{r}, t) + \mathbf{F}_{\text{sup}}(\mathbf{r}, t). \quad (11)$$

Here $\mathbf{F}_{\text{ad}}(\mathbf{r}, t)$ is the adiabatic force density profile, as given formally via the explicit equilibrium free energy derivative (10) and directly accessible in simulations via the custom flow method [52, 53]. The custom flow algorithm allows to systematically construct a hypothetical adiabatic (equilibrium) system that shares its density profile with the nonequilibrium system at the given time.

Then sampling the internal force density in the adiabatic system yields results for $\mathbf{F}_{\text{ad}}(\mathbf{r}, t)$.

The second, superadiabatic contribution in equation (11), $\mathbf{F}_{\text{sup}}(\mathbf{r}, t)$, contains all effects that are not expressible as an instantaneous density functional. This includes forces that lead to viscous and to nonequilibrium structure forming phenomena, as we exemplify below in a concrete model compressional flow situation. Formally, the superadiabatic force density is generated from the superadiabatic excess free power functional $P_t^{\text{exc}}[\rho, \mathbf{J}]$ upon functional differentiation with respect to the one-body current via [43, 54]:

$$\mathbf{F}_{\text{sup}}(\mathbf{r}, t) = -\rho(\mathbf{r}, t) \frac{\delta P_t^{\text{exc}}[\rho, \mathbf{J}]}{\delta \mathbf{J}(\mathbf{r}, t)}. \quad (12)$$

The functional dependence of $P_t^{\text{exc}}[\rho, \mathbf{J}]$ on the density and current is causal, i.e. on the values of these fields at prior times to t ; density and current need to satisfy the continuity equation. Upon using equation (11) the force density balance (6) attains the following form:

$$\begin{aligned} \gamma \mathbf{J}(\mathbf{r}, t) = & -k_B T \nabla \rho(\mathbf{r}, t) + \mathbf{F}_{\text{ad}}(\mathbf{r}, t) \\ & + \mathbf{F}_{\text{sup}}(\mathbf{r}, t) + \rho(\mathbf{r}, t) \mathbf{f}_{\text{ext}}(\mathbf{r}, t). \end{aligned} \quad (13)$$

This relationship holds beyond gradient forms of $\mathbf{f}_{\text{ext}}(\mathbf{r}, t)$, i.e. for external force fields that contain non-conservative contributions. Crucially, $\mathbf{F}_{\text{sup}}(\mathbf{r}, t)$ will in general also acquire nonconservative contributions, such as e.g. damping effects that represent viscous behaviour. Moreover, nonequilibrium structure-forming effects will also arise in general. These affect directly the shape of the density profile, whether this evolves in time or persists in a nonequilibrium steady state.

If one wishes to eliminate the explicit occurrence of the current from the dynamics, then inputting the force density balance (13) into the continuity equation (5) leads to the following formally exact form of the equation of motion for the density profile:

$$\begin{aligned} \frac{\partial \rho(\mathbf{r}, t)}{\partial t} = & D_0 \nabla^2 \rho(\mathbf{r}, t) + \nabla \cdot \frac{\rho(\mathbf{r}, t)}{\gamma} \nabla \frac{\delta F_{\text{exc}}[\rho]}{\delta \rho(\mathbf{r}, t)} \\ & - \nabla \cdot \frac{\rho(\mathbf{r}, t)}{\gamma} [\mathbf{f}_{\text{sup}}(\mathbf{r}, t) + \mathbf{f}_{\text{ext}}(\mathbf{r}, t)]. \end{aligned} \quad (14)$$

Here it is apparent that the superadiabatic force field $\mathbf{f}_{\text{sup}}(\mathbf{r}, t) = \mathbf{F}_{\text{sup}}(\mathbf{r}, t)/\rho(\mathbf{r}, t)$ has a direct effect on the system dynamics. The effect is similar to that of the external force field. Crucially though, both force fields are independent of each other: the external force field represents a prescribed and inert influence on the system. In contrast, the superadiabatic force field is an emergent phenomenon that arises due to interparticle interactions and, from the functional point of view, depends non-locally in position and causally in time on the one-body density and on the current profile.

Although setting $\mathbf{f}_{\text{sup}}(\mathbf{r}, t) = 0$ yields the DDFT (1), the superadiabatic force field $\mathbf{f}_{\text{sup}}(\mathbf{r}, t)$ was demonstrated to exist [55–61] and in general to play a major role in the dynamics on the one-body level and, based on test-particle concepts [62–67], two-body correlation functions [68–70], and for active matter [71–75]. Both the flow properties as well as the spatial structure formation in the system are affected.

To reveal additional physics, it is useful to split into ‘structural’ and ‘flow’ contributions. This was established e.g. for complex flow patterns that occur in driven BD [56, 60], for active Brownian particles which form a self-sustained interface at motility-induced phase coexistence [71–75], as well as very recently

for a sheared three-body colloidal gel former [61]. Before we demonstrate these concepts for an example of steady nonequilibrium below, we first describe two simple model power functionals that respectively generate structure and viscously dampen the motion and that, as we will see, give a good account of the nonequilibrium flow considered below.

We concentrate on the low-order terms that are relevant for compressional/extensional flow, i.e. for situations where $\nabla \cdot \mathbf{v}(\mathbf{r}, t) \neq 0$. We focus on cases where there is no rotational motion (such as shearing) and hence $\nabla \times \mathbf{v}(\mathbf{r}, t) = 0$. The velocity gradient superadiabatic power functional consists of a sum,

$$P_t^{\text{exc}}[\rho, \mathbf{v}] = P_t^{\text{flow}}[\rho, \mathbf{v}] + P_t^{\text{str}}[\rho, \mathbf{v}]. \quad (15)$$

Here the flow and structural [56, 60] contributions are approximated, respectively, by the following time-local (Markovian) and space-semilocal (i.e. involving ∇) forms

$$P_t^{\text{flow}}[\rho, \mathbf{v}] = \frac{\eta}{2} \int d\mathbf{r} [\rho(\mathbf{r}, t) \nabla \cdot \mathbf{v}(\mathbf{r}, t)]^2, \quad (16)$$

$$P_t^{\text{str}}[\rho, \mathbf{v}] = -\frac{\chi}{3} \int d\mathbf{r} [\rho(\mathbf{r}, t) \nabla \cdot \mathbf{v}(\mathbf{r}, t)]^3, \quad (17)$$

where the overall prefactors η and χ control the respective magnitude and they play the role of transport coefficients (see below). The flow functional (16) is quadratic both in density and in the velocity field; the structural functional (17) is of cubic order in each of these variables. Explicit higher-order functionals exist [60] and they become relevant when driving the system strongly. We will return to the consequences of equations (16) and (17) after laying out in section 5 the actual flow situation that we use as a model to exemplify the implications for the physics. Before doing so, we briefly describe several further key aspects of the power functional framework.

Power functional theory provides a formal mechanism for the inclusion of time- and space-nonlocal dynamics [57, 69, 80]. While equation (12) applies to overdamped dynamics, the acceleration field becomes a further relevant degree of freedom if inertia are relevant [79–82] whether classically in molecular dynamics [79, 80] or in quantum dynamics [81, 82]. Here the memory functions act as convolution kernels on specific kinematic fields and rotational and compressional contributions to the dynamics are genuinely built in. As laid out above, the framework is based on an exact variational concept [43, 54], and the resulting functional mapping was shown to be explicitly accessible in many-body simulation via the custom flow computer simulation method [52, 53].

Even simple mathematical model forms for the nonequilibrium contribution to the power functional, such as equations (16) and (17), already capture essential physics (as we demonstrate below) and dynamical two-body correlation functions are accessible via test particle dynamics [9, 10, 62–70]. The power functional is thereby not to be confused with the often vague concept of a ‘nonequilibrium free energy’. The proper equilibrium free energy functional does play a central role in power functional theory though, via providing the description of the adiabatic reference state [43], see the generation of the force density distribution via functional differentiation (10), as is relevant for the interparticle force splitting (11), and the full density equation of motion (14).

The relevance of superadiabatic contributions to the dynamics, i.e. of those effects that lie beyond equation (1), has been amply demonstrated in the literature [55–60, 68–70]. Both adiabatic and superadiabatic effects arise from integrating out the dynamical degrees of freedom of the many-body problem.

Ensemble differences between canonical dynamics and grand canonical equilibrium have been systematically addressed [76–78] and these do not account for the observed differences between adiabatic and superadiabatic dynamics. The kinematic dependence on the motion of the system arises formally [43], it can be explicitly traced in many-body computer simulation work [60], and it is amenable to machine learning, as we demonstrate in section 7. Before doing so, we first formulate the representative flow problem that we will use to apply the above concepts.

5. Nonequilibrium steady states

We restrict ourselves to flow situations with one-body fields that are inhomogeneous in position but independent of time, i.e. $\rho(\mathbf{r})$ and $\mathbf{v}(\mathbf{r})$. Then trivially $\partial\rho(\mathbf{r})/\partial t = 0$ and the continuity equation (5) constrains both fields to satisfy $\nabla \cdot [\rho(\mathbf{r})\mathbf{v}(\mathbf{r})] = 0$. As a representative case we illustrate in figure 1(a) nonequilibrium steady state of a three-dimensional liquid undergoing unidirectional compressional flow. Flow along a single given direction occurs e.g. under the influence of gravity, where sedimentation of colloids leads to both compression in the lower parts of the sample and expansion in the upper parts of the sample. Here we disregard transient phenomena and investigate an idealized periodic system, where flowing steady states can form.

This chosen uniaxial flow in planar geometry is complementary to DDFT, as density gradients are relevant and the density profile alone already contains much non-trivial information about the dynamics that the system undergoes. Hence this specific geometry is often used to carry out generic tests; see e.g. the investigation of the quality of force-based DDFT [47, 48]. In contrast, shear flow is very different, as any motion that occurs perpendicular to the density gradient is not captured by equation (1); we refer the reader to [41, 42] for a description of efforts to include these effects within DDFT via different types of modifications of equation (1).

In order to elucidate the physics in the chosen uniaxial compressional setups, we follow the splitting (15) of the superadiabatic power functional into structural and flow contributions and hence decompose the superadiabatic force field accordingly as

$$\mathbf{f}_{\text{sup}}(\mathbf{r}) = \mathbf{f}_{\text{str}}(\mathbf{r}) + \mathbf{f}_{\text{flow}}(\mathbf{r}), \quad (18)$$

where the right hand side consists of the nonequilibrium structural force field $\mathbf{f}_{\text{str}}(\mathbf{r})$ and the flow force field $\mathbf{f}_{\text{flow}}(\mathbf{r})$. Both of these force contributions arise from the microscopic interparticle interactions, as coarse-grained in a microscopically sharp way to the one-body level. We lay out in the following the benefits of the structure-flow splitting (18) and its definition via flow reversal symmetry.

First, on the more practical level, equation (18) allows to carry out a corresponding splitting of the force density balance (13) (we divide by $\rho(\mathbf{r})$ to obtain force fields). The result is a set of two coupled equations of motion, with one of them depending explicitly on the velocity profile and the second one depending explicitly on the density profile:

$$\gamma\mathbf{v}(\mathbf{r}) = \mathbf{f}_{\text{flow}}(\mathbf{r}) + \mathbf{f}_{\text{ext},f}(\mathbf{r}), \quad (19)$$

$$0 = \mathbf{f}_{\text{str}}(\mathbf{r}) - k_B T \nabla \ln \rho(\mathbf{r}) + \mathbf{f}_{\text{ad}}(\mathbf{r}) + \mathbf{f}_{\text{ext},s}(\mathbf{r}). \quad (20)$$

Building the sum of equations (19) and (20) and multiplying by the density profile restores the full force density balance (13). The external force field is split

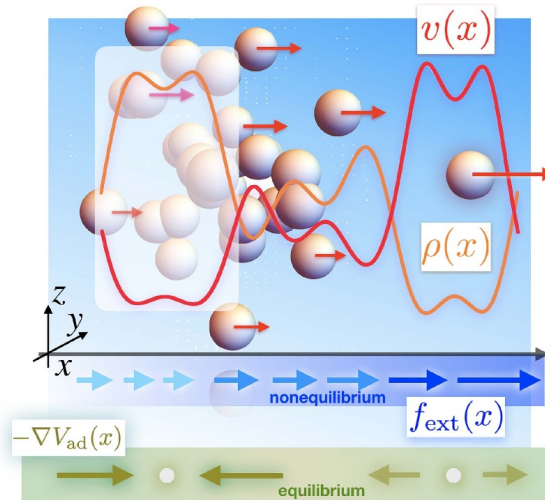


Figure 1. Illustration of unidirectional compressional flow of a liquid. The three-dimensional system is set into motion (red arrows) by the action of an external force profile $f_{\text{ext}}(x)$ (blue arrows) which acts along the x -axis. The system retains planar geometry such that spatial inhomogeneities only occur as a function of x . The density profile $\rho(x)$ (orange curve) and the velocity profile $v(x)$ (red curve) are both stationary in time but inhomogeneous in position. The local one-body current $J(x) = \rho(x)v(x) = \text{const}$ and as a result the system is in a nonequilibrium steady state. The corresponding adiabatic system is in equilibrium (it has no mean flow) and it has by construction an unchanged density profile $\rho(x)$. In the adiabatic system the spatial variation of $\rho(x)$ is stabilized by the action of an external force field $-\nabla V_{\text{ad}}(x)$ (olive arrows), which acts solely in the adiabatic system.

according to $\mathbf{f}_{\text{ext}}(\mathbf{r}) = \mathbf{f}_{\text{ext},f}(\mathbf{r}) + \mathbf{f}_{\text{ext},s}(\mathbf{r})$, where the two terms couple to the flow via $\mathbf{f}_{\text{ext},f}(\mathbf{r})$ in equation (19) and to the structure via $\mathbf{f}_{\text{ext},s}(\mathbf{r})$ in equation (20).

On the superficial level the two equations (19) and (20) appear to be independent of each other, as no single field appears explicitly in both equations. However, the two equations are indeed intimately coupled to each other by the interparticle interactions, as represented by both the adiabatic and the two superadiabatic (flow and structural) force fields. These three intrinsic force contributions provide the physical representation of the true nonequilibrium steady state dynamics.

The flow-structure splitting (18) is uniquely determined by the symmetry properties of the forces upon motion reversal of the system [60]. Motion reversal is a discrete symmetry operation, and hence different from continuous invariances where Noether's theorem applies [45–51]. One considers a 'reversed' system, which is also in steady state and possesses an unchanged density profile $\rho(\mathbf{r})$. The flow, however, is directed against the velocity orientation in the original 'forward' system. Hence the velocity profile in the reversed system is simply $-\mathbf{v}(\mathbf{r})$. As a result the current also acquires a minus sign, $-\rho(\mathbf{r})\mathbf{v}(\mathbf{r})$, which however does not affect the (vanishing) divergence, $\nabla \cdot [-\rho(\mathbf{r})\mathbf{v}(\mathbf{r})] = 0$. Thus the reversed state indeed is stationary. The two superadiabatic contributions are then defined to be unchanged [$\mathbf{f}_{\text{str}}(\mathbf{r})$] and inverted [$-\mathbf{f}_{\text{flow}}(\mathbf{r})$] in the reversed system. Consequentially, the superadiabatic force field in the reversed system is the difference $\mathbf{f}_{\text{str}}(\mathbf{r}) - \mathbf{f}_{\text{flow}}(\mathbf{r})$.

Analyzing the symmetry properties of the adiabatic force field is straightforward. We recall that $\mathbf{f}_{\text{ad}}(\mathbf{r})$ is a density functional via equation (10). The density profiles in the forward and in the reversed systems are identical though. Hence $\mathbf{f}_{\text{ad}}(\mathbf{r})$ is invariant under motion reversal. Motion reversal is a useful device in order to (i) rationalize the nonequilibrium behaviour according to

the split force balance (19) and (20), and to (ii) classify the dependence of superadiabatic forces on the velocity field into even powers, which constitute $\mathbf{f}_{\text{str}}(\mathbf{r})$, and odd powers, which form $\mathbf{f}_{\text{flow}}(\mathbf{r})$.

We can demonstrate this mechanism explicitly on the basis of the above flow and structural power functionals (16) and (17). Superadiabatic force fields are generated via the functional derivative (12) with respect to the current or, analogously, by functionally deriving by $\mathbf{v}(\mathbf{r}, t)$ and dividing the result by $\rho(\mathbf{r}, t)$. The resulting superadiabatic one-body force field consists of two components. The viscous flow force and [56, 59] and the structural force follow respectively as

$$\mathbf{f}_{\text{flow}}(\mathbf{r}) = \frac{\eta}{\rho(\mathbf{r})} \nabla[\rho(\mathbf{r})^2 \nabla \cdot \mathbf{v}(\mathbf{r})], \quad (21)$$

$$\mathbf{f}_{\text{str}}(\mathbf{r}) = -\frac{\chi}{\rho(\mathbf{r})} \nabla\{\rho(\mathbf{r})^3 [\nabla \cdot \mathbf{v}(\mathbf{r})]^2\}, \quad (22)$$

where equation (21) is odd (linear) and equation (22) is even (quadratic) in the derivatives of the velocity field, as desired and we re-iterate that both expressions are only valid for small enough velocity gradients.

One might wonder where all this genuine nonequilibrium physics leaves the DDFT! Some readers will find the instantaneous dynamics, as generated from an adiabatic free energy according to (1), to be more appealing and intuitive than the thinking in terms of the above described apparently intricate functional relationships. Why not live with equation (1), use it, and simply accept its defects? In order to address this question and to demonstrate why this path is severely restricted from the outset, we turn in section 7 to an explicit demonstration of the functional relationship that governs the nonequilibrium physics, i.e. the kinematic functional map from the one-body mean motion to the internal force field. Before doing so, we demonstrate that Noether’s theorem of invariant variations has much to say about our present setup.

6. Noether force sum rules

We discuss one of the arguably simplest cases of exploitation of the inherent symmetries of a thermal many-body system, that of global translational invariance of its statistical mechanics [45, 46]. We consider a ‘shifting’ transformation, where all particle coordinates change according to the map $\mathbf{r}_i \rightarrow \mathbf{r}_i + \boldsymbol{\epsilon}$, where $\boldsymbol{\epsilon} = \text{const}$. This uniform shifting operation leaves all interparticle distance unchanged, $\mathbf{r}_i - \mathbf{r}_j \rightarrow (\mathbf{r}_i + \boldsymbol{\epsilon}) - (\mathbf{r}_j + \boldsymbol{\epsilon}) \equiv \mathbf{r}_i - \mathbf{r}_j$. As a consequence the interparticle potential is invariant under the transformation, which we can express as the identity $u(\mathbf{r}_1, \dots, \mathbf{r}_N) = u(\mathbf{r}_1 + \boldsymbol{\epsilon}, \dots, \mathbf{r}_N + \boldsymbol{\epsilon})$. Here equality holds irrespectively of the magnitude and the direction of the shifting vector $\boldsymbol{\epsilon}$.

The Noether argument proceeds with a twist. Despite the absence of dependence on $\boldsymbol{\epsilon}$, we can nevertheless differentiate both sides of the equation with respect to $\boldsymbol{\epsilon}$ and the result will be a valid identity. We obtain $0 = \partial u(\mathbf{r}_1 + \boldsymbol{\epsilon}, \dots, \mathbf{r}_N + \boldsymbol{\epsilon}) / \partial \boldsymbol{\epsilon} = \sum_i \nabla_i u(\mathbf{r}_1, \dots, \mathbf{r}_N)$, where we have set $\boldsymbol{\epsilon} = 0$ after taking the derivative. We multiply by -1 and insert $1 = \int d\mathbf{r} \delta(\mathbf{r} - \mathbf{r}_i)$, which yields

$$-\int d\mathbf{r} \sum_i \delta(\mathbf{r} - \mathbf{r}_i) \nabla_i u(\mathbf{r}^N) = 0. \quad (23)$$

The expression on the left hand side allows to identify the locally resolved interparticle force operator $\hat{\mathbf{F}}_{\text{int}}(\mathbf{r}) = -\sum_i \delta(\mathbf{r} - \mathbf{r}_i) \nabla_i u(\mathbf{r}^N)$, such that equation (23) attains the form $\int d\mathbf{r} \hat{\mathbf{F}}_{\text{int}}(\mathbf{r}) = 0$. This identity holds for each microstate \mathbf{r}^N and hence it remains trivially valid upon averaging over the

many-body distribution function, irrespective of whether this is in- or out-of-equilibrium. We can hence conclude the vanishing of the global interparticle force, expressed as the integral over the mean force density $\mathbf{F}_{\text{int}}(\mathbf{r}) = \langle \hat{\mathbf{F}}_{\text{int}}(\mathbf{r}) \rangle$ as

$$\int d\mathbf{r} \mathbf{F}_{\text{int}}(\mathbf{r}, t) = 0. \quad (24)$$

Equation (24) holds at all times t and it can be viewed as a consequence of Newton's third law, see the discussion in [45]. Using the adiabatic-superadiabatic force splitting (11) one can further conclude that the both global contributions need to vanish individually,

$$\int d\mathbf{r} \mathbf{F}_{\text{ad}}(\mathbf{r}, t) = 0, \quad (25)$$

$$\int d\mathbf{r} \mathbf{F}_{\text{sup}}(\mathbf{r}, t) = 0. \quad (26)$$

The proof can either be based on the fact that equation (25) is merely equation (24) for the special case of an equilibrium system, from which then equation (26) follows from the force splitting (11). Alternatively and starting from a very fundamental point of view, the global translational invariance of the excess free energy functional $F_{\text{exc}}[\rho]$ and of the superadiabatic free power functional $P_t^{\text{exc}}[\rho, \mathbf{v}]$, here considered instantaneously at time t , lead directly to equations (25) and (26), see [45, 46] for detailed derivations.

It is interesting to apply the Noether concept to the flow-structure splitting equation (18) of the superadiabatic force field. One can see straightforwardly, from the symmetry upon motion reversal, that both the global structural force and the global flow force need to vanish individually:

$$\int d\mathbf{r} \rho(\mathbf{r}) \mathbf{f}_{\text{flow}}(\mathbf{r}) = 0, \quad (27)$$

$$\int d\mathbf{r} \rho(\mathbf{r}) \mathbf{f}_{\text{str}}(\mathbf{r}) = 0. \quad (28)$$

We prove by contradiction and assume that it is not the case, i.e. that each integral gives the same global force, but with opposite sign, such that the sum vanishes and equation (26) remains valid. Per construction, $\mathbf{f}_{\text{flow}}(\mathbf{r})$ changes sign in the motion reversed system, but $\mathbf{f}_{\text{str}}(\mathbf{r})$ does not. Hence equation (26) can only be satisfied in the motion-reversed system provided that both the flow and structural contribution vanish separately.

We can explicitly test the validity of the sum rules (27) and (28) for the above analytical force approximations (21) and (22). The respective integrals are $\eta \int d\mathbf{r} \nabla[\rho(\mathbf{r})^2 \nabla \cdot \mathbf{v}(\mathbf{r})] = 0$ and $\chi \int d\mathbf{r} \nabla\{\rho(\mathbf{r})^3 [\nabla \cdot \mathbf{v}(\mathbf{r})]^2\} = 0$, which follows from the divergence theorem, as boundary terms vanish. Hence the simple non-local velocity gradient power functional approximations (16) and (17) have passed the global Noether validation test. This is nontrivial, as the proof rests on the specific structure of the integrands being gradients, which for more general analytical forms will not be the case. This exemplifies the merits of Noether sum rules for assessing and by extension also constructing theoretical nonequilibrium force approximations.

The Noether concept carries much further. Hermann and Schmidt [45] present a generalization of the global sum rules, such as the vanishing of the total superadiabatic force (26), for so-called time direct correlation functions. These

are defined via functional derivatives of the superadiabatic power functional, in generalization of the superadiabatic force density as generated via the derivative (12) with respect to the current distribution. We have shown [45] that these time direct correlation functions satisfy additional memory sum rules and we expect the corresponding identities to be helpful in the study of temporal nonlocality. Further work was addressed at the variance of global fluctuations, which were shown to be constrained by Noether invariance at the second order global level [50]. Noether’s theorem also yields the locally resolved force balance relationship in quantum mechanical many-body systems [49]. Very recently, striking two-body force-force and force-gradient correlation functions for the precise and novel characterization of disordered (liquid and gel) systems [51] were revealed. Exploiting Noether’s concept in a statistical mechanical setting is robust against changes of ensemble, [46] presents the transfer of the grand ensemble formalism [45] to canonical systems. Considering global rotational invariance leads to (classical) spin–orbit coupling of torque identities [45].

We return to steady states and demonstrate that the seemingly entirely formal functional relationships do in fact apply to real systems. We present in the following new computational methodology that we use to demonstrate the functional point of view. We will also demonstrate that the sum rules (26) and (27) are highly valuable in providing checks for numerical results.

7. Machine learning the kinematic map

Machine learning proves itself to be an increasingly useful tool in a variety of settings in soft matter, ranging from soft matter characterization [83], engineering of colloidal self-assembly [84], to the inverse design of soft materials [85]. Pivotal studies were addressed at colloidal structure detection [86], the identification of combinatorial rules in mechanical metamaterials [87], the learning of many-body interaction potentials for spherical [88] and for anisotropic particles [89], and the prediction of the dynamics of supercooled liquids from their static properties [90].

Concerning slow dynamics, machine learning was used for obtaining memory kernels for generalised Langevin dynamics [91], classifying the age [92], assessing the structural heterogeneity [93], and investigating dimensionality reduction of local structure [94] of glasses. Machine learning was applied to equilibrium reactive processes such as molecular isomerization [95] and to the behaviour of rare diffusive molecular dynamics trajectories [96].

Machine learning plays an important role in the inverse design for self-assembly of soft materials [97, 98]. Examples thereof include sequence-specific aggregation of copolymers [99], inverse design of multicomponent colloidal crystals by reverse engineering the Hamiltonian of the system [100], characterizing the self-assembly of three-dimensional colloidal systems [101], controlling colloidal crystals via morphing energy landscapes [102], and learning free energy landscapes using artificial neural networks [103].

In a liquid state theory-informed approach, Limmer and his coworkers have considered potentials based on local representations of atomic environments, in order to learn intermolecular forces at liquid-vapor interfaces [104]. They relate their machine-learning approach to the local molecular field theory by Weeks and coworkers [105, 106], see [107] for a description of the relationship of this approach to DFT.

More specifically, in the context of classical density functional theory, an early and pioneering study formulated a neural-network approach to liquid crystal ordering in confinement [108]. Free energy density functionals were obtained for one-dimensional fluids from a convolutional neural network [109] and an analytical form of an excess free energy functional was generated from an equation learning network [110]. Cats *et al* [111] recently used machine learning

to improve the standard mean-field approximation of the excess Helmholtz free-energy functional for a three-dimensional LJ system at a supercritical temperature. These significant research efforts were devoted to tailoring analytical forms of model free energy functionals, by training certain key components such as spatial convolution kernels, and much insight into the inner workings of excess free energy functionals was gained [109–111]. Very recent developments include using physics-constrained Bayesian inference of state functions [112] and to emulate functionals by active learning with error control [113]. The results of DFT calculations were also used as training data for investigating gas solubility in nanopores [114].

However, here we proceed very differently and moreover do so out-of-equilibrium. We use the LJ model and the identical planar geometry as in [111], such that the density profile $\rho(x)$ depends only on a single position coordinate x . We consider steady states and retain planar symmetry by considering flow that is directed in the x -direction, such that the current $\mathbf{J}(x) = J(x)\mathbf{e}_x$, where $J(x)$ is the magnitude of the current and \mathbf{e}_x is the unit vector in the x -direction. Both the density profile $\rho(x)$ and the velocity field $v(x) = J(x)/\rho(x)$ are independent of time. The continuity equation (5) then implies $0 = \partial\rho(x)/\partial t = -\partial[v(x)\rho(x)]/\partial x$, from which one obtains by spatial integration $\rho(x)v(x) = J_0 = \text{const}$. Here the value of J_0 determines the intensity of the flow; we recall the illustration shown in figure 1.

We base the machine learning procedure on a convolutional neural network, as was done e.g. in [109], and following [109–111] we use many-body computer simulations to provide training, validation, and test data. In contrast to these equilibrium studies though, in order to address the nonequilibrium problem we need to represent the physical time evolution on the many-body trajectory level. We use the recently developed highly performant adaptive BD algorithm [7] and apply it to the three-dimensional LJ fluid. As laid out above, in order to address situations of planar symmetry we drive the system only along the \mathbf{e}_x -direction. The specific form of the driving force field $f_{\text{ext}}(x)\mathbf{e}_x$ is however irrelevant, as the training data only serves to extract the intrinsic kinematic functional relationship.

In order to cover a sufficiently broad range of flow situations, we represent the external force field as a truncated Fourier series $f_{\text{ext}}(x) = \sum_{n=0}^{n_{\text{max}}} A_n \sin(2\pi nx/L + B_n)$, where L is the size of the cubic simulation box with periodic boundary conditions, A_n are random amplitudes with zero mean and uniform distribution inside of a given finite interval, and B_n are random phases. We truncate at order $n_{\text{max}} = 4$ such that the length scale $L/(2\pi n_{\text{max}})$ is comparable to the LJ molecular size σ . Ten percent of our simulation runs are carried out in equilibrium, i.e. for $A_0 = 0$. We use $N = 500$ LJ particles inside of a cubic simulation box of size $L = 10\sigma$. The temporal duration of each run is 1000τ , where $\tau = \sigma^2/D_0$ is the Brownian time scale. After initialization the system is randomized for 1τ at a very high temperature. Then we wait for 100τ to allow the system to reach a steady state and then collect data during the remaining time. In total we use 1000 such simulation runs; these are subdivided for purposes of training (520), validation (280) and testing (200). The maximal current encountered during training was $J_0\sigma^2\tau = 4.93$. A more detailed account of our machine-learning strategy is given in the [appendix](#)

Our aim is to machine-learn and hence to explicitly demonstrate the kinematic map, $\rho(\mathbf{r}), \mathbf{v}(\mathbf{r}) \rightarrow \mathbf{f}_{\text{int}}(\mathbf{r})$ in steady state. We present the learning algorithm with inputs $\rho(x), v(x)$ and target $f_{\text{int}}(x)$. The data for these three fields are obtained from building steady state averages via the adaptive BD over the corresponding one-body operators. We recall the microscopic definition of the interparticle one-body force density $\mathbf{F}_{\text{int}}(\mathbf{r})$ via equation (7) and we refer the reader to appendix of [52] for a description of several methods to sample the current in BD and hence obtain the overdamped velocity profile $\mathbf{v}(\mathbf{r})$. Finally, we use the

standard counting method for the density profile $\rho(\mathbf{r})$, although more efficient ‘force sampling’ methods [115–118] exist. At this stage we neither impose adiabatic-superadiabatic splitting (11), nor structure-flow splitting (18), nor do we use any analytical model form of the functional relationship. We rather work on the level of the bare one-body simulation data, generated in the above described randomized uniaxial flow situations of the desired planar symmetry.

We refer to the result of this procedure as the machine-learned internal force field $f_{\text{int}}^*(x, [\rho, v])$. This represents a ‘surrogate model’ in the sense of the terminology of the machine learning community. By construction this data structure depends functionally on the density profile and on the velocity profile. Importantly the external force field $f_{\text{ext}}(x)$, as given by the above described randomized Fourier series, has not been used in the training, which was rather based solely on the intrinsic force field and its kinematic dependence on the density profile and the velocity field.

In order to test the validity of the functional relationship and to address the question whether $f_{\text{int}}^*(x, [\rho, v])$ indeed represents the true $\mathbf{f}_{\text{int}}(\mathbf{r}, t, [\rho, v])$ of power functional theory, as restricted to the present planar and steady situation, we consider a toy flow situation as an application. We choose the density profile to consist of a single (co)sinusoidal deviation from the bulk, $\rho(x) = [0.5 + 0.2 \cos(2\pi x/L)]\sigma^{-3}$. In order for the system to be in steady state, the velocity then necessarily needs to satisfy $v(x) = J_0/\rho(x)$, where the strength of the current $J_0 = \text{const}$ is a free parameter.

We proceed in two ways. First, we check for self-consistency. Therefore we solve the force density balance relationship (6) for the external force field, which yields the explicit result:

$$f_{\text{ext}}(x) = k_B T \frac{\partial \ln \rho(x)}{\partial x} + \gamma v(x) - f_{\text{int}}^*(x, [\rho, v]). \quad (29)$$

As is explicit in equation (29), inputting the toy state $\rho(x), v(x)$ on the right hand side yields a concrete machine learning prediction for the external force field on the left hand side. We then input this result for $f_{\text{ext}}(x)$ as the driving force field in a single adaptive BD simulation run and expect this procedure to reproduce the density and velocity profile of the toy state. The reproductive success will however materialize only provided that (i) the functional kinematic dependence actually exists and that (ii) it is accurately represented by the neural network.

The results, shown in figure 2, demonstrate the accomplishment of the reconstruction of the toy state. This establishes that the machine learned functional provides a numerically highly accurate representation of the true internal force functional. That quantitative differences between results from direct BD and from machine learning occur for the case of strongest flow ($J_0\sigma^2\tau = 5$) is not surprising, given that the value of the current is beyond the maximum encountered during training ($J\sigma^2\tau = 4.93$). However, despite the quantitative deviations of the prediction for the interparticle force field, the qualitative behaviour of the network remains entirely reasonable.

We take this validation via the machine learning to be a practical, data-science-level verification of the existence of the power functional kinematic map. We recall the original formal construction [43, 54] and its subsequent confirmation via custom flow [52, 53].

Turning to the physics of the compressional flow, we use the adiabatic-superadiabatic decomposition (11) together with the flow-structure splitting (18) to analyze both the machine-learned functional $f_{\text{int}}^*(x, [\rho, v])$ as well as the direct simulation results. As anticipated, both flow and structural force fields have nontrivial spatial variation, see figure 2. The flow force primarily contains viscous effects that stem from the dissipation that the compressional and extensional regions of the flow pattern generate. The structural force field

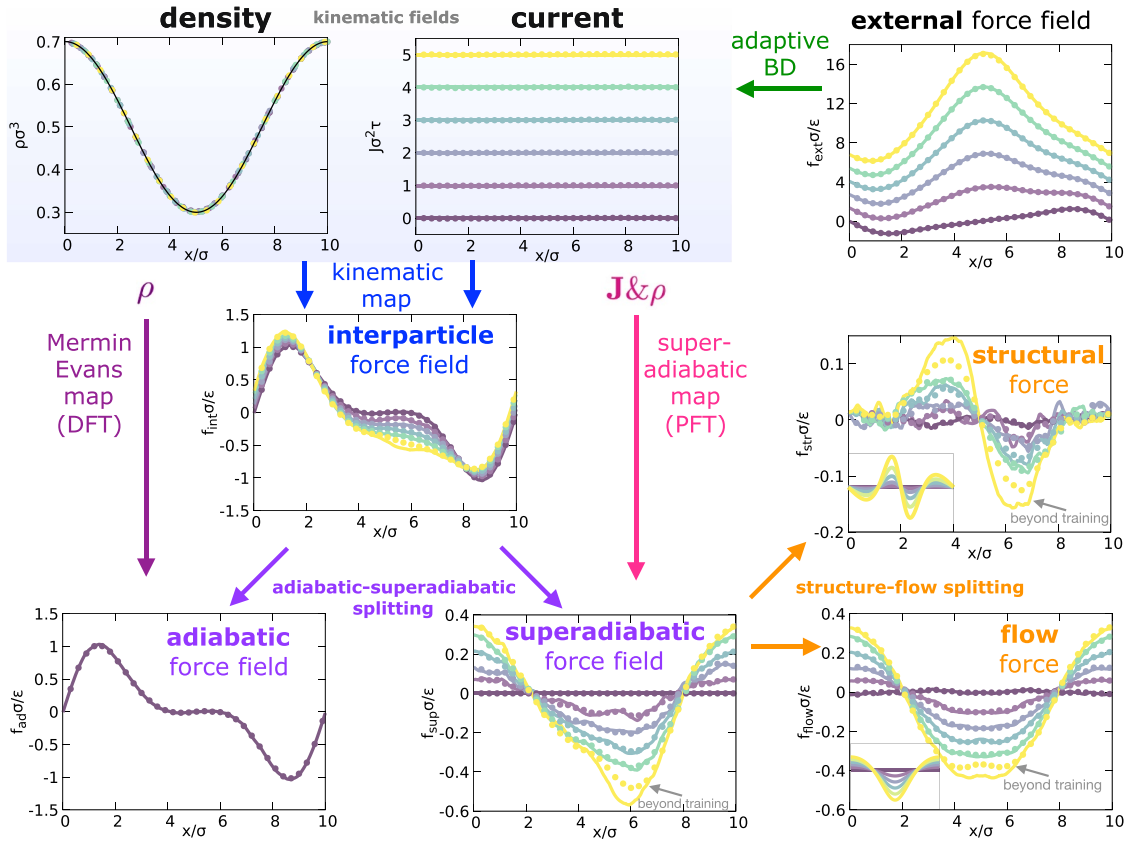


Figure 2. Kinematic profiles and force fields for uniaxial compressional flow of the LJ fluid. Results are shown from machine learning (lines) and from direct adaptive BD simulations (symbols). Functional relationships are represented by vertical arrows. Shown are the density profile $\rho(x)$, the one-body current $J(x)$ and the external force field $f_{\text{ext}}(x)$ (top row) as a function of the scaled distance x/σ , where σ is the LJ length scale and $k_B T/\epsilon = 1.5$ throughout. The density and the current functionally determine both the interparticle force field $f_{\text{int}}(x)$ via the kinematic map and the superadiabatic force field $f_{\text{sup}}(x)$ via the superadiabatic kinematic map (middle row). The internal force field $f_{\text{int}}(x)$ splits into superadiabatic and adiabatic force contributions. The adiabatic force field $f_{\text{ad}}(x)$ is a density functional via the Mermin-Evans map of density functional theory. The structural and flow force fields are split according to their symmetry upon motion reversal. The colour code represents different values of the current $J_0 \sigma^2 \tau = 0, 1, 2, 3, 4, 5$ (from violet to yellow, see the center panel in the top row). The two insets show the predictions from the analytical velocity gradient functionals (21) and (22) on the same scale as the respective main panel; the transport coefficients are chosen as $\eta/(\epsilon \tau \sigma^3) = 0.35$ and $\chi/(\epsilon \tau^2 \sigma^6) = 0.075$ to give good agreement with the quasi-exact data. The system with $J_0 = 0$ is at rest in equilibrium and it doubles as the adiabatic state because its density profile is identical to that of the flowing systems (as shown in the first panel). The small differences in superadiabatic forces from BD and from machine learning for the case of the highest current considered, $J_0 \sigma^2 \tau = 5$, occur as this value is beyond those encountered in the training data.

becomes more strongly inhomogeneous and also larger in magnitude upon increasing the amplitude of the flow. This trend is necessary to provide a balance for the increasingly asymmetric and growing external force field, which in turn is required to keep the density profile unchanged upon increasing the throughput through the prescribed density wave.

The power functional predictions (21) and (22) capture these effects reasonably well given the simplicity of the analytical expressions, see the insets in figure 2. We find our numerical results to satisfy the Noether sum rules (26)

and (27) to very good accuracy. The values of the prefactors η and χ in equations (21) and (22) characterize the dominant behaviour of the system in response to spatial variation of the flow. The parameter $\eta/(\epsilon\tau\sigma^3) = 0.35$ measures viscosity and $\chi/(\epsilon\tau^2\sigma^6) = 0.075$ quantifies the strength of nonequilibrium structure formation. We regard these amplitudes as being well-defined transport coefficients, which will determine the leading behaviour of the system in situations where higher-order gradient contributions are small or even irrelevant. Using our methodology, the precise values of η and χ can be obtained systematically from straightforward comparison to the data from the BD simulations or the machine learning model.

It remains to point out the stark contrast with the standard DDFT (1), which gives a trivial null result in the present setup by construction: the density profile remains unchanged upon increasing flow, and so does the adiabatic force field. So the DDFT provides no mechanism to account for the genuine nonequilibrium physics; see the [appendix](#) for further details.

8. Conclusions

For the purpose of assessing the status of the DDFT equation of motion (1) we have first described two exact limits that this approximation reproduces: the dynamics of the noninteracting diffusive ideal gas (see equation (4)) and the spatially inhomogeneous static equilibrium limit (see equation (2)). On general grounds one expects the DDFT to perform well when the situation under consideration is close to one of these limits. In particular near the static case this is nontrivial, as the system might be dense and spatially highly structured, as evident by a strongly inhomogeneous density profile. Provided that the dynamics are driven weakly enough via a time-dependent external potential then the DDFT [41, 42] can be a highly useful device, which enables one to describe the temporal evolution as a chain of equilibrium states, labelled by time. As the strictly static case (DFT) can correctly describe arbitrary spatial inhomogeneities, such adiabatic time evolution can provide highly nontrivial information. It is challenging, however, to know a priori whether or not the nonequilibrium situation under investigation will be close to adiabatic. Leaving the use of bare physical intuition aside, we are not aware of any simple quantitative criterion that would allow one to judge a priori whether DDFT is reliable or not. In this sense, the DDFT approximation can be viewed as being uncontrolled.

In general the contributions beyond the equilibrium physics will be relevant. On the level of the formally exact one-body equation of motion (14), the superadiabatic force field $\mathbf{f}_{\text{sup}}(\mathbf{r}, t)$ will then contribute and will potentially do very significantly so. Together with the adiabatic force field, which follows from the equilibrium excess free energy functional via $-\nabla\delta F_{\text{exc}}[\rho]/\delta\rho(\mathbf{r}, t)$, their sum constitutes the full interparticle forces. These force fields are coarse-grained, in a microscopically sharp way, to the one-body level of dynamical correlation functions. We have argued (i) that power functional theory is a concrete formal structure that allows to obtain $\mathbf{f}_{\text{sup}}(\mathbf{r}, t)$ from a generating functional and (ii) that simple approximate forms already capture much relevant nonequilibrium physics and they do so in a transparent and systematic way, and (iii) that machine learning can be used as a practical representation.

We have described and exemplified for uniaxial steady compressional flow of the three-dimensional LJ fluid the kinematic functional map that governs the exact nonequilibrium dynamics on the one-body level of dynamic correlation functions. As this description is based on a single position coordinate and a single time variable, it is of both conceptual and practical simplicity. As described by power functional theory the superadiabatic interparticle force field functionally depends on the density and the velocity field, i.e. $\mathbf{f}_{\text{sup}}(\mathbf{r}, t, [\rho, \mathbf{v}])$, for overdamped

Brownian motion. The functional dependence is causal, i.e. on the values of the density profile and velocity field at previous times, in general up to an initial state. The superadiabatic force field carries this kinematic dependence, i.e. on the history of $\rho(\mathbf{r}, t)$ and $\mathbf{v}(\mathbf{r}, t)$, but crucially it is independent of the external force field that drives the system.

We have explicitly demonstrated the functional map $\rho(\mathbf{r}, t), \mathbf{v}(\mathbf{r}, t) \rightarrow \mathbf{f}_{\text{int}}(\mathbf{r}, t)$ by establishing this functional relationship via machine learning the intrinsic force field. This includes as a special case the equilibrium map $\rho(\mathbf{r}, t) \rightarrow \mathbf{f}_{\text{ad}}(\mathbf{r}, t)$, as it is relevant for the approximative adiabatic time evolution via the DDFT (1). Using the force balance then gives direct access to the form of the required external force field via equation (29). The machine-learned model of the functional map hence enables ‘instant custom flow’ at negligible computational cost at the time of use. We recall that the custom flow method [52, 53] is based on the kinematic functional map, such that from knowing the kinematic one-body fields, the external force field that is necessary to generate the given time evolution follows straightforwardly from the exact force balance (6).

An analytical approach to one-body functional maps leads to the simple structure of velocity gradient forms for the viscous and structural superadiabatic forces, as exemplified in equations (16) and (17) for compressional flow, i.e. for velocity fields with nonvanishing divergence. As we have shown, the resulting predictions for the flow force (21) and for the structural force field (22) represent a reasonable description of the simulation data and its representation via the machine-learned functional. We attribute the remaining differences to higher-order terms [60] which we have not addressed here for simplicity and which we expect to become increasingly relevant under stronger driving. As we have shown, our results from direct simulation, from machine learning, and from the analytical approximations, satisfy exact global Noether sum rules.

We have restricted our discussion to a single and relatively easily accessible type of nonequilibrium dynamics, that of stationary uniaxial compressional flow that represents a model steady (batch) sedimentation situation. The power functional approach allows to go much further, including the treatment of viscoelasticity [57], as arising from superadiabatic memory, deconfinement under shear [58], the dynamic decay of the van Hove pair correlation function as governed by drag, viscous and structural forces [69, 70], and the complex forms of both flow and structural forces that arise under spatially complex forms of driving [60]. Time-dependent uniaxial flow is relevant in a variety of situations, including colloidal stratification [119, 120] and sedimentation [121].

Although power functional theory operates on the one-body level of dynamical correlation functions, two-body correlation functions are accessible both formally via the nonequilibrium Ornstein–Zernike route [43] and explicitly by the dynamical test particle limit. The latter is the dynamic generalization of Percus’ static test particle limit [62], which identifies two-point correlation functions, such as $g(r)$ as also recently shown to be intimately related to thermal Noether invariance at second order [51], with one-body density profiles in an external potential. This is set equal to the interparticle pair potential.

The dynamical test-particle limit goes further in that it describes the test particle via its own dynamical degrees of freedom, which are coupled to those of all other particles in the system. The concept was originally formulated as an approximation within DDFT [63, 64] and formally exactly within power functional theory [67]. Two-body superadiabatic effects were shown via simulation work to be significant [68–70] and they arise naturally in an exact formulation of the test particle dynamics [67]. The test particle limit allowed for a rationalization of the dynamical pair structure as e.g. experimentally observed in

two-dimensional colloids [10]. Recently an approach to DDFT based on the two-body level was formulated [122] and earlier work was addressed at construction of dynamical density functional theories from exactly solvable limits [123]; we recall that [41, 42] provide exhaustive overviews. In event-driven BD simulations superadiabatic forces were shown to consist of drag, viscous, and structural contributions [69, 70]; see [43] for an extended discussion. The physics of active particles [71–75] is very significantly governed by a vigorous interplay between superadiabatic and adiabatic forces, both of which are very strong, as the tendency of these systems to self-compress leads naturally to very high local densities.

Furthermore, relevant and interesting microscopic models that go beyond the simple fluid paradigm of a pair potential, such as the monatomic water model by Molinero and Moore [124, 125] and the three-body gel by Saw *et al* [126, 127], are accessible. Despite the complexity of both its defining Hamiltonian and the intricate transient network structure, the inhomogeneous viscous response of the three-body gel was recently demonstrated [61] to be surprisingly well captured by a simple power functional flow approximation. We finally recall that superadiabatic effects transcend overdamped dynamics, and are relevant both in quantum dynamics [43, 81, 82] and in classical molecular dynamics [43, 79, 80].

While we have restricted ourselves to discussing the point of view of functional relationships, it would be interesting to explore in future work possible cross connections to other theoretical approaches, such as Onsager’s variational principle for soft matter [128–131], stochastic thermodynamics [132], large deviation theory [133, 134], mode-coupling theory [135, 136], generalized hydrodynamics [137], local molecular field theory for nonequilibrium systems [138], as well as to the physics of nonequilibrium phase transitions [139], Brownian solitons [140], and crystal dynamics [141–144] and non-isothermal situations [145]. Implications of the machine-learning methodology are summarized at the end of the [appendix](#).

Data availability statement

The data cannot be made publicly available upon publication because they are not available in a format that is sufficiently accessible or reusable by other researchers. The data that support the findings of this study are available upon reasonable request from the authors.

Acknowledgments

This work is supported by the German Research Foundation (DFG) via Projects No. 436306241 and No. 447925252.

Appendix. Simulation and training details

Initialization

The nonequilibrium many-body physics that we investigate falls into the class of temporal initial value problems. This holds true both on the full many-body (phase space) level, as accessible via the simulations or formally via the Smoluchowski equation [43], as well as on the reduced one-body level of the temporal kinematic fields, i.e. the time-dependent density profile and current distribution. Evidently one-body initial data needs to be available in order to start the time evolution according to either the approximate DDFT (1) or the formally

exact power functional equation of motion (14). In typical applications of one of these frameworks to a dynamical problem, the system is taken to be in an equilibrium state at a starting time t_0 such that the current vanishes and the density profile is known. Standard ways [146] to specify an initial state include choosing the bulk and possibly applying (simple) external fields and letting the system relax therein. The DFT point of view allows for more general initializations as one can choose an equilibrium system with an arbitrary spatially inhomogeneous density profile $\rho(\mathbf{r}, t_0)$ as the starting point.

We recall from section 1 that for an equilibrium system with given interparticle interactions, knowledge of the density profile [in the present case $\rho(\mathbf{r}, t_0)$] is sufficient to formally exactly determine all static thermal properties. This fact [4, 150] constitutes one of the major virtues of static DFT. Leaving representability issues aside, prescribing a (physically sensible) form of $\rho(\mathbf{r}, t_0)$ is feasible, as one can picture this as being generated by an appropriate form of corresponding external potential $V_{\text{ext}}(\mathbf{r}, t_0)$, where t_0 acts as a mere label to specify the initial state. As laid out above in section 1, the description formally requires to have access to the free energy density functional $F[\rho]$, which implicitly contains the full static information about the thermal physics of the system.

In particular, the equilibrium many-body probability distribution function $\Psi(\mathbf{r}^N, t_0)$ is uniquely determined, for given interparticle interactions and given knowledge of the density profile [3, 4, 150]. (In the notation we have dropped the dependence on momenta, which is trivial in the present situation.) One pictures the system to have been in the same equilibrium state also at all prior times $t < t_0$ and having undergone time evolution in this quiescent state up to t_0 . As an aside, the equilibrium dynamics can then be characterized for bulk liquids on the two-body level by the van Hove dynamical correlation function [3, 63–70, 147–149], with much recent progress from the power functional point of view [69, 70].

Obtaining a statistical description requires in principle to average over the initial distribution of microstates. In the context of many-body simulations, in practice this necessitates to carry out a sufficient number of independent realizations of the time evolution that is under consideration. Representative studies relied on e.g. 10^4 realizations for the transient dynamics of hard spheres under a temporally switched shear field [57], and on 2×10^6 realizations [80] for investigating superadiabatic acceleration effects that occur in Molecular Dynamics. There are also special cases, such as test particle concepts that allow efficient sampling of the bulk van Hove function via building moving averages [69, 70]. We also point out work [151, 152] which address the initial state dependence in the context of quantum mechanical time-dependent density functional theory.

Steady states

In the present model situation of uniaxial compressional steady flow (we recall its graphical illustration in figure 1) there is no need to temporally resolve the one-body fields, as these are invariant in time. Hence we proceed in the standard way of replacing the average over an ensemble of initial states with a temporal average over a single trajectory of sufficiently long duration. Recalling the details that are given in section 7, we average over time evolutions each with duration 1000τ , with $\tau = \sigma^2/D_0$ denoting the Brownian time scale for self diffusion with diffusion constant $D_0 = k_B T/\gamma$, where γ is the friction constant against the background. The strategy of identifying temporal and ensemble averages relies on having an ergodic system of which the time evolution indeed explores the entirety of the ensemble. As we deal with a liquid in the present illustrative case, we expect ergodicity to hold.

In order to validate this expectation, we have investigated the possibility of dependence of the steady state results on the initial state of the simulation; see figure 3 for illustrations of the chosen four different (crystalline and disordered) microstates. We recall that we evolve the system over a waiting time of 100τ before starting to sample the one-body correlation functions. The resulting steady state profiles, see figure 3, bear no traces of the different initialization, and the data of each of the four runs collapse onto each other. As this behaviour is already observed on the level of starting with individual differing microstates, we expect no changes if we were to start with a representative sample of, say 10^4 , microstates in order to numerically approximate an entire distribution.

Training procedure

The results shown in figure 3 also serve to illustrate our training procedure in more detail. We use randomized forms of the external force field $f_{\text{ext}}(x)$ via superimposing Fourier modes that are compatible with the box size L via: $f_{\text{ext}}(x) = \sum_{n=0}^{n_{\text{max}}} A_n \cos(2\pi nx/L + B_n)$, which we cut off at $n_{\text{max}} = 4$. The amplitudes A_n and phases B_n are generated randomly within a cutoff, which i) makes the specific training protocol free of having to perform manual choices and ii) removes any further bias thus easing the interpretation of the quality of the machine learning predictions. Our currently adopted random training strategy is suited to investigate issues of generality, universality and transferability both of the underlying mathematical structure of power functional theory and of its presently proposed specifically tailored implementation via supervised machine learning. Nevertheless, as our supervised learning procedure is general, one could well tune for specific applications and rather train on the basis of situations that are close to the eventual use of the network, see e.g. [111] for a corresponding enlightening study.

Our supervision protocol operates on the level of the simulation output in a specifically organized way of (functional) dependencies of the obtained histograms that represent the one-body distributions. All three involved functions are taken from straightforward sampling in adaptive BD. The density profile $\rho(x)$ is obtained from the standard counting method. (We recall reduced-variance sampling techniques such as force sampling [115–117], which could help in acquiring numerical training data more efficiently.)

The current distribution $J(x)$ can be sampled via the force balance equation or alternatively via a temporally centered derivative of the particle trajectories. Here the position resolved histogram is filled with the displacement vector of each particle, between the position in the next and in the previous time step; see the appendix of [52] for an in-depth description. The velocity profile then follows straightforwardly from $v(x) = J(x)/\rho(x)$.

Finally the interparticle force density $F_{\text{int}}(x)$ is sampled in an analogous way on the basis of a position-resolved histogram that simply accepts the instantaneous interparticle force that acts on each given particle. The interparticle force field is then obtained by simple normalization with the density profile, $f_{\text{int}}(x) = F_{\text{int}}(x)/\rho(x)$.

From a data science point of view, and possibly even when working in a physics-informed way, one might use the information in all three fields $\rho(x)$, $v(x)$ and $f_{\text{int}}(x)$ to analyze and make predictions of the dynamical behaviour of the system. However, our present approach is very specific and leaves no choice in the general setup of the supervised learning. We have $\rho(x)$ and $v(x)$ as inputs and $f_{\text{int}}(x)$ as the output or target of the neural network; we recall the description in section 4 of the functional relationships that apply to the nonequilibrium physics. As concrete illustration we show three representative training data sets in figure 3. We find the success of the learning procedure to be robust against changes in even simple network topology and choice of hyperparameters. We attribute these

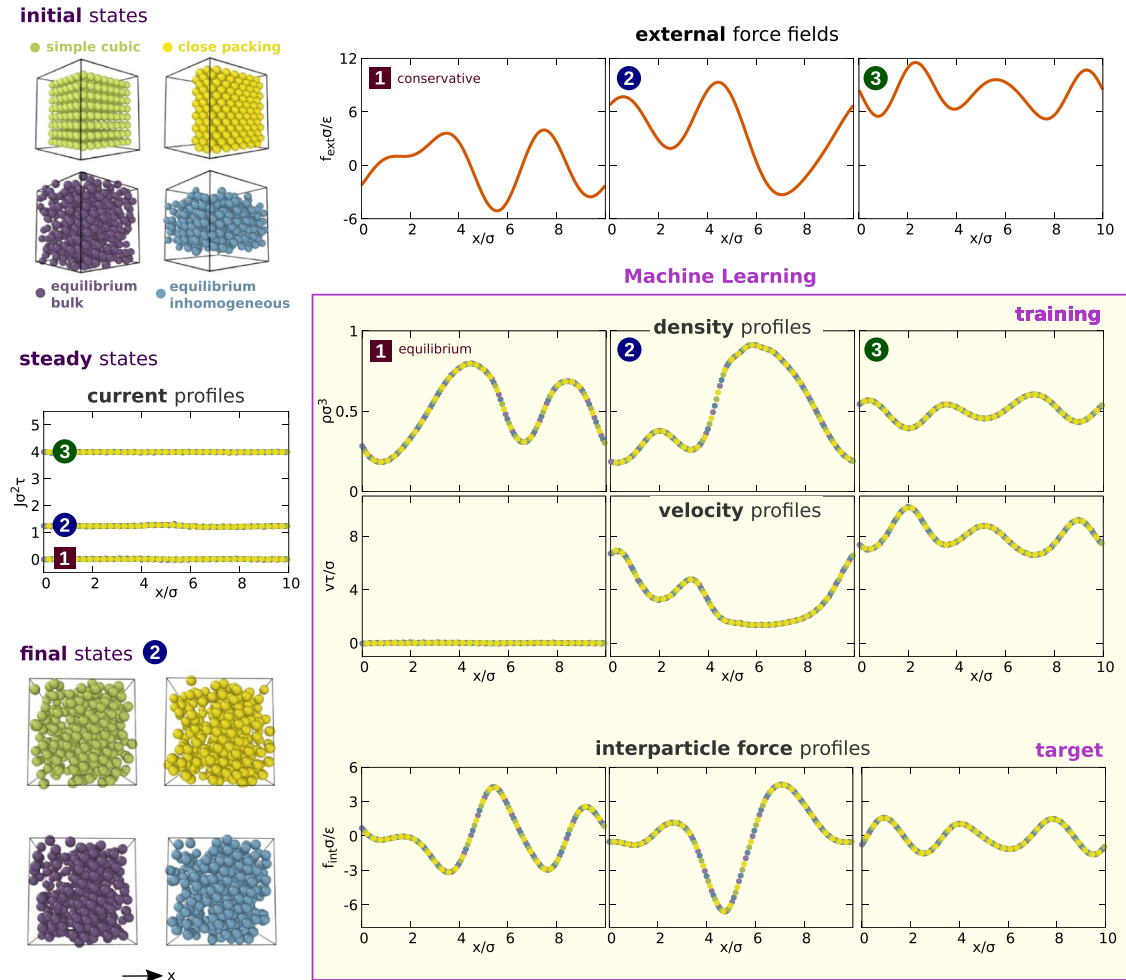


Figure 3. Three representative cases (systems 1, 2, and 3) of nonequilibrium steady states under external driving, as used for training the neural network. The results are obtained from adaptive BD simulations under the influence of a temporally static external force field $f_{\text{ext}}(x)$ (top row) that consists of a random superposition of spatial Fourier modes. The zeroth Fourier mode represents a constant force offset, which either vanishes (system 1) or drives the system out of equilibrium (systems 2 and 3). The steady states are characterized by spatially and temporally constant currents $J(x) = J_0 = \text{const}$, with $J_0 = 0$ in equilibrium (system 1) and $J_0 > 0$ under drive (systems 2 and 3). The density profile $\rho(x)$ (second row) is temporally constant and spatially inhomogeneous, as induced by the action of the external force field. The inhomogeneous velocity profile is simply the inverse $v(x) = J_0/\rho(x)$ (third row). For each system 1, 2 and 3, the results for the respective steady state profiles $\rho(x)$, $v(x)$, and the interparticle force field $f_{\text{int}}(x)$ (fourth row) are independent of the type of initialization, as demonstrated by the results from the four differently initialized simulation runs (indicated by differently coloured symbols) lying on top of each other. Here each system is alternatively initialized via one of four protocols to select the initial microstate: simple cubic (green) or close packed (yellow) crystals or an equilibrated bulk liquid state (violet) or an inhomogeneous slab-like confined liquid (blue). Representative simulation snapshots in steady state ('final states' after 1000τ) for system 2 illustrate the spatial structure of the flowing liquid; no imprints of the initialization can be perceived. The machine learning is based on training data $\rho(x)$ and $v(x)$ [or alternatively to the latter $J(x)$ or $\partial v(x)/\partial x$] that lead to the target interparticle force field $f_{\text{int}}(x)$ for each given training system (1000 in total) in the supervised learning. While we here solely illustrate the training procedure, we show in figures 2, 4, and 5 how the trained model can be used to both predict and design nonequilibrium steady states.

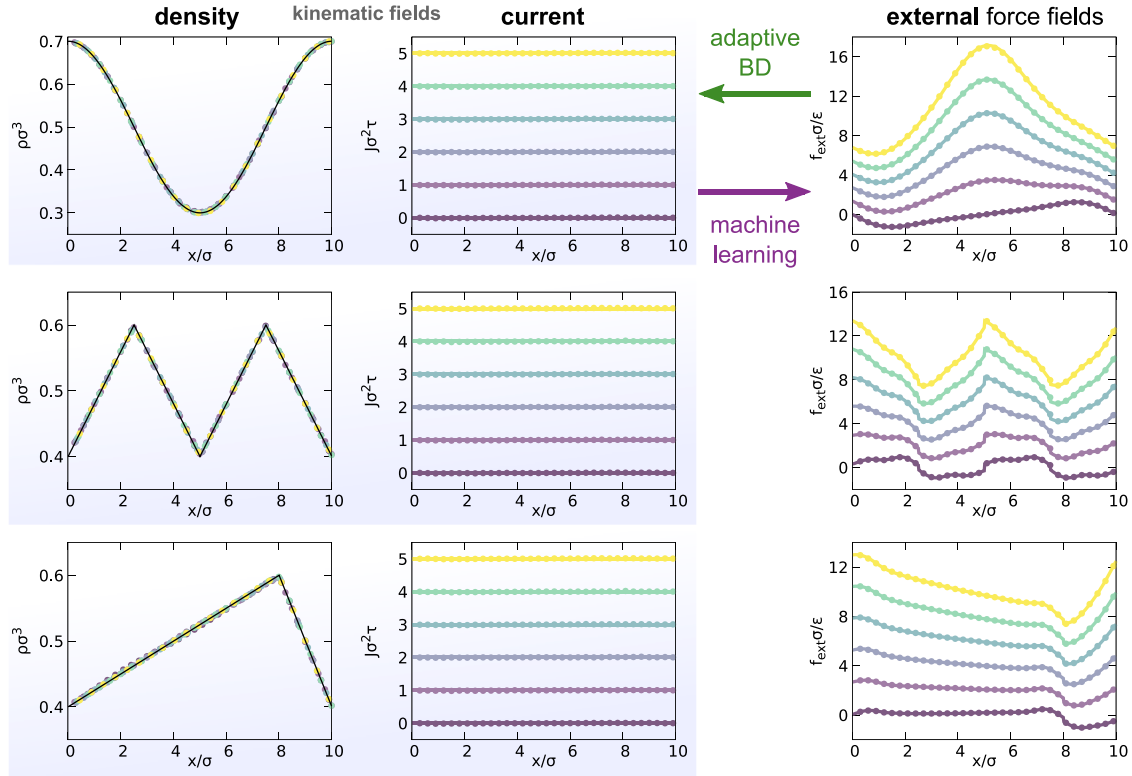


Figure 4. Demonstration of the machine-learned kinematic force map and its use in the design of nonequilibrium steady states. Shown are three different target shapes of the density profile $\rho(x)$ (left column): cosine wave (top row, results are identical to those shown in figure 2), triangle wave (second row), and sawtooth-like wave (third row). For each of the three density waves the current profile (second column) $J(x) = J_0 = \text{const}$, and we prescribe alternative values $J_0\tau/\sigma^2 = 0$ (equilibrium), 1, 2, 3, 4, and 5 (all nonequilibrium). Our aim is to obtain the specific form of $f_{\text{ext}}(x)$ via our trained machine learning model which then generates the target shapes of $\rho(x)$ and $J(x)$. That this procedure indeed is successful is validated with BD simulations as shown via the symbols, as both $\rho(x)$ and $J(x)$ are reproduced to high accuracy. Each of the three target density profiles $\rho(x)$ (lines) is strikingly matched by the simulation results (symbols); the data for the external force profile $f_{\text{ext}}(x)$ (right column) coincide per construction, as the output from machine learning is taken as the input force field in the many-body simulations that are carried out to assess the accuracy of the design procedure.

features to the fact that the mapping is formally exact, as summarized in the main text and reviewed in detail in [43].

Universality and inverse design

The thus obtained functional relationship $f_{\text{int}}^*(x, [\rho, v])$ not merely interpolates between the training situations, but it rather captures the genuine correlated nature of the statistical physics under consideration. We recall the target cosine-shaped density wave (presented in figure 2 and replotted in the first row of figure 4 as a reference). This situation was not genuinely part of the training but certainly close in character. As a further demonstration we apply the network to a triangular density wave (second row in figure 4) and also to a sawtooth-like density wave (third row in figure 4), which are further removed from the situations encountered during training. The excellent match with the direct simulation results of the density profile and current distribution validates our approach.

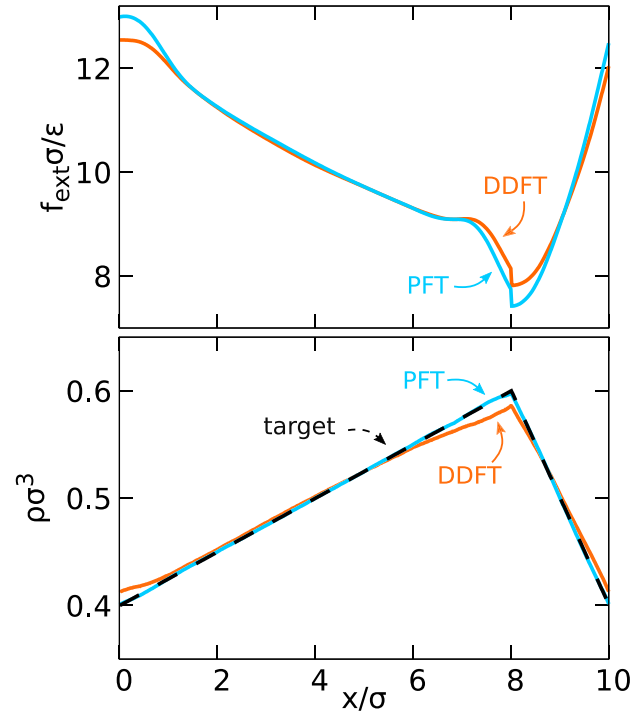


Figure 5. Shape of the external force field $f_{\text{ext}}(x)$ (upper panel) that stabilizes the target nonequilibrium sawtooth density profile $\rho(x)$ (lower panel) with current strength $J_0\sigma^2/\tau = 5$ (as also shown in the third row of figure 4). The force field is generated either from power functional theory via equation (A1) or from machine learning DDFT via equation (A2). While capturing the correct shape of the external force profile, the DDFT produces in this case a quantitative error between maximal and minimal force of size ϵ/σ . The respective results for the density profiles are obtained from direct simulations. The power functional design meets the target profile in a quasi-exact way, whereas quantitative deviations occur in DDFT in particular near the cusps of the wave.

We finally return to the DDFT and to the purpose of the present Perspective of discussing its virtues and shortcomings. We present as a final example, see figure 5, its application to the sawtooth state. Shown is the external force profile, as obtained from the machine-learned power functional, via the instant custom flow equation (29), which we reproduce for convenience:

$$f_{\text{ext}}(x) = \gamma \frac{J_0}{\rho(x)} + k_B T \frac{\partial \ln \rho(x)}{\partial x} - f_{\text{int}}^*(x, [\rho, v]). \quad (\text{A1})$$

In the present case this constitutes a (numerical) quasi-exact solution; we recall the excellent agreement of the resulting kinematic profiles, shown in figure 4, with the direct simulation results. We can now easily compare this to the adiabatic DDFT prediction, as the equilibrium states were part of our training protocol (cases of vanishing zeroth mode of the external force field). We can straightforwardly implement this on the level of the neural network by simply considering no flow, i.e. setting the velocity profile $v(x) = 0$, which yields a quasi-exact representation of the adiabatic force; we recall the perfect agreement shown in figure 4 for the cases with no flow, where $J_0 = 0$ (dark purple symbols and lines). Hence within DDFT the instant custom flow equation (A1) reduces to

the following simple form:

$$f_{\text{ext}}^{\text{DDFT}}(x) = \gamma \frac{J_0}{\rho(x)} + k_B T \frac{\partial \ln \rho(x)}{\partial x} - f_{\text{ad}}^*(x, [\rho]). \quad (\text{A2})$$

Here the machine-learned adiabatic force field is obtained simply by evaluating the full network at vanishing velocity, i.e. $f_{\text{ad}}^*(x, [\rho]) = f_{\text{int}}^*(x, [\rho, v = 0])$. The comparison shown in figure 5 indicates qualitatively correct behaviour of the DDFT but quantitative errors of magnitude ϵ/σ .

The effects being quantitatively small should not lead one to conclude that the physics are irrelevant. First, as laid out above, the planar uniaxial geometry is intrinsically favorable for the DDFT. Secondly, we have chosen moderate values for temperature and for density to ease our current pilot study for the use of machine learning. This renders the situation relatively simple. However, as emphasized above, a priori it is very difficult to assess whether or not the DDFT will be sufficient to obtain a reliable estimate of the real time evolution. For a very recent demonstration of quantitatively large superadiabatic (viscous and structural) forces, we point the reader to the study by Sammüller *et al* [61] of the nonequilibrium dynamics of a three-body colloidal gel former [126, 127].

Implications and related work

We take the quantitative success and computational ease of applying supervised machine learning to the formal functional dependencies of nonequilibrium many-body flow, as presently considered in a simple uniaxial flow geometry, as an incentive to summarize several possible connections that could be explored in future work. Our approach fits into the broader picture of coarse-graining many-body systems out of equilibrium [44] and it is very specific in terms of input and output variables of the neural network. The supervised machine learning method gives the interparticle force field directly, in contrast to approaches that are based on learning the excess free energy functional [109–112] which then upon differentiation according to equation (10) give the (adiabatic approximation for the) interparticle force density. DDFT was also used in learning the physics of pattern formation from images [153], and for importance sampling in adaptive multiscale simulations, see [42, 154] for a list of several further examples.

In the terminology of multiscale simulation methods for soft matter systems [155], in our method we learn the characteristics of a fine-grained model (chosen as the LJ fluid in the present model study) and, while not strictly obtaining a coarse-grained model, are able to reduce the fine-grained information systematically to the one-body level in a microscopically resolved way. It would be interesting to see whether our approach is useful in the context of adaptive simulation techniques [156–158] as applied e.g. to coupling boundaries of open systems [159].

We would need to go beyond the presently considered steady states to address memory effects, as are relevant both in classical [69, 70, 160, 161] and in quantum systems [151, 152]. Given the recent interest in force-based quantum-mechanical density functional theory [162, 163], we could imagine that apart from quantum power functional theory [43, 49, 81, 82] our study could potentially be inspirational in other force-based approaches to quantum dynamics [164–167].

ORCID iDs

Daniel de las Heras  <https://orcid.org/0000-0003-3219-0518>
 Toni Zimmermann  <https://orcid.org/0009-0005-1181-1188>
 Florian Sammüller  <https://orcid.org/0000-0002-3605-329X>
 Sophie Hermann  <https://orcid.org/0000-0002-4012-9170>

Matthias Schmidt  <https://orcid.org/0000-0002-5015-2972>

References

- [1] Nagel S R 2017 Experimental soft-matter science *Rev. Mod. Phys.* **89** 025002
- [2] Evans R, Frenkel D and Dijkstra M 2019 From simple liquids to colloids and soft matter *Phys. Today* **72** 38
- [3] Hansen J P and McDonald I R 2013 *Theory of Simple Liquids* 4th edn (London: Academic)
- [4] Evans R 1979 The nature of the liquid-vapour interface and other topics in the statistical mechanics of non-uniform, classical fluids *Adv. Phys.* **28** 143
- [5] Marconi U M B and Tarazona P 1999 Dynamic density functional theory of fluids *J. Chem. Phys.* **110** 8032
- [6] Hohenberg P C and Halperin B I 1977 Theory of dynamic critical phenomena *Rev. Mod. Phys.* **49** 435
- [7] Sammüller F and Schmidt M 2021 Adaptive Brownian dynamics *J. Chem. Phys.* **155** 134107
- [8] Royall C P, Dzubiella J, Schmidt M and van Blaaderen A 2007 Non-equilibrium sedimentation of colloids on the particle scale *Phys. Rev. Lett.* **98** 188304
- [9] Bier M, van Roij R, Dijkstra M and van der Schoot P 2008 Self-diffusion of particles in complex fluids: temporary cages and permanent barriers *Phys. Rev. Lett.* **101** 215901
- [10] Stopper D, Thorneywork A L, Dullens R P A and Roth R 2018 Bulk dynamics of Brownian hard disks: dynamical density functional theory versus experiments on two-dimensional colloidal hard spheres *J. Chem. Phys.* **148** 104501
- [11] Perez C M, Rey M, Goddard B D and Thijssen J H J 2021 Changing the flow profile and resulting drying pattern of dispersion droplets via contact angle modification (arXiv:2111.00464)
- [12] Evans R 1992 Density functionals in the theory of nonuniform fluids *Fundamentals of Inhomogeneous Fluids* ed D Henderson (New York: Dekker)
- [13] For an overview of new developments in classical density functional theory, see: Evans R, Oettel M, Roth R and Kahl G 2016 New developments in classical density functional theory *J. Phys.: Condens. Matter* **28** 240401
- [14] Evans R, Stewart M C and Wilding N B 2019 A unified description of hydrophilic and superhydrophobic surfaces in terms of the wetting and drying transitions of liquids *Proc. Natl Acad. Sci.* **116** 23901
- [15] Coe M K, Evans R and Wilding N B 2022 Density depletion and enhanced fluctuations in water near hydrophobic solutes: identifying the underlying physics *Phys. Rev. Lett.* **128** 045501
- [16] Coe M K, Evans R and Wilding N B 2023 Understanding the physics of hydrophobic solvation *J. Chem. Phys.* **158** 034508
- [17] Martin-Jimenez D, Chacón E, Tarazona P and Garcia R 2016 Atomically resolved three-dimensional structures of electrolyte aqueous solutions near a solid surface *Nat. Commun.* **7** 12164
- [18] Hernández-Muñoz J, Chacón E and Tarazona P 2019 Density functional analysis of atomic force microscopy in a dense fluid *J. Chem. Phys.* **151** 034701
- [19] Cats P, Evans R, Härtel A and van Roij R 2021 Primitive model electrolytes in the near and far field: decay lengths from DFT and simulations *J. Chem. Phys.* **154** 124504
- [20] Rosenfeld Y 1989 Free-energy model for the inhomogeneous hard-sphere fluid mixture and density-functional theory of freezing *Phys. Rev. Lett.* **63** 980
- [21] Roth R 2010 Fundamental measure theory for hard-sphere mixtures: a review *J. Phys.: Condens. Matter* **22** 063102
- [22] Roth R, Evans R, Lang A and Kahl G 2002 Fundamental measure theory for hard-sphere mixtures revisited: the White Bear version *J. Phys.: Condens. Matter* **14** 12063
- [23] Hansen-Goos H and Roth R 2006 Density functional theory for hard-sphere mixtures: the White Bear version mark II *J. Phys.: Condens. Matter* **18** 8413
- [24] Archer A J and Evans R 2004 Dynamical density functional theory and its application to spinodal decomposition *J. Chem. Phys.* **121** 4246
- [25] Chan G K-L and Finken R 2005 Time-dependent density functional theory of classical fluids *Phys. Rev. Lett.* **94** 183001
- [26] Español P and Löwen H 2009 Derivation of dynamical density functional theory using the projection operator technique *J. Chem. Phys.* **131** 244101
- [27] Marconi U M B and Melchionna S 2007 Phase-space approach to dynamical density functional theory *J. Chem. Phys.* **126** 184109
- [28] Dzubiella J and Likos C N 2003 Mean-field dynamical density functional theory *J. Phys.: Condens. Matter* **15** L147
- [29] Lutsko J F and Oettel M 2021 Reconsidering power functional theory *J. Chem. Phys.* **155** 094901
- [30] Szamel G 2022 An alternative, dynamic density functional-like theory for time-dependent density fluctuations in glass-forming fluids *J. Chem. Phys.* **156** 191102

- [31] Goddard B D, Mills-Williams R D, Ottobre M and Pavliotis G 2020 Well-posedness and equilibrium behaviour of overdamped dynamic density functional theory (arXiv:2002.11663)
- [32] Archer A J 2006 Dynamical density functional theory for dense atomic liquids *J. Phys.: Condens. Matter* **18** 5617
- [33] Archer A J 2009 Dynamical density functional theory for molecular and colloidal fluids: a microscopic approach to fluid mechanics *J. Chem. Phys.* **130** 014509
- [34] Stierle R and Gross J 2021 Hydrodynamic density functional theory for mixtures from a variational principle and its application to droplet coalescence *J. Chem. Phys.* **155** 134101
- [35] Goddard B D, Nold A, Savva N, Pavliotis G A and Kalliadas S 2012 General dynamical density functional theory for classical fluids *Phys. Rev. Lett.* **109** 120603
- [36] Rex M and Löwen H 2009 Dynamical density functional theory for colloidal dispersions including hydrodynamic interactions *Eur. Phys. J. E* **28** 139
- [37] Dzubiella J and Moncho-Jordá A 2020 Controlling the microstructure and phase behavior of confined soft colloids by active interaction switching *Phys. Rev. Lett.* **125** 078001
- [38] Bley M, Dzubiella J and Moncho-Jordá A 2021 Active binary switching of soft colloids: stability and structural properties *Soft Matter* **17** 7682
- [39] Goddard B D, Gooding B, Pavliotis G A and Short H 2022 Noisy bounded confidence models for opinion dynamics: the effect of boundary conditions on phase transitions *IMA J. Appl. Math.* **87** 80
- [40] te Vrugt M, Bickmann J and Wittkowski R 2020 Effects of social distancing and isolation on epidemic spreading modeled via dynamical density functional theory *Nat. Commun.* **11** 5576
- [41] te Vrugt M, Löwen H and Wittkowski R 2020 Classical dynamical density functional theory: from fundamentals to applications *Adv. Phys.* **69** 121
- [42] te Vrugt M and Wittkowski R 2023 Perspective: new directions in dynamical density functional theory *J. Phys.: Condens. Matter* **35** 041501
- [43] Schmidt M 2022 Power functional theory for many-body dynamics *Rev. Mod. Phys.* **94** 015007
- [44] Schilling T 2022 Coarse-grained modelling out of equilibrium *Phys. Rep.* **972** 1
- [45] Hermann S and Schmidt M 2021 Noether’s theorem in statistical mechanics *Commun. Phys.* **4** 176
- [46] Hermann S and Schmidt M 2022 Why Noether’s theorem applies to statistical mechanics *J. Phys.: Condens. Matter* **34** 213001
- [47] Tschopp S M, Sammüller F, Hermann S, Schmidt M and Brader J M 2022 Force density functional theory in- and out-of-equilibrium *Phys. Rev. E* **106** 014115
- [48] Sammüller F, Hermann S and Schmidt M 2023 Comparative study of force-based classical density functional theory *Phys. Rev. E* **107** 034109
- [49] Hermann S and Schmidt M 2022 Force balance in thermal quantum many-body systems from Noether’s theorem *J. Phys. A: Math. Theor.* **55** 464003
- [50] Hermann S and Schmidt M 2022 Variance of fluctuations from Noether invariance *Commun. Phys.* **5** 276
- [51] Sammüller F, Hermann S, de las Heras D and Schmidt M 2023 What is liquid, from Noether’s perspective? (arXiv:2301.11221)
- [52] de las Heras D, Renner J and Schmidt M 2019 Custom flow in overdamped Brownian dynamics *Phys. Rev. E* **99** 023306
- [53] Renner J, Schmidt M and de las Heras D 2021 Custom flow in molecular dynamics *Phys. Rev. Res.* **3** 013281
- [54] Schmidt M and Brader J M 2013 Power functional theory for Brownian dynamics *J. Chem. Phys.* **138** 214101
- [55] Fortini A, de las Heras D, Brader J M and Schmidt M 2014 Superadiabatic forces in Brownian many-body dynamics *Phys. Rev. Lett.* **113** 167801
- [56] Stuhlmüller N C X, Eckert T, de las Heras D and Schmidt M 2018 Structural nonequilibrium forces in driven colloidal systems *Phys. Rev. Lett.* **121** 098002
- [57] Treffenstädt L L and Schmidt M 2020 Memory-induced motion reversal in Brownian liquids *Soft Matter* **16** 1518
- [58] Jahreis N and Schmidt M 2020 Shear-induced deconfinement of hard disks *Col. Pol. Sci.* **298** 895
- [59] de las Heras D and Schmidt M 2018 Velocity gradient power functional for Brownian dynamics *Phys. Rev. Lett.* **120** 028001
- [60] de las Heras D and Schmidt M 2020 Flow and structure in nonequilibrium Brownian many-body systems *Phys. Rev. Lett.* **125** 018001
- [61] Sammüller F, de las Heras D and Schmidt M 2023 Inhomogeneous steady shear dynamics of a three-body colloidal gel former *J. Chem. Phys.* **158** 054908
- [62] Percus J K 1962 Approximation methods in classical statistical mechanics *Phys. Rev. Lett.* **8** 462
- [63] Archer A J, Hopkins P and Schmidt M 2007 Dynamics in inhomogeneous liquids and glasses via the test particle limit *Phys. Rev. E* **75** 040501(R)

- [64] Hopkins P, Fortini A, Archer A J and Schmidt M 2010 The van Hove distribution function for Brownian hard spheres: dynamical test particle theory and computer simulations for bulk dynamics *J. Chem. Phys.* **133** 224505
- [65] Stopper D, Roth R and Hansen-Goos H 2015 Communication: dynamical density functional theory for dense suspensions of colloidal hard spheres *J. Chem. Phys.* **143** 181105
- [66] Stopper D, Marolt K, Roth R and Hansen-Goos H 2015 Modeling diffusion in colloidal suspensions by dynamical density functional theory using fundamental measure theory of hard spheres *Phys. Rev. E* **92** 022151
- [67] Brader J M and Schmidt M 2015 Power functional theory for the dynamic test particle limit *J. Phys.: Condens. Matter* **27** 194106
- [68] Schindler T and Schmidt M 2016 Dynamic pair correlations and superadiabatic forces in a dense Brownian liquid *J. Chem. Phys.* **145** 064506
- [69] Treffenstädt L L and Schmidt M 2021 Universality in driven and equilibrium hard sphere liquid dynamics *Phys. Rev. Lett.* **126** 058002
- [70] Treffenstädt L L, Schindler T and Schmidt M 2022 Dynamic decay and superadiabatic forces in the van Hove dynamics of bulk hard sphere fluids *SciPost Phys.* **12** 133
- [71] Hermann S, de las Heras D and Schmidt M 2019 Non-negative interfacial tension in phase-separated active Brownian particles *Phys. Rev. Lett.* **123** 268002
- [72] Hermann S, Krinninger P, de las Heras D and Schmidt M 2019 Phase coexistence of active Brownian particles *Phys. Rev. E* **100** 052604
- [73] Krinninger P, Schmidt M and Brader J M 2016 Nonequilibrium phase behaviour from minimization of free power dissipation *Phys. Rev. Lett.* **117** 208003
- [74] Krinninger P and Schmidt M 2019 Power functional theory for active Brownian particles: general formulation and power sum rules *J. Chem. Phys.* **150** 074112
- [75] Hermann S, de las Heras D and Schmidt M 2021 Phase separation of active Brownian particles in two dimensions: anything for a quiet life *Mol. Phys.* **119** e1902585
- [76] de las Heras D and Schmidt M 2014 Full canonical information from grand potential density functional theory *Phys. Rev. Lett.* **113** 238304
- [77] de las Heras D, Brader J M, Fortini A and Schmidt M 2016 Particle conservation in dynamical density functional theory *J. Phys.: Condens. Matter* **28** 244024
- [78] Schindler T, Wittmann R and Brader J M 2019 Particle-conserving dynamics on the single-particle level *Phys. Rev. E* **99** 012605
- [79] Schmidt M 2018 Power functional theory for Newtonian many-body dynamics *J. Chem. Phys.* **148** 044502
- [80] Renner J, Schmidt M and de las Heras D 2022 Shear and bulk acceleration viscosities in simple fluids *Phys. Rev. Lett.* **128** 094502
- [81] Schmidt M 2015 Quantum power functional theory for many-body dynamics *J. Chem. Phys.* **143** 174108
- [82] Brütting M, Trepl T, de las Heras D and Schmidt M 2019 Superadiabatic forces via the acceleration gradient in quantum many-body dynamics *Molecules* **24** 3660
- [83] Clegg P S 2021 Characterising soft matter using machine learning *Soft Matter* **17** 3991
- [84] Dijkstra M and Luijten E 2021 From predictive modelling to machine learning and reverse engineering of colloidal self-assembly *Nat. Mater.* **20** 762
- [85] Coli G M, Boattini E, Filion L and Dijkstra M 2022 Inverse design of soft materials via a deep learning-based evolutionary strategy *Sci. Adv.* **8** eabj6731
- [86] Boattini E, Dijkstra M and Filion L 2019 Unsupervised learning for local structure detection in colloidal systems *J. Chem. Phys.* **151** 154901
- [87] van Mastrigt R, Dijkstra M, van Hecke M and Coulais C 2022 Machine learning of implicit combinatorial rules in mechanical metamaterials *Phys. Rev. Lett.* **129** 198003
- [88] Campos-Villalobos G, Boattini E, Filion L and Dijkstra M 2021 Machine learning many-body potentials for colloidal systems *J. Chem. Phys.* **155** 174902
- [89] Campos-Villalobos G, Giunta G, Marín-Aguilar S and Dijkstra M 2022 Machine-learning effective many-body potentials for anisotropic particles using orientation-dependent symmetry functions *J. Chem. Phys.* **157** 024902
- [90] Ciarella S, Chiappini M, Boattini E, Dijkstra M and Janssen L M C 2023 Dynamics of supercooled liquids from static averaged quantities using machine learning (arXiv:2212.09338)
- [91] Winter M K, Pihlajamaa I, Debets V E and Janssen L M C 2023 A deep learning approach to the measurement of long-lived memory kernels from generalised Langevin dynamics (arXiv:2302.13682)
- [92] Janzen G, Smit C, Visbeek S, Debets V E, Luo C, Storm C, Ciarella S and Janssen L M C 2023 Classifying the age of a glass based on structural properties: a machine learning approach (arXiv:2303.00636)
- [93] Paret J, Jack R L and Coslovich D 2020 Assessing the structural heterogeneity of supercooled liquids through community inference *J. Chem. Phys.* **152** 144502
- [94] Coslovich D, Jack R L and Paret J 2022 Dimensionality reduction of local structure in glassy binary mixtures *J. Chem. Phys.* **157** 204503
- [95] Singh A N and Limmer D T 2023 Variational deep learning of equilibrium transition path ensembles (arXiv:2302.14857)

- [96] Das A, Rose D C, Garrahan J P and Limmer D T 2021 Reinforcement learning of rare diffusive dynamics *J. Chem. Phys.* **155** 134105
- [97] Lindquist B A, Jadrlich R B and Truskett T M 2016 Communication: inverse design for self-assembly via on-the-fly optimization *J. Chem. Phys.* **145** 111101
- [98] Sherman Z M, Howard M P, Lindquist B A, Jadrlich R B and Truskett T M 2020 Inverse methods for design of soft materials *J. Chem. Phys.* **152** 140902
- [99] Statt A, Kleeblatt D C and Reinhart W F 2021 Unsupervised learning of sequence-specific aggregation behavior for a model copolymer *Soft Matter* **17** 7697
- [100] Mahynski N A, Mao R, Pretti E, Shena V K and Mittal J 2020 Grand canonical inverse design of multicomponent colloidal crystals *Soft Matter* **16** 3187
- [101] O’Leary J, Mao R, Pretti E J, Paulson J A and Mittal J 2021 Deep learning for characterizing the self-assembly of three-dimensional colloidal systems *Soft Matter* **17** 989
- [102] Zhang J, Yang J, Zhang Y and Bevan M A 2020 Controlling colloidal crystals via morphing energy landscapes and reinforcement learning *Sci. Adv.* **6** eabd6716
- [103] Sidky H and Whitmer J K 2018 Learning free energy landscapes using artificial neural networks *J. Chem. Phys.* **148** 104111
- [104] Niblett S P, Galib M and Limmer D T 2021 Learning intermolecular forces at liquid-vapor interfaces *J. Chem. Phys.* **155** 164101
- [105] Weeks J D, Selinger R L B and Broughton J Q 1995 Self-consistent treatment of repulsive and attractive forces in nonuniform liquids *Phys. Rev. Lett.* **75** 2694
- [106] Weeks J D 2002 Connecting local structure to interface formation: a molecular scale van der Waals theory of nonuniform liquids *Annu. Rev. Phys. Chem.* **53** 533
- [107] Archer A J and Evans R 2013 Relationship between local molecular field theory and density functional theory for nonuniform liquids *J. Chem. Phys.* **138** 014502
- [108] Santos-Silva T, Teixeira P I C, Anquetil-Deck C and Cleaver D J 2014 Neural-network approach to modeling liquid crystals in complex confinement *Phys. Rev. E* **89** 053316
- [109] Lin S-C and Oettel M 2019 A classical density functional from machine learning and a convolutional neural network *SciPost Phys.* **6** 025
- [110] Lin S-C, Martius G and Oettel M 2020 Analytical classical density functionals from an equation learning network *J. Chem. Phys.* **152** 021102
- [111] Cats P, Kuipers S, de Wind S, van Damme R, Coli G M, Dijkstra M and van Roij R 2021 Machine-learning free-energy functionals using density profiles from simulations *APL Mater.* **9** 031109
- [112] Yatsyshin P, Kalliadasis S and Duncan A B 2022 Physics-constrained Bayesian inference of state functions in classical density-functional theory *J. Chem. Phys.* **156** 074105
- [113] Fang X, Gu M and Wu J 2022 Reliable emulation of complex functionals by active learning with error control *J. Chem. Phys.* **157** 214109
- [114] Qiao C, Yu X, Song X, Zhao T, Xu X, Zhao S and Gubbins K E 2020 Enhancing gas solubility in nanopores: a combined study using classical density functional theory and machine learning *Langmuir* **36** 8527
- [115] Rotenberg B 2020 Use the force! Reduced variance estimators for densities, radial distribution functions and local mobilities in molecular simulations *J. Chem. Phys.* **153** 150902
- [116] Borgis D, Assaraf D R, Rotenberg B and Vuilleumier R 2013 Computation of pair distribution functions and three-dimensional densities with a reduced variance principle *Mol. Phys.* **111** 3486
- [117] de las Heras D and Schmidt M 2018 Better than counting: density profiles from force sampling *Phys. Rev. Lett.* **120** 218001
- [118] Renner J, Schmidt M and de las Heras D 2023 Reduced-variance orientational distribution functions from torque sampling *J. Phys.: Condens. Matter* **35** 235901
- [119] He B, Martin-Fabiani I, Roth R, Tóth G I and Archer A J 2021 Dynamical density functional theory for the drying and stratification of binary colloidal dispersions *Langmuir* **37** 1399
- [120] Kundu M and Howard M P 2022 Dynamic density functional theory for drying colloidal suspensions: comparison of hard-sphere free-energy functionals *J. Chem. Phys.* **157** 184904
- [121] Sui J, Doiab M and Ding Y 2018 Dynamics of the floating nematic phase formation in platelet suspension with thickness polydispersity by sedimentation *Soft Matter* **14** 8956
- [122] Tschopp S M and Brader J M 2022 First-principles superadiabatic theory for the dynamics of inhomogeneous fluids *J. Chem. Phys.* **157** 234108
- [123] Scacchi A, Krüger M and Brader J M 2016 Driven colloidal fluids: construction of dynamical density functional theories from exactly solvable limits *J. Phys.: Condens. Matter* **28** 244023
- [124] Molinero V and Moore E B 2009 Water modeled as an intermediate element between carbon and silicon *J. Phys. Chem. B* **113** 4008–16
- [125] Coe M K, Evans R and Wilding N B 2022 The coexistence curve and surface tension of a monatomic water model *J. Chem. Phys.* **156** 154505
- [126] Saw S, Ellegaard N L, Kob W and Sastry S 2009 Structural relaxation of a gel modeled by three body interactions *Phys. Rev. Lett.* **103** 248305

- [127] Saw S, Ellegaard N L, Kob W and Sastry S 2011 Computer simulation study of the phase behavior and structural relaxation in a gel-former modeled by three-body interactions *J. Chem. Phys.* **134** 164506
- [128] Doi M 2011 Onsager's variational principle in soft matter *J. Phys.: Condens. Matter* **23** 284118
- [129] Doi M 2015 Onsager principle as a tool for approximation *Chin. Phys. B* **24** 020505
- [130] Wang H, Qian T and Xu X 2021 Onsager's variational principle in active soft matter *Soft Matter* **17** 3634
- [131] Wang X, Dobnikar J and Frenkel D 2022 Numerical test of the Onsager relations in a driven system *Phys. Rev. Lett.* **129** 238002
- [132] Seifert U 2012 Stochastic thermodynamics, fluctuation theorems and molecular machines *Rep. Prog. Phys.* **75** 126001
- [133] Jack R L and Sollich P 2010 Large deviations and ensembles of trajectories in stochastic models *Prog. Theory Phys. Suppl.* **184** 304
- [134] Jack R L and Sollich P 2015 Effective interactions and large deviations in stochastic processes *Eur. Phys. J. Spec. Top.* **224** 2351
- [135] Janssen L M C 2018 Mode-coupling theory of the glass transition: a primer *Front. Phys.* **6** 97
- [136] Janssen L M C and Reichman D R 2015 Microscopic dynamics of supercooled liquids from first principles *Phys. Rev. Lett.* **115** 205701
- [137] Mazzuca G, Grava T, Kriecherbauer T, McLaughlin K T-R, Mendl C B and Spohn H 2023 Equilibrium spacetime correlations of the Toda lattice on the hydrodynamic scale (arXiv:2301.02431)
- [138] Baker E B, Rodgers J M and Weeks J D 2020 Local molecular field theory for nonequilibrium systems *J. Phys. Chem. B* **124** 5676
- [139] Lips D, Ryabov A and Maass P 2018 Brownian asymmetric simple exclusion process *Phys. Rev. Lett.* **121** 160601
- [140] Antonov A P, Ryabov A and Maass P 2022 Solitons in overdamped Brownian dynamics *Phys. Rev. Lett.* **129** 080601
- [141] Haussmann R 2016 The way from microscopic many-particle theory to macroscopic hydrodynamics *J. Phys.: Condens. Matter* **28** 113001
- [142] Haussmann R 2022 Microscopic density-functional approach to nonlinear elasticity theory *J. Stat. Mech.* **05** 3210
- [143] Ganguly S, Shrivastav G P, Lin S-C, Häring J, Haussmann R, Kahl G, Oettel M and Fuchs M 2022 Elasticity in crystals with a high density of local defects: insights from ultra-soft colloids *J. Chem. Phys.* **156** 064501
- [144] Lin S-C, Oettel M, Häring J, Haussmann R, Fuchs M and Kahl G 2021 The direct correlation function of a crystalline solid *Phys. Rev. Lett.* **127** 085501
- [145] Anero J G, Español P and Tarazona P 2013 Functional thermo-dynamics: a generalization of dynamic density functional theory to non-isothermal situations *J. Chem. Phys.* **139** 034106
- [146] Zwanzig R 2001 *Nonequilibrium Statistical Mechanics* (Oxford: Oxford University Press)
- [147] van Hove L 1954 Correlations in space and time and Born approximation scattering in systems of interacting particles *Phys. Rev.* **95** 249
- [148] Brader J M and Schmidt M 2014 Dynamic correlations in Brownian many-body systems *J. Chem. Phys.* **140** 034104
- [149] Brader J M and Schmidt M 2013 Nonequilibrium Ornstein-Zernike relation for Brownian many-body dynamics *J. Chem. Phys.* **139** 104108
- [150] Mermin N D 1965 Thermal properties of the inhomogeneous electron gas *Phys. Rev.* **137** A1441
- [151] van Leeuwen R 1999 Mapping from densities to potentials in time-dependent density-functional theory *Phys. Rev. Lett.* **82** 3863
- [152] Maitra N T, Burke K and Woodward C 2002 Memory in time-dependent density functional theory *Phys. Rev. Lett.* **89** 023002
- [153] Zhao H, Storey B D, Braatz R D and Bazant M Z 2020 Learning the physics of pattern formation from images *Phys. Rev. Lett.* **124** 060201
- [154] Bhatia H *et al* 2021 Machine-learning-based dynamic-importance sampling for adaptive multiscale simulations *Nat. Mach. Intell.* **3** 401
- [155] Schmid F 2022 Editorial: multiscale simulation methods for soft matter systems *J. Phys.: Condens. Matter* **34** 160401
- [156] Ebrahimi Viand R, Höfling F, Klein R and Delle Site L 2021 Theory and simulation of open systems out of equilibrium *J. Chem. Phys.* **153** 101102
- [157] Delle Site L, Krekeler C, Whittaker J, Agarwal A, Klein R and Höfling F 2019 Molecular dynamics of open systems: construction of a mean-field particle reservoir *Adv. Theory Simul.* **2** 1900014
- [158] Baptista L A, Dutta R C, Sevilla M, Heidari M, Potestio R, Kremer K and Cortes-Huerto R 2021 Density-functional-theory approach to the Hamiltonian adaptive resolution simulation method *J. Phys.: Condens. Matter* **33** 184003

- [159] Gholami A, Höfling F, Klein R and Delle Site L 2021 Thermodynamic relations at the coupling boundary in adaptive resolution simulations for open systems *Adv. Theory Simul.* **4** 2000303
- [160] Klippenstein V, Tripathy M, Jung G, Schmid F and van der Vegt N F A 2021 Introducing memory in coarse-grained molecular simulations *J. Phys. Chem. B* **125** 4931
- [161] Jung G, Hanke M and Schmid F 2017 Iterative reconstruction of memory kernels *J. Chem. Theory Comput.* **13** 2481
- [162] Tchenkoue M-L M, Penz M, Theophilou I, Ruggenthaler M and Rubio A 2019 Force balance approach for advanced approximations in density functional theories *J. Chem. Phys.* **151** 154107
- [163] Tarantino W and Ullrich C A 2021 A reformulation of time-dependent Kohn-Sham theory in terms of the second time derivative of the density *J. Chem. Phys.* **154** 204112
- [164] Tokatly I V 2005 Quantum many-body dynamics in a Lagrangian frame: I. Equations of motion and conservation laws *Phys. Rev. B* **71** 165104
- [165] Tokatly I V 2005 Quantum many-body dynamics in a Lagrangian frame: II. Geometric formulation of time-dependent density functional theory *Phys. Rev. B* **71** 165105
- [166] Ullrich C A and Tokatly I V 2006 Nonadiabatic electron dynamics in time-dependent density-functional theory *Phys. Rev. B* **73** 235102
- [167] Tokatly I V 2007 Time-dependent deformation functional theory *Phys. Rev. B* **75** 125105



Neural functional theory for inhomogeneous fluids: Fundamentals and applications

Florian Sammüller^{a,1}, Sophie Hermann^a, Daniel de las Heras^a, and Matthias Schmidt^{a,1}

Edited by Robert Evans, University of Bristol, Bristol, United Kingdom; received July 21, 2023; accepted October 7, 2023 by Editorial Board Member Daan Frenkel

We present a hybrid scheme based on classical density functional theory and machine learning for determining the equilibrium structure and thermodynamics of inhomogeneous fluids. The exact functional map from the density profile to the one-body direct correlation function is represented locally by a deep neural network. We substantiate the general framework for the hard sphere fluid and use grand canonical Monte Carlo simulation data of systems in randomized external environments during training and as reference. Functional calculus is implemented on the basis of the neural network to access higher-order correlation functions via automatic differentiation and the free energy via functional line integration. Thermal Noether sum rules are validated explicitly. We demonstrate the use of the neural functional in the self-consistent calculation of density profiles. The results outperform those from state-of-the-art fundamental measure density functional theory. The low cost of solving an associated Euler–Lagrange equation allows to bridge the gap from the system size of the original training data to macroscopic predictions upon maintaining near-simulation microscopic precision. These results establish the machine learning of functionals as an effective tool in the multiscale description of soft matter.

classical density functional theory | machine learning | statistical mechanics | soft matter

The problem with density functional theory (DFT) is that you do not know the density functional. Although this quip by the late and great Yasha Rosenfeld (1) was certainly meant in jest to a certain degree, it does epitomize a structural assessment of classical DFT (2–5). As a general formulation of many-body statistical physics, the framework comprises a beautiful and far-reaching skeleton of mathematical formalism centered around a formally exact variational minimization principle (2, 6). In practice, however, the theory needs to be fleshed out by approximations of all means conceivable in our efforts to get to grips with the coupled many-body problem that is under consideration. Specifically, it is the excess (over ideal gas) intrinsic Helmholtz free energy $F_{\text{exc}}[\rho]$, expressed as a functional of the position-resolved density profile $\rho(\mathbf{r})$, which needs to be approximated.

Decades of significant theoretical efforts have provided us with a single exact functional, that for nonoverlapping hard rods in one spatial dimension, as obtained by another hero in the field, Jerry Percus (7). Nevertheless, useful DFT approximations range from the local density approximation for large-scale features which are decoupled from microscopic length scales, to square-gradient functionals with their roots in the 19th century, to the arguably most important modern development, that of the fundamental measure theory (FMT) as kicked off by Rosenfeld (8) and much refined ever since (9–16). FMT is a geometry-based framework for the description of hard sphere systems and it has deep roots in the Percus–Yevick (17) and scaled-particle theories (4), which Rosenfeld was able to unify and generalize based on his unique theoretical insights (18).

The realm of soft matter (19–21) stretches far beyond the hard sphere fluid. FMT remains relevant though in the description of a reference system as used, e.g., in studies of hydrophobicity, where the behavior of realistic water models (22, 23) is traced back to the simpler Lennard-Jones fluid, which in turn is approximated via the hard sphere FMT functional plus a mean-field contribution for describing interparticle attraction (20, 24, 25). Further topical uses of FMT include the analysis of the three-dimensional electrolyte structure near a solid surface (26, 27) and the problem of the decay length of correlations in electrolytes (28).

There is a current surge in the use of machine learning techniques in soft matter, e.g., for its characterization (29), engineering of self-assembly (30), structure detection (31), and for learning many-body potentials (32, 33). Within classical DFT, machine learning was used to address ordering of confined liquid crystals (34), and free energy functionals were

Significance

Classical density functional theory (DFT) is a powerful approach for predicting inhomogeneous fluid equilibria. The development of functionals that model the rich interparticle correlations remains a major theoretical challenge though. Here, we introduce a universal machine learning scheme for training a neural network with Monte Carlo simulation data in order to represent the density functional relationship via direct one-body correlations. We show for the well-studied hard sphere fluid that the resulting neural correlation functional exceeds in accuracy all current analytic approaches and that it provides immediate access to the full structure of homogeneous and heterogeneous fluid states. The corresponding neural DFT yields density profiles at near-simulation precision, and it applies directly to multiscale problems at low computational cost.

Author contributions: F.S., D.d.l.H., and M.S. designed research; F.S. and S.H. performed research; F.S. analyzed data; and F.S., S.H., D.d.l.H., and M.S. wrote the paper.

The authors declare no competing interest.

This article is a PNAS Direct Submission. R.E. is a guest editor invited by the Editorial Board.

Copyright © 2023 the Author(s). Published by PNAS. This article is distributed under Creative Commons Attribution-NonCommercial-NoDerivatives License 4.0 (CC BY-NC-ND).

¹To whom correspondence may be addressed. Email: florian.samueller@uni-bayreuth.de or Matthias.Schmidt@uni-bayreuth.de.

This article contains supporting information online at <https://www.pnas.org/lookup/suppl/doi:10.1073/pnas.2312484120/-/DCSupplemental>.

Published December 7, 2023.

obtained for one-dimensional systems from convolutional (35) and equation-learning (36) networks as well as within a Bayesian inference approach (37). Cats et al. (38) used machine learning to improve the standard mean-field approximation of the excess Helmholtz free-energy functional for the Lennard-Jones fluid. In nonequilibrium, de las Heras et al. (39) have reported a method to machine-learn the functional relationship of the local internal force for a steady uniaxial compressional flow of a Lennard-Jones fluid at constant temperature. As prescribed by power functional theory (40, 41), the functional dependence in nonequilibrium not only incorporates the density profile but also the one-body current.

In this work, we return to the problem of describing and predicting the structure and thermodynamics of inhomogeneous equilibrium fluids. We show that a neural network can be trained to accurately represent the functional dependence of the one-body direct correlation function with respect to the density profile. The presented methods are directly applicable to virtually arbitrary fluids with short-ranged interparticle interactions. In the following, we focus on the well-studied hard sphere fluid in order to exemplify our framework and to challenge the available highly accurate analytic approaches from liquid integral equation theory and FMT. We give more details about the feasibility of generalizations in the discussion. Reference data for training and testing the model are provided by grand canonical Monte Carlo (GCMC) simulations that cover a broad range of randomized inhomogeneous environments in planar geometry.

We implement functional calculus on the basis of the trained neural functional to infer related physical quantities and demonstrate their consistency with known literature results both in bulk and in inhomogeneous systems. In particular, we highlight the accessibility of the fluid pair structure, the determination of free energies and equations of state as well as the validation of thermal Noether sum rules (42). These results corroborate that the neural functional exceeds its role as a mere interpolation device and instead possesses significant representational power as a genuine density functional for the prediction of nontrivially related physical properties. We apply the trained neural network in the DFT Euler–Lagrange equation, which enables the self-consistent calculation of density profiles and which hence constitutes a neural-network-based DFT or short neural DFT. This method alleviates conventional DFT from the burden of having to find suitable analytic approximations while still surpassing even the most profound existing treatments of the considered hard sphere fluid via FMT functionals (8, 13, 14) in accuracy. We further demonstrate the fitness of the method for the straightforward application to multiscale problems. Neural DFT therefore provides a way to transfer near-simulation microscopic precision to macroscopic length scales, which serves as a technique to predict properties of inhomogeneous systems which far exceed typical box sizes of the original training data.

This work is structured as follows. The relevant physical background of liquid state theory is provided in Section A.1. Details of the simulations as well as of the neural network are given in Sections A.2 and A.3. The training procedure and results for the achieved metrics that measure its convergence are presented in Section A.4. We proceed by testing physical properties of the trained model and use automatic differentiation of the neural network in Section B.1 to access pair correlations, which are then compared to bulk results from both the Percus–Yevick theory and from simulations. The consistency of the neural direct correlation functional to satisfy thermal Noether sum rules is validated in Section B.2, and different ways to obtain the bulk equation

of state as well as free energies in inhomogeneous systems are given in Section B.3. In Section C.1, we show the application of the neural functional to the self-consistent calculation of density profiles via the DFT Euler–Lagrange equation and describe the technical details and conceptual advantages of this neural DFT over analytic approaches. In Section C.2, the results are compared to those from FMT, and in Section C.3, the relevance of the method for making macroscopic predictions is illustrated for cases of randomized external potential and for sedimentation between hard walls on length scales that far exceed the training simulation box sizes. We conclude with a discussion of the results and give an outlook on possible improvements and extensions of the method as well as to its application for different fluid types, in more general geometries and in nonequilibrium.

Results

A. Machine Learning Intrinsic Correlations.

A.1. Physical background. We start with the standard relation for the one-body direct correlation function $c_1(\mathbf{r})$ of liquid state theory (4),

$$c_1(\mathbf{r}) = \ln \rho(\mathbf{r}) + \beta V_{\text{ext}}(\mathbf{r}) - \beta \mu, \quad [1]$$

where \mathbf{r} denotes the spatial position and $\beta = 1/(k_B T)$ with the Boltzmann constant k_B and absolute temperature T . The three terms on the right-hand side of Eq. 1 represent respectively the ideal gas contribution, the external potential $V_{\text{ext}}(\mathbf{r})$ and the influence of the particle bath at chemical potential μ . The logarithm in Eq. 1 is understood as $\ln[\Lambda^3 \rho(\mathbf{r})]$ with the thermal wavelength Λ , which can be set to the particle size σ without any loss of information in the present classical context. For a prescribed external potential $V_{\text{ext}}(\mathbf{r})$, knowledge of the corresponding equilibrium density profile $\rho(\mathbf{r})$ allows to compute $c_1(\mathbf{r})$ explicitly via Eq. 1. This relationship can be viewed as a locally resolved chemical potential balance: the contribution from the ideal gas, $k_B T \ln \rho(\mathbf{r})$, from the external potential, $V_{\text{ext}}(\mathbf{r})$, and from interparticle interactions, $-k_B T c_1(\mathbf{r})$, add up at each position to μ , which is necessarily uniform throughout an equilibrium system.

However, the notation in Eq. 1 is oblivious to a central result shown by Evans (2), thereby kicking off a modern theory for the description of inhomogeneous fluids. For given type of internal interactions, the spatial variation of the function $c_1(\mathbf{r})$ is already uniquely determined by the spatial form of the density profile $\rho(\mathbf{r})$ alone, without the need to invoke the external potential explicitly. From this vantage point of classical DFT, the dependence of $c_1(\mathbf{r})$ on $\rho(\mathbf{r})$ is not merely pointwise but rather with respect to the values of the entire density profile, which determine $c_1(\mathbf{r})$ at each given position \mathbf{r} . Formally, this relationship is exact (2, 4), and it constitutes a functional dependence $c_1(\mathbf{r}; [\rho])$, which is indicated by brackets here and in the following and which is in general nonlinear and nonlocal. As we will demonstrate, the existence of such a universal functional mapping makes the problem of investigating inhomogeneous fluids particularly amenable to supervised machine learning techniques.

In most formulations of classical DFT, one exploits the fact that the intrinsic excess free energy functional $F_{\text{exc}}[\rho]$ acts as a functional generator such that the one-body direct correlation function is obtained via functional differentiation with respect to the density profile,

$$c_1(\mathbf{r}; [\rho]) = -\frac{\delta \beta F_{\text{exc}}[\rho]}{\delta \rho(\mathbf{r})}. \quad [2]$$

A compact description of standard formulae for the calculation of functional derivatives can be found in ref. 41. In order to make progress in concrete applications, one typically needs to rely on using an approximate form of $F_{\text{exc}}[\rho]$ for the specific model under consideration, as determined by its interparticle interactions. DFT is a powerful framework, as using $c_1(\mathbf{r}; [\rho])$ obtained from Eq. 2 with a suitable expression for $F_{\text{exc}}[\rho]$ turns Eq. 1 into an implicit equation for the equilibrium density profile $\rho(\mathbf{r})$. In the presence of a known form of $V_{\text{ext}}(\mathbf{r})$, one can typically solve Eq. 1 very efficiently, allowing ease of parameter sweeps, e.g., for exhaustive phase diagram explorations. On the downside, $F_{\text{exc}}[\rho]$ and thus also $c_1(\mathbf{r}; [\rho])$ remain approximate, and the development of analytic tools has certainly slowed down over several years if not decades.

Here, we proceed differently and bypass the excess free energy functional $F_{\text{exc}}[\rho]$ at first. Instead, we use a deep neural network to learn and to represent the functional relationship $\rho(\mathbf{r}) \rightarrow c_1(\mathbf{r})$ directly, which has significant advantages both for the generation of suitable training data as well as for the applicability of the model in the determination of fluid equilibria. This investigation is based on GCMC simulations that serve to provide training, validation, and test data. Discriminating between these three roles of use is standard practice in machine learning and we give further details below.

A.2. Simulation method. Generating the simulation data is straightforward, and we use the following strategy, adopted to planar situations where the position dependence is on a single position variable x while the system remains translationally invariant in the y and z direction. This geometry is highly relevant to identify the physics in planar capillary and adsorption situations and facilitates ease of accurate sampling. We employ randomized simulation conditions by generating external potentials of the form

$$V_{\text{ext}}(x) = \sum_{n=1}^4 A_n \sin\left(\frac{2\pi nx}{L} + \phi_n\right) + \sum_n V_n^{\text{lin}}(x), \quad [3]$$

where A_n and ϕ_n are randomly selected Fourier coefficients and phases, respectively, and L is the simulation box length in the x direction. The phases ϕ_n are chosen uniformly in the interval $[0, 2\pi)$, and values of A_n are drawn from a normal distribution with zero mean and variance 2.5. We choose $L = 20\sigma$, although there is no specific compliance requirement for the neural network (see below), and the lateral box lengths are set to 10σ to minimize finite-size effects. Periodic boundary conditions apply in all spatial directions. The sinusoidal terms in $V_{\text{ext}}(x)$ are complemented by up to five piecewise linear functions $V_n^{\text{lin}}(x) = V_1 + (V_2 - V_1)(x - x_1)/(x_2 - x_1)$ for $x_1 < x < x_2$ and 0 otherwise, for which the parameters $0 < x_1 < x_2 < L$, V_1 , and V_2 are again chosen randomly. The locations x_1 and x_2 are distributed uniformly while V_1 and V_2 follow again from an unbiased normal distribution with variance 4. Additionally to the discontinuous linear segments, we explicitly impose planar hard walls in a subset of the simulations by setting $V_{\text{ext}}(x) = \infty$ for $x < x_w/2$ and $x > L - x_w/2$, i.e., near the borders of the simulation domain; the width x_w of the wall is chosen randomly in the interval $1 \leq x_w/\sigma \leq 3$. To cover a broad range from dilute to dense systems, the chemical potential is chosen uniformly within the range $-5 \leq \beta\mu \leq 10$ for each respective GCMC simulation run. The observed mean densities range from $0.006\sigma^{-3}$ to $0.803\sigma^{-3}$, yet smaller and much larger local densities occur due to the inhomogeneous nature of the systems.

In total, 750 such GCMC runs are used, where for given form of $V_{\text{ext}}(x)$, the planar one-body profiles $\rho(x)$ and $c_1(x)$ are

obtained. The former is acquired from straightforward histogram filling and the latter from evaluating Eq. 1 on the basis of the sampled histogram for $\rho(x)$ as well as the known form of $V_{\text{ext}}(x)$ and value of μ for the specific run under consideration. As Eq. 1 is undefined for vanishing density, we have excluded regions where $\rho(x) = 0$ such as within the hard walls. By modern standards of computational resources, the workload for the generation of the simulation data is only moderate at a total CPU time of $\sim 10^4$ h.

A.3. Neural network. We use a deep neural network (43) to represent the functional map from the density profile to the local value of the one-body direct correlation function at a given point. That is, instead of the entire function, we construct the network to output only the scalar value $c_1(x)$ for a certain position x when supplied with the surrounding inhomogeneous density. The relevant section of the density profile comprises the values of $\rho(x)$ in a specified window around a considered location x , as described below. Despite the locality of the method, access to the entire (discretized) one-body direct correlation profile is immediate via evaluation of the neural network at pertinent positions x across the domain of interest. Multiple local evaluations of the network remain performant on highly parallel hardware such as GPUs when passing the input accordingly in batches. A schematic picture of the network architecture is given in Fig. 1 and is explained in the following.

The functional dependence on the density profile is realized by providing discretized values of $\rho(x)$ on an equidistant grid with resolution $\Delta x = 0.01\sigma$. As $c_1(x; [\rho])$ depends only on the immediately surrounding density profile around a fixed location x , we restrict the input range x' to a sufficiently large window $x' \leq |x - x_c|$. We choose the cutoff $x_c = 2.56\sigma$ based on simulation data for the bulk direct correlation function (44) and on the evaluation of training metrics for different window sizes x_c . Increasing the value of x_c further led to no improvement in the performance of the trained neural network.

This behavior is expected from theoretical considerations, as the one-body direct correlation function vanishes quickly for short-ranged pair potentials (4). We recall that in FMT, $x_c = \sigma$ by construction. Note that the choice of $c_1(x; [\rho])$ as our target functional is not coincidental but that its quick spatial decay rather is a pivotal characteristic central to the success of our

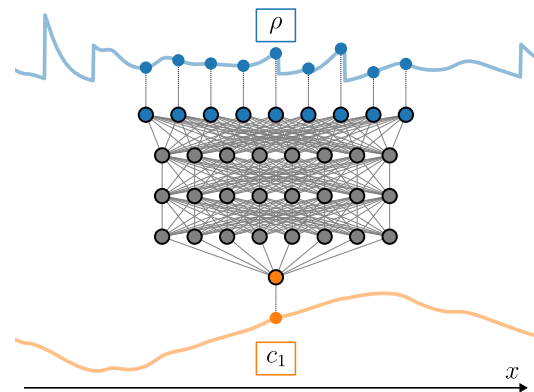


Fig. 1. We represent the functional mapping from the density profile $\rho(x)$ to local values of the one-body direct correlation function $c_1(x)$ in planar geometry via a neural network. The density profile is discretized on a regular spatial grid with resolution 0.01σ and given within a region around the location of interest to the input layer. Three fully connected layers with continuously differentiable activation functions enable the inference of the nonlinear and nonlocal functional map. The output layer consists of a single node which yields the predicted value of $c_1(x)$ at the chosen location.

method. To contrast this, assume that one attempts to model the functional mapping $\mu_{\text{loc}}(x) = \mu - V_{\text{ext}}(x) \rightarrow \rho(x)$, thereby naively imitating the simulation procedure. This task poses major challenges due to the long-range nature of density correlations induced by an external potential, which is circumvented in our case by the choice of a more manageable target functional.

The input layer involves 513 nodes and is followed by three fully connected hidden layers with 512 units each. The output layer consists of a single node for the scalar value of $c_1(x)$ at the specified location x . In order to realize a nonlinear input–output mapping of the neural network, activation functions are applied to the output of each node within a hidden layer (see also ref. 43 for a pedagogical introduction to the design of neural networks). We deviate here from the most common choice of a rectified linear unit (ReLU) and instead employ continuously differentiable activation functions such as the exponential linear unit or the softplus function (45). This choice leads to substantial improvements during training and in particular when using automatic differentiation to evaluate two-body quantities; see Sections B.1 and B.2. We attribute the superior performance to the fact that activation functions which are not continuously differentiable and which vanish in certain domain ranges (such as ReLU) reinforce sparsity of the activation output, i.e., the tendency to set many units of a hidden layer identically to zero (46). While this property is desired in many machine learning tasks (e.g., for classification), it hinders the accurate representation of the functional relation $c_1(x; [\rho])$ in our case. The resulting neural functional for the one-body direct correlation function is denoted in the following by $c_1^*(x; [\rho])$ and related quantities which follow from it by inference are marked accordingly by a superscript star.

A.4. Training procedure and metrics. The machine learning routines are implemented in Keras/Tensorflow (43) and we use the standard Adam (47) optimizer for the adjustment of the network parameters in order to fit $c_1^*(x; [\rho])$ against the simulation reference $c_1(x)$. The problem at hand is a regression task. Hence, the mean squared error is chosen as a suitable loss function and the mean average error serves as a validation metric. Since the model shall infer the pointwise value $c_1(x)$ from a density section around a specified location x , see Fig. 1, the simulation data cannot be passed as they are to the neural network. Instead, windowed views of the density profile have to be generated prior to the training loop, which correspond to the target value $c_1(x)$ at the center x of the respective window. A periodic continuation of all simulation profiles is valid due to periodic boundary conditions. Additionally, we use data augmentation to benefit from the inherent mirror symmetry (i.e., $x \rightarrow -x$) of the problem and thus effectively double the number of training datasets. As is customary, we separate the independent simulation results prior to performing the machine learning routines: 150 are kept aside as a test set, 150 serve as validation data to monitor training progress and 450 are used for the actual training of the neural network.

Modeling the functional relationship of $c_1(x; [\rho])$ locally, i.e., inferring pointwise values individually instead of outputting the entire profile at once, has numerous conceptual and practical advantages. Regarding the feasibility of the neural network in concrete applications, one is free to choose an arbitrary box length L when gathering training data and more importantly to readjust the value of L when using the trained neural network for making predictions (cf. Section C.3). From a physical point of view, providing only local density information has the merit of already capturing the correlated short-range behavior of $c_1(x; [\rho])$. If the neural network were to output the entire one-body direct correlation profile from a given density profile $\rho(x)$ at once,

this inherent locality would have to be learned instead, hence leading to a much more elaborate training process. Last, the fine-grained nature of the training data turns out to be highly beneficial from a machine learning perspective. Note that one can generate $9 \cdot 10^5$ input–output pairs from 450 training simulations in the present context (with the values being doubled after data augmentation). The increased cardinality of the training set enables better generalization of the model and also prevents overfitting, e.g., to the statistical noise of the sampled profiles.

We train the model for 100 epochs in batches of size 256 and decrease the learning rate exponentially by $\sim 5\%$ per epoch from an initial value of 0.001. This results in a best mean average error of 0.0022 over the validation set, which is of the same order as the estimated average noise of the simulation data for $c_1(x)$. Therefore, we deem our neural network to possess full representational power of the local functional relationship $c_1(x; [\rho])$ within the conditions of the provided simulation data.

B. Examining the Neural Correlation Functional.

B.1. Two-body bulk correlations. Besides monitoring standard metrics such as the mean average error over a test set, arguably deeper physical insights into the rigorous structure of the statistical mechanics at hand serve for assessing the quality of the neural functional $c_1^*(x; [\rho])$. We first ascertain that the model gives an accurate representation of the physics of bulk fluids. Despite the apparent simplicity of this case, this is a highly nontrivial test as the training data solely covered (strongly) inhomogeneous situations. For this, we investigate the pair structure and aim at implementing the two-body direct correlation functional, which is formally defined as the functional derivative (4)

$$c_2(\mathbf{r}, \mathbf{r}'; [\rho]) = \frac{\delta c_1(\mathbf{r}; [\rho])}{\delta \rho(\mathbf{r}')} \quad [4]$$

On the basis of the neural network, we can make use of the powerful automatic differentiation techniques. This allows to create an immediate analog of Eq. 4 via $c_2^*(x, x'; [\rho]) = \delta c_1^*(x; [\rho]) / \delta \rho(x')$, where the functional derivative $\delta / \delta \rho(x')$ is evaluated by reverse mode automatic differentiation with respect to the input values of the discretized density profile. In common machine learning frameworks, this requires only high-level code, e.g., GradientTape in Keras/Tensorflow (43). The numerical evaluation of $c_2^*(x, x'; [\rho])$ is performed as reverse mode automatic differentiation generates executable code that is suitable for building derivatives with respect to multiple input variables simultaneously.

We obtain the bulk direct correlation function in planar geometry as the special case $\bar{c}_2^b(x, \rho_b) = c_2(0, x; [\rho_b])$, where we have introduced the bulk density $\rho_b(x) = \rho_b = \text{const.}$ (In the notation, the parametric dependence on ρ_b is dropped in the following). Note that $\bar{c}_2^b(x)$ is distinct from the more common radial representation $c_2^b(r)$, as our geometry implies an integration over the lateral directions y and z , i.e.,

$$\begin{aligned} \bar{c}_2^b(x) &= \int dy dz c_2^b\left(r = \sqrt{x^2 + y^2 + z^2}\right) \\ &= 2\pi \int_x^\infty dr r c_2^b(r), \end{aligned} \quad [5]$$

where the last equality follows from using radial coordinates and substitution. The standard radial form $c_2^b(r)$ can however be recovered by differentiating Eq. 5 with respect to x such that

$$c_2^b(r) = -\frac{\bar{c}_2^{b'}(r)}{2\pi r}, \quad [6]$$

where $\bar{c}_2^{b'}(r)$ denotes the derivative of $\bar{c}_2^b(x)$ evaluated at $x = r$. Numerical artifacts might occur particularly for small values of r as evaluating Eq. 6 requires the numerical derivative of $\bar{c}_2^b(x)$ as well as a division by r .

We perform a Fourier transform of the planar real space representation $\bar{c}_2^b(x)$ and utilize radial symmetry in Fourier space. This acts as a deconvolution of Eq. 5 and directly yields the radial Fourier (Hankel) transform of $c_2^b(r)$,

$$\tilde{c}_2^b(k) = \frac{4\pi}{k} \int_0^\infty dr r \sin(kr) c_2^b(r). \quad [7]$$

The inverse transform is identical to Eq. 7 up to a factor of $(2\pi)^{-3}$ upon interchanging r and k . To go further, the bulk Ornstein–Zernike equation (4)

$$\tilde{c}_2^b(k) = \frac{\tilde{h}(k)}{1 + \rho_b \tilde{h}(k)}, \quad [8]$$

is used to obtain the total correlation function $\tilde{h}(k)$ from $\tilde{c}_2^b(k)$ in Fourier space after rearrangement. Recall that the radial distribution function follows directly via $g(r) = h(r) + 1$; here, $h(r)$ is the real space representation of $\tilde{h}(k)$. The static structure factor $S(k)$ is then given as:

$$S(k) = 1 + \rho_b \tilde{h}(k). \quad [9]$$

In Fig. 2, results of $\bar{c}_2^b(x)$, $c_2^b(r)$, $\tilde{c}_2^b(k)$, $\tilde{h}(k)$, and $S(k)$ are shown for different bulk densities $\rho_b \sigma^3 = 0.4, 0.7, 0.9$. From our neural functional, we obtain $\bar{c}_2^{b*}(x) = \delta c_1^*(0; [\rho]) / \delta \rho(x)|_{\rho=\rho_b}$, i.e. the autodifferentiated network is evaluated at spatially constant density ρ_b . The total correlation function and the static structure factor follow from Eqs. 8 and 9 after having computed $\tilde{c}_2^{b*}(k)$ via a numerical Fourier transform of $\bar{c}_2^{b*}(x)$. For comparison, we also depict reference data obtained analytically from the Percus–Yevick theory (17) and reproduced from simulation results of Groot et al. (44). Good agreement is found between simulation and the autodifferentiated neural network, while the Percus–Yevick result shows noticeable deviations in $\bar{c}_2^b(x)$. The latter overestimates the depth of the core region $x < \sigma$, and this discrepancy increases for larger bulk densities. The neural functional yields a clear improvement over the Percus–Yevick theory and shows only marginal differences to the simulation results of ref. 44 for both the planar real space and the radial Fourier space representation of the two-body direct correlation function. In $\tilde{h}(k)$ and $S(k)$, the severity of the discrepancies of simulation and machine learning data to the Percus–Yevick results decreases, but a difference is still noticeable in particular for large bulk densities. A slight mismatch to the simulation reference is observed in the magnitude and phase of the oscillations of the Percus–Yevick static structure factor $S_{PY}(k)$, and this correction is reproduced very well by the neural functional. Note that although one arrives at radial representations of the quantities $\tilde{h}(k)$ and $S(k)$ in Fourier space, performing the radial backtransform to real space numerically according to the inverse of Eq. 7 is generally a “notoriously difficult task” (48) and is not considered here.

This successful test reveals that, while being trained solely with one-body profiles, the neural functional $c_1^*(x; [\rho])$ contains full two-body information equivalent in bulk to the radial

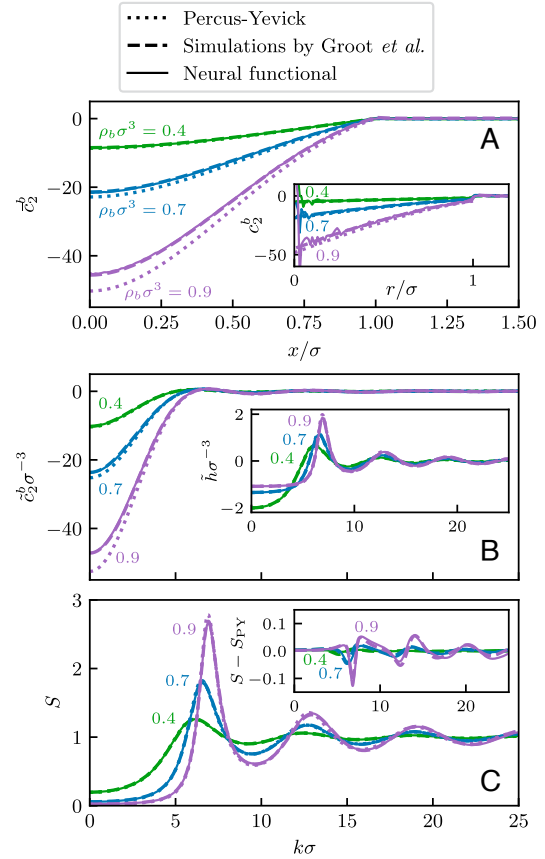


Fig. 2. We compare (A) the planar direct correlation function $\bar{c}_2^b(x)$, (B) its radial Fourier space representation $\tilde{c}_2^b(k)$, and (C) the static structure factor $S(k)$ for different bulk densities $\rho_b \sigma^3 = 0.4, 0.7, 0.9$ (as indicated). Data are shown as obtained from the Percus–Yevick theory (dotted), from simulation results by Groot et al. (44) (dashed) and from our neural functional $c_1^*(x; [\rho])$ (solid), where $\bar{c}_2^b(x)$ is acquired via automatic differentiation. The inset in panel (A) shows the radial direct correlation function $c_2^b(r)$ as obtained via Eq. 6. In panel (B), the inset depicts the total correlation function $\tilde{h}(k)$ in Fourier space, which follows from $\tilde{c}_2^b(k)$ via the bulk Ornstein–Zernike Eq. 8. The inset in panel (C) displays the deviation of $S(k)$ to the Percus–Yevick result $S_{PY}(k)$ for the simulation data and the neural functional. Simulation and machine learning results are in very good agreement with each other while the Percus–Yevick theory shows quantitative discrepancies.

distribution function $g(r)$. The pair correlations can be accessed via automatic differentiation at low computational cost, and they are consistent with known bulk results. We recall that this is a mere by-product of the neural network and that no such two-body information has been explicitly incorporated into the training. More so, Fig. 2 demonstrates that the bulk quantities $\bar{c}_2^b(x)$, $\tilde{c}_2^b(k)$, $\tilde{h}(k)$, and $S(k)$ as obtained from $c_1^*(x; [\rho])$ substantially outperform the Percus–Yevick theory and almost attain simulation quality. In *SI Appendix*, we illustrate that higher-order correlations such as the three-body direct correlation functional $c_3^*(x, x', x''; [\rho])$ follow analogously via nested automatic differentiation. On this level, differences to FMT results are even more prominent than the deviations to the two-body Percus–Yevick results. As we will show in Section C.2, the accuracy of predictions from the neural network also holds in inhomogeneous situations, where FMT serves again as an analogous and arguably even more challenging theoretical

baseline than the Percus–Yevick bulk theory. Before doing so, we lay out additional consistency tests and quality assessments that are applicable in inhomogeneous systems.

B.2. Noether sum rules. In order to further elucidate whether $c_1^*(x; [\rho])$ quantitatively reproduces fundamental properties of equilibrium many-body systems, we make use of exact sum rules that follow from thermal Noether invariance (42):

$$\nabla c_1(\mathbf{r}) = \int d\mathbf{r}' c_2(\mathbf{r}, \mathbf{r}') \nabla' \rho(\mathbf{r}'), \quad [10]$$

$$\int d\mathbf{r} \rho(\mathbf{r}) \int d\mathbf{r}' \rho(\mathbf{r}') \nabla c_2(\mathbf{r}, \mathbf{r}') = 0. \quad [11]$$

Both Eqs. 10 and 11 apply in any equilibrated inhomogeneous system regardless of the type of internal interactions. While the interparticle interaction potential does not appear explicitly in Eqs. 10 and 11, it nevertheless determines the functionals $c_1(\mathbf{r}; [\rho])$ and $c_2(\mathbf{r}, \mathbf{r}'; [\rho])$. Recall that the spatial gradient of the one-body direct correlation function can be identified with the internal equilibrium force profile, $\mathbf{f}_{\text{int}}(\mathbf{r}) = k_B T \nabla c_1(\mathbf{r})$ (41).

We verify that the neural functional complies with the above sum rules Eqs. 10 and 11 as follows. Analogous to Section B.1, we use autodifferentiation to evaluate Eq. 4, but this time, we retain the full inhomogeneous structure of $c_2^*(x, x'; [\rho])$. The left-hand side of Eq. 10 is obtained straightforwardly from simple evaluation of the neural functional and numerical spatial differentiation. As input for $\rho(x)$, we use the simulated density profiles of the test set. Care is required when evaluating the spatial gradients $\nabla \rho(x)$, $\nabla c_1^*(x; [\rho])$ and $\nabla c_2^*(x, x'; [\rho])$ due to the amplification of undesired noise, which we reduce by applying a low-pass filter after having taken the numerical derivatives. The volume integrals reduce in planar geometry to $\int d\mathbf{r} = A \int dx$, where A is the lateral system area.

In Fig. 3, three typical profiles for the left- and right-hand side of Eq. 10 are shown. In all three systems, both sides of the equation coincide up to numerical noise due to the required spatial derivatives. Additionally, we define errors via scalar deviations from equality in Eqs. 10 and 11 respectively as

$$e_1 = \left\| \nabla c_1(x) - A \int dx' c_2(x, x') \nabla' \rho(x') \right\|_{\infty}, \quad [12]$$

$$e_2 = A^2 \int dx \rho(x) \int dx' \rho(x') \nabla c_2(x, x'), \quad [13]$$

where $\|\cdot\|_{\infty}$ denotes the maximum norm. Fig. 3 *A* and *B* depict results for e_1 and e_2 resolved with respect to the mean density $\bar{\rho} = \int d\mathbf{r} \rho(\mathbf{r})/V$ for all 150 density profiles of the test set, where V denotes the volume of the system. The small magnitudes of the observed error values indicate that the neural network satisfies the Noether identities 10 and 11 to very high accuracy. Outliers are caused mostly by the moderate numerical noise of the spatial gradients (Fig. 3, *III*) and are no hindrance in practical applications of the neural functional.

This confirmation demonstrates that our method transcends the neural network from a mere interpolation device of the simulation training data to a credible standalone theoretical object. The fact that one is able to carry out consistent and performant functional calculus indeed renders $c_1^*(x; [\rho])$ a neural-network-based density functional. Besides functional differentiation, we show next that functional line integration acts as the inverse operation and provides access to the corresponding free energy. *SI Appendix* gives further insight into the symmetry properties of $c_2^*(x, x'; [\rho])$, which serve as a prerequisite for the

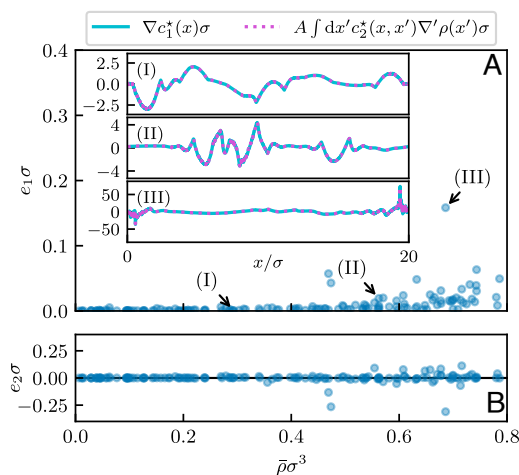


Fig. 3. Typical profiles of the right- and left-hand sides of Eq. 10 are shown for three test scenarios in panels (I), (II), and (III), where one can verify their high level of agreement across the entire inhomogeneous systems. Additionally, the respective scalar discrepancies e_1 and e_2 of the Noether identities Eqs. 10 and 11 are displayed, defined as (A) the maximum norm of the difference of left- and right-hand side of Eq. 10 and (B) the value of the left-hand side of Eq. 11. Across all mean densities $\bar{\rho}$ of the test set, the sum rules are satisfied to very high accuracy by our model. Some outliers remain which we attribute to the numerical computation of spatial gradients appearing in Eqs. 10 and 11; see also panel (III) for an example of the noise that this introduces in the respective terms of Eq. 10 particularly in the vicinity of hard walls.

existence of a generating excess free energy functional $F_{\text{exc}}^*[\rho]$; we recall Eq. 2.

B.3. Equation of state and free energy. Although the machine learning procedure operates on the level of the one-body direct correlation function, the excess free energy $F_{\text{exc}}[\rho]$ is accessible by functional line integration (49):

$$\beta F_{\text{exc}}[\rho] = - \int_0^1 d\alpha \int d\mathbf{r} \rho(\mathbf{r}) c_1(\mathbf{r}; [\rho_\alpha]). \quad [14]$$

Here, $\rho_\alpha(\mathbf{r}) = \alpha \rho(\mathbf{r})$ is a sequence of density profiles that are linearly parametrized by α in the range $0 \leq \alpha \leq 1$. The limits are $\rho_0(\mathbf{r}) = 0$ such that $F_{\text{exc}}[0] = 0$, and $\rho_1(\mathbf{r}) = \rho(\mathbf{r})$, which is the target density profile that appears as the functional argument on the left-hand side of Eq. 14. Other parametrizations of $\rho_\alpha(\mathbf{r})$ are conceivable but change the concrete form of Eq. 14. On the basis of $c_1^*(x; [\rho])$, we implement Eq. 14 via $\beta F_{\text{exc}}^*[\rho] = -A \int_0^1 d\alpha \int dx \rho(x) c_1^*(x; [\rho_\alpha])$ and evaluate the integrals numerically; as before, A denotes the lateral system area.

We first return to bulk systems and illustrate in the following three different routes toward obtaining the bulk equation of state from the neural network. For this, we introduce the excess free energy density as $\psi_b(\rho_b) = F_{\text{exc}}[\rho_b]/V$. From the neural functional, the excess free energy density $\psi_b^*(\rho_b)$ can be acquired via $F_{\text{exc}}^*[\rho_b]$ from functional line integration along a path of bulk densities according to Eq. 14. Alternatively and equivalently, one can simply evaluate the neural direct correlation functional at bulk density ρ_b and due to translational symmetry at arbitrary location (e.g., $x = 0$) such that $c_1^{b*} = c_1^*(0; [\rho_b])$. Simplifying Eq. 2 in bulk reveals that

$$\psi_b^*(\rho_b) = -k_B T c_1^{b*}, \quad [15]$$

where the prime denotes the derivative with respect to the bulk density argument. The excess free energy density $\psi_b^*(\rho_b)$ follows

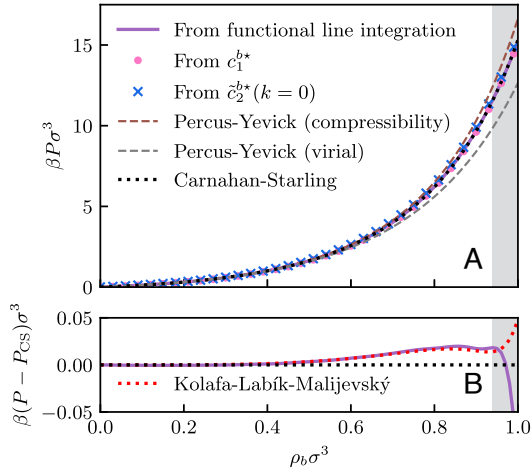


Fig. 4. We show (A) the equation of state $P(\rho_b)$ obtained via different methods and (B) deviations to the Carnahan–Starling result $P_{CS}(\rho_b)$ (dotted black line). The neural equation of state $P^*(\rho_b)$ is calculated via Eq. 16 in which the excess free energy density follows from functional line integration according to Eq. 14 (solid purple line), from evaluation of the bulk value c_1^{b*} (pink dots), see Eq. 15, and via the low-wavelength limit of $\tilde{c}_2^{b*}(k)$ (blue crosses), see Eq. 17. For comparison, the Percus–Yevick equations of state according to the virial (dashed gray line) and compressibility (dashed brown line) route are shown. Bulk densities ρ_b beyond the stable fluid phase are shaded in gray. All three routes coincide very well up to and within the metastable region, with functional line integration leading to the most accurate results. We additionally depict a simulation-based equation of state (B, dotted red line) due to Kolafa et al. (50), which our neural functional is able to reproduce very accurately in the stable fluid region, hence exceeding in precision the Carnahan–Starling equation of state.

from ordinary numerical integration across bulk densities up to the target value ρ_b . The numerical accuracy to which both routes coincide serves as a further valuable consistency test.

Additionally, one obtains the bulk pressure $P(\rho_b)$ from the excess free energy density via

$$P(\rho_b) = (\psi'_b(\rho_b) + k_B T) \rho_b - \psi_b(\rho_b). \quad [16]$$

The pressure is equally accessible from a further route which incorporates previous results for the bulk pair structure via their low-wavelength limits according to ref. (4):

$$\beta \left. \frac{\partial P}{\partial \rho_b} \right|_T = \frac{\beta}{\rho_b \chi_T} = \frac{1}{S(0)} = \frac{1}{1 + \rho_b \tilde{c}_2^b(0)} = 1 - \rho_b \tilde{c}_2^b(0), \quad [17]$$

where one can identify the isothermal compressibility $\chi_T = \rho_b^{-1}(\partial \rho_b / \partial P)_T$. From Eq. 17, $P(\rho_b)$ is obtained by evaluation of either of the bulk correlation functions (Section B.1) in Fourier space at $k = 0$ for different bulk densities and by subsequent numerical integration toward the target value of ρ_b .

We compare the results in Fig. 4, where the equation of state $P^*(\rho_b)$ of the neural network was acquired from functional line integration across bulk systems, cf. Eq. 14, from evaluation of one-body bulk correlation values c_1^{b*} , cf. Eq. 15, and from the low-wavelength limit of two-body bulk correlations, cf. Eq. 17. One finds that the results of all three routes are consistent with each other and that they match very well the Carnahan–Starling equation of state (51), thus outperforming the Percus–Yevick theory as already observed for the bulk pair structure in Section B.1. A slight deviation can be noticed when evaluating $P^*(\rho_b)$ via Eq. 17, which constitutes the

most indirect route detouring to two-body correlations. This may reflect the small discrepancy of the neural functional to simulation results (cf. Fig. 2) and the sensitivity of the low-wavelength limit of the static structure factor to remaining finite size effects (52). Notably, functional line integration is the most reliable method, and the corresponding results even surpass the Carnahan–Starling equation of state in accuracy. Fig. 4B shows the reproduction of a highly accurate simulation-based equation of state due to Kolafa et al. (50). We recall again that neither bulk information nor data for free energies or pressures was given explicitly in the training of the neural network. Instead, the beyond-Carnahan–Starling precision is achieved solely by extracting direct one-body correlations from simulation data of randomized inhomogeneous systems in planar geometry. In *SI Appendix*, we additionally demonstrate that the neural functional is fit for the application of dimensional crossover (53) in order to obtain the bulk equation of state for the two-dimensional hard disk fluid within a reasonable range of packing fractions.

For a concise comparison of free energies in inhomogeneous situations, additional reference data have to be acquired from simulations. In our grand canonical setting, thermodynamic integration (54) with respect to the chemical potential can be used to measure the grand potential according to

$$\Omega[\rho] = - \int_{-\infty}^{\mu} d\mu' \langle N \rangle. \quad [18]$$

Here, the integration starts from an empty system with $\Omega[0] = 0$ and traverses the chemical potential up to the target value μ . One needs to measure the mean number of particles $\langle N \rangle$ in a sufficient number of simulations with intermediate chemical potentials $-\infty < \mu' \leq \mu$ to evaluate Eq. 18 numerically. The excess free energy then follows directly from

$$F_{\text{exc}}[\rho] = \Omega[\rho] - F_{\text{id}}[\rho] - \int d\mathbf{r} \rho(\mathbf{r})(V_{\text{ext}}(\mathbf{r}) - \mu), \quad [19]$$

where $F_{\text{id}}[\rho] = k_B T \int d\mathbf{r} \rho(\mathbf{r})(\ln \rho(\mathbf{r}) - 1)$ is the ideal gas free energy. Thermodynamic integration according to Eq. 18 has been performed for 22 systems of the test set to yield reference values $F_{\text{exc}}^{\text{sim}}$ for the excess free energy via Eq. 19. The systems were selected to cover a broad range of excess free energy values, and FMT results for F_{exc} were used as a further theoretical estimate for this selection.

In Table 1 and Fig. 5, we show errors of F_{exc} to the quasi-exact simulation values when calculating the excess free energy via Rosenfeld and White Bear MkII FMT as well as from functional

Table 1. The absolute and relative mean average error of the excess free energy F_{exc} as obtained via the Rosenfeld and White Bear MkII FMT functionals is compared to the result from functional line integration of the neural correlation functional

	$\beta \langle F_{\text{exc}} - F_{\text{exc}}^{\text{sim}} \rangle$	$\langle F_{\text{exc}} - F_{\text{exc}}^{\text{sim}} / F_{\text{exc}}^{\text{sim}} \rangle$
Rosenfeld	0.540	1.75%
White Bear MkII	0.0159	0.104%
Neural functional	0.0127	0.097%

The reference values $F_{\text{exc}}^{\text{sim}}$ were obtained via thermodynamic integration according to Eqs. 18 and 19 for a subset of the test systems. The results of the neural functional surpass the Rosenfeld FMT significantly and even yield a slight improvement over the highly accurate White Bear MkII theory. The angular brackets denote an average over the 22 test simulations.

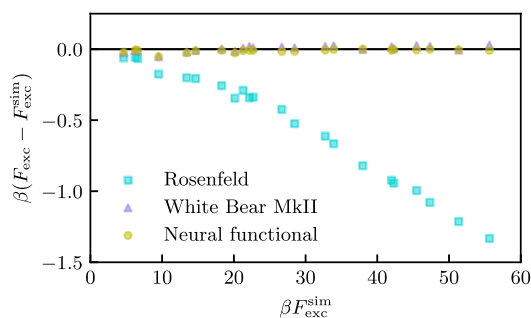


Fig. 5. We compare free energies of inhomogeneous test systems as obtained via Rosenfeld (turquoise squares) and White Bear (purple triangles) FMT as well as with functional line integration of the neural correlation functional $c_1^*(x; [\rho])$ (yellow circles). The discrepancy $F_{\text{exc}} - F_{\text{exc}}^{\text{sim}}$ of the respective method to the simulation result $F_{\text{exc}}^{\text{sim}}$ is shown. Rosenfeld FMT systematically underestimates F_{exc} , whereas White Bear MkII FMT as well as our neural functional yield almost exact results. The neural network performs slightly better for large excess free energies as occur primarily in dense systems.

line integration according to Eq. 14 of the neural functional. For both FMT methods, a DFT minimization (cf. Section C.1) is performed to yield a self-consistent density profile $\rho(x)$, which serves as input to the respective analytic FMT expression for $F_{\text{exc}}[\rho]$. Hence, we compare consistently equilibrium states (according to the respective theory) corresponding to the same form of the external potential.

The comparison reveals that the neural functional significantly outperforms Rosenfeld FMT and still yields slightly more accurate values for the excess free energy than the very reliable White Bear theory. Regarding the above-described bulk results for the free energy, this behavior is both consistent and expected, as the Rosenfeld and White Bear MkII functionals can be associated with the Percus–Yevick compressibility and Carnahan–Starling bulk equations of state respectively. Still, the test in inhomogeneous systems is a more rigorous one than in bulk, as the full nonlocal functional representation is invoked when providing $c_1^*(x; [\rho])$ with an inhomogeneous density profile as input. Given that the functional line integration of $c_1^*(x; [\rho])$ via Eq. 14 is practically immediate, one can deem $F_{\text{exc}}^*[\rho]$ itself a corresponding neural functional for the excess free energy that enables a full description of the thermodynamics of inhomogeneous fluids to high accuracy. As we present below, this quantitative precision is preserved when applying the neural functional in a predictive manner in the self-consistent calculation of density profiles.

C. Predicting Inhomogeneous Fluids via Neural DFT.

C.1. Going beyond analytic approximations. In the previous section, the trained model has been put to test by deriving related quantities such as $c_2^*(x, x'; [\rho])$ from autodifferentiation and $F_{\text{exc}}^*[\rho]$ from functional line integration in order to assess its performance against analytic and numerical reference results. We now turn to the application of the neural functional $c_1^*(x; [\rho])$ in the context of the self-consistent determination of density profiles according to the DFT Euler–Lagrange equation. This is achieved by rearranging Eq. 1 to the standard form (2, 4)

$$\rho(\mathbf{r}) = \exp(-\beta(V_{\text{ext}}(\mathbf{r}) - \mu) + c_1(\mathbf{r}; [\rho])). \quad [20]$$

A fixed-point (Picard) iteration with mixing parameter α can be used to determine the density profile from Eq. 20 according to

$$\rho(\mathbf{r}) \leftarrow (1 - \alpha)\rho(\mathbf{r}) + \alpha \exp(-\beta(V_{\text{ext}}(\mathbf{r}) - \mu) + c_1(\mathbf{r}; [\rho])). \quad [21]$$

The degree of convergence is determined from the remaining difference of right- and left-hand side of Eq. 20. With the trained neural functional at hand, one can evaluate the one-body direct correlation function in Eq. 21 via the surrogate $c_1^*(x; [\rho])$ in each iteration step. In the following, the use of $c_1^*(x; [\rho])$ in this context will be referred to as neural DFT.

We note two minor technical points concerning the use of the neural functional in the Picard iteration. It was observed that a conservative choice of α is necessary during the first few iterations to ensure numerical stability. After this burn-in, the mixing parameter can be set to usual values (e.g. $\alpha = 0.05$). Furthermore, the convergence criterion has to be relaxed as compared to typical choices in analytic DFT methods due to the remaining intrinsic uncertainty of $c_1^*(x; [\rho])$. The mean average error after training, cf. Section A.4, provides an estimate for the expected relative uncertainty of the density profile according to Eq. 20. Depending on the specific problem, the error might not decrease any further than that during the iteration of Eq. 21. Neither of these points caused any practical hindrance in applications.

The treatment of Eq. 20 in neural DFT is conceptually not different from that in standard DFT methods. However, the model $c_1^*(x; [\rho])$ relieves the theory from being restricted by the available approximations for the one-body direct correlation function as generated from analytic expressions of the excess free energy functional $F_{\text{exc}}[\rho]$ via Eq. 2. We emphasize that, unlike in previous work (35, 37), no analytic ansatz had to be provided and that our method is generic for the determination of a suitable functional from a given model Hamiltonian, thus indeed constituting a “machine learning black box” (35) regarding the training procedure. However, in contrast to a closed black box, the inner workings of the resulting neural correlation functional can be inspected very thoroughly via the neural functional calculus laid out above. Also note that, while the model works at the level of the one-body direct correlation function, the free energy is readily available from functional line integration, cf. Section B.3. Last, we point out that $c_1^*(x; [\rho])$ captures the entirety of the intrinsic correlations and that further improvements are conceivable by only learning differences to an analytic reference functional. To demonstrate the capabilities of our method, we refrain from this route and show that the trained neural functional alone already exceeds the accuracy of FMT.

C.2. Comparison to FMT. In the following, we benchmark the self-consistent inhomogeneous density profiles obtained via neural DFT against FMT results. For this comparison, the Rosenfeld (8) and White Bear MkII (13) FMT functionals are considered and the simulated density profiles are taken as quasi-exact reference data. The FMT functionals are the most profound analytic description of the hard sphere fluid with the White Bear MkII theory being the state-of-the-art treatment of short-ranged intermolecular repulsion in classical DFT. Nevertheless, measurable and systematic deficiencies still remain, e.g., in highly correlated systems (55). We point the reader to ref. 14 for a thorough account of FMT and to ref. 56 for a very recent quantitative assessment. Note that the tensorial weights of Tarazona (15) to describe hard sphere freezing are not included in our investigation.

The comparison is set up as follows. For each hard sphere system of the test set (Section A.4), we determine the density profile $\rho(x)$ from the Rosenfeld and White Bear MkII FMT functionals as well as from $c_1^*(x; [\rho])$ via the Picard iteration Eq. 21 of the Euler–Lagrange Eq. 20. For this, only the known

form of the external potential $V_{\text{ext}}(x)$ and the value μ of the chemical potential are prescribed. As reference density profiles are available from GCMC simulations, we can evaluate the error $\Delta\rho(x)$ of each of the DFT results relative to the simulation data for $\rho(x)$. From here, different scalar metrics for the quantitative agreement of self-consistent DFT profiles and simulation results are considered.

In Fig. 6, both global and local error measures for the deviation of FMT as well as neural DFT to simulation data are depicted. For the assessment of the global error, we show the L_2 -norm $\|\Delta\rho\|_2$ of the discrepancy to the reference profile, which is normalized by the mean density $\bar{\rho}$ of each system respectively. As the test data cover very dilute to very dense systems, this relative global error measure is plotted as a function of $\bar{\rho}$ to discern the behavior with respect to varying global average density. Similarly, we define an estimate for the relative local error by evaluating the maximum norm $\|\Delta\rho\|_\infty$ of the density deviation divided by the maximum value $\|\rho\|_\infty$ of the GCMC density profile. This quantity is resolved against the maximum $\|\rho\|_\infty$ of the respective

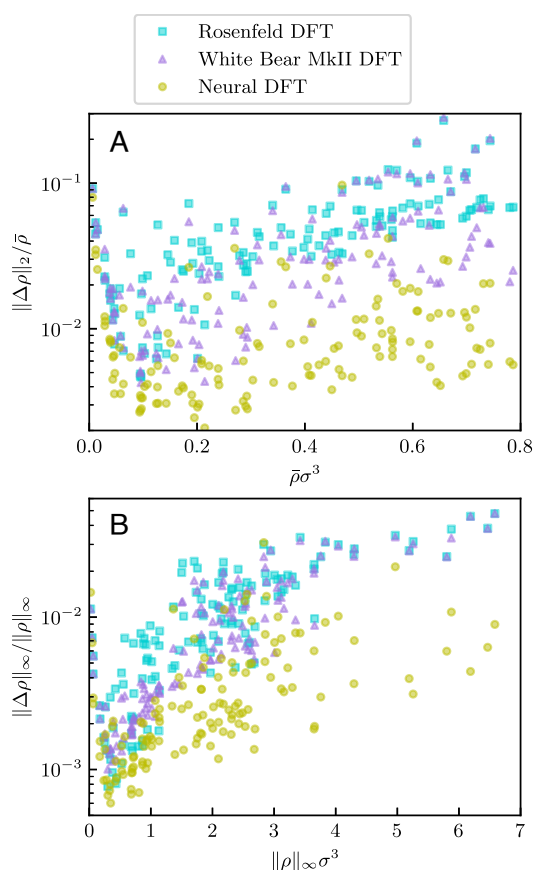


Fig. 6. Measures of discrepancy of self-consistent density profiles to simulation results across the test set are presented. We show (A) the normalized L_2 -norm $\|\Delta\rho\|_2/\bar{\rho}$ as a function of the mean density $\bar{\rho}$ for judgment of the average error over the inhomogeneous system, and (B) the relative maximum norm $\|\Delta\rho\|_\infty/\|\rho\|_\infty$ as a function of the largest local density $\|\rho\|_\infty$ to reveal the magnitude of local errors, e.g. at density peaks. The self-consistent density profiles are obtained from Rosenfeld (turquoise squares) and White Bear MkII (purple triangles) as well as from employing our neural functional $c_1^*(x; [\rho])$ in the DFT Euler–Lagrange equation (yellow circles). Regarding both global and local error, the neural network outperforms the analytic FMT functionals and reduces the respective errors up to an order of magnitude, especially in large-density regimes.

inhomogeneous density, thus enabling the detection of local discrepancies, e.g., in the vicinity of maxima and discontinuities of the density profile.

One recognizes that neural DFT yields substantially better results than the FMT functionals with regard to both error measures. Compared to the Rosenfeld results, both the global and the local errors are decreased by approximately an order of magnitude. Surprisingly, even the White-Bear MkII functional is not able to match the accuracy of the neural DFT, which is noticeable especially for large values of $\bar{\rho}$ and of $\|\rho\|_\infty$.

C.3. Simulation beyond the box. A particular advantage of the local nature of the neural functional $c_1^*(x; [\rho])$ is its applicability to systems of virtually arbitrary size. As explained in Section A.3, it is sufficient to provide the density profile within a rather narrow window as input to the neural network to infer the value of the one-body direct correlation function at the center of the density section. The model $c_1^*(x; [\rho])$ can therefore be used directly in the Euler–Lagrange Eq. 20 for the prediction of planar systems of arbitrary length. Due to the low computational demands of solving this equation self-consistently, this method is suitable even in multiscale problems where macroscopic length scales compete with and are influenced by microscopic correlations and packing features. Although one could argue that analytic DFT methods already account for such tasks, importantly the neural functional $c_1^*(x; [\rho])$ acts as a drop-in replica of the (almost) simulation-like description of the intrinsic correlations. Therefore, neural DFT facilitates to fuse simulation data with common DFT methods, thus providing a means to “simulate beyond the box.”

Simulation beyond the box is demonstrated in Fig. 7, where the system size has been increased to $1,000\sigma$ while the numerical grid size remains unchanged at 0.01σ . Our setup implies that for colloids of, say, size $\sigma = 1 \mu\text{m}$, we have spatial resolution of 10 nm across the entirety of a system of macroscopic size 1 mm. We consider both a highly correlated fluid in a rapidly varying external potential as well as the diffusive sedimentation behavior (57) in a weak gravitational potential. The former case is realized by generating a sequence of randomized external potentials via Eq. 3 which are spatially connected; the chemical potential is set to zero. Neural DFT yields a highly inhomogeneous density profile in this system and resolves the microscopic variations accurately at low computational cost. In the sedimentation column, a local chemical potential $\mu_{\text{loc}}(x) = \mu - V_{\text{ext}}(x) = (10 - 0.01x/\sigma)k_B T$ is imposed which decreases linearly with respect to the height x , and the system is bounded from the bottom ($x = 0$) and the top ($x = 1,000\sigma$) by hard walls. The spatial variation of $\mu_{\text{loc}}(x)$ is chosen small enough to enable thermal diffusion across the whole sedimentation column and to yield locally an almost bulk-like behavior except near the upper and lower hard walls. The method reproduces both the highly correlated nature of $\rho(x)$ in the vicinity of the walls as well as its intermediate behavior within the sedimentation column, which follows closely the bulk equation of state (Section B.3), as one would expect within a local density approximation (4). In both cases, the computational cost for the determination of $\rho(x)$ with neural DFT is negligible as compared to analogous many-body simulations, which are hardly feasible on such length scales.

Discussion

In this work, we have outlined and validated a machine learning procedure for representing the local functional map from the density profile to the one-body direct correlation function via a neural network. The resulting neural functional was shown

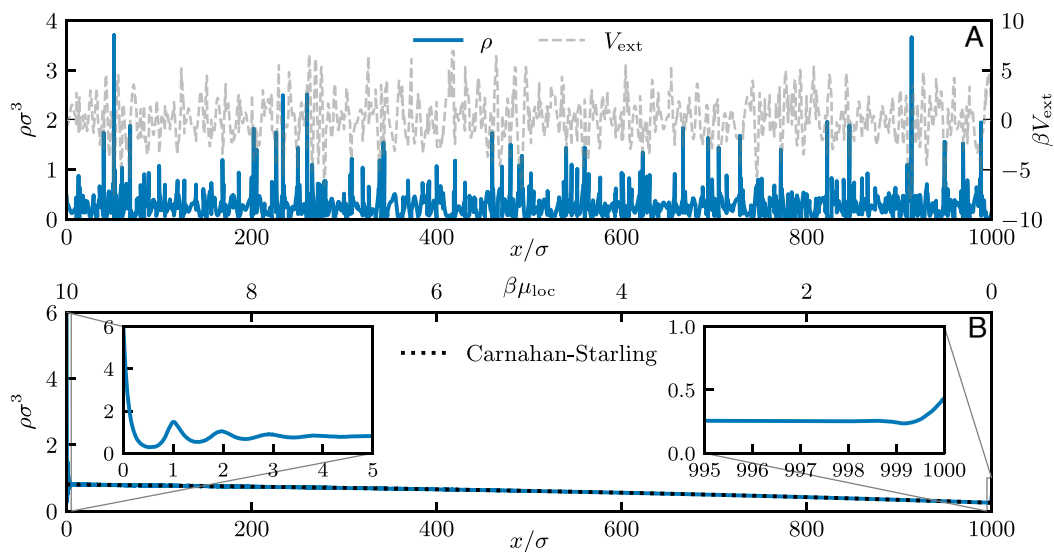


Fig. 7. Neural DFT is used to obtain the density profile $\rho(x)$ (blue lines) of the hard sphere fluid (A) in a highly correlated system with randomized external potential $V_{\text{ext}}(x)$ (gray dashed line) and (B) in a sedimentation column of height $1,000\sigma$ that is bounded by hard walls at the bottom and at the top of the system. Near-simulation microscopic accuracy is retained at low computational cost by the application of neural DFT in the highly correlated large-scale system. For the case of sedimentation, strongly oscillating behavior at the lower wall as well as mild adsorption at the top can be resolved. As the spatial variation of the local chemical potential $\mu_{\text{loc}}(x)$ is negligible, the density profile reproduces the equation of state within the sedimentation column, which is verified by a comparison to the Carnahan–Starling equation of state (dotted black line).

to be applicable as a powerful surrogate in the description of inhomogeneous equilibrium fluids. This was demonstrated for the hard sphere fluid, where we have used GCMC simulations in randomized inhomogeneous planar environments for the generation of training, validation, and test data. Density and one-body direct correlation profiles followed respectively from direct sampling and from evaluation of Eq. 1.

DFT elevates the role of the one-body direct correlation function $c_1(x)$ to that of an intrinsic functional $c_1(x; [\rho])$ depending on the density profile $\rho(x)$ but being independent of the external potential. We exploited this fact in the construction of our neural network, which takes as input a local section of the discretized density profile around a fixed location x and outputs the value of the one-body direct correlation functional $c_1(x; [\rho])$ at that specific location. Establishing a pointwise inference of $c_1(x; [\rho])$ instead of trying to represent the global functional mapping of the entire one-body profiles comes with various advantages, such as independence of the box size, the correct description of the short-range behavior of $c_1(x; [\rho])$, and a very significant improvement of training statistics.

The nonlinear and nonlocal relationship was realized by fully connected hidden layers with smooth activation functions and a standard supervised training routine was used. The achieved mean average error over the test set was of the same order of magnitude as the noise floor of the simulations, thus being indicative of full representational power of the neural correlation functional within the considered simulation data. Whether the quality of the model can be improved further by performing more extensive sampling to reduce the statistical noise of the simulation profiles remains to be investigated in the future. Additionally, active and reinforcement machine learning techniques could be useful for interleaving the training and simulation process, thereby guiding the generation of reference data in order to explore the space of inhomogeneous systems more efficiently and exhaustively.

The neural functional was put to test by verifying numerous physical relations in bulk and in inhomogeneous systems.

In particular, it was shown that the two-body direct correlation functional $c_2(x, x'; [\rho])$ as well as higher-order correlations are accessible from the model via automatic differentiation. In bulk, the pair structure as described by the neural network significantly outperforms the Percus–Yevick theory and is even able to compete with simulation results (44), although no bulk data was used during training. In inhomogeneous situations, the conformance of the neural functional to the thermal Noether sum rules Eqs. 10 and 11 as well as to spatial symmetry requirements holds to high accuracy. The excess free energy $F_{\text{exc}}[\rho]$ is readily and efficiently available via functional line integration of the model according to Eq. 14 and the results agree with those obtained from simulations. The bulk equation of state can be acquired consistently from various routes with the results attaining simulation quality (50) and in particular exceeding the very reliable Carnahan–Starling equation of state (51) in accuracy. Dimensional crossover is feasible for the calculation of the bulk equation of state for the two-dimensional hard disk system.

Arguably the most important consequence of the neural functional framework is the applicability of $c_1^*(x; [\rho])$ in the self-consistent calculation of density profiles by solving the Euler–Lagrange equation (20) of classical DFT. As the one-body direct correlation function is faithfully represented by the neural network, one is exempted from having to find analytic approximations for $c_1(x; [\rho])$ or for its generating functional $F_{\text{exc}}[\rho]$. Although FMT provides such approximations for the hard sphere fluid with high precision, we could demonstrate that our neural functional outperforms both the Rosenfeld (8) as well as the White Bear MkII (13) functional. For this, Eq. 20 was solved self-consistently for all 150 randomized local chemical potentials of the test set to obtain $\rho(x)$, where $c_1(x; [\rho])$ was given either analytically by FMT or evaluated via $c_1^*(x; [\rho])$. The comparison of the results to the simulated density profiles reveals that neural DFT yields global and local errors that are up to an order of magnitude lower than those of FMT.

Furthermore, due to the flexibility that comes with the local functional mapping, the neural network could be used as a means

to “simulate beyond the box.” That is, while the training was based solely on simulation data from systems of manageable size, the resulting model $c_1^*(x; [\rho])$ is directly applicable for predictions on much larger length scales. We demonstrated this by imposing a spatial sequence of randomized external potentials on a length of $1,000\sigma$. While the explicit numerical simulation of such a system is comparatively cumbersome, neural DFT offers a way to achieve close to simulation-like accuracy at low computational effort. Furthermore, we have considered a sedimentation column with a height of $1,000\sigma$ that is bounded by hard walls. Neural DFT is capable of both resolving microscopically the adsorption at the walls as well as efficiently capturing the long-range density decay with increasing height. The presented fusion of machine learning and DFT can therefore be another useful technique to make headway in the multiscale description of soft matter (58–60).

Even though we saw no need for a more sophisticated training procedure in our investigations, it could be useful to consider physics-informed machine learning (61) as a technique for enforcing exact physical relations of the underlying problem directly during training. Sum rules in bulk or in inhomogeneous systems, e.g., the thermal Noether identities Eqs. 10 and 11, might be suitable candidates for this task. Analogous to the evaluation of derivatives in physics-informed neural networks, we have shown the necessary quantities to be accessible by automatic differentiation of the neural functional.

When considering nonequilibrium systems, power functional theory (PFT) (40, 41) establishes an exact functional many-body framework which is analogous to that of DFT in equilibrium. A central ramification of PFT is the existence of a functional map from the time-dependent one-body density $\rho(\mathbf{r}, t)$ and current $\mathbf{J}(\mathbf{r}, t)$ to the internal force profile $\mathbf{f}_{\text{int}}(\mathbf{r}, t; [\rho, \mathbf{J}])$, which is in general nonlocal in space and causal in time t . Recent work by de las Heras et al. (39) demonstrated that machine learning this kinematic internal force functional yields highly promising results and overcomes the analytic and conceptual limitations of dynamical density functional theory. In this regard, our method can be put into a more general context as it may be viewed as a mere special case for equilibrium systems where $\mathbf{J}(\mathbf{r}, t) = 0$. The topical problem of accurately describing nonequilibrium many-body physics is certainly a natural contender for the application and extension of our neural functional framework, with many practical questions arising, e.g., concerning the generation of training data or the choice of neural network architecture.

While much insight could be gained by considering the hard sphere fluid, the application of our machine learning procedure is arguably even more useful for particle models that lack satisfactory analytic density functional approximations. Although mean-field descriptions account surprisingly well for soft and attractive contributions (62, 63), e.g., in the Lennard-Jones fluid, analytic efforts to go beyond this approximation are sparse (64–66). We demonstrate the generality of our method in *SI Appendix*, where we show that the machine learning routine applies directly to the (truncated) Lennard-Jones interaction potential in an isothermal supercritical setting. In the future, providing the temperature as a further input quantity to a modified neural network is a valuable goal in order to tackle the full physics of such thermal systems. As a proper treatment of the arising phase transitions and interfacial phenomena is already subtle in simulation, the machine learning perspective might provide further insights. We expect the general method to hold up even for complex particle models, e.g., containing many-body interactions (22), provided that sufficiently accurate training data of sufficient quantity can be generated.

For the treatment of anisotropic particles, the neural network must be extended to accommodate for the additional orientational degrees of freedom. Recent advances in molecular DFT could be helpful in guiding appropriate augmentations of our method (67, 68). Related to the increased dimensionality due to anisotropy, the extension of the machine learning procedure from planar symmetry to more general geometries is worth contemplating. Especially for fully inhomogeneous three-dimensional problems, the amount of required training data seems restrictive at first. However, we have shown in this work that results obtained in planar geometry already capture the essence of internal interactions. Therefore, it may be feasible to base the machine learning predominantly on data in reduced geometrical settings and to incorporate remaining nontrivial effects due to the more general geometry by supplementing only a few selected higher-dimensional simulations. In particular, we highlight in this context the promising development of equivariant neural networks (69–72), which serve as a means of casting underlying symmetries of a problem directly into the neural network architecture. Recent applications in the physical domain show that this method facilitates robust training and generalization on the basis of much reduced datasets as compared to common machine learning approaches which do not intrinsically enforce symmetry (73–75). In our case, exploiting inherent symmetries of the direct correlation functional via the use of equivariant neural networks is certainly valuable when further orientational or spatial degrees of freedom are to be considered.

Last, we point out useful cross-fertilization of machine learning ideas regarding topical applications in quantum DFT (76). In particular, the analogous functional mapping to the classical one-body direct correlation functional $c_1(\mathbf{r}; [\rho])$ is given quantum mechanically by the exchange-correlation potential $v_{\text{xc}}(\mathbf{r}; [n])$ which depends functionally on the one-body electron density $n(\mathbf{r})$. Due to the immediate analogy, obtaining the exchange-correlation energy functional $E_{\text{xc}}[n]$ might be feasible with functional line integration similar to our treatment of $F_{\text{exc}}[\rho]$ via Eq. 14, which here becomes $E_{\text{xc}}[n] = \int_0^1 d\alpha \int d\mathbf{r} n(\mathbf{r}) v_{\text{xc}}(\mathbf{r}; [n_\alpha])$ with $n_\alpha(\mathbf{r}) = \alpha n(\mathbf{r})$. Albeit lacking the neural functional calculus that we presented here, Zhou et al. (77) have successfully demonstrated the machine learning of the functional mapping from the electron density to local values of the exchange-correlation potential $v_{\text{xc}}(\mathbf{r})$. Specifically, they trained a convolutional neural network on the basis of three-dimensional quantum chemical simulation data of small molecules and could obtain accurate predictions for larger molecules. This success is akin to the multiscale applicability of our neural correlation functional $c_1^*(\mathbf{r}; [\rho])$. In general, however, most machine learning strategies in quantum DFT have considered different functional mappings (78–83). In light of our results for classical systems, we deem the analogous machine learning of the local functional relationship of $v_{\text{xc}}(\mathbf{r}; [n])$ the arguably most promising approach in the development of a neural quantum DFT with the goal of chemical accuracy and generic applicability.

Data, Materials, and Software Availability. Code, data sets and models have been deposited in Zenodo (84)

ACKNOWLEDGMENTS. We thank T. Zimmermann, T. Eckert, and N. C. X. Stuhl Müller for useful comments. This work is supported by the German Research Foundation (DFG) via Project No. 436306241.

Author affiliations: ^aTheoretische Physik II, Physikalisches Institut, Universität Bayreuth, Bayreuth D-95447, Germany

1. R. Evans, J. P. Hansen, H. Löwen, Foreword. *J. Phys.: Condens. Matter* **14**, 1 (2002).
2. R. Evans, The nature of the liquid-vapour interface and other topics in the statistical mechanics of non-uniform, classical fluids. *Adv. Phys.* **28**, 143–200 (1979).
3. R. Evans, *Density Functionals in the Theory of Non-Uniform Fluids* D. Henderson, Eds. (M. Dekker, New York, 1992), pp. 85–175.
4. J. P. Hansen, I. R. McDonald, *Theory of Simple Liquids With Applications to Soft Matter* (Elsevier Science & Technology Books, 2013).
5. R. Evans, M. Oettel, R. Roth, G. Kahl, New developments in classical density functional theory. *J. Phys.: Condens. Matter* **28**, 240401 (2016).
6. N. D. Mermin, Thermal properties of the inhomogeneous electron gas. *Phys. Rev.* **137**, A1441–A1443 (1965).
7. J. K. Percus, Equilibrium state of a classical fluid of hard rods in an external field. *J. Statist. Phys.* **15**, 505–511 (1976).
8. Y. Rosenfeld, Free-energy model for the inhomogeneous hard-sphere fluid mixture and density-functional theory of freezing. *Phys. Rev. Lett.* **63**, 980–983 (1989).
9. E. Kierlik, M. L. Rosinberg, Free-energy density functional for the inhomogeneous hard-sphere fluid: Application to interfacial adsorption. *Phys. Rev. A* **42**, 3382–3387 (1990).
10. E. Kierlik, M. L. Rosinberg, Density-functional theory for inhomogeneous fluids: Adsorption of binary mixtures. *Phys. Rev. A* **44**, 5025–5037 (1991).
11. S. Phan, E. Kierlik, M. L. Rosinberg, B. Bildstein, G. Kahl, Equivalence of two free-energy models for the inhomogeneous hard-sphere fluid. *Phys. Rev. E* **48**, 618–620 (1993).
12. R. Roth, R. Evans, A. Lang, G. Kahl, Fundamental measure theory for hard-sphere mixtures revisited: The White Bear version. *J. Phys.: Condens. Matter* **14**, 12063–12078 (2002).
13. H. Hansen-Goos, R. Roth, Density functional theory for hard-sphere mixtures: The White Bear version mark II. *J. Phys.: Condens. Matter* **18**, 8413–8425 (2006).
14. R. Roth, Fundamental measure theory for hard-sphere mixtures: A review. *J. Phys.: Condens. Matter* **22**, 063102 (2010).
15. P. Tarazona, Density functional for hard sphere crystals: A fundamental measure approach. *Phys. Rev. Lett.* **84**, 694–697 (2000).
16. P. Tarazona, J. Cuesta, Y. Martínez-Ratón, “Density functional theories of hard particle systems” in *Theory and Simulation of Hard-Sphere Fluids and Related Systems* (Springer, Berlin, 2008), pp. 247–341.
17. J. K. Percus, G. J. Yeveck, Analysis of classical statistical mechanics by means of collective coordinates. *Phys. Rev.* **110**, 1–13 (1958).
18. Y. Rosenfeld, Scaled field particle theory of the structure and the thermodynamics of isotropic hard particle fluids. *J. Chem. Phys.* **89**, 4272–4287 (1988).
19. S. R. Nagel, Experimental soft-matter science. *Rev. Mod. Phys.* **89**, 025002 (2017).
20. R. Evans, D. Frenkel, M. Dijkstra, From simple liquids to colloids and soft matter. *Phys. Today* **72**, 38–39 (2019).
21. J. L. Barrat, J. P. Hansen, *Basic Concepts for Simple and Complex Liquids* (Cambridge University Press, 2003).
22. V. Molinero, E. B. Moore, Water modeled as an intermediate element between carbon and silicon. *J. Phys. Chem. B* **113**, 4008–4016 (2008).
23. M. K. Coe, R. Evans, N. B. Wilding, The coexistence curve and surface tension of a monatomic water model. *J. Chem. Phys.* **156**, 154505 (2022).
24. M. K. Coe, R. Evans, N. B. Wilding, Density depletion and enhanced fluctuations in water near hydrophobic solutes: Identifying the underlying physics. *Phys. Rev. Lett.* **128**, 045501 (2022).
25. M. K. Coe, R. Evans, N. B. Wilding, Understanding the physics of hydrophobic solvation. *J. Chem. Phys.* **158**, 034508 (2023).
26. D. Martín-Jiménez, E. Chacon, P. Tarazona, R. García, Atomically resolved three-dimensional structures of electrolyte aqueous solutions near a solid surface. *Nat. Commun.* **7**, 12164 (2016).
27. J. Hernández-Muñoz, E. Chacón, P. Tarazona, Density functional analysis of atomic force microscopy in a dense fluid. *J. Chem. Phys.* **151**, 034701 (2019).
28. P. Cats, R. Evans, A. Härtel, R. van Roij, Primitive model electrolytes in the near and far field: Decay lengths from DFT and simulations. *J. Chem. Phys.* **154**, 124504 (2021).
29. P. S. Clegg, Characterising soft matter using machine learning. *Soft Matter* **17**, 3991–4005 (2021).
30. M. Dijkstra, E. Luijten, From predictive modelling to machine learning and reverse engineering of colloidal self-assembly. *Nat. Mater.* **20**, 762–773 (2021).
31. E. Boattini, M. Dijkstra, L. Filion, Unsupervised learning for local structure detection in colloidal systems. *J. Chem. Phys.* **151**, 154901 (2019).
32. G. Campos-Villalobos, E. Boattini, L. Filion, M. Dijkstra, Machine learning many-body potentials for colloidal systems. *J. Chem. Phys.* **155**, 174902 (2021).
33. G. Campos-Villalobos, G. Giunta, S. Marín-Aguilar, M. Dijkstra, Machine-learning effective many-body potentials for anisotropic particles using orientation-dependent symmetry functions. *J. Chem. Phys.* **157**, 024902 (2022).
34. T. Santos-Silva, P. I. C. Teixeira, C. Anquetil-Deck, D. J. Cleaver, Neural-network approach to modeling liquid crystals in complex confinement. *Phys. Rev. E* **89**, 053316 (2014).
35. S. C. Lin, M. Oettel, A classical density functional from machine learning and a convolutional neural network. *SciPost Phys.* **6**, 025 (2019).
36. S. C. Lin, G. Martius, M. Oettel, Analytical classical density functionals from an equation learning network. *J. Chem. Phys.* **152**, 021102 (2020).
37. P. Yatsyshin, S. Kalliadas, A. B. Duncan, Physics-constrained Bayesian inference of state functions in classical density-functional theory. *J. Chem. Phys.* **156**, 074105 (2022).
38. P. Cats *et al.*, Machine-learning free-energy functionals using density profiles from simulations. *APL Mater.* **9**, 031109 (2021).
39. D. de las Heras, T. Zimmermann, F. Sammler, S. Hermann, M. Schmidt, Perspective: How to overcome dynamical density functional theory. *J. Phys.: Condens. Matter* **35**, 271501 (2023).
40. M. Schmidt, J. M. Brader, Power functional theory for Brownian dynamics. *J. Chem. Phys.* **138**, 214101 (2013).
41. M. Schmidt, Power functional theory for many-body dynamics. *Rev. Mod. Phys.* **94**, 015007 (2022).
42. S. Hermann, M. Schmidt, Noether’s theorem in statistical mechanics. *Commun. Phys.* **4**, 176 (2021).
43. F. Chollet, *Deep Learning with Python* (Manning Publications, 2017).
44. R. D. Groot, J. P. van der Eerden, N. M. Faber, The direct correlation function in hard sphere fluids. *J. Chem. Phys.* **87**, 2263–2270 (1987).
45. S. R. Dubej, S. K. Singh, B. B. Chaudhuri, Activation functions in deep learning: A comprehensive survey and benchmark. *Neurocomputing* **503**, 92–108 (2022).
46. X. Glorot, A. Borde, Y. Bengio, “Deep sparse rectifier neural networks” in *Proceedings of the Fourteenth International Conference on Artificial Intelligence and Statistics (JMLR Workshop and Conference Proceedings)* (2011), pp. 315–323.
47. D. P. Kingma, J. Ba, Adam: A method for stochastic optimization (2014).
48. D. Henderson, E. W. Grundke, Direct correlation function: Hard sphere fluid. *J. Chem. Phys.* **63**, 601–607 (1975).
49. J. M. Brader, M. Schmidt, Free power dissipation from functional line integration. *Mol. Phys.* **113**, 2873–2880 (2015).
50. J. Kolafa, S. Labík, A. Malijevský, Accurate equation of state of the hard sphere fluid in stable and metastable regions. *Phys. Chem. Chem. Phys.* **6**, 2335–2340 (2004).
51. N. F. Carnahan, K. E. Starling, Equation of state for nonattracting rigid spheres. *J. Chem. Phys.* **51**, 635–636 (1969).
52. F. Höfling, S. Dietrich, Finite-size corrections for the static structure factor of a liquid slab with open boundaries. *J. Chem. Phys.* **153**, 054119 (2020).
53. Y. Rosenfeld, M. Schmidt, H. Löwen, P. Tarazona, Fundamental-measure free-energy density functional for hard spheres: Dimensional crossover and freezing. *Phys. Rev. E* **55**, 4245–4263 (1997).
54. D. Frenkel, B. Smit, *Understanding Molecular Simulation: From Algorithms to Applications* (Elsevier Science & Technology, 2023).
55. R. L. Davidchack, B. B. Laird, R. Roth, Hard spheres at a planar hard wall: Simulations and density functional theory. *Condens. Matter Phys.* **19**, 23001 (2016).
56. F. Sammler, S. Hermann, M. Schmidt, Comparative study of force-based classical density functional theory. *Phys. Rev. E* **107**, 034109 (2023).
57. D. de las Heras, M. Schmidt, The phase stacking diagram of colloidal mixtures under gravity. *Soft Matter* **9**, 8636 (2013).
58. L. D. Site *et al.*, Molecular dynamics of open systems: Construction of a mean-field particle reservoir. *Adv. Theory Simul.* **2**, 1900014 (2019).
59. L. A. Baptista *et al.*, Density-functional-theory approach to the Hamiltonian adaptive resolution simulation method. *J. Phys.: Condens. Matter* **33**, 184003 (2021).
60. F. Schmid, Editorial, Multiscale simulation methods for soft matter systems. *J. Phys.: Condens. Matter* **34**, 160401 (2022).
61. G. E. Karniadakis *et al.*, Physics-informed machine learning. *Nat. Rev. Phys.* **3**, 422–440 (2021).
62. A. J. Archer, B. Chacko, R. Evans, The standard mean-field treatment of inter-particle attraction in classical DFT is better than one might expect. *J. Chem. Phys.* **147**, 034501 (2017).
63. S. M. Tschoop, H. D. Vuijk, A. Sharma, J. M. Brader, Mean-field theory of inhomogeneous fluids. *Phys. Rev. E* **102**, 042140 (2020).
64. M. Schmidt, Density-functional theory for soft interactions by dimensional crossover. *Phys. Rev. E* **60**, R6291–R6294 (1999).
65. M. Schmidt, Fluid structure from density-functional theory. *Phys. Rev. E* **62**, 4976–4981 (2000).
66. K. L. Finster, E. J. Krebs, C. J. May, P. A. Kreuzberg, D. Roundy, Soft fundamental measure theory functional for the Weeks-Chandler-Andersen repulsive potential. *Phys. Rev. E* **106**, 064134 (2022).
67. G. Jeanmairet, M. Levesque, R. Vuilleumier, D. Borgis, Molecular density functional theory of water. *J. Phys. Chem.* **4**, 619–624 (2013).
68. L. Ding, M. Levesque, D. Borgis, L. Belloni, Efficient molecular density functional theory using generalized spherical harmonics expansions. *J. Chem. Phys.* **147**, 094107 (2017).
69. T. S. Cohen, M. Welling, Group equivariant convolutional networks (2016).
70. M. Weiler, M. Geiger, M. Welling, W. Boomsma, T. Cohen, 3D steerable CNNs: Learning rotationally equivariant features in volumetric data (2018).
71. M. Finzi, S. Stanton, P. Izmailov, A. G. Wilson, Generalizing convolutional neural networks for equivariance to Lie groups on arbitrary continuous data (2020).
72. V. G. Satorras, E. Hoogeboom, M. Welling, “(E)n equivariant graph neural networks” in *Proceedings of the 38th International Conference on Machine Learning, Proceedings of Machine Learning Research*, M. Meila, T. Zhang, Eds. (PMLR, 2021), vol. 139, pp. 9323–9332.
73. S. Batzner *et al.*, E(3)-equivariant graph neural networks for data-efficient and accurate interatomic potentials. *Nat. Commun.* **13**, 2453 (2022).
74. S. Batzner, A. Musaelian, B. Kozinsky, Advancing molecular simulation with equivariant interatomic potentials. *Nat. Rev. Phys.* **5**, 437–438 (2023).
75. A. Musaelian *et al.*, Learning local equivariant representations for large-scale atomistic dynamics. *Nat. Commun.* **14**, 579 (2023).
76. R. Pederson, B. Kalita, K. Burke, Machine learning and density functional theory. *Nat. Rev. Phys.* **4**, 357–358 (2022).
77. Y. Zhou, J. Wu, S. Chen, G. Chen, Toward the exact exchange-correlation potential: A three-dimensional convolutional neural network construct. *J. Phys. Chem. Lett.* **10**, 7264–7269 (2019).
78. R. Nagai, R. Akashi, S. Sasaki, S. Tsuneyuki, Neural-network Kohn-Sham exchange-correlation potential and its out-of-training transferability. *J. Chem. Phys.* **148**, 241737 (2018).
79. J. Schmidt, C. L. Benavides-Riveros, M. A. L. Marques, Machine learning the physical nonlocal exchange-correlation functional of density-functional theory. *J. Phys. Chem. Lett.* **10**, 6425–6431 (2019).
80. R. Nagai, R. Akashi, O. Sugino, Completing density functional theory by machine learning hidden messages from molecules. *npj Comput. Mater.* **6**, 43 (2020).
81. L. Li *et al.*, Kohn-Sham equations as regularizer: Building prior knowledge into machine-learned physics. *Phys. Rev. Lett.* **126**, 036401 (2021).
82. H. Li *et al.*, Deep-learning density functional theory Hamiltonian for efficient ab initio electronic-structure calculation. *Nat. Comput. Sci.* **2**, 367–377 (2022).
83. J. Wang, Y. Wang, R. X. Xu, G. Chen, X. Zheng, A semilocal machine-learning correction to density functional approximations. *J. Chem. Phys.* **158**, 154107 (2023).
84. F. Sammler, S. Hermann, D. de las Heras, M. Schmidt, Neural functional theory for inhomogeneous fluids: Fundamentals and applications. Zenodo. <https://zenodo.org/records/8380003>. Deposited 26 September 2023.



Supporting Information for

Neural functional theory for inhomogeneous fluids: Fundamentals and applications

Florian Sammüller, Sophie Hermann, Daniel de las Heras, and Matthias Schmidt

Florian Sammüller.

E-mail: florian.samueller@uni-bayreuth.de

Matthias Schmidt.

E-mail: Matthias.Schmidt@uni-bayreuth.de

This PDF file includes:

Supporting text

Figs. S1 to S4

SI References

Supporting Information Text

Higher-order correlations. Analogous to Sec. B.1, we demonstrate that higher-order correlations can be obtained from the neural correlation functional by nested automatic differentiation. This is due to the fact that the hierarchy of direct correlation functions $c_n(\mathbf{r}, \mathbf{r}', \dots, \mathbf{r}^{(n-1)}; [\rho])$, $n \geq 2$, is accessible from successive functional derivatives of the one-body direct correlation functional (1),

$$c_n(\mathbf{r}, \mathbf{r}', \dots, \mathbf{r}^{(n-1)}; [\rho]) = \frac{\delta^{n-1} c_1(\mathbf{r}; [\rho])}{\delta \rho(\mathbf{r}') \dots \delta \rho(\mathbf{r}^{(n-1)})}. \quad [1]$$

As illustrated in the main text, translational symmetry can be applied in bulk fluids such that the resulting bulk correlation function $c_n^b(\mathbf{r}, \dots, \mathbf{r}^{(n-2)}) = c_n(0, \mathbf{r}, \dots, \mathbf{r}^{(n-2)}; [\rho_b])$ only incorporates $n - 2$ remaining position coordinates.

We specialize again to the planar geometry of our neural functional and show in Fig. S1 the three-body bulk correlation function $\bar{c}_3^{b*}(x, x')$ for a bulk density of $\rho_b = 0.7\sigma^{-3}$. While the computation of $\bar{c}_2^{b*}(x)$ is practically immediate via a single reverse mode autodifferentiation pass, going to the three-body correlation function comes at the price of having to evaluate the Hessian of $c_1^*(x; [\rho])$, for which different strategies exist (2). In principle, one can proceed by nesting autodifferentiation layers to obtain further members of the hierarchy Eq. (1), albeit being restricted by the practicability of the actual evaluation and the efficacy of the result. Note that the computational effort at the three-body level is by no means restrictive and that growing numerical demands are expected when considering higher-order correlations. The computation and analysis of $\bar{c}_3^b(x, x')$ might be especially useful for more complex fluid models, e.g. containing internal three-body interactions (3).

We compare $\bar{c}_3^{b*}(x, x')$ to analytic approximations based on FMT. For both the Rosenfeld and the White Bear MkII functional, the three-body bulk direct correlation function is analytic in Fourier space. We point the reader to Ref. (4) for an expression of the original Rosenfeld result in terms of vectorial weight functions and to Refs. (5, 6) for an equivalent representation via scalar weights. As the weight functions remain unchanged, the White Bear MkII result follows immediately from the modification of the excess free energy density as laid out in Ref. (7).

A cumulant expansion of the bulk result of the three-body direct correlation function in Fourier space can be transformed to real space analytically, which in planar geometry gives

$$\bar{c}_3^b(x, x') = -\frac{bR^4}{a} \exp\left(\frac{-x^2 + xx' - x'^2}{aR^2}\right), \quad [2]$$

where the width parameter a and the prefactor b are determined by

$$a = \frac{\nu}{\kappa} \frac{3}{5} \frac{53 - 25\eta + 8\eta^2}{30 + 2\eta + 5\eta^2 - \eta^3}, \quad [3]$$

$$b = \kappa \frac{8\pi}{3\sqrt{3}} \frac{30 + 2\eta + 5\eta^2 - \eta^3}{(1 - \eta)^5}, \quad [4]$$

with the packing fraction $\eta = \pi\rho_b/6$. The correction factors ν and κ are set to unity in the Rosenfeld FMT and attain the forms

$$\nu = \frac{53 - 35\eta + \eta^2 + 5\eta^3}{53 - 25\eta + 8\eta^2}, \quad [5]$$

$$\kappa = \frac{30 - 6\eta}{30 + 2\eta + 5\eta^2 - \eta^3}, \quad [6]$$

in the White Bear MkII case.

The comparison reveals that the form of the neural three-body bulk correlation function $\bar{c}_3^{b*}(x, x')$ is plausible and that it captures genuine features which go beyond both FMT descriptions. The Rosenfeld FMT yields a large discrepancy in the core region $x, x' \approx 0$, which is significantly underestimated as compared to the results from the neural functional and from the White Bear theory. We recall that, as in Sec. C.2, the tensorial weights of Tarazona (8) have not been used in the FMT functionals and that their inclusion might be particularly relevant on the level of higher-order correlations. In this vein, investigating members of the direct correlation hierarchy Eq. (1) with the neural correlation functional could be a valuable aid for testing and refining analytic FMT functionals.

Spatial symmetry of the neural two-body direct correlation functional. A further consistency test of $c_2^*(x, x'; [\rho])$ arises due to its expected symmetry with respect to an interchange of the planar position coordinates x and x' . Recall that the excess free energy functional $F_{\text{exc}}[\rho]$ generates the two-body direct correlation function according to

$$c_2(\mathbf{r}, \mathbf{r}'; [\rho]) = -\frac{\delta^2 \beta F_{\text{exc}}[\rho]}{\delta \rho(\mathbf{r}) \delta \rho(\mathbf{r}')}, \quad [7]$$

see Eq. (2) and Eq. (4) of the main text. One can directly recognize from the symmetry of the second functional derivative in Eq. (7) that $c_2(\mathbf{r}, \mathbf{r}'; [\rho]) = c_2(\mathbf{r}', \mathbf{r}; [\rho])$ must hold.

On the basis of the neural direct correlation functional in planar geometry, assessing the validity of the identity

$$c_2^*(x, x'; [\rho]) = c_2^*(x', x; [\rho]) \quad [8]$$

is a highly nontrivial test. This is due to the fact that $c_2^*(x, x'; [\rho])$ evaluated at certain positions x and x' follows from automatic differentiation of $c_1^*(x; [\rho])$, where the input density window is centered around the location x , see Sec. B.1. On the other hand, when formally evaluating $c_2^*(x', x; [\rho])$, where the arguments x and x' are now reversed, the density window is centered around x' , hence constituting a generally very different and a priori unrelated input profile. One can expect Eq. (8) to be recovered only if the physical implications of Eq. (7) are captured correctly by the neural functional. Note that Eq. (8) is a necessary condition for the existence of a unique neural excess free energy functional $F_{\text{exc}}^*[\rho]$, which can practically be obtained via functional line integration, see Sec. B.3. We exemplify in Fig. S2 that the neural two-body direct correlation functional $c_2^*(x, x'; [\rho])$ obtained via autodifferentiation of $c_1^*(x; [\rho])$ indeed satisfies the symmetry requirement Eq. (8) to very high accuracy.

Neural equation of state for hard disks via dimensional crossover. Although the neural functional $c_1^*(x; [\rho])$ was acquired explicitly for the three-dimensional hard sphere fluid, dimensional crossover techniques can be used to obtain bulk results for the two-dimensional hard disk system. This is facilitated by investigating the behavior of the hard sphere fluid under narrow confinement, which constitutes a quasi-two-dimensional scenario. With this method, one obtains the equation of state for the hard disk fluid from $c_1^*(x; [\rho])$, as we demonstrate in the following.

We proceed similar to Sec. B.3 and utilize Eq. (16) to express the pressure $P(\rho_b)$ via the excess free energy density $\psi_b(\rho_b)$, which we aim to compute for a range of bulk densities ρ_b . Whereas $c_1^*(x; [\rho])$ was evaluated for the three-dimensional bulk fluid at spatially constant density, cf. Eq. (15), here a suitable density profile $\rho_{2D}(x)$ is constructed as input to the neural direct correlation functional in order to emulate narrow planar confinement. For this, we choose

$$\rho_{2D}(x) = \frac{\rho_b}{x_w} \Theta\left(\left|x - \frac{x_w}{2}\right|\right) \quad [9]$$

with the Heaviside function $\Theta(\cdot)$; note that Eq. (9) is a Dirac series and yields the Dirac distribution for $x_w \rightarrow 0$. The neural direct correlation functional is then evaluated at the center of this assumed slit, and the values $c_1^*(0; [\rho_{2D}])$ are used analogous to Sec. B.3 for the determination of $P_{2D}^*(\rho_b)$. The equation of state for the associated two-dimensional hard disk system follows formally for $x_w \rightarrow 0$. As this limit is not directly accessible in practice, we assess the obtained values for finite but small slit widths $0.3 \leq x_w/\sigma \leq 1$ and extrapolate to $x_w = 0$ via a quadratic fit.

The resulting equation of state $P_{2D}^*(\rho_b)$ for the two-dimensional hard disk fluid as obtained from this dimensional crossover on the basis of the neural network is shown in Fig. S3. We additionally display analytic equations of state from scaled particle theory (9) and by Henderson (10) which serve as reference. One recognizes that reasonable results can be achieved for low and medium densities, but that deviations to analytic results become noticeable for $\rho_b > 0.7\sigma^{-2}$. Nevertheless, it is both surprising and reassuring that the neural functional is capable of predicting correlations in narrow confinement, as no such situations were explicitly included in the training data. Recall that hard walls were imposed only at the borders of the simulation box of length $L = 20\sigma$ and that the inhomogeneous external potential within the simulation domain consisted solely of Fourier modes and of piecewise linear functions, cf. Eq. (3) in the main text. Presumably, improvements over the results presented in Fig. S3 could be obtained especially for large densities by including situations of very narrow confinement explicitly in the training data. From our outset, the successful achievement of a viable two-dimensional equation of state serves as a demonstration that $c_1^*(x; [\rho])$ indeed captures the intricate functional relationship of the underlying physical problem instead of acting as a mere interpolation tool with respect to the encountered training data.

Neural DFT for the Lennard-Jones fluid. We illustrate the generalizability of our machine learning framework to other particle types by considering the truncated Lennard-Jones fluid with pairwise interparticle potential

$$\phi(r) = \begin{cases} 4\epsilon \left[\left(\frac{\sigma}{r}\right)^{12} - \left(\frac{\sigma}{r}\right)^6 \right], & r \leq r_c, \\ 0, & r > r_c, \end{cases} \quad [10]$$

where r is the interparticle distance, ϵ is the dispersion energy and the cutoff radius is set to $r_c = 2.5\sigma$. Analogous to Sec. A.2 of the main text, reference data is generated via GCMC simulations of 800 systems with randomized external conditions of which 500 are used for training and 150 respectively for validation and testing. We focus on the isothermal behavior of the supercritical fluid and hence set $k_B T = 1.5\epsilon$. The chemical potential varies uniformly in a range of $-8 \leq \beta\mu \leq 4$ and the external potential is generated as described in the main text, cf. Eq. (3).

To accommodate the longer-ranged interactions compared to the hard sphere fluid, the size of the density window to be input into the neural network is increased to $x_c = 4\sigma$ whilst keeping the design of the hidden layers unchanged (see Sec. A.3). The training results in a mean average error of 0.0035 and larger values of x_c led to no further improvement in the training statistics. The slight increase of the mean average error as compared to the hard sphere case (see Sec. A.4) can be attributed to noisier simulation data, which results from the decreased efficiency of GCMC method when simulating soft interactions with larger cutoff radius instead of hard spherical particles with an interaction range of σ .

After successfully training the neural functional for the Lennard-Jones fluid, we employ $c_1^*(x; [\rho])$ in neural DFT to determine self-consistent density profiles for all 150 test systems. The Picard iteration proceeds without problems and analogously to Sec. C.1. The results are compared with the standard mean field DFT treatment of the Lennard-Jones fluid. Here, the repulsive part of Eq. (10) is approximated by a hard core interaction, for which we utilize the White Bear MkII FMT functional. An additive mean field contribution $F_{\text{MF}}[\rho] = \int d\mathbf{r} \int d\mathbf{r}' \rho(\mathbf{r})\rho(\mathbf{r}')\phi_{\text{att}}(|\mathbf{r} - \mathbf{r}'|)/2$ to the excess free energy functional incorporates

the attractive part $\phi_{\text{att}}(r)$ of the Lennard-Jones potential. The function $\phi_{\text{att}}(r)$ is equal to Eq. (10) for $r \geq r_{\text{min}} = 2^{1/6} \sigma$ and it is set to $-\epsilon$ for $r < r_{\text{min}}$.

Local and global deviations of both neural DFT and the analytic mean field DFT to the simulation reference data are presented in Fig. S4. The neglect of correlations in the mean field treatment leads to considerable errors across the whole test set. Contrarily, the neural DFT achieves close-to-simulation results and outperforms the analytic DFT by up to two orders of magnitude in the considered error measures.

This successful test demonstrates the transferability of our machine learning framework across particle models and indicates its utility especially for Hamiltonians which lack satisfactory analytic DFT treatments. Although the considered interparticle potential Eq. (10) is still short-ranged, we see much potential to extend our method to long-ranged interactions as occur e.g. in charged systems. The resulting algebraic decay of direct correlations could be tackled in various ways: i) It might be sufficient in some cases (e.g. for screened interactions) to simply extend the cutoff range x_c of the density input. ii) In order to achieve a better scaling of the number of input nodes with growing x_c , one could change the corresponding discretization of $\rho(x)$ to employ variably spaced sampling points instead of a fixed discretization interval. This would still enable to finely resolve the vicinity of the considered location x while also incorporating information about long-range density correlations. iii) An alternative approach emerges by treating the long-range behavior of $c_1(\mathbf{r}; [\rho])$ analytically, similar to the treatment of the Hartree term in quantum DFT, see e.g. Ref. (11). Hence, the neural functional could be trained as is on the remaining short-ranged part of $c_1(\mathbf{r}; [\rho])$ to recover full quasi-exact information about intrinsic correlations.

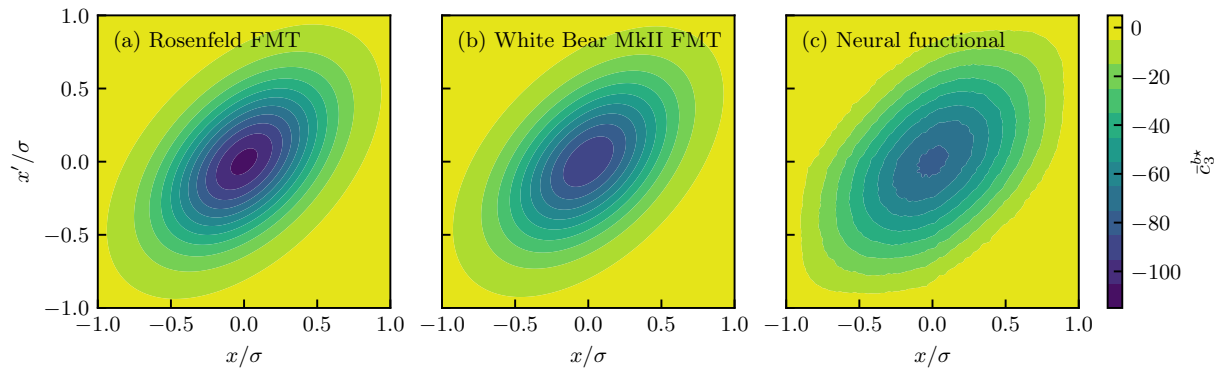


Fig. S1. The three-body direct correlation function is shown in bulk at density $\rho_b = 0.7\sigma^{-3}$. We depict (a) the Rosenfeld and (b) the White Bear MkII FMT results for the planar representation $\bar{c}_3^b(x, x')$, which were obtained analytically according to Eq. (2) by a cumulant expansion in Fourier space and a subsequent backtransform. Within our neural functional framework (c), $\bar{c}_3^{b*}(x, x')$ is acquired via nested automatic differentiation of $c_1^*(x; [\rho])$.

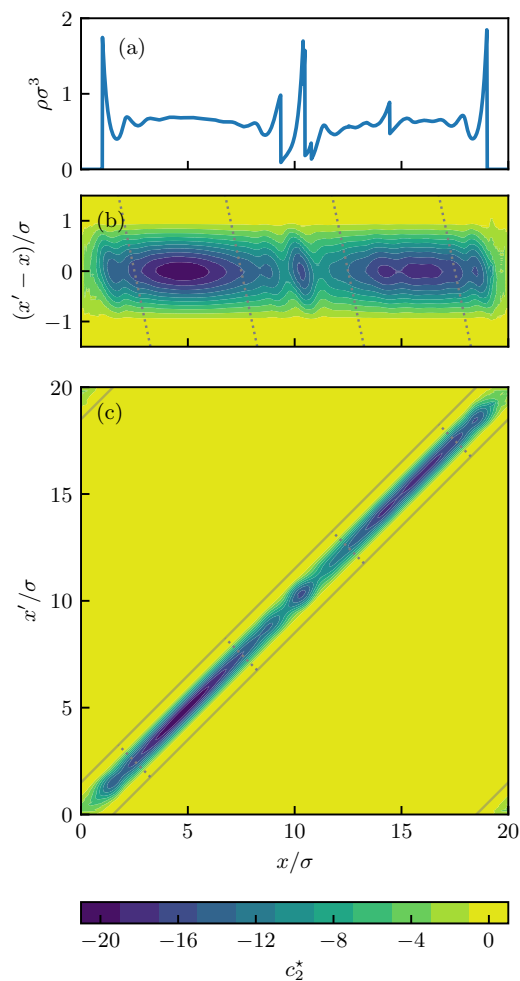


Fig. S2. We show (a) the density profile $\rho(x)$ of an inhomogeneous system of the test set and (b) the corresponding neural two-body direct correlation function, which is obtained for each position x with respect to $x' - x$. A linear transformation is applied to display $c_2^*(x, x'; [\rho])$ as a function of x and x' in panel (c). This transformation is visualized by corresponding gray lines in panels (b) and (c) which indicate the extent of the detailed view (solid) and slices where $x + x' = \text{const.}$ (dotted). The results exemplify that the neural network reproduces the symmetry property Eq. (8) of the two-body direct correlation function very accurately.

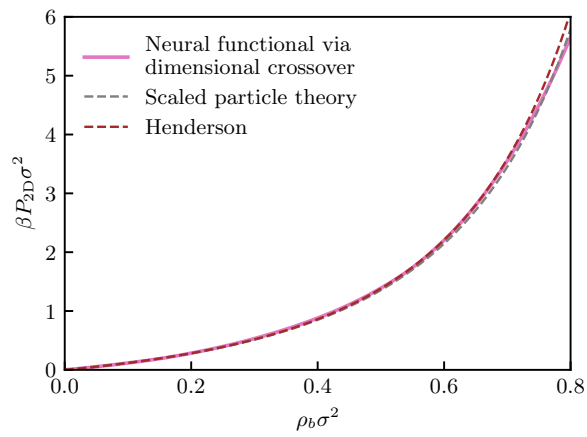


Fig. S3. The equation of state $P_{2D}(\rho_b)$ for two-dimensional hard disks is depicted, which is obtained from the neural functional via dimensional crossover. For comparison, we show analytic results according to scaled particle theory (9) and by Henderson (10). Although the training data for the three-dimensional hard sphere fluid did not cover narrow confinement within hard walls, $c_1^*(0; [\rho])$ reproduces very reasonable behavior when applied to such quasi-two-dimensional situations and yields acceptable results for densities up to $\rho_b \approx 0.7\sigma^{-2}$.

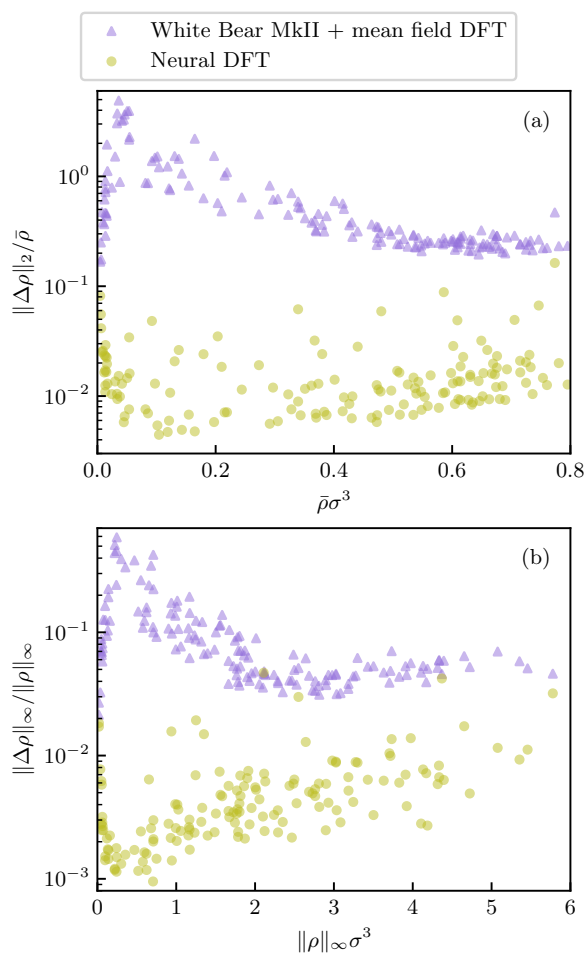


Fig. S4. Neural DFT (yellow circles) is compared to the standard mean field DFT (purple triangles) for the truncated Lennard-Jones fluid. As in Fig. 6, (a) the normalized L_2 -norm $\|\Delta\rho\|_2/\bar{\rho}$ as a function of the mean density $\bar{\rho}$, and (b) the relative maximum norm $\|\Delta\rho\|_\infty/\|\rho\|_\infty$ as a function of the largest local density $\|\rho\|_\infty$ are considered. While considerable deviations to the reference profiles are observed for the hard sphere plus mean field treatment, neural DFT achieves almost simulation-like accuracy with global and local errors being decreased by up to two orders of magnitude.

References

1. JP Hansen, IR McDonald, *Theory of Simple Liquids With Applications to Soft Matter*. (Elsevier Science & Technology Books), (2013).
2. L Dixon, Automatic differentiation: Calculation of the Hessian in *Encyclopedia of Optimization*. (Springer US), pp. 133–137 (2008).
3. V Molinero, EB Moore, Water modeled as an intermediate element between carbon and silicon. *J. Phys. Chem. B* **113**, 4008–4016 (2008).
4. Y Rosenfeld, Free-energy model for the inhomogeneous hard-sphere fluid mixture and density-functional theory of freezing. *Phys. Rev. Lett.* **63**, 980–983 (1989).
5. E Kierlik, ML Rosinberg, Free-energy density functional for the inhomogeneous hard-sphere fluid: Application to interfacial adsorption. *Phys. Rev. A* **42**, 3382–3387 (1990).
6. S Phan, E Kierlik, ML Rosinberg, B Bildstein, G Kahl, Equivalence of two free-energy models for the inhomogeneous hard-sphere fluid. *Phys. Rev. E* **48**, 618–620 (1993).
7. H Hansen-Goos, R Roth, Density functional theory for hard-sphere mixtures: the White Bear version mark II. *J. Phys.: Condens. Matter* **18**, 8413–8425 (2006).
8. P Tarazona, Density functional for hard sphere crystals: A fundamental measure approach. *Phys. Rev. Lett.* **84**, 694–697 (2000).
9. H Reiss, HL Frisch, JL Lebowitz, Statistical mechanics of rigid spheres. *J. Chem. Phys.* **31**, 369–380 (1959).
10. D Henderson, A simple equation of state for hard discs. *Mol. Phys.* **30**, 971–972 (1975).
11. Y Zhou, J Wu, S Chen, G Chen, Toward the exact exchange-correlation potential: A three-dimensional convolutional neural network construct. *J. Phys. Chem. Lett.* **10**, 7264–7269 (2019).

Topical Review

Why neural functionals suit statistical mechanics

Florian Sammüller , Sophie Hermann  and Matthias Schmidt* 

Theoretische Physik II, Physikalisches Institut, Universität Bayreuth, D-95447 Bayreuth, Germany

E-mail: Matthias.Schmidt@uni-bayreuth.de

Received 29 November 2023, revised 14 February 2024

Accepted for publication 11 March 2024

Published 21 March 2024



CrossMark

Abstract

We describe recent progress in the statistical mechanical description of many-body systems via machine learning combined with concepts from density functional theory and many-body simulations. We argue that the neural functional theory by Sammüller *et al* (2023 *Proc. Natl Acad. Sci.* **120** e2312484120) gives a functional representation of direct correlations and of thermodynamics that allows for thorough quality control and consistency checking of the involved methods of artificial intelligence. Addressing a prototypical system we here present a pedagogical application to hard core particle in one spatial dimension, where Percus' exact solution for the free energy functional provides an unambiguous reference. A corresponding standalone numerical tutorial that demonstrates the neural functional concepts together with the underlying fundamentals of Monte Carlo simulations, classical density functional theory, machine learning, and differential programming is available online at <https://github.com/sfalmo/NeuralDFT-Tutorial>.

Keywords: density functional theory, statistical mechanics, machine learning, inhomogeneous fluids, fundamental measure theory, neural functional theory, differential programming

1. Introduction

The discovery of the molecular structure of matter was still in its infancy when van der Waals predicted in 1893 on theoretical grounds that the gas–liquid interface has finite thickness. The theory is based on a square-gradient treatment of the density inhomogeneity between the coexisting phases [1, 2] and it is consistent with van der Waals' earlier treatment of the gas–liquid phase separation in bulk. Both the bulk and the interfacial treatments are viewed as simple yet physically correct

descriptions of fundamental phase coexistence phenomena by modern standards of statistical mechanics.

What was unknown then is that an underlying formally exact variational principle exists. This mathematical structure was recognized only much later, first quantum mechanically by Hohenberg and Kohn [3] for the groundstate of a many-body system, subsequently by Mermin [4] for finite temperatures, and then classically by Evans [5]. The variational principle forms the core of density functional theory and the intervening history between the quantum [4] and classical milestones [5] is described by Evans *et al* [6]; much background of the theory is given in [7–9]. Kohn and Sham [10, 11] re-introduced orbitals via an effective single-particle description, which facilitates the efficient treatment of the many-electron quantum problem.

Practical applications of density functional theory require one to make concrete approximations for the central

* Author to whom any correspondence should be addressed.



Original Content from this work may be used under the terms of the [Creative Commons Attribution 4.0 licence](https://creativecommons.org/licenses/by/4.0/). Any further distribution of this work must maintain attribution to the author(s) and the title of the work, journal citation and DOI.

functional. (We recall that a functional maps an entire function to a number.) Quantum mechanically one needs to approximate the exchange-correlation energy functional $E_{xc}[n]$, as depending on the electronic density profile $n(\mathbf{r})$, and classically one needs to get to grips with the excess (over ideal gas) intrinsic Helmholtz free energy $F_{exc}[\rho]$, as a functional of the local particle density $\rho(\mathbf{r})$.

A broad range of relevant problems and intriguing collective and self-organization effects in soft matter [12] have been investigated on the basis of classical density functional theory [5–9]. Exemplary topical studies include investigations of hydrophobicity [13–16], the orientation-resolved molecular structure of liquids [16], the three-dimensionally resolved atomic structure of electrolytes [17, 18], and the asymptotic decay of ionic structural correlations [19].

Owing to its rigorous formal foundation, density functional theory provides a microscopic, first-principles treatment of the many-body problem. The numerical efficiency of (in practice often approximate) implementations allows for exhaustive model parameter sweeps, for systematic investigation of bulk and interfacial phase transitions, and for the discovery and tracing of scaling laws. Exact statistical mechanical sum rules [20–23] integrate themselves very naturally into the scheme and they provide consistency checks and can form the basis for refined approximations. Nevertheless, at the core of such studies lies usually an approximate functional and hence resorting to explicit many-body simulations is common in a quest for validation of the predicted density functional results.

Inline with topical developments in other branches of science, the use of machine learning is becoming increasingly popular in soft matter research. Recent applications of machine learning range from the characterization of soft matter [24], reverse-engineering of colloidal self-assembly [25], local structure detection in colloidal systems [26], to the investigation of many-body potentials for isotropic [27] and for anisotropic [28] colloids. Brief overviews of machine learning in physics [29] and in particular in liquid state theory [30] were given recently.

Density functional theory lends itself towards machine learning due the necessity of finding an approximation for the central functional. Corresponding research was carried out in the classical [31–42] and quantum realms [43–51]. The classical work addressed liquid crystals in complex confinement [31], the functional construction of a convolutional network [32] and of an equation-learning network [33], the improvement of the standard mean-field approximation for the three-dimensional Lennard–Jones system [34] with the aim of addressing gas solubility in nanopores [35], the use physics-informed Bayesian inference [36, 37], active learning with error control [38], and the physics of patchy particles [39].

The quantum mechanical problem was addressed on the basis of machine learning the exchange-correlation potential [43–45], testing its out-of-training transferability [43], using a three-dimensional convolutional neural network construct [45], considering hidden messages from molecules [46], and using the Kohn–Sham equations already during training via a regularizer method [47]. The Hamiltonian itself was targeted via deep learning with the aim of efficient electronic-structure

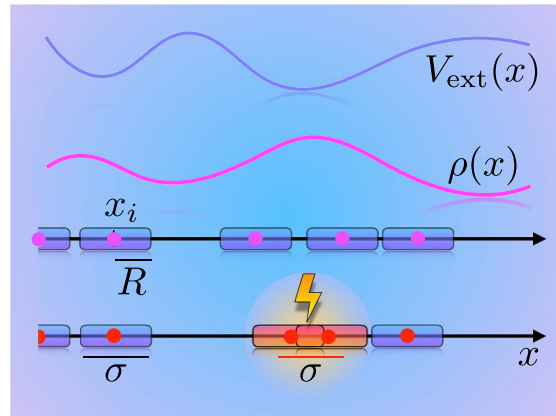


Figure 1. Illustration of hard rods in one spatial dimension that are exposed to a position-dependent external potential $V_{\text{ext}}(x)$. In response to the external influence a spatially inhomogeneous density profile $\rho(x)$ emerges in equilibrium at temperature T and chemical potential μ . The particles with position coordinates x_i and particle index $i = 1, \dots, N$ have radius R and diameter $\sigma = 2R$. A configuration is forbidden (bottom row) if any two particles overlap, i.e. if their mutual distance is smaller than the particle diameter σ .

calculation [48]. A recent perspective on these and more developments was given by Burke and co-workers [50]. Huang *et al* [51] argue prominently that quantum density functional theory plays a special role in the wider context of the use of artificial intelligence methods in chemistry and in materials science.

While the central problem of quantum density functional theory is to deal with the exchange and correlation effects between electrons that are exposed to the external field generated by the nuclei, classical statistical mechanics of soft matter relies on a much more varied range of underlying model Hamiltonians. The effective interparticle interactions in soft matter systems cover a wide gamut of different types of repulsive and attractive, short- and long-ranged, hard-, soft-, and penetrable-core behaviours.

In particular the hard core model plays a special role. For hard core particles the pair potential between two particles is infinite if the particle pair overlaps and it vanishes otherwise. Hard core particles are relatively simple as temperature becomes an irrelevant variable while the essence of short-ranged repulsion and the resulting molecular packing remain captured correctly [52, 53]. The statistical mechanics of the bulk of one-dimensional hard core particles was solved early by Tonks [54]. The free energy functional is known exactly due to Percus [55–59] and his solution provides the general structure and thermodynamics of the system when exposed to an external potential, see figure 1 for an illustration. The mathematical form of Percus’ free energy functional was one of the sources of inspiration [60] for Rosenfeld’s powerful fundamental measure density functional for three-dimensional hard spheres [61–68]. One-dimensional hard rods are also central for nonequilibrium physics [69–73] and the Percus functional forms a highly useful reference for developing and testing

machine learning techniques in classical density functional theory [32, 33, 36–38].

In recent work, de las Heras *et al* [40] and Sammüller *et al* [41] have put forward machine learning strategies that operate on the one-body level of correlation functions. Here we address in detail the neural functional theory [41] for inhomogeneous fluids in equilibrium. We argue that this approach constitutes a neural network-based theory, where multiple different and mutually intimately related neural functionals form a genuine theoretical structure that permits investigation, testing, and to ultimately gain profound insight into the nature of the coupled many-body physics. Thereby the training is only required for a single neural network, from which then all further neural functionals are created in straightforward ways. The method allows for multi-scale application [41] as is pertinent for many areas of soft matter [74–76]. It is furthermore applicable to general interactions, as exemplified by successfully addressing a supercritical Lennard–Jones fluid [41], thus complementing analytical efforts to construct density functional approximations. Such work was based, e.g. on hierarchical integral equations [77, 78], on functional renormalization group methods [79–81], and on fundamental measure theory [82–84].

Here we use the one-dimensional hard core model to illustrate the key concepts of the neural functional theory, as the required sampling can be performed easily and Percus’ functional provides an analytical structure that we can relate to the neural theory. The Percus functional is one of the very few general classical free energy density functionals that is analytically known for a continuum model (see e.g. also [85, 86]) and this fact provides further motivation for our study. A hands-on tutorial that demonstrates the key concepts of constructing a neural direct correlation functional, generating the required data from Monte Carlo simulations, testing against a numerical implementation of the Percus functional, and working with automatic differentiation is available online [42].

The paper is structured into individual subsections, as described in the following; each subsection is self-contained to a significant degree such that Readers are welcome to select the description of those topics that match their own interests and individual backgrounds. An overview of key concepts of the one-body neural functional approach is given in section 1.1. This hybrid method draws on classical density functional concepts, as summarized in section 1.2. Functional differentiation and integration methods are described in section 1.3.

Readers who are primarily interested in the use of machine learning may want to skip the above material and rather start with section 2.1, where we describe how to construct and train the neural correlation functional on the basis of many-body simulation data. We concentrate on the specific model of one-dimensional hard core particles and complement and contrast the neural functional by the known exact analytical results for this model, as described in section 2.2. Model applications for predicting inhomogeneous systems based on neural density functional theory are described in section 2.3.

Several methods of neural functional calculus are described in section 3. Manipulating the neural correlation functional by

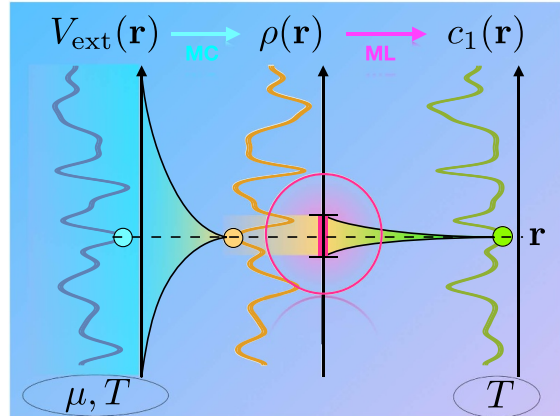


Figure 2. Illustration of the relevant functional maps of the neural functional theory. The external potential $V_{\text{ext}}(\mathbf{r})$ generates a one-body density profile $\rho(\mathbf{r})$ that is associated with a one-body direct correlation function $c_1(\mathbf{r})$. At given temperature T , chemical potential μ , and for a specific form of the external potential $V_{\text{ext}}(\mathbf{r})$, Monte Carlo simulations provide data for the corresponding density profile $\rho(\mathbf{r})$ and for the direct correlation function $c_1(\mathbf{r})$. Machine learning is used to represent the functional map $\rho \rightarrow c_1$ via a deep neural network. The functional dependence of $c_1(\mathbf{r})$ on the density profile is of much shorter spatial range as compared to the training data obtained from $V_{\text{ext}} \rightarrow \rho$.

functional integration and automatic functional differentiation is described in sections 3.1 and 3.2, respectively. The application of Noether sum rules as a standalone means for quality control of the neural network is presented in section 3.3. Functional integral sum rules are shown in section 3.4. A brief overview of key concepts of neural functional representations in nonequilibrium are presented in section 4. We give conclusions in section 5.

1.1. Neural functional concepts

The neural functional framework [41] rests on a combination of simulation, density functional theory, and machine learning. Data that characterizes the underlying many-body system is generated via grand canonical Monte Carlo simulations of well-defined, but random external conditions. Based on these results the one-body direct correlation functional is constructed as a neural network that accepts as an input the relevant local section of the density profile. This method allows for very efficient data handling as only short-ranged correlations contribute; figure 2 depicts an illustration.

The neural one-body direct correlation functional $c_1(\mathbf{r}, [\rho])$ forms the mother network for the subsequent functional calculus. Automatically differentiating the mother network with respect to its density input yields the two-body direct correlation functional $c_2(\mathbf{r}, \mathbf{r}', [\rho])$ as a daughter functional. Two-body direct correlations are central in liquid state theory [8] and they are here represented by a standalone numerical object that is created via straightforward application of automatic differentiation. This workflow is very different and arguably

much simpler in practice than the standard technique of carrying out the functional differentiation analytically and then implementing the resulting expression(s) via numerical code.

Differentiating the daughter network yields a granddaughter network, which represents the three-body direct correlation functional $c_3(\mathbf{r}, \mathbf{r}', \mathbf{r}'', [\rho])$. Again this is an independent and standalone numerical computing object. Very little is known about three-body direct correlations, with e.g. Rosenfeld's early investigation for hard spheres [61] and the freezing studies by Likos and Ashcroft [87, 88] being notable exceptions. The neural functional method [41] offers arguably unprecedented detailed access.

Tracing the genealogy in the reverse direction requires functional integration, which is a general and standard technique in functional calculus. In the present case again a quasi-standalone numerical object can be built based on mere network evaluation and standard numerical integration, both of which are fast operations. In this way, functionally integrating the mother one-body direct correlation functional creates as the grandmother the excess free energy functional $F_{\text{exc}}[\rho]$. This mathematical object is the ultimate generating functional in classical density functional theory for all n -body *direct* correlation functions [5, 8, 9]. We give more details about the interrelationships within the family of functionals below in section 1.3.

When applied to the three-dimensional hard sphere fluid and restricted to planar geometry, such that the density distribution is inhomogeneous only along a single spatial direction, the neural functional theory outperforms the best available hard sphere density functional (the formidable White Bear Mk. II fundamental measure theory [65]) in generic inhomogeneous situations. For spatially homogeneous fluids the neural functional even surpasses the 'very accurate equation of state' [8] by Carnahan and Starling [52], despite the fact that no explicit information about *any* bulk fluid properties was used during training.

Formulating reliable strategies of how to test machine-learning predictions constitutes in general a complex yet very important task, not least in the light of ongoing and projected increased use of artificial intelligence in science [51]. The neural functional theory offers a wealth of concrete self-consistency checks besides the standard benchmarking techniques. Commonly and following best practice in machine learning, benchmarking is performed by dividing the reference data, as here obtained from many-body simulations, into training, validation and test data. The simulations in the test data set have not been used during training and hence can serve to assess the performance of the trained network. In our present model application, we can perform testing directly with respect to the exact Percus theory.

Assessing extrapolation capabilities beyond the underlying data set requires the availability of further reference data. In [41] this is provided by comparing (favourably) against a highly accurate bulk equation of state [89] as well as comparing against free energy reference results obtained from simulation-based thermodynamic integration of inhomogeneous systems.

However, due to its computational efficiency the neural approach allows to make predictions for system sizes that outscale significantly the dimensions of the original simulation box. Sammüller *et al* [41] describe systems of micron-sized colloids confined between parallel walls with macroscopic separation distance. The density profile is resolved over a system size of 1 mm with nanometric precision on a numerical grid with 10 nm spacing. Such 'simulation beyond the box' is both powerful in terms of multiscale description of soft matter [74–76], but is also serves as template for the more general situation of using artificial intelligence methods far outside their original training realm.

In order to provide quality control, the neural functional theory hence allows to carry out a second type of test. This is less generic than the above benchmarking but it can nevertheless provide inspiration for machine learning in wider contexts. In the present case, the specific statistical mechanical nature of the underlying equilibrium many-body system implies far-reaching mathematical structure, as it lies at the very heart of Statistical Mechanics. Specifically, it is the significant body of equilibrium sum rules that provide formally exact interrelations between different types of correlation functions. These sum rules hold universally, i.e. independent of the specific inhomogeneous situation that is under consideration and they hence constitute formally exact relationships between functionals.

As the neural functional theory expresses direct correlation functions using neural network methods, the sum rules directly translate to identities that connect the different neural functionals and their integrated and differentiated relatives with each other. Crucially, these connections have both different mathematical form, as well as different physical meaning, as compared to the bare genealogy provided by the automatic functional differentiation and functional integration. Without overstretching the analogy, one could view the sum rules as genetic testing the entire family for absence of inheritable disease.

While the body of statistical mechanical sum rules is both significant and diverse [20–23], here we rely on the recent Noether invariance theory [90–98] as a systematic means to create both known and new functional identities from the thermal invariance of the underlying statistical mechanics [90, 91]. In particular from invariance against local shifting one obtains sum rules that connect different generations of direct correlation functionals with each other in both locally-resolved and global form. We present exemplary cases below in section 3.3. Generic sum rules that emerge from the mere inverse relationship of functional integration and functional differentiation are presented in section 3.4.

1.2. Introduction to classical density functional theory

We give a compact account of some key concepts of classical density functional theory; for more details see [5–9]. Readers who are primarily interested in machine learning of neural functionals can skip this and the next subsection and directly proceed to section 2.

In a statistical mechanical description of a many-body system the local density acts as a generic order parameter that measures the probability of finding a particle at a specific location. The formal definition of the one-body density distribution as a statistical average is:

$$\rho(\mathbf{r}) = \left\langle \sum_i \delta(\mathbf{r} - \mathbf{r}_i) \right\rangle, \quad (1)$$

where the sum over i runs over all N particles, \mathbf{r}_i is the position coordinate of particle $i = 1, \dots, N$, and $\delta(\cdot)$ indicates the Dirac distribution, here in three dimensions. The angles indicate a thermal average over microstates, which can e.g. be efficiently carried out in Monte Carlo simulations.

For completeness, we give a formal description of the equilibrium average based on the grand ensemble, where it is defined as $\langle \cdot \rangle = \text{Tr} \cdot e^{-\beta(H - \mu N)} / \Xi$. Here the inverse temperature is $\beta = 1/(k_B T)$, with the Boltzmann constant k_B and absolute temperature T , the Hamiltonian H , chemical potential μ and grand partition sum Ξ . The classical trace is defined as $\text{Tr} \cdot = \sum_{N=0}^{\infty} (h^{dN} N!)^{-1} \int d\mathbf{r}^N \int d\mathbf{p}^N$, where h denotes the Planck constant and $\int d\mathbf{r}^N \int d\mathbf{p}^N$ is a shorthand for the high-dimensional phase space integral over all particle positions and momenta in d spatial dimensions. Pedagogical introductions can be found in standard textbooks [8] and an introductory compact account together with a description of the force point of view is provided in [91].

The Hamiltonian has the following standard form:

$$H = \sum_i \frac{\mathbf{p}_i^2}{2m} + u(\mathbf{r}^N) + \sum_i V_{\text{ext}}(\mathbf{r}_i), \quad (2)$$

where \mathbf{p}_i is the momentum of particle i , the interparticle interaction potential $u(\mathbf{r}^N)$ depends on all position coordinates $\mathbf{r}^N = \mathbf{r}_1, \dots, \mathbf{r}_N$, and $V_{\text{ext}}(\mathbf{r})$ is an external potential energy function that depends on position \mathbf{r} . Hence the sum in equation (2) comprises kinetic, interparticle, and external energy contributions. For the common case of particles interacting via a pair potential $\phi(r)$ that only depends on the interparticle distance r , the interparticle energy reduces to $u(\mathbf{r}^N) = \sum_{ij(i \neq j)} \phi(|\mathbf{r}_i - \mathbf{r}_j|)/2$ where the double sum runs only over distinct particle pairs ij with $i \neq j$ and the factor 1/2 corrects for double counting.

For the ideal gas the interparticle interactions vanish, $u(\mathbf{r}^N) \equiv 0$, and the density profile is given by the generalized barometric law [8]:

$$\rho_{\text{id}}(\mathbf{r}) = e^{-\beta(V_{\text{ext}}(\mathbf{r}) - \mu)} / \Lambda^d, \quad (3)$$

where Λ denotes the thermal de Broglie wavelength, which in the present classical case can be set to $\Lambda = \sigma$, with σ denoting the particle size; for simplicity of notation here we use $\Lambda = 1$.

Taking the logarithm of equation (3) and collecting all terms on the left hand side gives the following ideal gas chemical potential balance:

$$\ln \rho_{\text{id}}(\mathbf{r}) + \beta V_{\text{ext}}(\mathbf{r}) - \beta \mu = 0. \quad (4)$$

For a mutually interacting system, where $u(\mathbf{r}^N) \neq 0$, equation (4) will not be true when replacing the ideal density profile $\rho_{\text{id}}(\mathbf{r})$ by the true density profile $\rho(\mathbf{r})$ as formally given by equation (1). Rather the sum of the three terms on the left hand side of equation (4) will not vanish, but yield a nontrivial contribution:

$$\ln \rho(\mathbf{r}) + \beta V_{\text{ext}}(\mathbf{r}) - \beta \mu = c_1(\mathbf{r}), \quad (5)$$

where the one-body direct correlation function $c_1(\mathbf{r})$ is in general nonzero and arises due to the presence of interparticle interactions in the system. (For hard core systems $c_1(\mathbf{r})$ typically features negative values.)

The machine learning strategy described below in section 2.1 is based on this pragmatic access to data for $c_1(\mathbf{r})$, as obtained by direct simulation of $\rho(\mathbf{r})$ on the basis of explicitly carrying out the average in equation (1) for given form of $V_{\text{ext}}(\mathbf{r})$ and prescribed values of the thermodynamic parameters μ and T . As the one-body direct correlation function is central in the neural functional theory, we combine equations (4) and (5), which yields the following equivalent form for the one-body direct correlation function,

$$c_1(\mathbf{r}) = \ln \left(\frac{\rho(\mathbf{r})}{\rho_{\text{id}}(\mathbf{r})} \right), \quad (6)$$

where $\rho_{\text{id}}(\mathbf{r})$ is given by equation (3) with $\Lambda = 1$. Equation (6) has the direct interpretation of $c_1(\mathbf{r})$ as the logarithm of the ratio of the actual density profile and the density profile of the ideal gas under identical conditions, as given by the external potential and thermodynamic statepoint.

In alternative terminology [8] one defines the intrinsic chemical potential as $\mu_{\text{int}}(\mathbf{r}) = \mu - V_{\text{ext}}(\mathbf{r})$. The intrinsic chemical potential and the one-body direct correlation function are related trivially to each other via $\mu_{\text{int}}(\mathbf{r}) = k_B T [\ln \rho(\mathbf{r}) - c_1(\mathbf{r})]$ as is obtained straightforwardly by rearranging equation (5).

The practical, computational, and conceptual advantage of density functional theory lies in avoiding the explicit occurrence of the high-dimensional phase space integral that underlies thermal averages; we recall the definition of the density profile (1) as such an expectation value. Instead, and without any principal loss of information, one works with functional dependencies. Rather than mere point-wise dependencies, such as between the functions $\rho(\mathbf{r})$, $V_{\text{ext}}(\mathbf{r})$, and $c_1(\mathbf{r})$ that hold at each point \mathbf{r} , see equation (5), a functional dependence is on the entirety of a function and it has in general a nonlocal and nonlinear structure.

Density functional theory is specifically based on the fact [3–5] that for a given type of fluid, as characterized by its interparticle interaction potential $u(\mathbf{r}^N)$, and known thermodynamic parameters μ and T , the form of density profile $\rho(\mathbf{r})$ is sufficient to determine the entirety of the external potential $V_{\text{ext}}(\mathbf{r})$. Hence a unique functional map exists [3–5]:

$$\rho \rightarrow V_{\text{ext}}. \quad (7)$$

Here we omit the position arguments on both sides to reflect in the notation that the functional map relates the entirety of the density profile to the entirety of the external potential.

Applying equation (7) to the external potential, as it occurs in equation (5), implies that the left hand side is determined from knowledge of the density profile alone, in principle without any need for *a priori* knowledge of the form of $V_{\text{ext}}(\mathbf{r})$. Via the identity (5) we can conclude the existence of the map:

$$\rho \rightarrow c_1, \quad (8)$$

where the entirety of the density profile determines the entirety of the direct correlation function. As a consequence the one-body direct correlation function actually is a density functional, $c_1(\mathbf{r}, [\rho])$, where the brackets indicate the functional dependence, i.e. on the entirety of the argument function, here $\rho(\mathbf{r})$. We will discuss below more explicitly that the dependence is effectively short-ranged for the case of short-ranged interparticle interaction potentials and that this can be exploited to great effect in the neural network methodology.

1.3. Density functional derivatives and integrals

While we have emphasized above the role of the one-body direct correlation functional $c_1(\mathbf{r}, [\rho])$, primarily due to $c_1(\mathbf{r})$ being directly measurable via equation (6), one typically rather starts with a parent functional, the excess free energy functional $F_{\text{exc}}[\rho]$, in standard accounts of classical density functional theory. The relationship of $F_{\text{exc}}[\rho]$ and $c_1(\mathbf{r}, [\rho])$ is established via functional calculus. Functional differentiation, see [9] for a practitioner's account, yields additional position dependence and we use the notation $\delta/\delta\rho(\mathbf{r})$ to denote the *functional* derivative with respect to the function $\rho(\mathbf{r})$. Functional integration is the inverse operation. We give a brief description of the functional relationships in the following. An overview is illustrated in figure 3 and we will return for a broader account below in section 3.

The method of *automatic differentiation* [99] is an integral part of the new computing paradigm of differentiable programming [100]. Automatic differentiation is based on a powerful set of techniques and it differs from both symbolic differentiation, as facilitated by computer algebra systems, and from numerical differentiation via finite difference, as is computational bread and butter. As shown in the tutorial [42] only high-level code is required to invoke automatic differentiation, and both neural *and* analytical functionals can be differentiated with little effort. As the derivative (of the functional) is with respect to its entire input data, the method constitutes a representation of a genuine functional derivative.

We give an overview. In the present context the functional calculus that relates the one-body direct correlations to the parent excess free energy functional is given by the following functional integration and functional differentiation relations:

$$\beta F_{\text{exc}}[\rho] = - \int d\mathbf{r} \rho(\mathbf{r}) \int_0^1 da c_1(\mathbf{r}, [\rho_a]), \quad (9)$$

$$c_1(\mathbf{r}, [\rho]) = - \frac{\delta \beta F_{\text{exc}}[\rho]}{\delta \rho(\mathbf{r})}. \quad (10)$$

In equation (9) we have parameterized the general formal integral $\int D[\rho]$ by using $\rho_a(\mathbf{r})$ as a scaled version of the density

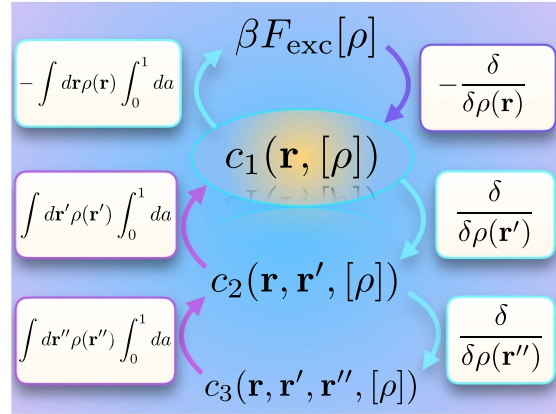


Figure 3. Illustration of four different generations of density functionals. Shown are the excess free energy functional $F_{\text{exc}}[\rho]$ and the one-, two-, and three-body direct correlation functionals. Upward arrows indicate the relationship via functional integration $\int d\mathbf{r} \rho(\mathbf{r}) \int_0^1 da$ with the integrand being evaluated at the scaled density $a\rho(\mathbf{r})$. Downward arrows indicate functional differentiation $\delta/\delta\rho(\mathbf{r})$. The neural functional theory is based on training $c_1(\mathbf{r}, [\rho])$ as the generating mother functional. Implementing the arrowed operations only requires high-level code. The resulting neural networks, as well as functionals derived from analytical expressions, are highly performant.

profile, with a simple linear relationship $\rho_a(\mathbf{r}) = a\rho(\mathbf{r})$. Hence the parameter value $a=0$ corresponds to vanishing density and $a=1$ reproduces the target density profile, as it occurs in the argument of $\beta F_{\text{exc}}[\rho]$ on the left hand side of equation (9). We emphasize that the integral over a in equation (9) is a simple one-dimensional integral over the coupling parameter a . The consistency between equations (9) and (10) is demonstrated below in section 3.4.

The perhaps seemingly very formal functional calculus acquires new and pressing relevance in light of the neural functional concepts of [41], which allow to work explicitly with both functional derivatives and functional integrals, which can be evaluated efficiently via the corresponding standalone neural functionals.

In light of these benefits it is fortunate that the functional differentiation-integration structure extends recursively to higher orders of correlation functions. The next level beyond equations (9) and (10) involves the two-body direct correlation functional $c_2(\mathbf{r}, \mathbf{r}', [\rho])$ and the integration and differentiation structure is as follows:

$$c_1(\mathbf{r}, [\rho]) = \int d\mathbf{r}' \rho(\mathbf{r}') \int_0^1 da c_2(\mathbf{r}, \mathbf{r}', [\rho_a]), \quad (11)$$

$$c_2(\mathbf{r}, \mathbf{r}', [\rho]) = \frac{\delta c_1(\mathbf{r}, [\rho])}{\delta \rho(\mathbf{r}')}, \quad (12)$$

and we refer to [8, 9, 101, 102] for background.

We can chain the functional derivatives together by inserting $c_1(\mathbf{r}, [\rho])$ as given by equation (10) into the definition (12) of $c_2(\mathbf{r}, \mathbf{r}', [\rho])$. In parallel, we can also chain the functional

integrals in equations (9) and (11). These procedures yield the following second order functional integration and differentiation relationships:

$$\beta F_{\text{exc}}[\rho] = - \int d\mathbf{r}\rho(\mathbf{r}) \int d\mathbf{r}'\rho(\mathbf{r}') \times \int_0^1 da \int_0^a da' c_2(\mathbf{r}, \mathbf{r}', [\rho_{a'}]), \quad (13)$$

$$c_2(\mathbf{r}, \mathbf{r}', [\rho]) = - \frac{\delta^2 \beta F_{\text{exc}}[\rho]}{\delta \rho(\mathbf{r}) \delta \rho(\mathbf{r}')}, \quad (14)$$

where the scaled density profile in equation (13) is $\rho_{a'}(\mathbf{r}) = a'\rho(\mathbf{r})$. The double parameter integral in equation (13) can be further simplified [7], as described at the end of section 3.4. The generalization of equation (14) to the n -th functional derivative defines the n -body direct correlation functional, which remains functionally dependent on the density profile and which possesses spatial dependence on n position arguments. Although increasing n yields objects that become very rapidly out of any practical reach, the neural functional concept provides much fuel for making progress. While we do not cover $c_3(\mathbf{r}, \mathbf{r}', \mathbf{r}'', [\rho])$ here, Sammüller *et al* have demonstrated its general accessibility and physical validity for bulk fluids in [41].

We have so far focused on the properties of the intrinsic excess free energy functional $F_{\text{exc}}[\rho]$ and its density functional derivatives. This is natural as classically $F_{\text{exc}}[\rho]$ is the central object that contains the effects of the interparticle interactions and thus depends in a nontrivial way on its input density profile. The functional $F_{\text{exc}}[\rho]$ is intrinsic in the sense that it is independent of external influence. We recall that we here work in the grand ensemble (see e.g. [103–106] for studies addressing the canonical ensemble of fixed particle number). Hence the appropriate thermodynamic potential is the grand canonical free energy or grand potential. This is required in order to determine $\rho(\mathbf{r})$.

When expressed as a density functional the grand potential consists of the following sum of ideal, excess, external, and chemical potential contributions:

$$\Omega[\rho] = F_{\text{id}}[\rho] + F_{\text{exc}}[\rho] + \int d\mathbf{r}\rho(\mathbf{r})[V_{\text{ext}}(\mathbf{r}) - \mu]. \quad (15)$$

The form of the ideal gas free energy functional is explicitly known as $F_{\text{id}}[\rho] = k_B T \int d\mathbf{r}\rho(\mathbf{r})[\ln \rho(\mathbf{r}) - 1]$ and the third term in equation (15) contains the effects of the external potential $V_{\text{ext}}(\mathbf{r})$ and of the particle bath at chemical potential μ .

The variational principle of classical density functional theory [4, 5, 105] ascertains that

$$\left. \frac{\delta \Omega[\rho]}{\delta \rho(\mathbf{r})} \right|_{\rho=\rho_0} = 0 \quad (\text{min}), \quad (16)$$

$$\Omega[\rho_0] = \Omega_0. \quad (17)$$

Equations (16) and (17) imply that the grand potential becomes minimal at $\rho_0(\mathbf{r})$, which is the real, physically realized density profile and Ω_0 is the equilibrium value of the grand potential. Recall that based on the many-body picture

we have $\Omega_0 = -k_B T \ln \Xi$ with the grand ensemble partition sum $\Xi = \text{Tr} e^{-\beta(H-\mu N)}$. We have used the subscript 0 to denote equilibrium but we drop this elsewhere in our presentation to simplify notation.

Inserting equation (15) into equation (16) and using the explicit form of the ideal free energy functional together with the definition (10) of $c_1(\mathbf{r}, [\rho])$ leads to equation (5) with the one-body direct correlations expressed as a density functional, as anticipated in section 1.2. Exponentiating and regrouping the terms then yields the following popular form of the Euler–Lagrange equation:

$$\rho(\mathbf{r}) = \exp(-\beta V_{\text{ext}}(\mathbf{r}) + \beta \mu + c_1(\mathbf{r}, [\rho])). \quad (18)$$

Equation (18) is a self-consistency relation that can be solved efficiently for the equilibrium density profile $\rho(\mathbf{r})$ via iterative methods, as detailed below in section 2.3. A prerequisite is that $c_1(\mathbf{r}, [\rho])$ is known, usually as an approximation that is obtained from an approximate excess free energy functional $F_{\text{exc}}[\rho]$ via functionally differentiating according to equation (10). Having obtained a numerical solution of equation (18) for the density profile, this can then be inserted into the grand potential functional (15) to obtain full thermodynamic information via equation (17), which by construction is consistent with the density profile.

We demonstrate in the following how this classical functional background can be put to formidable use via hybridization with simulation-based machine learning. As our aim is pedagogical, we choose the one-dimensional hard core system as a concrete example to demonstrate the general methodology [41]. We complement the neural functional structure with a description of Percus’ analytical solution, which then allows for mirroring of the neural theory.

2. Neural functional theory

Jerry Percus famously wrote in the abstract of his 1976 statistical mechanics landmark paper [55]: ‘The external field required to produce a given density pattern is obtained explicitly for a classical fluid of hard rods. All direct correlation functions are shown to be of finite range in all pairs of variables.’ Here we relate his achievement to the neural functional theory, which allows to reproduce numerically a variety of properties of the exact solution. We emphasize that the neural functional theory remains generic in its applicability to further model fluids; see the supplementary information of [41] for the successful treatment of the supercritical Lennard–Jones fluid in three dimensions. We refer the Reader to the provided online resources [42] for a programming tutorial on the concrete application of the following concepts. Figure 4 shows a schematic of the workflow that is inherent in the neural functional concept, as described in the following.

2.1. Training the neural correlation functional

The classical fluid of hard rods that Percus considers has one-dimensional position coordinates x_i , with particle index $i = 1, \dots, N$ and a pairwise interparticle interaction potential $\phi(x)$

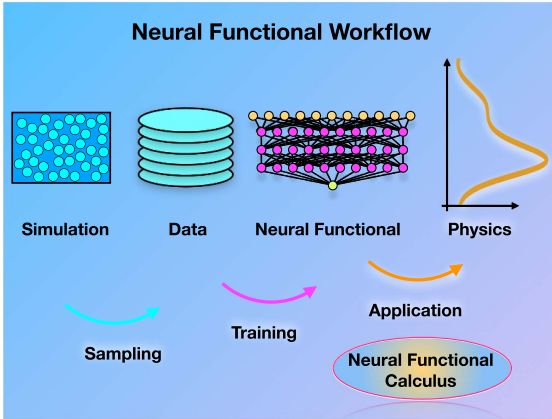


Figure 4. Schematic of the workflow of the neural functional theory. Many-body simulations under randomized conditions are used to sample statistically averaged and spatially resolved data that characterize the inhomogeneous response of the considered system. A neural network is then trained to represent the direct correlation functional, which is subsequently applied numerically and via neural functional methods to investigate the physics of the system in the desired target situations.

which is infinite if the distance x between the two particles is smaller than their diameter, $x < \sigma$, and it vanishes otherwise. The system is exposed to an external potential $V_{\text{ext}}(x)$, which is a function of position x across the system, and this in general creates an inhomogeneous ‘density pattern’ $\rho(x)$.

We adjust the definition (1) of the density distribution to the present one-dimensional case:

$$\rho(x) = \left\langle \sum_i \delta(x - x_i) \right\rangle, \quad (19)$$

where $\delta(\cdot)$ here indicates the Dirac distribution in one dimension and the brackets indicate a grand canonical thermal average. Due to the hard core nature of the model, the statistical weight of each ‘allowed’ microstate is particularly simple and given by $\exp[-\beta \sum_i V_{\text{ext}}(x_i) + \beta \mu N] / \Xi$, where Ξ is a normalizing factor. Allowed microstates are those for which all distinct particle pairs ij are spaced far enough apart, $|x_i - x_j| \geq \sigma$. If already a single overlap occurs, then the microstate is ‘forbidden’ as the interparticle potential becomes formally infinite, which then creates vanishing statistical weight; we recall the illustration in figure 1.

Despite the apparent simplicity of the many-body probability distribution, the Statistical Mechanics of the hard rod model is nontrivial. The particles interact nonlocally over the lengthscale σ and the external potential has no restrictions on its shape or on the lengthscale(s) of variation. Hence features such as jumps and positive infinities that represent hard walls are allowed. In bulk, $V_{\text{ext}}(x) = 0$, and the solution is straightforward [8, 54]. The general case is however highly nontrivial, which makes Percus’ above quoted opening a very remarkable one. We present more details of his work

further below, after first laying out the general machine learning strategy of [41]. This neural functional method is neither restricted to hard cores nor to one-dimensional systems, but addressing this case here is useful to highlight the salient features of the approach.

We aim for explicitly sampling the microstates of the system according to their probability distribution via particle-based simulations. This can be implemented efficiently, and for the present introductory purposes in also an intuitively accessible way, via grand canonical Monte Carlo (GCMC) sampling. Excellent accounts of this method are given in [8, 107–109]. Briefly, a Markov chain of microstates is constructed, where based on a given configuration, a trial step is proposed, which is accepted with a probability given by a Metropolis function involving the energy difference ΔE between the original and the trial state.

Three trial moves are used in the simplest yet powerful scheme: (i) Selecting one particle i randomly and displacing it uniformly within a given maximal cutoff distance. If the displacement creates overlap, then the trial move is discarded. If otherwise there is no overlap in the new configuration, the energy difference is due to only the external potential, $\Delta E = V_{\text{ext}}(x'_i) - V_{\text{ext}}(x_i)$, where the prime denotes the trial position of particle i . (ii) A new particle j is inserted at a random position x_j with energy change that accounts for both the external potential and the chemical equilibrium with the particle bath and hence $\Delta E = V_{\text{ext}}(x'_j) - \mu$. (iii) Correspondingly, a randomly selected particle i is removed from the system. The acceptance of the removal happens again with a probability given by the Metropolis function with energy difference $\Delta E = -V_{\text{ext}}(x_i) + \mu$.

Despite its conceptual simplicity GCMC is a very powerful method for the investigation of complex effects [107–109] and significant extensions exist both in the form of histogram techniques [108, 109] and the tailoring of more complex and collective trial moves. Investigating a typical physical problem, as specified by the interparticle interactions $u(\mathbf{r}^N)$ and the type of considered external influence, such as walls as represented by a model form of $V_{\text{ext}}(\mathbf{r})$, requires e.g. scanning of the thermodynamic parameters and acquiring good enough statistics at each statepoint. Our ultimate goal (section 2.3) is to perform this tasks with significant gain in efficiency via the neural theory; we re-iterate the availability via [42] of hands-on code examples for the present hard rod model.

We base the training on the following rewriting and adaptation of the chemical potential balance equation (5) to the one-dimensional system:

$$c_1(x) = \ln \rho(x) + \beta V_{\text{ext}}(x) - \beta \mu. \quad (20)$$

All quantities on the right hand side are either prescribed *a priori* or are accessible via the GCMC simulations: Specifically, the density profile $\rho(x)$ is obtained by filling a position-resolved histogram according to the encountered microstates as specified by its particle coordinates x_i . We recall the formal definition (19) of $\rho(x)$ via the Dirac distribution, which in practice is discretized such that sufficient finite spatial resolution, say 0.01σ , is obtained. This ‘counting’ method is arguably the

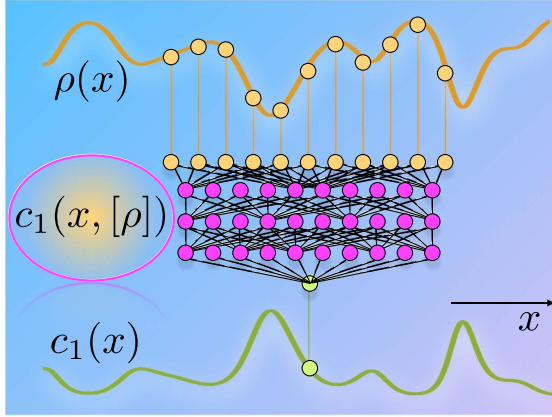


Figure 5. Illustration of the neural one-body direct correlation functional $c_1(x, [\rho])$ represented by a fully connected neural network with three hidden layers. The topology maps a small finite window of the density profile $\rho(x)$ to the local value of the direct correlation function $c_1(x)$.

most intuitive one to obtain data for the density profile. As an aside, there is a number of force-sampling techniques that can improve the statistical variance significantly [97, 110–112] and that also can serve to gauge the quality of sampling of the equilibrium ensemble [97].

While the issues of Monte Carlo sampling efficiency and quality assessment of thermal averages can be pertinent in higher dimensions and in physically more complex situations, the simplicity of the present one-dimensional hard core model makes counting according to equation (19) an appropriate choice to obtain data for $\rho(x)$. Then adding up the three contributions on the right hand side of equation (20) yields results for $c_1(x)$. We proceed at this data-generation stage somewhat heretically and ignore at first the central role that $c_1(x)$ plays for the physics of inhomogeneous systems.

In contrast to the typical deterministic setup for investigating a specific physical situation described above, training the neural network proceeds on the basis of randomized situations rather than with the ultimate application in mind; we recall the illustration of the neural functional workflow shown in figure 4. The motivation for using this strategy comes from the goal of capturing via the machine learning the intrinsic direct correlations of the many-body system that then transcend the specific inhomogeneous situations that were under consideration during training. Figure 5 depicts an illustration of the neural network topology of the trained central neural network $c_1(x, [\rho])$ and its relation to the physical input and output quantities, i.e. to $\rho(x)$ and $c_1(x)$.

We hence perform a sequence of simulation runs, where each run has an input value $\beta\mu^{(k)}$ and an input functional shape $\beta V_{\text{ext}}^{(k)}(x)$, both of which are generated randomly. Specifically, we combine sinusoidal functions with periodicities that are commensurate with the box length L , linear discontinuous segments, and hard walls in the creation of $V_{\text{ext}}^{(k)}(x)$; see [41, 42] for further details. The superscript k enumerates the

different GCMC simulation runs and in practice we perform 512 of these. The result is a set of corresponding density profiles $\rho^{(k)}(x)$. We then use equation (20) to obtain for each run the one-body direct correlation profiles from simply adding up: $c_1^{(k)}(x) = \ln \rho^{(k)}(x) + \beta V_{\text{ext}}^{(k)}(x) - \beta\mu^{(k)}$. As a result of the simulation protocol we have generated a bare data set $\{\beta\mu^{(k)}, \beta V_{\text{ext}}^{(k)}(x), \rho^{(k)}(x), c_1^{(k)}(x)\}$ for all positions x and for all different runs k . As a practical detail, this requires to exclude regions where $\rho(x) = 0$ and $V_{\text{ext}}(x) = \infty$.

In order to address our declared goal to learn a functional dependence of $c_1(x)$, we have to carve out a nontrivial dependence relationship and hence restrict the data input. Motivated by the physics, one might see the scaled chemical potential $\beta\mu^{(k)}$ and the scaled external potential $\beta V_{\text{ext}}^{(k)}(x)$ to be the true mechanical origin of the shape of the direct correlation function $c_1^{(k)}(x)$. However, the insights provided by density functional theory hint at the fact that this is not the best possible choice of functional relationship to consider.

We recapitulate that the GCMC simulations yield data according to:

$$\left\{ V_{\text{ext}}^{(k)}(x') - \mu^{(k)} \right\}_0^L \longrightarrow \left\{ \rho^{(k)}(x) \right\}_0^L, \quad (21)$$

where the curly brackets indicate all function values inside of the system box, with ranges $0 \leq x' \leq L$ and $0 \leq x \leq L$; the arrow indicates an input-output relationship. Applying equation (20) to the entire data set also allows to have the direct correlation function as an output according to:

$$\left\{ V_{\text{ext}}^{(k)}(x') - \mu^{(k)} \right\}_0^L \longrightarrow \left\{ c_1^{(k)}(x) \right\}_0^L. \quad (22)$$

If one were to mimic the simulations directly by the neural network one would be tempted to base the training directly upon equation (22). In less clearcut machine-learning situations than considered here, it can be a standard strategy to attempt to represent the causal relationship, which governs the complex mathematical or real-world system under consideration, by a surrogate artificial intelligence model. The present functional formulation of Statistical Mechanics hints at potential caveats, such as the necessity of dealing with the full input and output data sets (parameter ranges of x and x') across the entire system. Furthermore the specific physics of the mutually interacting rods appears to play no role.

The density functional-inspired training (section 1.2) proceeds very differently. We here take a pragmatic stance and attempt to create via training a neural representation of the dependence of $c_1(x)$ on $\rho(x)$ alone. This leads to a surrogate model $c_1(x, [\rho])$ based on the following mapping

$$\left\{ \rho^{(k)}(x') \right\}_{x-x_c}^{x+x_c} \longrightarrow c_1^{(k)}(x), \quad (23)$$

where the input on the left hand side consists of function values $\rho^{(k)}(x')$ that lie inside the density window centered at x , i.e. only the values x' that lie within a narrow interval $x - x_c \leq x' \leq x + x_c$. Here x_c is a cutoff parameter that for short-ranged interparticle potentials is of the order of the particle size. For

the present one-dimensional hard core system we set $x_c = \sigma$. Instead of having to output an entire function, as would be the case when attempting to learn via equation (22), here the output is merely the single value of the direct correlation function at the center of the density window. We recall that this target value is obtained from the simulation data via equation (20) such that $c_1^{(k)}(x) = \ln \rho^{(k)}(x) + \beta V_{\text{ext}}^{(k)}(x) - \beta \mu^{(k)}$ for each run k . A simple GCMC code is provided online [42], along with a pre-generated simulation data set and a pre-trained neural functional.

We choose the loss function to be the mean squared error of the neural network output compared to the simulation reference value for $c_1(x)$, as obtained via equation (20). As a further metric to gauge the training progress, we make use of the mean absolute error of reference and output. Both choices are standard [100]. The quadratic loss is convenient as it is analytical and hence the machine-learning gradient-based methods directly apply. The mean absolute error is nonanalytical due to the modulus involved, but it is a useful supporting quantity that has a very direct interpretation.

After training the mean absolute error was of the order of ~ 0.013 , which implies that the neural network prediction deviates on average by this value from the simulation data. Although the simulation data carries some statistical noise, its effect is comparatively smaller, when taking the numerical solution of the Percus theory (detailed below) as the reference.

Our training data consists of 512 simulation runs using a simulation box size of $L = 10\sigma$. Each of the simulation runs requires only about three minutes runtime on a single CPU core of a standard desktop machine.

We use a standard fully-connected artificial neural network with three hidden layers that respectively possess 128, 64 and 32 nodes. We use 201 input nodes to represent the density profile in a finite window of size 1σ and spatial bin size 0.01σ , where we recall that σ is the particle size. To accommodate the local functional mapping, we reshape the training data into input density windows and corresponding output values of $c_1(x)$, where we also apply twofold data augmentation by exploiting mirror symmetry of the simulation results. Excluding regions where $V_{\text{ext}}(x) = \infty$ and hence where equation (20) is not defined, this results in $\sim 10^6$ input-output pairs.

From the above description and without considering the background in density functional theory it is not evident that the training will be successful and minimize the loss satisfactorily to yield a trained network $c_1(x, [\rho])$. From a mathematical point of view, this raises the questions whether a corresponding object $c_1(x, [\rho])$ indeed exist and whether it is unique. And if so, is its structure simple enough that it can be written down explicitly?

2.2. Percus' exact direct correlation functional

Due to Percus singular achievement [55] the one-body direct correlation functional $c_1(x, [\rho])$ for interacting hard rods in one spatial dimension is known analytically and this has triggered much subsequent progress, see e.g. [56–58, 60–65]. The functional dependence on the density profile is nonlocal,

as one would expect from the fact that the rods interact over the finite distance σ , and it is also nonlinear, as is consistent with the behaviour of a nontrivially interacting many-body system. The spatial dependence is characterized by convolution operations which, despite performing the task of coarse-graining, retain the full character of the microscopic interactions. The Percus functional provided motivation for developing so-called weighted-density approximations [8], where the density profile is convolved with one or several weight functions that are then further processed to give the ultimate value of the density functional.

We here give the Percus direct correlation functional in Rosenfeld's geometry-based fundamental measure representation, see [59] for a historical perspective. Instead of working with the particle diameter σ as the fundamental length-scale, Rosenfeld rather bases his description on the particle radius $R = \sigma/2$, which allows to find deep geometric meaning in Percus' expressions and to also generalize to higher dimensions [60, 61, 65].

The exact form [60] of the one-body direct correlation functional is analytically given as the following sum:

$$c_1(x, [\rho]) = -\frac{\Phi_0(x-R) + \Phi_0(x+R)}{2} - \int_{x-R}^{x+R} dx' \Phi_1(x'). \quad (24)$$

Here the two functions $\Phi_0(x)$ and $\Phi_1(x)$ each depend on two weighted densities $n_0(x)$ and $n_1(x)$ in the following form:

$$\Phi_0(x) = -\ln[1 - n_1(x)], \quad (25)$$

$$\Phi_1(x) = \frac{n_0(x)}{1 - n_1(x)}. \quad (26)$$

The weighted densities $n_0(x)$ and $n_1(x)$ are obtained from the bare density profile via spatial averaging:

$$n_0(x) = \frac{\rho(x-R) + \rho(x+R)}{2}, \quad (27)$$

$$n_1(x) = \int_{x-R}^{x+R} dx' \rho(x'). \quad (28)$$

The discrete spatial averaging at positions $x \pm R$ in the weighted density (27) parallels that in the first term of equation (24). Similarly the position integral over the interval $[x-R, x+R]$ in equation (28) appears analogously in the second term of equation (24). These similarities are not by coincidence. The structure is rather inherited from the grand-mother (excess free energy) functional, as is described in section 3.1.

Having the analytical solution (24)–(28) for $c_1(x, [\rho])$ allows for carrying out numerical evaluation and comparing against results from the neural functional $c_1(x, [\rho])$. The range of nonlocality, i.e. the distance across which information of the density profile enters the determination of $c_1(x, [\rho])$ via equations (24)–(28) is strictly finite, as announced in Percus' abstract [55]. As two averaging operations, each with range $\pm R$, are chained together, the composite procedure has a range of $\pm 2R = \pm \sigma$, inline with our truncation of the density profiles

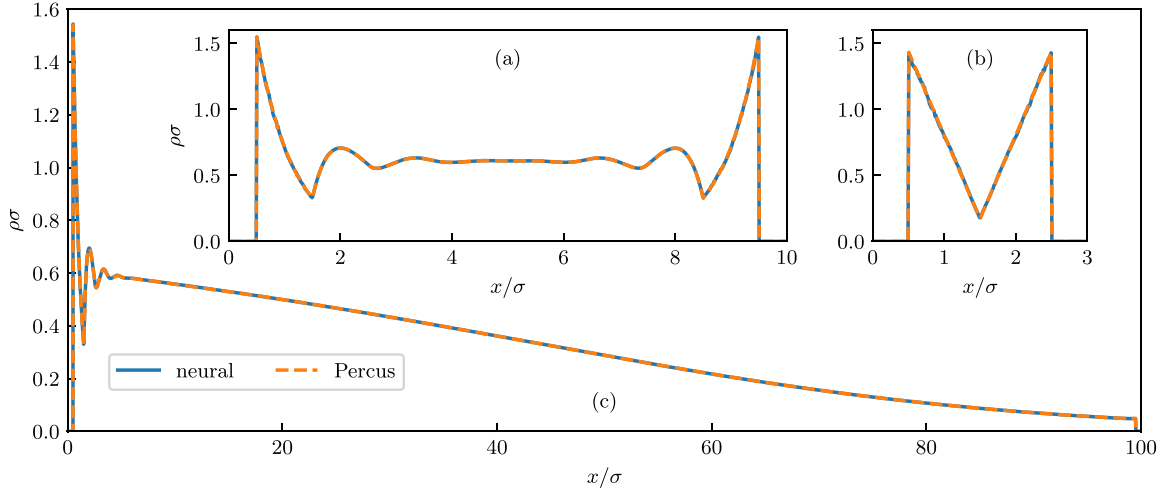


Figure 6. Representative density profiles that the inhomogeneous hard rod system exhibits under the influence of an external potential. The results are obtained from numerically solving equation (29) upon using either the neural direct correlation functional $c_1(x, [\rho])$ or Percus exact solution thereof. The three cases comprise (a) two hard walls with separation distance 9σ and chemical potential $\beta\mu = 2$, (b) two hard walls with much smaller separation distance 2σ and identical chemical potential $\beta\mu = 2$, and (c) sedimentation-diffusion equilibrium under gravity with a locally varying chemical potential, $\beta\mu_{loc}(x) = \beta\mu - \beta V_{ext}(x) = 2 - 0.05x/\sigma$; here the linearly varying contribution accounts for the influence of gravity on the system and confinement is provided by two widely spaced hard walls at $x = 0.5\sigma$ and $x = 99.5\sigma$. Note the crossover in panel (c) from the strongly oscillatory behaviour near the lower wall to a very smooth density decay, effectively following a local density approximation [8], upon increasing the scaled height x/σ .

in the training data sets according to equation (23). A numerical implementation of Percus direct correlation functional is available online [42].

2.3. Application inside and beyond the box

Actually making the predictions for the hard rod model is now straightforward as we can resort to density functional theory and its standard use in application to physical problems. The arguably most common method for solving the Euler–Lagrange equation self-consistently is based on equation (18), which we re-express for the one-dimensional case considered:

$$\rho(x) = \exp(-\beta V_{ext}(x) + \beta\mu + c_1(x, [\rho])). \quad (29)$$

We recall that the range of nonlocality of $c_1(x, [\rho])$ is limited to only the particle size σ and that we were able to extract the functional dependence from simulation data obtained by sampling in boxes of size L . Although the value of L could in principle be imprinted in subtle finite size effects that $c_1(x, [\rho])$ has acquired, the size L of the original simulation box has vanished and the application of the neural functional in equation (29) is fit for use to predict properties of much larger systems. As an example, [41] demonstrates the scaling up by a factor of 100 from the original simulation box to the predicted system of three-dimensional hard spheres under gravity.

The numerical solution of equation (29) can be efficiently performed on the basis of Picard iteration where an initial guess of the density profile is inserted on the right hand side and the resulting left hand side is used to nudge the initial

guess in the correct direction toward the self-consistent solution. This is numerically fast and straightforward to implement, see the tutorial [42]. A common choice is to mix five percent of the new solution to the prior estimate.

As laid out above, we choose the one-dimensional hard core model due to both the availability of Percus’ functional and the computational ease of both numerical evaluation of the analytical expressions and of carrying out many-body simulations. On the downside, the model does not form a very credible platform for assessing the numerical efficiency gain of the neural theory, as in general one will be interested in more complex systems and more complex physical situations than addressed here. Nevertheless, to give a rough idea about the required computational workload, minimizing the neural density functional takes of the order of seconds on a GPU, while the GCMC simulation runtime is of the order of several minutes. Minimizing the analytical Percus functional is faster than using the neural network, due to the simple structure of equations (24)–(28), which facilitates using very high-performance fast Fourier transforms.

We show three representative examples of density profiles for narrow to wide confinement between impenetrable walls in figure 6. In all cases the results from using the neural functional are numerically identical to those from the Percus functional on the scale of the plot. The profiles in narrow (figure 6(a)) and in moderately wide (figure 6(b)) pores show very distinct features with the strongly confined system in (a) having a striking V-shape, which arises from having at most two particles in the system, to the more generic damped oscillatory behaviour in the moderately wide pore (b). The main panel figure 6(c)

shows the influence of a weak gravitational field, which creates a continuously varying density inhomogeneity across the entire system. The decay in local density occurs with a much larger length scale as compared to the particle packing effects that are localized near the lower wall.

The behaviour shown in figure 6(c) away from the walls is well-represented by a local density approximation [8] (see e.g. [113] for recent mathematical work). The local density approximation can be a useful tool when investigating e.g. macroscopic ordering under gravity, where the occurring stacking sequences of different thermodynamic phases can be traced back to the phase diagram [114, 115]. In particular the effects on mixtures were rationalized by a range of techniques, from generalization of Archimedes' principle [116, 117] to analyzing stacking sequences [114, 115]. We stress that the present model applications constitute very significant extrapolations from the training data that we recall was obtained in a fixed box size $L = 10\sigma$ and under the influence of randomized external and chemical potentials. This is relevant in particular for both the very confined system (figure 6(b)) and the large system (figure 6(c)).

As a further potential application of the neural functional theory, the dynamical density functional theory [5, 69, 118] is similarly easy to implement numerically as equation (29) and it is a currently popular choice to study time-dependent problems [119, 120]. We comment on the status of the approach [40] and how machine learning can help to overcome its limitations in section 4 below.

3. Neural functional calculus

We have seen in section 2 how a neural one-body direct correlation functional can be efficiently trained on the basis of a pool of pre-generated Monte Carlo simulation data that are obtained under randomized conditions. The specific way of organizing the simulation data into training sets mirrors the functional relationships given by classical density functional theory. We have then shown that the neural functional can efficiently be used to address physical problems, taking the one-dimensional hard rod system as a simple example of a mutually interacting many-body system.

We here proceed by exemplifying the depth of physical insight that can be explored by acknowledging the functional character of the trained neural correlation functional. Hence we lay out functional integration (section 3.1) and functional differentiation (section 3.2). We show sum rule construction via Noether invariance (section 3.3), via exchange symmetry (also section 3.3), and via functional integration (section 3.4). The presentation in each subsection is self-contained to a considerable degree and we illustrate the generality of the methods both by application to the neural functional as well as by revisiting the analytic Percus theory.

3.1. Functional integration of direct correlations

Having captured the essence of molecular packing effects, as they arise from the short-ranged hard core repulsion between

the particles, via the neural functional $c_1(x, [\rho])$, begs for speculation whether additional and as yet hidden physical structure can be revealed. We give two plausibility arguments why one should expect to be able to postprocess $c_1(x, [\rho])$ in a meaningful way to retrieve global information.

First, thermodynamics is based on the existence of very few and well-defined unique and global quantities, such as the entropy, the internal energy, and the free energy. Carrying out parametric derivatives, with powerful interrelations given by the Maxwell relations, enables one to obtain equations of state, susceptibilities and further measurable global quantities. Our neural direct correlation functional in contrast is a local object with finite range of nonlocality. So how does this relate to the global information?

The second argument is more formal. Suppose we prescribe the form of the density profile and then evaluate the neural functional $c_1(x, [\rho])$ at each position x . This procedure yields a numerical representation of the corresponding direct correlation function $c_1(x)$. In the practical numerical implementation we have a set of discrete grid points that represent the function values at these spatial locations x . Hence the entire data set forms a numerical array or numerical vector, indexed by x . One can then ask whether this vector could potentially be the gradient of an overarching parent object?

The physical and the formal question can both be answered affirmatively due to the existence of the excess free energy density functional $F_{\text{exc}}[\rho]$. Its practical route of access, based on functional integration along a continuous sequence of states (a 'line') in the space of density functions, is strikingly straightforward within the neural method. The core of the method is to evaluate $c_1(x, [\rho_a])$ as described above, but for a range of scaled versions of the prescribed density profile $\rho_a(x)$ and then integrating in position to obtain the excess free energy as a global value, see the functional integral given in equation (9).

Specifically, we define a scaled version of the density profile as $\rho_a(x) = a\rho(x)$, such that $a=0$ generates the empty state that has vanishing density profile, $\rho_{a=0}(x) = 0$. On the other end $a=1$ yields the actual density profile of interest, $\rho_{a=1}(x) = \rho(x)$. The excess free energy functional is then obtained easily via functional integration according to

$$\beta F_{\text{exc}}[\rho] = - \int dx \rho(x) \int_0^1 da c_1(x, [\rho_a]). \quad (30)$$

The numerical evaluation requires evaluating $c_1(x, [\rho_a])$ at all positions x in the system and for a range of intermediate values $0 \leq a \leq 1$ such that the parametric integral over a can be accurately discretized.

Analytically carrying out the functional integral (30) on the basis of the analytical direct correlation functional $c_1(x, [\rho])$ as given by equations (24)–(28) is feasible. The result [56], again expressed in the more illustrative Rosenfeld fundamental measure form, is given by:

$$\beta F_{\text{exc}}[\rho] = \int dx \Phi(n_0(x), n_1(x)), \quad (31)$$

$$\Phi(n_1(x), n_2(x)) = -n_0(x) \ln[1 - n_1(x)]. \quad (32)$$

Here the integrand $\Phi(n_0(x), n_1(x))$ plays the role of a localized excess free energy density which depends on the weighted densities $n_0(x)$ and $n_1(x)$ as given via the spatial averaging procedures in equations (27) and (28), respectively. Inserting equation (32) into equation (31) yields the hard rod excess free energy functional in the following more explicit form:

$$\beta F_{\text{exc}}[\rho] = - \int dx n_0(x) \ln[1 - n_1(x)]. \quad (33)$$

Equation (33) is strikingly compact, given that it describes the essence of a system of mutually interacting hard cores exposed to an arbitrary external potential.

Although the result of the functional integral (30) has lost all position dependence, the specific form of the density profile $\rho(x)$ is deeply baked into the resulting output value of the functional via both the prefactor $\rho(x)$ in the integrand in equation (30) and the evaluation of the direct correlation functional at the specifically scaled form $\rho_\alpha(x)$. In parallel with this mathematical structure, the explicit form (33) of the Percus functional clearly demonstrates that the resulting value will depend nontrivially on the shape of the input density profile.

Having demonstrated that $F_{\text{exc}}[\rho]$ as a global quantity can be obtained from appropriate functional integration of a locally resolved correlation functional $c_1(x, [\rho])$ naturally leads to the question whether a reverse path exists that would mirror the inverse structure provided by integration and differentiation known from ordinary calculus.

The availability of a corresponding derivative structure for functionals is quite significant, as this by construction generates spatial dependence, as indicated by $\delta/\delta\rho(x)$; see e.g. [9] for details. We can hence retrieve, or generate, the direct correlation functional as the functional density derivative of the intrinsic excess free energy functional:

$$c_1(x, [\rho]) = - \frac{\delta \beta F_{\text{exc}}[\rho]}{\delta \rho(x)}. \quad (34)$$

While we turn to more general functional differentiation below, we here address again the analytical case, which is useful as it reveals the origin of the double appearance of the two spatial weighting processes in equations (24)–(28). Rosenfeld [61] introduced two weight functions $w_0(x)$ and $w_1(x)$, which respectively describe the end points of a particle and its interior one-dimensional ‘volume’:

$$w_0(x) = \frac{\delta(x-R) + \delta(x+R)}{2}, \quad (35)$$

$$w_1(x) = \Theta(R - |x|), \quad (36)$$

where $\Theta(x)$ indicates the Heaviside unit step function, i.e. $\Theta(x \geq 0) = 1$ and 0 otherwise. The weighted densities $n_0(x)$ and $n_1(x)$, as given respectively by equations (27) and (28), can then be represented via convolution of the respective weight function of type $\alpha = 0, 1$ with the density profile according to

$$n_\alpha(x) = \int dx' w_\alpha(x-x') \rho(x'). \quad (37)$$

In more compact notation we can express equation (37) as $n_\alpha(x) = (w_\alpha * \rho)(x)$, where the asterisk denotes the spatial convolution. Then the direct correlation functional is given by

$$c_1(x, [\rho]) = - \sum_{\alpha=0,1} (w_\alpha * \Phi_\alpha)(x), \quad (38)$$

which is an exact rewriting of the form given in equation (24). The functions Φ_α are obtained as partial derivatives of the scaled free energy density (32) via $\Phi_\alpha = \partial\Phi/\partial n_\alpha$. This derivative structure reveals the mechanism for the generation of the explicit forms $\Phi_0(x)$ and $\Phi_1(x)$, as respectively given by equations (25) and (26).

3.2. Functional differentiation of direct correlations

While the above described use of functional differentiation in an analytical setting might appear to be very formal and perhaps limited in its applicability, we emphasize that the concept is indeed very general. Given a prescribed functional of a function $\rho(x)$, the functional derivative $\delta/\delta\rho(x)$ simply gives the gradient of the functional with respect to a change in the input function at a specific location x .

By applying the functional derivative in the present one-dimensional context to a given functional form of $c_1(x, [\rho])$, one obtains the two-body direct correlation functional and we recall the generic expression (12):

$$c_2(x, x', [\rho]) = \frac{\delta c_1(x, [\rho])}{\delta \rho(x')}. \quad (39)$$

Using the Percus version (38) of the one-body direct correlation functional and carrying out the functional derivative on the right hand side of equation (39) gives via an analytical calculation the following nonlocal result:

$$c_2(x, x', [\rho]) = - \sum_{\alpha\alpha'} (w_\alpha * \Phi_{\alpha\alpha'} * w_{\alpha'})(x, x'). \quad (40)$$

We make the double asterisk convolution structure more explicit below. The coefficient functions in equation (40) are obtained as second partial derivatives via $\Phi_{\alpha\alpha'} = \partial^2\Phi/\partial n_\alpha \partial n_{\alpha'}$. Explicitly, we have $\Phi_{00}(x) = 0$ and the symmetry $\Phi_{01}(x) = \Phi_{10}(x)$. The remaining terms are given by

$$\Phi_{01}(x) = \frac{1}{1 - n_1(x)}, \quad (41)$$

$$\Phi_{11}(x) = \frac{n_0(x)}{[1 - n_1(x)]^2}. \quad (42)$$

Inserting these results into equation (40) and making the convolutions explicit yields the following expression:

$$c_2(x, x', [\rho]) = -2 \int dx'' \frac{w_0(x-x'') w_1(x'-x'')}{1 - n_1(x'')} - \int dx'' \frac{w_1(x-x'') n_0(x'') w_1(x'-x'')}{[1 - n_1(x'')]^2}. \quad (43)$$

We recall the definitions (35) and (36) of the weight functions $w_0(x)$ and $w_1(x)$. The convolution structure couples two weight functions together and each of them has a range of R . Hence indeed the two-body direct correlations are of finite range $2R = \sigma$ in the position difference $x - x'$ [55].

While the above results for the Percus theory have been derived by pen-and-paper symbolic calculations, the neural functional is not amenable to such conventional techniques. Fortunately, the framework of automatic differentiation [99] provides a powerful alternative to both symbolic and numerical differentiation methods, and it is a natural choice to consider in the context of machine learning [100]. Via the implementation of either modified algebra or of computational graphs, automatic differentiation facilitates to obtain derivatives directly in the form of executable code, and crucially there is no need of any manual intervention. Automatic differentiation thereby is free of the numerical artifacts that are typical of finite difference schemes. The method is applicable in broad contexts, which we illustrate in the online tutorial [42] by computing the Percus result for $c_2(x, x', [\rho])$ via automatic differentiation of equation (38) rather than by manual implementation of equation (43).

For completeness, we can recover the one-body direct correlation functional by functional integration. We reproduce equation (11) for the present one-dimensional geometry:

$$c_1(x, [\rho]) = \int dx' \rho(x') \int_0^1 dac_2(x, x', [\rho_a]). \quad (44)$$

On the basis of the neural representations of the direct correlation functionals, this identity can be used to check for consistency and for correctness of the automatic differentiation.

3.3. Noether invariance and exchange symmetry

In its standard applications Noether's theorem is used to relate symmetries of a dynamical physical system with associated conservation laws. Obtaining linear momentum conservation from a symmetry of the underlying action integral is a primary example, see e.g. [91] for an introductory presentation. Besides such deterministic applications, the Noether theorem is currently seeing an increased use in a variety of statistical mechanical settings [121–128].

The recent statistical Noether invariance theory [90–98] is based on specific spatial displacement ('shifting') and rotation operations. These transformations are carried out in three-dimensional physical space and their effect is traced back to underlying invariances on the high-dimensional phase space and its associated thermal and nonequilibrium ensembles.

The central statistical Noether invariance concept [90, 91] was demonstrated in a range of studies, addressing the strength of force fluctuations via their variance [92], the formulation of force-based classical density functional theory [93, 94], and the force balance in quantum many-body systems [95]. The invariance theory has led to the discovery of force-force and force-gradient two-body correlation functions. These correlators were shown to deliver profound insight into

the microscopic spatial liquid structure beyond the pair correlation function for a broad range of model fluids [96, 98]. Noether invariance is relevant for any thermal observable, as associated sum rules couple the given observable to forces via very recently identified hyperforce correlations [97].

The statistical Noether sum rules are exact identities that can serve a variety of different purposes, ranging from theory building via combination with approximate closure relations, testing for sufficient sampling in simulation [97], carrying out force sampling to improve statistical data quality and, last but not least, testing neural functionals [40, 41]. Having the latter purpose in mind, here we describe a selection of these Noether identities.

As a fundamental property, the interparticle interaction potential only depends on the relative particle positions and not on the absolute particle coordinate values. Specifically, whether two particles overlap in the one-dimensional system is unaffected by displacing the entire microstate uniformly. This invariance against global translation leads to associated sum rules for direct correlation functions; we recall that the direct correlations arise solely from the interparticle interactions and hence they are not directly dependent on the external potential. We quote two members of an infinite hierarchy of identities, which is originally due to Lovett, Mou, Buff, and Wertheim [129, 130], see equations (45) and (46) below. We group these together with a recent curvature sum rule (47) [92]. Ultimately the identities (45) and (46) express the vanishing of the global interparticle force, as obtained by summing over the interparticle forces on all particles. The three sum rules read as follows:

$$\int dx \rho(x) \nabla c_1(x, [\rho]) = 0, \quad (45)$$

$$\int dx \rho(x) \int dx' \rho(x') \nabla c_2(x, x', [\rho]) = 0, \quad (46)$$

$$\begin{aligned} \int dx [\nabla \rho(x)] \int dx' [\nabla' \rho(x')] c_2(x, x', [\rho]) \\ = - \int dx \rho(x) \nabla \nabla c_1(x), \end{aligned} \quad (47)$$

where in the one-dimensional system the gradient is a simple scalar position derivative, $\nabla = d/dx$. Briefly, equation (45) is obtained by noting that $F_{\text{exc}}[\rho] = F_{\text{exc}}[\rho_\epsilon]$, where the displaced density profile is given by $\rho_\epsilon(\mathbf{r}) = \rho(\mathbf{r} + \epsilon)$ with displacement vector ϵ (in three dimensional systems). Building the gradient with respect to ϵ yields the result $0 = \partial \beta F_{\text{exc}}[\rho_\epsilon] / \partial \epsilon|_{\epsilon=0} = \int d\mathbf{r} (\delta \beta F_{\text{exc}}[\rho] / \delta \rho(\mathbf{r})) \nabla \rho(\mathbf{r})$, which gives equation (45) upon integration by parts, resorting to the one-dimensional geometry, and identifying the one-body direct correlation functional via equation (34); for more details of the derivation we refer the Reader to [90, 91]. Equation (46) is then obtained as the density functional derivative of equation (45) and reusing equation (45) to simplify the result. Equation (47) is a curvature sum rule that follows from spatial Noether invariance at second order in the global shifting parameter ϵ [90].

Using a locally resolved shifting operation, where the displacement $\epsilon(\mathbf{r})$ is local and depends on the spatial position \mathbf{r}

and hence constitutes a vector field (in the case of a three-dimensional system), yields in one dimension the following position-resolved identity:

$$\nabla c_1(x, [\rho]) = \int dx' c_2(x, x', [\rho]) \nabla' \rho(x'). \quad (48)$$

The left hand side has the direct interpretation of the mean interparticle force field, expressed in units of the thermal energy $k_B T$. This force both acts in equilibrium and it drives the adiabatic part of the time evolution in nonequilibrium [9]; we describe some details of the nonequilibrium theory for time evolution in section 4.

When inserting the relationship (34) of $c_1(x, [\rho])$ to the free energy functional $F_{\text{exc}}[\rho]$ into the definition (39) of $c_2(x, x', [\rho])$ we obtain

$$c_2(x, x', [\rho]) = -\frac{\delta^2 \beta F_{\text{exc}}[\rho]}{\delta \rho(x) \delta \rho(x')}, \quad (49)$$

which is the one-dimensional version of the general relationship (14). As the order of the two functional derivatives is irrelevant we obtain the following exact symmetry with respect to the exchange of the two position arguments:

$$c_2(x, x', [\rho]) = c_2(x', x, [\rho]). \quad (50)$$

When applied to the neural functional, the exchange symmetry relationship (50) is highly nontrivial, as the density windows that enter the functionals on the left and on the right hand sides differ markedly from each other, as do the corresponding evaluation positions. That both displacement effects cancel each other and lead to the identity (50) is nontrivial and can serve both for testing the quality of the neural direct correlation functional and for demonstrating the existence of an overarching grandmother functional $F_{\text{exc}}[\rho]$.

In order to illustrate the theoretical structure, we display numerical results in figure 7. We select a representative oscillatory density profile, as shown in figure 7(a), and take this as an input to evaluate the one-body direct correlation functional $c_1(x, [\rho])$. This procedure yields a specific form of the direct correlation function $c_1(x)$, displayed in figure 7(b), which belongs to the prescribed density profile $\rho(x)$. The spatial variations of $\rho(x)$ and $c_1(x)$ are roughly out-of-phase with each other. The nonlinear and nonlocal nature of the functional relationship $\rho \rightarrow c_1$ is however very apparent in the plot. The results from choosing the neural functional or Percus' analytical one-body direct correlation functional agree with each other to excellent accuracy. The agreement is demonstrated in figure 7(b), where the two resulting direct correlation profiles are identical on the scale of the plot.

As laid out above, the exchange symmetry (50) constitutes a rigorous test for the two-body direct correlation functional $c_2(x, x', [\rho])$. Both the neural and the analytical functional pass with flying colours, see figures 7(c) and (d) respectively, where the symmetry of the respective ‘heatmap’ graph against mirroring at the diagonal is strikingly visible.

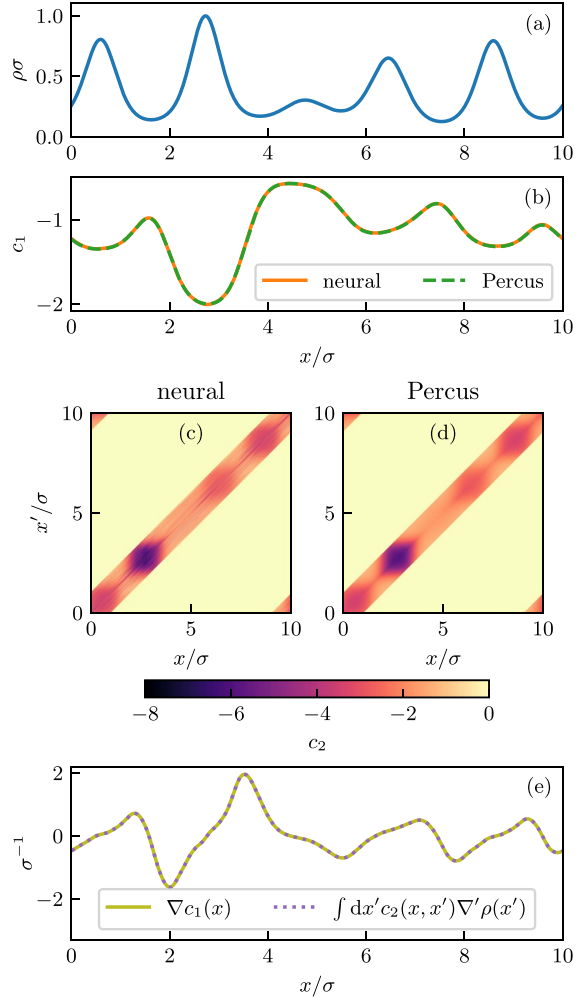


Figure 7. Numerical results for functional calculus and Noether invariance. The results are shown for an exemplary oscillatory density profile displayed in panel (a). Results for the neural prediction for $c_1(x)$ are compared to numerically evaluating Percus' analytical direct correlation functional (24) in panel (b). The two-body direct correlation function $c_2(x, x')$ as a function of x/σ and x'/σ , as obtained from automatic differentiation of the neural functional is shown in panel (c) and compared to the result from using Percus' analytical expression (43) in panel (d). Using the neural functionals, the agreement of the left and right hand side of the Noether force sum rule (48) is shown in panel (e). In all cases the neural functional and Percus theories give numerically identical results on the scale of the respective plot.

As a representative case for the use of a Noether sum rule as a quantitative test for the accuracy of the neural functional methods, we show in figure 7(e) the numerical results of evaluating both sides of equation (48) for the same given density profile (shown in figure 7(a)). We find that both sides of the equation agree with high numerical precision with each other.

3.4. Functional integral sum rules

We next address general identities that emerge from exploiting the inverse nature of functional differentiation and integration. For this, we recall the functional integral form (9) of $F_{\text{exc}}[\rho]$ and the functional derivative form (10) of $c_1(\mathbf{r}, [\rho])$, which both are central for the following derivations. That equation (9) is the inverse of equation (10) can be seen explicitly by functionally differentiating equation (9) as follows:

$$\frac{\delta \beta F_{\text{exc}}[\rho]}{\delta \rho(\mathbf{r})} = - \int d\mathbf{r}' \int_0^1 da \frac{\delta}{\delta \rho(\mathbf{r})} \rho(\mathbf{r}') c_1(\mathbf{r}', [\rho_a]). \quad (51)$$

We have interchanged the order of integration and functional differentiation on the right hand side of equation (51) as these operations are independent of each other. The functional density derivative now acts on the product $\rho(\mathbf{r}') c_1(\mathbf{r}', [\rho_a])$ and we need to differentiate both factors according to the product rule. Differentiating the first factor gives the Dirac distribution, $\delta \rho(\mathbf{r}') / \delta \rho(\mathbf{r}) = \delta(\mathbf{r} - \mathbf{r}')$. Differentiating the second factor generates the two-body direct correlation functional according to equation (39) and hence $\delta c_1(\mathbf{r}', [\rho_a]) / \delta \rho(\mathbf{r}) = ac_2(\mathbf{r}, \mathbf{r}', [\rho_a])$, where multiplication by the scaling factor a arises from the identity $\delta / \delta \rho(\mathbf{r}) = a \delta / \delta (a \rho(\mathbf{r})) = a \delta / \delta \rho_a(\mathbf{r})$.

We can hence reformulate equation (51) by rewriting the left hand side via equation (10) and expressing the right hand side by the two separate terms. Upon multiplication by -1 the result is the following functional integral identity:

$$c_1(\mathbf{r}, [\rho]) = \int_0^1 da c_1(\mathbf{r}, [\rho_a]) + \int d\mathbf{r}' \rho(\mathbf{r}') \int_0^1 da ac_2(\mathbf{r}, \mathbf{r}', [\rho_a]). \quad (52)$$

In the first term on the right hand side of equation (52) the position integral has cancelled out due to the presence of the Dirac function, which leaves over the position dependence on \mathbf{r} , as occurring in all other terms.

In order to prove equation (52) and hence to establish that indeed equations (9) and (10) are inverse of each other, we integrate by parts in a addressing the first integral on the right hand side of equation (52). This yields a sum of boundary terms and an integral: $c_1(\mathbf{r}, [\rho]) - 0 - \int_0^1 da a \partial c_1(\mathbf{r}, [\rho_a]) / \partial a$. The derivative with respect to the parameter a generates the second term in equation (52) up to the minus sign upon carrying out the parametric derivative via $\partial / \partial a = \int d\mathbf{r}' \rho(\mathbf{r}') \delta / \delta \rho_a(\mathbf{r}')$ and identifying $c_2(\mathbf{r}, \mathbf{r}', [\rho_a]) = \delta c_1(\mathbf{r}, [\rho_a]) / \delta \rho_a(\mathbf{r}')$. Hence the two integrals cancel each other. Only the upper boundary term $c_1(\mathbf{r}, [\rho])$ remains, which is the left hand side of equation (52), and hence completes the proof.

Despite this explicit derivation via functional calculus, as both $c_1(\mathbf{r}, [\rho])$ and $c_2(\mathbf{r}, \mathbf{r}', [\rho])$ are directly available as neural functionals, the functional integral sum rule (52) provides yet again fresh possibility for carrying our consistency and accuracy checks.

Going through the analogous chain of arguments one generation younger leads to the following functional integral

relationship between the two- and three-body direct correlation functionals:

$$c_2(\mathbf{r}, \mathbf{r}', [\rho]) = \int_0^1 da c_2(\mathbf{r}, \mathbf{r}', [\rho_a]) + \int d\mathbf{r}'' \rho(\mathbf{r}'') \int_0^1 da ac_3(\mathbf{r}, \mathbf{r}', \mathbf{r}'', [\rho_a]). \quad (53)$$

The neural functional calculus allows to obtain $c_3(\mathbf{r}, \mathbf{r}', \mathbf{r}'', [\rho])$ via automatic generation of the Hessian of $c_1(\mathbf{r}, [\rho])$ [41], which elevates equation (53) beyond mere formal interest.

The structure of equations (52) and (53) expresses a general functional relationship. When applied to the excess free energy functional itself the result is:

$$\beta F_{\text{exc}}[\rho] = \int_0^1 da \beta F_{\text{exc}}[\rho_a] - \int d\mathbf{r} \rho(\mathbf{r}) \int_0^1 da ac_1(\mathbf{r}, [\rho_a]). \quad (54)$$

We furthermore demonstrate explicitly the relationship from daughter to grandmother via functional integration of the two-body correlation functional to obtain the excess free energy functional:

$$\beta F_{\text{exc}}[\rho] = - \int d\mathbf{r} \rho(\mathbf{r}) \int d\mathbf{r}' \rho(\mathbf{r}') \times \int_0^1 da \int_0^a da' c_2(\mathbf{r}, \mathbf{r}', [\rho_{aa'}]), \quad (55)$$

where again the scaled density profile is $\rho_{a'}(\mathbf{r}) = a' \rho(\mathbf{r})$. That equation (55) holds can be seen by chaining together the two levels of functional integrals (9) and (44) and then simplifying the two nested parameter integrals. The double parametric integral in equation (55) can alternatively be written with fixed parametric boundaries as $\int_0^1 da a \int_0^1 da' c_2(\mathbf{r}, \mathbf{r}', [\rho_{aa'}])$, where the twice scaled density profile is defined as $\rho_{aa'}(\mathbf{r}) = aa' \rho(\mathbf{r})$.

Evans [7] goes further than equation (55) by using the identity $\int_0^1 da \int_0^a da' f(a') = \int_0^1 da (1-a) f(a)$, which is valid for any function $f(a)$, as can either be shown geometrically by considering the triangle-shaped integration domain in the two-dimensional (a, a') -plane or, more formally, by integration by parts. The identity allows to express equation (55) in a form that requires to carry out only a single parametric integral:

$$\beta F_{\text{exc}}[\rho] = - \int d\mathbf{r} \rho(\mathbf{r}) \int d\mathbf{r}' \rho(\mathbf{r}') \times \int_0^1 da (1-a) c_2(\mathbf{r}, \mathbf{r}', [\rho_a]). \quad (56)$$

Evans [7] also considers more general cases where the parameter a linearly interpolates between a nontrivial initial density profile $\rho_i(\mathbf{r}) \neq 0$ and the target profile $\rho(\mathbf{r})$ via $\rho_a(\mathbf{r}) = \rho_i(\mathbf{r}) + a[\rho(\mathbf{r}) - \rho_i(\mathbf{r})]$. In our present description we have

restricted ourselves to empty initial states, $\rho_i(\mathbf{r}) = 0$, but the functional integration methodology is more general, see [7].

Throughout we have notated the functional integrals via an outer position integral over \mathbf{r} and an inner parametric integral over a . This structure allows to take the common factor $\rho(\mathbf{r})$ out of the inner integral. Standard presentations often reverse the order of integration. Taking the functional integral over the one-body direct correlation functional as an example, both versions are identical:

$$\int d\mathbf{r}\rho(\mathbf{r}) \int_0^1 da c_1(\mathbf{r}, [\rho_a]) = \int_0^1 da \int d\mathbf{r}\rho(\mathbf{r}) c_1(\mathbf{r}, [\rho_a]). \quad (57)$$

Our (mild) preference for the order on the left hand side of equation (57) has two reasons. (i) In a numerical scheme, where one discretizes on a grid of positions \mathbf{r} and of values of a , the multiplication by $\rho(\mathbf{r})$ is only required to be carried out once at each gridpoint \mathbf{r} , when using the left hand side, not also for every value of a as on the right hand side. (ii) Although the result of the inner integral, $\int_0^1 da c_1(\mathbf{r}, [\rho_a])$, depends on the specific chosen parameterization $\rho_a(\mathbf{r})$ and is hence not unique from the viewpoint of the entire functional, it nevertheless constitutes a well-defined localized function of \mathbf{r} .

4. Nonequilibrium dynamics

We have so far demonstrated that the equilibrium properties of correlated many-body systems can be investigated on a very deep level by using neural networks to represent the functional relationship that are inherent in the statistical physics. The required computational workload is thereby only quite moderate. The neural functionals that encapsulate the nontrivial information about correlations and about thermodynamics are lean, robust and they can be manipulated efficiently by the neural functional calculus outlined above.

These features of the neural theory naturally lead one to wonder about the potential applicability beyond equilibrium, i.e. to situations where the considered system is driven by external forces such that flow is generated. The recent nonequilibrium machine-learning method by de las Heras *et al* [40] is based on the dynamical one-body force balance relationship for overdamped Brownian motion. The required dynamical functional dependencies are those given by power functional theory [9]. The power functional approach is formally exact and it goes beyond dynamical density functional theory [5, 69, 118, 131–133] in that it also captures nonequilibrium interparticle force contributions that exceed those generated by the free energy functional; see [9, 119, 120, 134] for recent reviews. Such genuine nonequilibrium effects include viscous and structural nonequilibrium force fields [9, 135–137], which for uniaxial compressional flow of a three-dimensional Lennard–Jones fluid were shown to be well-represented by a trained neural network [40].

The neural nonequilibrium force fields were successfully compared against analytical power functional approximations, where simple and physically motivated semi-local dependence on both the local density and local velocity gradients

was shown to capture correctly the essence of the forces that occur in the nonequilibrium situation. Together with the exact force balance equation, this allows to predict and to design nonequilibrium steady states [40]. The approach offers a systematic way to go beyond dynamical density functional theory and to address genuine nonequilibrium beyond a free energy description. We recall studies based on dynamical density functional theory that addressed non-equilibrium sedimentation of colloids [138], the self-diffusion of particles in complex fluids [139], and the behaviour of the van Hove two-body dynamics of colloidal Brownian hard disks [140] and of hard spheres [141, 142].

Several current statistical mechanical research threads are dedicated to the force point of view. This includes novel force-sampling techniques that significantly reduce the seemingly inherent statistical noise in many-body simulation results for key quantities such as the density profile [110–112, 143]. The statistical Noether invariance theory [90–98] generates formal expressions for force correlation functions very naturally. Corresponding exact sum rules interrelate correlations that involve forces, force gradients, and more general observables in a hyperforce framework [97]. Force-based density functional approaches were put forward both quantum mechanically [144–148] and classically [93, 94].

We have briefly touched on the concept of forces when discussing the direct correlation sum rule (48). Locally resolved force fields are central to power functional theory [9, 149–151] for the description of the nonequilibrium dynamics of underlying many-body systems. The connection to the present framework is via the locally resolved interparticle force density $\mathbf{F}_{\text{int}}(\mathbf{r}, t)$. When expressed in correlator form, this vector field is given as the following nonequilibrium average:

$$\mathbf{F}_{\text{int}}(\mathbf{r}, t) = -\left\langle \sum_i \delta(\mathbf{r} - \mathbf{r}_i) \nabla_i u(\mathbf{r}^N) \right\rangle. \quad (58)$$

The dependence on time t arises as the average on the right hand side of equation (58), which is taken over the instantaneous nonequilibrium many-body probability distribution, as given by temporal evolution of the Smoluchowski equation for the case of overdamped dynamics. The interparticle force density $\mathbf{F}_{\text{int}}(\mathbf{r}, t)$ can be split into a sum of an equilibrium-like ‘adiabatic’ force density $\mathbf{F}_{\text{ad}}(\mathbf{r}, t)$ and a genuine nonequilibrium ‘superadiabatic’ contribution $\mathbf{F}_{\text{sup}}(\mathbf{r}, t)$. Making the functional dependencies explicit, as they arise in power functional theory [9], gives the following sum of two contributions:

$$\mathbf{F}_{\text{int}}(\mathbf{r}, t, [\rho, \mathbf{v}]) = \mathbf{F}_{\text{ad}}(\mathbf{r}, t, [\rho]) + \mathbf{F}_{\text{sup}}(\mathbf{r}, t, [\rho, \mathbf{v}]). \quad (59)$$

Here the functional arguments are the density profile $\rho(\mathbf{r}, t)$ and the one-body velocity field $\mathbf{v}(\mathbf{r}, t) = \mathbf{J}(\mathbf{r}, t)/\rho(\mathbf{r}, t)$, which are both microscopically resolved in space and in time. The numerator is the one-body current, which is given as an instantaneous nonequilibrium average via $\mathbf{J}(\mathbf{r}, t) = \langle \sum_i \delta(\mathbf{r} - \mathbf{r}_i) \mathbf{v}_i \rangle$, where $\mathbf{v}_i(\mathbf{r}^N, t)$ is the velocity of particle i in the underlying many-body overdamped Brownian dynamics.

De las Heras *et al* [40] present a demonstration of the validity of the functional dependence on $\rho(\mathbf{r}, t)$ and $\mathbf{v}(\mathbf{r}, t)$ via

successful machine-learning of $\mathbf{F}_{\text{int}}(\mathbf{r}, t, [\rho, \mathbf{v}])$ for inhomogeneous nonequilibrium steady states. The strategy for constructing the neural network is similar to that described here, but it is based on predicting the locally resolved nonequilibrium forces rather than the equilibrium one-body direct correlations. One important connection between equilibrium and nonequilibrium is given by the adiabatic construction [9] that relates $\mathbf{F}_{\text{ad}}(\mathbf{r}, t, [\rho])$ in the nonequilibrium system to an instantaneous equilibrium system with identical density profile $\rho(\mathbf{r}, t)$. The adiabatic force field is then given as a density functional via the standard relationship

$$\mathbf{F}_{\text{ad}}(\mathbf{r}, t, [\rho]) = k_B T \rho(\mathbf{r}, t) \nabla c_1(\mathbf{r}, [\rho]), \quad (60)$$

where the density argument of the one-body direct correlation functional $c_1(\mathbf{r}, [\rho])$ is the instantaneous density distribution $\rho(\mathbf{r}, t)$.

For overdamped Brownian dynamics with friction constant γ , the one-body current $\mathbf{J}(\mathbf{r}, t)$ appears in the force density balance, which is given by

$$\gamma \mathbf{J}(\mathbf{r}, t) = -k_B T \nabla \rho(\mathbf{r}, t) + \mathbf{F}_{\text{int}}(\mathbf{r}, t) + \rho(\mathbf{r}, t) \mathbf{f}_{\text{ext}}(\mathbf{r}, t), \quad (61)$$

where $\mathbf{f}_{\text{ext}}(\mathbf{r}, t)$ is an external force field that acts on the system, in general in a time- and position-dependent fashion. The prescription for the current is complemented by the microscopically resolved continuity equation, $\partial \rho(\mathbf{r}, t) / \partial t = -\nabla \cdot \mathbf{J}(\mathbf{r}, t)$. Upon neglecting the superadiabatic force density in equation (59) and hence only taking adiabatic forces into account, i.e. approximating $\mathbf{F}_{\text{int}}(\mathbf{r}, t, [\rho, \mathbf{v}]) \approx \mathbf{F}_{\text{ad}}(\mathbf{r}, t, [\rho])$, one arrives at the dynamical density functional theory [5, 69, 118]. Its inherent central approximation is hence to replace the nonequilibrium forces by effective equilibrium forces that are obtained from the free energy functional via the adiabatic construction [9].

Returning to the one-dimensional geometry of the hard rod model, this leads to the following closed approximate equation of motion for the time-dependent density profile:

$$\frac{\partial \rho(x, t)}{\partial t} = D_0 \nabla [\nabla \rho(x, t) - \rho(x, t) (\nabla c_1(x, [\rho]) + \beta f_{\text{ext}}(x, t))]. \quad (62)$$

The derivative is simply $\nabla = \partial / \partial x$ in one dimension and the diffusion constant $D_0 = k_B T / \gamma$ is the ratio of thermal energy and the friction constant. Equation (62) can be efficiently propagated in time with a simple forward Euler algorithm and the neural representation of $c_1(x, [\rho])$ can be used in lieu of an analytic approximation. However superadiabatic forces, i.e. force contributions that go beyond the adiabatic approximation of working with a free energy functional, are neglected. These include viscous and structural nonequilibrium contributions; we refer the Reader to [9] for background and to [40] for a recent perspective on the description of microscopic nonequilibrium dynamics of fluids in the light of machine learning on the basis of power functional theory.

5. Conclusions and outlook

In conclusion we have given a detailed account of the recent neural functional theory [41] for the structure and thermodynamics of spatially inhomogeneous classical many-body systems. The approach is based on input data obtained from Monte Carlo simulations that provide results for averaged density profiles. Thereby the training systems are exposed to the influence of randomized external potentials. Based on the functional relationships that are rigorously given by classical density functional theory, the training data is used to construct a neural network representation of the one-body direct correlation functional, which acts as a fundamental ‘mother’ object in the neural functional theory.

From automatic functional differentiation of the one-body direct correlation functional follow daughter and granddaughter functionals that represent two- and three-body direct correlation functionals. Conversely, functional integration yields the neural excess free energy functional, which acts as the ultimate grandmother functional in the genealogy. We have shown that chaining together the functional differentiation and integration operations yields exact functional sum rules. Further exact identities are given by the statistical mechanical Noether invariance theory [90–98], by variety of fundamental liquid state techniques [8, 20–23] and by functional calculus alone [5, 7]. We have described a selection of these sum rules in detail and have shown how their validity can be used to carry out consistency and accuracy checks for the different levels of mutually related neural density functionals.

We have here in particular focused on the one-dimensional hard rod systems for reasons of ease of data generation via simulations [42], the availability of Percus’ exact functional [55], the possibility of analytical manipulations to be carried out, and not least the fundamental character of this classical model [54]. A beginner-friendly interactive code tutorial is provided online [42], together with stand-alone documentation that describes the key strategies and the essence of the methods that constitute the neural functional theory [41]. We have discussed prototypical applications for ‘simulation beyond the box’, where the neural functional is used for system sizes that outscale the dimension of the original training box that was used to generate the underlying Monte Carlo data [41]. We have also given an overview of nonequilibrium methods and have emphasized the important role of the occurring force fields and their functional dependencies.

We recall that a detailed description of the setup of the paper is given before the start of section 1.1; the modular structure of the paper invites for selective reading. An overview of the relevant statistical mechanical concepts is given in section 1. The neural functional theory is described in detail in section 2 and we have emphasized the important concept of *local* learning, as illustrated in figure 2, which facilitates very efficient network construction and training. The neural functional approach allows to explicitly carry out functional calculus as presented in section 3 and it is relevant for nonequilibrium as described in section 4. We once more highlight the availability of the online tutorial [42], which covers all key

aspects of our study and includes a practitioner’s account of automatic differentiation and differentiable programming.

The neural functional theory is a genuine hybrid method that draws with comparable weight from computer simulations, machine learning, and density functional theory. The computational and conceptual complexities of the involved methods from each respective field are relatively low. Yet their combination offers a new and arguably unprecedented view of the statistical physics of many-body systems. We lay out in the following why the approach is interesting from the viewpoints of each of the three constituent approaches.

From the machine-learning perspective it seems unusual to have a large set of testable self-consistency conditions available. These conditions stem from statistical mechanical sum rules, as they follow e.g. from the Noether invariance theory, the functional integration-differentiation structure, and exchange symmetry. Taking the latter case as an example, that the automatic derivative of a neural network satisfies the exchange symmetry of its two (position) arguments is very remarkable, see the graphical demonstration of the diagonal symmetry in figure 7(c). This is a purely structural test for the quality of the network that does not require any independent reference data as a benchmark. All presented sum rules are of this type and they hence provide intrinsic constraints, either genuinely following from the underlying Statistical Mechanics or from mere functional calculus alone, which is the case for the functional integration-differentiation formalism outlined in section 3.4. Crucially, in our methodology the constraints are not enforced during training the network, as is done in methods of physics-informed machine learning in the classical density functional [37] and wider [152, 153] contexts.

From a computer simulation point of view the neural functional methods offer a new way of designing simulation work. Instead of direct simulation of the physical problem at hand, an intervening step of constructing the direct correlation functional is introduced. We have shown that the direct correlation functional can thereby be obtained explicitly and accurately. Rather than playing the role of a formal object, its availability as a trained neural network facilitates making fast and precise predictions in nontrivial situations. This application stage of the neural functional theory requires very little effort both in terms of the required numerical algorithmic structure and the computational workload; we recall the illustration of the neural functional workflow shown in figure 4.

From a density functional perspective the neural approach is arguably unprecedented in its degree of access to the excess free energy functional. We find it highly remarkable that so much of the seemingly very abstract functional relationships and formal concepts can be inspected and tested in computationally straightforward and highly efficient ways. The range of these methods includes automatic differentiation to generate direct correlation functions as well as performant functional integration routines. The neural functional framework offers the possibility to work numerically with exact functional identities with great ease. Hence the neural network technology relieves one from the task of constructing an approximate analytical functional and manipulating it on paper.

This leaves over the question of the status of analytical density functionals in the light of the neural network capabilities. We have here deliberately chosen the exact Percus functional for one-dimensional hard rods to demonstrate how much insight can be gleaned from the analytical manipulations; as a representative example see the nonlinear convolutional structure of equations (24)–(28) along with the excellent numerical comparison against the neural functional as shown in figure 7(b). As the neural functional method is not restricted to the hard core system, one can expect that having an accurate neural functional for a given system can be of very significant help when attempting first-principles construction of analytical free energy functionals. After all we should make use of the tools that van der Waals did not have at his disposal!

In summary, in light of the progress reported in [40, 41] and the present model investigation, we anticipate that a wealth of deep questions can be addressed from the viewpoint of the neural functional theory, including fundamental questions of phase coexistence [154] as well as the possible construction of fundamental measure functionals [155, 156]. While we here have restricted ourselves to hard core systems, the principal applicability of the neural functional theory for soft potentials was demonstrated in [41] for (planar) inhomogeneities of the supercritical three-dimensional Lennard–Jones fluid. Going beyond planar geometry and addressing spatial inhomogeneity in two or three dimensions could benefit from the use of equivariant neural networks [157–163], which possess the fundamental symmetry properties of Euclidean space.

For complex Hamiltonians the required amount of simulation work to provide training data might seem as a limitation. We are however optimistic that the subsequent efficient use of the direct correlation functionals in the form of neural networks can by far outweigh the training cost. Hence the application to complex models such as the monatomic Molinero–Moore water model [164, 165] might not be out of reach. Furthermore it is inspiring to think that potential progress could be made in the treatment of dielectric [166] and long-ranged forces [167].

As a final note, we re-emphasize the successful application of the neural method to nonequilibrium flow problems presented in [40] and it is certainly very inspiring to speculate whether this facilitates making progress concerning questions of slow dynamics in soft matter [153, 168, 169] and beyond that [170].

Data availability statement

The data and code that support the findings of this study are openly available at the following URL: <https://github.com/sfalmo/NeuralDFT-Tutorial> [42].

Acknowledgments

We thank Daniel de las Heras and Bob Evans for useful discussions and the organizers and participants of HISML 2023 [170] for inspiring feedback throughout the workshop. This

work is supported by the German Research Foundation (DFG) via Project No. 436306241.

ORCID iDs

Florian Sammüller  <https://orcid.org/0000-0002-3605-329X>

Sophie Hermann  <https://orcid.org/0000-0002-4012-9170>

Matthias Schmidt  <https://orcid.org/0000-0002-5015-2972>

References

- [1] van der Waals J D 1894 Thermodynamische Theorie der Kapillarität unter Voraussetzung stetiger Dichteänderung (Thermodynamic theory of capillarity under the hypothesis of a continuous variation of density) *Z. Phys. Chem.* **13U** 657 Rowlinson J S 1979 *J. Stat. Phys.* **20** 197 (Engl. transl.)
- [2] Rowlinson J S and Widom B 2002 *Molecular Theory of Capillarity* (Dover)
- [3] Hohenberg P and Kohn W 1964 Inhomogeneous electron gas *Phys. Rev.* **136** B864
- [4] Mermin N D 1965 Thermal properties of the inhomogeneous electron gas *Phys. Rev.* **137** A1441
- [5] Evans R 1979 The nature of the liquid-vapour interface and other topics in the statistical mechanics of non-uniform, classical fluids *Adv. Phys.* **28** 143
- [6] Evans R, Oettel M, Roth R and Kahl G 2016 New developments in classical density functional theory *J. Phys.: Condens. Matter* **28** 240401
- [7] Evans R 1992 Density functionals in the theory of nonuniform fluids *Fundamentals of Inhomogeneous Fluids* ed D Henderson (Dekker) ch 3
- [8] Hansen J P and McDonald I R 2013 *Theory of Simple Liquids* 4th edn (Academic)
- [9] Schmidt M 2022 Power functional theory for many-body dynamics *Rev. Mod. Phys.* **94** 015007
- [10] Kohn W and Sham L J 1965 Self-consistent equations including exchange and correlation effects *Phys. Rev.* **140** A1133
- [11] Kohn W 1999 Nobel lecture: electronic structure of matter—wave functions and density functionals *Rev. Mod. Phys.* **71** 1253
- [12] Evans R, Frenkel D and Dijkstra M 2019 From simple liquids to colloids and soft matter *Phys. Today* **72** 38
- [13] Levesque M, Vuilleumier R and Borgis D 2012 Scalar fundamental measure theory for hard spheres in three dimensions: application to hydrophobic solvation *J. Chem. Phys.* **137** 034115
- [14] Evans R, Stewart M C and Wilding N B 2019 A unified description of hydrophilic and superhydrophobic surfaces in terms of the wetting and drying transitions of liquids *Proc. Natl Acad. Sci.* **116** 23901
- [15] Coe M K, Evans R and Wilding N B 2022 Density depletion and enhanced fluctuations in water near hydrophobic solutes: identifying the underlying physics *Phys. Rev. Lett.* **128** 045501
- [16] Jeanmairet G, Levesque M and Borgis D 2013 Molecular density functional theory of water describing hydrophobicity at short and long length scales *J. Chem. Phys.* **139** 154101
- [17] Martin-Jimenez D, Chacón E, Tarazona P and Garcia R 2016 Atomically resolved three-dimensional structures of electrolyte aqueous solutions near a solid surface *Nat. Commun.* **7** 12164
- [18] Hernández-Muñoz J, Chacón E and Tarazona P 2019 Density functional analysis of atomic force microscopy in a dense fluid *J. Chem. Phys.* **151** 034701
- [19] Cats P, Evans R, Härtel A and van Roij R 2021 Primitive model electrolytes in the near and far field: decay lengths from DFT and simulations *J. Chem. Phys.* **154** 124504
- [20] Baus M 1984 Broken symmetry and invariance properties of classical fluids *Mol. Phys.* **51** 211
- [21] Evans R and Parry A O 1990 Liquids at interfaces: what can a theorist contribute? *J. Phys.: Condens. Matter* **2** SA15
- [22] Henderson J R 1992 Statistical mechanical sum rules *Fundamentals of Inhomogeneous Fluids* ed D Henderson (Dekker) ch 2
- [23] Upton P J 1998 Fluids against hard walls and surface critical behavior *Phys. Rev. Lett.* **81** 2300
- [24] Clegg P S 2021 Characterising soft matter using machine learning *Soft Matter* **17** 3991
- [25] Dijkstra M and Luijten E 2021 From predictive modelling to machine learning and reverse engineering of colloidal self-assembly *Nat. Mater.* **20** 762
- [26] Boattini E, Dijkstra M and Filion L 2019 Unsupervised learning for local structure detection in colloidal systems *J. Chem. Phys.* **151** 154901
- [27] Campos-Villalobos G, Boattini E, Filion L and Dijkstra M 2021 Machine learning many-body potentials for colloidal systems *J. Chem. Phys.* **155** 174902
- [28] Campos-Villalobos G, Giunta G, Marín-Aguilar S and Dijkstra M 2022 Machine-learning effective many-body potentials for anisotropic particles using orientation-dependent symmetry functions *J. Chem. Phys.* **157** 024902
- [29] Rodrigues F A 2023 Machine learning in physics: a short guide *Europhys. Lett.* **144** 22001
- [30] Wu J and Gu M 2023 Perfecting liquid-state theories with machine intelligence *J. Phys. Chem. Lett.* **14** 10545
- [31] Santos-Silva T, Teixeira P I C, Anquetil-Deck C and Cleaver D J 2014 Neural-network approach to modeling liquid crystals in complex confinement *Phys. Rev. E* **89** 053316
- [32] Shang-Chun L and Oettel M 2019 A classical density functional from machine learning and a convolutional neural network *SciPost Phys.* **6** 025
- [33] Lin S-C, Martius G and Oettel M 2020 Analytical classical density functionals from an equation learning network *J. Chem. Phys.* **152** 021102
- [34] Cats P, Kuipers S, de Wind S, van Damme R, Coli G M, Dijkstra M and van Roij R 2021 Machine-learning free-energy functionals using density profiles from simulations *APL Mater.* **9** 031109
- [35] Qiao C, Yu X, Song X, Zhao T, Xu X, Zhao S and Gubbins K E 2020 Enhancing gas solubility in nanopores: a combined study using classical density functional theory and machine learning *Langmuir* **36** 8527
- [36] Yatsyshin P, Kalliadas S and Duncan A B 2022 Physics-constrained Bayesian inference of state functions in classical density-functional theory *J. Chem. Phys.* **156** 074105
- [37] Malpica-Morales A, Yatsyshin P, Duran-Olivencia M A and Kalliadas S 2023 Physics-informed Bayesian inference of external potentials in classical density functional theory *J. Chem. Phys.* **159** 104109
- [38] Fang X, Gu M and Wu J 2022 Reliable emulation of complex functionals by active learning with error control *J. Chem. Phys.* **157** 214109
- [39] Simon A, Weimar J, Martius G and Oettel M 2024 Machine learning of a density functional for anisotropic patchy particles *J. Chem. Theory Comput.* **20** 1062
- [40] de las Heras D, Zimmermann T, Sammüller F, Hermann S and Schmidt M 2023 Perspective: How to overcome

- dynamical density functional theory *J. Phys.: Condens. Matter* **35** 271501
- [41] Sammüller F, Hermann S, de las Heras D and Schmidt M 2023 Neural functional theory for inhomogeneous fluids: fundamentals and applications *Proc. Natl Acad. Sci.* **120** e2312484120
- [42] Sammüller F 2023 Neural functional theory for inhomogeneous fluids—tutorial (available at: <https://github.com/sfalmo/NeuralDFT-Tutorial>)
- [43] Nagai R, Akashi R, Sasaki S and Tsuneyuki S 2018 Neural-network Kohn-Sham exchange-correlation potential and its out-of-training transferability *J. Chem. Phys.* **148** 241737
- [44] Schmidt J, Benavides-Riveros C L and Marques M A L 2019 Machine learning the physical nonlocal exchange-correlation functional of density-functional theory *J. Phys. Chem. Lett.* **10** 6425
- [45] Zhou Y, Wu J, Chen S and Chen G 2019 Toward the exact exchange-correlation potential: a three-dimensional convolutional neural network construct *J. Phys. Chem. Lett.* **10** 7264
- [46] Nagai R, Akashi R and Sugino O 2020 Completing density functional theory by machine learning hidden messages from molecules *npj Comput. Mater.* **6** 43
- [47] Li L, Hoyer S, Pederson R, Sun R, Cubuk E D, Riley P and Burke K 2021 Kohn-Sham equations as regularizer: building prior knowledge into machine-learned physics *Phys. Rev. Lett.* **126** 036401
- [48] Li H, Wang Z, Zou N, Ye M, Xu R, Gong X, Duan W and Xu Y 2022 Deep-learning density functional theory Hamiltonian for efficient ab initio electronic-structure calculation *Nat. Comput. Sci.* **2** 367
- [49] Gedeon J, Schmidt J, Hodgson M J P, Wetherell J, Benavides-Riveros C L and Marques M A L 2022 Machine learning the derivative discontinuity of density-functional theory *Mach. Learn.: Sci. Technol.* **3** 015011
- [50] Pederson R, Kalita B and Burke K 2022 Machine learning and density functional theory *Nat. Rev. Phys.* **4** 357
- [51] Huang B, von Rudorff G F and von Lilienfeld O A 2023 The central role of density functional theory in the AI age *Science* **381** 170
- [52] Santos A, Yuste S B and de Haro M L 2020 Structural and thermodynamic properties of hard-sphere fluids *J. Chem. Phys.* **153** 120901
- [53] Royall C P, Charbonneau P, Dijkstra M, Russo J, Smallegange F, Speck T and Valeriani C 2023 Colloidal hard spheres: triumphs, challenges and mysteries (arXiv:2305.02452)
- [54] Tonks L 1936 The complete equation of state of one-, two- and three-dimensional gases of hard elastic spheres *Phys. Rev.* **50** 955
- [55] Percus J K 1976 Equilibrium state of a classical fluid of hard rods in an external field *J. Stat. Phys.* **15** 505
- [56] Robledo A and Varela C 1981 On the relationship between the density functional formalism and the potential distribution theory for nonuniform fluids *J. Stat. Phys.* **26** 513
- [57] Vanderlick T K, Davis H T and Percus J K 1989 The statistical mechanics of inhomogeneous hard rod mixtures *J. Chem. Phys.* **91** 7136
- [58] Bakhti B, Schott S and Maass P 2012 Exact density functional for hard-rod mixtures derived from Markov chain approach *Phys. Rev. E* **85** 042107
- [59] Percus J K 2013 A random walk to fundamental measure theory—a mini-review at a personal level *J. Stat. Phys.* **150** 601
- [60] Rosenfeld Y 1988 Scaled field particle theory of the structure and the thermodynamics of isotropic hard particle fluids *J. Chem. Phys.* **89** 4272
- [61] Rosenfeld Y 1989 Free-energy model for the inhomogeneous hard-sphere fluid mixture and density-functional theory of freezing *Phys. Rev. Lett.* **63** 980
- [62] Tarazona P 2000 Density functional for hard sphere crystals: a fundamental measure approach *Phys. Rev. Lett.* **84** 694
- [63] Roth R, Evans R, Lang A and Kahl G 2002 Fundamental measure theory for hard-sphere mixtures revisited: the White Bear version *J. Phys.: Condens. Matter* **14** 12063
- [64] Hansen-Goos H and Roth R 2006 Density functional theory for hard-sphere mixtures: the White Bear version mark II *J. Phys.: Condens. Matter* **18** 8413
- [65] Roth R 2010 Fundamental measure theory for hard-sphere mixtures: a review *J. Phys.: Condens. Matter* **22** 063102
- [66] Kierlik E and Rosinberg M L 1990 Free-energy density functional for the inhomogeneous hard-sphere fluid: application to interfacial adsorption *Phys. Rev. A* **42** 3382
- [67] Kierlik E and Rosinberg M L 1991 Density-functional theory for inhomogeneous fluids: adsorption of binary mixtures *Phys. Rev. A* **44** 5025
- [68] Phan S, Kierlik E, Rosinberg M L, Bildstein B and Kahl G 1993 Equivalence of two free-energy models for the inhomogeneous hard-sphere fluid *Phys. Rev. E* **48** 618
- [69] Marconi U M B and Tarazona P 1999 Dynamic density functional theory of fluids *J. Chem. Phys.* **110** 8032
- [70] Lips D, Ryabov A and Maass P 2018 Brownian asymmetric simple exclusion process *Phys. Rev. Lett.* **121** 160601
- [71] Lips D, Ryabov A and Maass P 2019 Single-file transport in periodic potentials: the Brownian asymmetric simple exclusion process *Phys. Rev. E* **100** 052121
- [72] Lips D, Ryabov A and Maass P 2020 Nonequilibrium transport and phase transitions in driven diffusion of interacting particles *Z. Naturforsch. A* **75** 449
- [73] Antonov A P, Ryabov A and Maass P 2022 Solitons in overdamped Brownian dynamics *Phys. Rev. Lett.* **129** 080601
- [74] Schmid F 2022 Editorial: Multiscale simulation methods for soft matter systems *J. Phys.: Condens. Matter* **34** 160401
- [75] Baptista L A, Dutta R C, Sevilla M, Heidari M, Potestio R, Kremer K and Cortes-Huerto R 2021 Density-functional-theory approach to the Hamiltonian adaptive resolution simulation method *J. Phys.: Condens. Matter* **33** 184003
- [76] Gholami A, Höfling F, Klein R and Delle Site L 2021 Thermodynamic relations at the coupling boundary in adaptive resolution simulations for open systems *Adv. Theory Simul.* **4** 2000303
- [77] Yagi T and Sato H 2021 Self-consistent construction of bridge functional based on the weighted density approximation *J. Chem. Phys.* **154** 124113
- [78] Yagi T and Sato H 2022 Self-consistent construction of grand potential functional with hierarchical integral equations and its application to solvation thermodynamics *J. Chem. Phys.* **156** 054116
- [79] Iso S and Kawana K 2019 Density renormalization group for classical liquids *Prog. Theor. Exp. Phys.* **2019** 013A01
- [80] Yokota T, Haruyamam J and Sugino O 2021 Functional-renormalization-group approach to classical liquids with short-range repulsion: a scheme without repulsive reference system *Phys. Rev. E* **104** 014124
- [81] Kawana K 2023 Note on general functional flows in equilibrium systems (arXiv:2309.10496)
- [82] Schmidt M 1999 Density-functional theory for soft potentials by dimensional crossover *Phys. Rev. E* **60** R6291
- [83] Schmidt M 2000 A density functional for additive mixtures *Phys. Rev. E* **62** 3799
- [84] Schmidt M 2000 Fluid structure from density functional theory *Phys. Rev. E* **62** 4976

- [85] Percus J K 1982 One-dimensional classical fluid with nearest-neighbor interaction in arbitrary external field *J. Stat. Phys.* **28** 67
- [86] Buschle J, Maass P and Dieterich W 2000 Exact density functionals in one dimension *J. Phys. A: Math. Gen.* **33** L41
- [87] Likos C N and Ashcroft N W 1992 Self-consistent theory of freezing of the classical one-component plasma *Phys. Rev. Lett.* **69** 316
- [88] Likos C N and Ashcroft N W 1993 Density-functional theory of nonuniform classical liquids: an extended modified weighted-density approximation *J. Chem. Phys.* **99** 9090
- [89] Kolafa J, Labík S and Malijevský A 2004 Accurate equation of state of the hard sphere fluid in stable and metastable regions *Phys. Chem. Chem. Phys.* **6** 2335
- [90] Hermann S and Schmidt M 2021 Noether's theorem in statistical mechanics *Commun. Phys.* **4** 176
- [91] Hermann S and Schmidt M 2022 Why Noether's theorem applies to statistical mechanics *J. Phys.: Condens. Matter* **34** 213001
- [92] Hermann S and Schmidt M 2022 Variance of fluctuations from Noether invariance *Commun. Phys.* **5** 276
- [93] Tschopp S M, Sammüller F, Hermann S, Schmidt M and Brader J M 2022 Force density functional theory in- and out-of-equilibrium *Phys. Rev. E* **106** 014115
- [94] Sammüller F, Hermann S and Schmidt M 2023 Comparative study of force-based classical density functional theory *Phys. Rev. E* **107** 034109
- [95] Hermann S and Schmidt M 2022 Force balance in thermal quantum many-body systems from Noether's theorem *J. Phys. A: Math. Theor.* **55** 464003
- [96] Sammüller F, Hermann S, de las Heras D and Schmidt M 2023 Noether-constrained correlations in equilibrium liquids *Phys. Rev. Lett.* **130** 268203
- [97] Robitschko S, Sammüller F, Schmidt M and Hermann S 2023 Hyperforce balance from thermal Noether invariance of any observable (arXiv:2308.12098)
- [98] Hermann S, Sammüller F and Schmidt M 2024 Noether invariance theory for the equilibrium force structure of soft matter (arXiv:2401.14971)
- [99] Baydin A G, Pearlmutter B A, Radul A A and Siskind J M 2018 Automatic differentiation in machine learning: a survey *J. Mach. Learn. Res.* **18** 1
- [100] Chollet F 2017 *Deep Learning With Python* (Manning Publications)
- [101] Brader J M and Schmidt M 2014 Dynamic correlations in Brownian many-body systems *J. Chem. Phys.* **140** 034104
- [102] Brader J M and Schmidt M 2013 Nonequilibrium Ornstein-Zernike relation for Brownian many-body dynamics *J. Chem. Phys.* **139** 104108
- [103] González A, White J A, Román F L, Velasco S and Evans R 1997 Density functional theory for small systems: hard spheres in a closed spherical cavity *Phys. Rev. Lett.* **79** 2466
- [104] White J A, González A, Román F L and Velasco S 2000 Density-functional theory of inhomogeneous fluids in the canonical ensemble *Phys. Rev. Lett.* **84** 1220
- [105] Dwandaru W S B and Schmidt M 2011 Variational principle of classical density functional theory via Levy's constrained search method *Phys. Rev. E* **83** 061133
- [106] de las Heras D and Schmidt M 2014 Full canonical information from grand potential density functional theory *Phys. Rev. Lett.* **113** 238304
- [107] Frenkel D and Smit B 2023 *Understanding Molecular Simulation: From Algorithms to Applications* 3rd edn (Academic)
- [108] Wilding N B 2001 Computer simulation of fluid phase transitions *Am. J. Phys.* **69** 1147
- [109] Brukhno A V, Grant J, Underwood T L, Stratford K, Parker S C, Purton J A and Wilding N B 2021 DL_MONTE: a multipurpose code for Monte Carlo simulation *Mol. Simul.* **47** 131
- [110] Borgis D, Assaraf R, Rotenberg B and Vuilleumier R 2013 Computation of pair distribution functions and three-dimensional densities with a reduced variance principle *Mol. Phys.* **111** 3486
- [111] de las Heras D and Schmidt M 2018 Better than counting: density profiles from force sampling *Phys. Rev. Lett.* **120** 218001
- [112] Rotenberg B 2020 Use the force! Reduced variance estimators for densities, radial distribution functions and local mobilities in molecular simulations *J. Chem. Phys.* **153** 150902
- [113] Jex M, Lewin M and Madsen P 2023 Classical density functional theory: the local density approximation (arXiv:2310.18028)
- [114] de las Heras D and Schmidt M 2015 Sedimentation stacking diagram of binary colloidal mixtures and bulk phases in the plane of chemical potentials *J. Phys.: Condens. Matter* **27** 194115
- [115] Eckert T, Schmidt M and de las Heras D 2021 Gravity-induced phase phenomena in plate-rod colloidal mixtures *Commun. Phys.* **4** 202
- [116] Buzzaccaro S, Tripodi A, Rusconi R, Vigolo D and Piazza R 2008 Kinetics of sedimentation in colloidal suspensions *J. Phys.: Condens. Matter* **20** 494219
- [117] Piazza R, Buzzaccaro S, Secchi E and Parola A 2012 What buoyancy really is. A generalized Archimedes' principle for sedimentation and ultracentrifugation *Soft Matter* **8** 7112
- [118] Archer A J and Evans R 2004 Dynamical density functional theory and its application to spinodal decomposition *J. Chem. Phys.* **121** 4246
- [119] te Vrugt M, Löwen H and Wittkowski R 2020 Classical dynamical density functional theory: from fundamentals to applications *Adv. Phys.* **69** 121
- [120] te Vrugt M and Wittkowski R 2023 Perspective: New directions in dynamical density functional theory *J. Phys.: Condens. Matter* **35** 041501
- [121] Baez J C and Fong B 2013 A Noether theorem for Markov processes *J. Math. Phys.* **54** 013301
- [122] Marvian I and Spekkens R W 2014 Extending Noether's theorem by quantifying the asymmetry of quantum states *Nat. Commun.* **5** 3821
- [123] Sasa S and Yokokura Y 2016 Thermodynamic entropy as a Noether invariant *Phys. Rev. Lett.* **116** 140601
- [124] Sasa S, Sugiura S and Yokokura Y 2019 Thermodynamical path integral and emergent symmetry *Phys. Rev. E* **99** 022109
- [125] Revzen M 1970 Functional integrals in statistical physics *Am. J. Phys.* **38** 611
- [126] Budkov Y A and Kolesnikov A L 2022 Modified Poisson-Boltzmann equations and macroscopic forces in inhomogeneous ionic fluids *J. Stat. Mech.* **053205**
- [127] Brandyshev P E and Budkov Y A 2023 Noether's second theorem and covariant field theory of mechanical stresses in inhomogeneous ionic fluids *J. Chem. Phys.* **158** 174114
- [128] Bravetti A, Garcia-Ariza M A and Tapias D 2023 Thermodynamic entropy as a Noether invariant from contact geometry *Entropy* **25** 1082
- [129] Lovett R A, Mou C Y and Buff F P 1976 The structure of the liquid-vapor interface *J. Chem. Phys.* **65** 570
- [130] Wertheim M S 1976 Correlations in the liquid-vapor interface *J. Chem. Phys.* **65** 2377
- [131] Chan G K-L and Finken R 2005 Time-dependent density functional theory of classical fluids *Phys. Rev. Lett.* **94** 183001

- [132] Goddard B D, Nold A, Savva N, Pavliotis G A and Kalliadasis S 2012 General dynamical density functional theory for classical fluids *Phys. Rev. Lett.* **109** 120603
- [133] Goddard B D, Mills-Williams R D, Ottobre M and Pavliotis G 2021 Well-posedness and equilibrium behaviour of overdamped dynamic density functional theory (arXiv:2002.11663)
- [134] Schilling T 2022 Coarse-grained modelling out of equilibrium *Phys. Rep.* **972** 1
- [135] de las Heras D and Schmidt M 2018 Velocity gradient power functional for Brownian dynamics *Phys. Rev. Lett.* **120** 028001
- [136] Stuhlmüller N C X, Eckert T, de las Heras D and Schmidt M 2018 Structural nonequilibrium forces in driven colloidal systems *Phys. Rev. Lett.* **121** 098002
- [137] de las Heras D and Schmidt M 2020 Flow and structure in nonequilibrium Brownian many-body systems *Phys. Rev. Lett.* **125** 018001
- [138] Royall C P, Dzubiella J, Schmidt M and van Blaaderen A 2007 Non-equilibrium sedimentation of colloids on the particle scale *Phys. Rev. Lett.* **98** 188304
- [139] Bier M, van Roij R, Dijkstra M and van der Schoot P 2008 Self-diffusion of particles in complex fluids: temporary cages and permanent barriers *Phys. Rev. Lett.* **101** 215901
- [140] Stopper D, Thorneywork A L, Dullens R P A and Roth R 2018 Bulk dynamics of Brownian hard disks: dynamical density functional theory versus experiments on two-dimensional colloidal hard spheres *J. Chem. Phys.* **148** 104501
- [141] Treffenhärdt L L and Schmidt M 2021 Universality in driven and equilibrium hard sphere liquid dynamics *Phys. Rev. Lett.* **126** 058002
- [142] Treffenhärdt L L, Schindler T and Schmidt M 2022 Dynamic decay and superadiabatic forces in the van Hove dynamics of bulk hard sphere fluids *SciPost Phys.* **12** 133
- [143] Renner J, Schmidt M and de las Heras D 2023 Reduced-variance orientational distribution functions from torque sampling *J. Phys.: Condens. Matter* **35** 235901
- [144] Tokatly I V 2005 Quantum many-body dynamics in a Lagrangian frame: I. Equations of motion and conservation laws *Phys. Rev. B* **71** 165104
- [145] Tokatly I V 2005 Quantum many-body dynamics in a Lagrangian frame: II. Geometric formulation of time-dependent density functional theory *Phys. Rev. B* **71** 165105
- [146] Tokatly I V 2007 Time-dependent deformation functional theory *Phys. Rev. B* **75** 125105
- [147] Tchenkoue M-L M, Penz M, Theophilou I, Ruggenthaler M and Rubio A 2019 Force balance approach for advanced approximations in density functional theories *J. Chem. Phys.* **151** 154107
- [148] Tarantino W and Ullrich C A 2021 A reformulation of time-dependent Kohn-Sham theory in terms of the second time derivative of the density *J. Chem. Phys.* **154** 204112
- [149] Schmidt M and Brader J M 2013 Power functional theory for Brownian dynamics *J. Chem. Phys.* **138** 214101
- [150] Schmidt M 2015 Quantum power functional theory for many-body dynamics *J. Chem. Phys.* **143** 174108
- [151] Schmidt M 2018 Power functional theory for Newtonian many-body dynamics *J. Chem. Phys.* **148** 044502
- [152] Karniadakis G E, Kevrekidis I G, Lu L, Perdikaris P, Wang S and Yang L 2021 Physics-informed machine learning *Nat. Rev. Phys.* **3** 422
- [153] Jung G, Biroli G and Berthier L 2023 Predicting dynamic heterogeneity in glass-forming liquids by physics-inspired machine learning *Phys. Rev. Lett.* **130** 238202
- [154] Binder K, Block B J, Virnau P and Tröster A 2012 Beyond the van der Waals loop: what can be learned from simulating Lennard–Jones fluids inside the region of phase coexistence *Am. J. Phys.* **80** 1099
- [155] Leithall G and Schmidt M 2011 Density functional for hard hyperspheres from a tensorial-diagrammatic series *Phys. Rev. E* **83** 021201
- [156] Schmidt M 2011 Statics and dynamics of inhomogeneous liquids via the internal-energy functional *Phys. Rev. E* **84** 051203
- [157] Cohen T S and Welling M 2016 Group equivariant convolutional networks *Proc. 33rd Int. Conf. on Machine Learning* (available at: <http://proceedings.mlr.press/v48/cohenc16.pdf>)
- [158] Weiler M, Geiger M, Welling M, Boomsma W and Cohen T 2018 3D steerable CNNs: learning rotationally equivariant features in volumetric data *Proc. 32nd Int. Conf. on Neural Information Processing Systems* (available at: https://proceedings.neurips.cc/paper_files/paper/2018/file/488e4104520c6aab692863cc1dba45af-Paper.pdf)
- [159] Finzi M, Stanton S, Izmailov P and Wilson A G 2020 Generalizing convolutional neural networks for equivariance to Lie groups on arbitrary continuous data *Proc. 37th Int. Conf. on Machine Learning* (available at: <http://proceedings.mlr.press/v119/finzi20a/finzi20a.pdf>)
- [160] Satorras V G, Hoogeboom E and Welling M 2021 E(n) equivariant graph neural networks *Proc. 38th Int. Conf. on Machine Learning (Proc. Machine Learning Research vol 139)* ed M Meila and T Zhang (PMLR) p 9323
- [161] Batzner S, Musaelian A, Sun L, Geiger M, Mailoa J P, Kornbluth M, Molinari N, Smidt T E and Kozinsky B 2022 E(3)-equivariant graph neural networks for data-efficient and accurate interatomic potentials *Nat. Commun.* **13** 2453
- [162] Batzner S, Musaelian A and Kozinsky B 2023 Advancing molecular simulation with equivariant interatomic potentials *Nat. Rev. Phys.* **5** 437
- [163] Musaelian A, Batzner S, Johansson A, Sun L, Owen C J, Kornbluth M and Kozinsky B 2023 Learning local equivariant representations for large-scale atomistic dynamics *Nat. Commun.* **14** 579
- [164] Molinero V and Moore E B 2009 Water modeled as an intermediate element between carbon and silicon *J. Phys. Chem. B* **113** 4008
- [165] Coe M K, Evans R and Wilding N B 2022 The coexistence curve and surface tension of a monatomic water model *J. Chem. Phys.* **156** 154505
- [166] Cox S J 2020 Dielectric response with short-ranged electrostatics *Proc. Natl Acad. Sci.* **117** 19746
- [167] Bui A T and Cox S J 2024 A classical density functional theory for solvation across length scales (arXiv:2402.02873)
- [168] Jung G *et al* 2023 Roadmap on machine learning glassy liquids (arXiv:2311.14752)
- [169] Sammüller F, de las Heras D and Schmidt M 2023 Inhomogeneous steady shear dynamics of a three-body colloidal gel former *J. Chem. Phys.* **158** 054908
- [170] Hierarchical Structure and Machine Learning (HISML) 2023 *Int. Workshop on the Physics and Chemistry of Many-Body Systems (Institute for Solid-State Physics, The University of Tokyo, Japan, 2–13 October 2023)*

A Efficient evaluation of the Stillinger-Weber potential

In simulations, the naive evaluation of the three-body interaction term (1.4) of the SW potential via the triple sum in Eq. (1.7) comes with significant computational disadvantages. On the one hand, although the SW potential is short-ranged (a common choice for the cutoff distance is 1.8σ [71, 74, 75]), the mediation by a third particle effectively doubles the interaction range, which must be considered when using advanced evaluation schemes such as cell lists [44]. On the other hand, an explicit computation of a triple sum remains tedious even when exploiting the finite interaction range and it would commonly render simulations of large and dense systems prohibitively expensive. Fortunately, the specific structure of Eq. (1.4) enables a rewriting of the internal energy (1.7) that avoids a loop over particle triplets, which remedies both of the above drawbacks. We reproduce here the gist of this reformulation as considered already in Refs. [171, 172] for the energy and in Ref. [75] for the force calculation.

We introduce the shorthand

$$g_{ij} = \exp\left(\frac{\gamma\sigma}{r_{ij} - a\sigma}\right) \quad (\text{A.1})$$

for $r_{ij} < a\sigma$ and $g_{ij} = 0$ otherwise and recall

$$\cos\theta_{ijk} = \hat{\mathbf{r}}_{ij} \cdot \hat{\mathbf{r}}_{ik}, \quad (\text{A.2})$$

where the hat indicates a unit vector $\hat{\mathbf{r}} = \mathbf{r}/r$. Note that Eq. (A.2) implies

$$\cos^2\theta_{ijk} = \text{Tr}((\hat{\mathbf{r}}_{ij}\hat{\mathbf{r}}_{ij}) \cdot (\hat{\mathbf{r}}_{ik}\hat{\mathbf{r}}_{ik})), \quad (\text{A.3})$$

whereby Tr denotes in this context the usual matrix trace (which is not to be confused with the phase space traces given in Sec. 1.3). From the multiplicative nature of the SW three-body interaction (1.4), one obtains

$$\phi_{\text{SW},3}(r_{ij}, r_{ik}, \theta_{ijk}) = \lambda\epsilon \left[\text{Tr}((g_{ij}\hat{\mathbf{r}}_{ij}\hat{\mathbf{r}}_{ij}) \cdot (g_{ik}\hat{\mathbf{r}}_{ik}\hat{\mathbf{r}}_{ik})) + 2\alpha(g_{ij}\hat{\mathbf{r}}_{ij}) \cdot (g_{ik}\hat{\mathbf{r}}_{ik}) + \alpha^2 g_{ij}g_{ik} \right] \quad (\text{A.4})$$

with $\alpha = -\cos\theta_0$. Observe that each additive contribution in Eq. (A.4) contains a product of identical functions of \mathbf{r}_{ij} and \mathbf{r}_{ik} .

We recall the computation of the total internal energy (1.7), which can be reinterpreted as the sum

$$u(\mathbf{r}^N) = \frac{1}{2} \sum_{i=1}^N U_i \quad (\text{A.5})$$

of single-particle energies

$$U_i = \sum'_j \phi_2(r_{ij}) + \sum'_j \sum'_{k \neq j} \phi_3(r_{ij}, r_{ik}, \theta_{ijk}), \quad (\text{A.6})$$

where a primed sum denotes the exclusion of particle index i . For three-body terms $\phi_3(r_{ij}, r_{ik}, \theta_{ijk})$ that possess a structure as given in Eq. (A.4), the double summation in Eq. (A.6) can be simplified via the introduction of the auxiliary quantities

$$\mathbf{T}_i = \sum'_j g_{ij} \hat{\mathbf{r}}_{ij} \hat{\mathbf{r}}_{ij}, \quad (\text{A.7})$$

$$\mathbf{s}_i = \sum'_j g_{ij} \hat{\mathbf{r}}_{ij}, \quad (\text{A.8})$$

$$h_i = \sum'_j g_{ij}. \quad (\text{A.9})$$

It is straightforward to show that

$$U_i = \sum'_j \phi_2(r_{ij}) + \lambda\epsilon \left[\text{Tr}(\mathbf{T}_i^2) + 2\alpha \mathbf{s}_i^2 + \alpha^2 h_i^2 \right] - w_i \quad (\text{A.10})$$

is equivalent to Eq. (A.6). A correction term

$$w_i = \sum'_j \phi_3(r_{ij}, r_{ij}, 0) = \sum'_j \lambda\epsilon(1 + \alpha)^2 g_{ij}^2 \quad (\text{A.11})$$

is required due to the inclusion of the case $j = k$ when squaring the quantities \mathbf{T}_i , \mathbf{s}_i and h_i as defined in Eqs. (A.7) to (A.9). Note that using Eq. (A.10) in Eq. (A.5) for the calculation of the total internal energy now only involves double sums. Recall as well that g_{ij} as given in Eq. (A.1) vanishes beyond a distance of $a\sigma$ and that hence Eqs. (A.7) to (A.11) do not suffer from an effective doubling of the interaction range as would be the case in an explicit evaluation of the triple sum in Eq. (A.6).

For completeness, we also give the results of the force calculation (taken from Ref. [75] and adapted to our notation), which follows from rigorous evaluation of $\mathbf{f}_i = -\nabla_i u(\mathbf{r}^N)$ with Eq. (A.5), where the single-particle energies enter in the rewritten form (A.10):

$$\begin{aligned} \mathbf{f}_i = & - \sum'_j \frac{\partial \phi_2(r_{ij})}{\partial r_{ij}} \hat{\mathbf{r}}_{ij} + \sum'_j 2\lambda\epsilon(1 + \alpha)^2 g_{ij} \frac{\partial g_{ij}}{\partial r_{ij}} \hat{\mathbf{r}}_{ij} \\ & - \sum'_j \lambda\epsilon(c_{ij} + c_{ji}) \hat{\mathbf{r}}_{ij} - \sum'_j 2\lambda\epsilon\alpha \frac{g_{ij}}{r_{ij}} (\mathbf{s}_i - \mathbf{s}_j) - \sum'_j 2\lambda\epsilon \frac{g_{ij}}{r_{ij}} (\mathbf{T}_i + \mathbf{T}_j) \cdot \hat{\mathbf{r}}_{ij} \end{aligned} \quad (\text{A.12})$$

with

$$c_{ij} = \alpha^2 \frac{\partial g_{ij}}{\partial r_{ij}} h_i + 2\alpha \left(\frac{\partial g_{ij}}{\partial r_{ij}} - \frac{g_{ij}}{r_{ij}} \right) \mathbf{s}_i \cdot \hat{\mathbf{r}}_{ij} + \left(\frac{\partial g_{ij}}{\partial r_{ij}} - \frac{2g_{ij}}{r_{ij}} \right) \hat{\mathbf{r}}_{ij} \cdot \mathbf{T}_i \cdot \hat{\mathbf{r}}_{ij}. \quad (\text{A.13})$$

B Measuring force-force and force-gradient correlations

In the following, we pursue the account given in Ref. [136] and provide further technical details for the sampling of the force-force and force-gradient correlations defined in Eqs. (3.35) and (3.36). Similar to the measurement of the standard pair correlation function $g(r)$, a loop over particle pairs is performed in order to calculate an average of a bulk two-body quantity. However, one not only counts the relative number of particles separated by a certain distance, but instead also involves the forces and force gradients of the particles in the calculation of the average.

Let \mathbf{r}_i and \mathbf{r}_j be the positions of two particles, such that $\mathbf{r} = \mathbf{r}_j - \mathbf{r}_i$ and $\hat{\mathbf{r}} = \mathbf{r}/|\mathbf{r}|$. The calculation of \mathbf{g}_{ff} proceeds straightforwardly by incorporating the forces \mathbf{f}_i and \mathbf{f}_j of particle i and j as given in Eq. (3.36). The radial and tangential components, which appear in Eqs. (3.37) and (3.38), are obtained by the projections

$$(\mathbf{f}_i \mathbf{f}_j)_{\parallel} = (\mathbf{f}_i \cdot \hat{\mathbf{r}})(\mathbf{f}_j \cdot \hat{\mathbf{r}}), \quad (\text{B.1})$$

$$(\mathbf{f}_i \mathbf{f}_j)_{\perp} = \frac{1}{2}[\mathbf{f}_i - (\mathbf{f}_i \cdot \hat{\mathbf{r}})\hat{\mathbf{r}}] \cdot [\mathbf{f}_j - (\mathbf{f}_j \cdot \hat{\mathbf{r}})\hat{\mathbf{r}}], \quad (\text{B.2})$$

where the factor of $1/2$ accounts for the two equal tangential contributions of \mathbf{g}_{ff} in a three-dimensional bulk fluid (there is only a single radial component).

For the calculation of $\mathbf{g}_{\nabla f}$, we employ numerical differentiation to evaluate the force gradients $\nabla_i \mathbf{f}_j$ that appear in Eq. (3.35). This is due to the fact that the implementation of analytic Hessians of the interaction potential would have been too cumbersome for the investigation of the various particle types in Ref. [4], in particular regarding more complex models such as the SW or the Gay-Berne potential. Automatic differentiation (see Sec. 4.1) could serve as a possible alternative to both numerical derivatives and the manual implementation of analytic derivatives in the future.

As before, a splitting of the force-gradient correlation function $\mathbf{g}_{\nabla f}$ into its radial and tangential components is performed. Assuming $\mathbf{f}_j \not\parallel \hat{\mathbf{r}}$, a tangential unit vector $\hat{\mathbf{t}} = \mathbf{t}/|\mathbf{t}| \perp \hat{\mathbf{r}}$ can be constructed by choosing $\mathbf{t} = \mathbf{f}_j - (\mathbf{f}_j \cdot \hat{\mathbf{r}})\hat{\mathbf{r}}$. The radial and tangential parts of $\mathbf{g}_{\nabla f}$ then follow via

$$(\nabla_i \mathbf{f}_j)_{\parallel} = D_{i, \hat{\mathbf{r}}}(\mathbf{f}_j \cdot \hat{\mathbf{r}}), \quad (\text{B.3})$$

$$(\nabla_i \mathbf{f}_j)_{\perp} = D_{i, \hat{\mathbf{t}}}(\mathbf{f}_j \cdot \hat{\mathbf{t}}), \quad (\text{B.4})$$

where $D_{i, \hat{\mathbf{a}}}$ is a directional derivative operator regarding the shifting of particle i along the direction specified by the general unit vector $\hat{\mathbf{a}}$. The evaluation of Eqs. (B.3) and

(B.4) is performed numerically in simulation, i.e. particle i is shifted by a small amount ($\sim 10^{-5}\sigma$) to calculate the arising finite difference in the force \mathbf{f}_j of particle j .

The above procedure for the evaluation of $g_{\nabla f \perp}$ is feasible for isotropic particles. However, anisotropic interactions, as are relevant e.g. in the considered Gay-Berne fluid [4, 80], necessitate to alter the determination of a suitable tangential unit vector for the evaluation of Eq. (B.4). In this case, taking the force \mathbf{f}_j of particle j as reference for the calculation of $\hat{\mathbf{t}}$ introduces an undesired bias in the chosen tangential directions (see also Ref. [173] for an overview of formulae and implementation techniques for anisotropic interactions of rigid bodies). To account for this caveat, we refrain here from using particle properties such as forces or orientations in the determination of $\hat{\mathbf{t}}$ and instead base its construction on a randomly drawn unit vector $\hat{\mathbf{r}}_{\text{rand}} \not\parallel \hat{\mathbf{r}}$. Then, one obtains an unbiased tangential unit vector $\hat{\mathbf{t}} = \mathbf{t}/|\mathbf{t}|$ with $\mathbf{t} = \hat{\mathbf{r}}_{\text{rand}} - (\hat{\mathbf{r}}_{\text{rand}} \cdot \hat{\mathbf{r}})\hat{\mathbf{r}}$, which can be used in Eq. (B.4) to acquire results for $g_{\nabla f \perp}$ that remain valid in the case of anisotropic interactions.

Neural functional theory for inhomogeneous fluids – Tutorial

Florian Sammüller

May 23, 2024

This material is available at <https://github.com/sfalmo/NeuralDFT-Tutorial> and it supplements the following publication:

Why neural functionals suit statistical mechanics

Florian Sammüller, Sophie Hermann, and Matthias Schmidt, *J. Phys.: Condens. Matter* **36**, 243002 (2024); [arXiv:2312.04681](https://arxiv.org/abs/2312.04681).

We show how the physics of simple fluids can be described with **many-body simulations** and **classical density functional theory** (DFT) and how the two approaches can be combined with the help of machine learning to a **neural functional theory**. The connection of the different methods is exemplified for the case of the one-dimensional hard rod fluid with hands-on code examples and exercises in the programming language Julia. Besides the pedagogical overview given here, a more in-depth account of the presented methodology with applications to the hard sphere and Lennard-Jones fluids in three dimensions can be found in

Neural functional theory of inhomogeneous fluids: Fundamentals and applications

Florian Sammüller, Sophie Hermann, Daniel de las Heras, and Matthias Schmidt, *Proc. Natl. Acad. Sci.* **120**, e2312484120 (2023); [arXiv:2307.04539](https://arxiv.org/abs/2307.04539).

Technical remarks

Running some of the tasks in this notebook requires a considerable amount of compute power, e.g. for the generation of simulation data and for the training of the neural network. Keep this in mind if you are using an online service with limited resources. For convenience, we also provide ready-to-use data sets and models, which can be downloaded and applied in the relevant parts.

Particularly for the machine learning tasks, we recommend using a GPU, as this speeds up training and inference considerably. Using a recent Nvidia GPU should work out of the box. For other GPU vendors, you might need to install the corresponding Julia packages, see <https://juliagpu.org/> for further details.

Part 1: Many-body simulations

Many-body simulations have long become a standard tool for the investigation of classical fluids. Conceptually, they offer a rather straightforward way to predict the behavior of a fluid from a microscopic description, i.e. by specifying the interactions of its constituent particles. However, simulations often come with a significant demand of computational resources.

In the following, we focus on Monte Carlo methods for the description of equilibrium systems. Specifically, we choose the grand ensemble where the temperature T and the chemical potential μ are kept fixed (we also specify the length L of the one-dimensional domain). The statistical mechanics of such a system is then determined by the equilibrium distribution function $\psi(x^{(N)}) \sim \exp(-\beta(U(x^{(N)}) - \mu N))$ where $\beta = 1/(k_B T)$ with the Boltzmann constant k_B . The potential energy $U(x^{(N)}) = u(x^{(N)}) + \sum_{i=1}^N V_{\text{ext}}(x_i)$ of a given microstate $x^{(N)} = (x_1, x_2, \dots, x_N)$ of N particles consists of a contribution due to an external potential $V_{\text{ext}}(x)$ and of the internal energy $u(x^{(N)})$. If the particles in the fluid possess pairwise interactions, $u(x^{(N)}) = \sum_{i=1}^N \sum_{j>i}^N \phi(|x_j - x_i|)$, where $\phi(r)$ is the interaction potential for a given distance r of two particles.

Monte Carlo is based on the generation of microstates according to their known equilibrium distribution. This is done iteratively by mutating an initial state A into a new state B with a probability such that a given distribution P of states is kept intact. The mutation happens in two stages: a trial transition selects a new state B , and a criterion $\text{acc}(A \rightarrow B)$ determines if the new state B shall be accepted or if the system shall be reset to the previous state A . Specifically, a valid choice for this acceptance probability is the Metropolis criterion $\text{acc}(A \rightarrow B) = \min(1, P(B)/P(A))$.

We now apply this scheme to the grand ensemble, which yields the standard grand canonical Monte Carlo (GCMC) method. There are three possible trial transitions: i) a particle is moved to a new position, ii) a particle is inserted, iii) a particle is removed. The goal distribution of states P is the grand canonical equilibrium distribution ψ (see above). When considering particle displacements, the Metropolis rate becomes

$$\text{acc}(x^{(N)} \rightarrow \tilde{x}^{(N)}) = \min(1, \exp[-\beta(U(\tilde{x}^{(N)}) - U(x^{(N)}))])$$

for moving a particle and changing the initial microstate $x^{(N)}$ to the new configuration $\tilde{x}^{(N)}$.

Let us now illustrate this trial move with code. For simplification, we provide some utilities for common tasks in `simulation.jl`, e.g. `calc_energy` for calculating the potential energy of one particle, `pb!` for applying periodic boundary conditions, and definitions of containers (structs) which hold the state of the `System` and the `Histograms`.

```
[1]: include("simulation.jl");

function trial_move(system::System; Δxmax=0.1)
    if isempty(system.particles) # If no particles are in the system, do nothing
        return
    end
    i = rand(1:length(system.particles)) # Select random particle with index i
    xbefore = system.particles[i] # Save its initial position
    Ebefore = calc_energy(system, i) # Calculate the initial potential energy of particle i
    system.particles[i] += Δxmax * (2 * rand() - 1) # Move particle to a new position
    pb!(system, i) # Apply periodic boundary conditions (this places the particle back in the box,
    ↪if it has moved outside of the valid range)
    Eafter = calc_energy(system, i) # Calculate the potential energy of particle i after it has been,
    ↪moved
    if rand() > exp(-system.β * (Eafter - Ebefore))
        system.particles[i] = xbefore # Trial move rejected. Reset particle to previous state
    end
end
end
```

```
[1]: trial_move (generic function with 1 method)
```

As the particle number can fluctuate in the grand ensemble, there are additional transitions which add and remove particles at random throughout the simulation. The acceptance probabilities of these transitions can be derived by considering particle exchanges of the system with a virtual reservoir. We spare this derivation here and only give the results

$$\text{acc}(x^{(N)} \rightarrow x^{(N+1)}) = \min\left(1, \frac{L}{N+1} \exp[\beta(\mu - U(x^{(N+1)}) + U(x^{(N)}))]\right),$$

$$\text{acc}(x^{(N)} \rightarrow x^{(N-1)}) = \min\left(1, \frac{N}{L} \exp[-\beta(\mu + U(x^{(N-1)}) - U(x^{(N)}))]\right).$$

These trial transitions are already provided as `trial_insert` and `trial_delete` in `simulation.jl`, feel free to take a look for the implementation details.

With all transitions being specified, we can write a simulation loop which consists of an equilibration stage and a stage in which measurements take place. For each simulation step, we perform a sweep over a fixed number of trial transitions which are chosen at random without introducing bias in the insertions and deletions.

```
[2]: using Dates

function sweep(system::System; transitions=10, insert_delete_probability=0.2)
    for _ in 1:transitions
        if rand() < insert_delete_probability # Randomly select trial transition: either move or
        ↪insert/delete
            rand() < 0.5 ? trial_insert(system) : trial_delete(system) # Do trial insertions and
        ↪removals with equal probability
        else
            trial_move(system)
        end
    end
end

function simulate(L::Number, μ::Number, T::Number, Vext::Function, φ::Function;
    ↪equilibration_time=Dates.Second(1), production_time=Dates.Second(2), sweep_transitions=10)
    system = System(L, μ, T, Vext, φ) # The state of the system is encapsulated in this struct
    histograms = Histograms(system)
    equilibration_start = now()
    while now() - equilibration_start < equilibration_time # Equilibration stage, no sampling
        sweep(system; transitions=sweep_transitions)
    end
    production_start = now()
    while now() - production_start < production_time
        sweep(system; transitions=sweep_transitions)
        sample(system, histograms)
    end
    get_results(system, histograms) # Normalizes histograms and returns (xs, ρ)
end
```

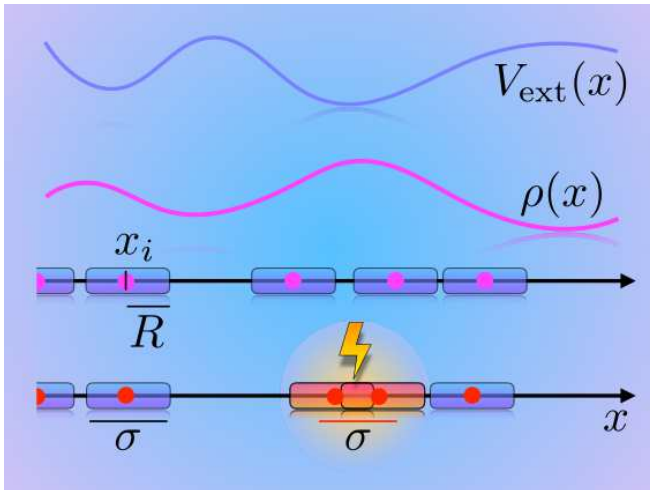
[2]: simulate (generic function with 1 method)

Equilibrium averages such as the one-body density profile $\rho(x) = \langle \sum_{i=1}^N \delta(x - x_i) \rangle$ are obtained by sampling. For this, the particle configuration is recorded in a position-resolved histogram, which yields the desired average after normalization:

```
[3]: function sample(system::System, histograms::Histograms)
    for x in system.particles
        bin = ceil(Int, x / L * histograms.bins) # Calculate the bin index from the given particle
        ↪position
        histograms.ρ[bin] += 1
    end
    histograms.count += 1 # Needed later for normalization
end
```

[3]: sample (generic function with 1 method)

Let us now do some simulations to illustrate the usage of the code. We just pass the length L of our system, the thermodynamic statepoint μ and T , the external potential $V_{\text{ext}}(x)$ and the pair interaction potential $\phi(r)$ to the `simulate` function. In this tutorial, we focus on the hard rod fluid, which is characterized by forbidding the overlap of particles as illustrated below.



This behavior is reflected by the pair interaction potential

$$\phi(r) = \begin{cases} \infty, & r < \sigma, \\ 0, & r \geq \sigma, \end{cases}$$

where σ specifies the particle size (we set $\sigma = 1$ in the code). As a simple test case, we choose confinement between hard walls by setting $V_{\text{ext}}(x) = \infty$ at the boundaries of the domain. Change the form of the external potential as well as the rest of the system parameters to explore the behavior of the hard rod fluid.

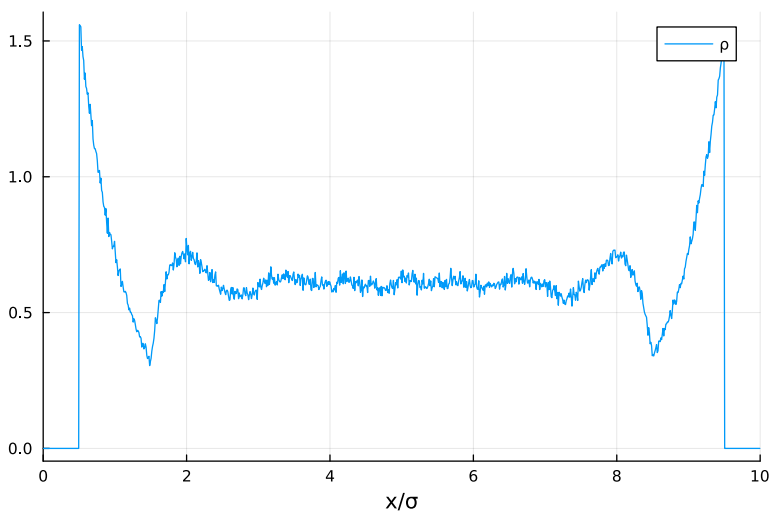
[4]: **using** Plots

```
L = 10.0
mu, T = 2.0, 1.0
Vext(x) = x < 0.5 || x > L - 0.5 ? Inf : 0 # Hard walls at the boundaries
phi(r) = r < 1.0 ? Inf : 0 # Hard core repulsion

xs, rho = simulate(L, mu, T, Vext, phi; equilibration_time=Dates.Second(1), production_time=Dates.
  Second(2), sweep_transitions=10)

plot(xs, rho, label="rho", xlims=(0, L), xlabel="x/sigma")
```

[4]:



Part 2: Classical density functional theory

Classical DFT is founded on a minimization principle of the grand potential $\Omega[\rho]$, which can be expressed as a functional of the one-body density profile $\rho(x)$. Its strength is therefore the reduction of a many-body problem (see Part 1) to a formally exact description on the level of one-body quantities. By writing out entropic, external and internal contributions of the grand potential, carrying out the functional derivative $\delta\Omega[\rho]/\delta\rho(x)$ and demanding that it vanishes at the equilibrium density, one arrives at the Euler-Lagrange equation of DFT,

$$c_1(x) = \ln \rho(x) + \beta(V_{\text{ext}}(x) - \mu),$$

where $c_1(x)$ is the one-body direct correlation function. This rather abstract object attains a fundamental meaning in classical DFT as it captures the nontrivial effects of the internal interactions within the fluid on the one-body level. Formally, it arises from a functional derivative,

$$c_1(x; [\rho]) = -\frac{\delta\beta F_{\text{exc}}[\rho]}{\delta\rho(x)},$$

where $F_{\text{exc}}[\rho]$ is the excess free energy, i.e. the part of $\Omega[\rho]$ which accounts for the beyond-ideal-gas behavior of the interacting fluid. As an immediate consequence of $F_{\text{exc}}[\rho]$ being a density functional, $c_1(x; [\rho])$ also attains a functional dependence on $\rho(x)$, which is made explicit by the bracket notation. In principle, $F_{\text{exc}}[\rho]$ and $c_1(x; [\rho])$ also depend parametrically on the temperature T , but this dependence becomes trivial for the hard rod fluid.

By rearranging the above equation to

$$\rho(x) = \exp(-\beta(V_{\text{ext}}(x) - \mu) + c_1(x; [\rho])),$$

we can reveal its use in actual DFT applications. Given a suitable expression for $c_1(x; [\rho])$ (which one has to obtain somehow for a given type of model fluid), a self-consistent iteration scheme can be used to solve for $\rho(x)$. One such method is the Picard iteration with mixing, in which the iteration is performed as follows:

$$\rho(x) \leftarrow (1 - \alpha)\rho(x) + \alpha\rho_{\text{EL}}(x).$$

Here, α is a mixing parameter and $\rho_{\text{EL}}(x) = \exp(-\beta(V_{\text{ext}}(x) - \mu) + c_1(x; [\rho]))$ is the right hand side of the rearranged Euler-Lagrange equation.

A simple DFT program proceeds as follows: The system parameters μ and T , an external potential $V_{\text{ext}}(x)$ and a functional form of $c_1(x; [\rho])$ are given, and the density profile is initialized (e.g. with a constant value) on a discrete numerical grid that spans the domain of length L . The iteration is then started and Picard steps are performed to update $\rho(x)$ as described above. If the change of $\rho(x)$ between iteration steps falls below a predefined numerical tolerance, the iteration is stopped and the converged self-consistent density profile is obtained as a result. We give an example of such a program in the following:

```
[5]: function minimize(L::Number, μ::Number, T::Number, Vext::Function, get_c1::Function; α::Number=0.03,
    ↪maxiter::Int=10000, dx::Number=0.01, floattype::Type=Float32, tol::Number=max(eps(floattype(1e3)),
    ↪1e-8))
    L, μ, T = floattype.(L, μ, T) # Technical detail: we will use Float32 in the machine learning
    ↪part as neural networks usually operate on single precision floats
    xs = collect(floattype, dx/2:dx:L) # Construct the numerical grid
    Vext = Vext.(xs) # Evaluate the external potential on the grid
    infiniteVext = isinf.(Vext) # Check where Vext is infinite to set ρ = 0 there
    ρ, ρEL = zero(xs), zero(xs) # Preallocate the density profile and an intermediate buffer for
    ↪iteration
    fill!(ρ, 0.5) # Start with a bulk density of 0.5
    c1 = get_c1(xs) # Obtain the c1 functional for the given numerical grid
    i = 0
    while true
```

```

ρEL .= exp.((μ .- Vext) ./ T .+ c1(ρ)) # Evaluate the RHS of the Euler-Lagrange equation
ρ .= (1 - α) .* ρ .+ α .* ρEL # Do a Picard iteration step to update ρ
ρ[infiniteVext] .= 0 # Set ρ to 0 where Vext = ∞
clamp!(ρ, 0, Inf) # Make sure that ρ does not become negative
Δρmax = maximum(abs.(ρ - ρEL)[.!infiniteVext]) # Calculate the remaining discrepancy to
↪check convergence
i += 1
if Δρmax < tol
println("Converged (step: $(i), ||Δρ|| = $(Δρmax) < $(tol) = tolerance)")
break # The remaining discrepancy is below the tolerance: break out of the loop and
↪return the result
end
if !isfinite(Δρmax) || i >= maxiter
println("Did not converge (step: $(i) of $(maxiter), ||Δρ||: $(Δρmax), tolerance: $(tol))")
return nothing # The iteration did not converge, there is no valid result
end
end
end
xs, ρ
end

```

[5]: minimize (generic function with 1 method)

The way in which $c_1(x; [\rho])$ appears both in the theory as well as in the code example above seems innocuous at first. However, the crux of DFT is finding a suitable functional expression for $c_1(x; [\rho])$ (or equivalently for $F_{\text{exc}}[\rho]$) for a given fluid model, and much of the ongoing research deals exactly with this problem. In Part 3, we will show how to efficiently use neural networks to capture such a nontrivial functional mapping from simulation data.

In the following, we proceed analytically as the focus lies on the hard rod system, which is at present one of very few model fluids where the exact excess free energy functional could be found. This success can be traced back to the purely geometrical nature of this particular system. For hard spheres in 3D, fundamental measure theory provides a similar geometric approach to the construction of excess functionals, although the results remain approximate in this more general geometry.

For the exact hard rod density functional, which is attributed to Jerry Percus, the excess free energy can be expressed as

$$\beta F_{\text{exc}}[\rho] = \int dx \Phi(n_0(x; [\rho]), n_1(x; [\rho]))$$

where the free energy density has the specific form $\Phi(n_0, n_1) = -n_0 \ln(1 - n_1)$. The functions $n_0(x; [\rho])$ and $n_1(x; [\rho])$ are *weighted* densities which arise from convolutions of the density profile with the weight functions $\omega_0(x) = (\delta(x - R) + \delta(x + R))/2$ and $\omega_1(x) = \Theta(R - |x|)$, i.e. $n_\alpha(x; [\rho]) = (\omega_\alpha \star \rho)(x)$. From this excess free energy functional, one can easily obtain by functional differentiation the result

$$c_1(x; [\rho]) = - \sum_{\alpha=0,1} \left(\omega_\alpha \star \frac{\partial \Phi}{\partial n_\alpha} \right) (x)$$

for the one-body direct correlation function.

We implement a method that constructs the Percus $c_1(x; [\rho])$ for a given numerical grid in the following. As assistance, we provide `conv_fft` to evaluate convolutions efficiently in Fourier space and `get_weights_Percus` to obtain $\omega_\alpha(x)$ on the numerical grid in the file `dft.jl`.

```

[6]: include("dft.jl")

function get_c1_Percus(xs)
    ω0, ω1 = get_weights_Percus(xs)

```

```

conv(f, g) = conv_fft(f, g; dx=xs[2]-xs[1])
function (ρ)
    n0, n1 = conv(ω0, ρ), conv(ω1, ρ) # Calculate the weighted densities
    ∂φ_∂n0 = -log.(1 .- n1) # Evaluate the partial derivatives of the excess free energy density
    ∂φ_∂n1 = n0 ./ (1 .- n1)
    -(conv(ω0, ∂φ_∂n0) .+ conv(ω1, ∂φ_∂n1)) # Return c1
end
end

```

[6]: `get_c1_Percus` (generic function with 1 method)

Now we can perform some DFT minimizations to see if the results match the simulations. Note that in general, you might have to adjust the mixing parameter α to ensure convergence of the Picard iteration (see the keyword arguments of `minimize`).

```

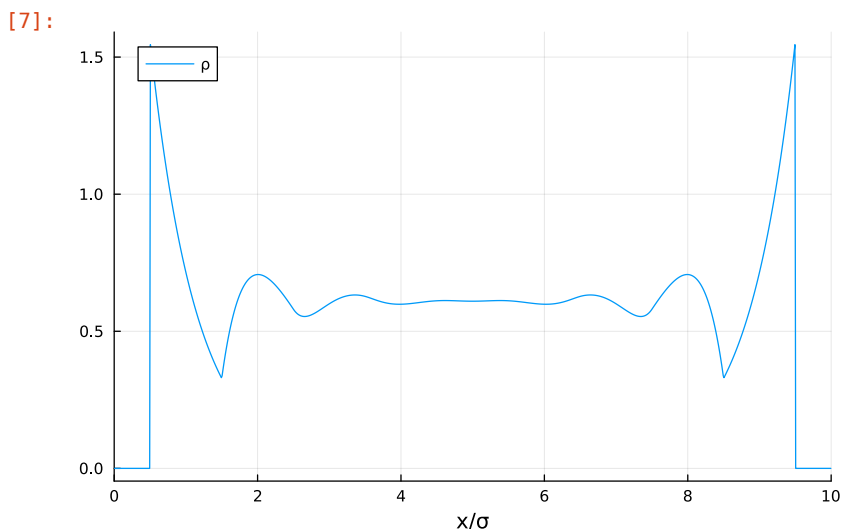
[7]: L = 10.0
μ, T = 2.0, 1.0
Vext(x) = x < 0.5 || x > L - 0.5 ? Inf : 0

xs, ρ = minimize(L, μ, T, Vext, get_c1_Percus)

plot(xs, ρ, label="ρ", xlims=(0, L), xlabel="x/σ")

```

Converged (step: 368, $\|\Delta\rho\| = 6.043911e-5 < 6.103515625e-5 = \text{tolerance}$)

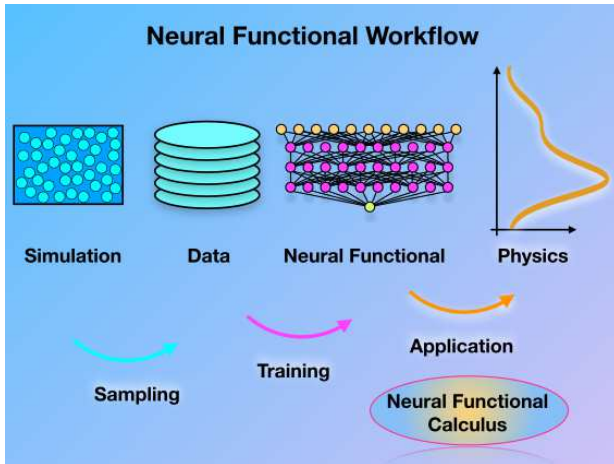


By comparing simulation and DFT results for the same choices of L , μ , T and $V_{\text{ext}}(x)$, we can cross-check the validity of the density profiles of the hard rod fluid. However, it is obvious that both methods have substantial (and quite contrary) restrictions: - The simulation data is noisy, which can only be improved with longer simulation runs. This quickly becomes prohibitively expensive, in particular if one wishes to perform many individual simulations to explore the behavior for different system parameters. However, one is free to change the type of considered fluid by simply modifying the form of the internal interactions. - The DFT calculation is fast and does not suffer from noisy results, thus enabling vast and efficient parameter studies. The results are exact for the case of hard rods, but as illustrated above, one had to find and implement a suitable density functional in order to capture the nontrivial intrinsic correlations. For more complex fluids, there is little hope in deriving an exact functional analytically, and the construction of good approximations often proves to be very difficult.

In the final part of this tutorial, we will combine the advantages of both methods with the help of machine

learning. We will demonstrate how to acquire an accurate and flexible representation of $c_1(x; [\rho])$ by training a neural network with simulation data. The resulting *neural functional* can be used in the minimization scheme as seen above, but it can also reveal more fundamental information about the statistical mechanics of the considered fluid.

Part 3: Neural functional theory



The survey in Part 2 indicates that classical DFT is a powerful concept for the determination of fluid equilibria, but that it is limited by the difficulty of finding analytic expressions for $c_1(x; [\rho])$. In the following, we will train a neural network with simulation data (see Part 1) to obtain a representation of $c_1(x; [\rho])$. We will then show applications of this neural functional, which include the prediction of density profiles and the investigation of neural functional calculus.

To generate a suitable data set, simulations of systems with randomized inhomogeneous external potentials $V_{\text{ext}}(x)$ and random values of the chemical potential μ are performed. For the construction of an appropriate form of $V_{\text{ext}}(x)$, we combine Fourier modes, linear segments and hard walls, which are defined in the following. We also write a method which generates a combination of these elementary functions with randomly chosen parameters.

```
[8]: Vext_sin(x; n::Int, A::Number, φ::Number, L::Number) = A * sin(2π * x * n / L + φ)

Vext_lin(x; x1::Number, x2::Number, E1::Number, E2::Number) = x > x1 && x < x2 ? E1 + (x - x1) * (E2 - E1) / (x2 - x1) : 0

Vext_wall(x; xw::Number, L::Number) = x < xw || x > L - xw ? Inf : 0

function generate_Vext(L::Number; num_sin=4, num_lin=rand(1:5), wall=true)
    Avar = 1.0
    sin_parameters = []
    for n in 1:num_sin # Generate random parameters for periodic sine functions with increasing frequency
        push!(sin_parameters, (n = n, A = randn() * Avar, φ = rand() * 2π, L = L))
    end
    Evar = 1.0
    lin_parameters = []
    for _ in 1:num_lin # Generate random parameters for discontinuous linear segments
        push!(lin_parameters, (x1 = round(rand() * L, digits=2), x2 = round(rand() * L, digits=2), E1 = randn() * Evar, E2 = randn() * Evar))
    end
end
```

```

end
xwmax = 1.0
wall_params = (xw = round(rand() * xwmax, digits=2), L = L) # Set a random wall width
function (x) # Return a method which evaluates a combination of all functions with the chosen_
↳parameters above
    result = 0.0
    for sin_params in sin_parameters
        result += Vext_sin(x; sin_params...)
    end
    for lin_params in lin_parameters
        result += Vext_lin(x; lin_params...)
    end
    if wall
        result += Vext_wall(x; wall_params...)
    end
    result
end
end
end

```

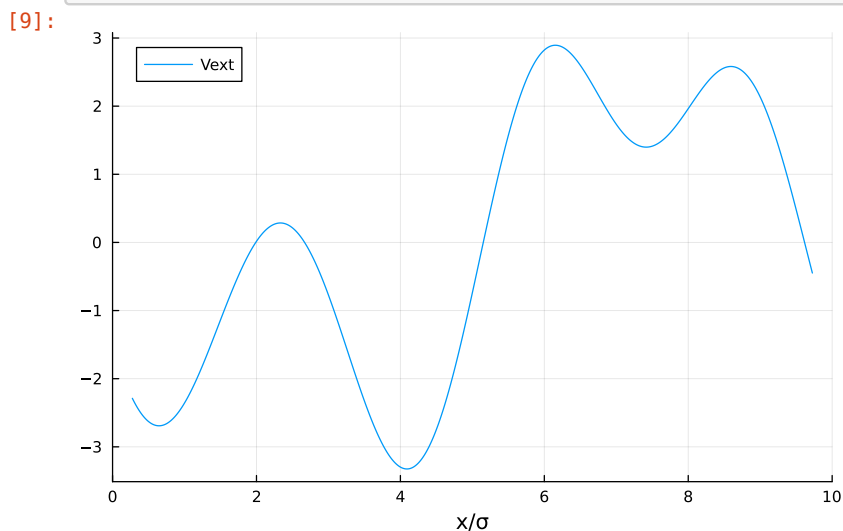
[8]: generate_Vext (generic function with 1 method)

To get an idea of the randomized inhomogeneous environments, let us generate and plot some $V_{\text{ext}}(x)$ profiles. Run the following code cell a few times:

```

[9]: L = 10.0
dx = 0.01
xs = dx/2:dx:L
Vext_generated = generate_Vext(L)
plot(xs, Vext_generated.(xs), label="Vext", xlims=(0, L), xlabel="x/σ")

```



We can now proceed to generate reference data by running simulations with these randomized external potentials and random values of the chemical potential as input. Of course, this requires spending some computational resources. You can run the simulations yourself, but be aware that this does take a considerable amount of compute time (~hours) if you want to get good data. For this, change `use_prepared_simulations` to `false` in the following code cell and set an appropriate number of simulations and the time to spend for the equilibration and production stage. Alternatively, you could “fake” the simulations by using the exact Percus DFT as illustrated in

Part 2.

For readers without the required computational resources and/or patience, we have prepared a ready-to-use data set for the following machine learning tasks, which is downloaded by default as follows:

```
[10]: using DelimitedFiles, Downloads

use_prepared_simulations = true # Choose if you want to use pregenerated simulations (true) or if you
    ↪ want to generate a simulation data set from scratch (false)

if use_prepared_simulations
    println("Downloading pregenerated simulation data set")

    Downloads.download("https://www.staff.uni-bayreuth.de/~bt306964/neuraldft-tutorial/data.tar", ↪
    ↪ "data.tar")
    run(`tar xf data.tar`) # You should now have a directory "data" with a bunch of simulation files
    datadir = "data"
else
    num_sim = 512
    equilibration_time = Dates.Second(10)
    production_time = Dates.Second(200)
    nthreads = Threads.nthreads()
    println("Generating simulation reference data from scratch. This will take approximately ↪
    ↪ $(canonicalize(num_sim * (equilibration_time + production_time) / nthreads)).")

    L = 10
    ϕ(r) = r < 1.0 ? Inf : 0 # Hard core repulsion
    μmin, μmax = -7.0, 5.0
    T = 1.0

    datadir = mkdir("data_$(now())")
    println("Saving results to $(datadir)")
    Threads.@threads for i in 1:num_sim
        μ = μmin + rand() * (μmax - μmin)
        Vext_generated = generate_Vext(L)
        println("Simulation $(i) running...")
        xs, ρ = simulate(L, μ, T, Vext_generated, ϕ; equilibration_time, production_time)
        μloc = μ .- Vext_generated.(xs)
        writedlm("$(datadir)/$(i).dat", [xs μloc ρ])
        println("Simulation $(i) done")
    end
end

println("There are $(length(readdir(datadir))) result files in the directory $(datadir)")
```

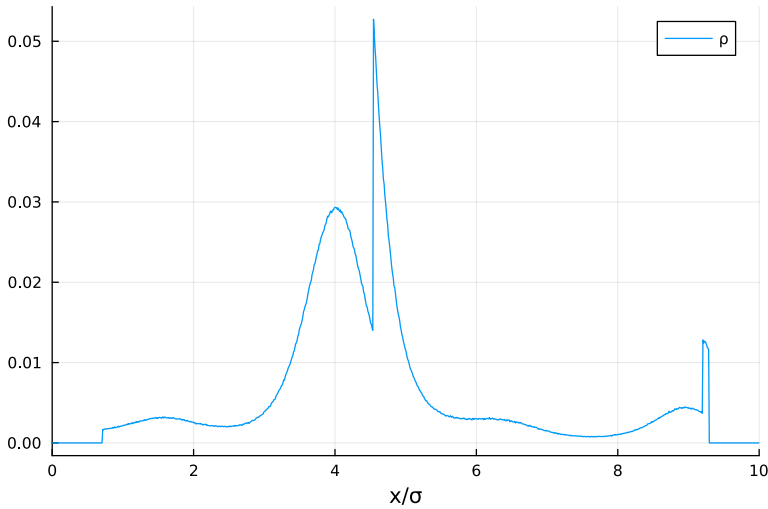
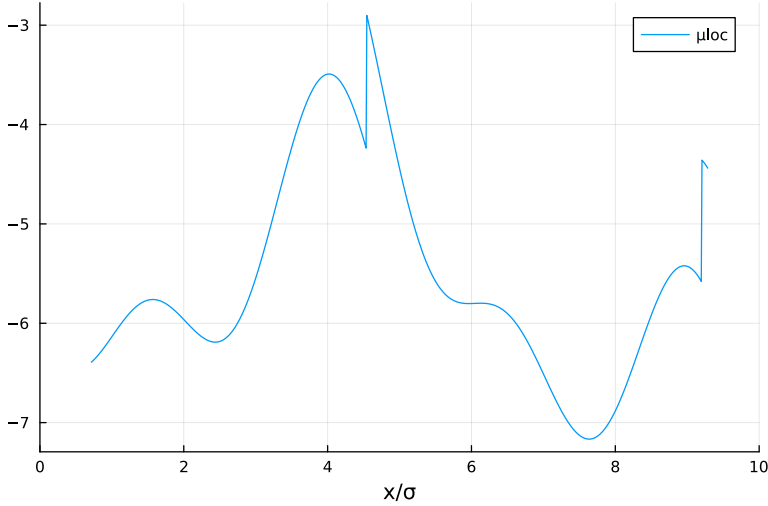
```
Downloading pregenerated simulation data set
There are 512 result files in the directory data
```

If you have generated your own training set, the results are now located in the directory `data_<timestamp>` (use the file explorer of JupyterLab on the left side). Otherwise, proceed with the pregenerated simulations which are located in `data` after successful download and unpacking.

Let us first plot some of the data files to check if they are reasonable:

```
[11]: datadir = "data" # ... or use your own simulation results from above

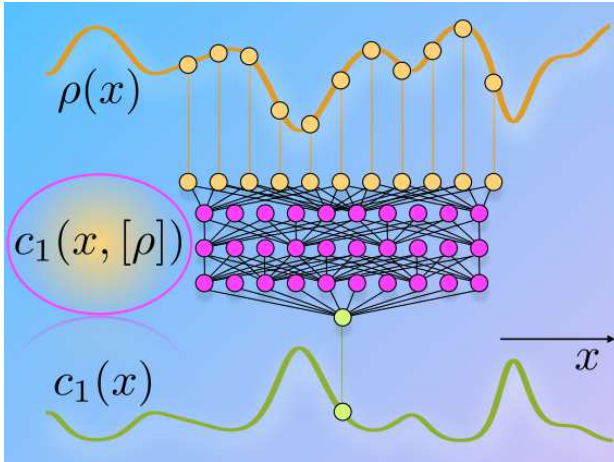
sim = rand(readdir(datadir, join=true)) # Select a random simulation within the data directory
xs, μloc, ρ = eachcol(readdlm(sim)) # Read the result file and split columns
display(plot(xs, μloc, label="μloc", xlims=(0, L), xlabel="x/σ"))
display(plot(xs, ρ, label="ρ", xlims=(0, L), xlabel="x/σ"))
```



Note that besides $\rho(x)$, we have saved the local chemical potential $\mu_{\text{loc}}(x) = \mu - V_{\text{ext}}(x)$ as a further one-body field. This additional information suffices to calculate the one-body direct correlation function $c_1(x) = \ln \rho(x) - \beta \mu_{\text{loc}}(x)$ for each x where $\rho(x) \neq 0$, which is the target of our following investigation.

In Part 2, we have shown that the one-body direct correlation function cannot only be obtained pointwise by the above relation, but that it also constitutes a universal functional $c_1(x; [\rho])$ of the density profile, without having to invoke the local chemical potential $\mu_{\text{loc}}(x)$ explicitly. In the following, we attempt to machine-learn this functional relationship with a neural network. For constructing the specific input-output mapping, we appeal to some physical background. Formally, the functional dependence on $\rho(x)$ is given with respect to the profile of the whole system. However, for short-ranged pair interactions, the influence of the surrounding density profile on the value of $c_1(x; [\rho])$ at a certain position x also remains very short-ranged. Therefore, we can adopt a *local*

learning strategy: the density profile is taken only within a narrow window around a given position as input to the neural network, which is trained to yield the *scalar value* of $c_1(x; [\rho])$ at that position. The whole one-body direct correlation profile can be recovered by evaluating the neural network at different positions across the system domain. The following schematic illustrates this setup.



Due to this specific construction, the data has to be prepared accordingly prior to the training, i.e. the input-output pairs of ρ -windows and c_1 -values have to be generated from the full profiles. For this, some utility functions are given in the file `neural.jl`. Note that we choose a window width of 1σ to each side. For the hard rod fluid, we know that this choice suffices, as the exact analytic solution for $c_1(x; [\rho])$ also has a convolutional range of 1σ . For other fluid models, one would have to determine the window width heuristically, for which the neural functional calculus (see below) could provide some guidance.

```
[12]: include("neural.jl")

ρ_profiles, c1_profiles = read_sim_data(datadir)
ρ_windows, c1_values = generate_inout(ρ_profiles, c1_profiles; window_width=1.0, dx=xs[2]-xs[1]) #
↳window width = 1σ suffices for hard rods

size(ρ_windows), size(c1_values)
```

```
[12]: ((201, 920866), (1, 920866))
```

The data is now ready to be given to a neural network for training. We choose a simple architecture with fully-connected hidden layers and continuous activation functions (e.g. `softplus`). For the construction of the neural network and the subsequent machine learning routines, the framework `Flux.jl` is used. We also specify a standard optimizer and give the generated input-output pairs to a data loader, which automates shuffling and batching during training. As this is a common regression task, we select the mean squared error as the loss function and the mean absolute error as the metric. The learning rate is decreased exponentially after the first few epochs, which improves the final training result.

You can choose in the following code cell via `use_pretrained_model` whether you want to download a ready-to-use model or whether you want to do the training yourself. Running the training on a GPU is recommended. Otherwise, the code runs as-is on the CPU, but training might be slow.

```
[13]: using BSON, Dates, Downloads, Flux, Printf
using CUDA # For Nvidia GPU support, defaults to CPU if no CUDA device is available. Switch out this
↳package if you have a different GPU manufacturer.
```

```

use_pretrained_model = true # Choose if you want to use the pretrained model (true) or if you want
↳to do the training yourself (false)

if use_pretrained_model
  println("Downloading pretrained model")

  Downloads.download("https://www.staff.uni-bayreuth.de/~bt306964/neuraldft-tutorial/model.bson",
↳"model.bson")
  BSON.@load "model.bson" model
else
  println("Training model from scratch")
  p_windows, c1_values = (p_windows, c1_values) |> gpu

  model = Chain(
    Dense(size(p_windows)[1] => 128, softplus),
    Dense(128 => 64, softplus),
    Dense(64 => 32, softplus),
    Dense(32 => 1)
  ) |> gpu

  display(model) # Show a summary of the model with the number of fittable parameters

  opt = Flux.setup(Adam(), model) # Set up a standard Adam optimizer

  loader = Flux.DataLoader((p_windows, c1_values), batchsize=256, shuffle=true) # Initialize the
↳DataLoader to yield shuffled batches

  loss(m, x, y) = Flux.mse(m(x), y) # Use mean squared error as loss
  metric(m, x, y) = Flux.mae(m(x), y) # Use mean absolute error as metric

  get_learning_rate(epoch; initial=0.0001, rate=0.03, wait=5) = epoch < wait ? initial : initial *
↳(1 - rate)^(epoch - wait)

  model_savefile = "model_$(now()).bson"
  println("Saving model to $(model_savefile)")
  for epoch in 1:250 # Do the training loop
    learning_rate = get_learning_rate(epoch)
    Flux.adjust!(opt, learning_rate)
    @printf "Epoch: %3i (learning_rate: %.2e)..." epoch learning_rate; flush(stdout)
    Flux.train!(loss, model, loader, opt)
    @printf " loss: %.5f, metric: %.5f\n" loss(model, p_windows, c1_values) metric(model,
↳p_windows, c1_values); flush(stdout)
    model = model |> cpu
    BSON.@save model_savefile model
    model = model |> gpu
  end
end

model

```

Downloading pretrained model

```
[13]: Chain(
  Dense(201 => 128, softplus),      # 25_856 parameters
  Dense(128 => 64, softplus),      # 8_256 parameters
  Dense(64 => 32, softplus),      # 2_080 parameters
  Dense(32 => 1),                  # 33 parameters
)                                     # Total: 8 arrays, 36_225 parameters, 142.004 KiB.
```

The model is now ready to be used for inference. For convenience, we write a method that lets us evaluate the whole c_1 -profile via the trained model for a given density profile. This is necessary due to the local nature of the mapping, which prevents $\rho(x)$ from being used directly as input. Instead, as shown above, the density profile must be restructured into appropriate windows which are passed to the model.

```
[14]: function get_c1_neural(model, xs)
  window_bins = length(model.layers[1].weight[1,:]) # Get the number of input bins from the shape
  ↪ of the first layer
  model = model |> gpu
  function (ρ)
    ρ_windows = generate_windows(ρ; window_bins) |> gpu # The helper function generate_windows
    ↪ is defined in neural.jl
    model(ρ_windows) |> cpu |> vec # Evaluate the model, make sure the result gets back to the
    ↪ CPU, and transpose it to a vector
  end
end
```

```
[14]: get_c1_neural (generic function with 1 method)
```

The central use of the neural functional is revealed by applying it for the self-consistent calculation of density profiles. Just like we have used the analytic functional due to Percus in Part 2, we can now employ the neural functional to obtain results for $c_1(x; [\rho])$ within a DFT minimization. Importantly, the specific minimization scheme to update and iterate $\rho(x)$ until convergence remains unchanged upon switching out the analytic one-body direct correlation functional with its neural counterpart. Hence, this *neural* DFT is an effective means to circumvent the cumbersome search for analytic functionals while retaining the merits of the DFT minimization procedure.

We show in the following that neural DFT indeed yields accurate results for the considered hard rod fluid. Exact reference data for comparison can be obtained immediately by the Percus theory (one would have to resort to simulation results for other fluid models).

```
[15]: L = 10.0
μ, T = 2.0, 1.0
Vext(x) = x < 0.5 || x > L - 0.5 ? Inf : 0

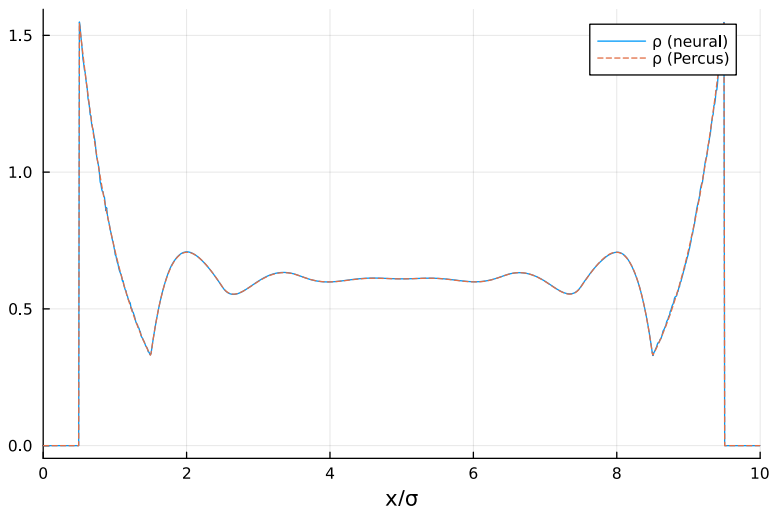
xs, ρ_neural = minimize(L, μ, T, Vext, xs -> get_c1_neural(model, xs))
xs, ρ_Percus = minimize(L, μ, T, Vext, get_c1_Percus)

plot(xs, [ρ_neural ρ_Percus], label=["ρ (neural)" "ρ (Percus)"], linestyle=[:solid :dash], xlims=(0,
  ↪ L), xlabel="x/σ")
```

```
Converged (step: 374, ||Δρ|| = 6.0796738e-5 < 6.103515625e-5 = tolerance)
```

```
Converged (step: 368, ||Δρ|| = 6.043911e-5 < 6.103515625e-5 = tolerance)
```

```
[15]:
```



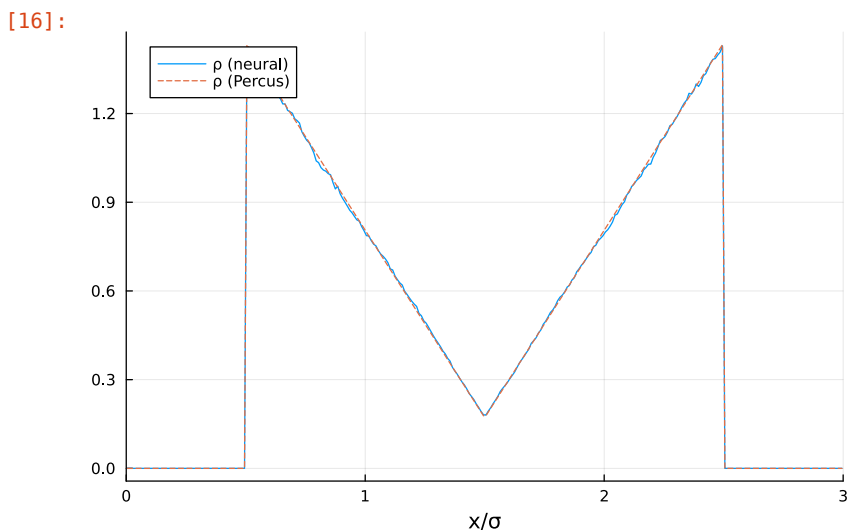
Although the box size has been kept constant during training and in the above example, we can immediately apply the neural functional for different choices of L due to its local nature. This also gives us the possibility to run some rather demanding quality checks. For narrow confinement, which has clearly not been included in our training data, the hard rod fluid yields very interesting density profiles. The following test reveals that the neural functional is able to extrapolate to these unseen cases and that the results from neural DFT match the analytic theory with surprising accuracy.

```
[16]: L = 3.0 # Try other values between 2.0 and 4.0, the density profiles will be interesting
μ, T = 2.0, 1.0
Vext(x) = x < 0.5 || x > L - 0.5 ? Inf : 0

xs, ρ_neural = minimize(L, μ, T, Vext, xs -> get_c1_neural(model, xs))
xs, ρ_Percus = minimize(L, μ, T, Vext, get_c1_Percus)

plot(xs, [ρ_neural ρ_Percus], label=["ρ (neural)" "ρ (Percus)"], linestyle=[:solid :dash], xlims=(0, L), xlabel="x/σ")
```

Converged (step: 368, $\|\Delta\rho\| = 6.043911e-5 < 6.103515625e-5 = \text{tolerance}$)
 Converged (step: 359, $\|\Delta\rho\| = 6.055832e-5 < 6.103515625e-5 = \text{tolerance}$)



We can also increase L significantly compared to the previous cases. The ability of the neural functional to be used straightforwardly in this manner creates the opportunity of efficient multiscale investigations. In the following, this is illustrated by considering the sedimentation of the hard rod fluid in a column with hard walls at the top and at the bottom. The external potential is chosen to slowly increase linearly with height x in order to model the effect of gravity. Within the sedimentation column, the density closely follows the equation of state of the hard rod fluid.

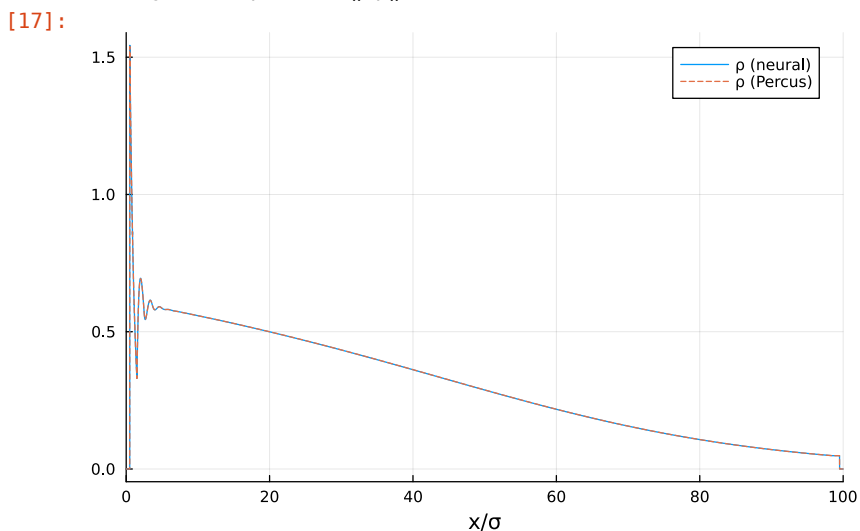
```
[17]: L = 100.0 # You can try to increase L even further
μ, T = 2.0, 1.0
Vext(x) = x < 0.5 || x > L - 0.5 ? Inf : 0.05 * x # Hard walls at the boundaries and linearly
        ↪ increasing within the sedimentation column

xs, ρ_neural = minimize(L, μ, T, Vext, xs -> get_c1_neural(model, xs))
xs, ρ_Percus = minimize(L, μ, T, Vext, get_c1_Percus)

plot(xs, [ρ_neural ρ_Percus], label=["ρ (neural)" "ρ (Percus)"], linestyle=[:solid :dash], xlims=(0, L),
      ↪ xlabel="x/σ")
```

Converged (step: 370, $\|\Delta\rho\| = 5.9962273e-5 < 6.103515625e-5 = \text{tolerance}$)

Converged (step: 364, $\|\Delta\rho\| = 6.067753e-5 < 6.103515625e-5 = \text{tolerance}$)



Besides using the trained model directly in DFT minimizations, we show in the following that one can extract much more fundamental physical information from the neural functional. For this, we aim at implementing functional calculus on the basis of the neural network. An important prerequisite for this is to understand the concept of automatic differentiation. In fact, we have used autodifferentiation already above to realize the adaptation of the neural network parameters during its training. This has been hidden within the `Flux.train!` method, which evaluates for the given training data the output of the neural network as well as gradients of the loss function with respect to all trainable parameters. These gradients are used to trace the error of the neural network predictions back to the weights in order to nudge them in the “right direction”, i.e. to decrease the loss.

Reverse mode automatic differentiation computes derivatives by recording individual subexpressions of a given composite function, e.g. of the neural network, during evaluation. The chain rule is then applied programmatically to yield the derivative of the function in a second computational pass. As this mechanism is central to machine learning, many frameworks come with ready-to-use implementations. For instance, `Flux.jl` provides the `gradient` method, which can be used as follows for scalar-valued functions:

```
[18]: f(x, y) = x^2 + sin(x * y) # Some arbitrary test function
df(x, y) = (2*x + y * cos(x * y), x * cos(x * y)) # Analytic derivative to test autodiff results

x, y = pi, 2.0 # Values for which the derivative will be computed

println("analytic: ", df(x, y))
println("autodiff: ", Flux.gradient(f, x, y))
```

```
analytic: (8.283185307179586, 3.141592653589793)
autodiff: (8.283185307179586, 3.141592653589793)
```

Similarly, we can derive the output of the neural functional with respect to the input density via autodifferentiation. But what do we get out of this?

In Part 2, we have seen that the one-body direct correlation functional is obtained from the functional derivative of the excess free energy, $c_1(x; [\rho]) = -\delta\beta F_{\text{exc}}[\rho]/\delta\rho(x)$, and that it is a central object in DFT calculations. Applying an additional functional derivative yields another important quantity, the two-body direct correlation function

$$c_2(x, x'; [\rho]) = \frac{\delta c_1(x; [\rho])}{\delta\rho(x')}.$$

In fact, a complete hierarchy of direct correlation functions $c_n(x, x', \dots; [\rho])$ is defined by iterating subsequent functional derivatives.

From fundamental physical considerations, further relations can be obtained for these direct correlation functions. In particular, by applying Noether's theorem to statistical mechanical systems, one arrives at so-called sum rules, which constrain the interrelation of different quantities of interest. One such sum rule which connects $c_1(x)$, $c_2(x, x')$ and $\rho(x)$ reads as follows:

$$\nabla c_1(x) = \int dx' c_2(x, x') \nabla' \rho(x').$$

As these identities emerge from fundamental invariances of equilibrium many-body systems, they can be used as further valuable tests to check the consistency of the neural functional.

We implement in the following a method to calculate $c_2(x, x'; [\rho])$ via autodifferentiation of a given function for $c_1(x; [\rho])$. Note that autodifferentiation can be used very generically, which gives us a way to obtain $c_2(x, x'; [\rho])$ also from the Percus $c_1(x; [\rho])$ without having to derive and implement the analytic expression by hand.

```
[19]: function get_c2_autodiff(c1_function, xs)
      dx = xs[2] - xs[1]
      function (rho)
          Flux.jacobian(c1_function, rho)[1] / dx
      end
end
```

```
[19]: get_c2_autodiff (generic function with 1 method)
```

First, we run some quick tests to illustrate the usage of this method. As test density input, we take profiles that follow from a randomized continuous external potential. Run the cell a few times to see different results for $c_2(x, x'; [\rho])$. Also try to switch out the neural correlation functional for the Percus expression, the use of autodifferentiation remains straightforward.

```
[20]: L = 10.0
mu, T = 0.0, 1.0

xs, rho = minimize(L, mu, T, generate_Vext(L; num_sin=5, num_lin=0, wall=false), get_c1_Percus)

c1_func = get_c1_neural(model, xs)
```

```

# c1_func = get_c1_Percus(xs) # The Percus c1 can also be used in the following autodifferentiation,
↳no need for a pen-and-paper derivation :)

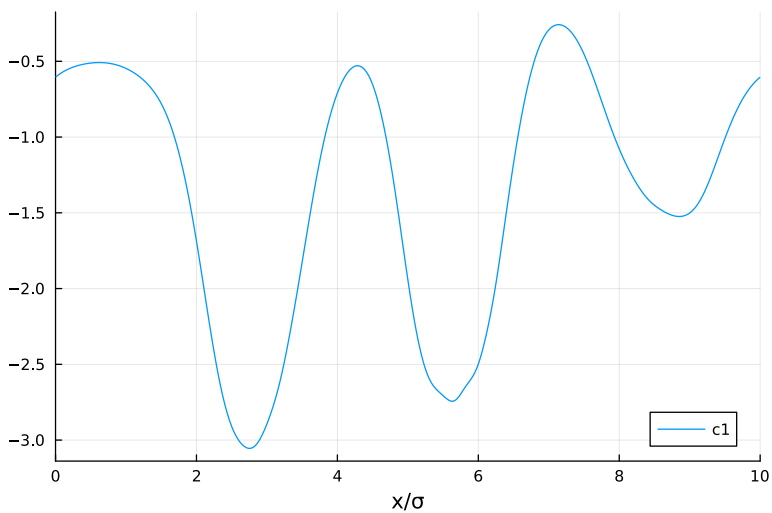
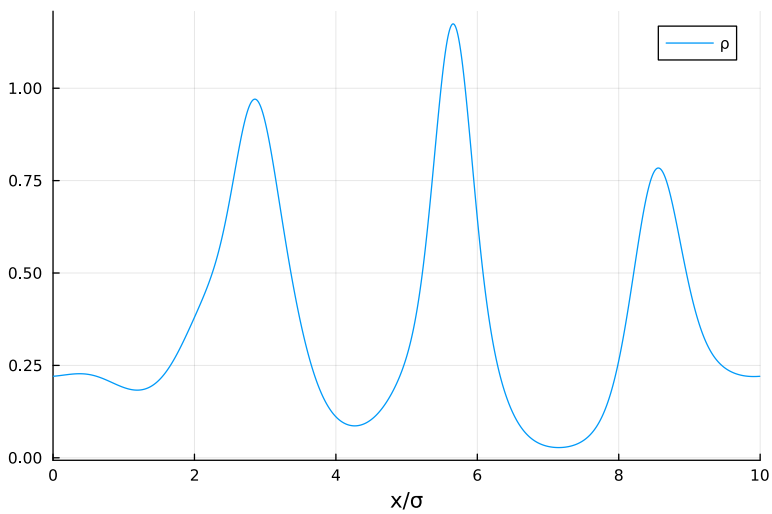
c2_func = get_c2_autodiff(c1_func, xs)

c1 = c1_func(ρ)
c2 = c2_func(ρ)

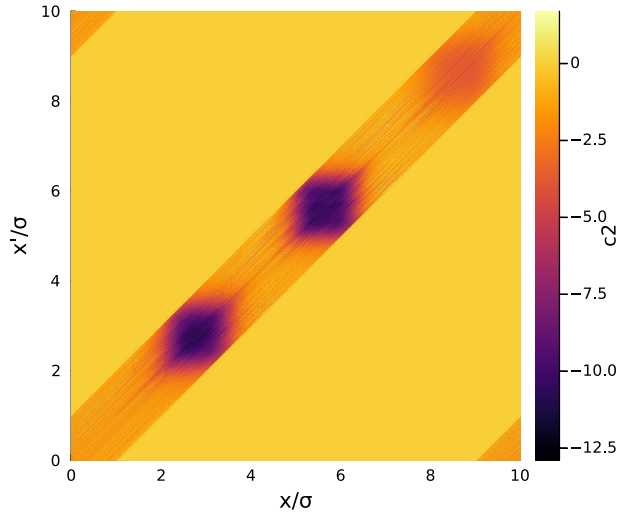
display(plot(xs, ρ, label="ρ", xlims=(0, L), xlabel="x/σ"))
display(plot(xs, c1, label="c1", xlims=(0, L), xlabel="x/σ"))
heatmap(xs, xs, c2, colorbar_title="c2", aspect_ratio=1, xlims=(0, L), ylims=(0, L), xlabel="x/σ",
↳ylabel="x'/σ")

```

Converged (step: 343, $\|\Delta\rho\| = 6.067753e-5 < 6.103515625e-5 = \text{tolerance}$)

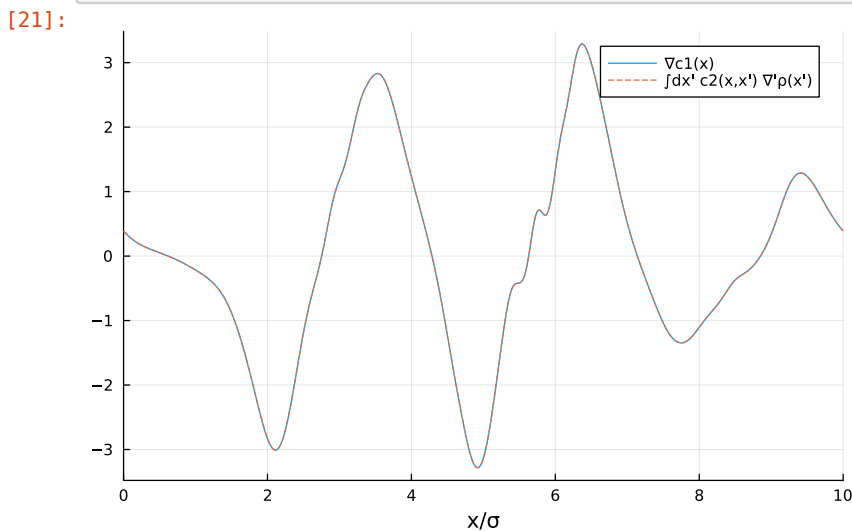


[20]:



Now we can check the above Noether sum rule. The gradients are evaluated numerically on the spatial grid via finite differences, for which we have supplied the function `finite_diff` in `neural.jl`. The following plot shows the right and left hand side of the identity, which coincide when evaluating the quantities with a neural functional that has been trained sufficiently well. Recall that we have neither specified $c_2(x, x'; [\rho])$ nor the Noether identity during training. The successful reproduction of such fundamental results implies that the neural functional does not merely interpolate values of $c_1(x; [\rho])$, but that it instead also captures the essential physics of the underlying many-body problem.

```
[21]: dx = xs[2] - xs[1]
grad_c1 = finite_diff(c1; dx)
grad_rho = finite_diff(rho; dx)
lhs = grad_c1 # Left hand side of the Noether sum rule
rhs = c2 * grad_rho * dx # Right hand side of the Noether sum rule
plot(xs, [lhs rhs], label=["∇c1(x)" "∫dx' c2(x,x') ∇'ρ(x')"], linestyle=[:solid :dash], xlims=(0, L),
      xlabel="x/σ")
```



To complete the functional calculus, we now consider the *inverse* operation of functional differentiation. This gives us direct access to the excess free energy $F_{\text{exc}}[\rho]$, as can be deduced from the definition of $c_1(x; [\rho])$ via its

functional derivative. Formally, functional line integration serves as such an inverse operation, and it amounts to performing a line integral in function space. By choosing a linear parameterization $\rho_a(x) = a\rho(x)$, one can derive the explicit result

$$\beta F_{\text{exc}}[\rho] = - \int dx \rho(x) \int_0^1 da c_1(x; [\rho_a]).$$

On the level of the neural functional (or, in fact, any representation of the one-body direct correlation functional), this expression is easy to evaluate numerically by discretizing both integrals. We write a method for this in the following.

```
[22]: function get_Fexc_funcintegral(c1_function, xs; num_a=100)
    dx = xs[2] - xs[1]
    da = 1 / num_a
    as = da/2:da:1
    function (ρ)
        aintegral = zero(ρ)
        for a in as
            aintegral .+= c1_function(a .* ρ)
        end
        -sum(ρ .* aintegral) * dx * da
    end
end
```

[22]: get_Fexc_funcintegral (generic function with 1 method)

In the following code cell, randomized inhomogeneous systems are considered as above to test the excess free energy calculation via functional line integration. We additionally implement the exact analytic Percus expression for $F_{\text{exc}}[\rho]$ (see Part 2) in order to judge the results. The values of $F_{\text{exc}}[\rho]$ as obtained by functional line integration of the neural correlation functional show almost no discrepancy to the exact analytic theory.

```
[23]: L = 10.0
μ, T = 0.0, 1.0

xs, ρ = minimize(L, μ, T, generate_Vext(L), get_c1_Percus)

c1_func = get_c1_neural(model, xs)
# c1_func = get_c1_Percus(xs)

Fexc_func = get_Fexc_funcintegral(c1_func, xs)

function get_Fexc_Percus(xs)
    dx = xs[2] - xs[1]
    ω0, ω1 = get_weights_Percus(xs)
    conv(f, g) = conv_fft(f, g; dx)
    function (ρ)
        n0, n1 = conv(ω0, ρ), conv(ω1, ρ)
        φ = n0 .* log.(1 .- n1)
        -sum(φ) * dx
    end
end

Fexc_Percus = get_Fexc_Percus(xs)

println("Fexc from analytic expression (Percus): ", Fexc_Percus(ρ))
```

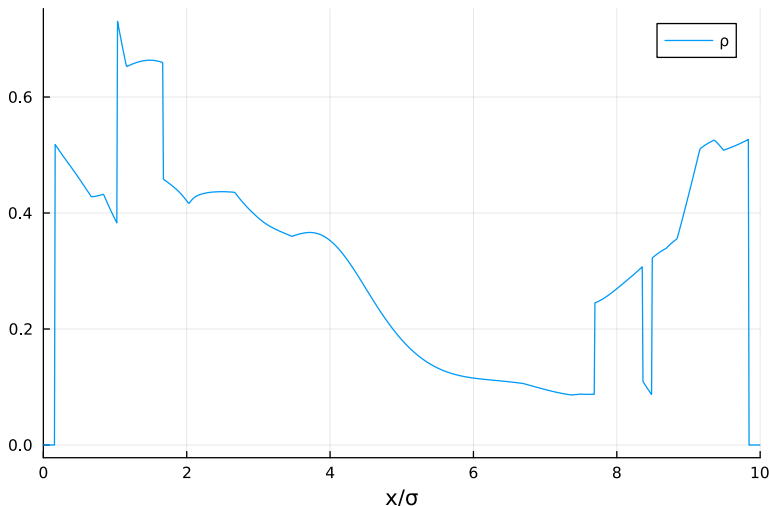
```
println("Fexc from functional line integral (neural): ", Fexc_func(ρ))
plot(xs, ρ, label="ρ", xlims=(0, L), xlabel="x/σ")
```

Converged (step: 302, $\|\Delta\rho\| = 6.0528517e-5 < 6.103515625e-5 = \text{tolerance}$)

Fexc from analytic expression (Percus): 1.5354127

Fexc from functional line integral (neural): 1.53711669921875

[23]:



Conclusions

In this tutorial, we have investigated various methods for the description of classical statistical many-body systems. In particular, we have focused on developing a machine learning framework based on classical DFT and many-body simulations, which combines the strengths of both methods and which facilitates to overcome their individual limitations.

As preparation, the fundamentals of GCMC simulations were laid out in Part 1. We have shown that many-body simulations are suitable to obtain equilibrium averages such as the density profile from the microscopic description of a system. This was exemplified specifically for the hard rod fluid in inhomogeneous environments. However, the computational demands of simulations often turn out to be too restrictive in concrete applications.

In Part 2, classical DFT was presented as a coarse-grained method that operates directly on the level of the one-body density rather than on the full many-body picture, which greatly reduces the computational complexity of the problem. For the case of the hard rod fluid, we have reproduced the exact analytic density functional due to Percus and have shown its application in a standard DFT minimization for the self-consistent calculation of density profiles. While DFT is formally exact for arbitrary fluid models, we have emphasized the difficulty of finding analytic functionals and the exceptionality of the hard rod result. These considerations led us to the application of machine learning with the goal of capturing functional maps from simulation data.

Part 3 gives a detailed account of our machine learning procedure, in which a neural network serves as the central object for the representation of a functional relationship. Training data has been acquired with GCMC simulations, and we have described in this regard how one can generate suitable external potentials randomly to cover diverse inhomogeneous environments. The actual training procedure was based on the functional mapping from the density profile $\rho(x)$ to the one-body direct correlation functional $c_1(x; [\rho])$, which were hence taken respectively as input and target output of the neural network. Crucially, however, we have adopted a *local* learning strategy. The neural network was constructed to yield only the scalar value of $c_1(x; [\rho])$ at a certain location x when provided with the surrounding density profile within a narrow window around x as input. This setup imposes no substantial restriction, as the whole profile of $c_1(x; [\rho])$ can be recovered by evaluating the neural network (in parallel) at multiple positions within the system domain. However, there are numerous benefits to considering the functional

relationship locally, such as an improvement of training statistics, the prescription of the short-ranged nature of $c_1(x; [\rho])$ and the applicability of the neural functional to multiscale problems.

We have then investigated applications of the trained neural correlation functional and its use in DFT minimizations. The results of this *neural* DFT were highly accurate even for unseen external environments, which could be demonstrated for the hard rod fluid by comparison to the exact Percus solution. Further, we have shown the implementation of functional calculus on the basis of the neural network, which enabled us to obtain related quantities such as the two-body direct correlation functional $c_2(x, x'; [\rho])$ or the excess free energy $F_{\text{exc}}[\rho]$. In this regard, automatic differentiation was utilized for the evaluation of functional derivatives, and a functional line integral served as the explicit inverse operation. The results of the neural functional calculus could be verified by the exact Percus theory. A special case, which has not been covered in this tutorial, is the application of the neural functional calculus to systems with spatially constant density, where important bulk properties such as the equation of state and the bulk pair structure can be determined. It is a valuable exercise to use the above tools for the investigation of these bulk results. Further details are given in our research paper ([doi:10.1073/pnas.2312484120](https://doi.org/10.1073/pnas.2312484120), [arXiv:2307.04539](https://arxiv.org/abs/2307.04539)).

As a further consistency check of the neural functional, we have shown the validity of a sum rule which arises from the application of Noether's theorem to statistical many-body systems, and which can hence be traced back to a fundamental invariance property of phase space. It is therefore nontrivial that the neural network reproduces the identity given that no such information was provided during training. There are many more sum rules which result from thermal Noether invariance and which are described in more detail in the accompanying manuscript ([arXiv:2312.04681](https://arxiv.org/abs/2312.04681)). We encourage the reader to implement and verify them; the above code provides the required utilities and may serve as guidance.

Even though we have focused on the hard rod fluid, which is owed to the pedagogical purpose of this tutorial and to the availability of exact theoretical results, the presented machine learning framework is generically applicable to other fluid models with short-ranged interactions. You can try this yourself by modifying the above code examples. Simulation data can be generated for a different type of fluid by simply changing the form of the pair potential $\phi(r)$ and by selecting appropriate parameters for the random generation of chemical and external potentials. The training routine of the neural functional then proceeds identically, provided that the input range of the density is chosen sufficiently large for the specific interaction type (this could be checked e.g. by evaluating $c_2(x, x'; [\rho])$ via autodifferentiation). The trained neural functional can be applied as before in DFT minimizations and in the functional calculus, which is particularly relevant for fluid models where no satisfactory analytic functionals exist. One could even go beyond an isothermal setting and include variations of the temperature, which then serves as a further input parameter to the neural correlation functional. In total, the neural functional theory leaves much room for further research and we have demonstrated here that it serves as a promising hybrid approach to the investigation of inhomogeneous fluids.

Eidesstattliche Versicherung

Hiermit versichere ich an Eides statt, dass ich die vorliegende Arbeit selbstständig verfasst und keine anderen als die von mir angegebenen Quellen und Hilfsmittel verwendet habe.

Weiterhin erkläre ich, dass ich die Hilfe von gewerblichen Promotionsberatern bzw. -vermittlern oder ähnlichen Dienstleistern weder bisher in Anspruch genommen habe, noch künftig in Anspruch nehmen werde.

Zusätzlich erkläre ich hiermit, dass ich keinerlei frühere Promotionsversuche unternommen habe.

Ort, Datum

Florian Sammüller